Lecture Notes in Mechanical Engineering

Yu Zhou
Yang Liu
Lixi Huang
Dewey H. Hodges *Editors*

# Fluid-Structure-Sound Interactions and Control

## Proceedings of the 2nd Symposium on Fluid-Structure-Sound Interactions and Control

Springer

# Lecture Notes in Mechanical Engineering

For further volumes:
http://www.springer.com/series/11236

Yu Zhou · Yang Liu · Lixi Huang
Dewey H. Hodges
Editors

# Fluid-Structure-Sound Interactions and Control

## Proceedings of the 2nd Symposium on Fluid-Structure-Sound Interactions and Control

Springer

*Editors*
Yu Zhou
Institute for Turbulence-Noise-Vibration Interaction and Control Shenzhen Graduate School
Harbin Institute of Technology
Shenzhen
China

Yang Liu
The Hong Kong Polytechnic University
Hong Kong
People's Republic of China

Lixi Huang
Laboratory of Aerodynamics and Acoustics
HKU Zhejiang Institute of Research and Innovation
Department of Mechanical Engineering
The University of Hong Kong
Hong Kong SAR
China

Dewey H. Hodges
Georgia Institute of Technology
Atlanta, GA
USA

ISSN 2195-4356 ISSN 2195-4364 (electronic)
ISBN 978-3-642-40370-5 ISBN 978-3-642-40371-2 (eBook)
DOI 10.1007/978-3-642-40371-2
Springer Heidelberg New York Dordrecht London

Library of Congress Control Number: 2013947818



Printed on acid-free paper

Springer is part of Springer Science+Business Media (www.springer.com)

# Preface

Fluid-related structural vibration and noise problems are widely encountered in many fields, causing increasingly grievous concerns. Turbulence clearly has a significant impact on all these problems. On the other hand, new possibilities are emerging with the advent of various new techniques such as signal processing, flow visualization and diagnostics, new functional materials, sensors and actuators, etc., revitalizing research activities in an interdisciplinary area. In this context, the Fluid-Structure-Sound Interactions and Control (FSSIC) conference series was launched jointly by China Aerodynamics Research and Development Center and The Hong Kong Polytechnic University in Yinchuan City, China, in 2011. This conference series aims to provide a forum for academics, scientists, and engineers working in all related branches to exchange and share the latest progress, ideas, and advances, and to bring them together, from both East and West, to chart the frontiers of FSSIC.

The meeting held in 20−23 May 2013 in Hong Kong and Macau was the second of this conference series and was an international event, attracting people from all over the world and featuring prominent keynote speakers such as R. A. Antonia, J. B. Grotberg, I. Marusic, A. J. Smits, and E. Rathakrishnan. This meeting also featured a broad range of talks on several topics: turbulence, fluid-structure interaction, fluid-related noise, and the control/management aspects of these research areas, many of which are clearly of an interdisciplinary nature. This book contains a selection of the talks presented. We trust it will be of interest to a rather broad engineering community.

Yu Zhou
Yang Liu
Lixi Huang
Dewey H. Hodges

# Acknowledgments

The editors are grateful for the valuable advice of Professor Robert Antonia, Chair of The Honorary Board for FSSIC2013, and the dedicated contribution of Dr. Chi Wai Wong, Deputy Secretary of FSSIC2013, to this book.

# Contents

# Part I
# Unsteady Fluid Dynamics and Turbulence

# A Look at the Turbulent Wake Using Scale-By-Scale Energy Budgets

**F. Thiesset, L. Danaila and R. A. Antonia**

**Abstract** It is now well established that coherent structures exist in the majority of turbulent flows and can affect various aspects of the dynamics of these flows, such as the way energy is transferred over a range of scales as well as the departure from isotropy at the small scales. Reynolds and Hussain (J Fluid Mech 54:263–288, 1972) were first to derive one-point energy budgets for the coherent and random motions respectively. However, at least two points must be considered to define a scale and allow a description of the mechanisms involved in the energy budget at that scale. A transport equation for the second-order velocity structure function, equivalent to the Karman-Howarth (1938) equation for the two-point velocity correlation function, was written by Danaila et al. (1999) and tested in grid turbulence, which represents a reasonable approximation to (structureless) homogenous isotropic turbulence. The equation has since been extended to more complicated flows, for example the centreline of a fully developed channel flow and the axis of a self-preserving circular jet. More recently, we have turned our attention to the intermediate wake of a circular cylinder in order to assess the effect of the coherent motion on the scale-by-scale energy distribution. In particular, energy budget equations, based on phase-conditioned structure functions, have revealed additional forcing terms, the most important of which highlights an additional cascade mechanism associated with the coherent motion. In the intermediate wake, the magnitude of the maximum energy transfer clearly depends on the nature of the coherent motion.

**Keywords** Coherent structure · Scale-by-scale budget · Wake flow

F. Thiesset (✉) · R. A. Antonia
School of Engineering, University of Newcastle, Newcastle, Australia
e-mail: Fabien.Thiesset@newcastle.edu.au

R. A. Antonia
e-mail: Robert.Antonia@newcastle.edu.au

L. Danaila
CORIA, UMR 6614, University of Rouen, Rouen, France
e-mail: danaila@coria.fr

Y. Zhou et al. (eds.), *Fluid-Structure-Sound Interactions and Control*,
Lecture Notes in Mechanical Engineering, DOI: 10.1007/978-3-642-40371-2_1,

## 1 Introduction

Turbulent flows give rise to a wide and continuous range of scales. The largest eddies reflect the way the kinetic energy is injected in the system and therefore depend on the type of flow. In contrast, one frequently asserts that the anisotropic and nonuniversal influence of the largest scales diminishes during the first nonlinear local interactions and is thus expected to decline at the smallest scales. Consequently, it is often postulated that *the smallest scales have the best prospect of being universal or quasi-universal* (Sreenivasan and Antonia 1997), this paradigm being usually related to its initiator (Kolmogorov 1941).

Recently, Kholmyansky and Tsinober (2008) argued that *neither the original derivation of the Kolmogorov 2/3 and 4/5 laws, nor all the subsequent derivations of the 4/5 law use the assumption of locality of interactions and the existence of a cascade*. Another analysis is provided by Hosokawa (2007) who demonstrated that the 4/5 law implies the statistical dependence of the difference and sum of velocities at two points separated by a distance $r$, the sum being a measure of the large scale motion (Hosokawa 2007; Mouri and Hori 2010). This analytical treatment was then accurately confirmed by the experiments of Kholmyansky and Tsinober (2008) in different high Reynolds number flows. Hence, we now dispose of very strong theoretical and experimental evidences that the way energy is distributed between different scales results from direct and bidirectional nonlocal interactions. The key argument in favor of the statistical universality of the smallest scales is thus worth investigating even at very high Reynolds number flows.

Moreover, the Reynolds number needed for the Kolmogorov theory to hold is usually beyond the reach of laboratory experiments. Consequently, large and small scales interact within a common range of scales, and remain correlated one with each other.

Because of the pioneering work of Townsend (1956) and of many other researchers, it is now well known that most shear flows give rise to so-called coherent structures. These are energy containing eddies at rather large scales, but in contrast with classical large scale turbulence, coherent structures strongly persist in time and/or in space. Their topology depends on initial conditions and their related statistics are not universal (Antonia et al. 2002; Thiesset et al. 2013). The information enclosed within coherent structures persists till the far field (Bisset et al. 1990; Thiesset et al. 2013; Zhou and Antonia 1995) and may thus influence small-scale statistics due to nonlocal interactions and finite Reynolds numbers effects.

Therefore, some new statistical tools must be developed to quantify the interactions between large (and in particular the CM) and small scales. To this end, one possible way is to consider velocity increments, which represent motions at scales $\leq r$ (not only at the particular scale $r$ Danaila et al. 2012; Mouri and Hori 2010), conditioned by another parameter characterizing motions at scales $\geq r$ (Mouri and Hori 2010).

The first study based on conditional structure functions is that of Praskovsky et al. (1993). The latter reported structure functions conditioned by the instantaneous

velocity in two different high Reynolds number shear flows. They pointed out a strong correlation between large and inertial subrange scales. These authors Praskovsky et al. (1993) finally concluded that these findings are in contradiction with the random sweeping decorrelation which was first stated (Tennekes 1975) by supposing statistical independence between eddies.

Subsequently, measured structure functions were conditioned by the instantaneous velocity in the atmospheric boundary layer (Sreenivasan and Dhruva 1998). In spite of the very high Reynolds number, a strong correlation between large and small scales was also emerged. According to Sreenivasan and Dhruva (1998), this result may highlight the persisting influence of the mean shear on the smallest scales.

More recently, Blum et al. (2010, 2011) measured structure functions conditioned by the average of the velocity at points $x$ and $x + r$ in different shearless flows. These authors pointed out that small scales were perturbed by the large scales at very different levels depending on the flow type. They concluded that conditional structure functions provide a reference tool for comparing large-scale effects in different flows.

Investigating the nature of the interactions between the coherent motion (CM) and the small scale motion is the principal motivation of the present work. A better understanding of the effect of the large-scale coherent motion on the smallest scales is of major practical interest, for example for designing new efficient subgrid scale models (Kang and Meneveau 2002; O'Neil and Meneveau 1997). This study addresses two specific issues: (1) Does the kinetic energy at a scale $r$ depend on the dynamics of the CM? (2) What are the energy budget equations based on phase-conditioned structure functions?

To unravel these issues, the way we condition structure functions is somewhat different to that presented previously. Based on the approach of e.g., (Reynolds and Hussain 1972), we propose to condition structure functions by a particular value of the phase $\phi$ arising from the phase-averaging operation.

This study focuses entirely on a circular cylinder wake flow, which is investigated by means of hot wire experiments. The wake flow is renowned for its coherent motion which persists far downstream from the obstacle [see e.g., Bisset et al. (1990)]. Different streamwise locations were studied, from $x = 10$ to 40 $D$ ($D$ is the cylinder diameter) leading to a decreasing amplitude of velocity coherent fluctuations. Investigations are mostly oriented on the wake centerline, for which the mean shear is absent. This allows us to focus only on the influence of the coherent motion, thus avoiding the additive effect of the mean shear (Sreenivasan and Dhruva 1998).

The paper is organized as follows. First, measurements are described. Then, onepoint statistics are presented, with particular emphasis on the typical topology of the wake flow. Afterwards, the interactions between the coherent and the random fluctuating fields are highlighted by means of second-order phase-conditioned structure functions. Finally, energy budget equations which concern both the random and coherent motions are derived and tested against experimental data.

## 2 Experiments

The reader can refer to Zhou et al. (2003) for more detailed information. We recall briefly the most important features of the experimental set-up and measurement technique.

Measurements were carried out in an open-circuit wind tunnel with a working section of $0.35 \times 0.35$ m$^2$ and 2.4 m long. The cylinder of diameter $D = 12.7$ mm is placed horizontally, spanning the full width of the working section. The upstream velocity $U\_0$ is $3\,\mathrm{ms}^{-1}$ corresponding to a Reynolds number $\mathrm{Re}_D = \frac{U_0 D}{\nu} = 2,540$ ($\nu$ is the kinematic viscosity). Measurements were made at different downstream locations: $x = 10,\ 20,\ 40\,\mathrm{D}$, and different transverse positions, from $y = 0$ to $y = 3D$. The Taylor micro-scale Reynolds number $R_\lambda = \frac{\sqrt{\overline{u^2}}\lambda}{\nu} \approx 70$ at $40D$. $\overline{u^2}$ is the streamwise velocity variance, $\lambda$ is the Taylor micro-scale $\lambda^2 = 15\,\nu\overline{u^2}/\bar{\varepsilon}$ and $\bar{\varepsilon}$ the mean dissipation rate [see Zhou et al. (2003) for the values and the procedure employed for measuring $\bar{\varepsilon}$]. A hot-wire probe, consisting of four cross-wires was used to measure simultaneously all three vorticity components [see Zhou et al. (2003) for more details about the probe].

Phase-averaged statistics are obtained as follows. The transverse velocity component $v$ is first digitally band-pass filtered at the Strouhal frequency, using an eighthorder Butterworth filter. The filtering operation is next applied to the magnitude of the Fourier transform of $v$ in order to avoid any phase shift. Then, the Hilbert transform $h$ of the filtered signal $v_f$ is obtained and the phase $\phi$ inferred from the relation $\phi = \arctan\left(\frac{h}{v_f}\right)$. Finally, the phase is divided into 41 segments and phase averaged statistics are calculated for each segment. The convergence of statistics was checked, by reducing the number of segments, and found to be satisfactory. By means of our method, phase-averaged quantities are calculated over the period $[-\pi,\ \pi]$. As was done by O'Neil and Meneveau (1997), the phase is doubled up to $[-2\pi,\ 2\pi]$ thanks to the periodicity, in order to enhance the visual display.

In Hill (2001), the geometrical space (location $x$ in the flow) and the separation space (turbulent scales $r$) are made independent by considering the geometrical location specified by the midpoint $X = \frac{1}{2}(x + x^+)$ with $x^+ = x + r$. The same idea is applied here to phase-conditioned structure functions for which the phase $\phi$ is defined as the phase at the midpoint $\phi = \phi(\mathbf{X})$. Therefore, each velocity component is decomposed into a triple contribution from the mean temporal average, the phase-averaged fluctuation and the random/turbulent fluctuation.

## 3 Flow Topology

Let us first briefly discuss the overall features of the coherent motion pertaining to the wake flow. One of the main advantages of using phase averaging is that the temporal dynamics associated with the presence of the CM is highlighted. As far

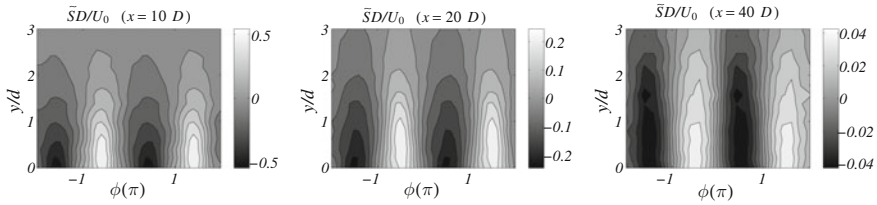


**Fig. 1** Coherent strain $\tilde{S} = \left(\frac{\partial \tilde{u}}{\partial y} + \frac{\partial \tilde{v}}{\partial x}\right)$ normalized by $D/U_0$ in the $(\phi, y)$ plane. **a** $x = 10D$, **b** $x = 20D$, **c** $x = 40D$

as the wake flow is concerned, one generally displays statistics in the $(\phi, y)$ plane (Bisset et al. 1990; Zhou and Antonia 1995) to relate the spatial organization of the kinetic energy to that of the coherent structures. Here, we focus particularly on the coherent strain which is generally enrolled in the creation of turbulent kinetic energy.

Iso-values of the coherent strain $\tilde{S} = \left(\frac{\partial \tilde{u}}{\partial y} + \frac{\partial \tilde{v}}{\partial x}\right)$ are reported in Fig. 1a–c. Note that $\phi = \pi/2 \pm k\pi$ and $y = 0$ corresponds to the location of the maximum (absolute values) of the coherent strain. Its amplitude decreases further downstream from the obstacle. For example, the extrema of $\tilde{S}$ at $40D$ are one order of magnitude smaller than at $10D$.

In the light of the previous remarks, in the remaining part of this study, we will focus entirely on the wake centerline, where the contribution of the coherent motion is maximum. In addition, this allows the effect of the coherent motion to be separated from that of the mean shear. The latter is known to influence the behaviour of the smallest scales even at large Reynolds numbers (Kholmyansky and Tsinober 2008; Praskovsky et al. 1993; Sreenivasan and Dhruva 1998).

## 4 Phase-Conditioned Structure Functions

The phase-averaging operation is now applied to the $n$th order structure functions. Structure functions are as usual functions of $r$, but specific to our methodology, they are also functions of the phase $\phi$. In the following, we assign brackets to phase-conditioned structure functions, viz.

$$\langle (\Delta u_\alpha)^n \rangle (r,\ \phi) = \langle (u_\alpha(x + r) - u_\alpha(x))^n \rangle (r, \phi) \tag{1}$$

which represent the ensemble average of the $n$th order increment $\Delta u_\alpha = u_\alpha(x + r) - u_\alpha(x)$ of the velocity component $u_\alpha$, for a particular value of $\phi$. Then, the conventional time-averaged structure functions are calculated by integrating $\langle (\Delta u_\alpha)^n \rangle$ over all values of $\phi \in [-\pi; \pi]$ (periodicity is invoked), and are denoted by a horizontal bar, i.e., $\langle (\Delta u_\alpha)^n \rangle$. An important remark is that for $n = 1$,

$$\langle \Delta u_\alpha \rangle = \Delta \tilde{u}_\alpha \neq 0. \tag{2}$$

Therefore, in contrast to classical structure functions, first-order phase-conditioned structure functions are non-zero for $r \neq 0$. However, $\overline{\langle \Delta u_\alpha \rangle} = 0$. Another result relates to the second-order structure functions,

$$\langle (\Delta u_\alpha) \rangle = (\Delta \tilde{u}_\alpha)^2 + \langle (\Delta u'_\alpha) \rangle, \tag{3}$$

i.e., the sum of the second-order structure functions of the random and coherent motions. The influence of the phase, on the total, organized or random fluctuating fields, can be thus assessed separately.

## 4.1 Focus on the Transverse Velocity Component

We present the phase-conditioned structure functions of the total transverse velocity fluctuations (Fig. 2a–c), of the coherent component (Fig. 2d–f), and of the randomly fluctuating field (Fig. 2g–i) for three downstream distances.

In homogenous turbulence, the second-order structure function should be equal to twice the velocity variance at large scales. In Fig. 2a–c, the values of the phase-conditioned second-order structure functions progressively increase as $r$ keeps increasing, and reach a maximum for $r = L_v/2$ ($L_v$ is the distance between two successive vortices) which overshoots $2\overline{v^2}$. Then, one notes a slight decrease of energy up to $r = L_v$ and this pattern is repeated with a period equal to $L_v$.

The influence of the phase (hereafter called phase-correlation) is clearly visible in Fig. 2a–c. The energy of the transverse velocity component $v$ is largest at phases $\phi = \frac{\pi}{2} \pm k\pi$ with a periodicity of $\pi$. These phase locations and periodicity are strongly linked to the maxima of the coherent shear (Fig. 1). Note finally that at $x = 40D$ the phase-correlation strongly diminishes at smallest scales, although it is still perceptible for scales larger than $r = 0.2\ L_v \approx 2\lambda$.

The phase-conditioned structure function of $v$ exhibits a topology analogous to that of $\tilde{v}$ (Fig. 2d–f). For example, the phase $\pi$-periodicity and the separation $L_v$-periodicity are recovered. Further, the local maxima or minima corresponds to that of the coherent motion. Therefore, as for one-point statistics, the energy distribution among scales of the total fluctuating field hides a non negligible contribution due to the presence of the coherent motion, which tends to decrease as we move away from the obstacle.

Using Eq. (3), we can calculate the structure function of the random velocity component $v'$ (Fig. 2g–i). At $x = 40D$, the phase-conditioned structure functions have similar shapes to the usual time-average structure functions, and the phase-correlation is lost. However, at $x = 10D$ and $20D$, there is still a strong influence of the phase, even at very small scales.

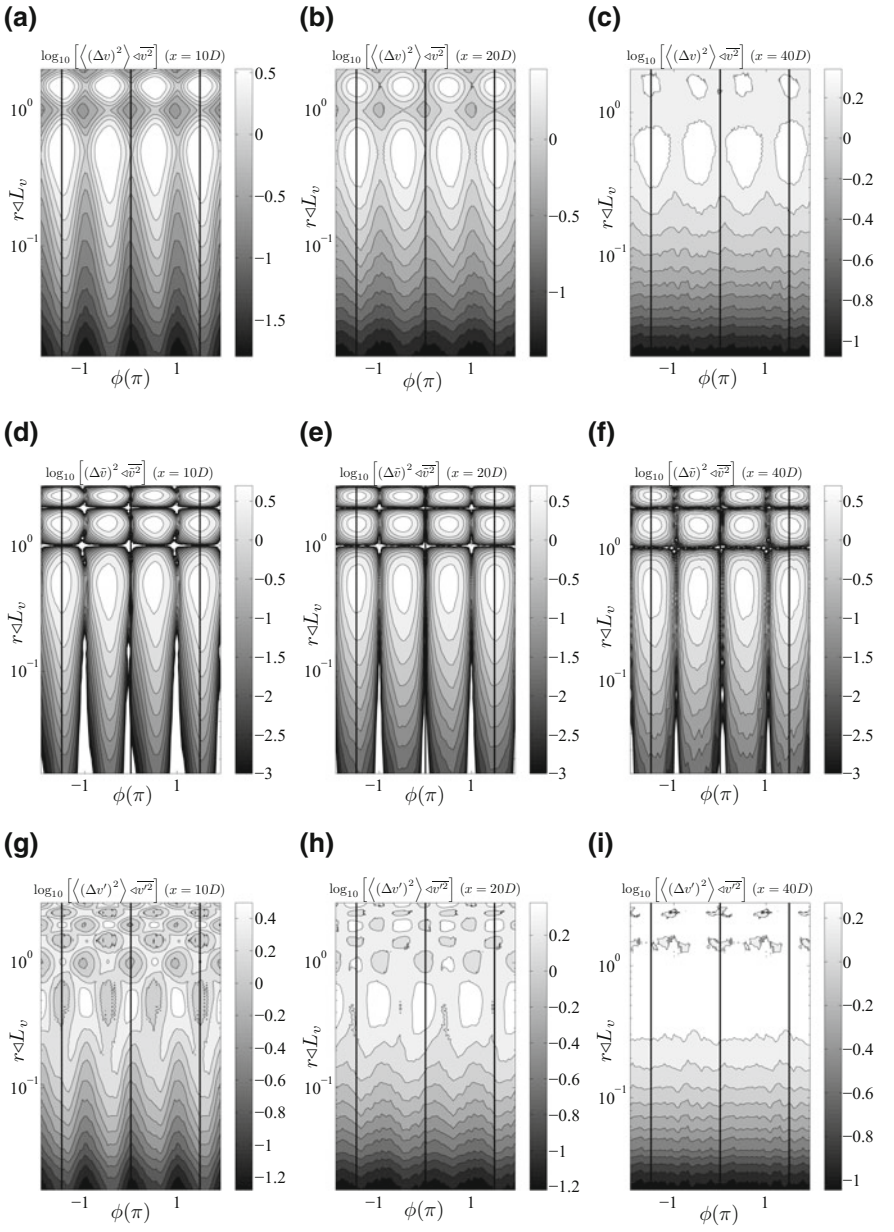


**Fig. 2** Phase-conditioned secondorder structure function of the transverse velocity component $v$ (using $\log_{10}$ scale). **a**, **b**, **c**: $\left\langle(\Delta v)^2\right\rangle/\overline{v^2}$. **d**, **e**, **f**: $(\Delta\tilde{v})^2/\overline{\tilde{v}^2}$. **g**, **h**, **i**: $\left\langle(\Delta v')^2\right\rangle/\overline{v'^2}$. (**a**, **d**, **g**) $x = 10D$, (**b**, **e**, **h**) $x = 20D$, (**c**, **f**, **i**) $x = 40D$. *Vertical solid lines* delineate phase references $\phi = \pm\frac{3\pi}{2}$ and $\phi = 0$

## 5 Energy Budget Equations

In flows where a phase-correlation at a given scale is strongly discernible, it might be interesting to derive an energy budget equation for second-order phase-conditioned structure function. One advantage of using the phase-average operation is that it allows writing transport equations for the two distinct energy contributions: that of the coherent motion and that of the purely random/turbulent part of the fluctuating field. The next section aims at deriving such kinds of budget equations.

### *5.1 General Formulation*

The starting point is the Navier–Stokes equation

$$\frac{\partial U_i}{\partial t} + U_j \frac{\partial U_i}{\partial x_j} = -\frac{\partial P}{\partial x_i} + \nu \frac{\partial^2 U_i}{\partial x_j \partial x_j}, \tag{4}$$

where $P$ is the kinematic pressure and $\nu$ the kinematic viscosity. In contrast to Danaila et al. (2002, 2004), we invoke the triple decomposition (Reynolds and Hussain 1972)

$$\begin{array}{cc} U_i = \bar{U}_i + \tilde{u}_i + u_i', & P = \bar{P} + \tilde{p} + p' \\ u_i = \tilde{u}_i + u_i', & p = \tilde{p} + p, \\ \langle u_i' \rangle = 0 & \langle p' \rangle = 0. \end{array} \tag{5}$$

By further using Eq. (5), Reynolds and Hussain (1972) obtained the dynamical equations of the coherent and random components, which are respectively

$$\frac{D\tilde{u}_i}{Dt} + \tilde{u}_j \frac{\partial \bar{U}_i}{\partial x_j} + \frac{\partial}{\partial x_j}\left(\tilde{u}_i \tilde{u}_j - \overline{\tilde{u}_i \tilde{u}_j}\right) + \frac{\partial}{\partial x_j}\left(\left\langle u_i' u_j' \right\rangle - \overline{u_i' u_j'}\right) = -\frac{\partial \tilde{p}}{\partial x_i} + \nu \frac{\partial^2 \tilde{u}_i}{\partial x_j \partial x_j}, \tag{6}$$

$$\frac{Du_i'}{Dt} + \tilde{u}_j \frac{\partial u_i'}{\partial x_j} + u_j' \frac{\partial \bar{U}_i}{\partial x_j} + u_j' \frac{\partial \tilde{u}_i}{\partial x_j} + \frac{\partial}{\partial x_j}\left(u_i' u_j' - \left\langle u_i' u_j' \right\rangle\right) = -\frac{\partial p'}{\partial x_i} + \nu \frac{\partial^2 u_i'}{\partial x_j \partial x_j}. \tag{7}$$

$\frac{D}{Dt} = \frac{\partial}{\partial t} + \overline{U_j} \frac{\partial}{\partial x_j}$ is the material derivative. Equations (6) and (7) are written at points $\mathbf{x}$ and $\mathbf{x}^+ = \mathbf{x} + \mathbf{r}$ separated by a distance $\mathbf{r}$. Then, the equation at point $\mathbf{x}$ is subtracted to that at point $\mathbf{x}^+$, so that

$$\begin{aligned} &\frac{\partial \Delta\tilde{u}_i}{\partial t} + \Delta\left(\bar{U}_j \frac{\partial \tilde{u}_i}{\partial x_j}\right) + \Delta\left(\tilde{u}_j \frac{\partial \bar{U}_i}{\partial x_j}\right) + \Delta\left(\frac{\partial}{\partial x_j}\left(\tilde{u}_i \tilde{u}_j - \overline{\tilde{u}_i \tilde{u}_j}\right)\right) \\ &\quad + \Delta\left(\frac{\partial}{\partial x_j}\left(\left\langle u_i' u_j' \right\rangle - \overline{u_i' u_j'}\right)\right) = -\Delta\left(\frac{\partial \tilde{p}}{\partial x_i}\right) + \nu\Delta\left(\frac{\partial^2 \tilde{u}_i}{\partial x_j^2}\right), \end{aligned} \tag{8}$$

is the dynamical equation of coherent velocity increments, and

$$\frac{\partial \Delta u_i'}{\partial t} + \Delta\left(\bar{U}_j \frac{\partial u_i'}{\partial x_j}\right) + \Delta\left(\tilde{u}_j \frac{\partial u_i'}{\partial x_j}\right) + \Delta\left(u_j' \frac{\partial \bar{U}_i}{\partial x_j}\right) + \Delta\left(u_j' \frac{\partial \tilde{u}_i}{\partial x_j}\right) + \Delta\left(\frac{\partial}{\partial x_j}\left(u_i' u_j' - \left\langle u_i' u_j' \right\rangle\right)\right) = -\Delta\left(\frac{\partial p'}{\partial x_i}\right) + \nu\Delta\left(\frac{\partial^2 u_i'}{\partial x_j^2}\right) \tag{9}$$

is the dynamical equation of random velocity increments.

As proposed by Danaila et al. (2002, 2004), Hill (2001), we use derivatives with respect to the midpoint X defined by $\mathbf{X} = (\mathbf{x} + \mathbf{x}^+)/2$, such as $\partial/\partial x_j = -\partial/\partial r_j + \partial/2\partial X_j$ and $\partial/\partial x_j^+ = \partial/\partial r_j + \partial/2\partial X_j$. We further assume the two points x and $x^+$ are independent (Danaila et al. 2002, 2004; Hill 2001), viz. $\partial u_i/x_j^+ = \partial u_i^+/x_j = 0$. After multiplying Eq. (8) by $2\Delta\tilde{u}_i$ and Eq. (9) by $2\Delta u_i'$, applying phase averaging followed by time averaging, and finally noting that

$$\left\langle \Delta u_j' \Delta u_i' \right\rangle = \left\langle \Delta u_i \Delta u_j \right\rangle - \Delta\tilde{u}_i \Delta\tilde{u}_j \tag{10}$$

$$\left\langle \Delta u_j \Delta q^2 \right\rangle = \Delta\tilde{u}_j \Delta\tilde{q}^2 + \Delta\tilde{u}_j \left\langle \Delta q'^2 \right\rangle + \left\langle \Delta u_j' \Delta q'^2 \right\rangle + 2\Delta\tilde{u}_i \left\langle \Delta u_j' \Delta u_i' \right\rangle, \tag{11}$$

We finally obtain the scale-by-scale energy budget of the coherent motion

$$\begin{aligned} &\overline{\frac{D}{Dt}\Delta\tilde{q}^2} + \frac{1}{2}\frac{\partial}{\partial X_j}\left[\overline{\Sigma\tilde{u}_j\Delta\tilde{q}^2} + \overline{2\left\langle \Sigma u_j' i' \right\rangle \Delta\tilde{u}_i} + 2\overline{\Delta\tilde{u}_i\Delta\tilde{p}}\right] + 2\overline{\Delta\tilde{u}_i\Delta\tilde{u}_j}\frac{\partial \bar{U}_i}{\partial x_j} \\ &\quad - \overline{\left\langle \Sigma u_j' \Delta u_i' \right\rangle \frac{\partial}{\partial X_j}\Delta\tilde{u}_i} + \frac{\partial}{\partial r_j}\overline{\Delta\tilde{u}_j\Delta\tilde{q}^2} + 2\Delta\tilde{u}_i \frac{\partial}{\partial r_j}\overline{\left\langle \Delta u_i' j' \right\rangle} \\ &\quad - \nu\left[\left(2\frac{\partial^2}{\partial r_j^2} + \frac{1}{2}\frac{\partial}{\partial X_j^2}\right)\overline{\Delta\tilde{q}^2} + 2\Sigma\left(\overline{\frac{\partial\tilde{u}_i}{\partial x_j}\frac{\partial\tilde{u}_j}{\partial x_i}}\right)\right] = -2\Sigma\bar{\tilde{\varepsilon}} \end{aligned} \tag{12}$$

For the random motion, the corresponding energy budget equation is

$$\begin{aligned} &\overline{\frac{D}{Dt}\Delta q'^2} + \frac{1}{2}\frac{\partial}{\partial X_j}\left[\overline{\Sigma u_j'\Delta q'^2} + \Sigma\tilde{u}_j\left\langle \Delta q'^2 \right\rangle + 2\overline{\Delta u_i'\Delta u_j'}\right] + 2\overline{\Delta u_i'\Delta u_j'}\frac{\partial \bar{U}_i}{\partial x_j} \\ &\quad + \overline{\left\langle \Sigma u_j'\Delta u_i' \right\rangle \frac{\partial}{\partial X_j}\Delta\tilde{u}_i} + \frac{\partial}{\partial r_j}\left(\overline{\left\langle \Delta u_j \Delta q^2 \right\rangle} - \overline{\Delta\tilde{u}_j\Delta\tilde{q}^2}\right) - 2\overline{\Delta\tilde{u}_i \frac{\partial}{\partial r_j}\left\langle \Delta u_i'\Delta u_j' \right\rangle} \\ &\quad - \nu\left[\left(2\frac{\partial^2}{\partial r_j^2} + \frac{1}{2}\frac{\partial^2}{\partial X_j^2}\right)\overline{\Delta q'^2} + 2\Sigma\left(\overline{\frac{\partial u_i'}{\partial x_j}\frac{\partial u_j'}{\partial x_i}}\right)\right] = -2\Sigma\overline{\varepsilon'} \end{aligned} \tag{13}$$

$\overline{\Delta\tilde{q}^2} = \overline{\Delta\tilde{u}_i\Delta\tilde{u}_i}$ and $\overline{\Delta q'^2} = \overline{\Delta u_i'\Delta u_j'}$ (the summation convention applies to repeated Latin indices) are the coherent and random kinetic energies at a given scale respectively. $\sum \cdot = \cdot(\mathrm{x} + \mathrm{r}) + \cdot(\mathrm{x})$ is the sum at two points separated by a distance

**r**. The quantities $\tilde{\varepsilon} = \frac{\nu}{2}\overline{\left(\frac{\partial \tilde{u}_i}{\partial x_j} + \frac{\partial \tilde{u}_j}{\partial x_i}\right)^2}$ and $\varepsilon' = \frac{\nu}{2}\overline{\left(\frac{\partial u'_i}{\partial x_j} + \frac{\partial u'_j}{\partial x_i}\right)^2}$ are the mean energy dissipation rates of the coherent and the random motions, respectively.For the sake of clarity, these equations are formally rewritten as

$$\mathscr{I}_c + \mathscr{A}_{cm} + \mathscr{D}_{cc} + \mathscr{D}^1_{rc} + \mathscr{D}_{cp} + \mathscr{P}_{cm} - \mathscr{P}_{rc} + \mathscr{T}_c + \mathscr{F}_c + \mathscr{V}_c = -2\Sigma\overline{\tilde{\varepsilon}} \quad (14)$$

$$\mathscr{I}_r + \mathscr{A}_{rm} + \mathscr{D}_{rr} + \mathscr{D}^2_{rc} + \mathscr{D}_{rp} + \mathscr{P}_{rm} + \mathscr{P}_{rc} + \mathscr{T} - \mathscr{T}_c - \mathscr{F}_c + \mathscr{V}_r = -2\Sigma\overline{\varepsilon'} \quad (15)$$

where $\mathscr{I}$, $\mathcal{A}$, $\mathscr{D}$, $\mathscr{P}$, $\mathscr{T}$, $\mathscr{F}$ et $\mathscr{V}$ denote respectively the nonstationarity, advection, diffusion, production, transfer, forcing and viscous terms. The subscripts $m$, $c$, $r$ correspond to the mean, coherent and random motions, and $\mathscr{D}_p$ indicates the pressure diffusion.

By comparison with Danaila et al. (2002, 2004), there are additional terms which emerge in the present equations, e.g., the terms $\mathscr{P}_{rc}$, $\mathscr{T}_c$ and $\mathscr{F}_c$ which can be identified as the production of random fluctuations by the coherent motion, the coherent kinetic energy transfer and the forcing associated by the presence of a coherent motion. All three are present in Eqs. (12) and (13), but with opposite signs. This means that what represents a loss of energy for the coherent motion Eq. (12), constitutes a gain of energy for randomly fluctuating motion (Eq. 13). Further, we can shed light on $\mathscr{D}^1_{rc}$ and $\mathscr{D}^2_{rc}$, the transport of random statistical quantities by the organized motion.

Equations (12) and (13) provide a general framework which allow the physics of the interaction between coherent and random fields to be unravelled.

In a globally homogenous context, the limit at the largest scales of Eqs. (12) and (13) is twice the one-point energy budgets provided by Reynolds and Hussain (1972). At this stage, Eqs. (12) and (13) are functions of the time $t$, the reference point vector $x$ and the separation vector $r$. This leads to a problem in seven dimensions (eight before time-averaging). In order to reduce the number of degrees of freedom, one generally invokes the local isotropy assumption. The practical consequence is that these isotropic forms lead themselves being tested experimentally, with the constraint that two-points statistics are usually evaluated along one particular direction. Further, this allows us to compare the present considerations to that already developed over the last half century (Antonia et al. 1997; Danaila et al. 2002, 2004; Kolmogorov 1941; Yaglom 1949).

## 5.2 *Locally Homogenous and Isotropic Context*

First, if homogeneity holds at the level of the viscous scales, then the viscous term reduces to (Hill 2001)

$$-\nu\left[\left(2\frac{\partial^2}{\partial r_j^2}+\frac{1}{2}\frac{\partial^2}{\partial X_j^2}\right)\overline{\Delta q'^2}+2\Sigma\left(\overline{\frac{\partial u_i'}{\partial x_j}\frac{\partial u_j'}{\partial x_i}}\right)\right]=-2\nu\frac{\partial^2}{\partial r_j^2}\overline{\Delta q'^2}, \tag{16}$$

Then, in the context of local isotropy, the divergence and the Laplacian operators are expressed in spherical coordinates (Danaila et al. 2002, 2004), and after multiplying (12) and (13) by $r^2 = r_j r_j$, integrating with respect to $r$ and dividing by $r^2$, we obtain

$$\begin{aligned}&\frac{1}{r^2}\int_0^r s^2\left(\mathscr{A}_{cm}+\mathscr{D}_{cc}+\mathscr{D}_{rc}^1+\mathscr{P}_{cm}+\mathscr{P}_{rc}+\mathscr{D}_{cp}\right)\mathrm{d}s\\&\quad+\overline{\Delta\tilde{u}_\parallel\Delta\tilde{q}^2}+\frac{2}{r^2}\int_0^r\overline{\Delta\tilde{u}_i\, s s^2\left\langle\Delta u_\parallel'\Delta u_i'\right\rangle}\,\mathrm{d}s-2\nu\frac{\partial}{\partial r}\overline{\Delta\tilde{q}^2}=-\frac{4}{3}\bar{\tilde{\varepsilon}}r;\end{aligned} \tag{17}$$

$$\begin{aligned}&\frac{1}{r^2}\int_0^r s^2\left(\mathscr{A}_{rm}+\mathscr{D}_{rr}+\mathscr{D}_{rc}^2+\mathscr{P}_{rm}-\mathscr{P}_{rc}+\mathscr{D}_{rp}\right)\mathrm{d}s+\overline{\left\langle\Delta u_\parallel\Delta q^2\right\rangle}-\overline{\Delta\tilde{u}_\parallel\Delta\tilde{q}^2}\\&\quad-\frac{2}{r^2}\int_0^r\Delta\tilde{u}_i\frac{\partial}{\partial s}s^2\left\langle\Delta u_\parallel'\Delta u_i'\right\rangle ds-2\nu\frac{\partial}{\partial r}\overline{\Delta q'^2}=-\frac{4}{3}\bar{\varepsilon}'r.\end{aligned} \tag{18}$$

Equations (17) and (18) are the energy budget equations for the coherent and random components in a locally isotropic context. Here, $s$ is a dummy variable and the subscript $\parallel$ denotes the direction parallel to the separation vector. When the spatial separation is inferred using Taylor hypothesis, this direction coincides with that of the mean flow.

The first line of Eqs. (17) and (18) represents the energy contribution of the largest scales (Danaila et al. 2002, 2004). The main difference with respect to the extended form of Kolmogorov's equation (Antonia et al. 1997), is the appearance of several extra terms due to the presence of CM. The effective energy transfer of the random velocity component is explicit and thus consists of the total energy transfer $\overline{\left\langle\Delta u_\parallel\Delta q^2\right\rangle}$ (including the coherent and random contributions), from which are subtracted the coherent energy transfer $\overline{\left\langle\Delta\tilde{u}_\parallel\Delta\tilde{q}^2\right\rangle}$ and the forcing term $\frac{2}{r^2}\int_0^r\overline{\Delta\tilde{u}_i\frac{\partial}{\partial_s}s^2\left\langle\Delta u_\parallel'\Delta u_i'\right\rangle}\,\mathrm{d}s$.

## 5.3 Comparison with Experiments

On the wake centerline, the locally isotropic scale-by-scale budget of the random motion is

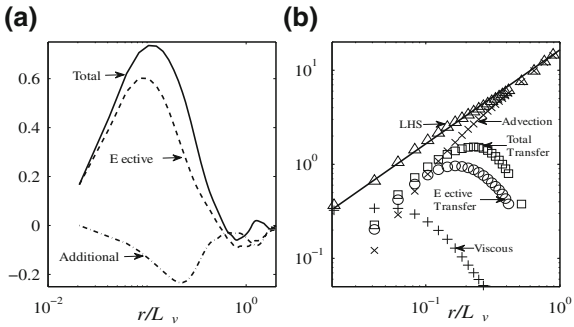


**Fig. 3** **a** Non linear transfer term divided by $\overline{\varepsilon'}r$. — total transfer term $-\overline{\langle \Delta u_\parallel \Delta q^2 \rangle}$, — • — coherent transfer and forcing term $\overline{\Delta\tilde{u}_\parallel \Delta\tilde{q}^2} + \frac{2}{r^2}\int_0^r \overline{\Delta\tilde{u}_i \frac{\partial}{\partial s} s^2 \left\langle \Delta u'_\parallel \Delta'_i \right\rangle}\,\mathrm{d}s$, — Sum $-\overline{\langle \Delta u_\parallel \Delta q^2 \rangle} + \overline{\Delta\tilde{u}_\parallel \Delta\tilde{q}^2} + \frac{2}{r^2}\int_0^r \overline{\Delta\tilde{u}_i \frac{\partial}{\partial s} s^2 \left\langle \Delta u'_\parallel \Delta'_i \right\rangle}\,\mathrm{d}s$. **b** Scale-by-scale budget of the random motion Eq. (19) divided by $\overline{\varepsilon'}$. —: $\frac{4}{3}\overline{\varepsilon'}r$, ×: $-\frac{1}{r^2}\int_0^r s^2 \mathcal{A}_{rm}\,\mathrm{d}s$, *square* $-\overline{\langle \Delta u_\parallel \Delta q^2 \rangle x}$, *circle* $-\overline{\langle \Delta u_\parallel \Delta q^2 \rangle} + \overline{\Delta\tilde{u}_\parallel \Delta\tilde{q}^2} + \frac{2}{r^2}\int_0^r \overline{\Delta\tilde{u}_i \frac{\partial}{\partial s} s^2 \left\langle \Delta u'_\parallel \Delta u'_i \right\rangle}\,\mathrm{d}s$, +: $2\nu \frac{\partial}{\partial r}\overline{\Delta q'^2}$, *triangle* Left hand side of Eq. (19)

$$-\frac{1}{r^2}\int_0^r s^2 \mathcal{A}_{rm}\,\mathrm{d}s - \overline{\langle \Delta u_\parallel \Delta q^2 \rangle}$$

$$+\overline{\Delta\tilde{u}_\parallel \Delta\tilde{q}^2} + \frac{2}{r^2}\int_0^r \Delta\tilde{u}_i \frac{\partial}{\partial s} s^2 \left\langle \Delta u'_\parallel \Delta u'_i \right\rangle \mathrm{d}s + 2\nu \frac{\partial}{\partial r}\overline{\Delta q'^2} = \frac{4}{3}\overline{\varepsilon'}r, \tag{19}$$

which means that in the limit of large scales, the advection term is almost entirely compensated by the energy dissipation rate, other large-scale terms such as longitudinal production or turbulent diffusion are negligible compared to the advection term.

Figure 3a reports the total non linear transfer $-\overline{\langle \Delta u_\parallel \Delta q^2 \rangle}$, the additional coherent transfer and forcing due to the coherent motion $\overline{\Delta\tilde{u}_\parallel \Delta\tilde{q}^2} + \frac{2}{r^2}\int_0^r \Delta\tilde{u}_i \frac{\partial}{\partial s} s^2 \left\langle \Delta u'_\parallel \Delta u'_i \right\rangle \mathrm{d}s$ and the effective transfer inferred from their sum, in function of the separation $r/Lv$. For weakly turbulent flows the nonlinear transfer term is smaller than $\frac{4}{3}\varepsilon r$, because of the cross-over between viscous and large-scale effects (Danaila et al. 2002, 2004). Here, $-\overline{\langle \Delta u_\parallel \Delta q^2 \rangle}/\varepsilon r \approx 0.63$. The additional energy transfer associated with the coherent motion is negative, its value being quite small, although non negligible. Its contribution is non zero for all separations, with a maximum contribution at about $2\lambda$. Finally, the maximum effective transfer of the random motion is smaller than the total transfer by about 12 %.

Even though the difference of 12 % between the total energy transfer and the effective energy transfer is quite weak, its influence may persist far from the injection of energy (Thiesset et al. 2013) and thus remains a key point to provide

some insight into the energy transfer along the cascade in the wake flow, for which the CM is discernible.

The extra-transfer term is nonzero over a large range of scales. However, one cannot claim that this quantifies the non local interactions between coherent and random fields because of the loss of localization in physical space as mentioned previously.

The balance between the right- and left-hand sides of (19) is reasonably satisfied at all scales. The weak imbalance at rather large scales appears to reflect that local isotropy no more holds or that another production and/or diffusion terms must taken into account in Eq. (19).

To conclude, the experimental investigation in the cylinder intermediate wake supports the analytical considerations provided by this study.

## 6 Conclusions

The connection between the temporal dynamics of the coherent motion and the energy distribution across all scales is highlighted by means of phase-conditioned structure functions. This original statistical tool allows us to assess what range of scales is affected by the CM dynamics. Moreover, we are able to separate the energy contributions of the coherent and random fluctuations. Phase-averaging the structure functions measured in a cylinder wake yields two main outcomes.

First, it is shown that, as the downstream location behind the cylinder increases, (1) the scale at which the forcing associated with the CM is perceptible continually increases; (2) phase-scale structure functions reveal also that a scale $r$ is correlated with that of the coherent shear, the effect of the latter being to locally enhance the energy at any scale $r$.

Second, energy budget equations which account for the organized motion are derived. Both general and isotropic formulations are obtained. They highlight a few additional terms. One of these may be interpreted as an additional forcing exerted by the CM on the random motion. At $x = 40D$, this term represents only about 12 % of the total transfer term, but its influence may persist far downstream. The isotropic formulation is tested against experimental data at the wake centreline. The weak imbalance between the analytical formulation and the measurements at rather large scales appears to underline the inadequacy of local isotropy at these scales.

**Acknowledgments** The financial support of the 'Agence Nationale de la Recherche' (ANR), under the project 'ANISO', is gratefully acknowledged. RAA acknowledges the support of the Australian Research Council. We thank T. Zhou who carried out the original experiments.

## References

Antonia RA, Ould-Rouis M, Anselmet F, Zhu Y (1997) Analogy between predictions of Kolmogorov and Yaglom. J Fluid Mech 332:395–409

Antonia RA, Zhou T, Romano GP (2002) Small-scale turbulence characteristics of two dimensional bluff body wakes. J Fluid Mech 459:67–92

Bisset DK, Antonia RA, Browne LWB (1990) Spatial organization of large structures in the turbulent far wake of a cylinder. J Fluid Mech 218:439–461
Blum DB, Bewley GP, Bodenschatz E, Gibert M, Gylfason A, Mydlarski L, Voth GA, Xu H, Yeung PK (2011) Signatures of non-universal large scales in conditional structure functions from various turbulent flows. New J Phys 13:113020
Blum DB, Kunwar SB, Johnson J, Voth GA (2010) Effects of nonuniversal large scales on conditional structure functions in turbulence. Phys Fluids 22:015107
Danaila L, Anselmet F, Antonia RA (2002) An overview of the effect of large scale inhomogeneities on small-scale turbulence. Phys Fluids 14:2475–2484
Danaila L, Antonia RA, Burattini P (2004) Progress in studying small-scale turbulence using 'exact' two-point equations. New J Phys 6:128
Danaila L, Antonia RA, Burattini P (2012) Comparison between kinetic energy and passive scalar energy transfer in locally homogeneous isotropic turbulence. Physica D 241:224–231
Hill RJ (2001) Equations relating structure functions of all orders. J Fluid Mech 434:379–388
Hosokawa I (2007) A paradox concerning the refined similarity hypothesis of Kolmogorov for isotropic turbulence. Prog Theor Phys 118:169
Kang HS, Meneveau C (2002) Universality of large eddy simulation model parameters across a turbulent wake behind a eated cylinder. J Turbul 3:1–27
Kholmyansky M, Tsinober A (2008) Kolmogorov 4/5 law, nonlocality, and sweeping decorrelation hypothesis. Phys Fluids 20:041704
Kolmogorov A (1941a) Dissipation of energy in the locally isotropic turbulence. Dokl Akad Nauk SSSR 125:15–17
Kolmogorov A (1941) The local structure of turbulence in incompressible viscous fluid for very large Reynolds numbers. Proc USSR Acad Sci (Trad Proc Roy Soc London 434 1991) 30:299–303
Mouri H, Hori A (2010) Two-point velocity average of turbulence: Statistics and their implications. Phys Fluids 22:115110
O'Neil J, Meneveau C (1997) Subgrid-scale stresses and their modelling in a turbulent plane wake. J Fluid Mech 349:253–293
Praskovsky AA, Gledzer E, Karyakin MY, Zhou Y (1993) The sweeping decorrelation hypothesis and energy-inertial range interaction in high Reynolds number flow. J Fluid Mech 248:493–511
Reynolds WC, Hussain AKMF (1972) The mechanics of an organised wave in turbulent shear flow. J Fluid Mech 54:263–288
Sreenivasan KR, Antonia RA (1997) The phenomenology of small-scale turbulence. Ann Rev Fluid Mech 29:435–472
Sreenivasan KR, Dhruva B (1998) Is there a scaling in high Reynolds-number turbulence? Prog Theor Phys 130:103
Tennekes H (1975) Eulerian and Lagrangian time microscales in isotropic turbulence. J Fluid Mech 67:561–567
Thiesset F, Danaila L, Antonia RA (2013) Dynamical effect of the total strain induced by the coherent motion on local isotropy in a wake. J Fluid Mech 720:393–423
Townsend AA (1956) The structure of turbulent shear flows. Cambridge University Press
Yaglom AM (1949) On the local structure of a temperature field in a turbulent flow. Dokl Akad Nauk SSSR 69:743
Zhou T, Zhou Y, Yiu MW, Chua LP (2003) Three-dimensional vorticity in a turbulent cylinder wake. Exp Fluids 35:459–471
Zhou Y, Antonia RA (1995) Memory effects in a turbulent plane wake. Exp Fluids 19:112–120

# Controlling the Large-Scale Motions in a Turbulent Boundary Layer

**I. Marusic, K. M. Talluru and N. Hutchins**

**Abstract** In this paper we consider a strategy to manipulate the large-scale structures in wall-bounded turbulent flows, which have recently been shown to be a key mechanism for modulating levels of the skin-friction drag. For this, we use a rectangular wall-normal jet to target the large-scale structures as detected by an upstream spanwise array of skin-friction sensors. A second spanwise array of sensors, located downstream of the jet, records any modifications to the large-scale structure. In addition, a traversing hotwire probe is mounted above the second spanwise array of sensors to study the effects across the depth of boundary layer. It is found that the jet is able to create a low-speed region and when targeted on a high-speed structure changes the associated footprint at the wall.

**Keywords** Large-scale structures · Skin-friction · Turbulent boundary layer · Wall-normal jet · Flow-control

## 1 Introduction

Over the past several decades, there has been growing understanding that turbulent boundary layers, despite their obvious randomness, possess certain recurrent features, commonly termed as 'coherent structures', and recent studies considerably expanded this view (Adrian 2007). Recent studies of high-Reynolds-number flows in pipe, channel and flat-plate boundary layers have revealed the presence of very large-scale motions (VLSMs, also referred to as superstructures) in the logarithmic regions of turbulent boundary layers, see Kim and Adrian (1999), Tomkins and Adrian (2003) and Hutchins and Marusic (2007a).

I. Marusic (✉) · K. M. Talluru · N. Hutchins
Department of Mechanical Engineering, The University of Melbourne,
Victoria 3010, Australia
e-mail: imarusic@unimelb.edu.au

Y. Zhou et al. (eds.), *Fluid-Structure-Sound Interactions and Control*,
Lecture Notes in Mechanical Engineering, DOI: 10.1007/978-3-642-40371-2_2,

Hutchins and Marusic (2007b) used a rake of 10 hotwires, and from the time-series data, they reported that these structures extend to large streamwise lengths and substantially meander in the spanwise direction. In addition, they inferred that the larger outer region motions extend down to the wall and modulate the flow in the inner layer, including the buffer layer. Such interactions were quantified by Mathis et al. (2009) and formed the basis of inner–outer motion interaction model by Marusic et al. (2010). Using the model, one could predict the statistics of the streamwise velocity fluctuations in the near-wall region from the large-scale velocity signal in the logarithmic region of a given flow. This idea was further strengthened in other recent studies by Chung and McKeon (2010) and Guala et al. (2011) and Hutchins et al. (2011). They reported methodologies describing how the large-scale features modulate the small-scale fluctuations near the wall. Through conditional average results, Hutchins et al. (2011) observed that associated with the low-skin-friction event, there is reduced small-scale activity near the wall switching to a regime of more intense small-scale fluctuations farther away from the wall.

Using the large-scale shear-stress footprint at the wall, Hutchins et al. (2011) conducted studies using a spanwise array of surface-mounted skin-friction sensors together with a traversing hotwire probe. From such experiments, they obtained a three-dimensional conditionally averaged view of the large-scale superstructures in a turbulent boundary layer. The conditional mean results indicated the presence of a forward-leaning low-speed and high-speed structures above low and high-skin-friction events, respectively, and with anti-correlated regions flanking them.

Many of the studies mentioned above rely only on streamwise velocity information. However, Hutchins and Marusic (2007b) identified counter-rotating roll-like structures associated with the largest scale events using a DNS channel flow database ($\mathrm{Re}_\tau = 950$). Dennis and Nickels (2011) computed various conditional averages from high-speed PIV measurements and showed a similar organization in the spanwise vicinity of large-scale structures. Also a study conducted in the atmospheric boundary layer by Hutchins et al. (2012) revealed identical results in the instantaneous velocity vector fields using linear stochastic estimation (LSE) technique.

In a more recent study conducted by Beresh et al. (2011), the focus was switched to wall pressure field from that of velocity field. Interestingly, they observed similar large-scale motions in the wall-pressure fluctuations beneath a supersonic turbulent boundary layer and attributed that such motions are the most possible explanation of the observed low-frequency pressure fluctuations in flight-vehicle vibrations.

In the past, Savill and Mumford (1988) attempted the use of large-eddy break-up (LEBU) devices and reported a significant drag reduction downstream of the LEBUs. They explained it in terms of interactions between the wake from the LEBUs and the large-scale motions in the outer layer of the boundary layer. However, such an approach suffered due to the form drag associated with the devices, diminishing the benefit in the skin-friction drag. Here, we are attempting to eliminate such drawbacks by using a non-intrusive wall-normal jet. Low-Reynolds-number

studies of a jet in cross-flows by Haven and Kurosaka (1997) revealed that a streamwise vortex pair is generated and that the strength of the pair depends on the aspect ratio of the jet. In this investigation, we are using a rectangular jet due to its high-aspect-ratio geometry.

Putting together the wall footprint of the large-scale structures, their modulating effect on the near-wall small-scale fluctuations, their associated streamwise roll modes, and their influence on the pressure fluctuations, it is possible to construct a well-targeted control scheme. With this intent, we are using a wall-normal jet that can generate a roll mode that acts as a retrograde to the naturally occurring roll modes associated with the large-scale structures in a turbulent boundary layer and thereby affect the acoustic noise and turbulence levels across the depth of the boundary layer.

## 2 Experimental Setup

Experiments were carried out in the high-Reynolds-number boundary layer wind tunnel (HRNBLWT) at the University of Melbourne. This open-return blower wind tunnel has dimensions of $27 \times 2 \times 1$ m with a nominally zero pressure gradient. Further details of the wind tunnel are given in Kulandaivelu (2012). In this current investigation, measurements are conducted in a turbulent boundary layer that has developed over a distance of 21 m from the trip. At a free-stream velocity of 20 m/s, the boundary layer thickness $(\delta)$ at the measuring station is 0.326 m. With the friction velocity, $U_\tau = 0.635$ m/s, a Reynolds number close to 14,000 is obtained in these experiments. Here, Reynolds number is defined as $\mathrm{Re}_\tau = U_\tau \delta / \nu$, where $U_\tau$ is the friction velocity, $\delta$ is the boundary layer thickness, and $\nu$ is the kinematic viscosity of air.

Figure 1 shows the experimental setup. The measurement array consists of a single hotwire attached to a moving traverse, two spanwise arrays of flush-mounted skin-friction sensors, and a rectangular jet. The two spanwise arrays are located $2\delta$ apart in the streamwise direction, with the jet positioned in between the two arrays. Each of the spanwise array consists of 9 skin-friction sensors, covering a spanwise domain of $0.64\delta$, with a spanwise resolution $\Delta y = 0.026$ m or $0.08\delta$. These sensors are Dantec 55R47 glue-on type sensors and are operated in constant-temperature mode using AA labs AN1003 anemometer with overheat ratio (OHR) set to 1.05.

The hotwire probe is mounted with its sensing element 550 mm upstream of the leading edge of the traversing sting. To minimize flow disturbance, the sting has an airfoil profile resembling NACA0016 with chord length of 180 mm. The hotwire prong has a spacing of 1.25 mm with 2.5-micron-diameter Wollaston platinum wire soldered between the prongs. Its etched length is 0.5 mm, keeping length to diameter ratio of 200, in accordance to the recommendations of Ligrani and Bradshaw (1987). It is operated with a OHR of 1.8 using an in-house-developed Melbourne University Constant Temperature Anemometer (MUCTA). The

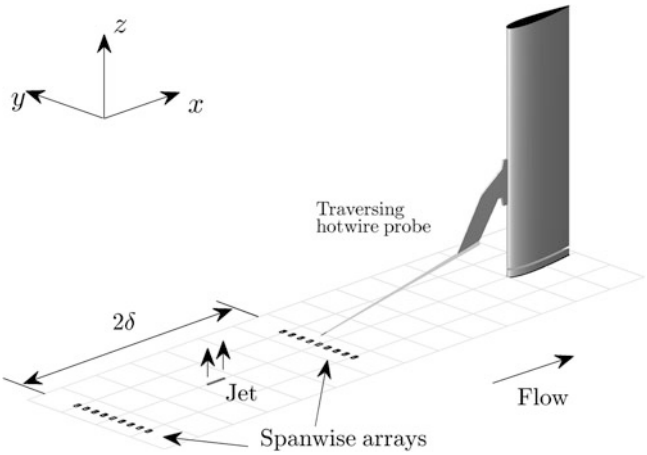


**Fig. 1** Schematic of experimental setup

dimensions, specifications, and relative positions of the skin-friction sensors in both the arrays are similar to the configuration used by Hutchins et al. (2011). Throughout this chapter, $x$, $y$, and $z$ represent the streamwise, spanwise, and wall-normal directions with $u$, $v$, and $w$ denoting the respective fluctuating velocity components.

The hotwire is calibrated in situ against a Pitot-static tube at 12 different free-stream velocities ranging from 0 to 25 m/s, while the hot-film sensors are calibrated using the friction velocity values at the above velocities obtained from previously reported results at the same location. Any errors in hot-film calibration will have only minimal effect on the analysis presented here since these sensors are merely used as low/high-skin-friction detection sensors.

## 3 Off-line Control Scheme

As a first step toward understanding the interactions of jet with the large-scale structures, an off-line control strategy is investigated. In these experiments, no real-time active controller is implemented, but the jet is periodically fired with fixed parameters, and during post-processing, the 'control' strategy is emulated in a conditional sense. The jet velocity is set at 10 m/s and is actuated for 0.1 s in a duty cycle of 0.4 s, while all the skin-friction sensors and hotwire are simultaneously sampled. In the post-processing stage, selective parts of the signal from the sensors are collected, where the jet has truly targeted a large-scale structure, as illustrated in Fig. 2. In this figure, the three signals, filtered upstream skin-friction signal, the jet, and the hotwire are shown with appropriate time shifts. Here, the length of hotwire signal enclosed by two dotted vertical lines is an example of

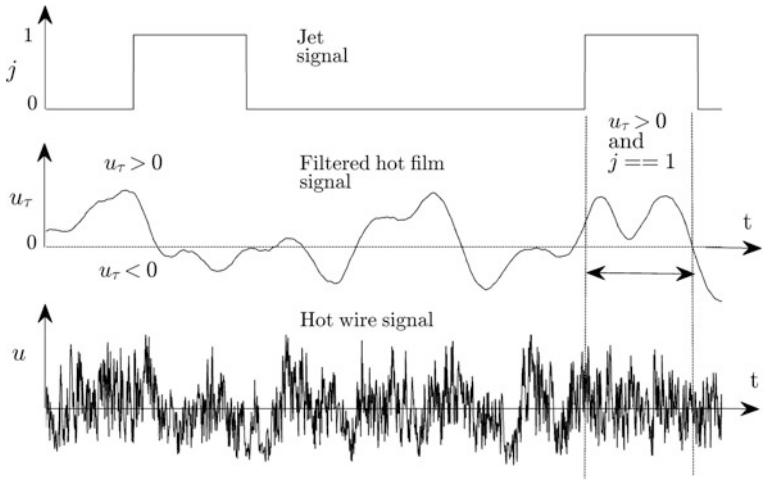


**Fig. 2** Off-line-simulated control scheme

large-scale high-skin-friction signal ($u_\tau > 0$) that is being targeted by the jet, and the effect is studied using the downstream hotwire signal.

## 4 Conditional Events

The interaction of the jet with the large-scale skin-friction fluctuations and the streamwise velocity fluctuations can be studied by computing conditional averages from the skin-friction sensors and the hotwire probe conditioned on the passage of a high-skin-friction event and also targeted by the jet after a certain time delay. The signal from the upstream wall shear-stress sensor is used to detect the structures convecting above it. This signal is filtered using a low-pass Gaussian filter of length 0.5 $\delta$ to get a signature of the large-scale skin-friction events. Using this large-scale signal, a high-skin-friction event is identified when the fluctuating friction velocity is greater than zero, and conversely, a value below zero indicates a low-skin-friction event. All the sensors including the control signal of the jet are simultaneously sampled. The conditional average is defined as

$$u|_{\mathrm{hj}}\,(\Delta t, \Delta y, z) = \langle u(t, y, z) | u_\tau(t - \Delta t, y - \Delta y) > 0 \,\&\, j(t - \Delta t + \Delta \mathrm{T}, y - \Delta y) = 1 \rangle \tag{1}$$

is a function of the wall-normal, spanwise, and temporal separation. Using Taylor's hypothesis with $x = -U_c\, t$, it can be converted to a function of all three spatial coordinates

$$u|_{\mathrm{hj}}(\Delta x, \Delta y, z) = \langle u(x, y, z) | u_\tau(x - \Delta x, y - \Delta y) > 0 \,\&\, j(x - \Delta x + \Delta X, y - \Delta y) = 1 \rangle \tag{2}$$

In these equations, $u$ is the streamwise velocity fluctuation and $u_\tau$ is the friction velocity fluctuation, $j$ is the binary control signal of the jet, $\Delta X$ is the physical separation between the jet and the downstream array, and $U_c$ is the convection velocity. In all the figures presented in this paper, $x = 0$ represents the streamwise location of upstream skin-friction sensor array, $x = 1\,\delta$ is the location of the jet, and $x = 2\,\delta$ is the location of the hotwire probe and the downstream array of sensors.

## *4.1 Two-Dimensional Conditional View*

Figure 3a shows the two-dimensional skin-friction fluctuations from the downstream array of hot-film sensors when conditioned on a positive skin-friction fluctuation on upstream sensor 5. A region of elongated positive skin-friction fluctuations is flanked on both sides by anti-correlated behavior with a spanwise separation of $0.7 - 0.8\,\delta$ between two positively correlated regions. Such behavior has been previously reported by Hutchins and Marusic (2007a), but in the current study, it is also possible to look at such a conditional high-skin-friction event when targeted by a jet, which is shown in Fig. 3b. It is evident that the jet has modified the elongated positive region along the line of symmetry at $\Delta y = 0$, but appears to have enhanced the positive skin-friction fluctuations on both sides of the centerline. However, merely analyzing the effect of the jet on the skin-friction footprint can be misleading. To resolve this, it is useful to look at the three-dimensional conditional view of the velocity fluctuations, which will be discussed in the following section.

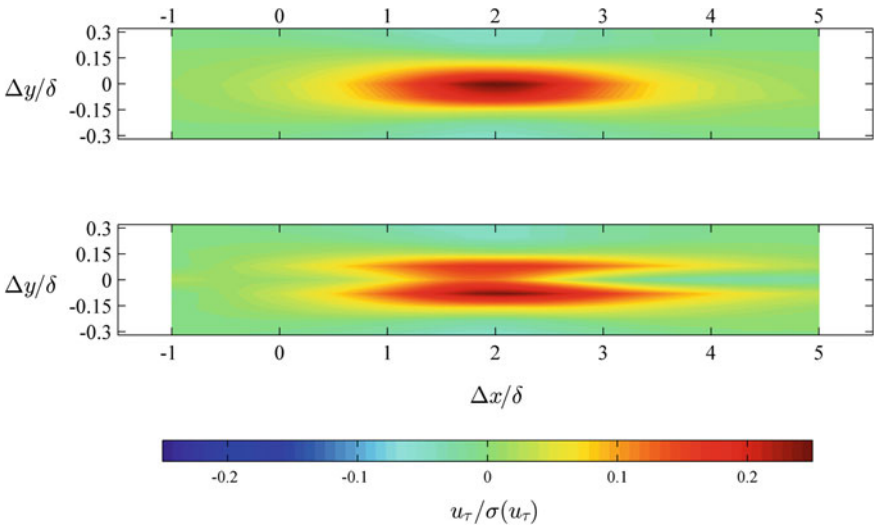


**Fig. 3** Isocontours of skin-friction fluctuations conditionally averaged on a high-skin-friction event (**a**) unmodified flow (**b**) simulated off-line control scheme

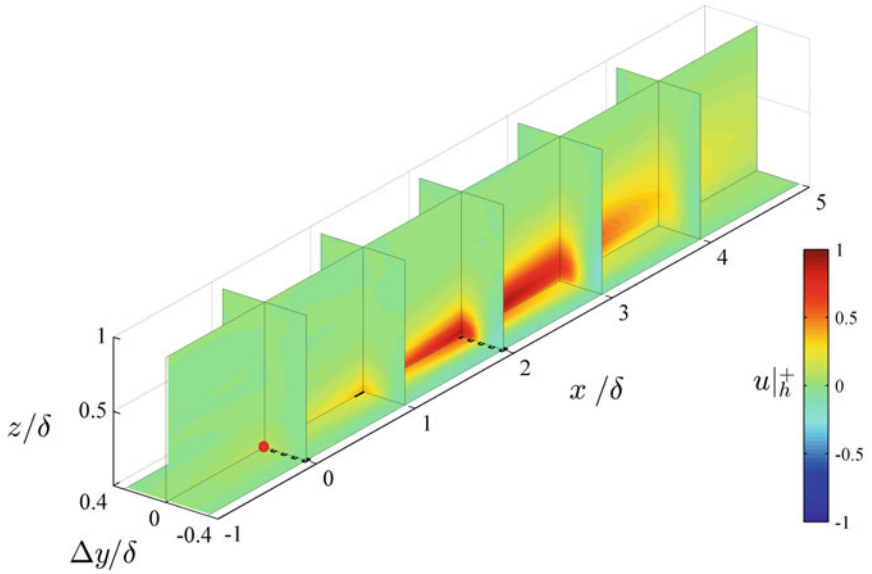


**Fig. 4** Isocontours of streamwise velocity fluctuations conditionally averaged on a high-skin-friction event

## *4.2 Three-Dimensional Conditional View*

Besides looking at the skin-friction fluctuations at the wall, the simultaneous time-series measurements from hotwire and skin-friction sensors allowed us to compute a conditionally averaged view of velocity fluctuations that occur in two cases: (1) unmodified and (2) modified high-skin-friction events. To build a three-dimensional conditional view, several experiments are conducted by positioning the jet in different spanwise locations in line with one of the nine skin-friction sensors. The data from these experiments have been used to compute the conditional averages in different spanwise planes according to Eq. 2, and by putting together all the data in such planes, a three-dimensional conditional view was built.

Figure 4 shows the isocontours of streamwise velocity fluctuations during an unmodified high-skin-friction event on upstream sensor 5 (shown as red dot), in different $x$–$y$, $y$–$z$, and $y$–$z$ planes, $x/\delta = 0, 1, .., 4$, $\Delta y/\delta = 0$, and $z/\delta = 10^{-4}$. The figure reveals an inclined, forward-leaning, high-speed structure extending over 3 $\delta$ in the streamwise direction. Such an observation is totally consistent with recent studies in the literature, see for example Hutchins et al. (2011). Flanking the high-speed region in the center, there are two low-speed regions in the spanwise

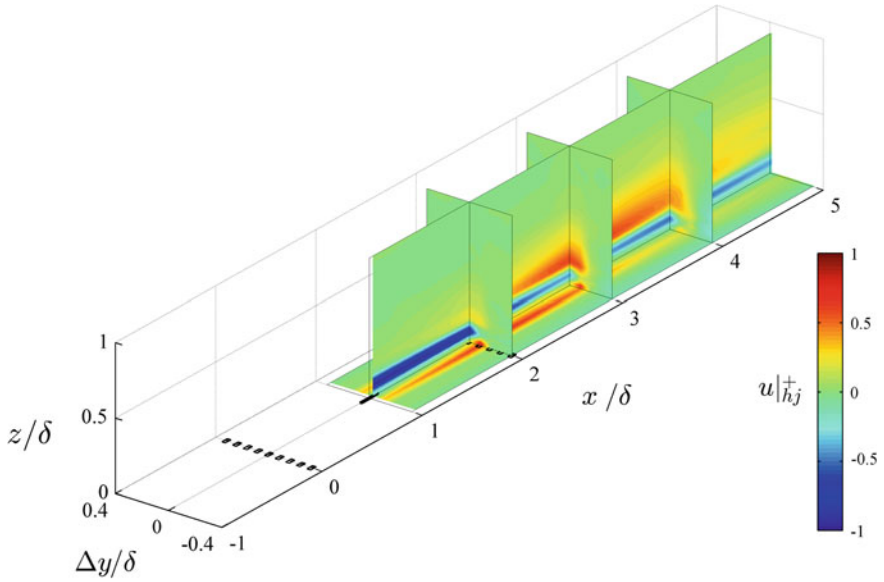


**Fig. 5** Isocontours of streamwise velocity fluctuations conditionally averaged on a high-skin-friction event and targeted by a jet

direction, separated by a distance of $0.7 - 0.8\,\delta$, similar to the result observed in the conditional wall shear-stress fluctuations in Fig. 3.

The motivation in this study is to modify the conditional high-skin-friction events using a wall-normal jet. As explained previously, a control scheme is simulated in the post-processing stage, and the results from the analysis are presented in Figs. 5 and 6. Note that in these figures, only the data behind the jet's location $(x/\delta = 1)$ are presented as Taylor's hypothesis is no longer valid upstream of the jet's location. Figure 5 shows that the jet has penetrated to a depth of $0.1\delta$ into the boundary layer, reducing the intensity of velocity fluctuations in the central plane corresponding to $\Delta y = 0$. However, its effect seems to be very localized with signs of increased skin-friction fluctuations on both sides.

To illustrate this better, the same result is plotted in Fig. 6 in three cross-planes at $x/\delta = 2, 3, 4$. Another inference that can be made here is that the jet has created a pair of streamwise roll modes, represented as circular arrows in the figure. Although this study only measured the streamwise component of the modified flow, the result seems to point toward this case. However, the scale of such roll modes is considerably small compared to the indicative naturally occurring roll modes, which are of the size $0.5\delta$, as reported by Talluru et al. (2012).

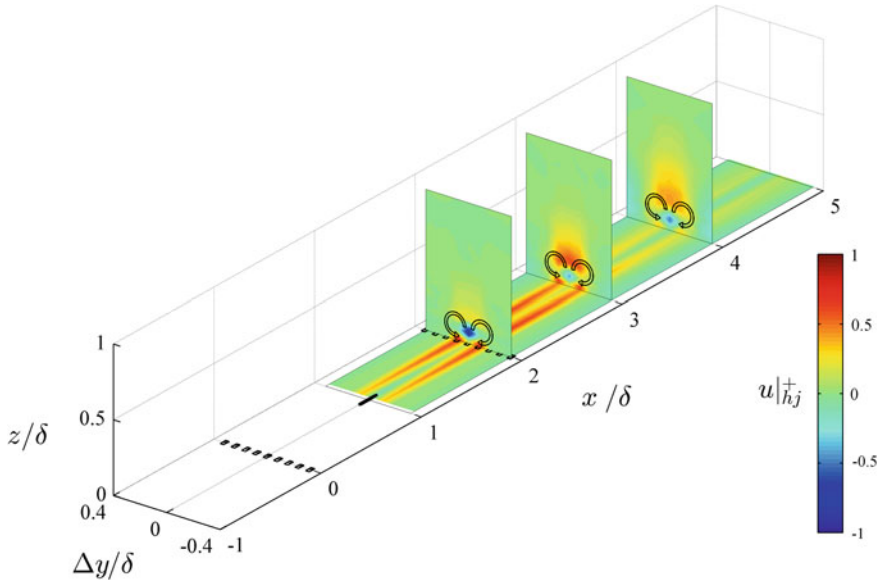


**Fig. 6** Isocontours of streamwise velocity fluctuations conditionally averaged on a high-skin-friction event shown in three streamwise cross-planes

## 5 Conclusions

Two spanwise arrays of glue-on hot-film sensors along with a wall-normal jet and a traversing hotwire probe are used to study the interaction of a jet with the large-scale structures that populate the logarithmic region of a turbulent boundary layer. Initial experiments were conducted with a periodic actuation of the jet, and the effects are studied in a conditional sense to emulate the behavior of an effective large-scale, real-time control scheme.

The conditional results show that the jet is able to generate a low-speed region along the symmetric plane, affecting the large-scale high-speed structure. However, it also appears to have increased the positive velocity and skin-friction fluctuations on both sides of the symmetric plane. An initial inference is made here; the jet actuation has induced streamwise counter-rotating roll modes into the flow; however, this observation has to be further justified by looking at the spanwise and wall-normal components of the velocity. Finally, the effect produced by the jet seems to be too localized and small compared to the scale of the large-scale high-skin-friction events and their associated streamwise roll modes. As a more general concluding statement, these results show prospects of using a wall-normal jet to target the large-scale control schemes when implemented at the correct scale.

## References

Adrian RJ (2007) Hairpin vortex organization in wall turbulence. Phys Fluids 19:041301

Beresh S, Henfling JF, Spillers RS, Pruett B (2011) Improved measurements of large-scale coherent structures in the wall pressure field beneath a supersonic turbulent boundary layer. In: 41st AIAA fluid dynamics conference and exhibit

Chung D, McKeon BJ (2010) Large-eddy simulation of large-scale structures in long channel flow. J Fluid Mech 661:341–364

Dennis DJC, Nickels TB (2011) Experimental measurement of large-scale three-dimensional structures in a turbulent boundary layer. Part 1: vortex packets. J Fluid Mech 673:180–217

Guala M, Metzger M, McKeon BJ (2011) Interactions across the turbulent boundary layer at high Reynolds number. J Fluid Mech 666:573–604

Haven BA, Kurosaka M (1997) Kidney and anti-kidney vortices in cross flow jets. J Fluid Mech 352:27–64

Hutchins N, Monty JP, Ganapathisubramani B, Ng HCH, Marusic I (2011) Three dimensional conditional structure of a high-Reynolds-number turbulent boundary layer. J Fluid Mech 673: 255–285

Hutchins N, Marusic I (2007a) Evidence of very long meandering features in the logarithmic region of turbulent boundary layers. J Fluid Mech 579:1–28

Hutchins N, Marusic I (2007b) Large-scale influences in near-wall turbulence. Phil Trans R Soc A 365:647–664

Hutchins N, Chauhan K, Marusic I, Monty J, Klewicki J (2012) Towards reconciling the large-scale structure of turbulent boundary layers in the atmosphere and laboratory. Bound-Layer Meteorol 1–34

Kim KC, Adrian RJ (1999) Very large-scale motion in the outer layer. Phys Fluids 11(2):417–422

Kulandaivelu V (2012) Evolution of zero pressure gradient turbulent boundary layers from different initial conditions. PhD Thesis, The University of Melbourne, Australia, 2012

Ligrani PM, Bradshaw P (1987) Spatial resolution and measurement of turbulence in the viscous sublayer using subminiature hot-wire probes. Exp Fluids 5:407–417

Marusic I, Mathis R, Hutchins N (2010) Predictive model for wall-bounded turbulent flow. Science 329(5988):193–196

Mathis R, Hutchins N, Marusic I (2009) Large-scale amplitude modulation of the small-scale structures in turbulent boundary layers. J Fluid Mech 628:311–337

Savill AM, Mumford JC (1988) Manipulation of turbulent boundary layers by outer-layer devices: skin-friction and flow-visualization. J Fluid Mech 191:389–418

Talluru KM, Morrill-Winter C, Ebner R, Hutchins N, Klewicki J, Marusic I (2012) Three dimensional conditional structure of large-scale structures in a high Reynolds number turbulent boundary layer. In: Proceedings of 18th Australasian Fluid Mechanics Conference, Launceston, Australia

Tomkins CD, Adrian RJ (2003) Spanwise structure and scale growth in turbulent boundary layers. J Fluid Mech 490:37–74

# Triangular Tabs for Supersonic Jet Mixing Enhancement

**E. Rathakrishnan**

**Abstract** The mixing promoting capability of right-angle triangular tab with sharp and truncated vertex has been investigated by placing two identical tabs at the extremities of an exit diameter of a Mach 2 axi-symmetric nozzle. The mixing promoting efficiency of these tabs have been quantified in the presence of adverse and almost zero pressure gradients. It is found that, at all levels of expansion of the present study though the core length reduction caused by both the tabs are appreciable, the mixing caused by the truncated tab is superior. The mixing promoting efficiency of the truncated tab is found to increase with increase of nozzle pressure ratio (that is, decrease of adverse pressure gradient). For all the nozzle pressure ratios of the present study, the core length reduction caused by the truncated tab is more than 95 %, with a maximum of 99 %, at NPRs 7 and 8. The present results clearly show that the mixing promoting capability of the tab is the best when the jet is almost correctly expanded (that is with almost zero pressure gradient).

## List of symbols

| | |
|---|---|
| NPR | Nozzle pressure ratio ($p_{0s}/p_a$) |
| $p_{0s}$ | Settling chamber pressure |
| $p_{0t}$ | Pitot pressure in the jet field |
| $p_e$ | Nozzle exit pressure |
| $p_a$ | Atmospheric pressure |
| $p_b$ | Backpressure ($p_a$) |
| $R$ | Distance along the radial direction of the uncontrolled jet |
| $Y$ | Coordinate normal to the tabs |
| $z$ | Coordinate along the tabs |

E. Rathakrishnan (✉)
Department of Aerospace Engineering, Indian Institute of Technology Kanpur, Kanpur, India
e-mail: erath@iitk.ac.in

Y. Zhou et al. (eds.), *Fluid-Structure-Sound Interactions and Control*,
Lecture Notes in Mechanical Engineering, DOI: 10.1007/978-3-642-40371-2_3,

## 1 Introduction

Jet control with tabs is an active research area, finding a lot of application. A concise compilation of the literature associated with jet control is recently compiled by Rathakrishnan (2010). From this survey it is evident that, for an efficient mixing of the mass entrained by the large scale vortices, at the boundary of a free jet, an appropriate proportion of mixing promoting vortices need to be introduced into the jet flow, to ensure rapid mixing. Indeed rapid mixing of the jet issuing from the engine nozzle with the cool air mass of the atmosphere, to which the jet is discharged, is essential to ensure that the length of the hot plume at the nozzle exit is reduced to as short as possible to minimize the infrared signature, resulting in high stealth capability for missiles. This kind of rapid mixing of the hot gases with the cold ambient air will results in the reduction of base heating, which is highly desirable for launch vehicles. Because of this kind of high-tech applications, large quantum of research has been done on jet mixing. However, until 2009 the school of thought was that the length of the mixing promoting tab should be within the boundary layer. This hypothesis is based on the vortex flow physics, namely that a vortex should have high vorticity and find large residential time to promote mixing efficiently. But in 2009, in his work on experimental studies on the limiting tab (Rathakrishnan 2009), Rathakrishnan demonstrated that the tab need not be within the boundary layer and indeed, the tab length can extend up to the nozzle radius. Following this Chiranjeevi Phanindra and Rathakrishnan (2010) showed that corrugations introduced at the tab edges result in a better mixing, owing to the generation of mixing promoting vortices of mixed size. However, they studied only rectangular tab with and without corrugation. Also, they studied only rectangular corrugation. Combining all these concepts, Arun Kumar and Rathakrishnan (2013a, b, c) studied triangular tabs and found that the triangular tabs shedding vortices of continuous variation in size is a better mixing promoter than tabs of rectangular geometry. But this investigation is with isosceles triangular tabs. Therefore, even though these tabs shed vortices of continuous variation in size, the vortices shed from the opposite edges at a given height from the tab base are of identical size. To improve the mixing process by introducing vortices of continuously varying size, even from the opposite edges at a given height, right-angle triangular tabs are investigated in the present study. In addition to right-angle triangular tabs, with sharp and truncated vertex, rectangular tabs were also studied for comparison.

## 2 Experimental Details

The experiments were conducted in the open jet facility at the high speed aerodynamics laboratory, Indian Institute of Technology Kanpur, India (Rathakrishnan 2009). The experimental model used in the present investigation is a Mach 2.0

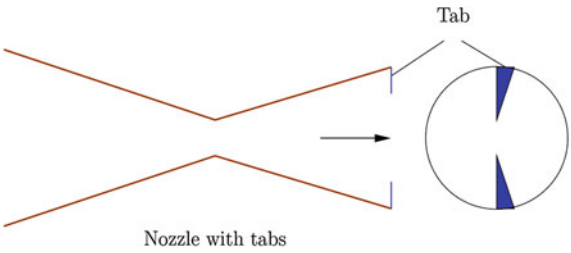


**Fig. 1** Schematic representation of nozzle and placement of tabs at the nozzle exit

axi-symmetric convergent-divergent nozzle of semi-divergence angle 7°, made of brass. The throat diameter of the nozzle is 10 mm and the exit diameter is 13 mm. The Reynolds numbers of the Mach 2.0 jet issuing out of the nozzle, based on nozzle exit diameter are 712,300 and 1,660,410, respectively, for the minimum and maximum NPRs of 4 and 8 of the present investigation. Tabs were made of 1 mm thick brass strips. The schematic diagram of the tabs placed at the nozzle exit is shown in Fig. 1.

The length of the tabs was kept constant at 4 mm, for both triangular and rectangular shapes. Schematic sketch of the tabs are shown in Fig. 2. The blockage offered by the two identical tabs placed at the nozzle exit, intruding the flow, with respect to the nozzle exit area, in the present investigation is 5 %.

The pressure in the jet field was measured using a pitot tube of 0.4 mm inner diameter and 0.6 mm outer diameter, mounted on a rigid three-dimensional traverse, following the same procedure used by Chiranjeevi and Rathakrishnan (2010). The waves prevailing in the supersonic jet core were visualized using a shadowgraph system with a helium spark arc-light source in conjunction with a concave mirror. The shadowgraph images were recorded using a still camera.

The settling chamber pressure during the experiments of present investigation was maintained within ±2 %, for all the NPRs studied. The movement of the pitot probe mounted on the traverse had a resolution of ±0.1 mm, in the linear translation. The repeatability of the pressure measurements was found to be within ±3 %.

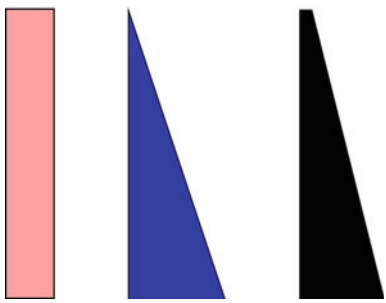

**Fig. 2** Schematic representation of *rectangular tab*, *right-angle triangular tab* with *sharp and truncated vertex*

## 3 Results and Discussion

It is important to note that, in a supersonic flow, the pitot probe measures the total pressure behind the bow shock that stands ahead of the probe nose and not the actual total pressure. If the actual total pressure is required, one has to correct the measured pressure for the pressure loss across the shock. The jet core is wave dominated and the Mach number in the core varies from point to point, and also the waves in different shock cells are of different strength. Therefore, it is difficult to correct the measured pitot pressure for shock loss. Hence, the results in supersonic regions should be considered only as qualitative and are good enough for comparative purposes (Rathakrishnan 2009, 2010).

### *3.1 Centerline Pitot Pressure Decay*

It is well established that the centerline pitot pressure decay is an authentic measure to quantify the jet core length, characteristic decay and far-field decay of free jet (Rathakrishnan 2010). For a supersonic jet, the jet core is the axial extent, from the nozzle exit, up to which the supersonic flow prevails or the axial extent at which the characteristic decay begins. The aim of the present investigation is to quantify the mixing promoting efficiency of right-angled triangular tabs with sharp and truncated vertex. The centerline decay of the jet, (that is, the reduction in core length caused by the tabs) can be taken as a measure, to quantify this feature. That is, fast decay implies better mixing.

The centerline decay of uncontrolled jet, and jet controlled with sharp and truncated triangular tabs, are compared in Fig. 3, for NPR4. The centerline pressure decay caused by rectangular tabs is also shown in this plot. For Mach 2 jet NPR4 is an overexpanded state, with an overexpansion level of about 49 % ($pe/pa = 0.511$). Therefore, at the nozzle exit there will be an oblique shock cone positioned, leading to the compression of the flow at a lower pressure at the nozzle exit to come to an equilibrium with the backpressure, namely the atmospheric pressure to which the jet is discharged. The oblique shocks of opposite family from the extremities of a diameter at the nozzle exit, would intersect at the jet axis and propagate towards the jet boundary. Thus, the maximum deceleration encountered by a overexpanded supersonic jet exiting the nozzle would be along the jet axis. The first pressure minimum in the centerline pressure decay plot is the point just ahead of the first shock cross-over point.

At NPR4 this point is found to be around 1.3D, downstream of the shock cross-over point the flow is forced to become subsonic, owing to the added strength of two oblique shocks, even though individual shocks are weak in nature. The subsonic flow downstream of the first shock cross-over point accelerates due to the flow of momentum from the higher momentum zone around the jet axis, where the flow continues to be supersonic even after passing through the weaker oblique

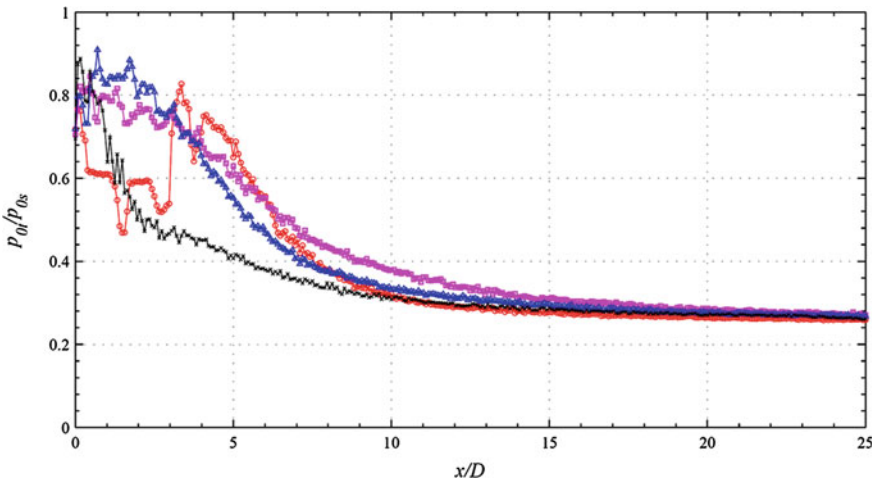


**Fig. 3** Centerline pressure decay of Mach 2.0 jet at NPR4 (overexpanded). *Red circle* uncontrolled jet, *pink rectangle* jet controlled with rectangular tabs, *blue triangle* jet controlled with right-triangular tabs, and *asterisk* jet controlled with truncated right-triangular tabs

shock. The accelerated subsonic flow downstream of the shock cross-over point, after reaching sonic speed (indicated by the pitot pressure maximum), accelerates further to supersonic level up to the second shock cross-over point. This process continues up to the end of the supersonic core, which is found to be around 4D, for the uncontrolled jet. The characteristic decay of the uncontrolled jet continues up to around 20D, for NPR4. For the rectangular tab, the core length is only marginally shorter than the uncontrolled jet core. But for the sharp vertex triangular tabs, the core length comes down to 3D, also the jet becomes fully developed as early as 15D. When the vertex of the triangular tab is truncated, the core length drastically comes down to about 0.5D, which corresponds to a reduction of about 87 %. Further, the characteristic decay for the truncated triangular tab is the steepest and the jet becomes fully developed as early as 10D. From these results it is obvious that, the mixing promoting performance of truncated triangular tab is the best among the tabs considered. A closer look into the flow physics of the momentum transfer process associated with the small scale vortices shed by the truncated tab would explain the reason for its mixing promoting superiority. It is well known that the vortices shed from an object is proportional to the half-width of the object normal to the stream direction (Rathakrishnan 2010).

For the rectangular tab the half-width is uniform all along the tab length, therefore the tab would shed mixing promoting vortices of only uniform size all along its edges, excepting the tip where there are two sharp corners and the vortices shed from the flat tip end and side wall are of different size and interact intensely. Also, the vortices shed from the tip would be of transverse type, whereas those shed from the edges are normal type. Therefore, the uniform vortices shed by the rectangular tab would travel some downstream distance before becoming

active in promoting mixing. Whereas, the triangular tab owing to its geometry would shed vortices of continuously varying size from its edges. An important feature to be noted is that the geometry of right-angle triangular tab is totally different from that of an isosceles triangular tab, recently studied by Arun Kumar and Rathakrishnan (2013a). The isosceles triangular tab, though capable of shedding vortices of continuously varying size along its edges, at every height from the base would be of identical size, though of opposite family. But, the mixing promoting vortices shed from the right-angle triangular tab would be of different size at all height, in addition to being of opposite family. This might be the primary reason for the intense interaction of vortices shed by the right-angle triangular tab leading to greatly enhanced mixing. Another important feature to be noted is that, near the sharp vertex tip, though the vortices shed are of different size and opposite family, their closer proximity would make them to interact intensely leading to loss of vorticity content. This might be the reason for lesser mixing promoting efficiency of the sharp vertex triangular tab compared to the truncated triangular tab. However, the mixing promoting efficiency of sharp triangular tab is higher than the rectangular tab due to the mixed size of vortices shed from the triangular tab. When the vertex is truncated, even at the tip, vortices of opposite family do not interact among themselves. This might be an advantage because almost entire vorticity content available with the mixing promoting vortices would be used for mixing promotion. This can be regarded as the primary reason for the better efficiency of the triangular tab with truncated vertex than the sharp vertex.

The centerline decay results for NPR5 are shown in Fig. 4. At NPR5 also Mach 2 jet is overexpanded, but with a reduced overexpansion level of only about 36 %. Therefore, the oblique shocks at the nozzle exit would be weaker than those for

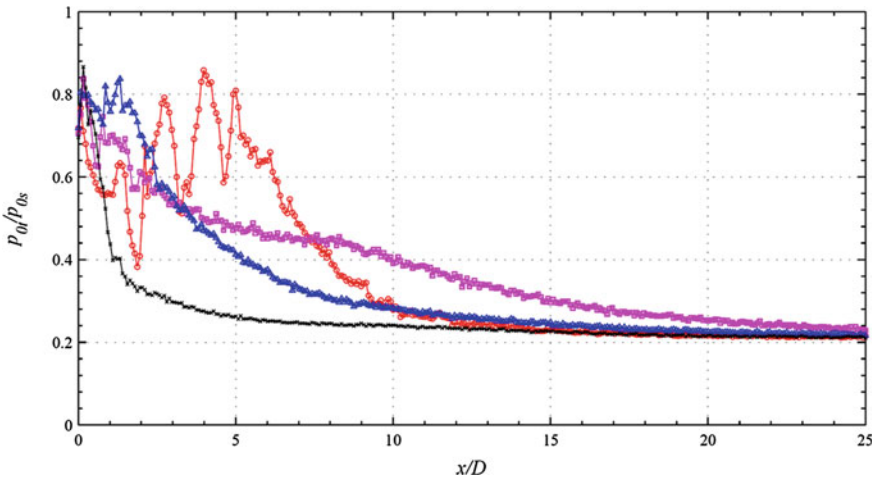


**Fig. 4** Centerline pressure decay of Mach 2.0 jet at NPR5 (overexpanded). *Red circle* uncontrolled jet, *pink rectangle* jet controlled with rectangular tabs, *blue triangle* jet controlled with right-triangular tabs, and *asterisk* jet controlled with truncated right-triangular tabs

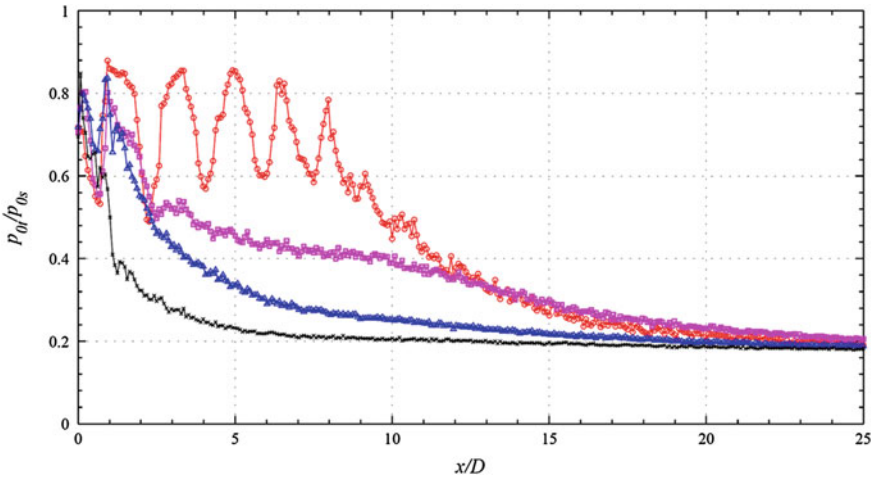


**Fig. 5** Centerline pressure decay of Mach 2.0 jet at NPR6 (overexpanded). *Red circle* uncontrolled jet, *pink rectangle* jet controlled with rectangular tabs, *blue triangle* jet controlled with right-triangular tabs, and *asterisk* jet controlled with truncated right-triangular tabs

NPR4. Due to the presence of weaker shocks, the pressure loss encountered by the flow in the near-field at NPR5 will be considerably less than that at NPR4. It is seen that the core length of the uncontrolled jet is 6D. At NPR5, the mixing caused by rectangular tab is significantly higher than at NPR4. The core length of the rectangular tab is about 2.5D. For the sharp triangular tab the core length is about 0.5D, whereas for the truncated triangular tab the core length is as short as about 0.2D. Further, for the truncated triangular tab, the flow is fully developed at around 6D itself. The characteristic decay is also much faster than that at NPR4. Thus, at NPR5 also the truncated triangular tab performance is the best among the tabs studied in the present investigation.

At NPR6, as seen from Fig. 5, the core length for the uncontrolled jet is about 10D. Whereas the core length for the rectangular, sharp vertex triangular and truncated vertex triangular tabs, respectively, are 3.5D, 1.2D and 1D. For NPR6 also the jet has become fully-developed at 6D, for the truncated triangular tab.

With increase of NPR to 7, the number of shock-cells is found to increase considerably, which is typical for a free jet. The core length has increased to about 14D, as seen in Fig. 6. At NPR7 the Mach 2 jet is with a marginal overexpansion level of about 10 %. For this overexpansion level also, the mixing promoting efficiency of all the tabs are found to be appreciable. But among the tabs, the mixing caused by truncated triangular tab is the best, reducing the core length to 0.2D, which is about 98.6 % reduction in core length. The mixing caused by the truncated triangular tab is found to be the best in both characteristics decay and fully-developed zones.

At NPR8, which is marginally underexpanded or almost correctly expanded state for Mach 2 jet, the core length for the uncontrolled jet extends up to about

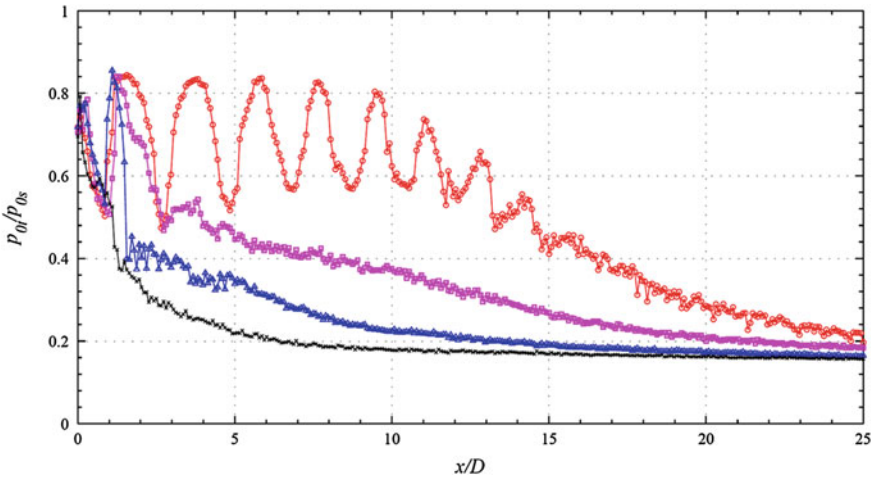


**Fig. 6** Centerline pressure decay of Mach 2.0 jet at NPR7 (overexpanded). *Red circle* uncontrolled jet, *pink rectangle* jet controlled with rectangular tabs, *blue triangle* jet controlled with right-triangular tabs, and *asterisk* jet controlled with truncated right-triangular tabs

15.5D, as seen in Fig. 7. The core length for the sharp and truncated vertex triangular tabs respectively are 0.3D and 0.2D. That is, core length reductions of about 98 and 99 % are achieved with the sharp and truncated tabs. These reductions are greatly higher than the reduction of 83 and 87 % (at NPR7 and NPR8) reported for isosceles triangular tabs (Arun Kumar and Rathakrishnan 2013a). In the presence of almost zero pressure gradient also, the tabs are found to perform

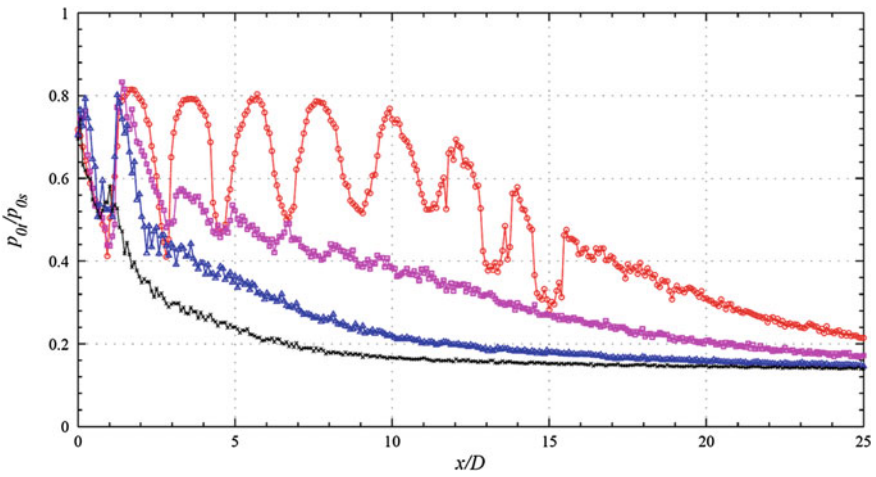


**Fig. 7** Centerline pressure decay of Mach 2.0 jet at NPR8 (almost correctly expanded). *Red circle* uncontrolled jet, *pink rectangle* jet controlled with rectangular tabs, *blue triangle* jet controlled with right-triangular tabs, and *asterisk* jet controlled with truncated right-triangular tabs

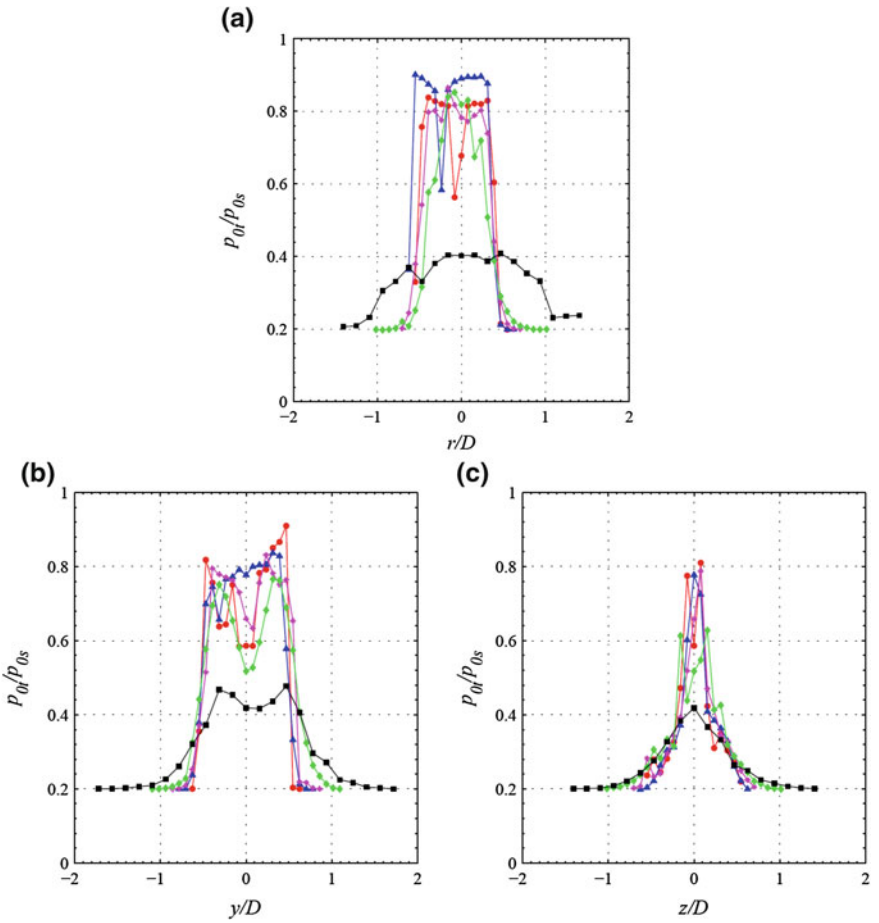


**Fig. 8** Radial pressure profiles of Mach 2.0 jet at NPR5 (overexpanded). *Filled red circle x/D* = 0.5, *filled blue triangle x/D* = 1, *asterisk x/D* = 2, *filled green diamond x/D* = 4 and *filled black rectangle x/D* = 8. **a** Uncontrolled jet *r*-direction. **b** Rectangular tabs *y*-direction. **c** Rectangular tabs *z*-direction. **d** Triangular tabs; *y*-direction. **e** Triangular tabs; *z*-direction. **f** Truncated triangular tabs; *y*-direction. **g** Truncated triangular tabs; *z*-direction

well. Among them, the performance of truncated triangular tab is once again the best leading to a core length reduction of about 0.2D, which is about 99 %.

From the centerline pressure decay results it is evident that, the mixing promotion caused by right-angle triangular tabs are significantly higher than that of isosceles triangular tab. Truncating the vertex of the tab is found to be of immense benefit in mixing promotion at all the three zones. Furthermore, the best efficiency of the tabs is around the correct expansion with almost zero pressure gradient at the nozzle exit. This aspect agrees with the findings of Rathakrishnan for limiting tab (Rathakrishnan 2009).

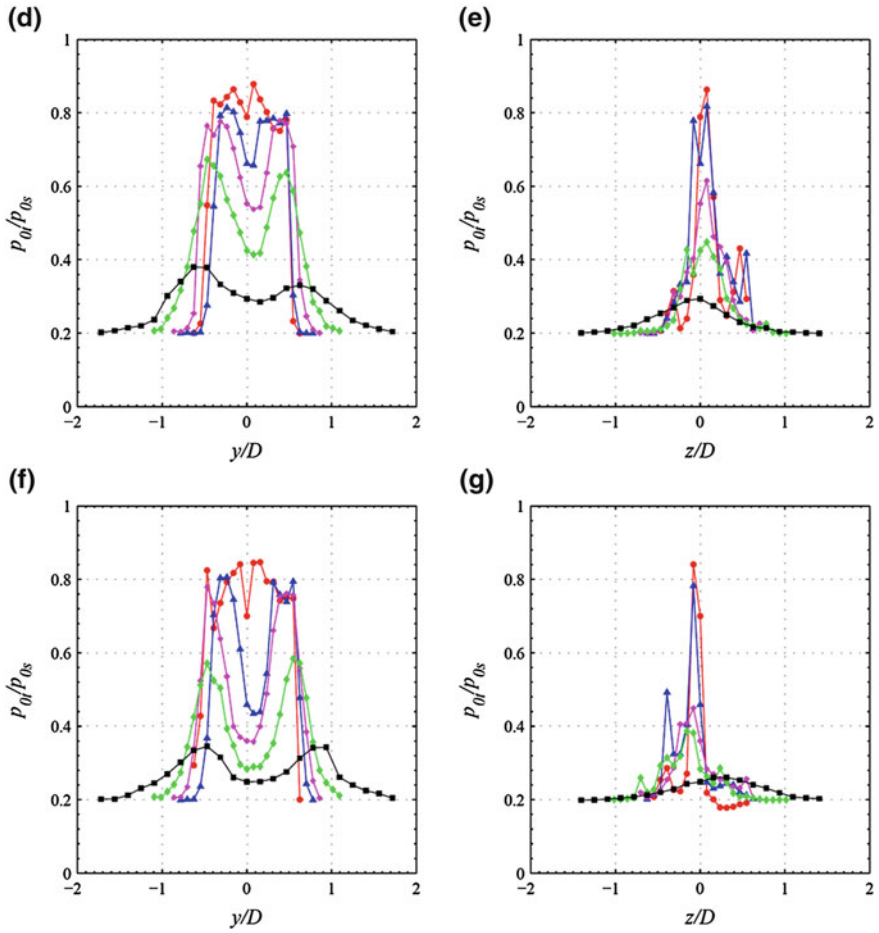


**Fig. 8** continued

## *3.2 Pressure Profiles*

It is desirable to ensure that the tabs cause appreciable mixing enhancement without making the jet highly unsymmetrical. To investigate this feature, the pressure profiles for the controlled jets, in the direction along the tabs ($z$-direction) and normal to the tabs ($y$-direction), were measured for the all possible combination of the flow and geometrical parameters of the present study. A representative set of pressure profile for the uncontrolled and controlled jet at NPR5 are given in Fig. 8. It is seen that, the triangular tabs do not introduce any asymmetry in the direction normal to the tab ($y$-direction). Whereas, in the direction along the tabs ($z$-direction) there is considerable level of asymmetry, especially at $x/D = 1$. This may because, the triangular tab used in the present study is right-angle

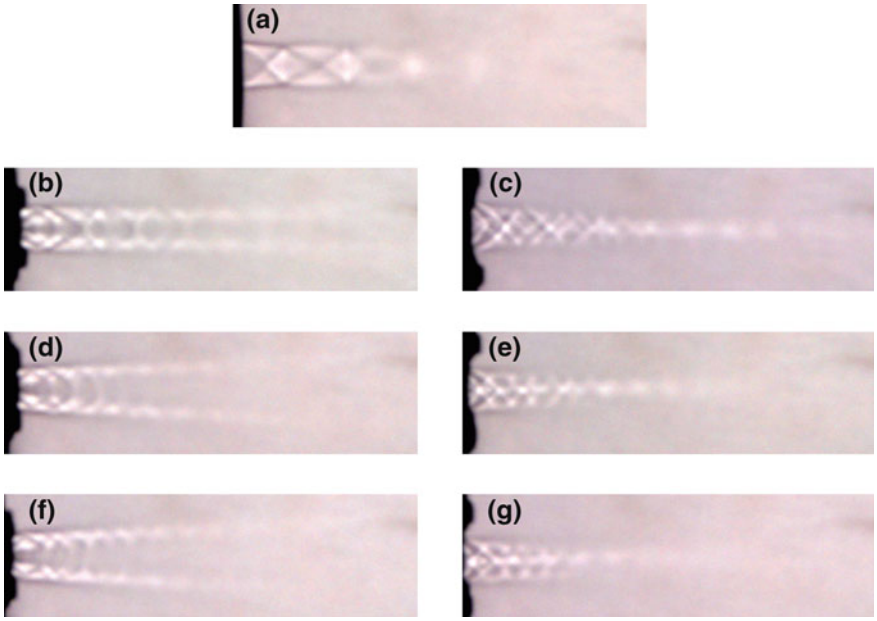


**Fig. 9** Shadowgraph pictures for Mach 2 jet at NPR5 (overexpanded). **a** Uncontrolled jet. **b** Jet controlled with rectangular tabs. **c** Jet controlled with rectangular tabs. **d** Jet controlled with right-triangular tabs. **e** Jet controlled with truncated right-triangular tabs. **f** Jet controlled with right-triangular tabs. **g** Jet controlled with right-triangular tabs

triangle and hence it is bound to cause asymmetry in the near-field, owing to the differential size of vortices shed at every height from the base. However, with increase in downstream distance the level of asymmetry gradually decreases forcing the jet to become symmetry, identical to the uncontrolled jet.

### *3.3 Flow Visualization*

The waves prevailing in the controlled and uncontrolled jet fields, at NPR5, are presented in Fig. 9. For the controlled jet the visualization was done viewing along and normal to the tabs. It is seen that there are three prominent shock-cells in the uncontrolled jet, that is exhibiting the shock cone at the nozzle exit, shock cross-over point at the nozzle axis and the reflection of expansion fans from just inside the inner boundary of the jet. With rectangular tabs, the waves in the shock-cells are perturbed, as seen in Fig. 9b and c. With sharp vertex triangular tabs (Fig. 9d and e), the wave spread is found to be larger than the rectangular tabs, and with truncated triangular tabs (Figs. 9f and g) the spread is found to be the highest and

the complexity of a waves in the jet field is the maximum. This could cause increased entropy production, leading to greatly enhanced mixing for the truncated triangular tabs (Rathakrishnan 2009).

## 4 Conclusions

The results of the present investigation clearly demonstrates that the mixing caused by right-angle triangular tab with truncated vertex is superior than the identical tab with sharp vertex and rectangular tab of equivalent blockage. The mixing promoting efficiency of the tab is found to increase with increase of NPR. The best performance of the tab is found to around correct expansion. At almost correctly expanded state, core length reduction of about 99 % is achieved with truncated triangular tab, which is much higher than the core length reduction of 87 %, reported for isosceles triangular tab of identical blockage at same Mach number (Arun and Rathakrishnan 2013a). It is found that, in-spite of the intense action of the mixing promoting vortices of continuously varying size shed by the triangular tabs, the jet does not become unduly asymmetry. The waves present in the jet field controlled by truncated triangular tab is found to be significantly weaker than the waves prevailing in the jet controlled by sharp triangular tab and rectangular tab.

## References

Arun Kumar P, Rathakrishnan E (2013a) Truncated triangular tabs for supersonic jet control. J Propul Power 29(1):50–65. doi:10.2514/1.B34642

Arun Kumar P, Rathakrishnan E (2013b) Corrugated triangular tabs for supersonic jet control. Proc Inst Mech Eng Part G: J Aero Eng 0(0):1–15. doi:10.1177/0954410013480098

Arun Kumar P, Rathakrishnan E (2013c) Corrugated truncated triangular tabs for supersonic jet control. J Fluids Eng 135:091104. doi:10.1115/1.4024204

Chiranjeevi Phanindra B, Rathakrishnan E (2010) Corrugated tabs for supersonic jet control. AIAA J 48(2):453–465

Rathakrishnan E (2009) Experimental studies on the limiting tab. AIAA J 47(10):2475–2485

Rathakrishnan E (2010) Applied gas dynamics. Wiley, NJ

# Development of a Feedback Model for the Self-Excited Impinging Planar Jet

**D. Arthurs and S. Ziada**

**Abstract** This article experimentally investigates the self-excited impinging planar jet flow, specifically, the development and propagation of large-scale coherent flow structures convecting between the nozzle lip and the downstream impingement surface. The investigation uses phase-locked PIV measurements and a new structure-tracking scheme to measure convection velocity and characterize the impingement mechanism near the plate in order to develop a new feedback model that can be used to predict the oscillation frequency as a function of flow velocity ($U_o$), impingement distance ($x_o$) and nozzle thickness ($h$). The resulting model prediction shows a good agreement with experimental tone frequency data.

**Keywords** Impinging jet · Self-excited flow · Acoustic tone · Flow-acoustic interaction · Feedback mechanism · Coherent structure · Vortices · Convection speed

## 1 Introduction

High-speed impinging planar jets are used in a myriad of important industrial applications; however, these flows are also known to be liable to the production of very intense narrow-band acoustic tones and strong self-excited flows. These phenomena are produced by a feedback mechanism between instabilities in the free shear layers of the jet and pressure fluctuations produced by the impingement

D. Arthurs (✉) · S. Ziada (✉)
Department of Mechanical Eng—JHE-316, McMaster University, 1280 Main Street West, Hamilton, ON L8S 4L7, Canada
e-mail: davidgarthurs@gmail.com

S. Ziada
e-mail: ziadas@mcmaster.ca

Y. Zhou et al. (eds.), *Fluid-Structure-Sound Interactions and Control*,
Lecture Notes in Mechanical Engineering, DOI: 10.1007/978-3-642-40371-2_4,

of large-scale coherent flow structures at the impingement surface. Previous investigations of the planar impinging jet have shown that the characteristics of the self-excited response of the system is different from other related geometries, such as the impinging axisymmetric jet, being self-excited over a much larger range of impingement ratio ($1.5 \leq x_o/h \leq 32.0$ for the planar cases, compared with $1.5 \leq x_o/D \leq 7.0$ for round jets) and beginning at lower flow velocities (Arthurs and Ziada 2012). These distinctions result in significant differences in both the structure of the flow, as well as the form of the jet oscillation modes compared to related systems, and as a result, the existing feedback models lead to relatively poor predictions of the oscillation frequency.

## 2 Experimental Details

Experiments were conducted using McMaster's planar jet noise facility, which employs a planar nozzle with a thickness of $h = 3$ mm, a total span of $L = 100$ mm, and uses compressed air as a flow source. Acoustic measurements have been performed with GRAS ¼" microphones, and flow measurements have been performed by means of a standard-speed PIV system using a phase-locked measurement technique, which acquires flow measurements at a specified point in the flow oscillation cycle using the periodic pressure signal obtained at the plate surface in the impingement region. Velocity vectors have been obtained using an iterative, multi-grid, deformation-based scheme with a final interrogation region size of 24 × 24 pixels and an overlap of 75 %. The resulting vector fields have less than 1 % interpolated vectors before the use of any vector replacement schemes.

## 3 Results and Discussion

### *3.1 Self-Excited Flow Oscillations*

Figure 1 shows pair of flow fields of the impinging planar jet, with part (a) showing a phase-averaged instantaneous velocity magnitude field, consisting of the average of 100 phase-locked measurements, along with a single contour of the velocity discriminant field proposed by Vollmers (2001) at an amplitude of $d_2 = 0$. This flow field is indicative of the typical form of the self-excited flow of the jet, which takes the form of a pronounced flapping motion of the jet column, along with an anti-symmetric distribution of coherent flow structures on either side of the jet centerline that convect from the nozzle to the plate, and with the number of structures varying with the mode number, $n$. The velocity discriminant parameter, which is a nonlinear combination of velocity shear terms, has been used

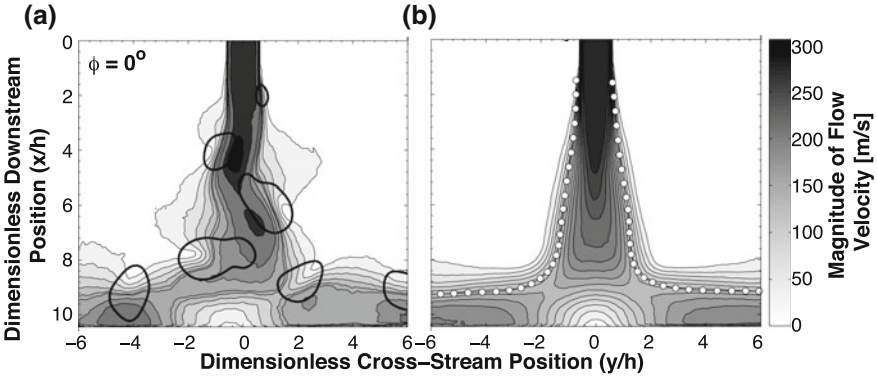


**Fig. 1** **a** Phase-locked velocity field and a single contour of the velocity discriminant ($d_2 = 0$) of the self-excited $n = 3$ hydrodynamic mode of the impinging planar jet with $U_o = 310$ m/s, $x_o/h = 10.5$, $h = 3$ mm, and **b** time-averaged velocity field and path of coherent structures

to identify and track coherent structures in the flow (Vollmers 2001). Part (b) of the figure shows the time-averaged velocity magnitude field, along with the position of the coherent structures extracted from eight phase-averaged flow fields evenly distributed over three repeated flow oscillation cycles.

## *3.2 Structure Convection Velocity and Mean Flow Effects*

Using the structure positions obtained from the phase-averaged flow fields, the convection velocity of the coherent structures in the downstream direction was obtained as a function of the downstream position. The results of these measurements are shown in Fig. 2, with part (a) illustrating the effect of changing flow velocity of the jet and part (b) showing the effect of varying impingement ratio. The results in part (a) show that the structures convect relatively slowly, at ~40 % of the free-stream velocity of the jet flow in the initial region and with the changing flow velocity of the jet having no effect on the dimensionless convection velocity. Furthermore, part (b) shows that as the impingement ratio is increased, the structure shows evidence of the structure slowing due to the effects of the transition region, where the jet flow experiences a bulk-slowing effect as the flow travels beyond the jet potential core and approaches the impingement surface.

$$u_c \approx k \times U_o \quad \text{for } x_o/h \leq 8.5 \tag{1}$$

$$u_c \approx k \times U_o \times 1.7 \times (x_o/h)^{-1/4} \quad \text{for } x_o/h > 8.5 \tag{2}$$

.

To account for the bulk-slowing effect brought on by the transition region for large impingement ratios, a set of expressions have been developed using the results

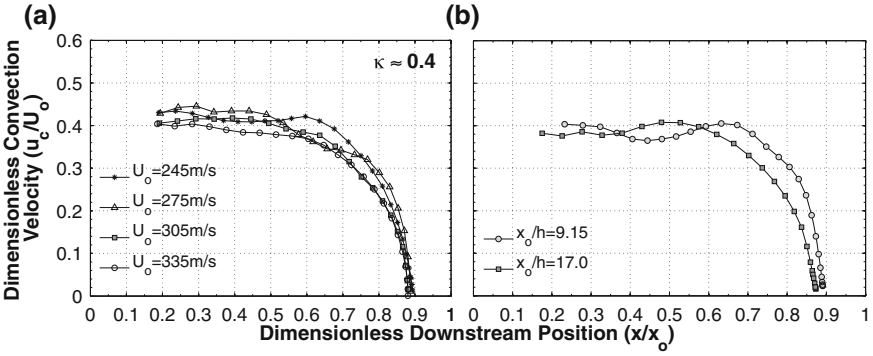


**Fig. 2** Downstream convection velocity extracted using the structure-tracking technique for **a** $x_o/h = 10.5$, $h = 3$ mm and $U_o = 245$, 275, 305 and 335 m/s, and **b** $U_o = 245$ m/s, $h = 3$ mm with $x_o/h = 9.15$ and 17.0

of time-averaged centerline velocity profiles obtained for impingement ratios between $x_o/h = 5.0$ and 30.0. The correction, given in Eqs. 1 and 2, gives the average downstream convection velocity in the developing region of the flow over two distinct ranges of impingement ratio: $x_o/h \leq 8.5$, where the transition region has a negligible effect, and $x_o/h > 8.5$ where significant bulk slowing of the flow occurs.

Because of the relatively large size of the structures and the flow diversion near the plate, it is clear that the structures will begin to impinge on the downstream surface having travelled less than the total impingement distance, $x_o$. In order to quantify this effect and to define an effective impingement length scale: $x_{eff}$, measurements of the structure circulation as a function of downstream position have been performed by integrating the vorticity field within the bound of each coherent flow structure determined by the velocity discriminant $d_2 = 0$ level. The results of these measurements are shown in Fig. 3, which illustrates that the structure circulation reaches a maximum value having travelled $\sim$75 % of the total impingement distance, after which it decreases sharply. The sudden decrease indicates the onset of structure impingement on the downstream surface. Measurements of other cases performed at various flow velocities and impingement ratios showed very similar results.

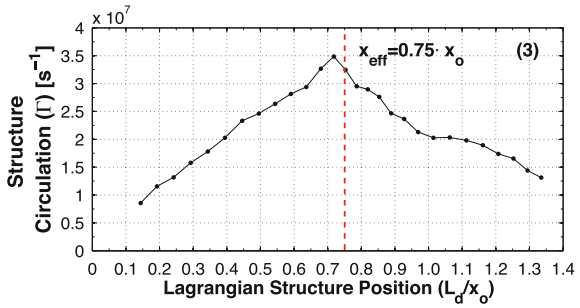


**Fig. 3** Total coherent structure circulation as a function of lagrangian structure position

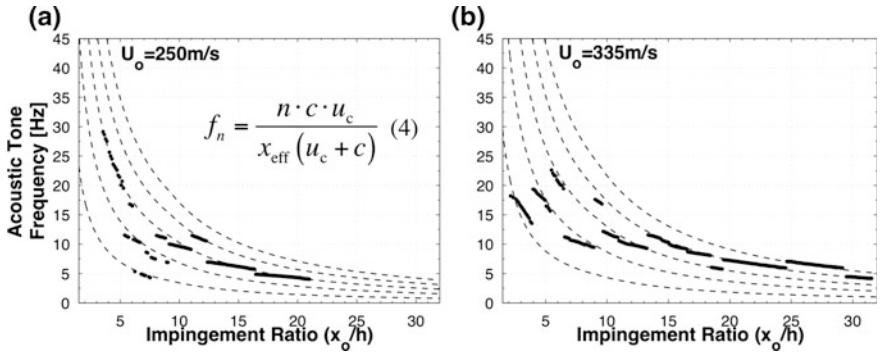


**Fig. 4** Predictions of the feedback model as a function of impingement ratio for flow velocities of **a** $U_o = 250$ m/s and **b** 335 m/s, and a nozzle thickness of $h = 3$ mm

### *3.3 Feedback Model*

A feedback model to predict the self-excited flow oscillation frequency is proposed based on the results of measured convection speed, mean flow characteristics and the effective impingement length. The model, which is conceptually based on the model developed by Alan Powell, is given in Eq. 4, with the predictions of the model shown in Fig. 4. The model has been found to have very good agreement with the measured oscillation frequency, typically within 10 %, for the complete range of sub-sonic flow velocity and impingement ratio for which the system is self-excited ($150 \leq U_o < 343$ m/s and $1.5 \leq x_o/h \leq 32.0$), as well as for a range of nozzle thicknesses ($1.0 \leq h \leq 4.0$ mm).

## 4 Conclusions

This article examined the development and propagation of large-scale coherent flow structures in the self-excited impinging planar jet flow in order to develop a feedback model capable of predicting the oscillation frequency. It was found that the coherent flow structures convect at $\sim$40 % of the jet velocity in the initial region and with the structures slowing due to the effects of the transition region for large impingement ratio. In addition, the large size of the structures and flow diversion near the plate results in interaction with the plate having propagated $\sim$75 % of the total impingement length. The feedback model that was developed using the present results shows a good agreement with experimental measured frequency for a wide range of flow velocity, impingement ratio and nozzle thickness.

## References

Arthurs D, Ziada S (2012) Self-excited oscillations of a high-speed impinging planar jet. J Fluids Struct 34:236–258

Vollmers H (2001) Detection of vortices and quantitative evaluation of their main parameters from experimental velocity data. Meas Sci Technol 12:1199–1207

# Self-Excited Oscillations of Two Opposing Planar Jets

**M. Hassaballa, D. Arthurs and S. Ziada**

**Abstract** The self-excited oscillation generated by two opposing planar jets is investigated experimentally. Strong flow oscillations resulting in intense acoustic tone generation are observed for wide ranges of jet flow velocity and distance between the opposing jet exits. A study of phase-locked particle image velocimetry (PIV) complemented with sound measurements is performed to clarify the self-excitation mechanism and the oscillation pattern(s) of the opposing jets.

**Keywords** Flow instability · Planar jet · Self-excited oscillation · Self-sustained oscillation

## 1 Introduction

Opposing planar jets are used in a variety of industrial applications, including the production of sheet steel, air/fuel mixing in combustion applications, in valves and piping systems, and in reactors used in the chemical industry (Tamir 1994; Johnson and Prud'homme 2003; Arthurs et al. 2012). In some applications, such flow can be problematic due to intense self-excited flow oscillations which can generate high vibration levels and/or intense acoustic tones; both of which can pose negative effects on the safety and ergonomic restrictions of the work place. Despite its use in many industrial applications, this flow geometry has hardly been investigated in the literature.

M. Hassaballa (✉) · D. Arthurs · S. Ziada
Department of Mechanical Engineering, McMaster University, 1280, Main Street West, Hamilton, ON L8S 4L7, Canada
e-mail: hassabmm@mcmaster.ca

Y. Zhou et al. (eds.), *Fluid-Structure-Sound Interactions and Control*,
Lecture Notes in Mechanical Engineering, DOI: 10.1007/978-3-642-40371-2_5,

## 2 Experimental Setup

Two planar nozzles, identical to that used by Arthurs and Ziada (2012), were employed in the present study (see Fig. 1). Each nozzle has a span of $L = 100$ mm thickness of $h = 2$ mm, giving an overall aspect ratio of $L/h = 50$. The working fluid is compressed air. Sound measurements, obtained by means of a GRAS ¼" condenser microphone, were acquired at a sample rate of 51.2 kHz and averaged over 100 spectra. Flow field measurements were performed using a particle image velocimetry (PIV) system consisting of a single PowerView 4 MP 12 bit digital camera and a 532 nm New Wave Solo 120XT pulsed Nd:YAG laser. A phase-locked measurement technique was utilized to obtain the PIV images at a particular instant in the flow oscillation cycle. This allows for the reconstruction of an *average* flow oscillation cycle. For the current study, 100 flow fields were averaged for each point in the phase.

## 3 Results and Discussion

### 3.1 Acoustic Response

Figure 2a shows a noise spectrum illustrating the general features of the self-excited response of the system at a jet exit velocity $U_0 = 200$ m/s and a normalized impingement length $z/h = 50$. An intense acoustic tone is observed at $f = 230$ Hz, with amplitude reaching 105 dB, as well as its higher harmonic near 460 Hz. The tone frequency, $f$, changes with both the impingement distance, $z$, and the flow velocity, $U_o$, but the Strouhal number, $S = fz/U_o$, remains nearly constant over wide ranges of $z$ and $U_o$, as it can be seen from the typical results shown in Fig. 2b.

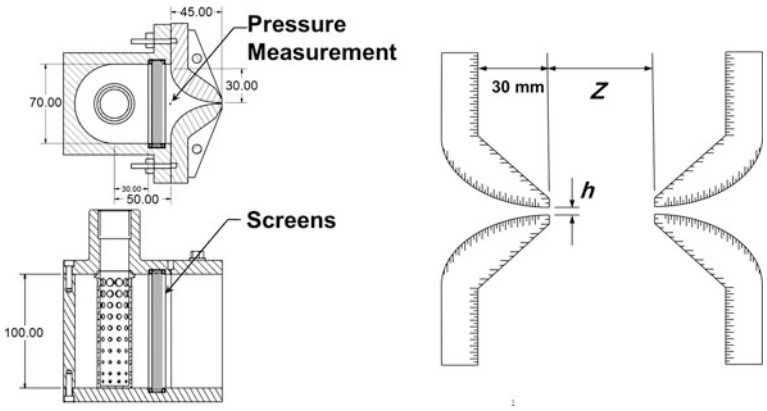


**Fig. 1** Planar jet nozzles

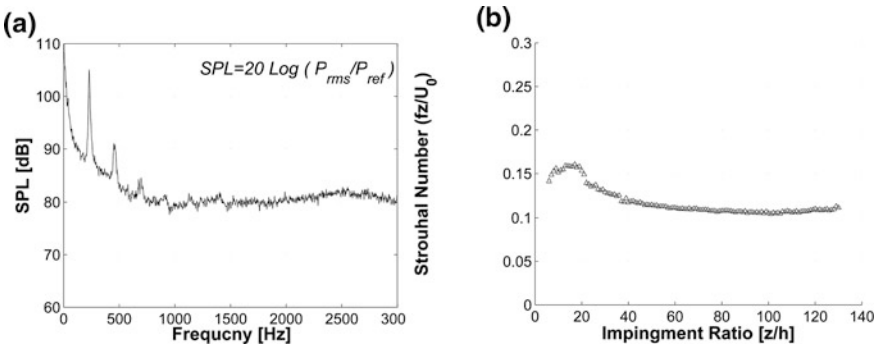


**Fig. 2** **a** Acoustic response of the planar opposing jets for a jet exit velocity of $U_0 = 200$ m/s and an impingement ratio of $z/h = 50$; **b** Strouhal number of the dominant tone as function of the impingement ratio for an exit velocity of $U_0 = 200$ m/s

## *3.2 Flow Field*

Figure 3 presents typical velocity contours of phase-averaged flow field; showing the flow oscillation cycle at eight phase angles separated by 45° of the oscillation cycle. These measurements were performed for a jet exit velocity of $U_0 = 200$ m/s ($Re_h = 25.5 \times 10^3$) and an impingement ratio of $z/h = 50$. The microphone signal was used to trigger the PIV system at different instants of the jet oscillation cycle. In inset (c) of the figure, the bottom jet column is seen be displaced to the left hand side, whereas the upper jet is displaced to the right. At 180° later, inset (g), the image is reversed, where the bottom jet is deflected to the right and the top jet to the left side. In the top two insets, also separated by 180°, the two jet columns exhibit the least deflection from their common axis and seem to have the shortest length due to the direct impingement on each other. This anti-symmetric *flapping* oscillation is the main pattern of the flow oscillation for the tested range of impingement length and flow velocity. This conclusion is based on the fact that the oscillation Strouhal number remains constant as indicated in Fig. 2. At present, PIV images taken for various flow velocities and impingement distances are being analyzed to better understand the excitation mechanism deriving the flow oscillation and a theoretical model is also being developed to predict the system oscillation frequency. The results of these additional analyses, including the vorticity and fluctuation velocity fields, will be discussed during the paper presentation.

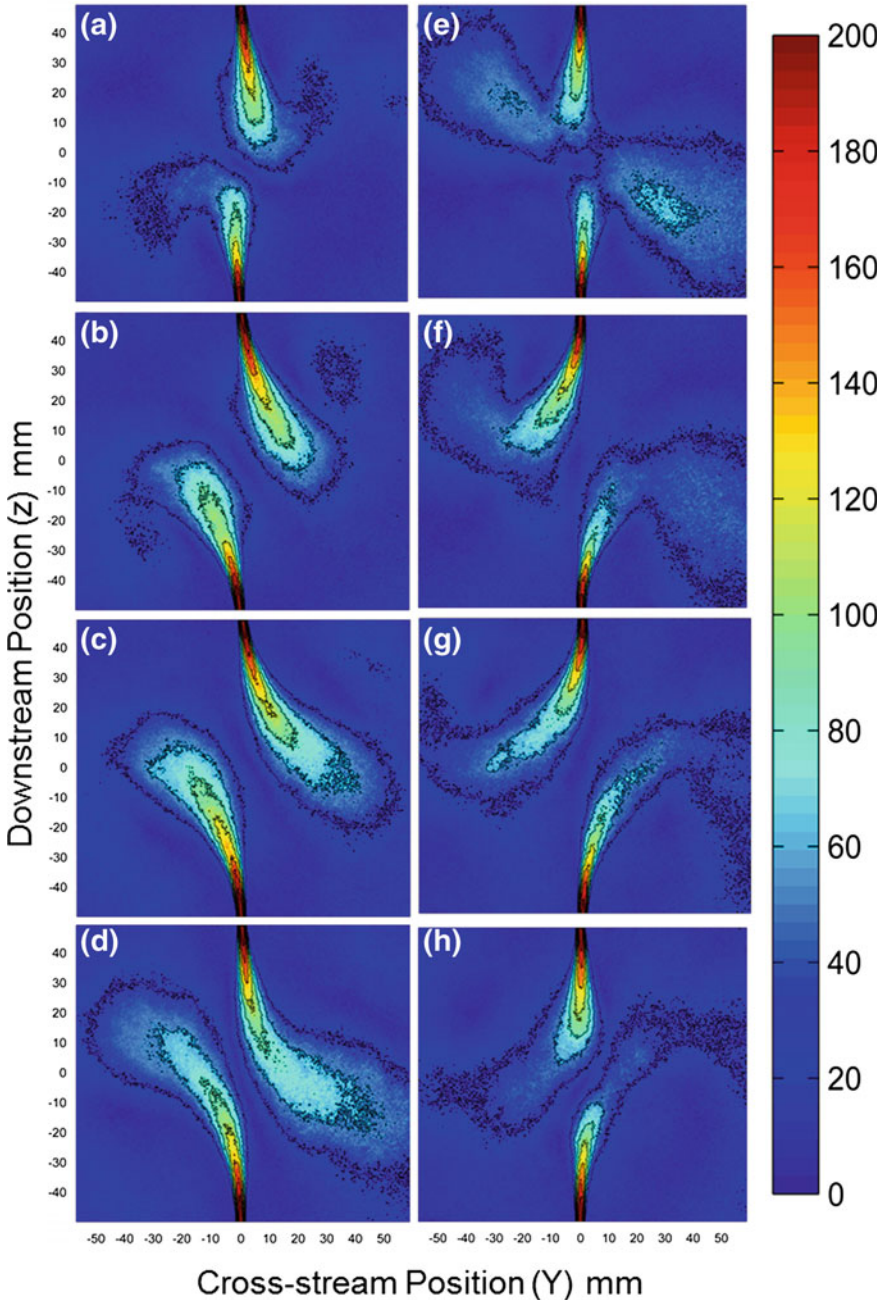


**Fig. 3** Phase averaged velocity magnitude contours showing complete oscillation cycle for $U_0 = 200$ m/s and $z/h = 50$ oscillating at a frequency of 230 Hz

## 4 Conclusions

Acoustic response measurements revealed that opposing planar jets produce intense acoustic tones at a well-defined, approximately constant Strouhal number, based on the distance between the jets. Phase-averaged PIV measurements revealed that the tone is generated by a self-excited flow oscillation where the two jets oscillate in an anti-symmetric *flapping* pattern. Further measurements and analysis are ongoing to examine the flow structures associated with the unsteady flow field.

## References

Arthurs D, Ziada S (2012) Self-excited oscillations of a high-speed impinging planar jet. J Fluids Struct 34:236–258

Arthurs D, Ziada S, Goodwin F (2012) Noise generation by the gas wiping jets of continuous galvanizing lines. J Fluids Therm Sci 1:85–129

Johnson BK, Prud'homme RK (2003) Chemical processing and micromixing in confined impinging jets. AIChE J 49:2264–2282

Tamir A (1994) Impinging-stream reactors: fundamentals and applications. Elsevier, Amsterdam

# Pressure Fluctuations in the Vicinity of a Wall-Mounted Protuberance

**Abdelkader Frendi and Philip Hahn**

**Abstract** Extensive numerical computations have been carried out to understand the effects of a wall-mounted protuberance on the fluctuating pressure field on the surrounding surfaces. The Mach 1.6 supersonic turbulent boundary layer is modeled using a hybrid RANS-LES approach known as detached eddy simulation (DES). The effects of protuberance height to boundary layer thickness as well as surface curvature are investigated. Comparisons of the surface pressure coefficients to existing experimental data showed good agreement. In addition, it was found that increasing the protuberance height resulted in higher sound pressure levels on the surface. Surface curvature led to the spreading of the high pressure region in the spanwise direction upstream of the protuberance. Convection velocities of the turbulent structures increased downstream of the protuberance and were in good agreement with published literature.

## 1 Introduction

In the last three decades, the rapid increase in computational power has led researchers in computational fluid dynamics to attempt to fully couple unsteady flows to flexible structures for simple geometries. Frendi (1997) showed the presence of a strong coupling between a supersonic turbulent boundary layer and a flexible structure. Handler et al. (1984) obtained the wall pressure fluctuations in a channel flow using a coarse direct numerical simulation (DNS). The coarse grid led to a lack of resolution of the high frequencies. Choi and Moin (1990) studied

A. Frendi (✉)
MAE Department, University of Alabama in Huntsville, 35899 Huntsville, AL, USA
e-mail: kader.frendi@uah.edu

P. Hahn
Blue Origin Corporation, Kent, WA, USA

Y. Zhou et al. (eds.), *Fluid-Structure-Sound Interactions and Control*,
Lecture Notes in Mechanical Engineering, DOI: 10.1007/978-3-642-40371-2_6,

the structure of the wall pressure fluctuations in a turbulent channel flow using a DNS database of Kim et al. (1987). Choi and Moin (1990) computed the wave number/frequency spectra and the convection velocities of the wall pressure fluctuations and found that small structures convected at a slower speed than large structures. Na and Moin (1998) studied the effect of an adverse pressure gradient on the structure of the wall pressure fluctuations using DNS. They found that adverse pressure gradients led to elongated two-point correlation maps in the spanwise direction and decreased convection velocities. Viazzo et al. (2001) studied the spectral features of the wall pressure fluctuations using a large eddy simulation database of a plane channel flow. They reported that a sinusoidal wall perturbation had a very weak effect in terms of time mean values. Wall pressure fluctuations and flow-induced noise from a turbulent boundary layer over a bump were investigated by Kim and Sung (2006) using DNS. They found that wall pressure fluctuations increased near the trailing edge of the bump along with the presence of large structures that convected rapidly downstream. The method used in this paper is referred to as a hybrid RANS-LES method, namely detached eddy simulation (DES) (Spalart et al. 1998) which has been used extensively and has shown promising results.

## 2 Numerical Approach

The equations solved are derived from the baseline RANS model of Menter et al. (1994) modified by Nichols and Nelson (2003) to become a hybrid RANS-LES. The numerical procedure followed is as follows: Once a RANS mean flow is obtained, several hybrid RANS/LES computations are carried out. The parameters investigated are the protuberance height to boundary layer thickness and the surface curvature. The flow parameters used are as follows: free stream Mach number 1.6, free stream air velocity 463.3 m/s, free stream air temperature 422 K and a Reynolds number per meter of 4.92 million. Protuberance height to boundary layer thickness ratios, $h/\delta$, studied are 0.5, 1.0 and 2.0, and the radius of curvature of the surfaces studied are as follows: 9.6, 4.8 cm and a flat surface. The 9.6 cm curved surface corresponds to the one used in the experiments (Hahn and Frendi 2013). All protuberances were cylindrical with a diameter, $D$, of 0.315 cm. When running a hybrid RANS/LES computation with a high Reynolds number, one needs to make sure the grid resolution is sufficient to capture the relevant flow physics of the problem. In the present computations, a hybrid unstructured grid is used with cell densities varying from 55 to 75 million depending on protuberance height. Near viscous walls, $y^+ < 1$, were enforced.

# 3 Results and Discussion

## *3.1 Overall Sound Pressure Level on the Surface*

Figure 1 shows the OASPL map on a flat surface for a small protuberance, Fig. 1a, and a tall protuberance, Fig. 1b. It is clear from the figure that the tall protuberance, Fig. 1b, has a huge impact on the surface in terms of high acoustic loads over a large area surrounding the protuberance. Figure 1c shows the OASPL contours on a curved surface for a protuberance having a height to boundary layer thickness ratio of 2.0. The curved surface has a radius of curvature of 9.6 cm. The figure shows that the presence of the curvature, Fig. 1c, leads to the spread of the high dB-levels area in the spanwise direction, i.e., *y*-direction, both upstream and downstream of the protuberance. Downstream of the protuberance, Fig. 1c, shows lower dB-levels over a larger area than that on a flat surface, Fig. 1b.

## *3.2 Surface Pressure Spectra, Two-Point and Space–Time Correlation*

Figure 2a shows that the wall pressure spectra at various distances downstream of the protuberance collapse well at low frequencies using the outer scaling but not so well at high frequencies. The ratio of protuberance height to boundary layer thickness in this case is 2.0. The two-point space correlation three-diameter downstream of the protuberance shows the presence of large structures with stretching in the spanwise direction, Fig. 2b. The space–time correlation, Fig. 2c, shows a short-lived coherence in both space and time. One can also deduce the convection velocity of the flow structures based on the slope of the curves; in this case, it is found to be between 0.6 and 0.77 of the free stream.

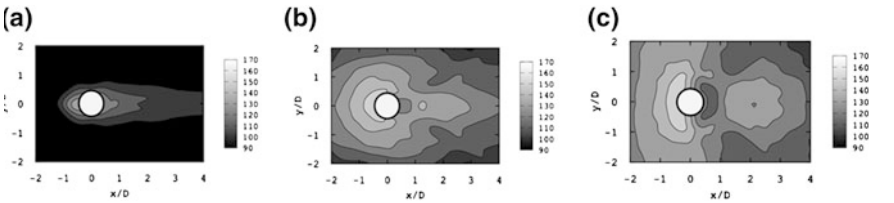


**Fig. 1** OASPL in dB on a *flat* surface for a protuberance height to boundary layer *thickness* of (**i**) 0.5 (**ii**) 2.0 and for a *curved* surface for a protuberance height to boundary layer *thickness* of 2.0

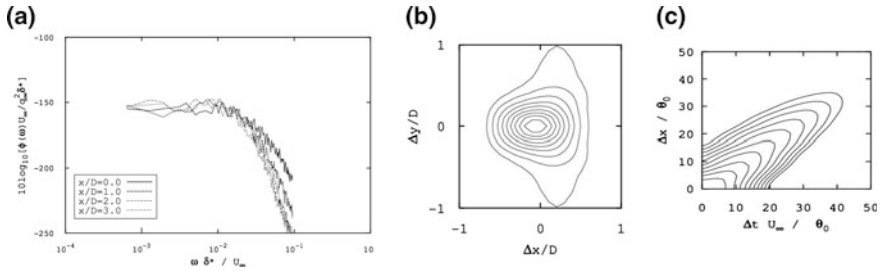


**Fig. 2** (**a**) Wall pressure spectra at various downstream locations from the protuberance, (**b**) two-point space correlation three-diameter downstream of the protuberance (**c**) two-point space–time correlation three-diameter downstream of the protuberance. The protuberance height to boundary layer thickness is 2.0, and for both the two-point and the space–time correlations, the contours levels are between 0.1 and 0.9

## 4 Conclusions

Results from an extensive numerical investigation on the effects of cylindrical protuberances on the wall pressure fluctuations in a supersonic turbulent boundary layer have been presented. The effects of protuberance height to boundary layer thickness and surface curvature on wall pressure fluctuations were studied. Our CFD results compared well to the experimental data for pressure coefficient and the fluctuating pressure coefficient. For tall protuberances, our results show an increase in overall sound pressure levels on the surface surrounding the protuberance. Surface curvature is found to increase the area affected by high overall sound pressure levels ahead of the protuberance but slightly decreases it downstream. Additional results can be found in (Hahn and Frendi 2013).

## References

Choi H, Moin P (1990) On the space-time characteristics of wall-pressure fluctuations. Phys Fluids A 2:1450–1460

Frendi A (1997) Coupling between a supersonic turbulent boundary layer and a flexible structure. AIAA J 35(1):58–66

Hahn VP, Frendi A (2013) Interaction of three-dimensional protuberances with a supersonic turbulent boundary layer. AIAA J. Accessed 7 May 2013. doi : http://arc.aiaa.org/doi/abs/10.2514/1.J052101

Handler RA, Hansen RJ, Sakell SA, Orszag SA, Bullister E (1984) Calculation of the wall-pressure field in a turbulent channel flow. Phys Fluids 27:579–582

Kim J, Sung HJ (2006) Wall pressure fluctuations and flow-induced noise in a turbulent boundary layer over a bump. J Fluid Mech 558:79–102

Kim J, Moin P, Moser R (1987) Turbulence statistics in fully developed channel flow at low Reynolds number. J Fluid Mech 177:133–166

Menter FR (1994) Two-equation eddy-viscosity turbulence models for engineering applications. AIAA 32(8):1598–1605

Na Y, Moin P (1998) Structure of wall-pressure fluctuations in turbulent boundary layers with adverse pressure gradient and separation. J Fluid Mech 377:347–373

Nichols RH, Nelson CC (2003) Application of hybrid RANS/LES turbulence models. AIAA-2003-0083

Spalart PR, Jou W, Strelets M, Allmaras S (1998) Comments on the feasibility of LES for wings, and on a hybrid RANS/LES approach. In Advances in DNS/LES, pp 137–147, 1998. First AFSOR International Conference on DNS/LES

Viazzo S, Dejoan A, Schiestel R (2001) Spectral features of the wall-pressure fluctuations in turbulent wall flows with and without perturbations using les. Int J Heat Fluid Flow 22:39–52

# Effects of Polymer Additive on Turbulent Bulk Flow: The Polymer Concentration Dependence

**Heng-Dong Xi, Haitao Xu and Eberhard Bodenschatz**

**Abstract** We report an experimental study of the effects of polymer additives on the turbulent bulk flow. Our results confirm that both the acceleration fluctuation $a$ and the velocity fluctuation $u$ of the flow are suppressed when the polymer additives are present and the suppression effect on $a$ is much stronger. We further found that polymer additives enhance the anisotropy of the flow at small scales, but do not affect the anisotropy at large scale very much. These results are qualitatively in agreement with a recent theory which predicts that only scales smaller than a critical scale are affected by the polymer additives.

## 1 Introduction

Minute amount of long-chain polymer additives can drastically change flow properties. Examples include the well-known drag reduction phenomenon in turbulent pipe/channel flows (Virk 1975) and the elastic turbulence phenomenon at low Reynolds numbers (Groisman and Steinberg 2001). The dynamics of the polymer-turbulence interaction are determined by the three control parameters, namely the Reynolds number $R_\lambda$, the Weissenberg number $Wi$ which is the ratio

H.-D. Xi (✉) · H. Xu · E. Bodenschatz
Max-Planck Institute for Dynamics and Self-Organization, D-37077 Göttingen, Germany
e-mail: hengdongxi@hitsz.edu.cn

H. Xu
e-mail: haitao.xu@ds.mpg.de

E. Bodenschatz
e-mail: eberhard.bodenschatz@ds.mpg.de

H.-D. Xi
Institute for Turbulence-Noise-Vibration Interaction and Control, Shenzhen Graduate School, Harbin Institute of Technology, Shenzhen, China

Y. Zhou et al. (eds.), *Fluid-Structure-Sound Interactions and Control*,
Lecture Notes in Mechanical Engineering, DOI: 10.1007/978-3-642-40371-2_7,

between the polymer relaxation time $\tau_p$ and the smallest time scale in turbulence $\tau_\eta$, and the polymer concentration $\phi$. In recent years, there have been a few experimental measurements of bulk turbulence in polymer solutions (Crawford et al. 2002; Liberzon et al. 2005; Liberzon et al. 2006; Crawford et al. 2008; Liberzon et al. 2009; Ouellette et al. 2009), which shed new light on our understanding of turbulence–polymer interactions. However, experiments systematically exploring the full parameter space are still lacking. It is therefore of great importance to have experiments that fully isolate the effect of the three control parameters. In this paper, we report an experimental study on the effects of minute high-molecular weight polymers on bulk turbulence, i.e., turbulence far away from the boundaries. We studied the polymer concentration dependence of the effects of polymer additive on the flow by using the three-dimensional Lagrangian particle tracking technique (LPT) with high temporal and spatial resolutions (Ouellette et al. 2006; Xu 2008). By differentiating the measured tracer particle trajectories once and two times, we obtained the fluid velocities and accelerations, respectively. By keeping both $R_\lambda$ and $Wi$ unchanged and varying solely the polymer concentration $\phi$, we studied the concentration dependence of the root-mean-square (RMS) acceleration $a$ and the RMS velocity $u$. We found that both $a$ and $u$ are suppressed when the polymers are present, and the suppression to $a$ is much stronger. Our results confirm that the suppression effect of polymer additives is much stronger on small scale than on large-scale quantities, and give for the first time the clear trends of the $\phi$ dependence of the suppressions. We further found that polymer additives enhance the anisotropy of the flow at small scales, but do not affect it at large scale very much.

## 2 Experimental Details

The experiments were carried out in a von Kàrmàn swirling flow system (Voth et al. 2002). The flow is generated in a cylinder with 63 cm in height and 49 cm in diameter by two counter-rotating baffled disks. The two baffled disks are 20 cm in diameter. The LPT system consists of three Phantom v12 CMOS cameras, a Q-switched Nd:YAG laser with power of 60 W and repetition frequency up to 120 kHz. The details of the LPT technique and the algorithms used here are described elsewhere (Ouellette et al. 2006; Xu 2008). The polymer we used is polyacrylamide (PAM) with molecular weight $Mw = 18 \times 10^6$. The experiments were done at three different Reynolds numbers $R_\lambda = 270, 342$ and $360$ which correspond to three different Wiessenberg numbers 5.94, 11.8, and 14.2, respectively. For each $R_\lambda$(or $Wi$), $\phi$ was varied from 0 to 10 ppm (part per million by weight). For the experiments with polymer solutions, we used the same $R_\lambda$ as that measured from the pure water case ($\phi = 0$) at the same rotating frequency of the propellers.

## 3 Polymer Concentration Dependence of the RMS Velocity and RMS Acceleration

We first examine the $\phi$ dependence of $u$ and $a$. In Fig. 1, we plot the measured $u$ and $a$ as functions of $\phi$ for three different $R_\lambda$, normalized by the corresponding value of the pure water case. The figure shows that $a(\phi)$ decreases very rapidly with $\phi$ for all the three $R_\lambda$, while $u$ decreases very slowly with $\phi$. For example, for $\phi = 10\,\text{ppm}$, $a$ is suppressed to about 30 %, while $u$ is suppressed to about 80 %, of those from the pure water case. Figure 1a suggests that the polymer additives suppress the small-scale properties such as $a$ much stronger than they do on large-scale property such as $u$, which confirms that the suppression effect of polymer additives is much stronger on small-scale than on large-scale quantities (Crawford et al. 2008; Ouellette et al. 2009; Tong et al. 1992).

A lot of efforts have been made to explain the strong polymer effect on the small scales. Lumley argued that only those fluctuations with time scale $\tau_r \leq \tau_p$ can stretch the polymer chain (Lumley 1973). This "time criterion," thus defines the Lumley scale $r^* \equiv (\varepsilon\tau_p^3)^{1/2}$ [see e.g., (Procaccia et al. 2008)], where $\varepsilon$ is the energy transfer rate per unit mass. The physical meaning of $r^*$ is that below this scale, the local fluid deformation would be strong enough to stretch polymers. Thus, only the scales smaller than $r^*$ will be affected by the polymers. Please note that the Lumley scale $r^*$ does not have $\phi$ dependence, thus it is not likely to explain the $\phi$ dependence of the suppression. To address this issue, we recently proposed a "energy flux balance theory" (Xi et al. 2013) based on de Gennes and Tabor's "energy balance theory" (De Gennes 1986; Tabor and de Gennes 1986). In our theory, we argued that the polymers start to affect the flow only if the energy transfer rate of the turbulent flow $\varepsilon$ is comparable to the elastic energy transfer rate by the polymers $\varepsilon_e(r) = \frac{kTc_p}{\tau_p \rho}\left(\frac{r^*}{r}\right)^{5n/2}$, where $c_p$ is the number of polymer chains per

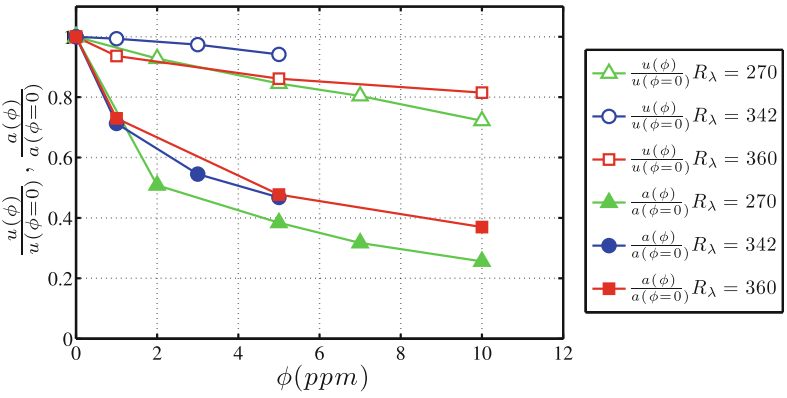


**Fig. 1** The polymer concentration dependence of the measured RMS velocity $u$ and RMS acceleration $a$. The *lines* are to guide the eyes

unit volume (which differs from $\phi$ only by a numerical factor), $k$ is the Boltzmann constant, $T$ is the temperature of the fluid, $\rho$ is the density of water, and $n$ is an unknown exponent that is related to the average stretching dimensions of the local flow field. The turbulent energy flux through the cascade (or the turbulent energy transfer rate from scale to scale) is gradually reduced by the energy transfer through stretching and recoiling of the polymer chains, with the elastic energy flux becoming dominant at small scales, and the balance of elastic and turbulent energy flux, $\varepsilon_T = \varepsilon_e(r_\varepsilon) = \frac{kTc_p}{\tau_p \rho}\left(\frac{r^*}{r_\varepsilon}\right)^{5n/2}$, gives a critical length scale $r_\varepsilon = (kT/\rho)^{\frac{2}{5n}} c_p^{\frac{2}{5n}} \varepsilon^{\frac{1}{2}-\frac{2}{5n}} \tau_p^{\frac{3}{2}-\frac{2}{5n}}$. All the scales less than $r_\varepsilon$ are affected by the polymers. We in addition identified from experiments that the unknown parameter $n$ is about 1.0. Thus, $r_\varepsilon \sim \phi^{0.4}\varepsilon^{0.1}\tau_p^{1.1}$. It is clear that $r_\varepsilon$ depends not only on $\varepsilon$ and $\tau_p$ but also on $\phi$. The future work will be to understand the $\phi$ dependence of $u$ and $a$ in the frame of the "energy flux balance theory."

## 4 Polymer Concentration Dependence of the Anisotropy

We then examine the effect of polymer additives on the anisotropy of the flow by studying the ratios between the different components of the RMS velocity, i.e., $u_x/u_z$ and $u_y/u_z$, as functions of $\phi$, as plotted in Fig. 2a. Similarly we plot $a_x/a_z$ and $a_y/a_z$ as functions of $\phi$ in Fig. 2b. It is seen from the plot both $u_x/u_z$ and $u_y/u_z$ stay largely the same as $\phi$ increases, which suggests that the large-scale anisotropy does not change much with the polymer additives. While both $a_x/a_z$ and $a_y/a_z$ increase roughly linearly with $\phi$, especially for the $R_\lambda = 270$ case, suggesting the polymer additives enhance the anisotropy of the flow at small scales. The observed enhancement of anisotropy is consistent with previous experiments (Crawford et al. 2008). Previously, it was suggested that the enhanced anisotropy is probably due to the theoretically predicted truncation of the energy cascade (Crawford et al. 2008). Recently, it is indeed shown that for the polymer solution case, the energy cascade is truncated at scale of the order $r_\varepsilon$ (Xi et al. 2013), as a result the inertial

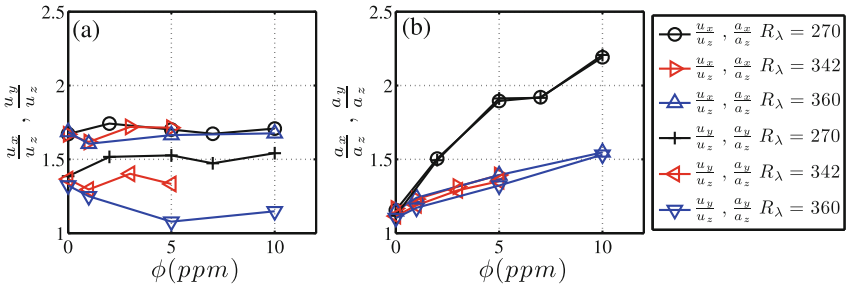


**Fig. 2** The ratios between RMS of different velocity components (**a**) and between RMS of different acceleration components (**b**), as functions of polymer concentration

range is postponed to larger scale compared with the Newtonian case. Thus, the separation between large and small scales is reduced and the anisotropy of the large scales would affect the small scales more, which is partially the reason for the enhanced anisotropy of the small scales. It is similar to the fact that the anisotropy increases with decreasing $R_\lambda$. This mechanism also explains the greater enhancement of anisotropy for smaller $R_\lambda$ as for smaller $R_\lambda$ the scale separation is even smaller.

## 5 Conclusion

In conclusion, we have studied the polymer concentration dependence of the effects of polymer additive on the turbulent bulk flow. We found that the fluid acceleration fluctuation is strongly suppressed, while the velocity fluctuation decreases slowly, with increasing concentration. Our results show that the suppression effect of polymer additives is much stronger on small-scale quantities than on the large-scale quantities. We further found that polymer additives enhance the anisotropy of the flow at small scales, but do not affect the anisotropy at large scale very much. These results are qualitatively in agreement with our recent theory which predicts that only scales smaller than a critical scale are affected by the polymer additives.

**Acknowledgments** We are grateful to the Max Planck Society and the Deutsche Forschungsgemeinschaft (through grant XU91-3) for their support. H.D. Xi also thanks the Alexander von Humboldt Foundation for the generous support.

## References

Crawford A et al (2002) Effect of dilute polymer solutions on dissipation range quantities in bulk turbulence. In: Castro IP, Hancock PE, Thomas TG (eds) Advances in turbulence IX: Proceedings of 9th European Turbulence Conference, CIMNE, Barcelona, pp 307–310

Crawford AM et al (2008) Fluid acceleration in the bulk of turbulent dilute polymer solutions. New J Phys 10:123015

De Gennes PG (1986) Towards a scaling theory of drag reduction. Physica A 140:9–25

Groisman A, Steinberg V (2001) Elastic turbulence in polymer solution flow. Nature 410:905–908

Liberzon A et al (2005) Turbulence in dilute polymer solutions. Phys Fluids 17:031707

Liberzon A et al (2006) On turbulent kinetic energy production and dissipation in dilute polymer solutions. Phys Fluids 18:125101

Liberzon A et al (2009) On turbulent entrainment and dissipation in dilute polymer solutions. Phys Fluids 21:035107

Lumley JL (1973) Drag reduction in turbulent flow by polymer additives. J Polymer Sci 7:263–290

Ouellette NT, Xu H, Bodenschatz E (2006) A quantitative study of three—dimensional Lagrangian particle tracking algorithms. Exp. Fluids 40:301–313

Ouellette NT, Xu H, Bodenschatz E (2009) Bulk turbulence in dilute polymer solutions. J Fluid Mech 629:375–385

Procaccia I, L'vov VS, Benzi R (2008) Theory of drag reduction by polymer in wall—bounded turbulence. Rev Mod Phys 80:225–247

Tabor M, de Gennes PG (1986) A cascade theory of drag reduction. Europhys Lett 2:519–522

Tong P, Goldburg WI, Huang JS (1992) Measured effects of polymer additives on turbulent—velocity fluctuations at various length scales. Phy Rev A 45:7231

Virk PS (1975) Drag reduction fundamentals. AIChE J 21:625–656

Voth GA et al (2002) Measurement of particle accelerations in fully developed turbulence. J Fluid Mech 469:121–160

Xi H-D, Xu H, Bodenschatz E (2013) Elastic Energy Flux by Flexible Polymers in Fluid Turbulence. Phys Rev Lett 111:024501

Xu H (2008) Tracking Lagrangian trajectories in physical—velocity space. Meas Sci Technol 19:075105

# Orthogonal Wavelet Analysis of Flow Structures in Asymmetric Wakes

**S. Fujimoto and A. Rinoshika**

**Abstract** The turbulent wake structures of various scales generated by an asymmetric bluff body have been experimentally investigated in this paper. Firstly, the instantaneous velocity and vorticity of turbulent wake were measured by the high-speed PIV technique at a Reynolds number of 8,960 in the circulating water channel. In order to decompose turbulent structures into a number of subsets based on their central frequencies, one- and two-dimensional wavelet multi-resolution technique is then used to analyze the instantaneous velocity and vorticity. It is found that the large-scale turbulent structure makes the largest contribution to the vorticity and Reynolds shear stresses. However, the small-scale structures make less contribution to the vorticity and Reynolds shear stresses.

**Keywords** PIV · Orthogonal wavelet multi-resolution technique · Reynolds shear stress · Vorticity · Wake

## 1 Introduction

It is a well-known fact that the turbulent wakes generated by a bluff body cause the aerodynamic drag, vibration, and noise. Until now, the most investigations focus on the symmetry bluff body wake, and the topology and transport characteristics of the turbulent structure in the wake flow have been well established (Hussain and Hayakawa 1987; Lin et al. 1996; Wei and Smith 1986). Recently, the multi-scale structures of various wakes are revealed based on the orthogonal wavelet multi-resolution analysis of the hot-wire data and PIV data (Rinoshika and Omori 2011;

S. Fujimoto · A. Rinoshika (✉)
Department of Mechanical Systems Engineering, Yamagata University, Yamagata, Japan
e-mail: rinosika@yz.yamagata-u.ac.jp

Y. Zhou et al. (eds.), *Fluid-Structure-Sound Interactions and Control*,
Lecture Notes in Mechanical Engineering, DOI: 10.1007/978-3-642-40371-2_8,

Rinoshika and Zhou 2005a, 2005b, 2009). However, there is little research on the multi-scale turbulent wakes generated by an asymmetric bluff body which will provide important information in industrial applications, thus becoming an objective of the present work.

In this study, the high-speed PIV was applied to measure a turbulent wake generated by an asymmetric body. Then, one- and two-dimensional wavelet multi-resolution technique was used to analyze the instantaneous velocity and vorticity. The turbulent structures were decomposed into a number of subsets based on their central frequencies. The contributions from the turbulent structures of various scales to Reynolds shear stresses and vorticity were examined.

## 2 Experimental Details

In this study, a compound of 1/4 circular and triangle cylinders is designed for the purpose of both reducing aerodynamic drag and producing a downward force. As a fundamental research, a two-dimensional asymmetric model having a scale of $L = 50$ mm and aspect ratio of eight with respect to their whole length, as shown in Fig. 1, is used as a wake generator. The experiment was conducted in a circulating water channel, which has 400 (width) × 200 (height) × 1,000 mm (length) working section. The high-speed PIV measurement system, as shown in Fig. 2, was carried out at a constant free stream velocity of $U_0 = 0.19$ m/s, corresponding to Reynolds number $Re$ ($\equiv U_0 L/\nu$) = 8,960.

Polystyrene particles with a diameter of 63–75 μm were seeded in the flow loop as PIV tracers. A high-speed camera (Photoron FASTCAM SA3) and a laser light sheet were used to capture the digital images at a frame rate of 500 fps (frame per second) with a resolution of 1,024 × 1,024 pixels and the shutter speed of each frame was set at 1 ms. 1,025 digital images were analyzed by ProVision PIV software. The measured flow area is about 200 × 200 mm behind bluff body.

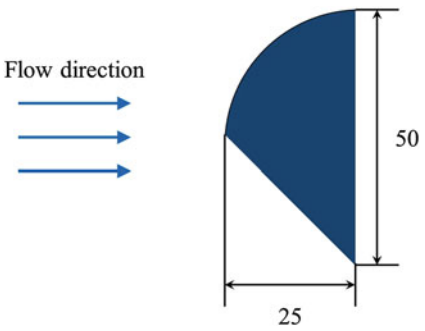


**Fig. 1** Experimental model

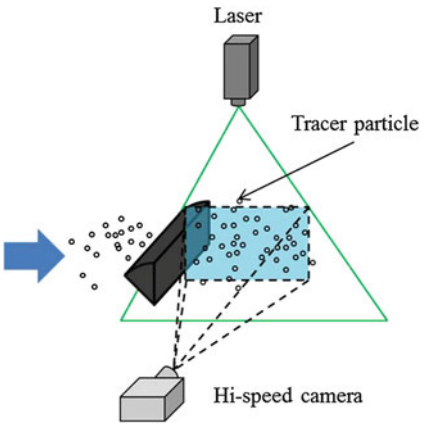


**Fig. 2** Experimental setup

## 3 Orthogonal Wavelet Multi-resolution Technique

In this study, the discrete serial data are decomposed into a number of wavelet components based on characteristic frequencies by using an orthogonal wavelet multi-resolution technique. As an example, a one-dimensional wavelet multi-resolution technique is briefly described in this section. A one-dimensional orthogonal discrete wavelet transform is often defined in matrix form by

$$\boldsymbol{S} = \boldsymbol{W}\boldsymbol{X} \tag{1.1}$$

where $\boldsymbol{X}$ is a one-dimensional data matrix. $\boldsymbol{S}$ and $\boldsymbol{W}$ are called the orthogonal wavelet coefficient matrix and the analyzing wavelet matrix, respectively. $\boldsymbol{W}$ is orthogonal. Therefore, the orthogonal discrete wavelet transform has the inverse transform, which is given by

$$\boldsymbol{X} = \boldsymbol{W}^T\boldsymbol{S} \tag{1.2}$$

In order to decompose the serial data into the grouped frequency components, the inverse wavelet transform is applied to the discrete wavelet coefficients at each level. This decomposition method is called the wavelet multi-resolution analysis and can be written as

$$\boldsymbol{X} = \boldsymbol{W}^T\boldsymbol{S}_1 + \boldsymbol{W}^T\boldsymbol{S}_2 + \ldots + \boldsymbol{W}^T\boldsymbol{S}_N \tag{1.3}$$

In this study, the Daubechies wavelet matrix with an order of 12 is used as the analyzing wavelet matrix. In case of two-dimensional wavelet multi-resolution analysis, wavelet coefficient matrix $\boldsymbol{S}$ is additionally transformed by $\boldsymbol{W}$ from another direction and wavelet multi-resolution analysis can be written as

$$\boldsymbol{X} = \boldsymbol{W}^T\boldsymbol{S}_1\boldsymbol{W} + \boldsymbol{W}^T\boldsymbol{S}_2\boldsymbol{W} + \ldots + \boldsymbol{W}^T\boldsymbol{S}_N\boldsymbol{W} \tag{1.4}$$

where the first term $\boldsymbol{W}^T\boldsymbol{S}_1\boldsymbol{W}$ and the last term $\boldsymbol{W}^T\boldsymbol{S}_N\boldsymbol{W}$ represent the data components at wavelet level 1 and level $N$, respectively. It is evident that the sum of all wavelet components can be used to reconstruct the original data in the case of the orthogonal wavelet bases.

## 4 Results and Discussion

### *4.1 Reynolds Shear Stress and Instantaneous Flow Structures*

Figure 3 shows the distribution of the normalized Reynolds shear stress contours of $\overline{uv}/U_0^2$ calculated by the measured instantaneous velocity, and instantaneous streamlines and normalized vorticity contour, $\omega_z L/U_0$. The color mappings have been assigned to the Reynolds shear stress and the vorticity values and the highest concentration is displayed as red and the lowest as blue, respectively. The distributions of $\overline{uv}/U_0^2$ exhibit the maximum values near the end of the separation region. The positive Reynolds shear stress of downside is more widely distributed than the negative Reynolds shear stress on the upside, suggesting the effect of the asymmetric body, and the lower side of body generates the high-intensity turbulence.

The asymmetric large-scale vortices with opposite sense of rotation shed from body are clearly observed. The large-scale spanwise structures originated from the lower (triangle) side become weak due to the effect of "rolls" structures shed from the upper (circle) side. It would be difficult to study the behaviors of the structures other than the large-scale ones.

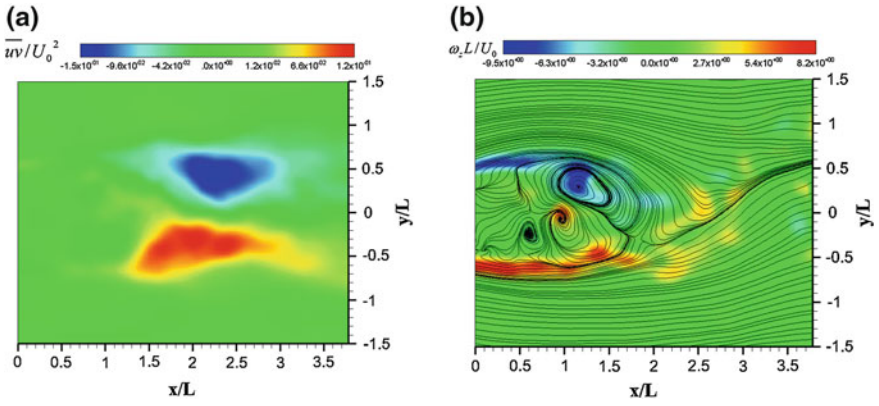


**Fig. 3** Asymmetric wake structure measured by PIV analysis

### 4.2 Reynolds Shear Stress of Different Wavelet Components

Figure 4 presents the normalized Reynolds shear stress contours of $\overline{uv}/U_0^2$ calculated from the wavelet components of the instantaneous fluctuation velocity at wavelet levels 1 and 7. The distributions of $\overline{uv}/U_0^2$ at level 1 exhibit the maximum values near the end of the separation region, corresponding well to the measured Reynolds shear stress contour. It indicates that the most significant contribution to the Reynolds shear stress comes from the large-scale structures, accounting for almost 76–83 % of the measured maximum $\overline{uv}/U_0^2$. At the level 7, the maximum Reynolds shear stress further decreases and only appears near the asymmetric body. It implies that less contribution to the Reynolds shear stresses comes from the small-scale structures.

### 4.3 Instantaneous Flow Structures of Different Wavelet Components

Figure 5 shows the two-dimensional streamlines and vorticity contours of the wavelet components at level 1, level 2, and levels 3 and 4. The streamlines and vorticity contours at level 1 coincide approximately with the measured data of Fig. 3b, implying the large-scale structures make the most contribution to the flow structure, and distinguishing vortex except redundant data is observed clearly. It is obvious that the large-scale structure is the energy-containing structure. At level 1, the body downside generates high positive vorticity and distributes widely. At level 2, as shown in Fig. 5b, relatively intermediate-scale structures are observed near the body. Compared with the vorticity of large-scale components, the strength

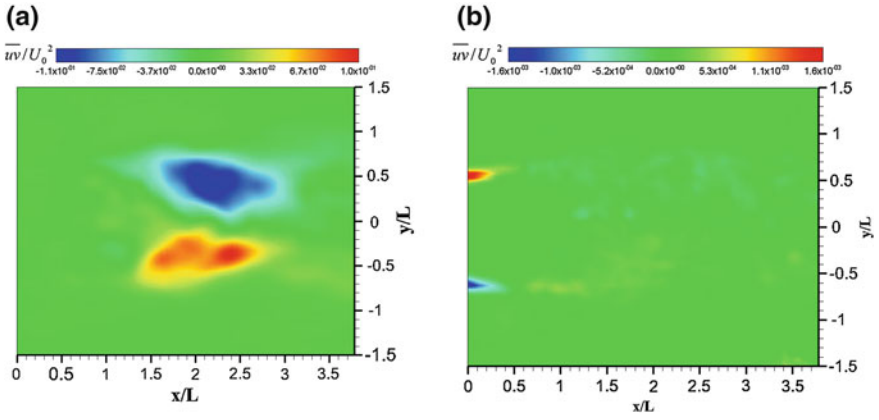


**Fig. 4** Reynolds shear stress contours of various wavelet components

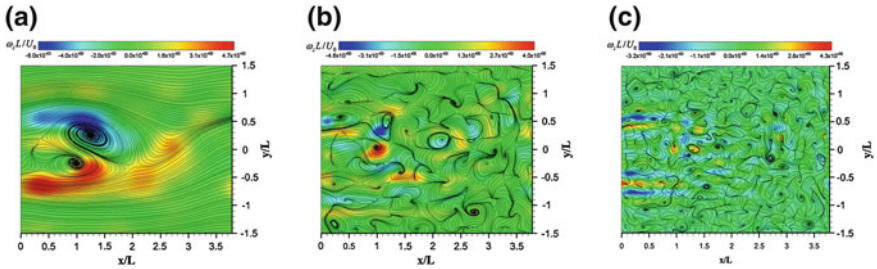


**Fig. 5** Streamlines and vorticity contours of various wavelet components

of the intermediate-scale component decreases. For the small-scale vorticity at levels 3 and 4, the small-scale structures are observed in the entire flow field. Especially, many strong vorticity peaks appear in the shear layer of separation region.

## 5 Conclusion

In this study, the following results can be drawn:

1. The maximum Reynolds shear stresses are distributed near the end of the separation region, and the lower side of asymmetric body generates the high-intensity turbulence.
2. The large-scale turbulent structures make the largest contribution to the Reynolds shear stress and vorticity. The contributions to the Reynolds shear stress from large-scale turbulent structures have a proportion of 76–83 % to the measured maximum Reynolds shear stress.
3. The small-scale structures are observed in all flow fields and the maximum Reynolds shear stress and vorticity appear in the separation shear layer. However, the small-scale structures make less contribution to Reynolds shear stresses and vorticity.

## References

Hussain AKMF, Hayakawa M (1987) Education of large-scale organized structures in a turbulent plane wake. J Fluid Mech 108:193–229

Lin J-C, Vorobieff P, Rockwell D (1996) Space-time imaging of a turbulent near-wake by high-image-density particle image cinematography. Phys Fluids 8:555–564

Rinoshika A, Omori H (2011) Orthogonal wavelet analysis of turbulent wakes behind various bluff bodies. Exp Thermal Fluid Sci 35:1231–1238

Rinoshika A, Zhou Y (2005a) Orthogonal wavelet multi-resolution analysis of a turbulent cylinder wake. J Fluid Mech 524:229–248

Rinoshika A, Zhou Y (2005b) Effects of initial conditions on a wavelet-decomposed turbulent near-wake. Phys Rev E 71(046303):1–8

Rinoshika A, Zhou Y (2009) Reynolds number effects on wavelet components of self-preserving turbulent structures. Phys Rev E 79(046332):1–11

Wei T, Smith CR (1986) Secondary vortices in the wake of circular cylinders. J Fluid Mech 169:513–533

# Phase Average Visualization of a Finite Cylinder Wake as Predicted by Large Eddy Simulation

**N. Moazamigoodarzi, D. J. Bergstrom, M. Einian and D. Sumner**

**Abstract** The current paper reports a large eddy simulation (LES) of turbulent flow over a finite-height square cylinder mounted normal to a ground plane. The cylinder aspect ratio is AR = 3 and the Reynolds number based on the cylinder width and inlet velocity is Re = 500. The flow field is complex, since the flow over the top of the cylinder interacts with the flow along the ground plane to create a complicated wake structure. The wake is characterized by a velocity field that changes rapidly in both direction and magnitude. Phase averaging based on the Strouhal number reveals a wake structure with quasi-periodic features that is much different from the structure suggested by the mean vorticity field.

**Keywords** Wake · Vortex structure · Finite square cylinder · Phase average · Large eddy simulation

## 1 Introduction

Turbulent flow over external bodies which is characterized by shear-layer separation is a complex phenomenon, e.g., it involves both the large-scale periodic motions associated with vortex shedding and smaller-scale motions associated with the fluid turbulence. In order to predict the aerodynamic forces on the body, as well as the potential for sound generation within the flow, the instantaneous and mean structure of the wake need to be understood. In this paper, we focus on the special case of a square cylinder, which is finite in length and mounted perpendicular to a

N. Moazamigoodarzi · D. J. Bergstrom (✉) · M. Einian · D. Sumner
Department of Mechanical Engineering, University of Saskatchewan, 57 Campus Drive, Saskatoon, Saskatchewan S7N 5A9, Canada
e-mail: don.bergstrom@usask.ca

Y. Zhou et al. (eds.), *Fluid-Structure-Sound Interactions and Control*,
Lecture Notes in Mechanical Engineering, DOI: 10.1007/978-3-642-40371-2_9,

ground plane. The flow approaching the cylinder is characterized by a boundary layer of thickness, $\delta$. An important characteristic of the flow is the aspect ratio AR = *H/D* (where *H* is the height and *D* is the width of the cylinder), which can be regarded as a measure of the slenderness of the cylinder. For a finite cylinder, the structure of the wake is influenced by both the flow over the top of the free end of the cylinder, as well as the boundary layer developing on the ground plane. Recent studies of finite (circular) cylinder flows (Sumner et al. 2004; Palau-Salvador et al. 2010) have indicated that at small aspect ratios, the wake structure becomes distinct from that at larger aspect ratios. The measurements of Wang and Zhou (2009) indicate both symmetric and staggered shedding, and they have also postulated a vortical structure for the cylinder wake. In contrast, Bourgeois et al. (2011) conclude that the wake structure should be understood in terms of the phase-average behavior. For the case of a square prism of AR = 4, they have identified a so-called half-loop structure. The present paper reports a large eddy simulation (LES) of a low Reynolds number (Re = *UD/v* = 500) flow over a square cylinder of aspect ratio AR = 3. The approaching boundary layer was thin and laminar. Two- and three-dimensional visualization of the phase-average structures was used to investigate the wake. It confirms the presence of quasi-periodic vortical structures, which is surprising at this low aspect ratio.

## 2 Numerical Methods

The mathematical model consisting of the filtered Navier–Stokes equations was discretized using the finite-volume method. A localized dynamic Smagorinsky model was used for the subgrid-scale stress terms. The resultant equation set was solved using a fractional step method, where the convective and diffusive terms were advanced in time using the Crank–Nicolson method, and a multi-grid (MG) method was used to efficiently solve the linear algebraic equation set. The initial velocity field was first developed in time to obtain a realistic turbulent flow. After this, velocity data were collected and processed to obtain the time-averaged or mean velocity field, the resolved-scale fluctuations, and the phase-average fields.

## 3 Results and Discussion

Sampling of the velocity field in the wake of the cylinder indicated a Strouhal number of St = 0.128. Based on the period inferred from the Strouhal number, the velocity field behind the cylinder was processed in terms of five distinct phases ($N = 1$ to 5) to give a picture of the periodicity of the flow. The results were averaged over five consecutive periods.

Figure 1 shows the mean streamwise vorticity and in-plane velocity vectors in a vertical plane section located at *X/D* = 2 (where *X* is the streamwise coordinate).

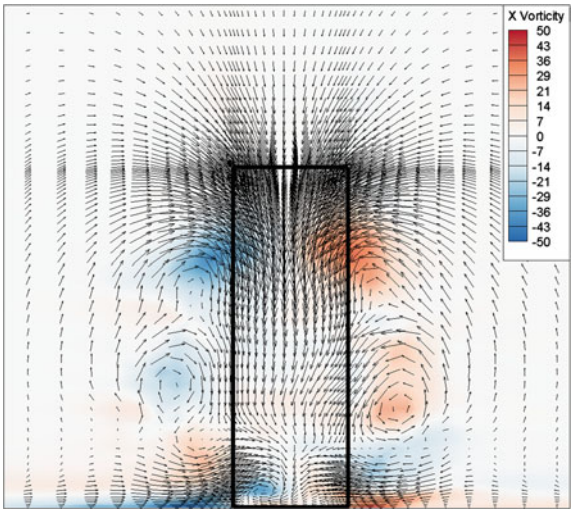


**Fig. 1** Mean streamwise vorticity and velocity vectors for a vertical section located at $X/D = 2$

Two pairs of tip vortices and much weaker base vortices are evident, and the flow field is almost symmetric about the center-plane.

Figure 2 shows a temporal trace of the instantaneous streamwise and crosswise velocity components and the associated power spectra at a reference point located in the cylinder wake. The velocity exhibits a strong periodic component with a frequency of $f = 2.4$ Hz.

Figure 3 shows the phase-averaged streamwise vorticity and velocity vectors in the same vertical plane as in Fig. 1. Two phases are shown, $N = 2, 4$. The velocity and vorticity fields are observed to sweep across the wake creating strongly asymmetric flow patterns. Similar to the mean velocity field shown in Fig. 1, Fig. 3 indicates that a strong downwash flow exists between the counter-rotating streamwise structures for each phase.

Figure 4 shows the velocity vectors and associated in-plane spanwise vorticity at a height of $Y/H = 1/4$ for phases $N = 2, 4$. The velocity vectors indicate patterns which are typical of vortex shedding, e.g., the dominant vortex immediately behind the cylinder is located at a different transverse location for each phase.

Figure 5 shows the three-dimensional structure of the wake (also for $N = 2, 4$) visualized by the contours of the second invariant of the velocity gradient tensor. The flow structure is clearly asymmetric for each phase, with the initially vertical vortex tubes being reoriented in the streamwise direction. There is some evidence of the half-loop structure as described by Bourgeois et al. (2011). The vortex patterns observed in Fig. 3 are seen to coincide with the streamwise structures shown in Fig. 5.

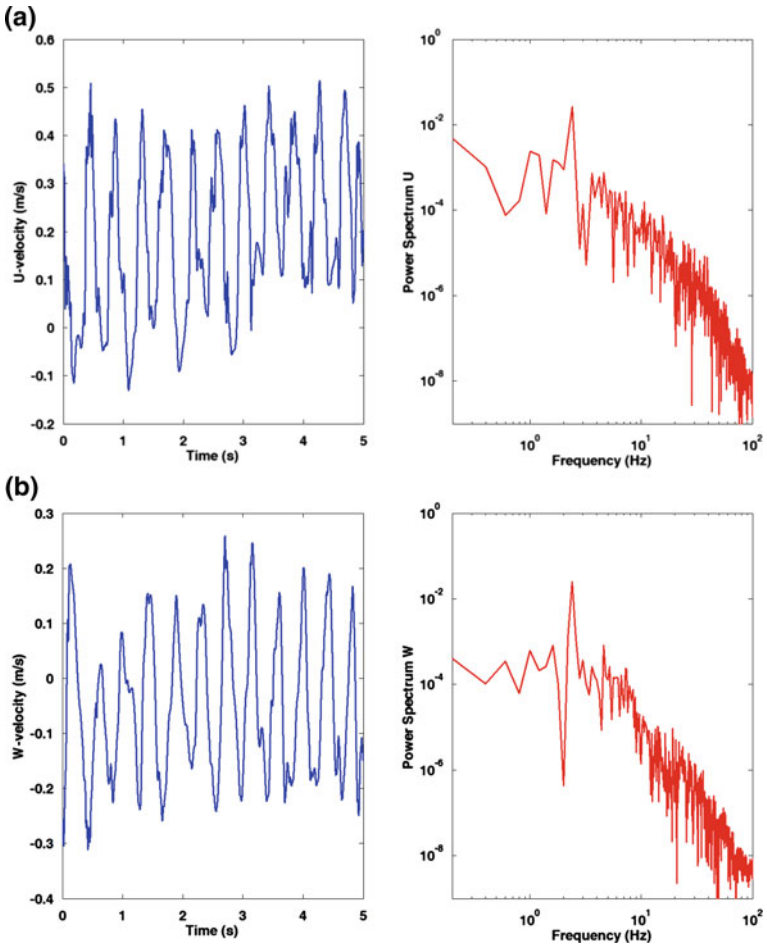


**Fig. 2** Trace and power spectrum of **a** streamwise and **b** cross-stream velocity at a point in the near-wake of the cylinder

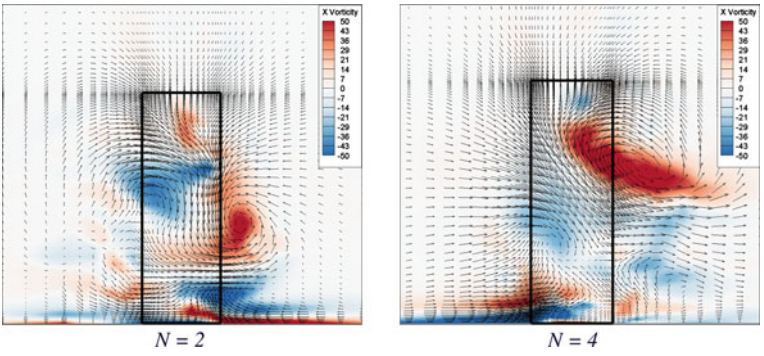


**Fig. 3** Phase-averaged streamwise vorticity and velocity vectors at $X/D = 2$ for phases $N = 2, 4$

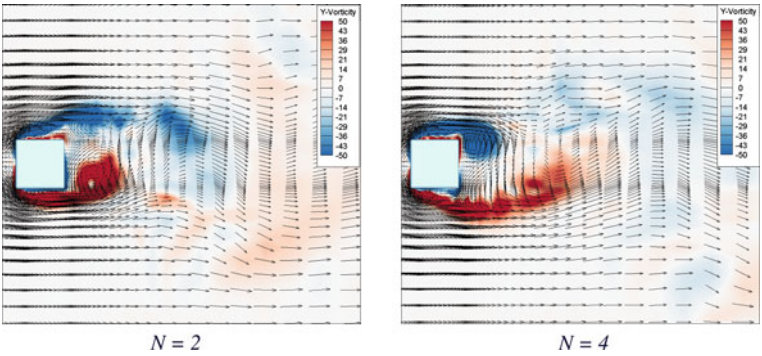


**Fig. 4** Phase-averaged vertical vorticity and velocity vectors at $Y/H = 0.25$ for phases $N = 2, 4$

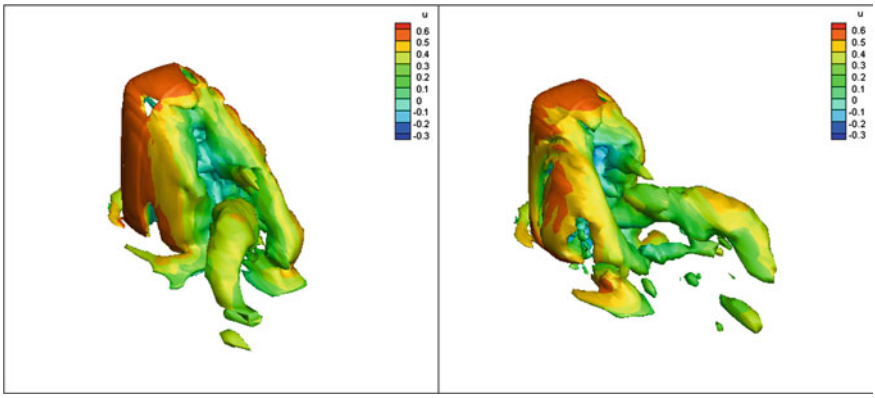


**Fig. 5** Visualization of the phase-averaged vorticity field using the second invariant ($Q = 200$), flooded by streamwise velocity for phases $N = 2, 4$

## 4 Conclusions

LES predictions of low Reynolds number flow over a finite-height square cylinder mounted on a ground plane are reported in this paper. The flow field predicted for this sub-critical aspect ratio of AR = 3 reveals a complex wake structure. Phase-average analysis of the cylinder wake reveals patterns of quasi-periodic vortical structures. The originally vertical-oriented vortex elements formed by the roll-up of the shear layers shed from the lateral sides of the cylinder evolve to create streamwise structures that connect back to the structures on the opposite side of the wake. The phase-averaged velocity field in transverse plane sections through the wake indicates strong downwash flow between pairs of dominant vortical streamwise structures that change their location over the course of a single phase-average cycle.

## References

Bourgeois JA, Sattari P, Martinuzzi RJ (2011) Alternating half-loop shedding in the turbulent wake of a finite surface-mounted square cylinder with a thin boundary layer. Phys Fluids 23:1–15

Palau-Salvador G, Stoesser T, Froehlich J, Kappler M, Rodi W (2010) Large Eddy simulations and experiments of flow around finite-height cylinders. Flow Turbul Combust 84(2):239–275

Sumner D, Heseltine JL, Dansereau OJP (2004) Wake structure of a finite circular cylinder of small aspect ratio. Exp Fluids 37:720–730

Wang HF, Zhou Y (2009) The finite-length square cylinder near wake. J Fluid Mech 638:453–490

# Three-Dimensional Wavelet Multi-resolution Analysis of Flow Structures Behind a Vehicle External Mirror

**A. Rinoshika and Y. Zheng**

**Abstract** The three-dimensional orthogonal wavelet multi-resolution technique was applied to analyze flow structures of various scales around an externally mounted vehicle mirror. Firstly, three-dimensional flow of the mirror wake was numerically analyzed by using the large eddy simulation (LES). Then, the instantaneous velocity and vorticity were decomposed into the large-, intermediate-, and relatively small-scale components by the wavelet multi-resolution technique. It was found that a three-dimensional large-scale vertical vortex dominates the mirror wake flow and makes a main contribution to vorticity. Some intermediate- and relatively small-scale vortices were extracted and were clearly identifiable.

**Keywords** LES · Vehicle mirror · Vortex · Wake · Wavelet multi-resolution analysis

## 1 Introduction

The aerodynamic noise and vibration caused by the vehicle door mirror has been much studied (Watkins and Oswald 1999), largely by numerical simulation (Ono et al. 1999). It is evident that the aerodynamic noise and vibration are strongly associated with the flow structures, and the unsteady behavior of the vortex causes the wind noise. Recently, the aero-acoustic characteristics of a vehicle door mirror were also studied by numerical simulation as well as experimental measurement (Reichl et al. 2005). Rinoshika et al. (2007) experimentally investigated the flow structure around an externally mounted vehicle mirror by the smoke-wire

A. Rinoshika (✉) · Y. Zheng
Department of Mechanical Systems Engineering, Yamagata University, Yamagata, Japan
e-mail: rinosika@yz.yamagata-u.ac.jp

Y. Zhou et al. (eds.), *Fluid-Structure-Sound Interactions and Control*,
Lecture Notes in Mechanical Engineering, DOI: 10.1007/978-3-642-40371-2_10,

visualization technique and high-speed PIV technique. It is found that the length scales of separation region are generally insensitive to Reynolds number, and the size of vortices and the vorticity concentration increase with Reynolds number. Rinoshika and Watanabe (2010) also applied one-dimensional wavelet multi-resolution technique to decompose Reynolds stress measured by high-speed PIV into various scales and analyzed the multi-scale flow structures behind a vehicle external mirror. But little attention has been paid to the analysis of the complex three-dimensional turbulent structures of various scales in the mirror wake from either the numerical or measurement data.

This work aims to apply the three-dimensional orthogonal wavelet multi-resolution technique to decompose the complex turbulent structures of the mirror wake into multi-scale structures based on the large eddy simulation and to provide both quantitative and qualitative information on the three-dimensional flow structures of various scales for designing the mirror with lower dynamic drag and noise.

## 2 Approach of Numerical Simulation

In this study, the commercial CFD software Fluent 6.3 is used to simulate the three-dimensional (3D) unsteady flow-field around a door mirror model. The LES turbulence model is adopted in which small eddies are modeled whereas large eddies are directly calculated.

A 1/3-scaled generic door mirror model, as shown in Fig. 1, is adopted and fixed on a flat plate. For simplifying the complex flows around the door mirror model, the flat plate is assumed to be the car body and the effect of the A-Pillar is neglected. The height of the mirror model is defined as characteristic length with $L = 100$ mm. The computational domain, in which the model is placed, is shown in Fig. 2, where the length, width, and height of the domains are 6, 2.5, and $2L$, respectively. The mesh of the hybrid volume, containing approximately 542,945 cells, is generated in the computational domain.

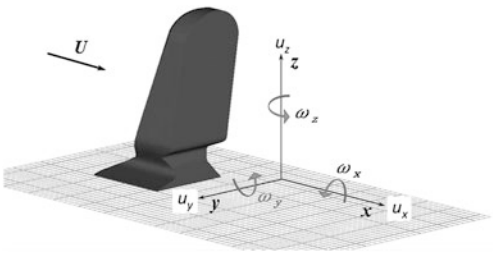


**Fig. 1** Model of door mirror

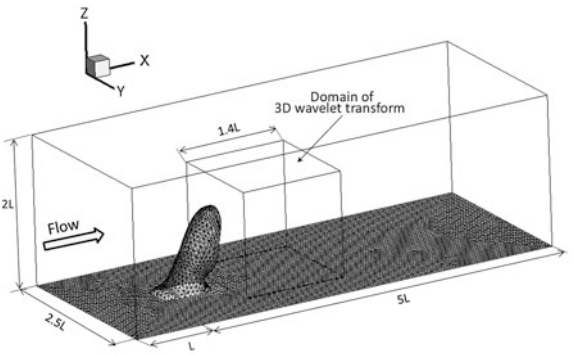


**Fig. 2** Computational domain

## 3 3D Orthogonal Wavelet Transform

Given a three-dimensional data matrix $V^N = \left[v_{i,j,k}\right]$ ($i = 1,\ldots,2^N$; $j = 1,\ldots,2^N$; $k = 1,\ldots,2^N$) having size of $2^N \times 2^N \times 2^N$, its coefficients of three-dimensional wavelet transform $\boldsymbol{S}$ can be obtained by

$$\boldsymbol{S} = \left(\boldsymbol{W}\left(\boldsymbol{W}\left(\boldsymbol{W}\boldsymbol{V}^{\boldsymbol{N}}\right)^{\boldsymbol{T}}\right)^{\boldsymbol{T}}\right)^{\boldsymbol{T}} \tag{1.1}$$

where $\boldsymbol{W}$ is constructed based on a cascade algorithm of the wavelet basis matrix and the permuting matrix for all level transform and satisfies $\boldsymbol{W}^{\boldsymbol{T}}\boldsymbol{W} = \boldsymbol{I}$, where $\boldsymbol{I}$ is a unit matrix. The inverse orthogonal discrete wavelet transform can be simply performed by reversing the procedure, that is,

$$\boldsymbol{V}^{\boldsymbol{N}} = \boldsymbol{W}^{\boldsymbol{T}}\boldsymbol{W}^{\boldsymbol{T}}\boldsymbol{S}^{\boldsymbol{T}}\boldsymbol{W} \tag{1.2}$$

In order to obtain the wavelet level components of the transformed data, similarly to one- and two-dimensional wavelet multi-resolution analysis (Rinoshika and Zhou 2005; Rinoshika and Omori 2011), the orthogonal wavelet coefficient matrix $\boldsymbol{S}$ is first decomposed into the sum of all levels:

$$\boldsymbol{S} = \boldsymbol{D}_1^N + \boldsymbol{D}_2^N + \cdots \boldsymbol{D}_i^N + \cdots + \boldsymbol{D}_{N-2}^N \tag{1.3}$$

where $\boldsymbol{D}_i^N$ consists of a wavelet coefficient matrix of level $i$ and a zero matrix, having size of $2^N \times 2^N \times 2^N$.

The inverse orthogonal wavelet transform is then applied to the coefficient of each level, viz.

$$\boldsymbol{V}^N = \boldsymbol{W}^T\boldsymbol{W}^T\boldsymbol{D}_1^T\boldsymbol{W} + \boldsymbol{W}^T\boldsymbol{W}^T\boldsymbol{D}_2^T\boldsymbol{W} + \cdots \boldsymbol{W}^T\boldsymbol{W}^T\boldsymbol{D}_i^T\boldsymbol{W} + \cdots + \boldsymbol{W}^T\boldsymbol{W}^T\boldsymbol{D}_{N-2}^T\boldsymbol{W} \tag{1.4}$$

where the first term $\boldsymbol{W}^T\boldsymbol{W}^T\boldsymbol{D}_1^T\boldsymbol{W}$ and the last term $\boldsymbol{W}^T\boldsymbol{W}^T\boldsymbol{D}_{N-2}^T\boldsymbol{W}$ represent the data components at wavelet level 1 (the highest grouped frequency) and level $N$-2

(the lowest grouped frequency), respectively. This decomposition method is referred to as the *three-dimensional wavelet multi-resolution technique*.

## 4 Spectral Characteristics of Wavelet Components

In order to analyze the three-dimensional flow structures of various scales, a three-dimensional wavelet multi-resolution technique is used to decompose the velocity and vorticity data of LES. The analysis region, as shown in Fig. 2, is focused on a volume of 140 × 140 × 140 mm behind the door mirror, which is divided into a mesh of 64 × 64 × 64. It results in a mesh size of 2.2 mm that represents the spatial resolution of LES.

To determine the scale characteristics of each wavelet component, the $u_y$ velocity signal is analyzed by the wavelet multi-resolution technique and is decomposed into three wavelet components. In this study, the instantaneous velocity field (64 × 64 × 64) extracted from LES is first decomposed into three wavelet levels or wavelet components by the three-dimensional orthogonal wavelet multi-resolution analysis. Then, the fast Fourier transform is used to analyze each wavelet component. The spectrum of each wavelet component displays a pronounced peak at a scale called the central scale. The wavelet level 1 having central scale of 16 mm represents the relatively small-scale structures, and the wavelet level 2 having central scale of 29 mm represents the intermediate-scale structure while the wavelet level 3 with central scale smaller than 62 mm refers the large-scale structure.

## 5 Results and Discussion

To quantify the flow structures around the mirror, the instantaneous velocity and pressure fields are simulated by LES at a constant free-stream velocity of 15 m/s, which corresponds to Reynolds number $Re$ ($\equiv UL/\nu$) = $10^5$. Figure 3 shows the representative instantaneous streamlines and corresponding vorticity contours, $\omega_y$ in the ($x$, $z$)-plane and $\omega_z$ in the ($x$, $y$)-plane. Here, the white and black represent positive and negative maximum values of vorticity, respectively. The streamlines and vorticity contours display the quasi-periodical large-scale vortices with opposite sense of rotation shed from the mirror in the separating region in both of the ($x$, $z$)- and ($x$, $y$)-plane. The large-scale structures are very similar to the Karman vortices of a cylinder wake. The largest vorticity concentration appears in the shear layer, which originates from the shear layer instability. This flow structure appears rather similar to the experimental results based on high-speed PIV (Rinoshika et al. 2007, 2010), thus providing a validation of the LES.

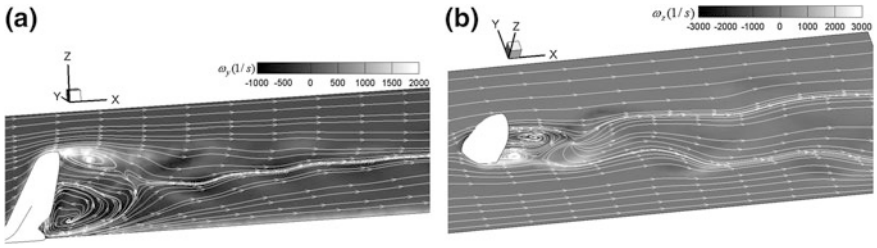


**Fig. 3** Instantaneous sectional streamlines and corresponding vorticity contours of the LES: **a** $\omega_y$, **b** $\omega_z$. The *white* and *black* represent positive and negative values of vorticity, respectively

In order to analyze the multi-scale flow structures of mirror wake, the 3D wavelet multi-resolution technique is used to decompose velocity and vorticity behind the mirror (as shown in Fig. 2). Figure 4 shows instantaneous velocity vectors and vorticity magnitude contours $|\omega| = (\sqrt{\omega_x^2 + \omega_y^2 + \omega_z^2})$ of the LES and wavelet components in the ($x$, $z$)-plane (the plan view). Two large-scale vortices, which originate from the tip and root of the mirror, respectively, are clearly

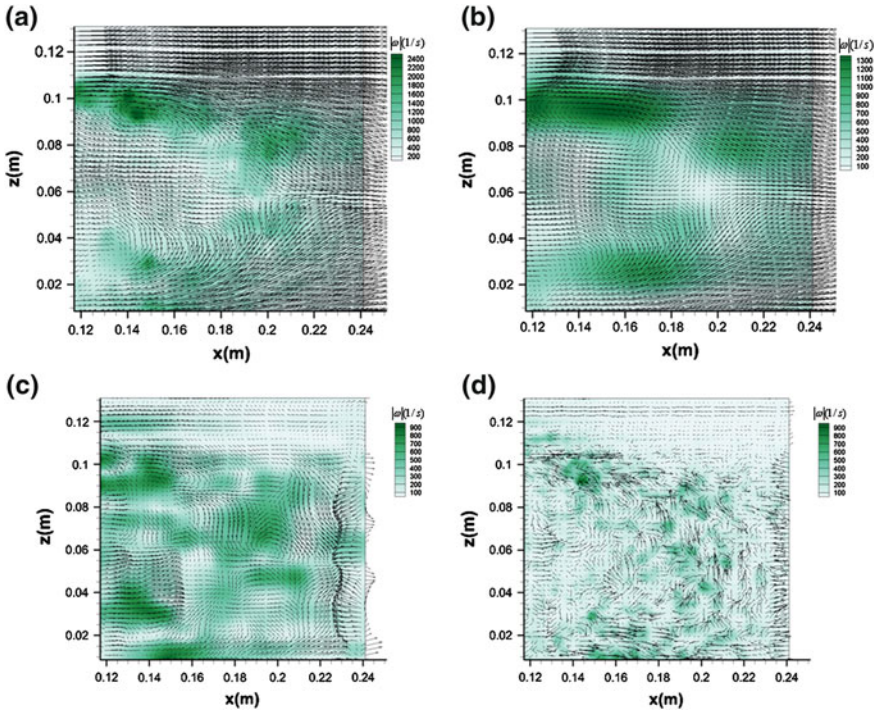


**Fig. 4** Instantaneous velocity vectors and vorticity magnitude contours $|\omega|$ of the LES and wavelet components in the ($x$, $z$)-plane

observed at central scale of 62 mm (level 3) in Fig. 4b. They correspond well to the large-scale structures of the LES (Fig. 4a). The vortex near the root is slightly larger than that at the tip. The large-scale vortices exhibit main contribution to the separation region. Besides the large-scale vortices observed in the LES (Fig. 4a), several intermediate-scale vortices shed from the mirror as well as the relatively small-scale ones are clearly identifiable at central scales of 29 mm and 16 mm (level 2 and 3) in Fig. 4c, d. However, the large-scale structures exhibit stronger vorticity concentration.

## 6 Conclusions

The three-dimensional orthogonal wavelet multi-resolution technique is applied to analyze LES data and the flow structure around an externally mounted vehicle mirror is decomposed into various scales. The following conclusions can be drawn.

1. Three-dimensional velocity and vorticity fields of the LES are decomposed into three wavelet components having large-, intermediate-, and relatively small-scale.
2. The large-scale structure dominates the mirror wake flow and its vorticity concentration makes main contribution. Several intermediate-scale vortices as well as the relatively small-scale ones, which cannot be observed in the LES, are clearly identifiable.

## References

Ono K, Himeno R, Fukushima T (1999) Prediction of wind noise radiated from passenger cars and its evaluation based on auralization. J Wind Eng Ind Aerodyn 81:403–419

Reichl C, Krenn C, Mann M, Lang H (2005) Application of numerical and experimental techniques for the aero-acoustic characterisation of a car rear-view mirror. Int J Aeroacoustics 4:185–212

Rinoshika A, Omori H (2011) Orthogonal wavelet analysis of turbulent wakes behind various bluff bodies. Exp Therm Fluid Sci 35:1231–1238

Rinoshika A, Watanabe K (2010) Orthogonal wavelet decomposition of turbulent structures behind a vehicle external mirror. Exp Therm Fluid Sci 34:1389–1397

Rinoshika A, Watanabe K, Nakano M (2007) Experimental investigation of flow structures around a car mirror. Dyn Continuous, Discrete & Impulsive Systems Ser B Applications & Algorithms 14(S8):78–90

Rinoshika A, Zhou Y (2005) Orthogonal wavelet multi-resolution analysis of a turbulent cylinder wake. J Fluid Mech 524:229–248

Watkins S, Oswald G (1999) The flow field of automobile add-ons with particular reference to the vibration of external mirrors. J Wind Eng Ind Aerodyn 83:541–554

# POD Study of a Turbulent Boundary Layer Over a Rough Forward-Facing Step

**Yanhua Wu and Hui Tang**

**Abstract** Large-scale fluctuating flow structures are studied using snapshot proper orthogonal decomposition (POD) in a turbulent boundary layer over a realistic rough forward-facing step (FFS) at $Re_h = 3{,}450$ and $\delta/h = 8$. It was observed that large-scale Q2 event induced by hairpin vortex packet and large-scale Q4 event are the dominant fluctuating flow structures that contribute significantly to the first POD mode for both smooth and rough steps. However, the flow structures close to the rough surface were affected differently by different roughness topographies.

**Keywords** Turbulent boundary layer · Forward-facing step flow · Turbulence structures · Proper orthogonal decomposition

## 1 Introduction

Turbulent flows over forward-facing steps (FFSs) have been the focus of many studies due to their importance in understanding the generation of noise and structural vibrations in various engineering applications. The unique features of the turbulent flows over a FFS include the existence of two recirculation regions: One is located in the lower front corner of the step, and the other one occurs downstream of the step's front and on the top surface of the step. A strong shear layer that is representative of a mixing layer exists above the downstream recirculation region. Near-wall turbulence statistics of the boundary layers over the FFS are investigated in few studies, which include Hattori and Nagano (2010) using DNS ($Re_h = 900$–$3{,}000$, $\delta/h = 1.5$–$3$) and Ren and Wu (2011) through PIV

Y. Wu (✉) · H. Tang
School of Mechanical and Aerospace Engineering, Nanyang Technological University, Singapore, Singapore
e-mail: yanhuawu@ntu.edu.sg

Y. Zhou et al. (eds.), *Fluid-Structure-Sound Interactions and Control*,
Lecture Notes in Mechanical Engineering, DOI: 10.1007/978-3-642-40371-2_11,

measurements ($Re_h = 3{,}450$, $\delta/h = 8$, where $\delta$ is the incoming boundary layer thickness). In both studies, a significant increase in Reynolds normal and shear stresses was observed in the downstream recirculation region. Ren and Wu (2011) also investigated the effects of realistic roughness topography on the turbulent boundary layer over the FFS. Their results showed that the separated turbulent flow in the downstream recirculation region had been significantly modified by the studied roughness. Even far less explored are the turbulent structures in the turbulent FFS flows. The objective of this work is to investigate the impacts of a realistic roughness on the turbulence structures imbedded in the turbulent FFS flow using proper orthogonal decomposition (POD). Since POD was introduced into fluid mechanics, it has become one of the most important tools to study the turbulence structures that contain significant turbulent kinetic energies (see, e.g., Wu and Christensen 2010).

## 2 Experiment

The particle image velocimetry (PIV) experiments were performed in an Eiffel-type, open circuit, boundary layer wind tunnel with a freestream turbulence intensity of $\sim$0.45 %. A rough block that is 90 mm (14 $h$) long, 169 mm (27 $h$) wide, and with a mean height of $h = 6.35$ mm is placed at the spanwise center of the boundary layer plate. The top surface of this block is highly irregular, while the

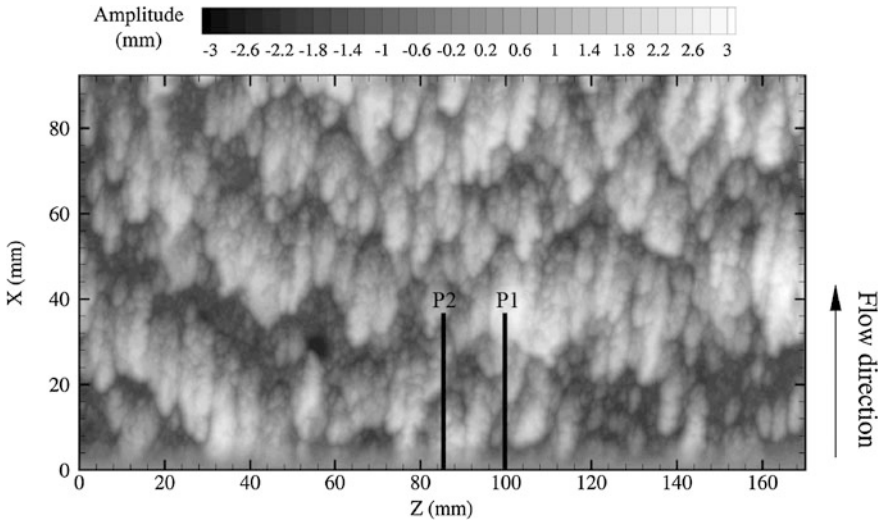


**Fig. 1** Topography of the roughness on the top surface of the rough block. The contour shows the fluctuating heights. P1 and P2 are the positions of PIV measurement planes

bottom surface is smooth. The roughness topography of the rough block's top surface is shown in Fig. 1.

High spatial resolution PIV measurements were performed in the streamwise wall-normal ($x$–$y$) planes at two distinct spanwise locations (P1 and P2 in Fig. 1) for both smooth and rough FFSs at $Re_h = (U_\infty\ h)/\nu = 3{,}450$. The experimental schematic is shown in Fig. 2. The particle images were obtained using an 8-bit frame-straddle CCD camera of 1,600 × 1,200 pixels. The pairs of PIV images were interrogated using a recursive two-frame cross-correlation method with interrogation window size of 20 × 20 pixels with 50 % overlap. The resulting velocity vector fields have a grid spacing of 0.2 mm or $h$/32. The ratio of incoming boundary layer thickness to the step height is $\delta/h = 8$. As described in Ren and Wu (2011), the most important difference in roughness between measurement positions P1 and P2 is that roughness profile at P2 starts with a strong positive slope while that at P1 starts with a strong negative slope.

## 3 Results and Discussion

Snapshot POD was only applied to the downstream recirculation region since it is this region where the turbulence statistics illustrate significant differences between the smooth and rough FFS flows (Ren and Wu 2011). In addition, in order not to include too much information on the turbulence structures in the incoming turbulent boundary layer, the flow area for the current POD analysis is confined in the region of $0 < x < 5\ h$ and $1 < y < 3\ h$ with the origin set at the lower corner of the step. The fractional contributions of the first POD mode, $\phi_1$, to the total turbulence kinetic energy $\langle u^2 + v^2 \rangle$ for the smooth step and the rough step at P1 and P2 locations are 20.38, 27.37, and 21.44 %, respectively. It is seen that the first

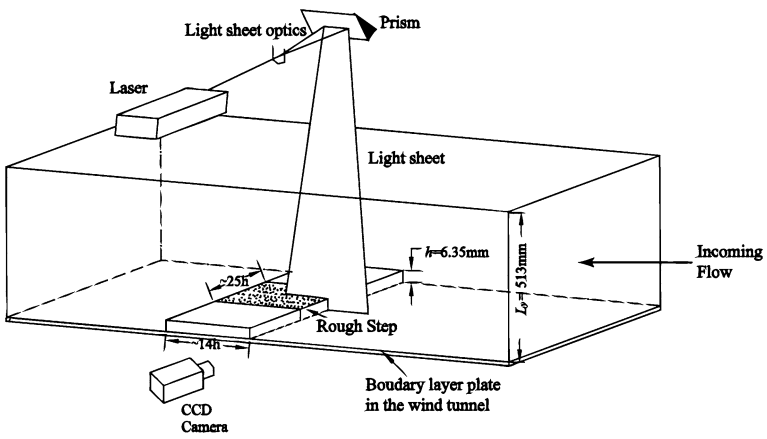


**Fig. 2** Schematic of experimental setup

mode at location P1 of the rough step contains significantly higher fractional energy.

The vector plots of the first POD mode for both smooth and rough steps are presented in Fig. 3. It can be observed that the first modes of all these cases illustrate large-scale Q4 or Q2 events that cover almost the whole field of view. $\phi_1$ of the smooth step shows a large Q4 event with a small region of Q1 event close to the step's front. On the other hand, the first POD mode for the rough step at either P1 or P2 location reveals a large Q2 event with the existence of a small region of Q3 event immediately downstream of the rough step's front. The vector plots do not show obvious differences between the first modes of the rough step at these two different spanwise locations although $\phi_1$ at P1 occupies about 28 % more fractional energy than that at P2.

In POD analysis, equation $\int_T a_i^2 \mathrm{d}t = \lambda_i$ indicates that the instantaneous fluctuating velocity field with a large value of POD coefficient squared ($a_1^2$) contributes more significantly to the eigenvalue, $\lambda_i$, a larger value of which represents a larger fraction of the kinetic energy from the *i*th POD mode. Therefore, although POD eigenfunctions are a set of basis functions *mathematically* extracted from the turbulent velocity fields, the instantaneous fluctuating flow structures that correspond to a particular eigenfunction may be crudely identified from velocity fields with large absolute values of $a$ for the first few dominant POD modes. In addition, since the contribution to $\lambda_i$ comes from $a_1^2$, instantaneous fluctuating velocity fields with either positive $a_i$ or negative $a_i$ contain equivalently important information on the flow structures relevant to the *i*th POD mode. To examine the fluctuating flow structures corresponding to the first POD mode of smooth and rough FFSs, the instantaneous velocity fields with large positive and negative $a_1$ values are presented in Fig. 4.

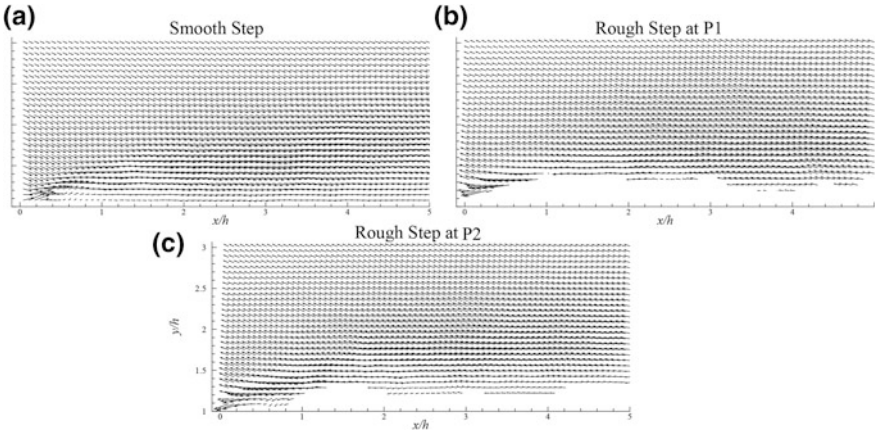


**Fig. 3** First POD eigenfunction, $\phi_1$, for **a** smooth step; **b** rough step at location P1; and **c** rough step at location P2

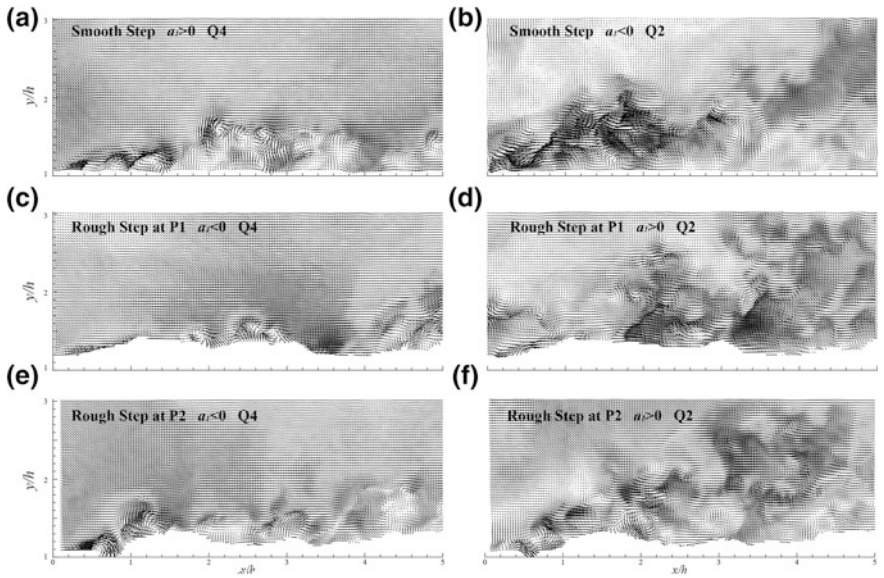


**Fig. 4** Examples of instantaneous fluctuating velocity fields with large values of $a_1^2$. Every other velocity vector is shown

For the smooth-step case, Fig. 4a illustrates a series of strong spanwise vortices within a large-scale Q4 event. The first three vortices appear to be produced by the roll-up of the fluctuating shear layer immediately downstream of the sharp front. The major flow structure shown in Fig. 4b is the large-scale and strong Q2 event particularly within $y = 2\ h$. This flow structure is consistent with the hairpin vortex packet observed in the smooth-wall turbulent boundary layer. For the rough step at location P1, Fig. 4c reveals a large-scale Q4 event occupying a large portion of the flow field. In contrast to the smooth-step one, there exist no trains of vortices within about 1.5 $h$ downstream of the step's front. As in the smooth-step case, a large-scale Q2 event that again appears to be induced by the hairpin vortex packet is also observed in Fig. 4d. Compared with the Q2 event in Fig. 4b within $x = 1.5\ h$ of the smooth step, that for the rough step at P1 is much weaker. Figure 4e, f shows the instantaneous fluctuating flow structures contributing significantly to the first POD mode of the rough step at P2. A large-scale Q4 event is shown in Fig. 4e with two obvious spanwise vortices within 1.5 $h$ downstream of the step while the fluctuating velocity vectors thereafter do not reveal well-defined vortices that, however, are clearly observed in Fig. 4a for the smooth step. Figure 4f shows a few counterclockwise-rotating vortices underneath the large-scale Q2 event, which indicates some topological changes in the vortices of the hairpin vortex packet close to the rough surface at location P2.

## 4 Summary and Conclusions

Snapshot POD was applied to a turbulent boundary layer over a realistic rough FFS at $Re_h = 3{,}450$ and $\delta/h = 8$ to investigate the large-scale fluctuating flow structures that contribute significantly to the turbulent kinetic energy. It was observed that both large-scale Q4 event and Q2 event induced by hairpin vortex packet are the dominant fluctuating flow structures that contribute significantly to the first POD mode for both smooth and rough steps. However, the specific roughness topographies affected the instantaneous flow structures close to the rough surface differently.

## References

Hattori H, Nagano Y (2010) Investigation of turbulent boundary layer over forward-facing step via direct numerical simulation. Int J Heat Fluid Flow 31:284–294

Ren H, Wu Y (2011) Turbulent boundary layers over smooth and rough forward-facing steps. Phys Fluids 23:045102

Wu Y, Christensen KT (2010) Spatial structure of a turbulent boundary layer with irregular surface roughness. J Fluid Mech 655:380–418

# Eulerian/Lagrangian Sharp Interface Schemes for Multimaterials

**Yannick Gorsse, Angelo Iollo and Thomas Milcent**

**Abstract** We present multimaterial simulations using both Eulerian and Lagrangian schemes. The methods employed are based on classical Godunov-like methods that are adapted to treat the case of interfaces separating different materials. In the models considered, the gas, liquids, or elastic materials are described by specific constitutive laws, but the governing equations are the same. Examples of gas–gas and gas–elastic material interactions in one- and two-spatial dimensions are presented.

## 1 Introduction

Physical and engineering problems that involve several materials are ubiquitous in nature and in applications. The main contributions in the direction of simulating these phenomena go back to Godunov (1978) for the model and Favrie et al. (2009) for numerical simulations. However, the numerical scheme presented in that paper is relatively complicated and has the disadvantage that the interface is diffused over a certain number of grid points. We propose a simple second-order accurate method to recover a sharp interface description keeping the solution stable and nonoscillating. This scheme can be adapted to both Eulerian and Lagrangian frameworks.

Y. Gorsse · A. Iollo
IMB and Inria, Bordeaux, France
e-mail: yannick.gorsse@math.u-bordeaux1.fr

A. Iollo
e-mail: angelo.iollo@math.u-bordeaux1.fr

T. Milcent (✉)
I2M and Arts et Metiers Paristech, Bordeaux, France
e-mail: thomas.milcent@u-bordeaux1.fr

Y. Zhou et al. (eds.), *Fluid-Structure-Sound Interactions and Control*,
Lecture Notes in Mechanical Engineering, DOI: 10.1007/978-3-642-40371-2_12,

## 2 Eulerian Model

The conservative form of elastic media equations in the Eulerian framework are

$$\begin{cases} \rho_t + \mathrm{div}_x(\rho u) = 0 \\ (\rho u)_t + \mathrm{div}_x(\rho u \otimes u - \sigma) = 0 \\ (\rho e)_t + \mathrm{div}_x(\rho e u - \sigma^T u) = 0 \\ (\nabla_x Y)_t + \nabla x\,(u \cdot \nabla_x Y) = 0 \end{cases} \tag{1}$$

The unknowns are the density $\rho(x,t)$, the velocity $u(x,\ \mathrm{t})$, the total energy per unit mass $e(x,t)$, and the backward characteristics of the problem $Y(x,t)$. Here, $\sigma(x,t)$ is the Cauchy stress tensor in the physical domain.

## 3 Lagrangian Model

The counterpart of these equations in the lagrangian framework are

$$\begin{cases} (\rho_0 X_t)_t - \mathrm{div}_\xi(\mathscr{T}) = 0 \\ (\rho_0 e)_t - \mathrm{div}_\xi(\mathscr{T}^T X_t) = 0 \end{cases} \tag{2}$$

The unknowns are the velocity $X_t(\xi,t)$ (the direct characteristics of the problem are $X(\xi,t)$ and the total energy per unit mass $e(\xi,t)$. Here, $\mathscr{T}(\xi,t)$ is the first Piola–Kirchhoff stress tensor in the reference domain and $\rho_0$ is the initial density.

## 4 Constitutive Law

To close the system, a constitutive law is chosen:

$$\varepsilon = e - \frac{1}{2}|u|^2 = \frac{\exp\left(\frac{s}{c_v}\right)\rho^{\gamma-1}}{\gamma - 1} + \frac{p_\infty}{\rho} + \frac{\chi}{\rho_0}(\mathrm{Tr}(\bar{B}) - 2) \tag{3}$$

where $s(x,t)$ is the entropy and $\bar{B}$ is the modified left Cauchy–Green tensor which depends on $\nabla_x Y$. The constants $c_v, \gamma, p_\infty, \chi$ characterize a given material. The two first terms of (3) represent a stiffened gas and the third one represents a Neo-Hookean elastic solid. The stress tensors $\sigma$ and $\mathscr{T}$ are then derived from this constitutive law as a function of the problem unknowns.

## 5 Approximate Riemann Solver

We have already developed a numerical scheme to solve the Eulerian equations of conservation (1). This scheme is based on a directional splitting on a fixed Cartesian mesh where the fluxes are computed by an HLLC approximate Riemann solver. The interface is kept sharp by using a nonconservative numerical flux for the computational cells that are crossed by the contact discontinuity. We refer for the 1D numerical results to Iollo et al. (2011) and Gorsse et al. (2012).

For the Lagrangian scheme, the ideas are the same but the contact discontinuity turns out to be steady by definition in this framework.

## 6 Results

### *6.1 Eulerian*

For the Eulerian framework, we provide numerical results of fluid–structure interaction involving 2D impacts. The initial configuration is a "T"-shaped domain (filled with copper or water) and surrounded by air. We impose an initial horizontal velocity on the protruding square of the "T". In Fig. 1, we present the numerical results obtained with our multimaterial scheme of air–copper (left) and air–water (right) media after the impact.

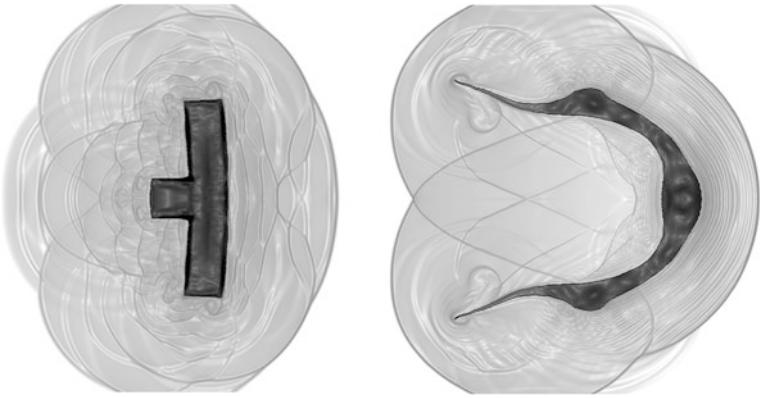

**Fig. 1** Schlieren image of the density for the air–copper (*left*) and air–water (*right*) after the impact

## 6.2 Lagrangian

As for the Lagrangian equations of conservation (2), we start by solving classical 1D shock-tube test cases for a perfect gas ($\gamma = 1.4$). First of all, we consider a Sod shock tube. The initial condition consists two piece-wise constant states. For the left state, $\rho_0 = 1$, $-\mathscr{T}^{11} = 1$, $X_t = 0$; for the right $\rho_0 = 0.125$, $-\mathscr{T}^{11} = 0.1$, $X_t = 0$. The results at the same times in the reference and in the physical plane are shown in Fig. 2 with second-order accuracy in space and 1,000 grid points. A similar test case has been performed with an elastic material whose characteristics model those of copper ($\gamma = 4.22$, $p_\infty = 3.42 \times 10^{10}$, $\chi = 3.42 \times 10^{10}$). We have also for the left state $\rho_0 = 8{,}900$, $-\mathscr{T} = 10^9$, $X_t^1 = 0$, $X_t^2 = 0$; for the right $\rho_0 = 8{,}900$, $-\mathscr{T} = 10^5$, $X_t^1 = 0$, $X_t^2 = 100$. We have discontinuous normal tensor components and discontinuous vertical velocity components. In Fig. 3, the results are shown for the

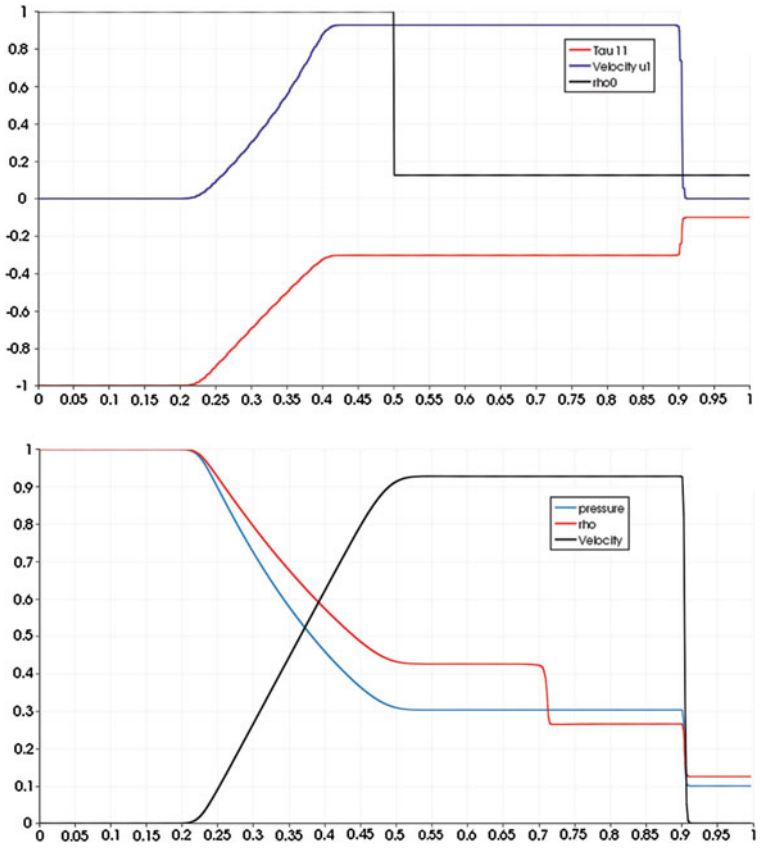


**Fig. 2** Sod test case. Reference domain (*up*) and physical domain (*down*)

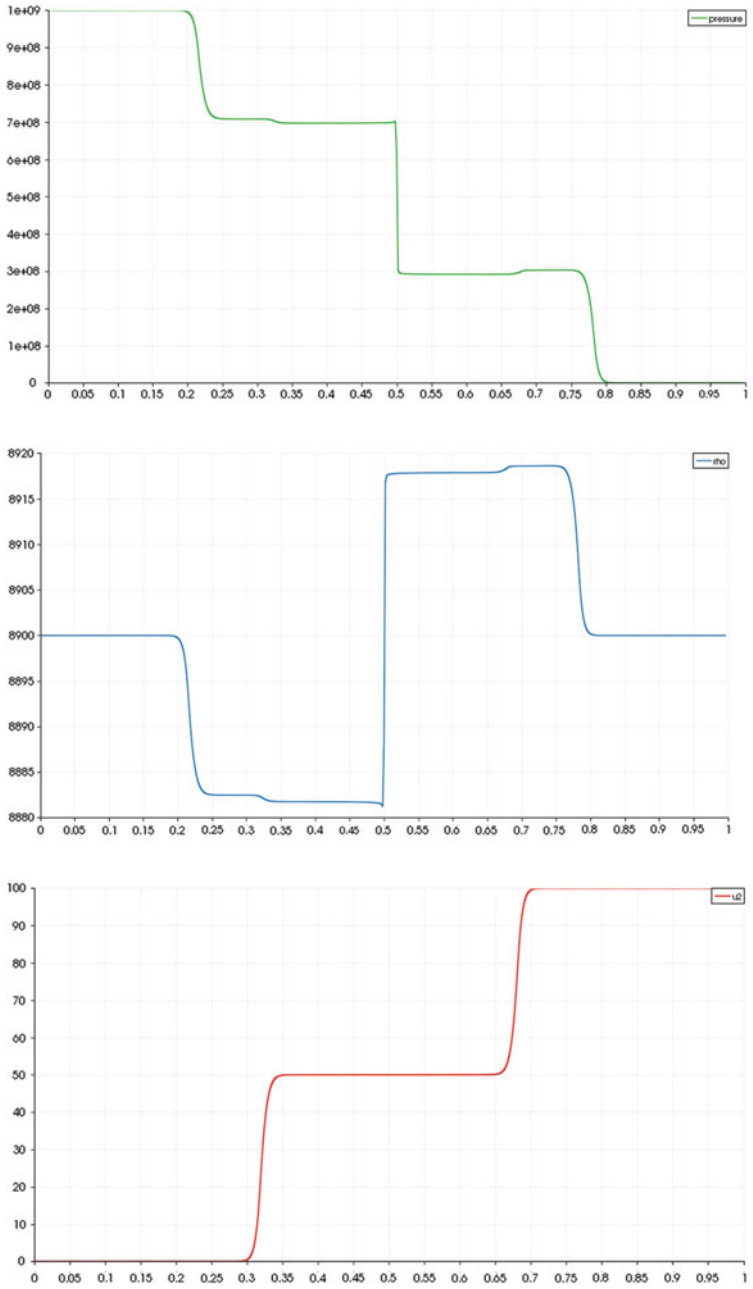


**Fig. 3** Copper test case. Five waves are present: the contact discontinuity is sharp; pressure is discontinuous at the contact discontinuity (but the stress tensor is continuous); the vertical speed is continuous at the contact discontinuity and at the normal perturbations, discontinuous at the shear waves

physical domain. They compare well with those presented in Favrie et al. (2009) and Iollo et al. (2011).

## 7 Conclusions

We have synthetically presented a model to deal with multimaterials in Eulerian and Lagrangian framework. For the Eulerian case, we show 2D results of stiff gas–structure and fluid–structure interaction. For the Lagrangian case, we have limited our scrutiny to 1D cases. Ongoing research addresses 2D models.

## References

Favrie N, Gavrilyuk SL, Saurel R (2009) Solid-fluid diffuse interface model in cases of extreme deformations. J Comput Phys 228(16):6037–6077

Godunov SK (1978) Elements of continuum mechanics. Nauka, Moskow

Gorsse Y, Iollo A, Milcent T, Telib H (2012) Accurate sharp interface scheme for multimaterial. In: International conference on computational fluid dynamics (ICCFD7). Hawaii

Iollo A, Milcent T, Telib H (2011) A sharp contact discontinuity scheme for multimaterial models. In: Proceedings of finite volumes for complex applications VI in Mathematics 4. Springer

# Turbulent Drag Reduction at High Reynolds Numbers

**Yongmann M. Chung and Edward Hurst**

**Abstract** Direct numerical simulations were performed to study the effect of streamwise travelling waves of spanwise wall velocity on turbulent channel flow. Simulations with various control parameters, scaled by wall units, are performed at four Reynolds numbers, corresponding to $Re_\tau = 200, 400, 800, 1600$. As the Reynolds number is increased the intensity of both the drag reduction and drag increase is reduced. This reduction does not scale universally, and the drag reduction deteriorates quickly with increased Reynolds number when the parameters used are close to optimal. The consequence of this variation in Reynolds scaling is that the value of the optimal forcing parameters change, even in wall units, with increased Reynolds number.

**Keywords** Drag reduction · Flow control · Wall oscillation · Reynolds number · DNS

## 1 Introduction

Turbulent skin friction drag reduction has been studied by applying the following forcing at the wall (Quadrio et al. 2009)

$$w(x, y = 0, z, t) = W_m \sin(\kappa_x x - \omega t), \tag{1}$$

where $W_m$ is the maximum wall velocity, $\kappa_x$ is the streamwise wavenumber and $\omega$ is the oscillation frequency. When $\kappa_x = 0$, the forcing becomes the purely temporal wall oscillation case, and the $\omega = 0$ case specifies the purely spatial stationary wave.

Y. M. Chung (✉) · E. Hurst
School of Engineering and CSC, University of Warwick, Coventry CV4 7AL, UK
e-mail: Y.M.Chung@warwick.ac.uk

Y. Zhou et al. (eds.), *Fluid-Structure-Sound Interactions and Control*,
Lecture Notes in Mechanical Engineering, DOI: 10.1007/978-3-642-40371-2_13,

As the previous numerical studies have been confined to low Reynolds numbers the Reynolds number effect is a requirement in finding out how useful the flow control method is at higher Re numbers (Ricco and Quadrio 2008; Choi et al. 2002; Touber and Leschziner 2012; Hurst and Chung 2012a). In this study, direct numerical simulations of turbulent channel flow subjected to streamwise travelling waves of spanwise wall velocity were performed at four Reynolds numbers with the intention of understanding the relationship between drag reduction and Re. The Reynolds numbers studied correspond to $\mathrm{Re}_\tau = 200$, 400, 800 and 1600, based on the no-control case. To the best of the authors' knowledge, this is the highest Re number attempted for flow control DNS (Hurst and Chung 2012b). A range of $\kappa_x^+$ and $\omega^+$ values were chosen while the maximum wall velocity was fixed at $W_m^+ = 12$ for all Re numbers considered.

## 2 Results

The results presented are generated by a second order finite-volume DNS code (Talha 2012), based on the fully implicit fractional step method presented by Kim et al. (2002), in which a Crank-Nicolson discretisation is used for both the diffusion and convective terms. First, direct numerical simulations of the fully developed turbulent channel flow were performed at four Reynolds numbers $\mathrm{Re}_\tau = 200$, 400, 800, 1600, based on the frictional velocity of the no control case, $u_{\tau_0}$. The simulations were run with a constant mass flow rate. The Reynolds numbers based on the bulk velocity, domain sizes, grid sizes and resolutions are shown in Table 1. Throughout this paper $+$ represents the wall units based on $u_{\tau_0}$. The no control case results compared well with available DNS data from the literature. Figure 1 shows the mean velocity and rms velocity fluctuation.

### 2.1 Drag Reduction Map

Figure 2 shows the drag reduction map in the $(\omega, \kappa_x)$ parameter space at $\mathrm{Re}_\tau = 200$ and 400. The DR map for the lower Re number compares very well with Quadrio et al. (2009). When comparing the parameters scaled by wall units, the

**Table 1** Direct numerical simulation parameters for the four Reynolds numbers studied

| $\mathrm{Re}_\tau$ | 200 | 400 | 800 | 1600 |
|---|---|---|---|---|
| Re | 3150 | 7000 | 15700 | 34500 |
| $L_x \times L_y \times L_z$ | 16 × 2×6 | 16 × 2 × 6 | 12 × 2 × 4 | 12 × 2 × 4 |
| $N_x \times N_y \times N_z$ | 320 × 140 × 240 | 640 × 240 × 480 | 960 × 384 × 640 | 1920 × 800 × 1280 |
| $\Delta_x^+, \Delta_y^+, \Delta_z^+$ | 10,0.4–6.5,5 | 10,0.4–7.2,5 | 10, 0.4–9.7,5 | 10,0.4–9.2,5 |

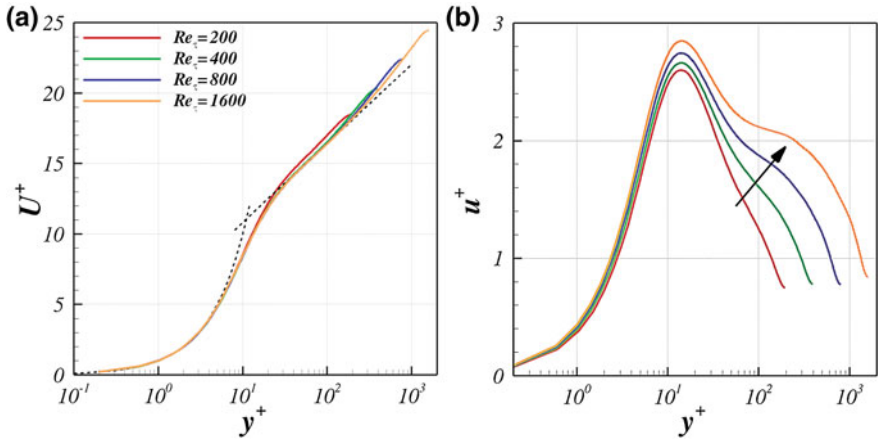


**Fig. 1** DNS of turbulent channel flow without wall forcing. **a** Log-law velocity profile, and **b** streamwise velocity fluctuation, $u_{\text{rms}}$

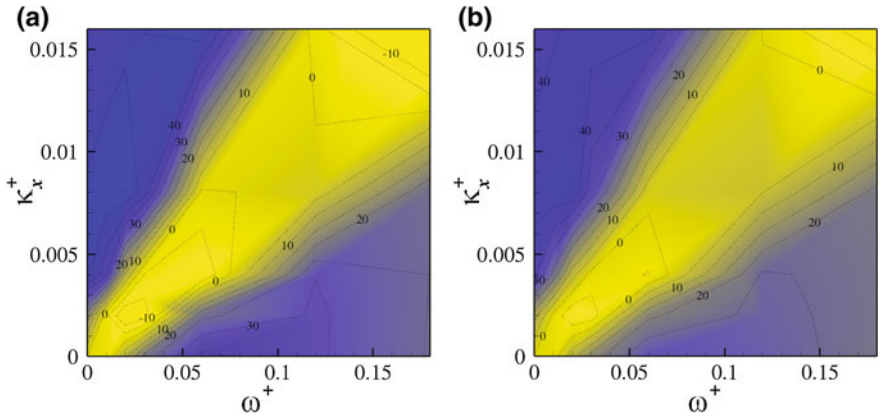


**Fig. 2** Drag reduction map for the forward travelling waves at **a** $\text{Re}_\tau = 200$ and **b** $\text{Re}_\tau = 400$ Contour levels are drawn at 5 % intervals. The bright (*yellow*) colour indicates a drag increase, and the dark (*blue*) indicates a drag reduction

drag reduction is seen to decrease as the Reynolds number increases. There is also a smaller drag increase in the $\text{Re}_\tau = 400$ case. One of the focuses of this work is to see whether the optimal values remain the same at different Reynolds numbers. This helps understand whether the optimal control parameters scale with the wall variables.

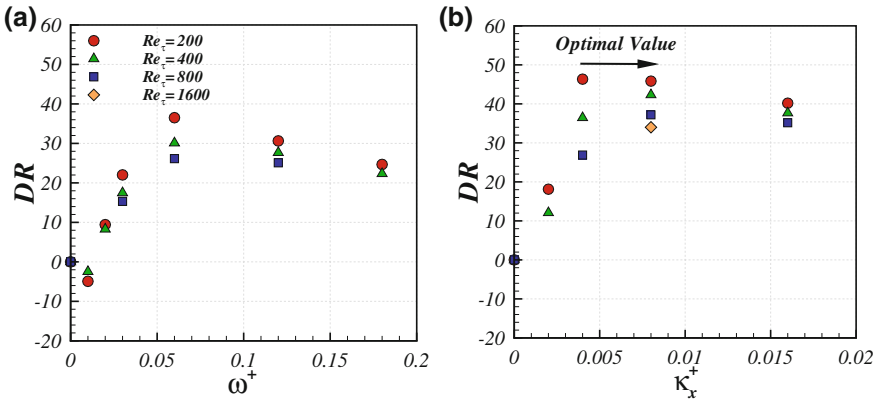


**Fig. 3** Drag reduction at the four Reynolds numbers studied for **a** the wall oscillation case, $\kappa_x^+ = 0$, and **b** the stationary wave case, $\omega^+ = 0$

## 2.2 Wall Oscillation

The Reynolds number effect of the wall oscillation and stationary wave cases is shown Fig. 3 for Reynolds numbers up to $\mathrm{Re}_\tau = 1600$. When comparing the parameters scaled by wall units, the drag reduction decreases as the Reynolds number increases for both wall oscillation and stationary wave cases. From the wall oscillation case, the reduction in DR is seen as Re increases. However, the extent of the variation is dependent on the oscillation frequency. It appears that the optimal oscillation frequency remains at $\omega^+ = 0.06$, corresponding to $T^+ = 100$, whilst it was found (Hurst and Chung 2012) that the optimal value for the stationary wave, based on the parameters studied, varies from $\kappa_x^+ = 0.006$ at $\mathrm{Re}_\tau = 200$ to $\kappa_x^+ = 0.008$ by $\mathrm{Re}_\tau = 400$.

The Re number effect for the travelling wave case was considered elsewhere (Hurst and Chung 2013). With fixed $\kappa_x^+ = 0.008$ the optimal frequency $\omega_{opt}^+$ decreases as $\mathrm{Re}_\tau$ increases, while with fixed $w^+ = 0.02$ the optimal wavenumber $\kappa_{x,\mathrm{opt}}^+$ appears to increase.

## 2.3 The Reynolds Number Effect

The Reynolds number effect can be expressed in the form of $\mathrm{DR} \sim \mathrm{Re}_\tau^{-\alpha}$; a large $\alpha$ value indicates a strong Re effect, i.e., a smaller drag reduction. Table 2 shows

**Table 2** DR scalings for (a) wall oscillation and (b) the stationary wave

| (a) | $\omega^+$ | 0.03 | 0.06 | 0.12 | (b) | $\kappa_x^+$ | 0.004 | 0.006 | 0.008 |
|---|---|---|---|---|---|---|---|---|---|
| | DR ∼ | $\mathrm{Re}_\tau^{-0.31}$ | $\mathrm{Re}_\tau^{-0.26}$ | $\mathrm{Re}_\tau^{-0.14}$ | | DR ∼ | $\mathrm{Re}_\tau^{-0.38}$ | $\mathrm{Re}_\tau^{-0.18}$ | $\mathrm{Re}_\tau^{-0.13}$ |

scalings calculated from the present DNS results at different values of $\omega^+$ and $\kappa_x^+$ parameters. A wide range of $\alpha$ values are observed in the wall oscillation and stationary wave cases, suggesting that the effect of the Re number cannot be represented by a simple scaling with a constant $\alpha$ value.

## 3 Conclusion

The effect of Reynolds number has been observed for travelling wave cases using direct numerical simulations for Reynolds numbers up to $\mathrm{Re}_\tau = 1600$. It is found that the drag reduction of the travelling wave becomes less efficient as Re increases. It is evident that the optimal control parameters change with Re number. The optimal $\kappa_x^+$ value for the stationary wave case appears to increase with the Re number while the changes in the optimal $\omega^+$ for the wall oscillation case is less prominent. A wide range of Re scaling is obtained for different travelling wave conditions from the DNS results.

**Acknowledgments** This work was supported by the EPSRC, Airbus Operations Ltd and EADS UK Ltd (EP/G060215/1). This work has also received support from European commission FP7 project AirPROM (Grant Agreement FP7 270194, www.airprom.eu), and the EPSRC through the UK Turbulence Consortium (EP/G069581/1). Computer resources were provided by the Centre for Scientific Computing, University of Warwick. This work made use of the facilities of HECToR, the UK's national high-performance computing service, which is provided by UoE HPCx Ltd at the University of Edinburgh, Cray Inc and NAG Ltd, and funded by the Office of Science and Technology through EPSRC's High End Computing Programme.

## References

Choi JI, Xu CX, Sung HJ (2002) Drag reduction by spanwise wall oscillation in wall-bounded turbulent flows. AIAA J 40(5):842–850

Hurst E, Chung YM (2012a) The Reynolds number effect of turbulent drag reduction. In 9th European Fluid Mechanics Conference, 9–13 September, Rome, Italy

Hurst E, Chung YM (2012b) Turbulent drag reduction by spanwise wall oscillation: the Reynolds number effect. In Joint ERCOFTAC/PLASMAERO Workshop, 10–12 December, Toulouse, France

Hurst E, Chung YM (2013) The effect of reynolds number on turbulent drag reduction by streamwise travelling waves. J Fluid Mech submitted

Kim K, Baek SJ, Sung HJ (2002) An implicit velocity decoupling procedure for the incompressible Navier-Stokes equations. Int J Numer Meth Fluids 38(2):125–138

Quadrio M, Ricco P, Viotti C (2009) Streamwise-travelling waves of spanwise wall velocity for turbulent drag reduction. J Fluid Mech 627:161–178

Ricco P, Quadrio M (2008) Wall-oscillation conditions for drag reduction in turbulent channel flow. Int J Heat Fluid Flow 29(4):891–902

Talha T (2012) A numerical investigation of three-dimensional unsteady turbulent channel flow subjected to temporal acceleration. PhD thesis, School of Engineering, University of Warwick, UK

Touber E, Leschziner MA (2012) Near-wall streak modification by spanwise oscillatory wall motion and drag-reduction mechanisms. J Fluid Mech 693:150–200

# Open- and Closed-Loop Control of a Turbulent Round Jet Based on Fluidic Means

**P. Zhang, H. L. Cao, J. Zhan and Y. Zhou**

**Abstract** This work investigates experimentally active control of an air round jet using radial unsteady air microjets. Two microjets were placed at diametrically opposite locations upstream of the nozzle exit. The Reynolds number was 8,000. The flow was measured in two orthogonal diametrical planes using various techniques. Under the open-loop control, the jet centreline decay rate $K$ exhibits a strong dependence on the mass flow ratio $C_m$ of microjets to the primary jet and excitation frequency ratio $f_e/f_0$ of microjets, where $f_e$ is the microjet excitation frequency and $f_0$ the preferred mode frequency of the uncontrolled jet. A closed-loop control technique has been developed to achieve automatically and rapidly the optimal control performance and the maximum $K$, as obtained from the open-loop control.

**Keywords** Jet · Open- and closed-loop control · Unsteady microjet

## 1 Introduction

The concept to use control jets to enhance jet mixing was proposed by Davis (1982), indicating that a jet may be controlled to achieve the optimized performance under different operation conditions. This work is a continuation of the

P. Zhang · Y. Zhou (✉)
Department of Mechanical Engineering, The Hong Kong Polytechnic University, Hong Kong, People's Republic of China
e-mail: yu.zhou@polyu.edu.hk

J. Zhan
Key Laboratory of Manufacture and Test Techniques for Automobile Parts, Ministry of Education, Chongqing University of Technology, Chongqing 400050, People's Republic of China

H. L. Cao · Y. Zhou
Shenzhen Postgraduate School, Harbin Institute of Technology, Shenzhen, China

Y. Zhou et al. (eds.), *Fluid-Structure-Sound Interactions and Control*,
Lecture Notes in Mechanical Engineering, DOI: 10.1007/978-3-642-40371-2_14,

study by Zhou et al. (2012), who deployed two steady microjets to manipulate a round jet, and aims to control the jet using two unsteady microjets. The Reynolds number was made the same for the two investigations. So is the jet control facility. In the open-loop control, the dependence of jet decay on the mass flow ratio $C_m$ of microjets to the primary jet and excitation frequency ratio $f_e/f_0$ of unsteady microjets to primary jet is investigated, where $f_e$ is the microjet excitation frequency and $f_0$ the preferred mode frequency in the uncontrolled jet. This is followed by the development of a closed-loop control.

## 2 Experimental Details

The jet facility consists of main jet and microjet assemblies (Fig. 1a, b). The exit Reynolds number $\mathrm{Re}_D = U_e D/\nu$ of the main jet is fixed at 8,000, where $U_e = 6$ m/s is the centreline velocity in the exit plane and $\nu$ the kinematic viscosity. The predominant vortex frequency $f_0$ is 143.5 Hz measured near the potential core end of the uncontrolled jet. The microjet assembly includes a stationary and a rotating disc both drilled with orifices of 1 mm in diameter. Once a stationary and a rotating orifice are aligned, an unsteady microjet emanates towards the main jet centreline. The $C_m$ and $f_e/f_0$ were varied from 0 to 15.4 % and 0 to 1.41, respectively. The origin of the coordinate system is chosen at the centre of the circular passage exit (Fig. 1b). The $x$ axis is along the streamwise direction, and the ($x$, $y$) plane is the non-injection plane orthogonal to the injection plane, i.e. the ($x$, $z$) plane where the two radial microjets lie in. A closed-loop controller is also developed, as shown in Fig. 1c. Three wires are deployed in different positions of the injection plane. Feedback wire 1 is placed at $x/D = 2$ and $z/D = 0.3$, serving for detecting the vortex frequency $f_{x/D=2}$. Feedback wire 2 at $x/D = 3$ and $z/D = 0$ is used to capture the instantaneous centreline velocity $U_{x/D=3}$. Another wire is placed at $x/D = 5$ and $z/D = 0$ for monitoring the decay rate $K$. The controller acts on the one hand to convert the $f_{x/D=2}$ value to the input voltage for the servo motor, which is linked to the frequency $f_e$ of unsteady microjets, and on the other hand to search $f_{x/D=2}$ corresponding to the minimum of $U_{x/D=3}$.

## 3 Results and Discussion

Figure 2 presents the dependence of the jet decay rate on $C_m$ and $f_e/f_0$. Following Zhou et al. (2012), the jet decay rate $K$ is estimated by $(U_e - U_{5D})/U_e$, where $U_{5D}$ is the centreline velocity at $x/D = 5$. Figure 2a presents the dependence of $K$ on $C_m$ which varies from 0 to 15.4 % at a given frequency ratio of $f_e/f_0 = 1.02$. Note that the present jet response may be divided into three types, i.e. I ($C_m < 2.0$ %),

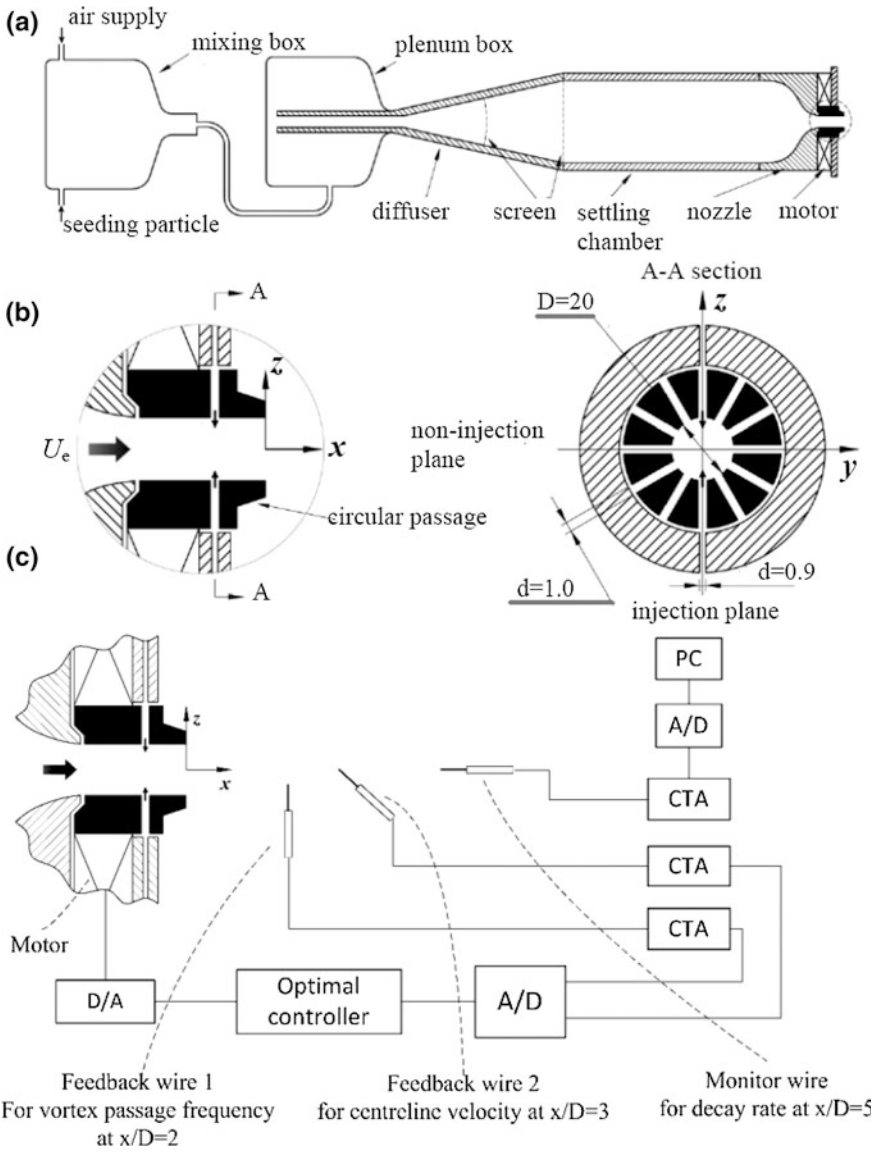


**Fig. 1** Schematic of jet control apparatus. **a** Main jet assembly. **b** Microjet assembly. **c** Experimental arrangement for the closed-loop-controlled jet

II ($C_m = 2.0$–$4.0$ %), and III ($C_m > 4.0$). As shown in Fig. 2b, the decay rate at $C_m = 0.8$ % is strongly dependent on $f_e/f_0$, showing a twin peak variation, one ($K = 0.144$) at $f_e/f_0 = 0.66$ and the other ($K = 0.215$) at $f_e/f_0 = 0.89$, along with a

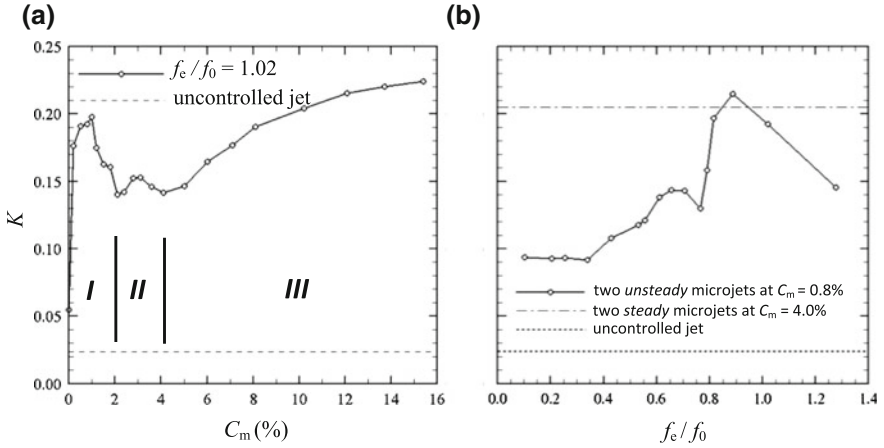


**Fig. 2** Dependence of jet decay rate on. **a** Mass flow ratio $C_m$ ($f_e/f_0 = 1.02$). **b** Excitation frequency ratio $f_e/f_0$ ($C_m = 0.8$ %)

trough ($K = 0.130$) at $f_e/f_0 = 0.77$ between the twin peaks. It is worth mentioning that two steady microjets require $C_m = 4$ % to achieve the same control performance as the unsteady ones, implying that the unsteady microjets may achieve a much higher control efficiency than their steady counterpart.

The flow in the controlled jet ($f_e/f_0 = 1.02$) displays distinct flow characteristics in these types, as illustrated in Fig. 3. Except the case of $C_m = 10.2$ % (Fig. 3d, e), the rollup and presence of coherent structures are evident for $x/D < 3.0$. Vortex pairing is also discernible in the non-injection plane, as marked in Fig. 3c. Due to microjet forcing, vortices near the exit appear to be appreciably larger in scale in the injection plane (Fig. 3b) than in the uncontrolled jet (Fig. 3a). Furthermore, vortices are relatively small in size in the non-injection plane (Fig. 3c). The vortex pairing observed in the non-injection plane deserves attention. Two neighbouring vortex rings at $x/D = 1.5$ ($C_m = 0.8$ %, Fig. 3c) are undergoing a phase of mutual induction during a typical vortex pairing after the shear layer rolls up into vortices owing to Kelvin–Helmholtz instability. At $C_m = 10.2$ % (type III), the flow appears turbulent in both planes even at $x/D = 0$ (Fig. 3d, e). At large $C_m$, the two microjets in the injection plane penetrate deeply into the potential core, as observed by Davis (1982), and even clash with each other around the centreline.

The strong disturbance is partially transferred into the non-injection plane, eventually leading to the transition of laminar vortices to the turbulent in both planes. Being turbulent, the vortices entrain more ambient fluid into the jet and thereby recover a high value of $K$ in type III, as suggested by Zhou et al. (2012). Thus, with increasing $C_m$, the jet gradually approaches a fully turbulent state with a bell-shaped rather than a top-hat mean velocity profile at jet exit and $K$ approaches an asymptotic value.

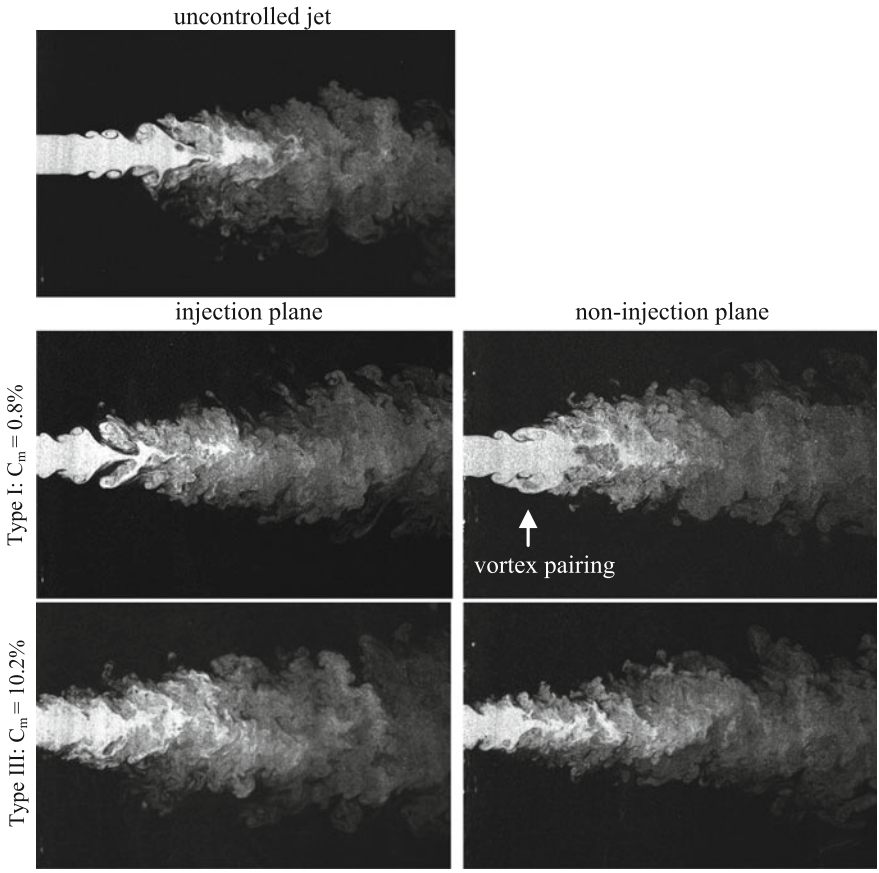


**Fig. 3** Photographs of typical flow structures captured from flow visualization in controlled jet ($f_e/f_0 = 1.02$) for different $C_m$

Figure 4 presents the performances of the closed-loop controlled jet ($C_m = 0.8$ %) when using different feedback signals. In the absence of the feedback signal from wire 2, $f_{x/D=2}/f_0$ (Fig. 4a), albeit converged rapidly, drifted upward. However, once the feedback signal from wire 2 was introduced, which provides the information on instantaneous centreline velocity $U_{x/D=3}$ at $x/D = 3$, $f_{x/D=2}/f_0$ (Fig. 4b) converged automatically and rapidly to the value almost the same as the optimal excitation frequency determined in the manual search of the open-loop control. The corresponding decay rate was 20.5 %, very close to the maximum (21.5 %) obtained in the open-loop control. The observation suggests the robustness of the technique.

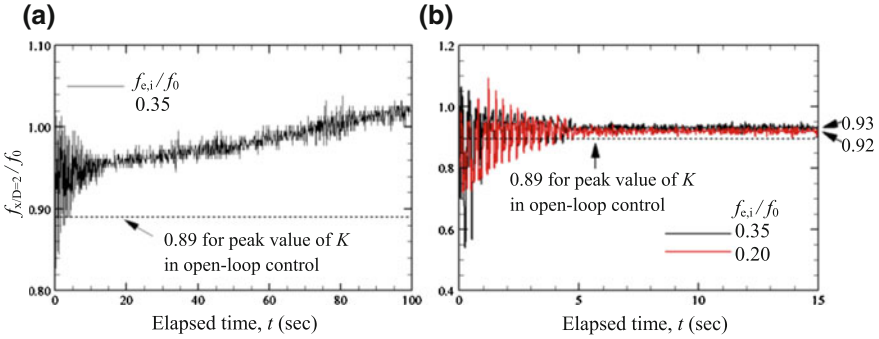


**Fig. 4** Performance of the closed-loop-controlled jet ($C_m = 0.8$ %). **a** Time history of the frequency component $f_{x/D=2}/f_0$ of the signal from wire 1 in the absence of wire 2. **b** with both feedback signals deployed

## 4 Conclusions

1. The effects of the mass ratio on the control performance can be three types. Type I corresponds to very small mass ratio, and the control excites the natural instability of jet, leading to significantly enhanced vortices. The control is highly effective. For type III, the mass ratio is large and the two control jets penetrate deeply into the potential core and even clash with each other, resulting in the transition of laminar vortices to the turbulent in both planes. The jet decay rate increases and approaches an asymptotic state with increasing $C_m$, though the control may be less efficient than type I. Type II is a transition between types I and III.
2. The jet decay rate depends strongly on the excitation frequency, showing one pronounced peak at $f_e/f_0 \approx 1$. The unsteady microjets can be much more efficient in control than their steady counterpart.
3. A closed-loop control is also developed, and the optimal control performance of the open-loop control can be achieved automatically and rapidly, suggesting the robustness of the technique.

**Acknowledgments** Authors wish to acknowledge support given to them from Research Grants Council of HKSAR through Grant PolyU 5350/10E and NSFC through Grant 51275550.

## References

Davis MR (1982) Variable control of jet decay. AIAA J. 20:606–609
Zhou Y, Du C, Mi J, Wang XW (2012) Turbulent round jet control using two steady minijets. AIAA J. 50:736–740

# Effect of Humpback Whale-like Leading-Edge Protuberances on the Low Reynolds Number Airfoil Aerodynamics

**M. M. Zhang, G. F. Wang and J. Z. Xu**

**Abstract** An experimental investigation of airfoil aerodynamics control at a low Reynolds number of $5 \times 10^4$ was conducted within the attack angle $\alpha$ of 0–90° using a leading-edge protuberance technique. The essence of the technique is to manipulate flow around the airfoil through the effect of a humpback whale-like leading edge. Whereas the mean lift force, drag force, and lift-to-drag ratio were measured using a 3-component force balance, the flow was mainly documented using a particle image velocimetry (PIV). The sinusoidal protuberances effectively suppressed the airfoil stall, although the corresponding aerodynamic performances were impaired to some extent. Meanwhile, the control significantly improved the airfoil aerodynamics in the post-stall $\alpha$ region, i.e., $16^\circ < \alpha < 70^\circ$, leading to a maximum 25.0 and 39.2 % increase in lift coefficient and lift-to-drag ratio, respectively, and maximum 20.0 % decrease in drag coefficient. The flow physics behind the observations were discussed.

**Keywords** Airfoil aerodynamics · Leading-edge protuberance · Stall

## 1 Introduction

Aerodynamic of airfoils operated at a low chord Reynolds number, i.e., $10^4 < \mathrm{Re}_c < 10^5$, has recently gained an increasing importance within the application fields of microair vehicles, small unmanned air vehicles, and small wind

The project was funded by NNSFC and MOST with Grant Nos. 51222606, 2010DFA62830, and CAS Hundred Talent Program.

M. M. Zhang (✉) · G. F. Wang · J. Z. Xu
Institute of Engineering Thermophysics, Chinese Academy of Sciences, No. 11 Beisihuan Road, Beijing 100190, People's Republic of China
e-mail: mmzhang@mail.etp.ac.cn

Y. Zhou et al. (eds.), *Fluid-Structure-Sound Interactions and Control*,
Lecture Notes in Mechanical Engineering, DOI: 10.1007/978-3-642-40371-2_15,

turbines. Nevertheless, the airfoils in this low $Re_c$ range are often subject to flow separation and even stall, resulting in poor aerodynamic performances and shortened fatigue lives. Therefore, effective control methods must be took to address this. Recently, a so-called leading-edge protuberance technique, inspired by the humpback whale flipper with rounded tubercles interspersed along its leading edge, has been given more and more attention. Within the last decade, many research works have been performed to investigate the effects of tubercles on the airfoil aerodynamic and hydrodynamic and good performances have been reported (Fish and Lauder 2006; Miklosovic et al. 2007; Johari et al. 2007; Goruney and Rockwell 2009; van Nierop et al. 2008). Even so, the detailed understanding of flow physics behind it is still very lacking, which may hinder the technique to be applied in the future. To this end, this paper presents an experimental study to investigate the nature of the modified airfoil aerodynamics by the presence of protuberances at low $Re_c$.

## 2 Experimental Details

Experiments were conducted in an open-loop wind tunnel with a test section of 0.5 × 0.5 × 2 m at Tsinghua University. The detailed setup was shown in Fig. 1. Two rectangular aluminum full-span $NACA63_4$-021 airfoils, i.e., a wavy airfoil with a sinusoidal leading edge (mimicking the cross-section to the flipper of a humpback whale) and a baseline airfoil with smooth leading edge, were chosen to be the test models. The mean $C_L$, $C_D$, and $L/D$ were measured using a 3-component force balance as $\alpha$ varied from $0^\circ$ to $90^\circ$, and the detailed flow structure is documented using particle image velocimetry (PIV). Measurements were carried out at a typical freestream velocity $U_\infty = 7.5$ m/s, corresponding to $Re_c$ of $5.0 \times 10^4$.

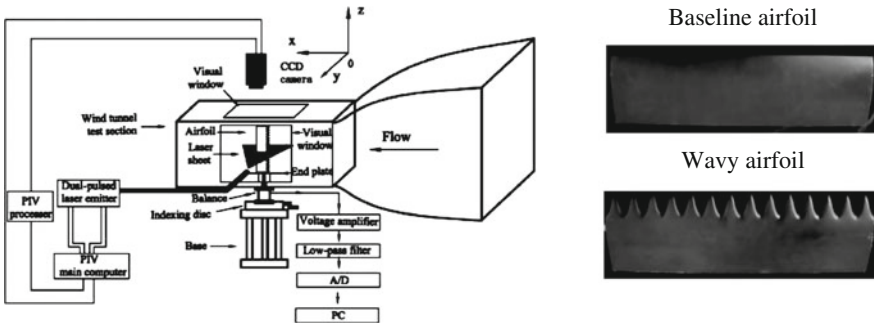


**Fig. 1** Experimental setup

## 3 Results and Discussion

### 3.1 Effect on Airfoil Aerodynamics

Figure 2 presents the dependences of the blockage-corrected mean $C_L$, $C_D$, and lift-to-drag ratio ($L/D$) on $\alpha$. Stall occurred at $\alpha = 13^{\circ}$, and then, $C_L$ displays another maximum at $\alpha = 45^{\circ}$. Compared with the baseline airfoil, all aerodynamic coefficients tend to be stable up to $\alpha = 3^{\circ}$. After that, as $3^{\circ} < \alpha \leq 16^{\circ}$, $C_L$ and $L/D$ evidently decrease (Fig. 2a, c) while $C_D$ mildly increases (Fig. 2b); the flow for the wavy airfoil case seems to not stall in the traditional sense of a rapid increase and thereafter a significant decrease in $C_L$, but $C_L$ gradually rises with $\alpha$, indicating the effectiveness of the passive control on inhibiting stall. The analogical phenomena on impairing the stall as well as detrimental to airfoil aerodynamics at the same time by leading-edge protuberances were also previously observed at the order of $Re_c$ magnitude of $10^5$ (Miklosovic et al. 2007; Johari et al. 2007). Moreover, the wavy airfoil exhibits rather good aerodynamic characteristics even when $\alpha$ varies from $16^{\circ}$ to $70^{\circ}$, resulting in the maximum 25.0 and 39.2 % increase in $C_L$ and $L/D$, respectively, and the maximum 20.0 % decrease in $C_D$, indicated in Fig. 2a–c.

### 3.2 Modified Stall Flow

To uncover the flow physics behind, two typical attack angle cases within stall and post-stall regions, i.e., $\alpha = 13^{\circ}$ and $40^{\circ}$, were selected for the following analysis. Figure 3a shows the contours of time-mean vorticity in $x$–$y$ plane out of 500 PIV images at $\alpha = 13^{\circ}$. The images for wavy airfoil cases were individually captured through the neighboring trough and peak location, which are near the airfoil mid-span. Clearly, flow separates at about $1/3c$ from the leading edge of the baseline airfoil. Once the wavy airfoil is introduced, flow in the trough-plane separates a little earlier while flow in the peak-plane adheres to the suction surface longer; the separated flow in the trough-plane reattaches to the suction surface and then moves toward the trailing edge for a while before leaving the surface again, resulting in

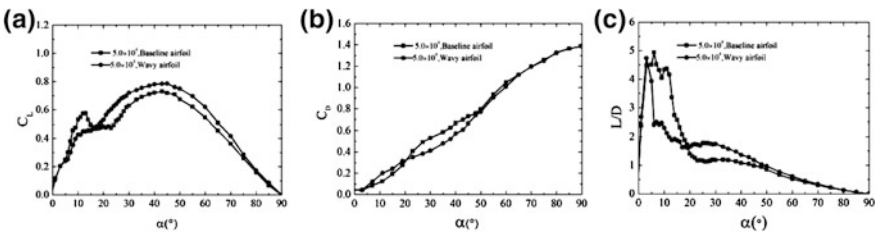


**Fig. 2** Airfoil aerodynamics with and without control

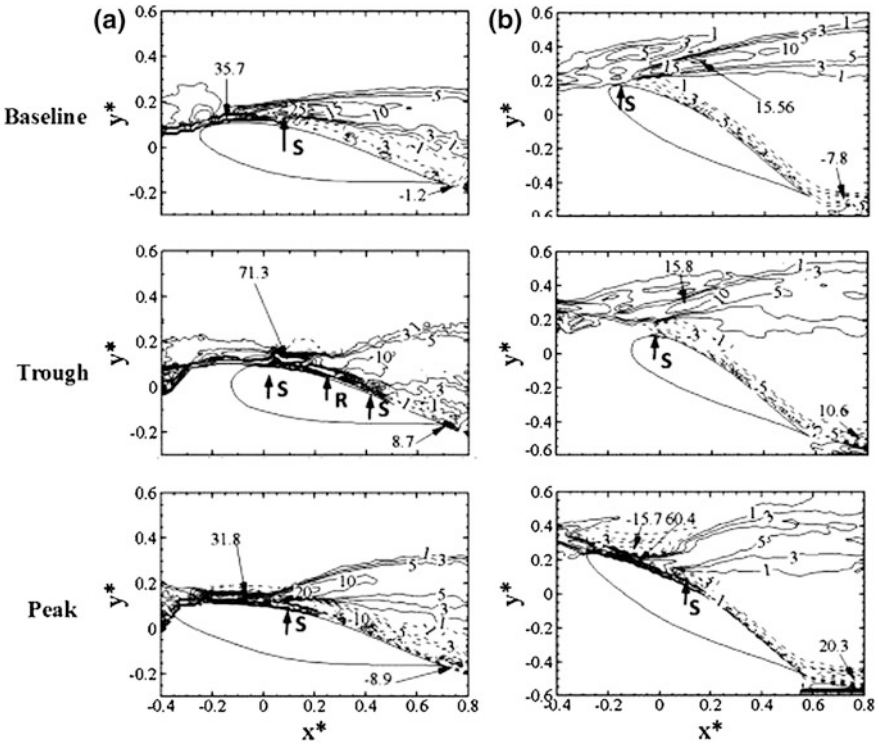


**Fig. 3** Contours of mean streamwise vorticity: **a** $\alpha = 13^{\circ}$; **b** $\alpha = 40^{\circ}$

much stronger separation than the baseline airfoil. Moreover, the typical averaged vorticity contours in $y$–$z$ plane at $x/c = 0.35$ (Fig. 4a) indicate that a pair of counter-rotating vortices are generated near each protuberance configuration, whose generation and subsequent mixing within neighboring valley region (Fish and Lauder 2006; Miklosovic et al. 2007; Johari et al. 2007; Goruney and Rockwell 2009; van Nierop et al. 2008) may partially account for more attached flow in the peak-plane as well as early separated and thereafter reattached flow in the trough-plane.

From another point of view, the typical profiles of mean streamwise velocity $\overline{U}^*$ above suction side at $\alpha = 13^{\circ}$ (Fig. 5a) show that the laminar flow separation occurs near $x/c = 0.1$ for the baseline case. In contrast, the separation takes place earlier for the trough case, and the reversed flow due to laminar separation successively weakens from $x/c = 0.1$ to 0.2 and quickly disappears between $x/c = 0.2$ and 0.3, suggesting that the flow transits and then reattaches to the airfoil surface again within the two $x/c$ ranges, respectively. The reversed flow appears again near $x/c = 0.4$, implying that the reattached turbulent boundary layer separates as $x > 0.4c$. The boundary thickness is about $0.12c$ at $x/c = 0.3$ and suddenly jumps to more than two times in magnitude ($0.25c$) at $x/c = 0.4$, which seemingly states

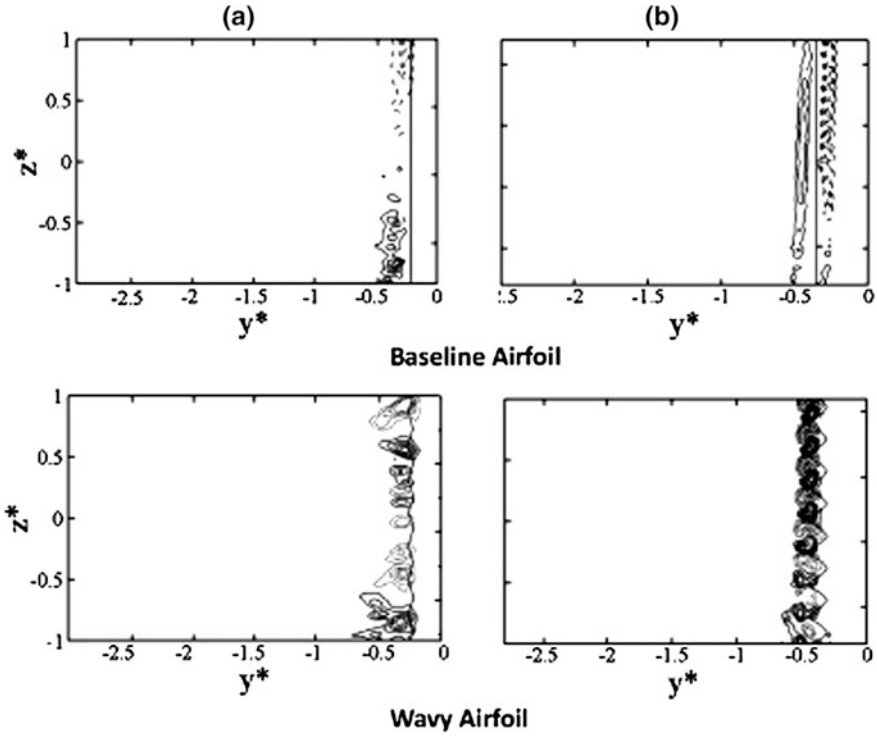


**Fig. 4** Contours of mean lateral vorticity: **a** $\alpha = 13^{\circ}$; **b** $\alpha = 40^{\circ}$

the thickened turbulent boundary layer due to the generation of streamwise vortices may be responsible for the detachment of turbulent flow in the trough-plane, consistent with the statements of Lissaman (1983). For the peak case, the occurrence of reversed flow moves backward to a location between $x/c = 0.1$ and $x/c = 0.2$, corresponding to a postponed laminar separation. Interestingly, such laminar separation in the peak-plane seems to be a little stronger than the baseline case near trailing edge, and the spanwise mixing of streamwise vortices at some distance behind airfoil leading edge may account for the extension of flow separation area.

Recalling that the aerodynamics of the wavy airfoil becomes worse in contrast to the baseline airfoil in the stall region (Fig. 2a–c, $3^{\circ} < \alpha \leq 16^{\circ}$), it implies that the enhanced separation originated from the complicated flow modification in the trough-plane might be responsible for the worse airfoil performance. This may further change the variation of $C_L$ with $\alpha$, leading to the impairment of airfoil stall.

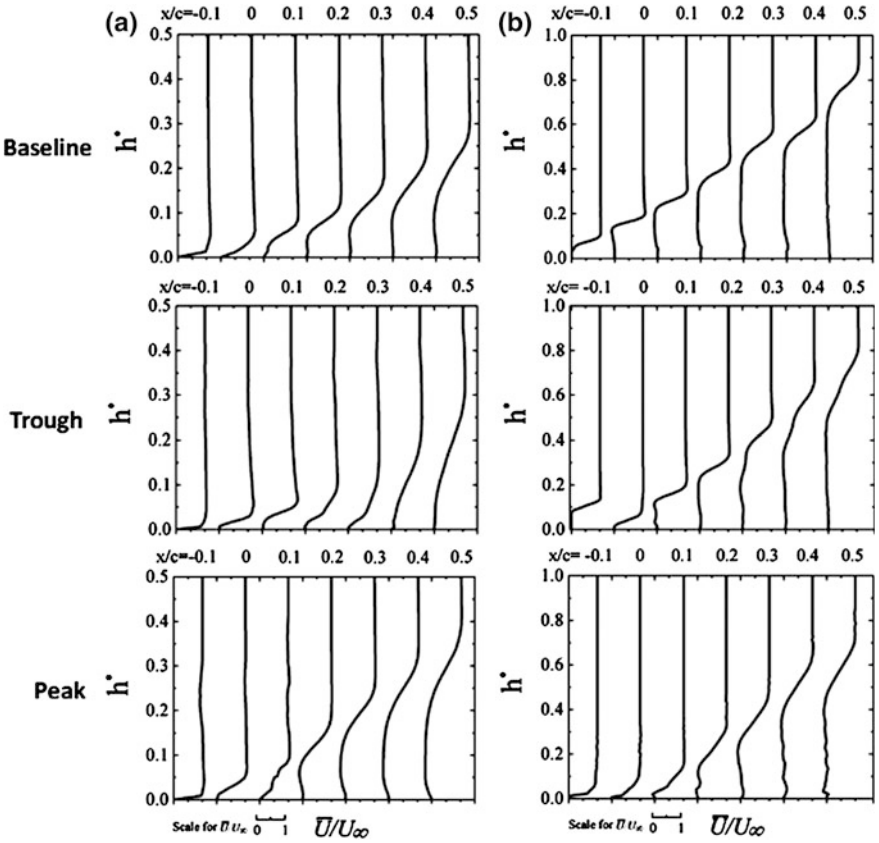


**Fig. 5** Mean streamwise velocity profiles of boundary layer: **a** $\alpha = 13^{\circ}$; **b** $\alpha = 40^{\circ}$

## *3.3 Modified Post-stall Flow*

For the typical post-stall case at $\alpha = 40^{\circ}$, the flow in the trough-plane tends to separate from the leading edge a little more seriously than the baseline case. Oppositely, the flow in the peak-plane still attaches to the suction side for a rather long distance (Fig. 3b), originated from the more generated vortex strengths in the peak-plane (Fig. 4b) to resist the negative pressure gradient and thus more attached flow than the baseline case, which may play a critical role in the improvements for the post-stall airfoil aerodynamics. Correspondingly, compared with the baseline airfoil case, the typical $\overline{U}^*$-profile (Fig. 5b) displays that the reversed flow pattern in the trough-plane does not change very much, while it is evidently impaired for the peak case. These results quantitatively point out that the impairment of flow separation and thus improvement of airfoil aerodynamics in post-stall originate from the effect of streamwise vortices induced by leading-edge protuberances.

## 4 Conclusions

The effects of sinusoidal leading-edge protuberances on two-dimensional full-span airfoil aerodynamics were experimentally investigated at low $Re_c$ of $5.0 \times 10^4$: (1) the airfoil stall was effectively inhibited while the post-stall airfoil aerodynamics was significantly improved in terms of $C_L$, $C_D$, and $L/D$. (2) In contrast with the baseline airfoil, the original stalled flow over trough section is subject to a series of complicated processes due to the protuberances-induced streamwise vortices, including laminar separation, laminar/turbulence transition, turbulent reattachment, and turbulent boundary layer detachment, leading to lessened lift as well as airfoil aerodynamics and an effective impairment in stall. (3) The post-stall airfoil performances were mainly manipulated by the flow over peak sections of protuberances, which remained attached well within a wide post-stall $\alpha$ range due to much stronger streamwise vortices, attributing to greatly enhanced momentum transfer and the corresponding significantly improved airfoil aerodynamics.

## References

Fish FE, Lauder GV (2006) Passive and active flow control by swimming fishes and mammals. Annu Rev Fluid Mech 38:193–224

Goruney T, Rockwell D (2009) Flow past a delta wing with a sinusoidal leading edge: near-surface topology and flow structure. Exp Fluids 47:321–331

Johari H, Henoch C, Custodio D, Levshin A (2007) Effects of leading-edge protuberances on airfoil performance. AIAA J 45(11):2634–2642

Lissaman PBS (1983) Low-reynolds-number airfoils. Annu Rev Fluid Mech 15:223–239

Miklosovic DS, Murray MM, Howle LE (2007) Experimental evaluation of sinusoidal leading edges. J Aircraft 44(4):1404–1407

Van Nierop EA, Alben S, Brenner MP (2008) How bumps on whale flippers delay stall: an aerodynamic model. Phy Rev Lett 100:054502

# Active Flow Control Over a Wing Model Using Synthetic-Jet-Actuator Arrays

**Hui Tang, Pramod Salunkhe, Jiaxing Du and Yanhua Wu**

**Abstract** In this study, synthetic-jet-actuator (SJA) arrays were designed, implemented, and tested on a straight-wing model for flow separation control. First, the characteristics of a single SJA were determined. The jet velocity appears a peak between 400 and 500 Hz, which corresponds to the SJA's Helmholtz resonance frequency. Second, two arrays of such SJAs were implemented at different chordwise locations on a straight-wing model. Force balance measurements and power spectrum analysis showed that both SJA arrays are able to effectively delay flow separation, with the front SJA array more effective than the rear one. For the front array, the improvement in $C_L$ and $C_D$ was 27.4 % and 19.6 %, respectively.

**Keywords** Synthetic jet · Synthetic-jet-actuator array · Active flow control · UAV

## 1 Introduction

Synthetic jet (SJ) technology has been proved to be a promising active flow control means in aeronautical applications, including flow separation control (Amitay and Glezer 2002; Zhong et al. 2007), mixing control (Pavlova et al. 2008), and turbulence control (Rathnasingham and Breuer 2003). As shown in Fig. 1, a typical synthetic jet actuator (SJA) consists of a cavity with an oscillatory diaphragm on one side and an orifice on another side. The oscillation of the diaphragm generates a succession of vortex structures that propagate away from the orifice, forming a so-called synthetic jet. Due to its well-known zero-net-mass-flux and compact

H. Tang (✉) · P. Salunkhe · J. Du · Y. Wu
School of Mechanical and Aerospace Engineering, Nanyang Technological University, Singapore, Singapore
e-mail: htang@ntu.edu.sg

Y. Zhou et al. (eds.), *Fluid-Structure-Sound Interactions and Control*,
Lecture Notes in Mechanical Engineering, DOI: 10.1007/978-3-642-40371-2_16,

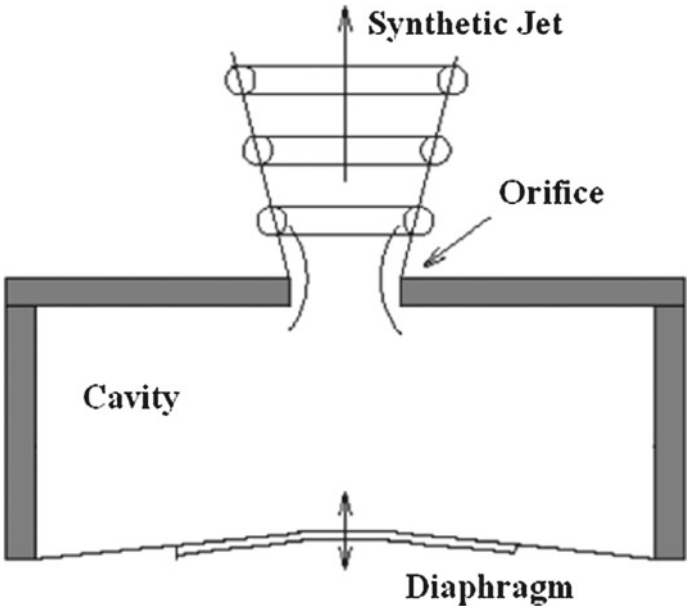


**Fig. 1** Schematic of a SJA

features, SJA can be easily implemented in arrays to achieve better flow control effects. As a study toward realizing active flow control for unmanned aerial vehicles (UAVs) by applying the SJ technology, the current investigation aims to design and deploy suitable SJA arrays to control the possible flow separation over a straight-wing model and hence enhance its aerodynamic performance. In addition, an experimental framework will be established for the investigation of the active flow control effectiveness and efficiency of SJA arrays on UAV wings.

## 2 Test Rig Setup and Instrumentation

Experiments were carried out in a subsonic closed-loop wind tunnel at a speed of 10 m/s. The test section size of the wind tunnel is 0.8 m ($W$) × 0.8 m ($H$) × 2 m ($L$). The wing model used in this study is based on the low-speed LS(1)-0421MOD airfoil, with chord length $c = 180$ mm and span $b = 255$ mm. In the present study, a new design of piezoelectric-driven SJA is proposed as shown in Fig. 2. It consists of four 20-mm-diameter piezoelectric ceramic disks attached to its four sidewalls. An O-ring is placed right above the opening on its top for a leak-proof fit. Multiple such SJAs can be arrayed and incorporated inside the cavity that is formed within the wing model. The orifice of the SJA consists of five 1-mm-diameter holes in a row on the wing model, with a distance of 1 mm

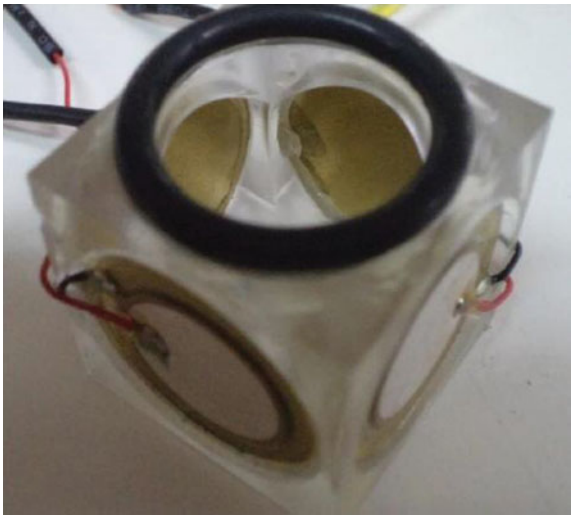

**Fig. 2** Current SJA design

between the successive holes. Ten such orifices were then arranged by keeping a 25-mm distance between each orifice. The array of SJAs was placed inside the cavity in such a way that each orifice is open to its respective SJA cavity.

In the present studies, two arrays of SJAs were incorporated in the wing model as shown in Fig. 3, each consisting of ten SJAs aligned in the spanwise direction. These two arrays are located at 23 % of the chord (denoted as front array) and 43 % of the chord (denoted as rear array) from the leading edge. A six-component force balance was used for the lift and drag measurement.

The SJAs were driven using a power amplifier (EPA-104 from Piezo Systems Inc.). The maximum output voltage is ±200 Vp, and the maximum output power is 40 Wp. Due to the limited power capacity of the amplifier and the large number of

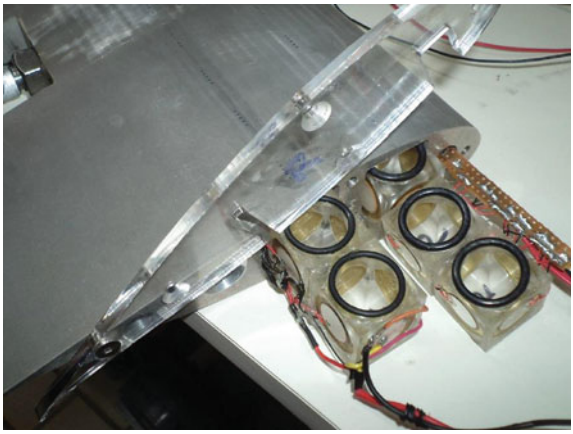

**Fig. 3** Two SJA arrays to be installed

the piezoelectric diaphragms (40 in total for one array), only one SJA array was driven at a time with a maximum frequency of 600 Hz. A function generator was used to generate the sinusoidal waveform and output voltages at various frequencies. The velocity measurement at various chordwise locations was carried out using a hot-wire anemometer (CTA 54T30 from Dantec Dynamics). A one-dimensional probe, 55P16, was used for this purpose. For spectral measurements, the hot-wire probe was placed 8 mm above the suction surface of the wing and traversed at three different locations, viz. 33 %, 50 %, and 67 % of the chord.

The present study aims to investigate the effect of the proposed SJA arrays on the flow separation control effectiveness on the wing model. Various measurement techniques were employed, including velocity measurements using a hot-wire anemometer and lift and drag measurements using a force balance.

## 3 Results and Discussions

The SJ velocity as generated by a single SJA was measured in quiescent conditions using a hot-wire anemometer. The hot-wire probe was placed 1 mm directly above one of the SJA's five holes. In this test, the four diaphragms were operated in phase at different voltages, namely, 100, 150, and 200 Vp. Figure 4 shows the variation of SJ velocity with frequency at various voltages. As expected, the jet peak velocity increases as the driving voltage increases, with the maximum velocity reaching about 7 m/s. All three curves demonstrate a velocity peak between 400 and 500 Hz. Since this frequency range is far below the diaphragm's natural frequency (1,500 Hz), it is believed that this peak corresponds to the SJA's Helmholtz resonance frequency. The test results indicate that the current SJA needs to be operated around its Helmholtz resonance frequency for higher jet velocities and hence better control effects if applied on the wing model.

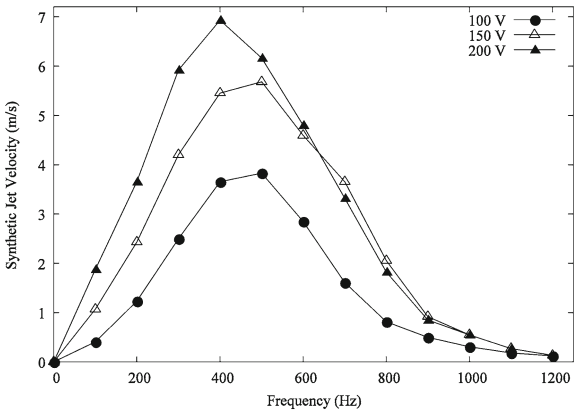


**Fig. 4** SJ velocity against frequency

The wing model with the two SJA arrays embedded was tested in the wind tunnel at a constant wind speed 10 m/s, the typical flight speed of small UAVs. The aerodynamic forces exerted on the wing model with and without the actuation of the SJA arrays at different angles of attack (AOAs) were measured using a six-component force balance. The SJA arrays were driven with the voltage of 200 Vp at three different frequencies, i.e., 200, 400, and 600 Hz.

Figure 5 shows the variation of lift coefficient ($C_L$) and drag coefficient ($C_D$) against AOAs, with and without SJA actuation. It was observed that after switching on the SJA arrays, $C_L$ increased substantially at higher AOAs, whereas $C_D$ decreased throughout the entire AOA range. The change in $C_L$ is believed to be associated with the delay of the flow separation on the suction surface of the wing model, indicating the SJA arrays are able to effectively delay the flow separation. It was also observed that the improvement in $C_L$ and $C_D$ was significant for actuation at 400 and 600 Hz compared to at 200 Hz over the without actuation case. The small improvement at 200 Hz may be attributed to the relatively low jet

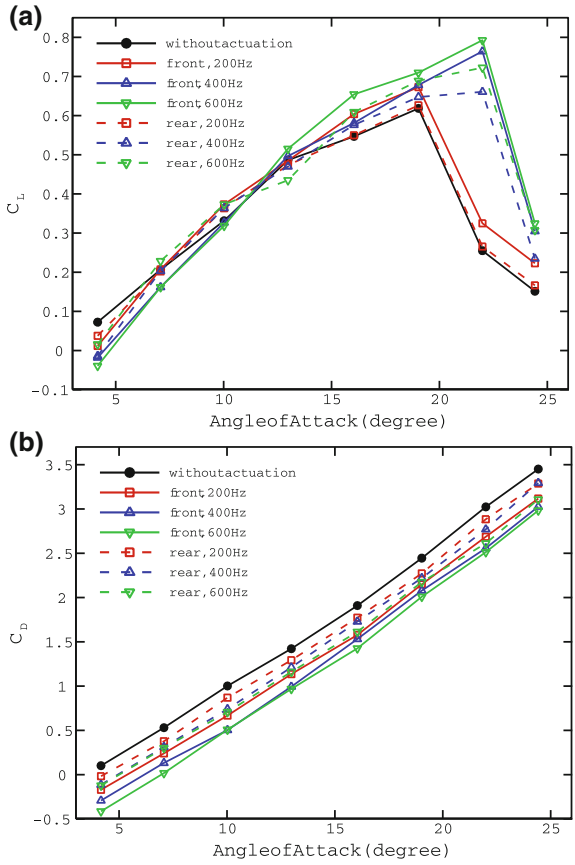


**Fig. 5** Variation of **a** $C_L$ and **b** $C_D$ against AOA, with and without the actuation of SJA arrays

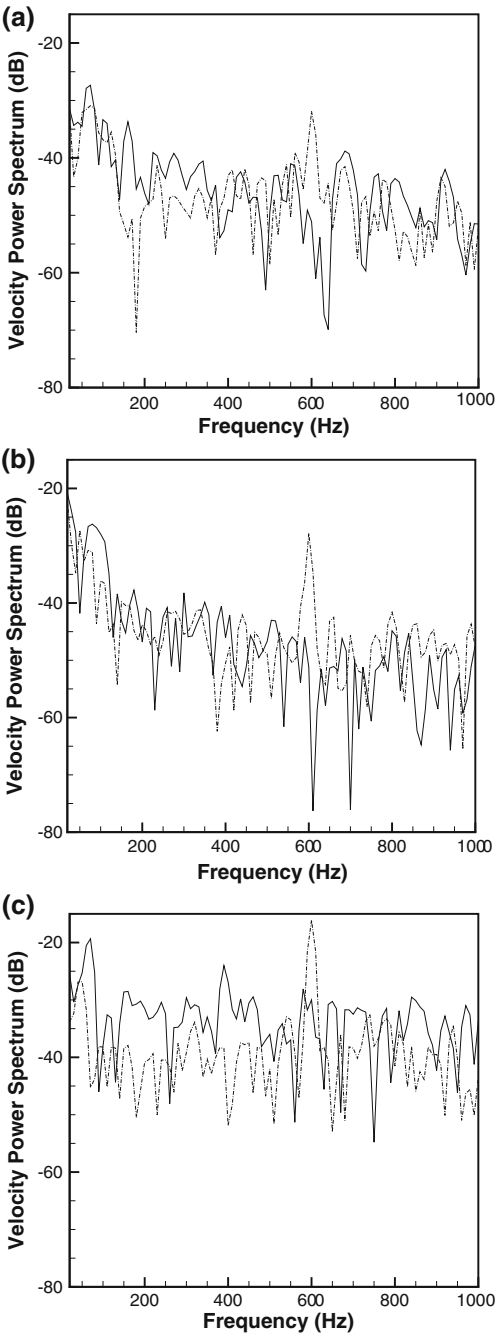


**Fig. 6** Power spectra of the velocity magnitude with and without the actuation of the front SJA array at **a** 0.33*c*, **b** 0.5*c*, and **c** 0.67*c*. The AOA of the wing model is 18°. *Solid line* spectra without actuation; *Dotted lines* spectra with SJA actuation at 600 Hz

velocity produced by the SJA arrays. From the hot-wire measurements shown in Fig. 4, the maximum SJ velocity at 200 Hz is only about 3.7 m/s, whereas it is 6.9 m/s at 400 Hz and 4.8 m/s at 600 Hz.

The flow separation control effectiveness of the two SJA arrays was also compared. At 600 Hz, for example, when the front array was in operation, the maximum $C_L$ increased from 0.62 to 0.79 resulting in a 27.4 % improvement over the without actuation case, and the average $C_D$ reduction was found to be 0.48, a 19.6 % improvement if normalized by the $C_D$ value at the stall AOA. For the rear SJA array, the improvement in the maximum $C_L$ and $C_D$ was found to be 16.1 % and 11.9 %, respectively. These numbers indicate that the front SJA array performs better than the rear SJA array.

Power spectra of the velocity magnitude fluctuations were measured with and without the actuation of the front SJA array at three chordwise stations ($0.33c$, $0.5c$, and $0.67c$) using a hot-wire anemometer. Figure 6 shows the spectra below 1 kHz, which represent large-scale motions associated with the flow separation. When the SJA array was not in operation, the mean power spectra at $0.33c$ and $0.5c$ were in the similar range between −55 dB and −45 dB, whereas they were significantly higher at $0.67c$ between −30 dB and −40 dB. This reveals that flow separation at the current AOA of 18° initiates after the second station 0.5 $c$, and the large-scale flow structures associating with flow separation dominate the rear portion of the suction surface. When the SJA array was actuated, a moderate improvement in flow separation control in terms of damping out of disturbances was observed at first two stations. For the third station $0.67c$, however, pronounced reduction in the power spectra was observed, indicating the previous large-scale flow structures were destroyed and the flow separation was successfully damped.

The flow separation delay indicated by the force measurements and power spectrum analysis may be attributed to two mechanisms: (1) the complex vortex structures produced by the interaction between the SJs and the cross flow bring the outer high-momentum flow into the wing-surface boundary layer; and (2) the oscillation of SJs triggers the instability of the separated-flow shear layer, breaking down large flow structures into small ones in the separated region. Both mechanisms are able to increase the momentum of the boundary layer and hence delay the flow separation. To determine which one is the dominant mechanism, however, further investigations are needed.

## 4 Conclusions

The present study proposed a new design of SJA arrays for the flow separation control over a straight-wing model. First, a single SJA was investigated to determine its characteristics. The jet velocity appears a peak between 400 and 500 Hz, which corresponds to the SJA's Helmholtz resonance frequency, and gives the preferred operational frequency range. Second, two arrays of such SJAs were implemented at different chordwise locations on a straight-wing model.

Force balance measurement results show that the SJA arrays can effectively increase the stall angle and maximum lift and reduce the drag at 400 and 600 Hz, whereas they marginally improve the aerodynamic performance of the wing model at 200 Hz due to the relatively low jet velocity. The power spectrum analysis confirmed these findings. It was also found that the front SJA array (at 0.23$c$ from the leading edge) is more effective than the rear SJA array (at 0.43$c$).

## References

Amitay M, Glezer A (2002) Role of actuation frequency in controlled flow reattachment over a stalled airfoil. AIAA J 40:209–216

Zhong S, Jabbal M, Tang H et al (2007) Toward the design of synthetic-jet actuators for full-scale flight conditions. Flow, Turbul Combust 78:283–307. doi:10.1007/s10494-006-9064-0

Pavlova AA, Otani K, Amitay M (2008) Active control of sprays using a single synthetic jet actuator. Int J Heat Fluid Fl 29:131–148. doi:10.1016/j.ijheatfluidflow.2007.06.004

Rathnasingham R, Breuer KS (2003) Active control of turbulent boundary layers. J Fluid Mech 495:209–233. doi:10.1017/S0022112003006177

# Initial Flow Structure Control of Jet Diffusion Using a Coaxial DBD Plasma Actuator

**M. Kimura, J. Asakura, M. Onishi, K. Sayo and N. Miyagi**

**Abstract** The dielectric barrier discharge plasma actuator (DBD PA) is applied to diffusion control of the jet flow issued at Reynolds numbers (based on a nozzle diameter) of $Re = 1.0 \times 10^3$ and $2.0 \times 10^3$ from a nozzle of 10 mm in diameter. The detailed flow structure is documented using particle image velocimetry, hot-wire anemometry, and laser flow visualization. In the experiment of the present study, the jet flow was controlled using a coaxial DBD PA, which generates an induced flow in the same direction as the jet direction. We investigated the difference in the influence of the flow induced by DBD PA on the main jet flow while varying the voltage, frequency, and intermittency. The induced flow was found to become stronger as the frequency and voltage increased. The diffusion of the jet flow was controlled.

## 1 Introduction

A number of jet diffusion control techniques, such as coaxial flow, sound excitation, and the use of a flap, have been proposed. In recent years, the dielectric barrier discharge plasma actuator (DBD PA), which is an atmospheric pressure plasma actuator, has been applied to wing separation control and cylinder wake control (Corke et al. 2010). However, a vortex ring of Kelvin–Helmholtz (K–H) instability is formed near the nozzle exit with a specific cycle. Since the characteristics of a jet are governed by the vortex ring at the early jet region, jet diffusion

M. Kimura (✉) · J. Asakura · M. Onishi · K. Sayo
Department of Mechanical Engineering, College of Science and Technology,
Nihon University, Tokyo, Japan
e-mail: kimura@mech.cst.nihon-u.ac.jp

N. Miyagi
Junior College Funabashi Campus, Nihon University, Funabashi, Japan

Y. Zhou et al. (eds.), *Fluid-Structure-Sound Interactions and Control*,
Lecture Notes in Mechanical Engineering, DOI: 10.1007/978-3-642-40371-2_17,

control can be carried out through a vortex ring generation and growth process. In the present study, the flow induced by a DBD PA made the main jet instability to increase. Diffusive mixing was controlled when the instability at the early jet region was generated by the induced flow. The influence of continuation DBD PA or intermittent DBD PA on a jet diffusion is investigated herein.

## 2 Experiment

Figure 1 shows a cross section of the coaxial-type DBD PA setup at the round nozzle exit, the main jet, and the overall view of the induced flow. The DBD PA consists of an exposed electrode, an insulated electrode, and a dielectric layer. In a convergent round nozzle having an exit inner diameter of $d = 10$ mm, the electrode was arranged coaxially with the nozzle. Plasma was generated by adding the alternating voltage of the impressed voltage of 2–6 kV, a frequency of 4–15 kHz, and the intermittency frequency from the power supply. The jet is at $\mathrm{Re} = 1.0 \times 10^3$ and $2.0 \times 10^3$ (based on a nozzle diameter). The laser light seat method was used. A photograph of the jet flow was visualized with a high-speed camera at 6,000 fps within the range of $x/d = 6$, where $x$ is the distance from the nozzle exit. Finally, the visualization picture was analyzed by PIV.

## 3 Results and Discussion

### 3.1 Change in Velocity Distribution by DBD PA

Figure 2 shows the velocity distribution chart for the case in which a plasma at $x/d = 1$ is not generated, and the velocity distribution chart for frequencies from 4 to 14 kHz for voltages of approximately 5.5 kV in case of continuous mode and a

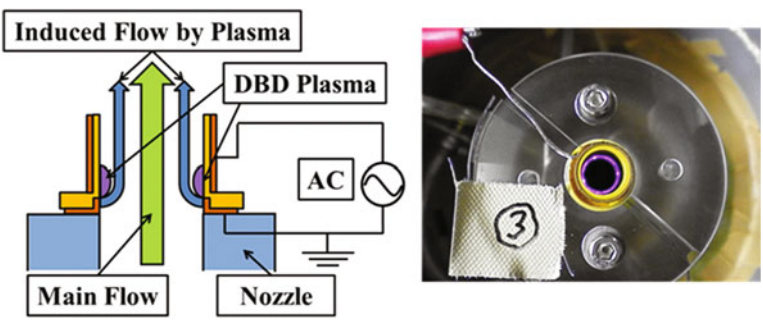


**Fig. 1** Cross section of the DBD PA and photograph of the nozzle

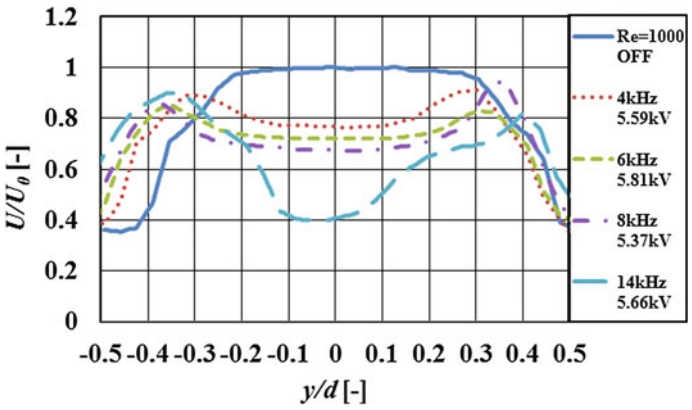


**Fig. 2** Velocity distribution around the nozzle at $x/d = 1$ (Re $= 1.0 \times 10^3$)

Re of $1.0 \times 10^3$. Here, $U_0$ is the center velocity of $x/d = 1$ when DBD PA is not generated. The velocity distribution in the free boundary layer is maximal at approximately $y/d = \pm 0.4$, and the velocity distribution at the center decreases as the frequency increases. This is because the flow in the vicinity of approximately $y/d = \pm 0.4$ was accelerated by the induced flow generated by the DBD PA. Since the supplied air mass flow rate is constant, if the velocity distribution is expanded radially, the law of conservation of mass indicates that the central velocity decreases.

## 3.2 Intermittency Frequency and Duty Ratio

Figure 3 shows photographs of typical flow structures at DBD PA for a frequency of 15 kHz, a voltage of approximately 4.9 kV, an intermittency frequency of 320 Hz, a duty ratio of 0 to 90 % (The duty ratio is defined as $B/A$, where $A$ is the

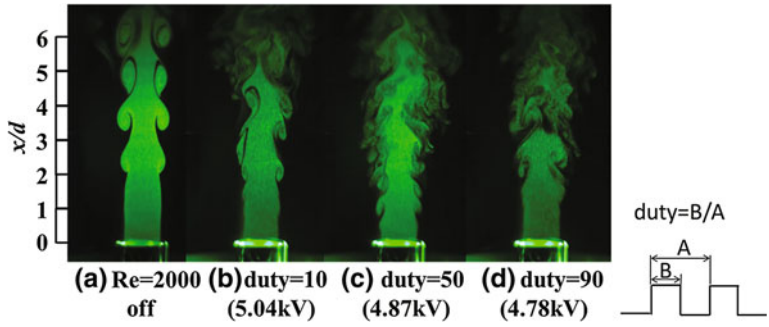


**Fig. 3** Typical flow visualizations at **a** off, **b** 10 %, **c** 50 %, and **d** 90 % (Re $= 2.0 \times 10^3$)

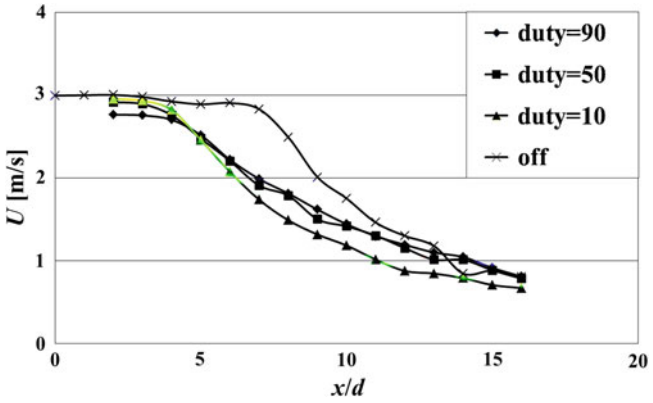


**Fig. 4** Velocity distribution on the jet axis (Re = 2.0 × $10^3$)

intermittency period and *B* is the plasma impression time. The duty ratio is 0 % when the DBD PA is in the off condition and 100 % when the DBD PA is operating in continuous mode.), and a Re of 2.0 × $10^3$. The intermittency frequency is twice the preferred frequency (approximately, 160 Hz at Re = 2.0 × $10^3$) of the jet stream. For the case in which the DBD PA is off, due to K–H instability, a vortex ring is generated in the neighborhood of $x/d = 2$, and a vortex ring sequence is formed. At $B/A = 50$ %, the instability approaches the nozzle, and the vortex ring has collapsed at an early stage. As *B/A* increases, the position at which the vortex ring is generated approaches the nozzle, and the interval of the vortex ring narrows.

## *3.3 Velocity Distribution on the Jet Axis*

Figure 4 shows the distribution of the mean velocity, *U*, along the jet axis for various duty ratios. For the case in which the DBD PA is off, the velocity potential core length is $x/d = 7$. For the case in which the DBD PA is on, the velocity potential core length is $x/d = 4$. This is thought to occur because the velocity at the surface of the nozzle wall increases as a result of the DBD PA, as discussed in Sect. 3.1. The potential core length is decreased sharply by turning on the DBD PA. K–H instability is enhanced by the DBD PA near the nozzle, and the application of intermittent plasma is believed to generate vortex rings near the nozzle that collapse at an early stage.

## 4 Conclusions

The flow velocity distribution in the vicinity of $y/d = \pm 0.4$ around the nozzle increases due to the flow induced by DBD PA, and the velocity at the center of the nozzle decreases in case of continuous mode. For the DBD PA at $B/A = 50$ % in case of intermittent mode, the instability approaches the nozzle, and the vortex ring collapses at an early stage. The potential core length is decreased sharply by the use of DBD PA at an early stage. K–H instability is enhanced by the DBD PA near the nozzle. Intermittent plasma is considered to generate vortex rings near the nozzle, and these vortex rings collapse at an early stage.

## References

Corke TC, Enloe CL, Wilkinson SP (2010) Dielectric barrier discharge plasma actuators for flow control. Ann Rev Fluid Mech 42:505–529

# End-Effects of a Finite Synthetic Jet on Flow Control

**Li-Hao Feng, Li-Qun Ma and Jin-Jun Wang**

**Abstract** The end-effects of a finite synthetic jet used for controlling the flow around a two-dimensional circular cylinder are experimentally investigated in this study. The Reynolds number based on the cylinder diameter is Re = 800, and the corresponding natural vortex shedding frequency $f_0$ is 0.24 Hz (St = 0.21). The synthetic jet is actuated at excitation frequency $f_e/f_0 = 2.08$, with the equivalent momentum coefficient $C_\mu = 0.139$. Six $x$–$y$ planes of view from the mid-span to one of the slot ends with identical interval 5 mm are measured using two-dimensional time-resolved PIV system. It is found that the end-effects of the finite synthetic jet do not have a crucial influence on flow fields in the mid-span regions, which are independent of the slot length if it is longer than one cylinder diameter.

**Keywords** Flow control · Finite synthetic jet · Circular cylinder · End-effects

## 1 Introduction

Synthetic jet is one of the most efficient flow control techniques, which has been applied in various fields (Zhang et al. 2008). Particular attention has been paid to control of flow around a circular cylinder in the previous investigations (Amitay et al. 1997; Tensi et al. 2002; Béra et al. 2000; Wang et al. 2007; Feng and Wang 2010, 2012; Feng et al. 2010, 2011; Ma and Feng 2013). The dimension problem is

Supported by the National Natural Science Foundation of China (Grant no. 11202015).

L.-H. Feng (✉) · L.-Q. Ma · J.-J. Wang
Fluid Mechanics Key Laboratory of Education Ministry, Beijing University of Aeronautics and Astronautics, Beijing 100191, People's Republic of China
e-mail: lhfeng@buaa.edu.cn

Y. Zhou et al. (eds.), *Fluid-Structure-Sound Interactions and Control*,
Lecture Notes in Mechanical Engineering, DOI: 10.1007/978-3-642-40371-2_18,

considered as one of the most important issues that potentially affects the global control results. A two-dimensional synthetic jet interacts with a two-dimensional flow filed, which usually is just the ideal situation. However, most of the flow fields in nature are highly three-dimensional, and sometimes the synthetic jet cannot be considered as a two-dimensional one in comparison with the controlled flow. For example, the length of the synthetic jet orifice was about two cylinder diameters in Amitay's et al. (1997) and Tensi's et al. (2002) experiments, while it was one cylinder diameter in Béra's et al. (2000) experiment. Consequently, the interactions between a finite synthetic jet and the flow around a two-dimensional circular cylinder are investigated experimentally in this study, where the particular attention is paid to the end-effects of the finite synthetic jet on the control effect.

## 2 Experimental Setup

The experiment was conducted in a recirculation water tunnel. The circular cylinder was horizontally mounted across the test section, and end plates were used in order to reduce the effects of the boundary layer developing on the test section walls. The outer diameter of the circular cylinder was $D = 30$ mm, the inner diameter was $d = 22$ mm, and the spanwise length was $L = 500$ mm, giving an aspect ratio of 16.7. The synthetic jet was issuing from a slot with width $h = 1$ mm and length $l = 50$ mm, which was arranged on the external surface of the circular cylinder. The slot was located in the mid-span region of the experimental circular cylinder and paralleled to its axis. During the experiment, the slot was arranged at the front stagnation point of the circular cylinder. Since the ratio of the synthetic jet length to the cylinder outer diameter was only about 1.7, the present synthetic jet could be considered as a finite one. The origin of the coordinate was located at the cylinder center in the mid-span of the slot, while the $x$-, $y$-, and $z$-axes pointed to the streamwise, vertical, and spanwise directions, respectively. More details about the experimental setup can be found in previous studies by the authors (Wang et al. 2007; Feng and Wang 2010, 2012; Feng et al. 2010, 2011; Ma and Feng 2013).

During the experiment, the free-stream velocity was fixed at $U_\infty = 34.5$ mm/s, corresponding to the Reynolds numbers $\mathrm{Re} = 800$ of the circular cylinder and the natural frequency $f_0 = 0.24$ Hz ($\mathrm{St} = 0.21$). The flow around the circular cylinder was belonged to the shear layer transition regime, where three-dimensional vortex structures developed in the wake. The synthetic jet was actuated at about twice of the natural frequency, namely $f_e/f_0 = 2.08$, with the equivalent momentum coefficient $C_\mu = 0.139$. In order to study the end-effects of the synthetic jet on the control effect, six $x$–$y$ planes of view from the mid-span to one of the slot ends with identical interval 5 mm were measured using two-dimensional time-resolved PIV system.

## 3 Results and Discussion

The objective of present investigation is to find out how much the flow field near the mid-span is influenced by the three-dimensional end-effects of the finite synthetic jet. To address this issue, by comparing the variances at different $x$–$y$ planes, two aspects have been considered as follows.

### *3.1 Characteristics of the Statistical Parameters*

Figures 1 and 2 show the distributions of the time-averaged streamwise velocity and its root mean square at different $x$–$y$ planes along the $y$-axis and the $x$-axis, respectively. It is shown that in the near-wake region, the velocities at planes of $z = 0$, 5, and 10 mm are nearly consistent with each other, though the velocities at planes of $z = 15$, 20, and 25 mm exhibit some differences due to the end-effects of the synthetic jet. It is indicated that the end-effects of the synthetic jet do have an influence on the flow fields within half-cylinder-diameter distance from each end. However, it does not have a crucial influence on flow fields in the mid-span regions, namely $-10 \text{ mm} \leq z \leq 10 \text{ mm}$. The wall visualization experiments conducted by Tensi et al. (2002) also showed the obvious three-dimensional effects near the slot ends; however, such effects decreased toward the mid-span of the slot.

### *3.2 POD Modes*

The proper orthogonal decomposition (POD) is a useful technique to analyze the complex flow phenomenon (Ma et al. 2000; Feng et al. 2010, 2011). Figure 3 presents the first 4 POD modes based on the vertical velocity downstream of the circular cylinder. Since most of the energy concentrates in the first few modes, the variations in the distributions of the first few modes can well reveal the variations in the vortex dynamics. For the control case, the POD modes in all $x$–$y$ planes are obviously different from the natural case. The modes at $z = 0$ mm show the most differences, which is followed by those at other $x$–$y$ planes, further indicating that the spanwise scale of the influenced scope of the finite synthetic jet can be at least the same scale as its length. The differences between different $x$–$y$ planes reveal the end-effects of the synthetic jet on the vortex dynamics.

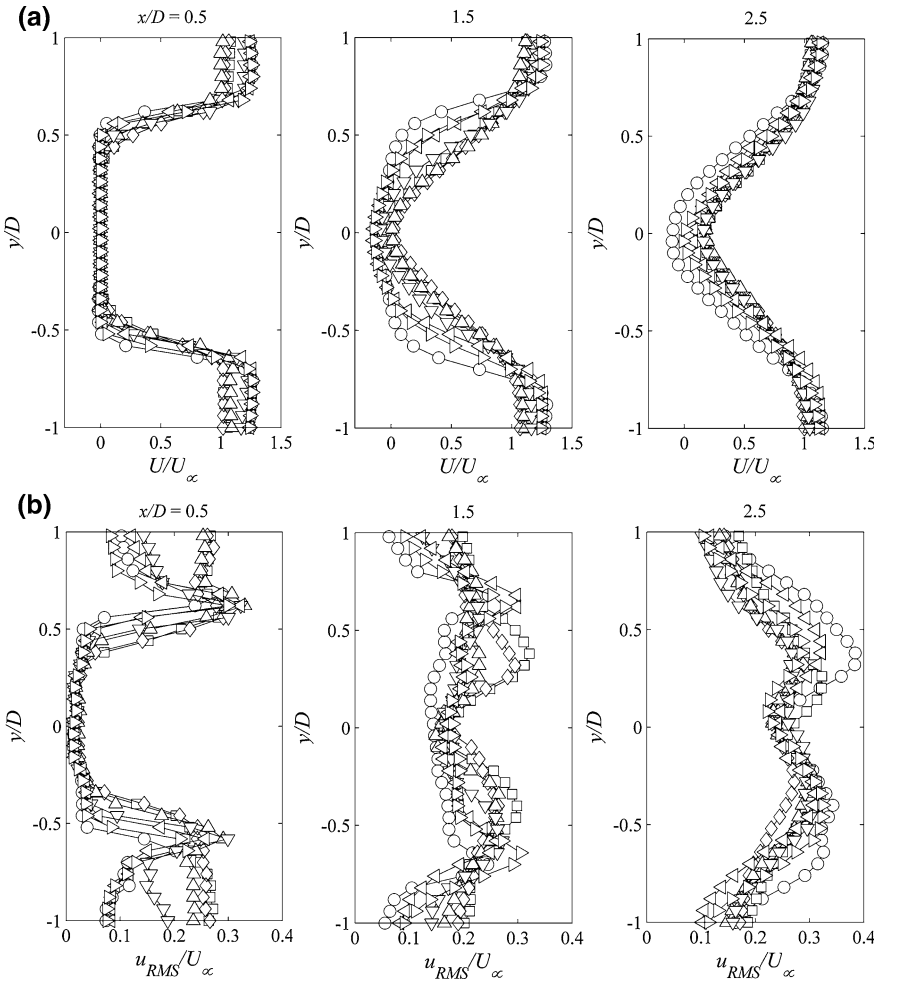


**Fig. 1** Vertical sectional distributions of time-averaged streamwise velocity $U/U_\infty$ (**a**) and root mean square of the streamwise velocity $u_{RMS}/U_\infty$ (**b**) at $x/D = 0.5$, 1.5, and 2.5 for different spanwise positions for Re = 800, $f_e/f_0 = 2.08$, $C_\mu = 0.139$. *Empty circle* natural case at $z = 0$, and control case at *empty square* $z = 0$, *empty diamond* 5 mm, *empty up-pointing triangle* 10 mm, *empty down-pointing triangle* 15 mm, *empty left pointing pointer* 20 mm, *empty right pointing pointer* 25 mm

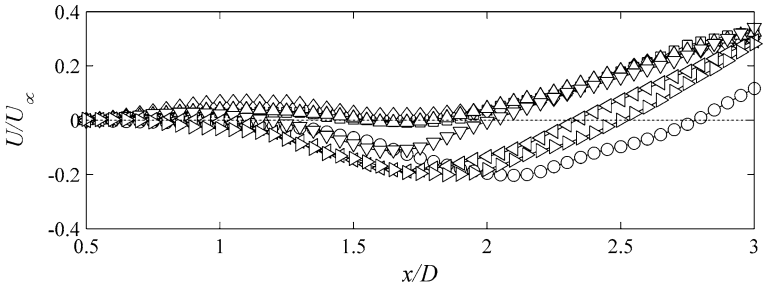


**Fig. 2** Streamwise sectional distributions of time-averaged streamwise velocity $U/U_\infty$ at $y/D = 0$ for different spanwise positions for Re = 800, $f_e/f_0 = 2.08$, $C_\mu = 0.139$. *Empty circle* natural case at $z = 0$, and control case at *empty square* $z = 0$, *empty diamond* 5 mm, *empty up-pointing triangle* 10 mm, *empty down-pointing triangle* 15 mm, *empty left pointing pointer* 20 mm, *empty right pointing pointer* 25 mm

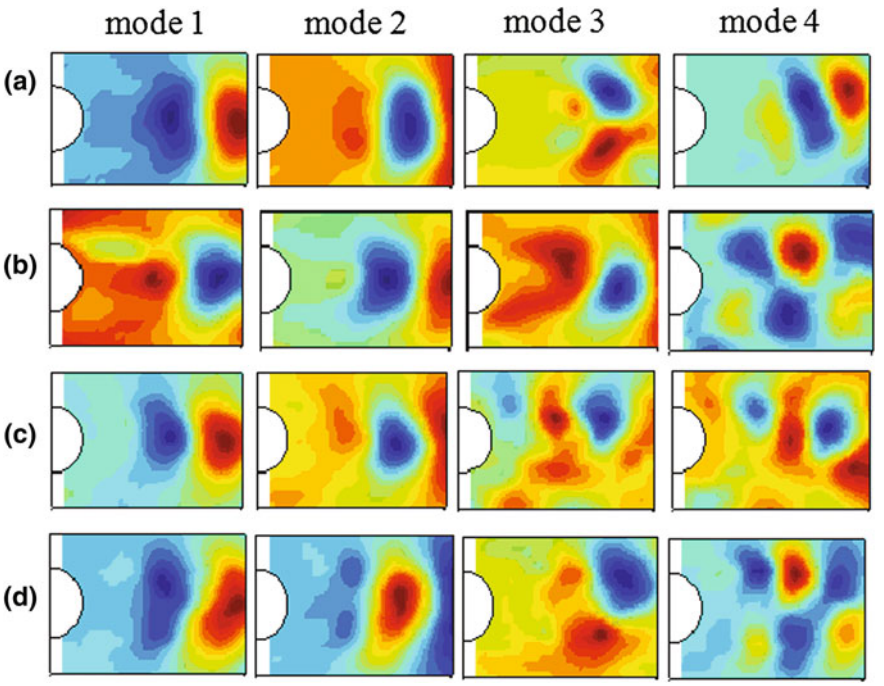


**Fig. 3** POD modes of the vertical velocity for the natural and control cases. **a** Natural case at $z = 0$, control case at **b** $z = 0$ mm, **c** $z = 10$ mm, **d** $z = 25$ mm

## 4 Conclusions

It can be concluded that the end-effects of the finite synthetic jet do have an influence on the flow fields within half-cylinder-diameter distance from each end. However, it does not have a crucial influence on flow fields in the mid-span regions, namely $-10$ mm $\leq z \leq 10$ mm. In other words, the flow field in the mid-span is independent of the slot length if it is longer than one cylinder diameter.

## References

Amitay M, Honohan A, Trautman M, Glezer A (1997) Modification of the aerodynamic characteristics of bluff bodies using fluidic actuators. AIAA paper 97–2004

Béra JC, Michard M, Sunyach M, Comte-Bellot G (2000) Changing lift and drag by jet oscillation: experiments on a circular cylinder with turbulent separation. Eur J Mech B/Fluids 19:575–595

Feng LH, Wang JJ (2010) Circular cylinder vortex-synchronization control with a synthetic jet positioned at the rear stagnation point. J Fluid Mech 662:232–259

Feng LH, Wang JJ (2012) Synthetic jet control of separation in the flow over a circular cylinder. Exp Fluids 53:467–480

Feng LH, Wang JJ, Pan C (2010) Effect of novel synthetic jet on wake vortex shedding modes of a circular cylinder. J Fluid Struct 26:900–917

Feng LH, Wang JJ, Pan C (2011) Proper orthogonal decomposition analysis of vortex dynamics of a circular cylinder under synthetic jet control. Phys Fluids 23:014106

Ma LQ, Feng LH (2013) Experimental investigation on control of vortex shedding mode of a circular cylinder using synthetic jets placed at stagnation points. Sci China Tech Sci 56:158–170

Ma M, Karamanos G-S, Karniadakis GE (2000) Dynamics and low-dimensionality of a turbulent near wake. J Fluid Mech 410:29–65

Tensi J, Boué I, Paillé F, Dury G (2002) Modification of the wake behind a circular cylinder by using synthetic jets. J Vis 5:37–44

Wang JJ, Feng LH, Xu CJ (2007) Experimental investigations on separation control and flow structure around a circular cylinder with synthetic jet. Sci China Ser E-Tech Sci 50:550–559

Zhang PF, Wang JJ, Feng LH (2008) Review on the zero-net-mass-flux jet and its application in separation flow control. Sci China Ser E-Tech Sci 51:1315–1344

# Streaky Structures in a Controlled Turbulent Boundary Layer

**H. L. Bai, Y. Zhou and W. G. Zhang**

**Abstract** This paper reports the modifications of near-wall low-speed streaks by local surface oscillations generated by a spanwise-aligned actuator array in a turbulent boundary layer over a flat plate at $Re_\theta = 1{,}000$. The streaks were educed from PIV-measured fluctuating velocities in the viscous sublayer using a procedure proposed by Schoppa and Hussain (2002). The wall-based perturbations, corresponding to a large skin-friction drag reduction (about 50 % at 17 wall units downstream of the actuator array), modified greatly the low-speed streaks, leading to a reduction by over 15 % in both the averaged width and spacing while an increase by 17 % in the streak center number. The alterations of velocity streak distributions are consistent with results from other techniques such as smoke-wire flow visualization and two-point cross-correlation, where the breakup of large-scale coherent structures into small-scale ones was observed.

**Keywords** Boundary-layer control · Drag reduction · Velocity streak eduction

## 1 Introduction

Active control of turbulent boundary layers (TBLs) for skin-friction drag reduction has been received a great deal of attention in fluid dynamics research community due to its significance in engineering applications. It has been widely accepted that

H. L. Bai (✉) · Y. Zhou
Shenzhen Graduate School, Harbin Institute of Technology, Shenzhen 518055, China
e-mail: hl_bai@126.comhlbai@hitsz.edu.cn

Y. Zhou
Department of Mechanical Engineering, The Hong Kong Polytechnic University, Hung Hom, Hong Kong SAR, China

W. G. Zhang
China Aerodynamics Research and Development Center, Mianyang 621000, China

Y. Zhou et al. (eds.), *Fluid-Structure-Sound Interactions and Control*,
Lecture Notes in Mechanical Engineering, DOI: 10.1007/978-3-642-40371-2_19,

large-scale coherent structures in the near-wall region of a TBL is closely connected to large skin-friction drag. Thus, manipulating these structures may affect the skin-friction drag. Recently, Bai et al. (2012) employed a spanwise-aligned PZT actuator array generating local surface perturbations to disturb the streaky structures. Under the optimum control parameters, they achieved a large reduction in local skin-friction drag by 50 % at 17 wall units downstream of the actuator array while observed a significant impairment of large-scale coherent structures. The alterations of near-wall flow structures by this technique were carefully examined based on extensive measurements via smoke-wire flow visualization, hotwire, hot-film, and PIV techniques. The present work aims to further study the modifications of near-wall structures based on PIV-measured fluctuating velocities in the viscous sublayer using a velocity streak eduction procedure proposed by Schoppa and Hussain (2002).

## 2 Experimental Details

Experiments were conducted in a closed-circuit wind tunnel with a 2.4-m-long test section of 0.6 × 0.6 m. With the leading edge tripped, a flat plate placed horizontally in the tunnel was used to produce a fully developed TBL. As shown in Fig. 1a, one array of 16 PZT actuators was deployed at 1.5 m downstream of the leading edge of the plate. Each actuator, having a dimension of 22 × 2 × 0.33 mm (length × width × thickness), was flush-mounted with the plate surface. The actuators are cantilever-supported, with its inactive part (2 mm long) glued to a substrate, which is embedded in a circular plug-base. There is a cavity under each actuator so that the active part (20 mm long) of the actuator can vibrate freely. The spacing between two adjacent actuators is 1 mm. All actuators

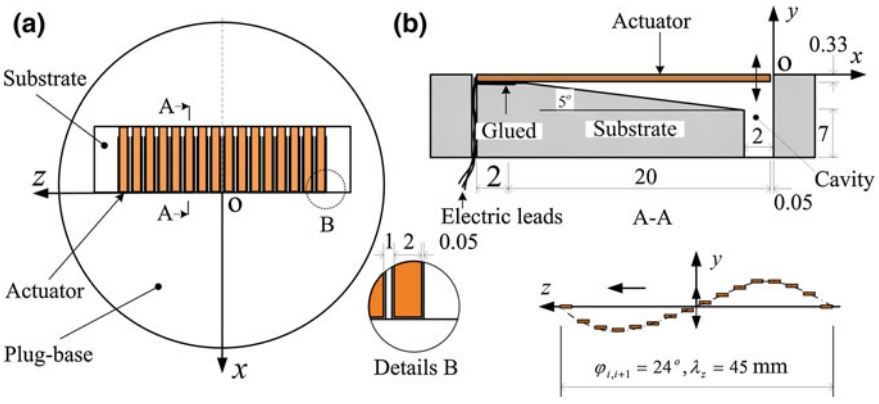


**Fig. 1** **a** Layout of 16 PZT actuators, **b** the cantilever-supported actuator and one spanwise wave formed at $\varphi_{i,i+1} = 24^{\circ}$ ($\lambda_z = 45$ mm or 312 wall units)

will generate individual wall-normal oscillations when driven by a sinusoidal voltage and, given a phase shift ($\varphi_{i,i+1}$) between two adjacent elements, a transverse travelling wave on the wall surface (Fig. 1b). At the actuation location, the TBL has a momentum thickness $\theta = 6.5$ mm, given a free-stream velocity $U_\infty = 2.4$ m/s, and a Reynolds number Re = 1,000 based $\theta$ and $U_\infty$. The origin of the coordinate system is at the actuator tip, with the $x$-, $y$-, and $z$-axes along the streamwise, normal, and spanwise directions, respectively (Fig. 1).

PIV measurements of fluctuating velocity ($u^+$) in the $xz$-plane of $y^+ = 5.5$ were conducted for the natural and disturbed flows. For the latter case, the actuators were operated under the optimum parameters, i.e., $A_o^+ = 2.22, f_o^+ = 0.65$, and $\varphi_{i,i+1} = 18^o$, where $A_o^+$ is the peak-to-peak oscillation amplitude at the actuator tip and $f_o^+$ is the oscillation frequency, corresponding to the maximum drag reduction of 50 % at $x^+ = 17$. Unless otherwise stated, superscript '+' denotes normalization based on the wall variables in the absence of control. The PIV image covers an area of $x^+ = 0$–306 and $z^+ = \pm 153$. Spatial cross-correlation, with an interrogation window of 64 × 64 pixels and a 50 % overlap along both directions, was calculated to determine velocity vectors. Over 2,000 pairs of images were taken during the measurements.

## 3 Results and Discussions

Table 1 presents a comparison of the statistical results from the streak eduction between the natural and controlled flows, i.e., identified low-speed streak center numbers $N$, and averaged low-speed streak spacing $\bar{S}^+$ and width $\bar{L}^+$. The number of low-speed streak centers was increased by about 17 %, while the averaged width and spacing were reduced by 15.5 and 17.3 %, respectively, by the wall-based oscillations.

Figure 2 shows histograms of the low-speed streak spacing $S^+$ and width $L^+$ with and without control. The distributions of $S^+$ (Fig. 2a) and $L^+$ (Fig. 2b) were greatly modified by the local surface oscillations. In the absence of control, the histogram of $S^+$ shows a positively skewed distribution, with the highest value at $S^+ \approx 60$. Under control, the $S^+$-distribution was more positively skewed, with its maximum shifted toward smaller $S^+$ ($\approx 50$). For the low-speed streak width, the highest probability occurs at $L^+ \approx 30$ in the natural flow but is shifted toward smaller $L^+$ under control, suggesting impaired streaks. The observations are in line

**Table 1** Statistical results of low-speed streaks at $y^+ = 5.5$

| | Natural TBL | Disturbed TBL |
|---|---|---|
| $N$ | 305,723 | 356,906 |
| $\bar{S}^+$ | 81.2 | 69.2 |
| $\bar{L}^+$ | 47.6 | 41.2 |

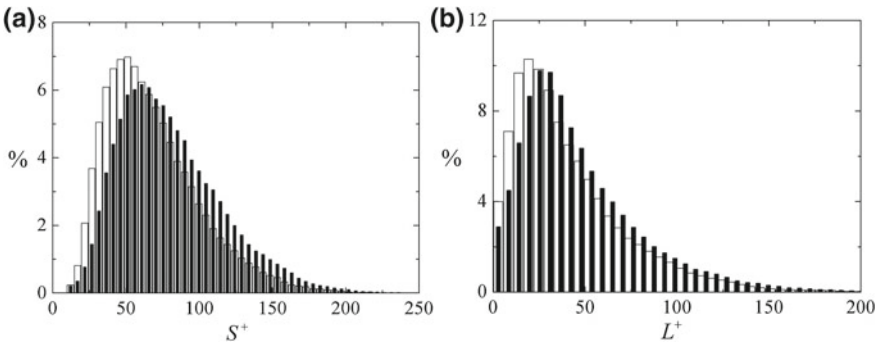


**Fig. 2** Histograms of low-speed streak spacing $S^+$ (**a**) and width $L^+$ (**b**): *filled square*, natural; *empty square*, controlled

with results from smoke-wire flow visualization (Fig. 3) and two-point cross-correlation function $R_{uu}$ of $u$ (Fig. 4). Large-scale coherent structures appear broken up, resulting in considerably smaller-scale longitudinal structures (Fig. 3). $R_{uu}$ in Fig. 4 indicates that lateral integral scale (areas under the curve) of the streaks was reduced by the wall-based oscillations.

Figure 5 shows the histograms of $\partial u^+/\partial x^+$ and $\partial u^+/\partial z^+$ at the streak borders with and without control, which characterize the internal shear layer and streamwise vortex generation. The histogram (Fig. 5a) appears positively skewed in the absence of oscillations, due to the fact that the magnitude of positive $\partial u^+/\partial x^+$ decreases across the streak border when fluid particles move from the inside to outside of a low-speed streak. Once the control was introduced, the histogram is more symmetrical, which is attributed to the occurrence of less

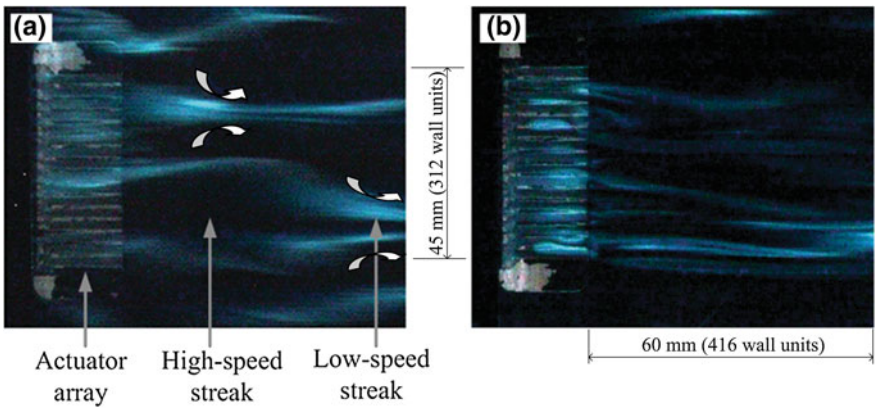


**Fig. 3** Typical photographs of instantaneous flow structure in the $xz$-plane at $y^+ = 10$ from smoke-wire flow visualization: **a** uncontrolled, **b** controlled. Flow at $U_\infty = 1.5$ m/s is left to right. *Circular arrows* indicate streamwise vortices

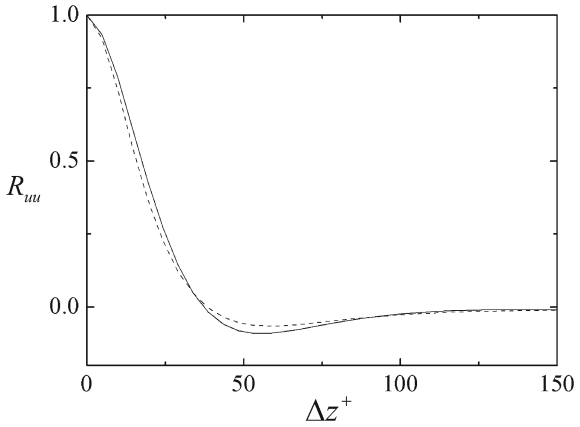


**Fig. 4** Two-point cross-correlation function $R_{uu}$ of $u$: *solid line*, natural; *dotted line*, controlled

coherent structures in the disturbed flow and thus consistent with observations from the flow visualization (Fig. 3). The higher probability of large $|\partial u^+/\partial x^+|$ in the histogram tails in the disturbed flow suggests that the low-speed streaks become less aligned with the streamwise flow and probably more wavy, compared to the natural case.

The histogram of $\partial u^+/\partial z^+$ (Fig. 5b) was modified by the wall-based oscillations, with the distribution mainly shifted to larger $|\partial u^+/\partial z^+|$ compared to the natural case. The $|\partial u^+/\partial z^+|$ at the streak borders is an indicator of the streak strength. Thus, the alteration of $\partial u^+/\partial z^+$ histogram in Fig. 5b suggests an increase in streak strength and an indication of strong formation of streamwise vortices due to the wall-based oscillations. This feature is distinct from that using other techniques (Du et al. 2002).

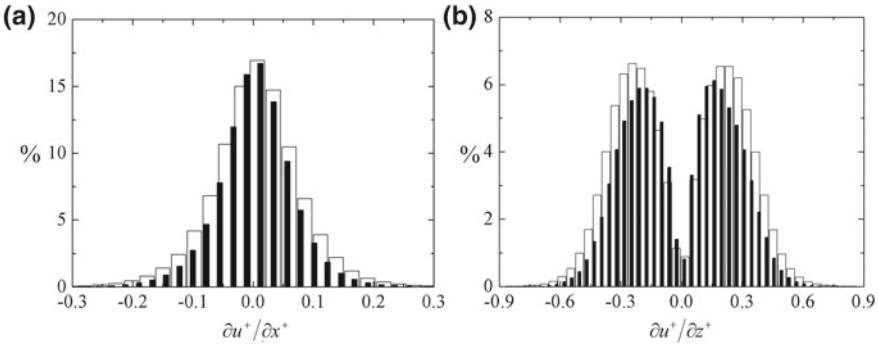


**Fig. 5** Histograms of $\partial u^+/\partial x^+$ (**a**) and $\partial u^+/\partial z^+$ (**b**) at streak borders: *filled square*, natural; *empty square*, controlled

## 4 Conclusions

The turbulent boundary layer is manipulated based on wall-normal oscillations generated by an array of 16 piezo-ceramic actuators flush-mounted to the wall surface; driven by a sinusoidal voltage, each oscillated independently and produced a perturbation to the flow. The maximum drag reduction reaches 50 % at $x^+ = 17$ under the optimum control parameters for the first time using an array of discrete actuators. The low-speed streaks in the viscous sublayer of this manipulated flow have been examined and detected based on PIV-measured $u^+$ of $y^+ = 5.5$. It has been found that the streaks decrease by over 15 % in width and spacing, though their strength is increased, in distinct contrast with the observation by others.

**Acknowledgments** This work is supported by grants PolyU 5329/11E (HKSAR) and 11172085 (NSFC).

## References

Bai HL, Zhou Y, Zhang WG, Xu SJ et al (2012) Active control of turbulent boundary layer based on local surface perturbation. J Fluid Mech (submitted)

Du Y, Symeonidis V, Karniadakis GE (2002) Drag reduction in wall-bounded turbulence via a transverse travelling wave. J Fluid Mech 457:1–34

Schoppa W, Hussain F (2002) Coherent structure generation in near-wall turbulence. J Fluid Mech 453:57–108

# Airfoil Flow Control Using DBD Plasma Actuators

**X. N. Wang, W. B. Wang, Y. Huang, Z. B. Huang and Z. H. Sheng**

**Abstract** Experiments were carried out to study the effect of plasma flow control on airfoil in an open-circuit low-speed wind tunnel. Lift and drag were measured by a five-component strain gauge balance. Particle image velocimetry (PIV) technology was applied to visualize the flow field over the airfoil. Influence of plasma actuator voltage, electrode position, and control evolution on NACA0015 airfoil was investigated, and the control mechanism was preliminarily analyzed. Lift enhancement validation experiment on NACA23018 two-element airfoil was carried out. The results show that the plasma actuators can efficiently increase the maximum lift and stall angle on a symmetric airfoil and a high-lift airfoil.

**Keywords** Flow control · DBD · Plasma

## 1 Introduction

Plasma technique has received much attention in recent decades due to its prospective applications in flow control (Roth et al. 1998). It can effectively control boundary-layer transition and separation, significantly improve lift-to-drag ratio and stall angle of the aircraft, etc (He et al. 2009). This work aims to investigate the influence of the control parameters, analyze the control mechanism, and validate the control effect on a high-lift airfoil.

X. N. Wang (✉) · W. B. Wang · Y. Huang · Z. B. Huang · Z. H. Sheng
China Aerodynamics Research and Development Center, Mianyang, Sichuan, China
e-mail: xunnian@sohu.com

X. N. Wang · W. B. Wang · Y. Huang · Z. B. Huang · Z. H. Sheng
State Key Laboratory of Aerodynamics, Mianyang, Sichuan, China

Y. Zhou et al. (eds.), *Fluid-Structure-Sound Interactions and Control*,
Lecture Notes in Mechanical Engineering, DOI: 10.1007/978-3-642-40371-2_20,

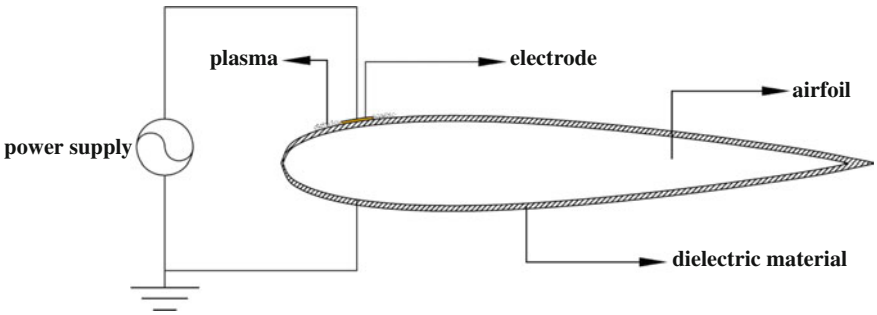


**Fig. 1** The layout of the plasma actuator on NACA0015 airfoil

## 2 Experimental Details

The experiment was conducted in the drawdown open-circuit low-speed wind tunnel, with a test section of 0.7 m (width) × 0.7 m (height) × 1.05 m (length). The flow speed in the experiments ranges from 20 to 40 m/s. NACA0015 airfoil and NACA23018 two-element airfoil used in the experiment are both with a chord length of 0.1 m and a span of 0.48 m. The airfoils are both made of aluminum. Lift and drag were measured by a five-component strain gauge balance. Flow field was measured by particle image velocimetry (PIV).

Influence of plasma actuator voltage, electrode position, and control evolution is investigated on NACA0015 airfoil. Lift enhancement validation experiment is carried out on NACA23018 two-element airfoil.

The plasma actuator consists of two electrodes separated by three layers of 0.1-mm-thick Kapton film, as shown in Fig. 1. One of the electrodes is made of 0.05-mm-thick copper foil tape, and the other one is the whole airfoil model. The upper electrode is arranged along spanwise with a width of 2 mm and a length of 440 mm. The DBD plasma is operated in steady mode.

## 3 Results and Discussion

Figure 2 presents $C_L$ and $C_D - C_L$ of NACA0015 airfoil at $V_\infty = 20$ m/s. The plasma actuator is located at $x/c = 0$ %. There is no visible lift enhancement on the airfoil at low angles of attack, but there is a significant lift increment at natural post-stall conditions. With control, $C_{L\max}$ and $\alpha_{\text{stall}}$ increase by 11 % and 6°, respectively, and lift-to-drag ratio improves as much as 199 %.

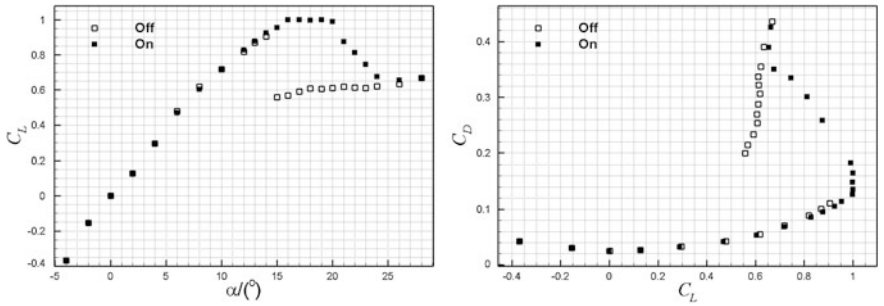


**Fig. 2** Lift coefficient versus angle of attack (*left*) and drag polar (*right*) for the NACA0015 airfoil ($x/c = 0$ %, $V = 4.0$ kV, $f = 3.0$ kHz)

## 3.1 Power Parameters

Effect of the actuator voltages on $C_L$ and $C_D$ is shown in Fig. 3. When the actuator voltage is not high enough, there is no improvement on $C_L$ and $C_D$. However, once a threshold voltage is reached, $C_L$ increases and $C_D$ decreases dramatically. Above this voltage, there is very little change in $C_L$ and $C_D$.

The threshold value is 1.6 kV at $\alpha = 15°$ and 17°, while the value is 2.4 kV at $\alpha = 18°$. At higher attack angle, the flow separation is much stronger and flow control is more difficult, resulting in higher actuator voltage threshold value.

## 3.2 Electrode Position

Table 1 lists the locations about the plasma actuators. Figure 4 shows $C_{L\max}$ and $\alpha_{stall}$ increments for various actuator locations at different velocities. The actuator near the leading edge of the airfoil can significantly improve stall character. At the range of the control $(0 \leq x/c \leq 6\,\%)$, the actuator near the trailing edge, $C_{L\max}$, apparently increases more.

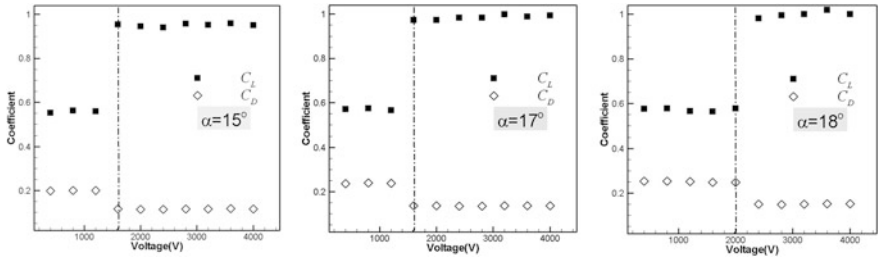


**Fig. 3** Effect of the actuator voltages on the lift and drag coefficient ($x/c = 0$ %, $V_\infty = 20$ m/s, $f = 3.0$ kHz)

**Table 1** The locations about the plasma actuators

| Case | $x/c$ (%) |
|---|---|
| 1 | 0 |
| 2 | 1 |
| 3 | 3.5 |
| 4 | 6 |

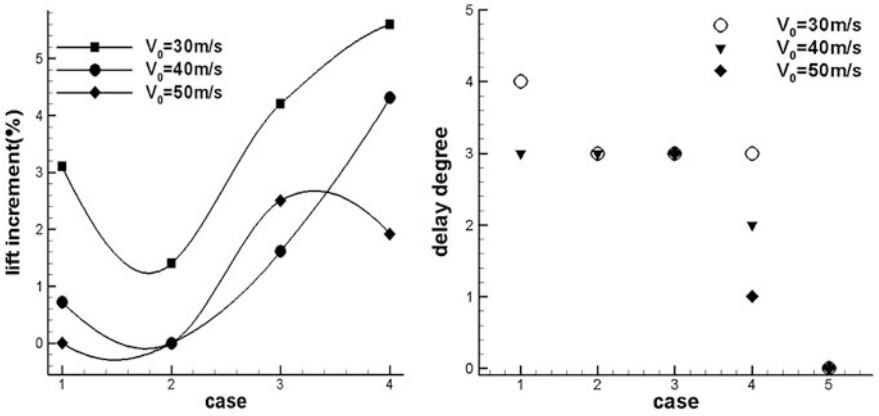


**Fig. 4** $C_{L\max}$ and $\alpha_{\text{stall}}$ increments for various actuator locations at different velocities ($V = 4.0$ kV, $f = 3.0$ kHz)

## 3.3 Velocity Field

Figure 5 shows the time-averaged PIV results of the NACA0015 airfoil at $\alpha = 16°$ before and after control. A large separation region covers the upper surface without control, while the flow is observed to be attached all over the upper surface with control.

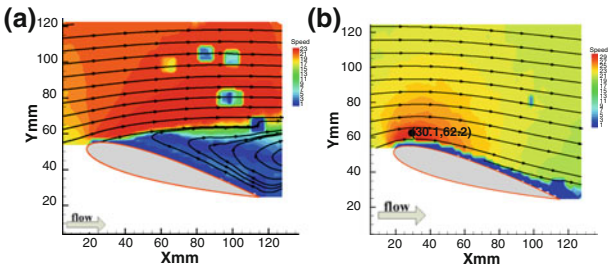


**Fig. 5** PIV results of the NACA0015 airfoil: **a** plasma off; **b** plasma on ($\alpha = 16°, V_\infty = 20$ m/s, $x/c = 0\%$, $V = 2.4$ kV, $f = 3.0$ kHz)

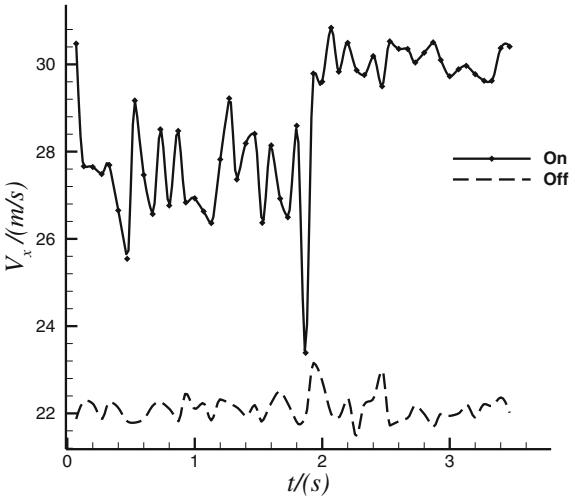


**Fig. 6** The streamwise velocity evolution ($\alpha = 16°, V_\infty = 20$ m/s, $x/c = 0$ %, $V = 2.4$ kV, $f = 3.0$ kHz)

Figure 6 gives the streamwise velocity evolution at point (30.1, 62.2) (shown in Fig. 4b). The streamwise velocity is around an average of 22 m/s before control, while it increases significantly after control, which fluctuates around 27 m/s, and it is about 30 m/s after 2 s. The rule that the streamwise velocity changes with time agrees with that of the change of flow field. When the actuator is on, the plasma disturbs the flow, so the control is effective instantaneously. With the flow field unsteady variation and the ion transferring, the actuator voltage is not high enough to maintain the plasma to a steady state, so the flow control is unsteady during a certain time. After a period of time, the ion cumulates to a density achieving a balance, so the control is steady.

Figure 7 gives the streamwise velocity at different locations before and after control. When there is no separation at $\alpha = 14°$, the streamwise velocity at the upper surface is no meaningful different with and without control. When there is large separation without control and the flow is reattached with control at $\alpha = 16°$,

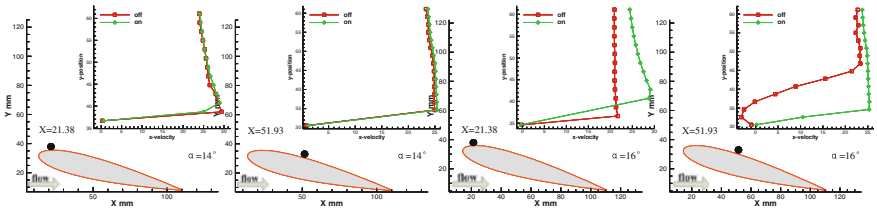


**Fig. 7** The x-velocity at different locations before and after control ($V_\infty = 20$ m/s, $x/c = 0$ %, $V = 2.4$ kV, $f = 3.0$ kHz)

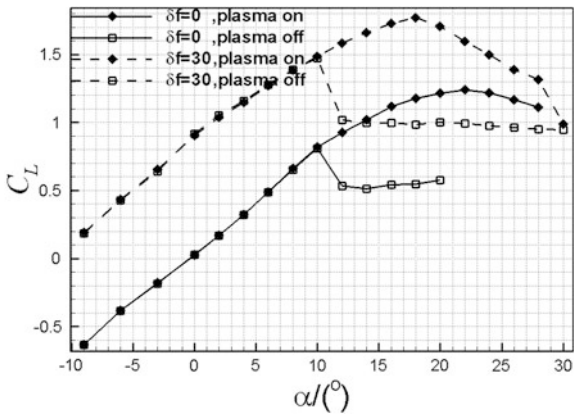


**Fig. 8** Lift coefficient versus angle of attack for the NACA23018 two-element airfoil ($V_\infty = 20$ m/s, $V = 2.4$ kV, $f = 3.0$ kHz)

the streamwise velocity at the upper surface is obviously increased after control. The mechanism of the plasma flow control is believed to be producing a disturbance in the flow that makes the high velocity flow and low velocity flow become mixed, and the flow over the boundary layer injects into the boundary layer, so the boundary-layer transition is delayed and the flow separation is restrained.

### *3.4 Lift Enhancement Validation*

Lift enhancement validation results of NACA23018 two-element airfoil are shown in Fig. 8. The plasma actuator is located at $x/c = 0.5$ %. When $V_\infty = 20$ m/s, $C_{L\max}$ increases 52 % and $\alpha_{\text{stall}}$ increases 12° with $\delta f = 0°$, and $C_{L\max}$ increases 18 % and $\alpha_{\text{stall}}$ increases 8° with $\delta f = 30°$. The plasma actuator has the same function as a leading-edge slat, and it can be used with other trailing-edge high-lift system, so it has a potential application foreground in the design of transport aircraft.

## 4 Conclusions

The leading-edge plasma actuators can efficiently increase $C_{L\max}$ and $\alpha_{\text{stall}}$ on a symmetric airfoil and a high-lift airfoil. At a given flow state, there exists threshold values for the actuator voltage on the actuator. The actuator located at different position has different contributions on $C_{L\max}$ and $\alpha_{\text{stall}}$. The mechanism of the plasma flow control is believed to be producing a disturbance in the flow.

## References

He C, Corke TC, Patel MP (2009) Plasma flaps and slats: an application of weakly ionized plasma actuators. J Aircr 46:864–873

Roth JR, Sherman DM, Wilkinson SP (1998) Boundary layer flow control with a one atmosphere uniform glow discharge surface plasma. AIAA, pp 1998–0328

# Comparison of the Near-Field Flow Structures of a Triangular Jet with and without the Initial Confinement of a Chamber

**M. Xu, S. K. Lee, J. Mi, P. Li and J. Zhang**

**Abstract** This paper reports a large eddy simulation (LES) of the precession-like oscillation produced by partially confining a triangular-jet flow with a short cylindrical chamber. The present LES, which has been verified by previous experimental data, shows that there is a strong inward swirl around the jet near the inlet end of the chamber. At the center of the swirl, there is a cluster of three sink foci, where each focus is aligned midway between the corners of the triangular inlet orifice. In the time-averaged flow field, the vortices rising from the foci are helically twisted about the core of the jet. As the flow passes through the chamber, the foci merge to form a closed-loop "bifurcation line" which separates the inward swirl and the core flow. The core of the emerging jet is visible as a source node at the approximate centerline of the chamber. If the chamber is removed, a cluster of six counter-rotating foci is produced in the "free" jet. When this happens, the net swirl circulation is zero and there is no jet oscillation.

**Keywords** Triangular jet · Flow structures · Oscillation · LES

## 1 Introduction

A nozzle, which consists of a cylindrical chamber with a concentric inlet orifice at one end and an exit lip at the other, can produce an oscillating-jet flow. The oscillation occurs naturally at low frequency and is a source of turbulent mixing

M. Xu
Marine Engineering College, Dalian Maritime University, 116026 Dalian, China

S. K. Lee
Australian Maritime College, University of Tasmania, Launceston, TAS 7250, Australia

J. Mi (✉) · P. Li · J. Zhang
College of Engineering, Peking University, Beijing 100871, China
e-mail: jcmi@coe.pku.edu.cn

Y. Zhou et al. (eds.), *Fluid-Structure-Sound Interactions and Control*,
Lecture Notes in Mechanical Engineering, DOI: 10.1007/978-3-642-40371-2_21,

with ambient fluid (e.g., Nathan et al. 2006; Mi et al. 2004; Lee 2009; England et al. 2010). From various tests leading up to Mi et al.'s international (invention) patent application and from the experimental studies by Lee (2009) and England et al. (2010), an equilateral triangle seemed to be the most promising shape for an inlet orifice because, for an inlet-diameter expansion ratio as low as about 2, it can sustain continuous large-scale oscillations.

The aim of this paper is to study the flow inside the oscillating-triangular-jet (OTJ) nozzle because this is the source of the large-scale oscillation. Conditionally sampled particle image velocimetry (PIV) measurements of non-axial velocity components in cross sections of the chamber (Lee 2009) have provided the location of critical points for deducing the topology of the flow. However, there are strong incentives to obtain a complete OTJ flow field to study the oscillation mechanism. An attempt to obtain a complete flow field is possible only by simulation. In the large eddy simulation (LES) of Xu et al. (2012), the simulated time-averaged external OTJ flow has been verified by PIV measurements (England et al. 2010). In the present study, we use the available LES data (Xu et al. 2012) of the internal OTJ flow to compare with new LES simulation of the same triangular inlet flow with the chamber removed. On the basis of the same inlet flow, any difference between the OTJ and the free triangular jet (FTJ) seems likely to be due to the presence or absence of the chamber.

## 2 Computational Details

Figure 1 shows the geometry of the FTJ (equivalent inlet diameter $D_e = 7.6$ mm; chamber length $L = 0$) and OTJ ($L = 8.75D_e$ with chamber diameter $D = 3.5D_e$; exit-lip diameter $d_2 = 0.82D$) nozzles. The flow fields produced by both nozzles are obtained using the LES technique described in detail by Xu et al. (2012). For both flows, the inlet-orifice Reynolds number is $\mathrm{Re} \equiv U_{De}/\nu = 17{,}900$, where $U_e$ is the mass-averaged velocity at the inlet orifice, and $\nu$ is the kinematic viscosity of the fluid. The large scales are obtained by solving the "filtered" governing equations of motions $\partial\overline{u_i}/\partial x_i = 0$, $\partial\overline{u_i}/\partial t + \partial\overline{u_i u_j}/\partial x_j = -\partial\overline{P}/\partial x_i + \mathrm{Re}^{-1}\partial^2\overline{u_i}/\partial x_j\partial x_j - \partial\tau_{ij}/\partial x_j$. For

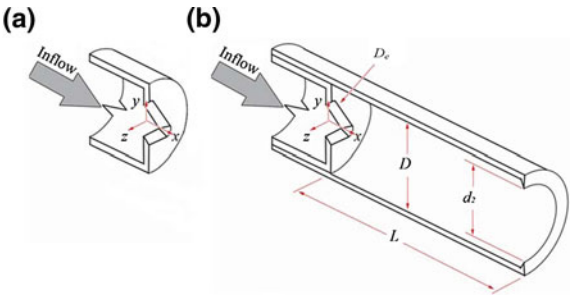


**Fig. 1** A schematic diagram of **a** the FTJ nozzle and **b** the OTJ nozzle showing notation. Here, $D = 3.5D_e$, $L = 8.75$ $D_e$, $d_2 = 0.82D$

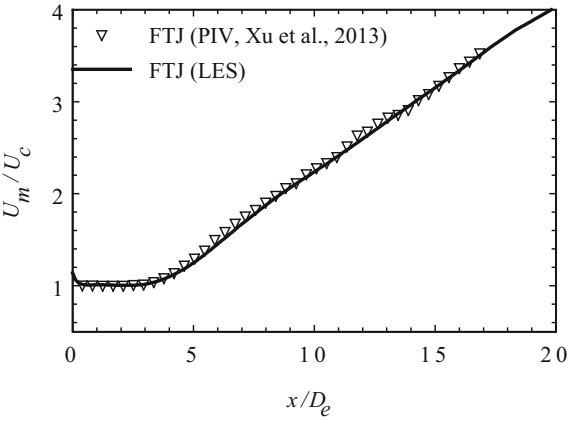


**Fig. 2** Streamwise variation of the mean centerline velocity for the FTJ flow; a comparison between the LES results and PIV measurements (Xu et al. 2013) at Re = 50,000

the fine scales, the subgrid-scale stress tensor, $\tau_{ij} = \overline{u_i u_j} - \overline{u_i}\,\overline{u_j}$, is calculated by using the dynamic model for turbulent viscosity (Xu et al. 2012). For the OTJ flow at Re = 17,900, Xu et al. (2012) have validated the present LES data against the PIV measurements of England et al. (2010); their study has shown reasonably good agreement between the LES and PIV data [see Figs. 3, 4, 5 of Xu et al. (2012)]. For the FTJ results shown in Fig. 2, the LES is validated against available PIV measurements at a slightly higher Reynolds number (Re = 50,000) (Xu et al. 2013); the close agreement between the FTJ simulation and measurements in Fig. 2 lends support for the validity of the present LES obtained at a slightly lower Reynolds number (i.e., Re = 17,900) to match that of the OTJ flow.

## 3 Results and Discussion

Figures 3 and 4 show different downstream cross sections of the time-averaged FTJ and OTJ flows, respectively. The streamlines ($y_s$, $z_s$), which show the direction of the in-plane flow and the presence of critical points (i.e., nodes, saddles) and bifurcation lines, are obtained by integrating the expression $\frac{dy_s}{V} = \frac{dz_s}{W}$, where $V$ and $W$ are the velocity components in the y and z directions, respectively. The axial ($x$) component of vorticity is given by $\omega_x = \frac{\partial W}{\partial y} - \frac{\partial V}{\partial z}$. In Fig. 4, the circulation is obtained by integrating vorticity over each selected cross section (of area $A$), where the positive circulation is defined by $\Gamma^+ = \iint \max(\omega_x, 0)\mathrm{d}A$, the negative circulation is $\Gamma^- = \iint \min(\omega_x, 0)\mathrm{d}A$, and the total circulation is the sum of the two quantities, i.e., $\Gamma = \Gamma^+ + \Gamma^-$.

In the FTJ flow (Fig. 3), there are three pairs of counter-rotating foci, where each pair is aligned midway between the corners of the triangular orifice. The vortices rising from the foci appear to evolve in a straightforward manner, where an increase in size of a vortex should be accompanied by a reduction in vorticity to

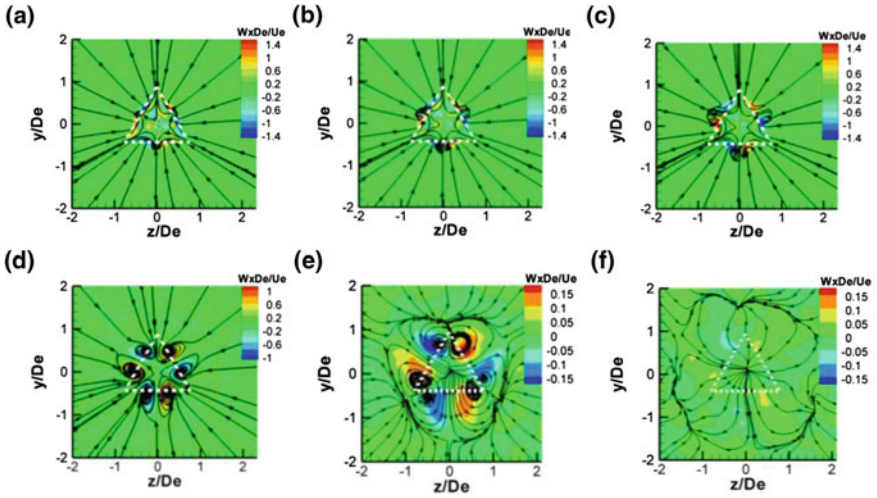


**Fig. 3** Streamlines and vorticity in cross sections of the FTJ flow at different values of x/$D_e$. **a** $x/D_e = 0.35$ **b** $x/D_e = 1$ **c** $x/D_e = 1.5$ **d** $x/D_e = 3$ **e** $x/D_e = 7$ **f** $x/D_e = 9$

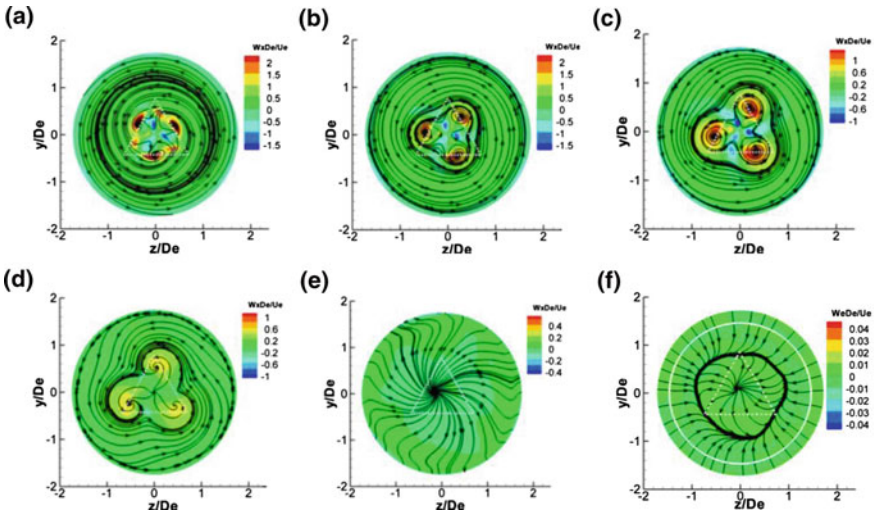


**Fig. 4** Streamlines and vorticity in cross sections of the OTJ flow at different values of x/$D_e$. **a** $x/D_e = 0.35$ **b** $x/D_e \approx 1$ **c** $x/D_e = 1.5$ **d** $x/D_e = 3$ **e** $x/D_e = 7$ **f** $x/D_e = 9$

maintain constant circulation (i.e., the Helmholtz's vortex law). The fact that there is a small variation in the FTJ circulation ($|\Gamma^+| = |\Gamma^-| \approx 0.375 \pm 0.075$ in Fig. 5a) along the axial direction may be due to (1) instantaneous vortex cores

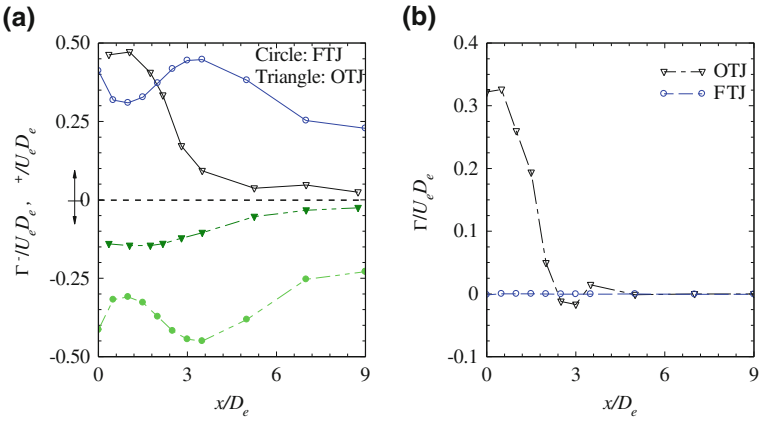


**Fig. 5** Circulation in the time-averaged FTJ and OTJ flows; **a** positive $\Gamma^+$ and negative $\Gamma^-$ contributions; **b** total circulation $\Gamma = \Gamma^+ + \Gamma^-$

varying with time and/or (2) spatial distortion of vortex cores by the jet flow spreading faster at midway between the corners of the triangle (a feature known as "axis-switching").

A major feature of the time-averaged OTJ flow is the presence of a strong inward swirl around the inlet jet. In Fig. 4, the precession of the OTJ is in the "clockwise" direction (see Xu et al. (2012), their Fig. 3). In the shear layer between the inlet jet and the swirling flow, there is a cluster of three corotating sink foci; both the swirl and the foci rotate in the same "counter-clockwise" direction. In the time-averaged flow (Fig. 4), the vortices rising from the three foci are helically twisted about the core of the jet; they merge to form a closed-loop "bifurcation line" which separates the core flow and the inward swirling flow. The emerging core flow appears as a source node near the centerline of the chamber. At the exit plane of the chamber ($x/D_e = 9$), a closed-loop bifurcation line forms between the emerging flow and the induced ambient flow.

The presence of the chamber clearly affects the near field of the triangular-jet flow (Figs. 3 and 4). This is demonstrated by the different OTJ and FTJ streamline patterns and their contributions to circulation in the range $0 < x/D_e < 9$ (Fig. 5a). The OTJ flow is highly asymmetric due to the presence of swirl trapped by the chamber; a counter-clockwise direction of the swirling flow implies positive circulation $|\Gamma^+| > |\Gamma^-|$ (Fig. 5b). The swirl is strongest at the inlet end of the chamber ($x/D_e \leq 1$). If the chamber is removed, the jet flow has a threefold axial symmetry with zero net circulation and this flow does not oscillate.

## 4 Conclusions

The present LES of a triangular-jet flow at Re = 17,900 shows that partially confining the triangular jet with a short chamber significantly alters the near flow field. With the chamber, there is large-scale jet oscillation and a strong swirling flow at the inlet end of the chamber; three longitudinal vortices spiral in the shear layer between the swirl and the jet. In the time-averaged flow, the vortices merge into a closed-loop bifurcation line; this line separates the swirling flow and the emerging jet. If the chamber is removed, there is no net swirl circulation and the large-scale oscillation stops.

**Acknowledgments** This project is financially supported by the Fundamental Research Funds for the Central Universities (Grant No. 3132013029) and the Nature Science Foundation of China (Grant Nos. 11072005 and 10921202).

## References

England G, Kalt P, Nathan G, Kelso R (2010) The effect of density ratio on the near field of a naturally occurring oscillating jet. Exp Fluids 48:69–80

Lee SK (2009) Study of a naturally oscillating triangular-jet flow. The University of Adelaide, South Australia. http://hdl.handle.net/2440/58581

Mi J, Nathan GJ, Luxton RE (2004) Family of oscillating jets. Pat App No. PCT/AU98/00959. The US Patent No. 6685102 (2004.2), European Pat. No. 1032789 (2004.9), Australian Pat. No. 746248 (2004.2), New Zealand Pat. No. 504470 (2003.7)

Nathan GJ, Mi J, Alwahabi ZT, Newbold GJR, Nobes DS (2006) Impacts of a jet's exit flow pattern on mixing and combustion performance. Prog Energy Combust Sci 32:496–538

Xu M, Mi J, Li P (2012) Large Eddy simulation of an initially-confined triangular oscillating jet. Flow, Turbulence Combus 88:1–20

Xu M, Zhang J, Mi J, Nathan GJ, Kalt PAM (2013) PIV measurements of turbulent jets issuing from triangular and circular orifice plates. Sci China, Ser G 56:1176–1186

# On Spectral Exponent Over Inertial Range in a Turbulent Square Jet

**J. Zhang, M. Xu, A. Pollard and J. Mi**

**Abstract** This paper reports a study that investigates the effects of the large-scale intermittency factor $\gamma$ and the mean shear $S$ on the inertial range spectral exponent $m$ in the far field of a turbulent square jet ($\gamma$ is defined as the fraction of time when the flow is turbulent at a specific location.). The exit Reynolds number is Re = 50,000. The turbulent energy recognition algorithm (TERA) method proposed by Falco and Gendrich (1990) is applied to estimate $\gamma$ from velocity signals. It is found that $\gamma$ has a strong impact on $m$ while the influence of $S$ is negligible. More specifically, $m$ varies with $\gamma$ following the relationship of $m = m_t + (\ln\gamma^{-0.0173})^{1/2}$, where $m_t$ denotes the scaling exponent in full turbulence. Moreover, self-similarity of $\gamma$ is observed in the far field of the jet.

**Keywords** Intermittency · Scaling exponent · Mean shear · Turbulent jet

## 1 Introduction

One famous result extended from the Kolomogrov (1941) theory, well known as K41, is the '−5/3' law, i.e., the energy spectrum in the inertial range (IR) follows a power relationship, $E(k) = C_0\varepsilon^{2/3}k^{-5/3}$, where $E(k)$ is the energy spectrum density function, $C_0$ is the Obukhov–Corrsin constant, $\varepsilon$ is the energy dissipation rate, and

J. Zhang · J. Mi (✉)
College of Engineering, Peking University, Beijing 100871, China
e-mail: jcmi@pku.edu.cn

M. Xu
Marine Engineering College, Dalian Maritime University, Dalian 116026, China

A. Pollard
Department of Mechanical and Materials Engineering, Queen's University at Kingston, Kingston, ON K7L-3N6, Canada

Y. Zhou et al. (eds.), *Fluid-Structure-Sound Interactions and Control*,
Lecture Notes in Mechanical Engineering, DOI: 10.1007/978-3-642-40371-2_22,

$k$ is the wavenumber. However, the scaling-range exponent (the absolute value of the exponent of $k$), denoted as $m$, is found to deviate from 5/3 by many studies (e.g., Mydlarski and Warhaft 1996). So far, the Taylor micro-scale Reynolds number $R_\lambda$, intermittency factor $\gamma$, and mean shear $S$ are found to influence $m$ (Kuznetsov et al. 1992; Mi and Antonia 2001). However, the individual effects of $\gamma$ and $S$ on $m$ have yet to be clarified.

In this context, we carefully investigate the respective effects of the intermittency $\gamma$ and the mean shear $S$ across the jet. The $\gamma$ profile for the present square jet is provided and a relationship between $m$ and $\gamma$ is proposed to assist in evaluating the influence of large-scale non-turbulent motion on $\gamma$. In addition, the present study is also to examine the self-similarity of $\gamma$ in the far field of the jet.

## 2 Experimental Details and Data Processing

The square jets investigated in the present study issued from a square duct whose dimensions were 25 × 25 × 2,000 mm and the equivalent diameter $D_e$ [$\equiv 2(A/\pi)^{1/2}$] was 28.2 mm (Fig. 1). The exit Reynolds number of the jet was $\mathrm{Re} = \rho U_j D_e/\nu = 50{,}000$, where $U_j$ is the bulk mean velocity of the square exit. Velocity signals were obtained using single hotwire. The sampling frequency $f_s$ for all measurements was 40 kHz. The turbulent energy recognition algorithm (TERA) method proposed by Falco and Gendrich (1990) was applied to estimate $\gamma$ from the velocity signals. The TERA method uses $u'\partial u'/\partial t$ as the detection function, and the criterion for the turbulence to occur is $\overline{u'\partial u'/\partial t} > C_0(u'\partial u'/\partial t)_{\mathrm{rms}}$, where $u'$ denotes the velocity fluctuation and $C_0$ is a preset threshold constant. Figure 2 illustrates the determination of $\gamma$.

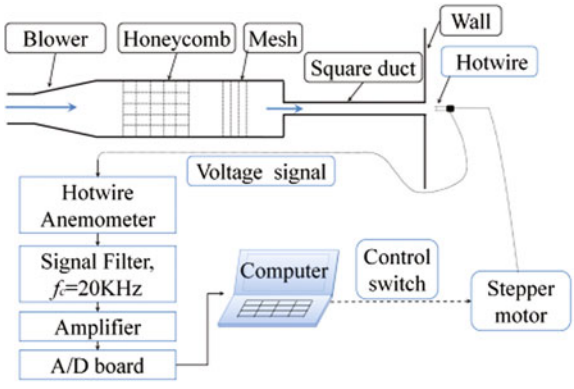


**Fig. 1** Schematic of the experimental arrangement

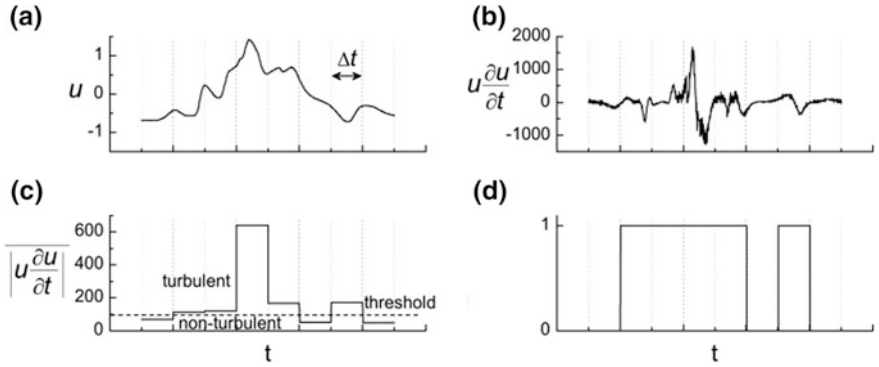


**Fig. 2** Illustration of $\gamma$ detection procedures from a velocity signal: **a** time-sequential velocity signal; **b** detector function calculated from the signal; **c** average of the detector function in a predefined time interval; **d** determination function of the signal ($\Delta t = 5$ ms)

## 3 Results and Discussion

### *3.1 Intermittency and Mean Shear*

The spanwise profile of $\gamma$ in various $x$-locations detected by the TERA method is shown in Fig. 3a. The threshold constant was set as $C_0 = 0.04$ to provide a good agreement between the present ($x/D_e \geq 25$) and previous results (Mi and Antonia 2001; Wygnanski and Fiedler 1996). Figure 3a also shows that the intermittency factor exhibits a self-similar characteristic in the far field at $x > 25D_e$, whose profile can be well fitted by a Gaussian error function $\gamma = 0.5\{1 - \mathrm{erf}[2.40(y/y_{1/2}-1.50)]\}$. Figure 3b shows the spanwise distribution of mean shear, which is obtained from the radial mean velocity distribution fitted by a Gaussian function $U/U_c = e^{-0.971 \ln 2 * \left(y/y_{1/2}\right)^2}$. Derivation of $U/U_c$ with respect to $y/y_{1/2}$ obtains the

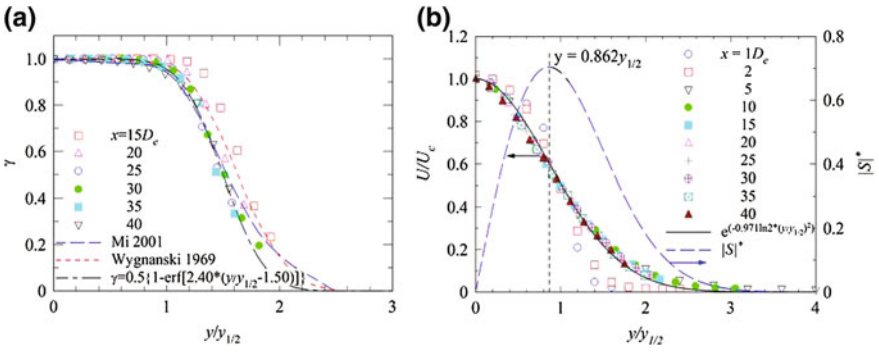


**Fig. 3** **a** Spanwise intermittency using the TERA method and **b** mean shear at various $x$-locations of the square jet

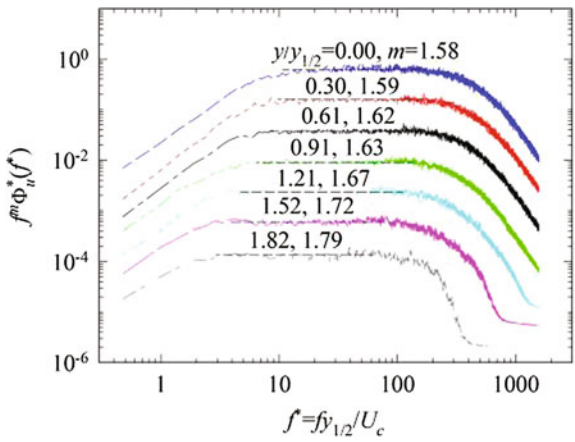


**Fig. 4** Compensated spectra of the streamwise velocity at different $y$-locations for $x = 30D_e$

normalized mean shear $|S^*| = (y_{1/2}/U_c)|dU/dy|$, whose profile is also given in Fig. 3b. The maximum mean shear occurs at $y = 0.862y_{1/2}$.

## 3.2 *Effect of the Intermittency and Mean Shear*

According to the K41 theory, $m$ should be 5/3. Yet, the present $m$ in the jet flow deviates from 5/3, as seen from the compensated spectra of $u$ obtained at $x = 30D_e$, see Fig. 4. By using the TERA method to identify the non-turbulent component and then remove them from the original velocity signal, we can investigate the intermittency impact on $m$. Figure 5 compares the scaling exponents with ($m$) and without ($m_t$) the effect of $\gamma$ at various $y$-locations in the far field of the jet. From these plots, it is observed that $m$ increases significantly with $y$ while $m_t$ does not.

Figure 6a presents the relationship between $m$ and $\gamma$ for different locations. It is shown that $m$ decreases as $\gamma$ increases. If the non-turbulent portion of the velocity signal is removed, the IR exponent, $m_t$, obtained from the corresponding spectrum should be related only to the turbulence. It follows that the difference $\Delta m = m - m_t$ should result solely from $\gamma$. Taking into account the error in the acquisition of $m$, $\Delta m$ varies with $\gamma$ in a certain pattern, as validated with the data of Mi and Antonia (2001) for a circular jet. A possible fitting with $\Delta m = (\ln\gamma^{-0.0173})^{1/2}$ is plotted in Fig. 6b as well, which is beneficial for estimating the $\gamma$ effect on $m$.

The mean shear effect on $m$ can be demonstrated by comparing the profiles of $m_t$ in Fig. 5. Virtually, within a margin of error, $m_t$ changes little along the $y$ direction and also along the axis. Recall in Fig. 3b that the mean shear $S$ reaches the maximum at $y = 0.862y_{1/2}$ for all locations where the mean velocity approaches the self-similar state. Thus, if $S$ has significant impact on $m$, a hump located at $y = 0.862y_{1/2}$ for $m_t$ is expected. Obviously, this expectation is not correct. To sum up, the mean shear has negligible effect on $m$.

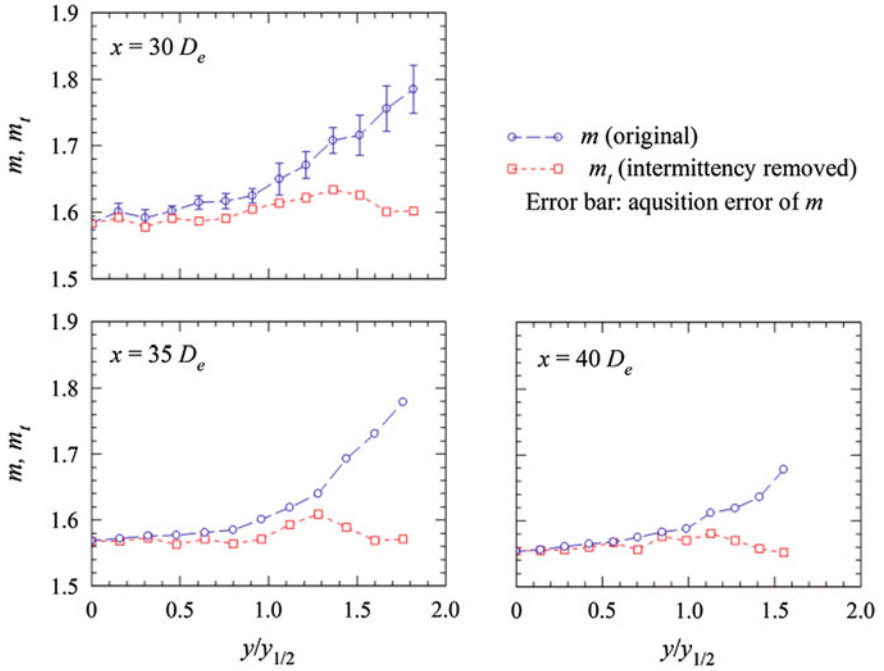


**Fig. 5** Intermittency impact on the scaling exponent $m$ at different far-field locations

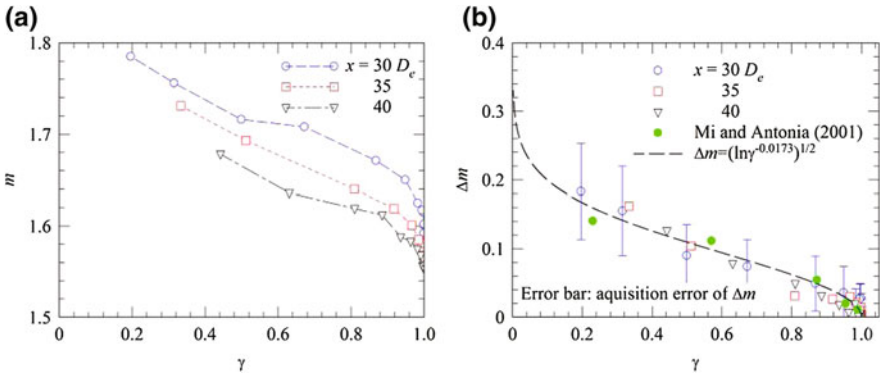


**Fig. 6** Relationships of **a** $m$ with $\gamma$ and **b** $\Delta m$ with $\gamma$ at different downstream locations

## 4 Conclusions

In this paper, we have investigated the effects of the intermittency factor $\gamma$ and the mean shear $S$ on the spectral scaling exponent $m$ in the self-similar far field ($x = 30$–$40D_e$) of a turbulent square jet at Re = 50,000. Using the TERA method

of Falco and Gendrich (1990), the magnitude of $\gamma$ was obtained from hot-wire signals. The present work has found: (1) The lateral distribution of $\gamma$ becomes self-similar at $x > 30D_e$ in the present jet and can be well fitted by the Gaussian error function $\gamma = 0.5\{1 - \mathrm{erf}[2.40(y/y_{1/2} - 1.50)]\}$; (2) The exponent $m$ depends strongly on $\gamma$ but weakly on the mean shear $S$.

## References

Falco RE, Gendrich CP (1990) The turbulence burst detection algorithm of Z. Zaric. Near-wall Turbul 1:911–931

Kolmogorov AN (1941) The local structure of turbulence in incompressible viscous fluid for very large Reynolds numbers. Dokl Akad Nauk SSSR 30(4):299–303

Kuznetsov VR, Praskovsky AA, Sabelnikov VA (1992) Fine-scale turbulent structure of intermittent shear flows. J Fluid Mech 243:595–622

Mi J, Antonia RA (2001) Effect of large-scale intermittency and mean shear on scaling-range exponents in a turbulent jet. Phys Rev E 64:026302

Mydlarski L, Warhaft Z (1996) On the onset of high-Reynolds-number grid generated wind tunnel turbulence. J Fluid Mech 320:331–368

Wygnanski I, Fiedler H (1969) Some measurements in the self-preserving jet. J Fluid Mech 38(03):577–612

# Wake Manipulation Using Control Cylinders in a Tandem Arrangement

**S. Rajagopalan, N. Lefeuvre, R. A. Antonia and L. Djenidi**

**Abstract** The drag reduction phenomenon of a circular cylinder is investigated, using an X-wire probe, by placing a smaller diameter control cylinder of either circular or square cross-sectional upstream of the main circular cylinder. The separation between the two cylinders was chosen so as to minimise the overall drag of the main cylinder. Although both configurations resulted in drag reduction, the square control cylinder yielded a bigger reduction and had a greater impact on the mean velocity and turbulent velocity fluctuations in the wake. Both control cylinders led to a reduction in the wake half-width. Spectra in the near wake did not indicate any suppression in vortex shedding.

**Keywords** Wake control · Cylinder wake · Tandem

## 1 Introduction

The drag of a circular cylinder and the vortex shedding phenomenon have been extensively investigated because of their importance in aerodynamic flows (Alam et al. 2011; Hu and Zhou 2008). Significant attention is now being focused on controlling the vortex shedding as well as reducing the drag by placing a control cylinder upstream of the main cylinder. The diameter of the control cylinder is generally smaller than that of the main cylinder. However, there have been few systematic investigations of the wake characteristics, such as mean velocity and turbulent velocity rms distributions, downstream of the main cylinder associated with the drag reduction phenomenon. The main aim of the present study is two-fold—firstly to investigate the drag reduction phenomenon by placing a small

S. Rajagopalan · N. Lefeuvre · R. A. Antonia · L. Djenidi (✉)
School of Engineering, University of Newcastle, Newcastle, NSW 2308, Australia
e-mail: lyazid.djenidi@newcastle.edu.au

Y. Zhou et al. (eds.), *Fluid-Structure-Sound Interactions and Control*,
Lecture Notes in Mechanical Engineering, DOI: 10.1007/978-3-642-40371-2_23,

diameter control cylinder upstream of the main cylinder and secondly to compare mean velocity, rms velocity fluctuations, and Reynolds stresses corresponding to the minimum drag configuration at several downstream locations with those for a single cylinder. The influence of the geometry of the control cylinder—e.g., circular, square, triangular and channel cross sections—on the drag reduction, vortex shedding, and wake turbulence characteristics is another objective of the present study although only results for circular and square control cylinders are given here.

## 2 Experimental Conditions

Measurements were made in a 2.2-m-long and 0.34 × 0.34 m test section of a low-speed wind tunnel at a Reynolds number $Re_D = 7{,}500$ based on the main cylinder diameter $D$ ($Re_D = U_0\, D/v$ where $D = 11.1$ mm and upstream velocity $U_0 = 10$ m/s). A 3-mm-diameter (d) control cylinder and a 3-mm-diameter square cylinder were used independently in the investigations. The control cylinders were placed upstream of the main cylinder on the centre line, and the separation between the two cylinders was varied by using two micrometre screws attached to the main cylinder. The drag of the main cylinder was estimated from surface pressure distribution and the drag of the combined cylinder arrangement was estimated from mean velocity measurements at $x/D = 40$ where $x$ is the longitudinal distance measured from the centre of the main cylinder. Figure 1 shows the experimental arrangement. An X-probe with 5-μm-diameter Pt-10 % Rh hot wires was used to measure mean velocity and longitudinal ($u$) and lateral ($v$) velocity fluctuations at several $y$ locations for $10 \leq x/D \leq 40$.

## 3 Results and Discussion

The gap between the cylinders that minimises the overall drag (for the tandem arrangement) was determined by measuring the difference in the (centre line) surface pressure between the upstream and downstream sides of the main cylinder for different values of $\Delta x$. It was observed by Rajagopalan and Antonia (2007) that

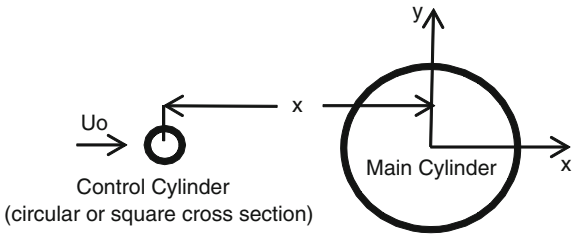


**Fig. 1** Experimental arrangement

the value of $\Delta x$ which minimises the pressure difference also yields minimum wake width and minimises the overall drag. For the circular control cylinder, the minimum drag was obtained for $\Delta x = 1.8D$, which is in agreement with the literature (Zdravkovich 1977a, b; Lee et al. 2004). The corresponding optimum $\Delta x$ for the square control cylinder is $1.75D$. Note that the optimum value of $\Delta x$ depends in general on the ratio $d/D$ and $\mathrm{Re}_D$.

To investigate the influence of the gap on the wake structure, both mean velocity ($U$) and longitudinal ($u$) and lateral ($v$) velocity fluctuations were measured at several downstream distances. Figure 2 compares the distributions of $U$ at three downstream locations $x/D = 10$, 20, and 40. With the control cylinders, $U$ tends to increase thus causing a decrease in the wake defect. This is qualitatively consistent square cylinder yields a larger drag reduction as is evident from the $U$ distribution. Distributions of $u'$ and $v'$ (the prime denotes an rms value) at $x/D = 10$ and 40 are shown in Fig. 3 where a reduction in $u'$ and $v'$ can be observed when the control cylinders are used. At $x/D = 10$, $v'$ is larger than $u$' whereas the opposite trend occurs at $x/D = 40$. As mentioned earlier, it was observed in Rajagopalan and Antonia (2007) that, at $x/D = 40$, the wake half-width exhibited a minimum for $\Delta x/D = 1.8$, suggesting that the minimum overall drag corresponds to a minimum half-width. Both Figs. 2 and 3 indicate a reduction in the wake half-width with the introduction of the control cylinders, as observed by Rajagopalan and Antonia (2007). However, Estimates of the wake half-width from mean velocity distributions at $x/D = 10$, 20, and 40 are shown in Fig. 4.

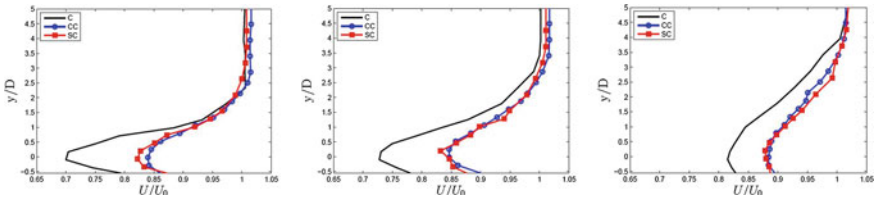


**Fig. 2** *C* main cylinder only (*black*), *CC* circular control cylinder (*blue*), *SC* square control cylinder (*red*)

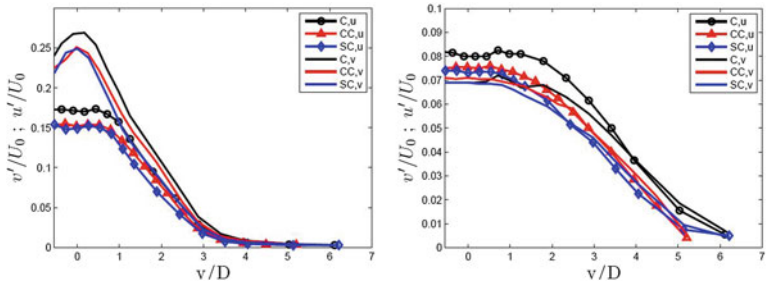


**Fig. 3** Distributions of $u'$ and $v'$ at $x/D = 10$ (*left*) and 40 (*right*)

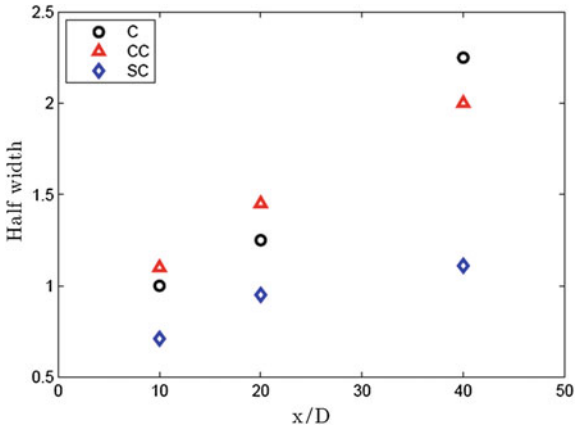


**Fig. 4** Streamwise variation of wake half-width

Once again, it can be seen that square the control cylinder has the maximum influence on the wake development as it yields the minimum wake half-width. At $x/D = 10$ and 20, the half-width of the undisturbed cylinder wake is slightly smaller than that with the circular control cylinder. However, at $x/D = 40$, the half-width of the single circular cylinder is larger than that for either tandem arrangement. Based on hot-wire measurements in a cylinder wake Antonia and Rajagopalan (1990) identified $x/D = 30$ as the minimum location where the contributions from the Reynolds normal stresses become negligible. At this location, a momentum balance can be applied to determine the drag as the velocity defect is fully representative of the cylinder drag. Values of the drag coefficient $C_D$, estimated from $U$ distributions at $x/D = 40$, were 1.3, 0.97, and 0.75 for the main cylinder and for the circular and square control cylinder arrangements, respectively. Spectra of u at $x/D = 10$ at a value of y aligned with the top edge of the main cylinder are shown in Fig. 5. There is a local peak at approximately 200 Hz which yields a Strouhal number $St_D = 0.22$, in agreement with established values for a circular cylinder. However, the introduction of the control cylinders does not suppress the formation of wake vortices. On the contrary, the amplitude of the peak at 200 Hz is increased by the control cylinders, the square cylinder having the largest effect. This suggests that the intensity of the vortices produced by square cylinder is larger than that in the other two wakes, which results in a reduction in the mean velocity gradients. This is supported by the measured mean velocity distributions. Figure 6 shows distributions of the Reynolds shear stress ($\overline{uv}$) at $x/D = 10$ and 40 for the three arrangements. At $x/D = 10$, the circular control cylinder yields a maximum in $\overline{uv}$ indicating enhanced mixing whereas the square cylinder produces a minimum value of $\overline{uv}$, which seems consistent with the magnitudes of the half-width at $x/D = 10$. At $x/D = 40$, $\overline{uv}$ values for the single cylinder are larger than the other two, the square cylinder yielding the smallest values. Once again, the nature of this distribution is consistent with the values of the wake half-width at this location. Clearly, the relative peak values of $\overline{uv}$ in the

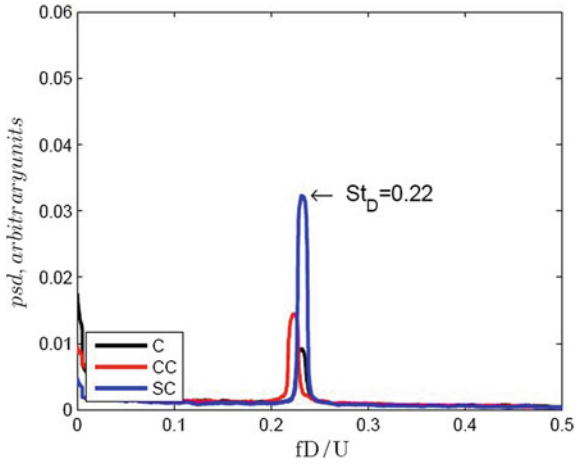


**Fig. 5** Spectra of $u$ at $x/D = 10$

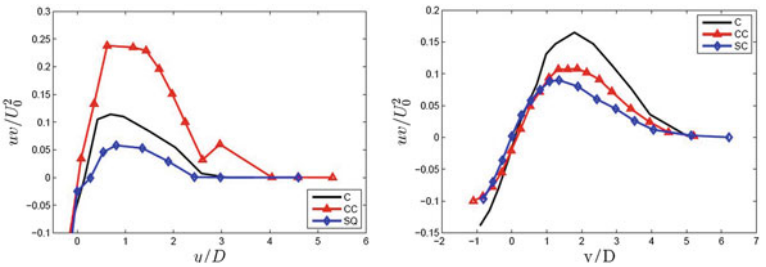


**Fig. 6** Distributions of the Reynolds shear stress across the wake at $x/D = 10$ (*left*) and 40 (*right*)

three different cases reflect the difference in momentum transfer (or turbulent mixing) and hence the drag.

## 4 Conclusions

Measurements in the wake of a circular cylinder show that with the insertion of a circular or square control cylinder upstream of the main cylinder, mean velocity distributions exhibit a fuller profile for the tandem arrangement compared with that for a single cylinder. This results in a reduction in the wake half-width and a smaller drag for the tandem arrangement. Rms turbulence intensities are reduced in the modified wake. Spectral measurements support the presence of a more intense wake vortex for the tandem arrangement compared to a single cylinder suggesting more effective mixing between the outer higher-velocity fluid and the

inner lower-velocity fluid. This scenario is consistent with the observation of a 'fuller' mean velocity (reduced wake defect) profile in the tandem arrangement. Although the Reynolds shear stress distributions can only be considered as preliminary at this stage, they show that the square control cylinder leads to a smaller value of $\overline{uv}$ and reduced turbulent mixing, in apparent agreement with the observation of a reduction in the wake half-width. The square control cylinder has a larger influence on the wake development compared to the circular control cylinder.

**Acknowledgments** The support of ARC and the technical assistance of Ken Sayce are acknowledged.

## References

Alam MM, Zhou Y, Wang XW (2011) The wake of two side by side square cylinders. J Fluid Mech 669:432–471

Antonia RA, Rajagopalan S (1990) Determination of drag of a circular cylinder. AIAA J 28:1834–1835

Hu J, Zhou Y (2008) Flow structure behind two staggered circular cylinders, part 1: downstream evolution and classification. J Fluid Mech 607:51–80

Lee SJ, Lee SI, Park CW (2004) Reducing the drag on a circular cylinder by upstream installation of a small control rod. Fluid Dyn Res 34:233–250

Rajagopalan S, Antonia RA (2007) Turbulence and drag control in jet and wake flows. Sadhana 32:133–144

Zdravkovich MM (1977a) Review of flow interference between two circular cylinders in various arrangements. J Fluids Eng 618–633

Zdravkovich MM (1997b) Flow around circular cylinders, vol 1. Oxford University Press

# Flow Above the Free End of a Surface-Mounted Finite-Height Cylinder

**N. Rostamy, D. Sumner, D. J. Bergstrom and J. D. Bugg**

**Abstract** The flow above the free end of a surface-mounted finite-height circular cylinder was studied experimentally in a low-speed wind tunnel using particle image velocimetry. Velocity measurements were taken in horizontal and vertical planes above the free end at a Reynolds number of $Re = 4.2 \times 10^4$. Four cylinder aspect ratios, of $AR = 9, 7, 5$, and 3, were examined. The turbulent boundary layer on the ground plane had a thickness of $\delta/D = 1.6$. The results revealed details of the mean recirculation zone, reattachment position, critical points, and vortex patterns in the flow field above the free end. The sensitivity of the free-end flow field to changes in AR was much less pronounced than what is observed for the near-wake region.

**Keywords** Finite circular cylinder · Separated flow · Vortex patterns · Wake · PIV

## 1 Introduction

The flow around surface-mounted finite-height circular cylinders [e.g., Sumner et al. (2004), Rostamy et al. (2012)] is more complex than the well-studied case of the "infinite" cylinder. In many engineering applications, such as high-rise buildings, oil storage tanks, and chimneys, the flow fields of these cylindrical structures are strongly three-dimensional owing to the flow around the free end and the flow around the body's junction with the ground plane. On the free-end surfaces of these structures [e.g., Kawamura et al. (1984), Roh and Park (2003), Pattenden et al. (2005), Hain et al. (2008), Krajnović (2011)], regions of

N. Rostamy · D. Sumner (✉) · D. J. Bergstrom · J. D. Bugg
Department of Mechanical Engineering, University of Saskatchewan, Saskatoon, SK, S7N 5A9, Canada
e-mail: david.sumner@usask.ca

Y. Zhou et al. (eds.), *Fluid-Structure-Sound Interactions and Control*,
Lecture Notes in Mechanical Engineering, DOI: 10.1007/978-3-642-40371-2_24,

recirculating flow, vortex patterns, and the flow separating from the curved leading edge act to influence the flow in the near-wake region.

Although the near wake of a surface-mounted finite-height cylinder has been reasonably well-studied, comparably less attention has been focused on the flow over the free end and its relationship to the rest of the local flow field. How the cylinder aspect ratio and the boundary layer thickness on the ground plane influence the free-end flow field is not yet well understood. Furthermore, there are different interpretations of the free-end flow patterns in the literature [e.g., Kawamura et al. (1984), Roh and Park (2003), Pattenden et al. (2005), Hain et al. (2008), Krajnović (2011)] which have yet to be fully resolved. In the present study, the flow field above the free end of a surface-mounted finite-height circular cylinder (Fig. 1) is investigated experimentally using particle image velocimetry (PIV). Of particular interest is the effect of aspect ratio (AR = $H/D$, where $H$ and $D$ are the cylinder's height and diameter, respectively).

## 2 Experimental Approach

The experiments were conducted in a low-speed wind tunnel at a Reynolds number of Re = $4.2 \times 10^4$. Finite-height circular cylinders with AR = 9, 7, 5, and 3 were mounted normal to a ground plane, with AR = 3 representing a cylinder below the critical AR (Sumner et al. 2004; Rostamy et al. 2012). The turbulent boundary layer on the ground plane had a thickness of $\delta/D = 1.6$ at the location of the cylinders.

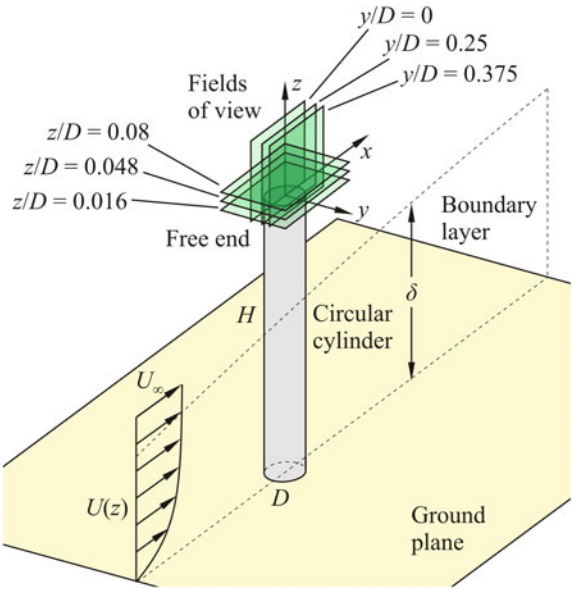


**Fig. 1** Schematic of the flow around a surface-mounted finite-height *circular cylinder* partially immersed in a flat-plate boundary layer (velocity profile $U(z)$, free stream velocity $U_\infty$); shown in the figure are the fields of view for the PIV measurements

Velocity measurements were made with a two-component PIV system in a set-up similar to Rostamy et al. (2012). Measurements were made in vertical ($x$–$z$) and horizontal ($x$–$y$) planes at different cross-stream ($y/D$) and wall-normal ($z/D$) positions, respectively, in the region above the free end of the cylinders (Fig. 1). In the $z$-direction, the horizontal plane nearest to the free-end surface was at $z/D = 0.016$, which was reasonably close to the surface to approximate the surface streamlines (Depardon et al. 2005). Mean velocity fields were obtained from ensembles of 1,000 and 528 image pairs in the ($x$–$z$) and ($x$–$y$) planes, respectively.

## 3 Results and Discussion

Figure 2 shows the mean streamlines in three vertical ($x$–$z$) planes above the free end of the cylinder of AR = 9. The flow separates from the sharp circumferential leading edge and a mean recirculation zone forms on the free-end surface. On the centre line (Fig. 2a), flow reattachment occurs at $x/D \approx 0.3$. A cross-stream vortex (referred to in the literature as the "arch vortex" or "mushroom vortex") can be seen within the mean recirculation zone [consistent with other studies, e.g., Hain et al. (2008), Krajnović (2011)]. Away from the centre line (Fig. 2b, c), the

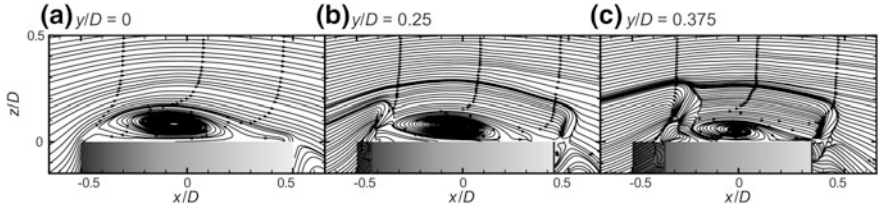


**Fig. 2** Mean streamlines in vertical ($x$–$z$) planes above the free end of a surface-mounted, finite-height *circular cylinder* of AR = 9: **a** $y/D = 0$, **b** $y/D = 0.25$, and **c** $y/D = 0.375$

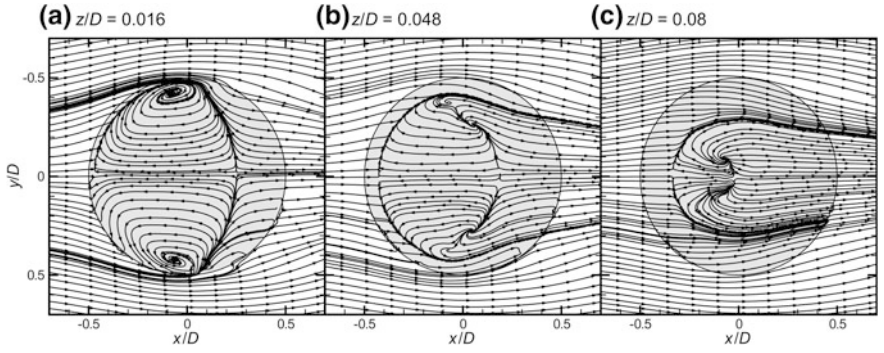


**Fig. 3** Mean streamlines in horizontal ($x$–$y$) planes above the free end of a surface-mounted, finite-height circular cylinder of AR = 7: **a** $z/D = 0.016$, **b** $z/D = 0.048$, and **c** $z/D = 0.08$

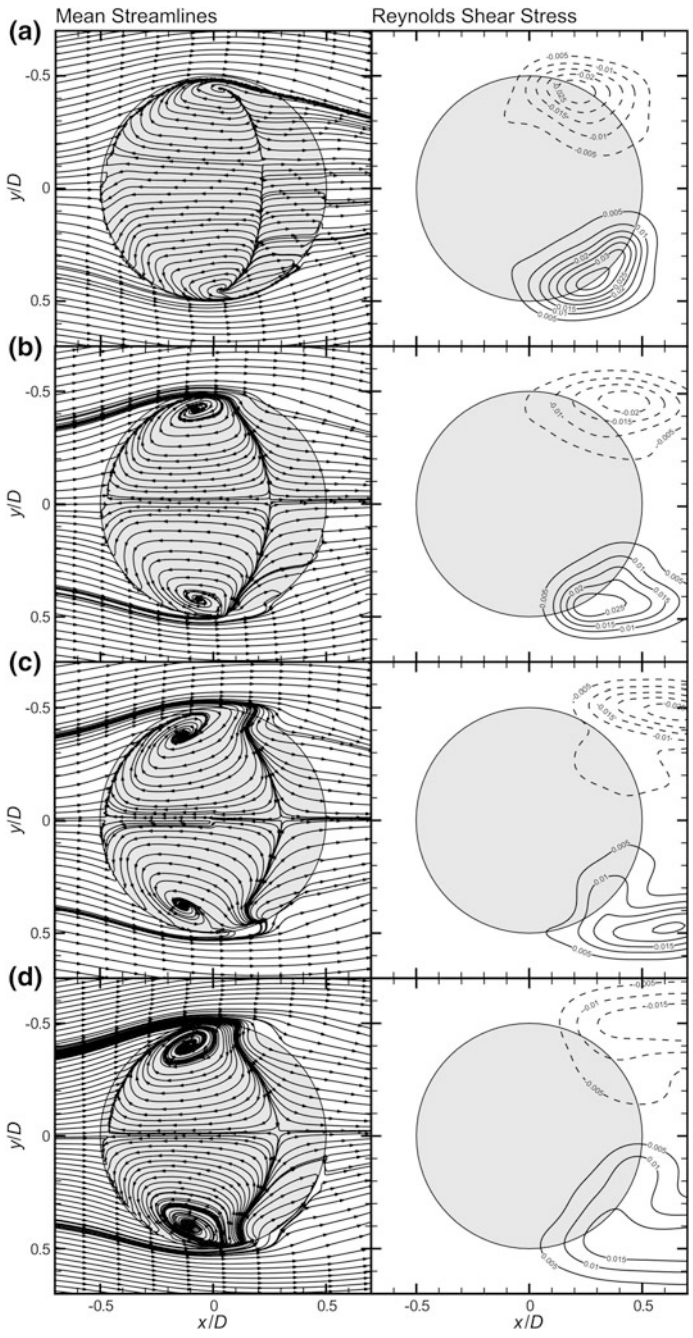


**Fig. 4** Flow in a horizontal plane (at $z/D = 0.016$) above the free end showing the mean streamlines (*left column*) and in-plane Reynolds shear stress (*right column*, contours of $-\langle u'v'\rangle'/U_\infty^2$): **a** AR = 9, **b** AR = 7, **c** AR = 5, and **d** AR = 3

streamlines are more complex owing to the three-dimensionality of the flow and the curved leading edge that defines the separation line. Reattachment moves upstream and the thickness of the zone reduces. Similar flow features are seen for the other aspect ratios (not shown).

Figure 3 shows the mean streamlines in three horizontal ($x$–$y$) planes above the free end of the cylinder of AR = 7. Very close to the surface (Fig. 3a) the curved reattachment line can be identified. Two foci are seen near the side edges of the free end and a saddle can be identified further downstream [consistent with other studies, e.g., Kawamura et al. (1984), Roh and Park (2003), Krajnović (2011)]. Away from the surface (Fig. 3b), the foci move away from the outer edges and towards the flow centre line. Farther away from the free end (Fig. 3c), there is no evidence of the foci, while a node is now observed.

The effects of AR are illustrated in Fig. 4 for measurements in the horizontal plane at $z/D = 0.016$. As AR decreases, the vortex structures represented by the foci become stronger, there are changes to the shape of the reattachment line near the outer edges of the free end, and reattachment moves towards the trailing edge. Also, with a decrease in AR, the contours of Reynolds shear stress extend into the near-wake region, and the lateral spacing between the two regions of elevated Reynolds shear stress, on either side of the cylinder, increases.

## 4 Conclusions

In the present study, the mean flow field above the free end of a surface-mounted, finite-height circular cylinder was studied using PIV. For aspect ratios of AR = 9, 7, 5, and 3, flow separating from the leading edge led to the formation of an enclosed mean recirculation zone containing a cross-stream vortex. The effect of aspect ratio on the free-end flow field was small and gradual compared to its effect on the near-wake region, with small changes to the shape and location of the mean reattachment line, the size and strength of the mean vortex patterns, and the turbulent shear stresses. Although the cylinder of AR = 3 was below the critical aspect ratio, from previous studies of the near-wake region (Rostamy et al. 2012), a distinct free-end flow pattern was not observed for this cylinder.

## References

Depardon S, Lasserre JJ, Boueilh JC, Brizzi LE, Borée J (2005) Skin friction pattern analysis using near-wall PIV. Exp Fluids 39:805–818

Hain R, Kähler CJ, Michaelis D (2008) Tomographic and time resolved PIV measurements on a finite cylinder mounted on a ground plane. Exp Fluids 45:715–724

Kawamura T, Hiwada M, Hibino T, Mabuchi T, Kumada M (1984) Flow around a finite circular cylinder on a flat plate. Bull JSME 27:2142–2150

Krajnović S (2011) Flow around a tall finite cylinder explored by large eddy simulation. J Fluid Mech 676:294–317

Pattenden RJ, Turnock SR, Zhang X (2005) Measurements of the flow over a low-aspect-ratio cylinder mounted on a ground plane. Exp Fluids 39:10–21

Roh SC, Park SO (2003) Vortical flow over the free end surface of a finite circular cylinder mounted on a flat plate. Exp Fluids 34:63–67

Rostamy N, Sumner D, Bergstrom DJ, Bugg JD (2012) Local flow field of a surface-mounted finite circular cylinder. J Fluids Struct 34:105–122

Sumner D, Heseltine JL, Dansereau OJP (2004) Wake structure of a finite circular cylinder of small aspect ratio. Exp Fluids 37:720–730

# Intermittency of Vortex Shedding in the Near Wake of a Finite-Length Square Prism

**H. Wang and M. Xu**

**Abstract** The flow around a finite-length square prism with aspect ratio of 5 is investigated using LES at $Re_d = 3{,}900$. Two typical flow modes are found in its near wake. One is characterized by staggered arranged spanwise vortices, similar to that in 2D cylinder wake; on the other hand, the spanwise vortices are symmetrically arranged for the second mode. These two modes occur intermittently in the near wake. When the first mode occurs, the pressure on prism side surface fluctuates periodically, corresponding to large values of drag and fluctuating lift; for the second mode, there is no obvious pressure fluctuation, and the drag and fluctuation lift are significantly smaller than those for the first mode.

**Keywords** Finite-length prism · Wake · Aerodynamic force · LES

## 1 Introduction

It has been clear that the near-wake structure of a finite-length cylinder depends strongly on its aspect ratio, $H/d$, where $H$ and $d$ are cylinder characteristic height and width, respectively. It was reported that when $H/d$ falls below a critical value, vortex shedding changes from anti-symmetrical to symmetrical, and the free-end downwash flow dominates the near wake (Okamoto and Sunabashiri 1992).

Financial support from the National Natural Science Foundation of China through grants 51108468 is acknowledged.

H. Wang (✉) · M. Xu
School of Civil Engineering, Central South University, Changsha, China
e-mail: wanghfme@gmail.com

Y. Zhou et al. (eds.), *Fluid-Structure-Sound Interactions and Control*,
Lecture Notes in Mechanical Engineering, DOI: 10.1007/978-3-642-40371-2_25,

Wang and Zhou (2009) suggested that the overall near-wake structure is arch type regardless of *H*/*d*. More recently, Sattari et al. (2011) observed two regimes for the flow around a wall-mounted finite prism with $H/d = 4$. Regime *A* corresponds to a high-amplitude fluctuation of pressure coefficient ($C_p$) and is associated with well-organized, alternate shedding vortices. On the other hand, regime *B* is observed during low-amplitude fluctuation of $C_p$ and is characterized by the coexistence of two-counter rotating vortices throughout the shedding cycle.

However, the relation between these two typical flow regimes and their effects on the aerodynamic forces are not thoroughly understood. The present paper aims to address these problems, utilizing large eddy simulation (LES) method.

## 2 Large Eddy Simulation Approach

Figure 1 presents the computational domain and coordinate system. The *H*/*d* of the prism was 5 and $d = 20$ mm. The oncoming velocity ($U_\infty$) is 3 m/s, $\mathrm{Re}_d = 3{,}900$. LES was utilized to solve the incompressible N–S and continuity equations. The algebraic eddy viscosity model (Smagorinsky 1963) was used in present LES for its simplicity and low computational cost. The computational grid was refined near the prism and bottom wall, which contains about 6.4 million cells. The dimensionless wall distance is smaller than 1 on most surface area, which ensures enough grid resolution. The time step was $3.4 \times 10^{-4}$ s, about 0.5 % of vertex shedding cycle.

## 3 Results and Discussions

Power spectral density function of lift on the prism is shown in Fig. 2, which presents a pronounced peak at $f^* = 0.105$. The superscript represents normalization by $U_\infty$ and/or *d*. It is deduced that there may be a periodic vortex shedding

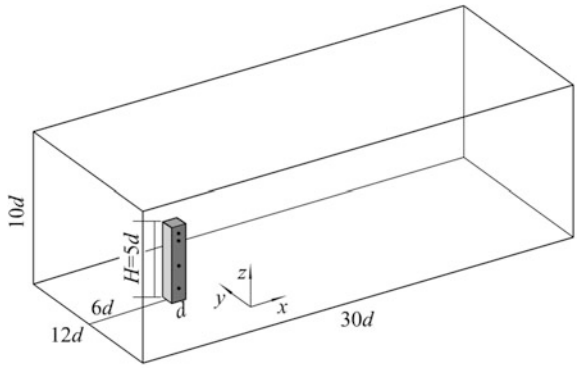


**Fig. 1** The computation domain and definition of coordinate system

occurring in the finite-length prism wake. The dominant vortex shedding frequency is slightly smaller than the corresponding value of 0.13 for a 2D prism (Wang and Zhou 2009).

The time tracers of drag and lift coefficients ($C_d$ and $C_l$) together with the time–frequency spectrum of $C_l$ are presented in Fig. 3. A number of observations can be made: firstly, the time-averaged value of $C_d$ is 1.64, about 78 % of the corresponding value (0.21) for a 2D square prism (Saha et al. 2003). Secondly, the variation of $C_d$ corresponds well with that of $C_l$. A local maximum value of $C_d$ occurs when $C_l$ fluctuates periodically with large amplitude, as indicated by mode 1; on the other hand, $C_d$ reduces significantly when there is no periodic fluctuation in $C_l$, as indicated by mode 2. The averaged value of $C_d$ is about 1.55–1.6 for mode 2; instead, its maximum value is about 1.85 for mode 1. The later is about 20 % larger than the former. Thirdly, both mode 1 and mode 2 occur randomly and intermittently in time. Although, the spectral energy concentrates at $f^* = 0.105$ in the time–frequency spectrum of $C_l$ (identical to that shown in Fig. 2), it is not continuous in time, as shown in Fig. 3c. The two pronounced energy peaks in Fig. 3c correspond to mode 1; on the other hand, there is no energy peak when mode 2 occurs. Lastly, when mode 1 occurs, the periodic large amplitude fluctuation of $C_l$ and the pronounced peak in the time–frequency spectrum suggest the occurrence of alternating spanwise vortex shedding, similar to that in a 2D cylinder wake. On the other hand for mode 2, this periodic vortex shedding may not exist.

Figure 4 presents the time tracers of the pressure coefficients on the side face at $z^* = 1$, 2.5, 4, and 4.5. The time–frequency spectrum of $C_l$ in 2–4 s is also shown for comparison. It is obvious that $C_p$ at all spanwise positions present remarkable periodic fluctuation for mode 1, but not for mode 2. This observation suggests that periodic vortex shedding occurs at most cylinder span for mode 1, but not for mode 2. The $C_p$ near the free end ($z^* = 4$ and 4.5) are smaller for mode 1 relative

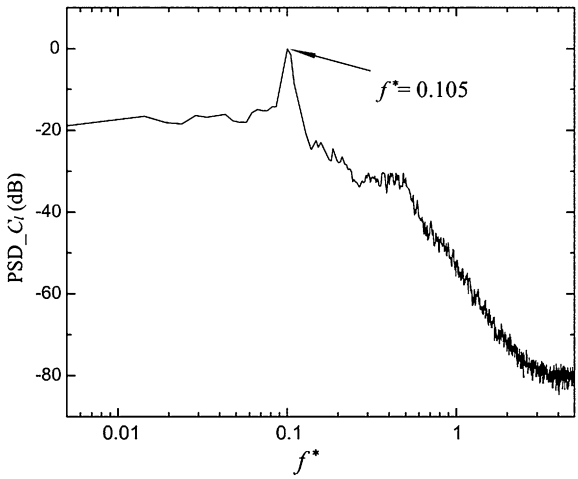


**Fig. 2** Power spectral density function of lift on the finite-length prism

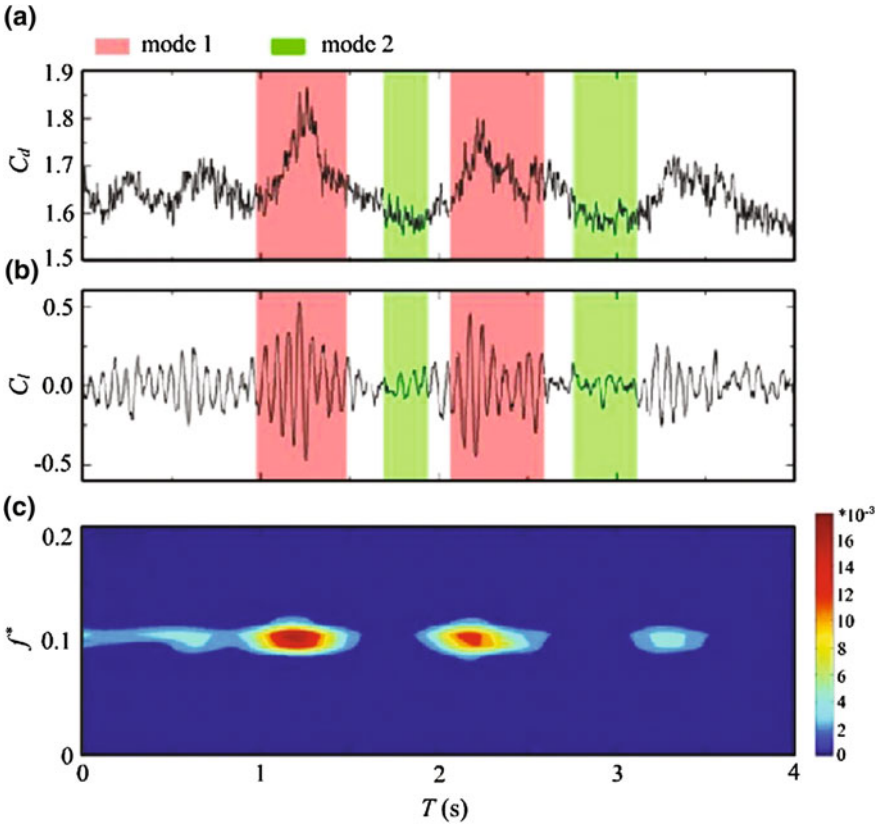


**Fig. 3** Time tracers of $C_d$ and $C_l$ (**a**, **b**), and the time–frequency spectrum of $C_l$ (**c**)

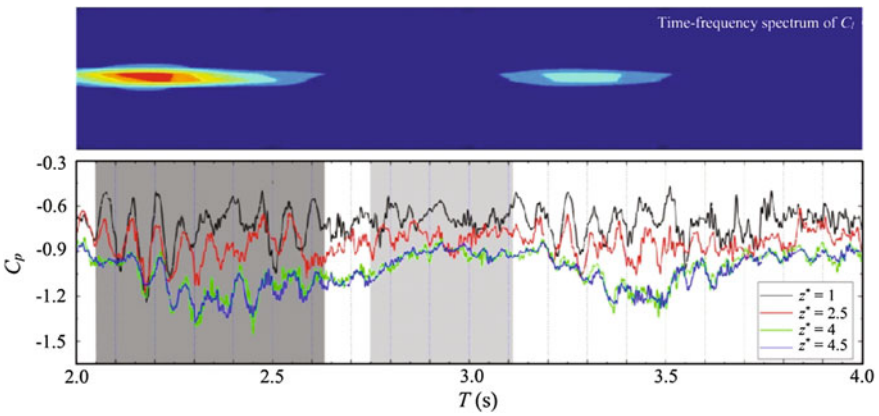


**Fig. 4** Time tracers of the pressure coefficients on prism side face at different heights

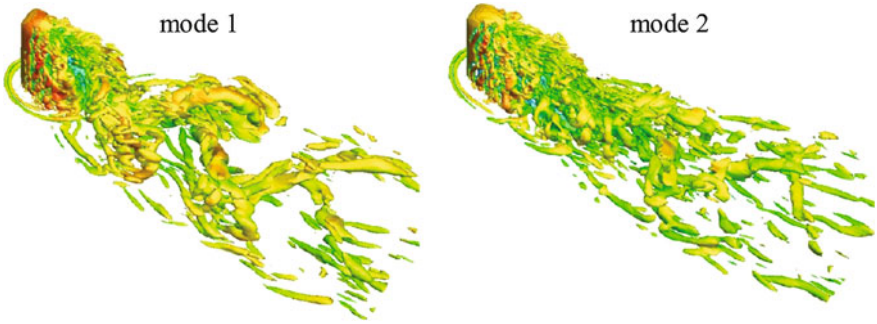


**Fig. 5** Iso-surface of $Q^* = 0.07$ for the two modes, colored by streamwise velocity

to those for mode 2. This is ascribed to the stronger flow separation for the former, resulting in smaller $C_p$.

Figure 5 presents two typical instantaneous vortex structures identified by $Q$ criterion (Hunt et al. 1988). For these two modes, the spanwise shear layers on both sides of the prism are connected by the free-end shear layer. That is, the initial overall vortex structure is arch type for the two modes, which is consistent with that observed by Wang and Zhou (2009). As proceeding further downstream, the near-wake structures are remarkably different. For mode 1, there are periodic alternating vortices similar to that in 2D prism wake, although it is more complicated and less organized. On the other hand, there is no periodic vortex street for mode 2.

## 4 Conclusions

Two typical modes occur in the near wake of a finite-length prism with $H/d = 5$ at $\mathrm{Re}_d = 3{,}900$. For mode 1, $C_l$ fluctuates periodically with large amplitude, and the corresponding $C_d$ is relatively larger. For mode 2, $C_l$ has no obvious periodicity and the corresponding $C_d$ is smaller compare to that for mode 1. For mode 1, staggered arranged large-scale spanwise vortices occur in the near wake, similar to those in 2D wake. On the other hand, for mode 2, no periodic vortex street occurs in the near wake. These two modes occur intermittently in the prism wake.

## References

Hunt JCR, Wray AA, Moin P (1988) Eddies, stream and convergence zones in turbulent flow. Center for Turbulence Research, report no. CTR-S88, p 193

Okamoto T, Sunabashiri Y (1992) Vortex shedding from a circular cylinder of finite length placed on a ground plane. J Fluids Eng 114:512–521

Saha AK, Biswas G, Muralidhar K (2003) Three-dimensional study of flow past a square cylinder at low Reynolds numbers. Int J Heat Fluid Flow 24:54–66

Sattari P, Bourgeois JA, Martinuzzi RJ (2011) On the vortex dynamics in the wake of a finite surface-mounted square cylinder. Exp Fluids 52:1149–1167

Smagorinsky J (1963) General circulation experiments with the primitive equations. Mon Weather Rev 91:99–164

Wang HF, Zhou Y (2009) The finite-length square cylinder near wake. J Fluid Mech 638:453–490

# Strouhal Numbers of Unsteady Flow Structures Around a Simplified Car Model

**B. F. Zhang, S. To and Y. Zhou**

**Abstract** This work aims to gain relatively thorough understanding of unsteady flow structures around an Ahmed body and associated predominated Strouhal numbers $St_{\sqrt{A}}$ based on the square root of the frontal area $A$. Extensive hotwire and flow visualization measurements were conducted in a wind tunnel at $Re_{\sqrt{A}} = 6.59 \times 10^4$ over the roof, the rear window, and behind the vertical base of this body with a slant angle of 25°. Four distinct Strouhal numbers have been identified. $St_{\sqrt{A}} = 0.196$ and 0.140 are detected above the roof. $St_{\sqrt{A}} = 0.196$ is captured again over the rear window, along with another unsteady structure of $St_{\sqrt{A}} = 0.265$. Behind the vertical base, the wake is dominated by the quasi-periodic structures of $St_{\sqrt{A}} = 0.442$. A conceptual flow structure model is proposed based on the present data as well as those in the literature.

## 1 Introduction

There has been recently a renewed interest in finding new technologies to reduce aerodynamic drag and hence fuel consumption in automotive industry because of the lasting high fuel costs in the past few years as well as the issue of global warming. Active control has been identified to be the most likely technique that may achieve substantial drag reduction further. The Ahmed body is perhaps the

B. F. Zhang · Y. Zhou (✉)
Department of Mechanical Engineering, The Hong Kong Polytechnic University, Kowloon, Hong Kong
e-mail: yu.zhou@polyu.edu.hk

S. To
State Key Laboratory of Ultra-precision Machining Technology, Department of Industrial and System Engineering, The Hong Kong Polytechnic University, Kowloon, Hong Kong

Y. Zhou
Shenzhen Postgraduate School, Harbin Institute of Technology, Shenzhen, China

Y. Zhou et al. (eds.), *Fluid-Structure-Sound Interactions and Control*,
Lecture Notes in Mechanical Engineering, DOI: 10.1007/978-3-642-40371-2_26,

most widely used simplified vehicle model in the active drag reduction research (Vino et al. 2005; Thacker et al. 2010). One piece of the crucial information required for the active control of drag is the Strouhal number $St_{\sqrt{A}}$ of unsteady flow structure around the Ahmed model. Previously reported $St_{\sqrt{A}}$ is rather scattered, 0.18 $\sim$ 0.50 over the rear window of $\varphi = 25^{\circ}$ and 0.36–0.53 behind the base. This work aims to clarify this issue and conduct a relatively thorough investigation on $St_{\sqrt{A}}$ in flow around the Ahmed model based on extensive hotwire and flow visualization measurements.

## 2 Experimental Details

Experiments were conducted in a closed-circuit wind tunnel, with a 2.4 m-long square test section (0.6 × 0.6 m). The 1/3 scaled Ahmed body was placed on a raised floor, which is used to control the boundary layer thickness. Figure 1 shows the dimensions of the model and the definition of the right-handed Cartesian coordinate system ($x$, $y$, $z$), with the origin $O$ at the midpoint of the lower edge of the model vertical base. Measurements were conducted at a free-stream velocity ($U_{\infty}$) of 8.33 m/s, corresponding to $Re_{\sqrt{A}} = 6.59 \times 10^4$. A single hot-wire fixed on a computer-controlled Dantec traverse system was used to measure streamwise fluctuating velocity $u$ to detect the predominant frequencies in flow. Flow visualization was conducted using a Dantec PIV system (PIV2100) in the ($x$, $z$) planes in order to capture the spanwise turbulent structures.

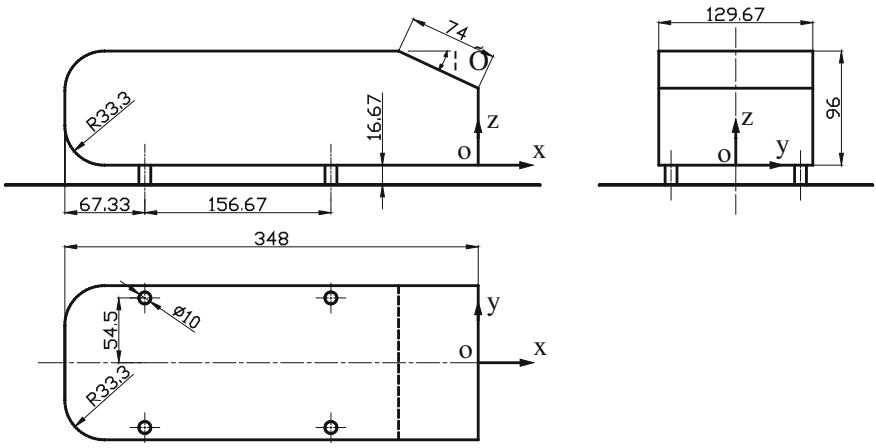


**Fig. 1** Dimensions of a 1/3-scaled Ahmed body

## 3 Results and Discussion

Figure 2a, b shows the power spectral density function $E_u$ of the single hot-wire signal $u$ measured above and the roof of the model at two stations downstream of the leading edge. The pronounced peak occurs at $St_{\sqrt{A}} = 0.196$ and 0.140 in Fig. 2a, depending on the spanwise location. Based on Spohn and Gillieron's (2002) flow visualization, the peak $St_{\sqrt{A}} = 0.196$ at $y^* = 0$ and 0.140 at $y^* = 0.14$ are ascribed to the vortices emanated from the recirculation bubble at the leading edge and the oscillation of the core of the longitudinal vortices originated from the bubble pulsation, respectively. Asterisk denotes normalization by $\sqrt{A}$ in this paper. At $y^* = 0.29$–$0.36$, the peak at $St_{\sqrt{A}} = 0.196$ is evident. The pronounced peak appears broadened at $y^* = 0.43$ under influence of the shear layer over the side surface. Further downstream, the peak at $St_{\sqrt{A}} = 0.140$ does not seem to be discernible in $E_u$ (Fig. 2b), due to the weakened longitudinal vortex as advected downstream.

Figure 2c presents $E_u$ measured at $A_1$–$A_4$ in the symmetry plane ($y^* = 0$) along the slant surface. The peak at $St_{\sqrt{A}} = 0.196$ is evident at $A_1$ and $A_2$, but becomes weaker further downstream at $A_3$ and vanishes at $A_4$. The observation is consistent with the previous report (Thacker et al. 2010) of $St_{\sqrt{A}} = 0.22$ measured near this location. The same pronounced peak at $St_{\sqrt{A}} = 0.196$ is observed at $B_1$–$B_4$ for $y^* = 0.36$ (Fig. 2d). The previously observed spanwise vortex roll (Wang et al. 2013) is probably responsible for the peak at $St_{\sqrt{A}} = 0.196$ in $E_u$ over the slant. However, the most pronounced peak occurs at $St_{\sqrt{A}} = 0.265$ near the side edge of

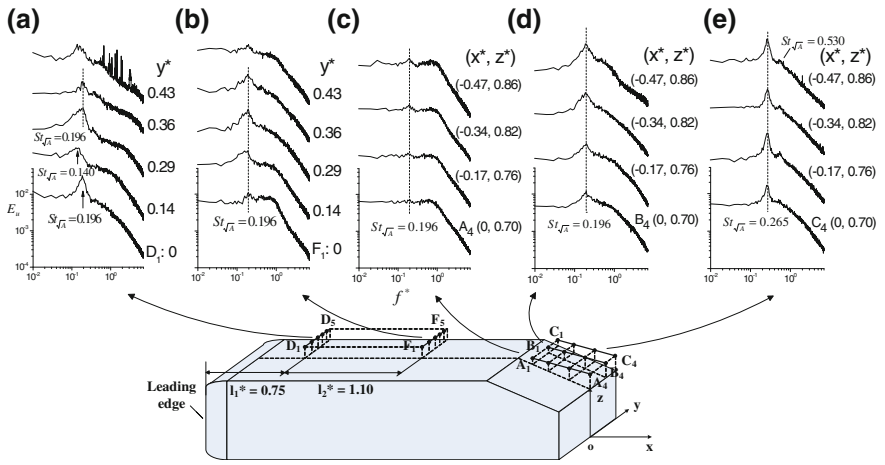


**Fig. 2** Power spectral density function $E_u$ of hot-wire signals measured along **a** $D_1$–$D_5$ ($x^* = -2.37$, $z^* = 0.94$), and **b** $F_1$–$F_5$ ($x^* = -1.27$, $z^* = 0.94$), respectively, above the roof, **c** $A_1$–$A_4$ ($y^* = 0$), **d** $B_1$–$B_4$ ($y^* = 0.36$), **e** $C_1$–$C_4$ ($y^* = 0.57$), respectively, over the slant

the rear window (Fig. 2e), coinciding with the location of the C-pillar vortex. Its second harmonic frequency $St_{\sqrt{A}} = 0.530$ is discernible.

Behind the vertical base, a predominant peak is observed in $E_u$ at $St_{\sqrt{A}} = 0.442$ for various downstream stations in the plane of $y^* = 0$ (Fig. 3). This peak is only discernible near the ground, i.e., at $K_1 - K_3$, at $x^* = 0.2$. But it grows considerably stronger and evident further away from the ground as x* increases up to 0.77, and then is weakened for larger $x^*$. Typical flow structures behind the vertical base (Fig. 4), captured from flow visualization, suggest that coherent structures are alternatively emanated from the upper and lower recirculation bubbles, which are responsible for the pronounced peaks at $St_{\sqrt{A}} = 0.442$ in $E_u$ (Fig. 3).

## 4 Summary and Conclusions

A total of four distinct predominant frequencies have been identified, each corresponding to distinct unsteady flow structures, as summarized below: (1) A quasi-periodical structure of $St_{\sqrt{A}} = 0.140$ is observed above the roof near the leading edge, which is ascribed to the pulsation of the separation bubble. (2) Another predominant frequency of $St_{\sqrt{A}} = 0.196$ is measured above the roof, due to the vortices shed from the bubble at the front. This peak is re-captured over the rear window, suggesting that spanwise vortices over the slant are connected to those formed over the roof. (3) A strong peak occurs at $St_{\sqrt{A}} = 0.265$ along the side edge of rear window, which is associated with the C-pillar vortex. (4) Other than the well-reported C-pillar vortices, the wake behind the vertical base is predominated

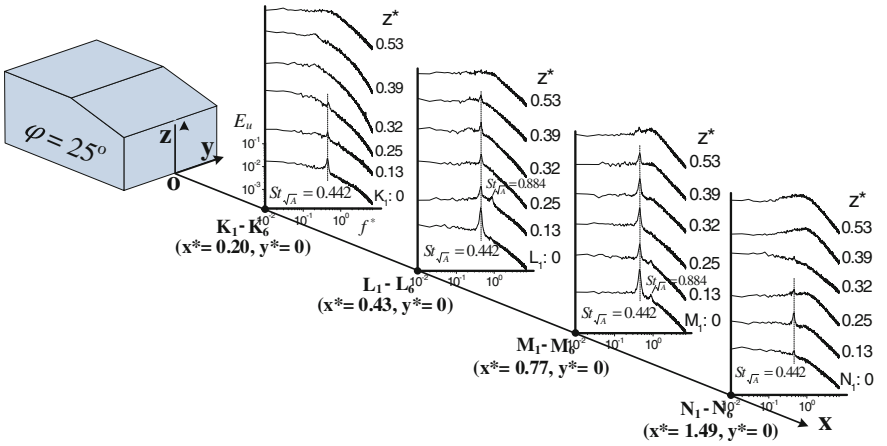


**Fig. 3** Power spectra $E_u$ of hot-wire signals measured at $K_1$–$K_6$, $L_1$–$L_6$, $M_1$–$M_6$, $N_1$–$N_6$, respectively, at $y^* = 0$ in behind the base

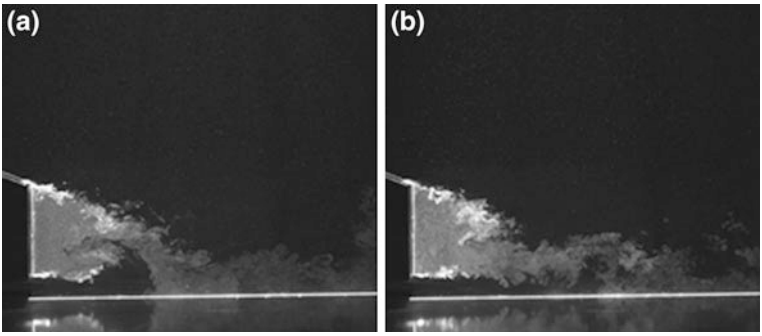


**Fig. 4** Typical photographs of flow structures in the symmetry plane ($y^* = 0$) of the wake: **a** flow disseminated from the upper recirculation bubble, and **b** from the lower bubble

by the quasi-periodical structures of $\mathrm{St}_{\sqrt{A}} = 0.442$, which are generated by alternate emanations of coherent structures from upper and lower recirculation bubbles, respectively.

One conceptual flow structure model around the Ahmed model is proposed, as sketched in Fig. 5. This model incorporates the presently found coherent structures, emanated from the upper and lower recirculation bubbles, with those observed by various investigators, including recirculation bubble and hairpin vortices above the roof, spanwise vortex roll and C-pillar vortices over the rear window, the upper and lower recirculation bubbles behind the base, the lower and

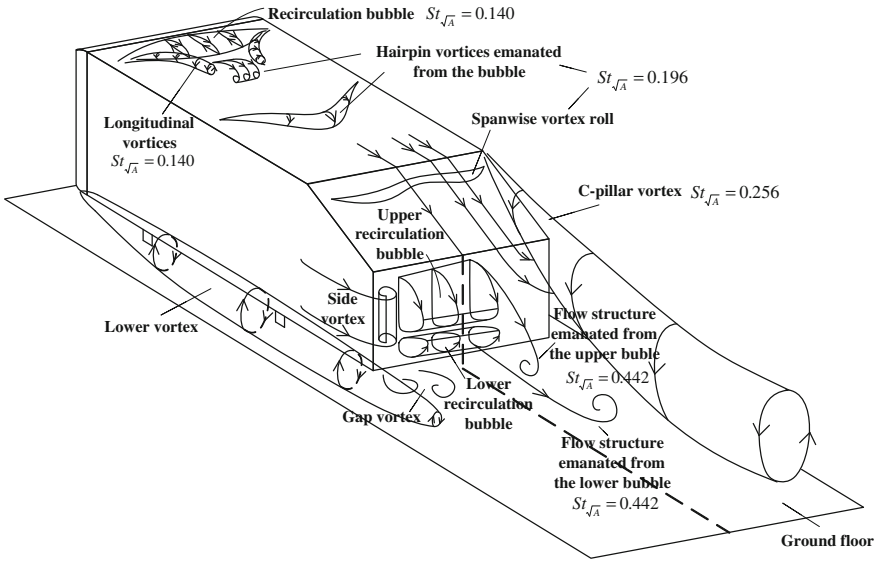


**Fig. 5** A conceptual model of the flow structure around the Ahmed model

side vortices on the side, and the gap vortex. Furthermore, the dimensionless predominant frequencies have been identified for the first time for all these unsteady coherent structures, thus providing a rather comprehensive picture of the flow structure and an explanation for the widely scattered frequencies in the literature.

**Acknowledgments** Authors wish to acknowledge support given to them from Research Grants Council of HKSAR through grant PolyU 5319/12E.

## References

Spohn A, Gillieron P (2002) Flow separations generated by a simplified geometry of an automotive vehicle. In: IUTAM symposium—unsteady separated flows, Toulouse, France

Thacker A, Aubrun S, Leroy A, Devinant P (2010) Unsteady analyses of the flow separation on the rear window of a simplified ground vehicle model. AIAA paper 2010-4569

Vino G, Watkins S, Mousley P, Watmuff J, Prasad S (2005) Flow structures in the near-wake of the Ahmed model. J Fluids Struct 20:673–695

Wang XW, Zhou Y, Pin YF, Chan TL (2013) Turbulent near wake of an Ahmed vehicle model. Exp Fluids (published online: 11 Apr 2013)

# Reynolds Number Effect on Flow Classification Behind Two Staggered Cylinders

**C. W. Wong, Y. Zhou and Md. Mahbub Alam**

**Abstract** This work aims to investigate based on the Strouhal number St and the flow structure, the dependence of flow classification on the Reynolds number Re in the wake of two staggered cylinders, with Re varying from $1.5 \times 10^3$ to $2.0 \times 10^4$. The cylinder center-to-center pitch, $P^* = P/d$ examined is 1.2–6.0 ($d$ is the cylinder diameter), and the angle ($\alpha$) between the incident flow and the line through the cylinder centers is 0°–90°. Two single hotwires were used to measure simultaneously the St behind each of the two cylinders at streamwise positions from $x^* = x/d = 2.5$–15. While the present data reconfirms the flow structure modes previously reported, the dependence of the flow modes on $P^*$ and $\alpha$ exhibits an appreciable dependence on Re. The observation is connected to the Re effect on the generic features of a two-cylinder wake such as flow separation, boundary layer thickness, gap flow deflection, and vortex formation length.

**Keywords** Two-cylinder wake · Vortex structure · Flow classification

## 1 Introduction

Flow behind two staggered cylinders in close proximity is by far more complicated than that behind an isolated cylinder, depending on the angle ($\alpha$) between incident flow and the line through the cylinders, and the cylinder center-to-center pitch $P^*$, in addition to the Reynolds number Re. In this paper, an asterisk denotes

C. W. Wong (✉) · Y. Zhou · Md. M. Alam
Institute of Turbulence-Noise-Vibration Interactions and Control, Shenzhen Graduate School, Harbin Institute of Technology, Harbin, China
e-mail: cwwong@hitsz.edu.cn

Y. Zhou
Department of Mechanical Engineering, The Hong Kong Polytechnic University, Kowloon, Hong Kong

Y. Zhou et al. (eds.), *Fluid-Structure-Sound Interactions and Control*,
Lecture Notes in Mechanical Engineering, DOI: 10.1007/978-3-642-40371-2_27,

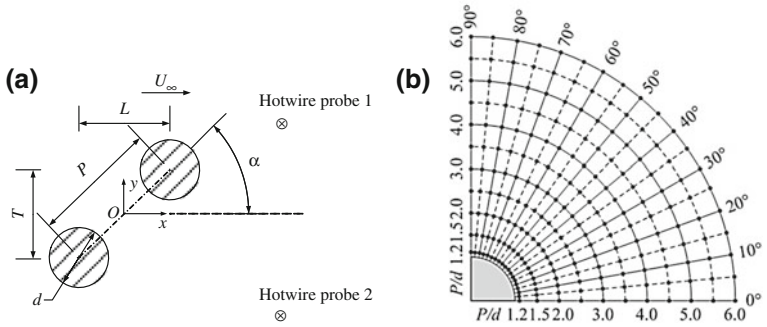


**Fig. 1** **a** Experimental arrangement, and **b** hotwire measurement grid in the $P^*-\alpha$ plane at $\mathrm{Re} = 7.0 \times 10^3$

normalization by $d$ and/or $U_\infty$. Naturally, flow classification in terms of $\alpha$ and $P^*$ is crucial for a thorough understanding of the flow and has received considerable attention in the literature [e.g., Sumner (2010)]. Hu and Zhou (2008) investigated the flow structures and their downstream evolutions in the wake of two staggered cylinders for $P^* = 1.2$–$4.0$ and $\alpha = 0°$–$90°$ ($\mathrm{Re} = 7.0 \times 10^3$). However, their flow structure classification suffered from a relatively coarse resolution in their measurement grid, $\Delta P^*$ and $\Delta\alpha$, which were 0.5 and 10°, respectively. Therefore, the first objective of this work is to provide an improved resolution in identifying the flow mode in the $P^*-\alpha$ plane. On the other hand, the dependence of flow classification on Re was not addressed in Hu and Zhou (2008). As such, the second objective of this work is to provide insight on how flow classification may be influenced by Re.

## 2 Experimental Details

Experiments were performed in a closed-circuit wind tunnel with a working section of $L \times W \times H = 2.4 \times 0.6 \times 0.6$ m. The test models were two identical brass cylinders of $d = 12.5$ mm. Both cylinders spanned 0.6 m and were mounted symmetrically with respect to the mid-plane, 0.2 m downstream of the exit plane of the contraction section of the wind tunnel. The length-to-diameter ratio of the cylinder was 48. Figure 1a shows the arrangement of the cylinders and the definitions of $P$ and $\alpha$. The $x$- and $y$-axis are defined along the free-stream and lateral directions, respectively, with their origin at the midpoint between the two cylinder centers. Two single hotwires (Pt-10 % Rh) of 5 μm in diameter and about 1 mm in length were used to measure simultaneously the streamwise velocity fluctuation $u$ behind each of the two cylinders at $x^* = 2.5$, 5, 10 and 15, and $y^* = \pm 1.3$–$\pm 3.0$, depending on the arrangement of the cylinders. The power spectral density function $E_u$ of $u$ was calculated using a fast Fourier transform. The Re range investigated was $1.5 \times 10^3$–$2.0 \times 10^4$. The measurement grid covers $\alpha = 0°$–$90°$,

with $\Delta\alpha$ of $10^{o}$ and $P^{*} = 1.2$, 1.5, 2.0, 2.5, 3.0, and 4.0 for $\mathrm{Re} = 1.5 \times 10^{3}$ and $2.0 \times 10^{4}$; $\Delta\alpha$ is reduced to 5° and $P^{*} = 1.2$–6.0 for $\mathrm{Re} = 7.0 \times 10^{3}$, as shown in (Fig. 1b).

## 3 Results and Discussion

### 3.1 Dependence of Flow Structure on $P^{*}$ and $\alpha$

The flow mode or structure is closely linked to its initial conditions such as Re and initial interactions between the four shear layers around the two cylinders. The shear layer interactions may have various types, as summarized in Hu and Zhou (2008). These interactions result in three types of the flow structure immediately behind the downstream cylinder, viz. a single vortex street, one wide street and one relatively short-lived narrow street, and two coupled streets, which may evolve downstream, forming different flow modes (i.e., S-Ia, S-Ib, S-II, T-I, and T-II) (Hu and Zhou 2008). The present classification, valid for $x^{*} \geq 5$, is compared in Fig. 2 with that reported by Hu and Zhou (2008). Unlike Hu and Zhou (2008), the border between different flow modes is presently identified with the midpoint between two adjacent measurement grid points where the flow structure changes from one mode to another (see example marked by points A and B in Fig. 2). The corresponding uncertainty is 0.15–0.25 in determining $P^{*}$ and $\pm$ 2.5° in $\alpha$. The two flow classifications show a general agreement with each other, though there is discernible variation in the border between different modes, which results from a

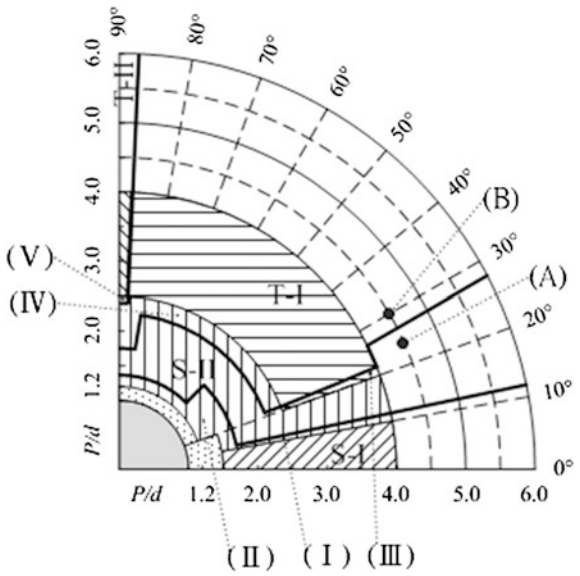


**Fig. 2** Dependence of the flow mode on $P^{*}$ and $\alpha$. Hatched area: Hu and Zhou (2008); thick solid line: present data. $\mathrm{Re} = 7.0 \times 10^{3}$

difference in determining the flow mode border as well as the present finer measurement grid. The differences between the flow classifications occur in five regions, marked by I through V in Fig. 2.

## 3.2 Dependence of Flow Structure on Re

Figure 3 presents flow classifications at $Re = 1.5 \times 10^3$, $7.0 \times 10^3$, and $2.0 \times 10^4$. It is immediately noted that a change in Re from $1.5 \times 10^3$ to $7.0 \times 10^3$ or from $7.0 \times 10^3$ to $2.0 \times 10^4$ results in an appreciable variation in the border between different flow regimes. To highlight the changes that occur in Fig. 4 shows the regions where the border has shifted with a variation in Re.

It is noteworthy that the upstream cylinder is subjected to uniform incident flow, as in an isolated cylinder wake, but the downstream is not. An increase in Re may result in the change in the isolated cylinder wake in a number of aspects (Zdravkovich 1997). As Re varies from $1.5 \times 10^3$ to $7.0 \times 10^3$, three regions (Fig. 4a), i.e., I through III, in the $P^* - \alpha$ plane are identified, where one flow mode

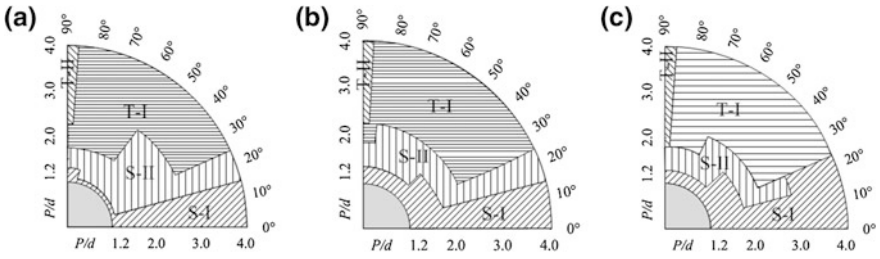


**Fig. 3** Dependence of flow structures on $P^*$ and $\alpha$ in the wake of two staggered circular cylinders: **a** $Re = 1.5 \times 10^3$, **b** $Re = 7.0 \times 10^3$, and **c** $Re = 2.0 \times 10^4$

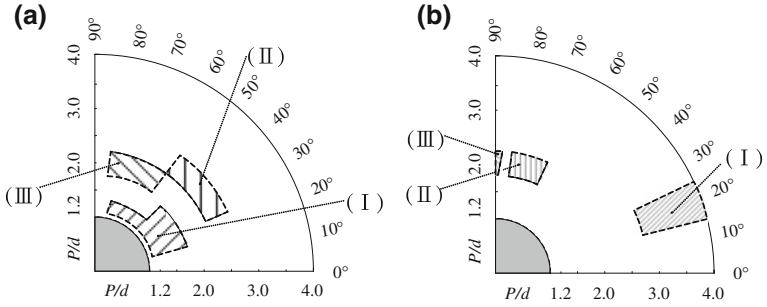


**Fig. 4** Comparison of dependence of the flow mode on $P^*$ and $\alpha$ (hatched area): **a** Re varies from $1.5 \times 10^3$ to $7.0 \times 10^3$, **b** Re varies from $7.0 \times 10^3$ to $2.0 \times 10^4$. The *solid* and *dashed lines* denote the borders of the flow regime at higher and lower Re, respectively

changes to another. Region I occurs due to the shift in separation point, an increase in separation angle, and an increase in wake width of the upstream cylinder. As such, the inner shear layer separating from the upstream cylinder does not go through the gap but reattaches on the downstream cylinder, that is, S-II changes to S-I. On the other hand, the aspects of reducing the boundary layer thickness and the vortex formation length of the upstream cylinder at a higher Re may assume a major role for the cause of region II. All these aspects enhance the stability of the narrow street. Therefore, the two streets formed persist, showing the characteristics of T-I. Similarly, the separation point and separation angle have a direct impact upon interactions between the streets. As such, a different change, from T-I to S-II, occurs in region III.

As Re varies from $7.0 \times 10^3$ to $2.0 \times 10^4$, three regions are identified, namely, I, II, and III in the $P^* - \alpha$ plane, where one flow mode changes to another (Fig. 4b). Given this range of the Re change, a single cylinder wake experiences a significantly reduced vortex formation length and thinner boundary layer (Zdravkovich 1997). Region I, changing from S-II to S-I, the inner shear layer of the upstream cylinder may roll up, forming vortices before reaching the downstream cylinder and producing a co-shedding flow. As such, the vortex shedding from the downstream cylinder is triggered by the vortices separated from the inner side of the upstream cylinder. Consequently, the frequency of vortex shedding is the same for the two cylinders, producing the S-I mode flow structure. In regions II and III, the flow mode changes from S-II to T-I and T-I to T-II, respectively, with Re varying from $7.0 \times 10^3$ to $2.0 \times 10^4$. In both cases, the boundary layers around both cylinders become thinner for the higher Re, implying greater streamwise momentum passing through the gap and a less deflection in the gap flow. All these enhance the stability of the vortex streets. Consequently, S-II changes to T-I and T-I changes to T-II.

## 4 Conclusions

The wake of two staggered cylinders is measured using two hotwires, with $\alpha = 0^o$–$90^o$, $P^* = 1.2$–$6.0$. The hotwire measurement grid at Re $= 7.0 \times 10^3$ was refined, compared to Hu and Zhou (2008). While the present flow classification is qualitatively in agreement with previous report by Hu and Zhou (2008), there is a departure in the border between different flow modes, which is partially ascribed to the different definitions of the border between different flow modes and partially the presently refined measurement grids, and hence an improved resolution in determining the flow mode. It has been found that the transition from one flow mode to another or the border of the flow regime in the $P^* - \alpha$ plane depends appreciably on the Re. From Re $= 1.5 \times 10^3$ to $7.0 \times 10^3$, the border varies appreciably in three regions. In region I, that is from S-II to S-I, the larger Re changes the path of the inner shear layer, separated from the upstream cylinder, from passing through the gap to reattaching on the downstream cylinder because of

the increased separation angle and separation between shear layers. In region II, the increased Re makes the boundary layer around the cylinders thinner and the vortex formation length shorter, contributing to a greater momentum through the gap and accounting for the flow structure change from S-II to T-I. The change from T-I to S-II in region III results from the reduced gap flow width and larger gap-flow deflection, due to a shift in flow separation toward the forward stagnation point and an increased separation angle. As $Re$ varies from $7.0 \times 10^3$ to $2.0 \times 10^4$, it has been found that the border of the flow regime varies again in three regions of the $P^*$-$\alpha$ plane. A reduced vortex formation length with increasing Re is responsible for the change from S-II to S-I in region I; though the changes from S-II to T-I in region II and from T-I to T-II in region III are ascribed to the thinner boundary layers over both cylinders, a greater streamwise momentum and less deflection of the gap flow.

**Acknowledgments** YZ wishes to acknowledge support given to him from Natural Science Foundation of China through grants 11172085 and 50930007.

## References

Hu JC, Zhou Y (2008) Flow structure behind two staggered circular cylinders, part 1. Downstream evolution and classification. J Fluid Mech 607:51–80

Sumner D (2010) Two circular cylinders in cross flow: a review. J Fluids Struct 26:849–899

Zdravkovich MM (1997) Flow around Circular Cylinders: Fundamentals, vol 1. Oxford Science, New York

# Simultaneously Measured Vorticity and Passive Heat in a Cylinder Wake

**H. Cao, T. Zhou, Y. Zhou and H. Zhang**

**Abstract** This work is an experimental study of the turbulent vortex structures and heat transport in the intermediate wake of a slightly heated cylinder. The three components of the vorticity vector were measured simultaneously with the fluctuating temperature at nominally the same point over $x/d = 10$–$40$ using a 3D vorticity probe and four cold wires. By using phase-averaging analysis, the contribution of coherent motion of various vorticity correlations such as vorticity-passive heat, as well as the velocity–vorticity correlations has been discussed, in conjunction with Reynolds shear stress and heat fluxes. The results indicate that coherent motion contributes significantly to the heat transport within the vortices while the incoherent motion mainly contributes between two vortices. The vorticity–velocity correlation involving spanwise vorticity component mainly contributes to the gradient of Reynolds shear stress.

**Keywords** Turbulent wake · Vorticity–velocity correlation · Phase-average

## 1 Introduction

The flow around a circular cylinder is one of the classical subjects due to its importance in engineering, and it has attracted a great deal of attention in the last few decades. Matsumura and Antonia (1993) presented two-dimensional vorticity field and momentum and heat transport in the intermediate wake of a cylinder.

H. Cao · T. Zhou (✉) · Y. Zhou · H. Zhang
Shenzhen Graduate school, Harbin Institute of Technology, Shenzhen, China
e-mail: tongming.zhou@uwa.edu.au

H. Zhang
School of Measurement Technology and Engineering, China Jiliang University, Hangzhou, China

Y. Zhou et al. (eds.), *Fluid-Structure-Sound Interactions and Control*,
Lecture Notes in Mechanical Engineering, DOI: 10.1007/978-3-642-40371-2_28,

Zhou et al. (2003) obtained three vorticity components using a multi-hot-wire vorticity probe. Zhou et al. (2002b) presented coherent and incoherent momentum and heat fluxes in a turbulent wake of two side-by-side cylinders, using a three-wire probe. One interesting question to be asked is how vorticity components would transport by the fluctuating velocity field? The objective of this work is to investigate the correlations between three components of vorticity and velocity, as well as temperature fluctuations, based on three vorticity components which are simultaneously measured.

## 2 Experimental Details

The experiments were conducted in a closed-loop wind tunnel with a working section of 1.2 m ($W$) × 0.8 m ($H$) and 2 m long at Nanyang Technological University. The free stream across the tunnel is uniform to within 0.5 %. The free stream turbulence intensity is less than 0.5 %. A circular cylinder with a diameter of $d = 12.7$ mm was used to generate the wake. The free stream velocity $U_\infty$ was 3 m/s, corresponding to a Reynolds number Re ($\equiv U_\infty d/v$) of 2,540. The measurement locations were at $x/d = 10$, 20, and 40 (where $x$ is the streamwise distance from the cylinder), and only the results of $x/d = 10$ are presented here. A probe consisting of four X-wires similar in design with that used by Zhou et al. (2002a) was used to measure the three vorticity components simultaneously. Four cold wires were arranged about 1 mm upstream of the four X-wires (or the 3D vorticity probe) to measure the temperature fluctuations at four locations. With these temperature signals, all three temperature gradients involved in the temperature dissipation rate are measured simultaneously with the vorticity signals. Another X-probe located at the edge of the wake was used to provide a phase reference for the measured vorticity signals. The phase-averaged method is similar to that used by Zhou et al. (2002b), and a total of 1,475 periods were used for the phase averaging.

## 3 Results and Discussion

### *3.1 Phase-Averaged Vorticity Field*

The phase-averaged contours of the three vorticity components $\left(\tilde{\omega}_x^*, \tilde{\omega}_y^* \text{and} \tilde{\omega}_z^*\right)$ and temperature $(\tilde{\theta}^*)$ are similar to that reported by Zhou et al. (2002b, 2003) and not shown here. Here an asterisk denotes normalization by $U_\infty$, $d$, and $T_0$ (where $T_0$ is the maximum temperature excess). The coherent contribution to three vorticity variances is also calculated (not shown), and the distribution of $\overline{\tilde{\omega}_z^2}/\overline{\omega_z^2}$ shows

good agreement with Yiu et al. (2004), where a single overbar denotes time averaging and a double overbar denotes structural averaging.

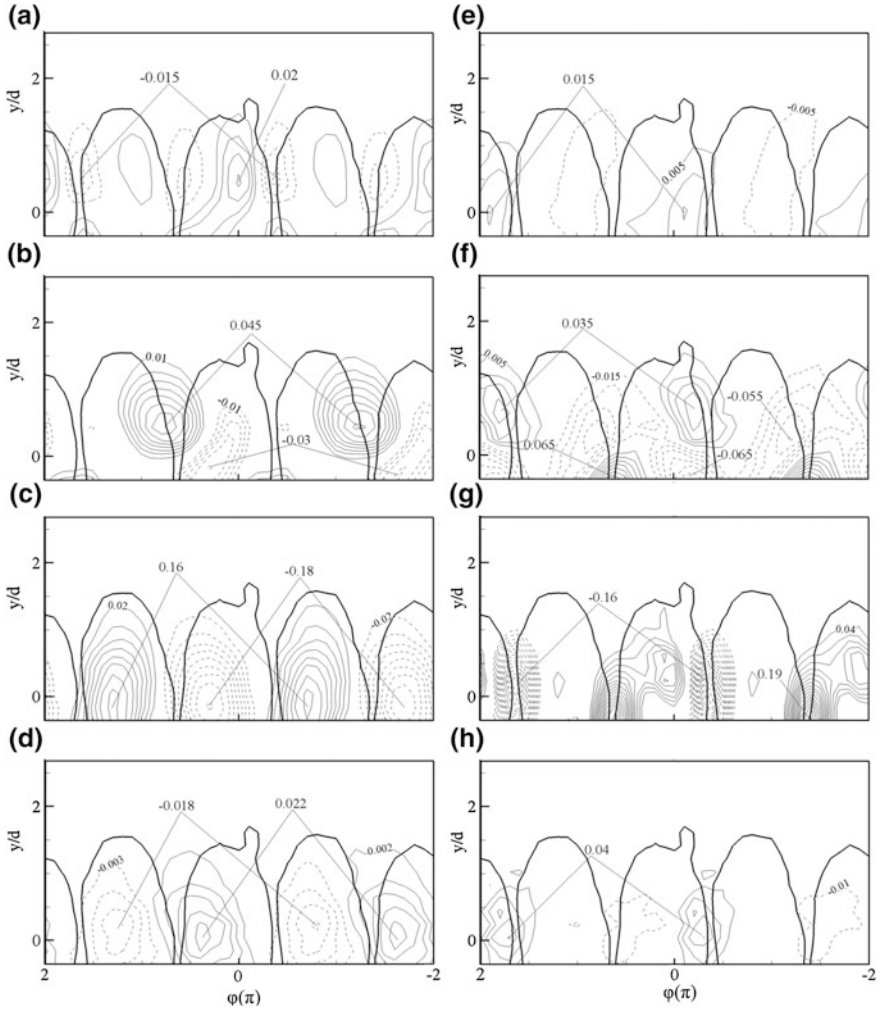


**Fig. 1** Phase-averaged coherent shear stress $\tilde{u}^*\tilde{v}^*$ (**a**), and heat fluxes $\left(\tilde{u}^*\tilde{\theta}^*, \tilde{v}^*\tilde{\theta}^*, \tilde{w}^*\tilde{\theta}^*\right)$ (**b–d**); incoherent shear stress $\langle u_r^* v_r^* \rangle$ (**e**), and incoherent heat fluxes $\left(\langle u_r^*\theta_r^* \rangle, \langle v_r^*\theta_r^* \rangle, \langle w_r^*\theta_r^* \rangle\right)$ (**f–h**). Contour interval = 0.005 for (**a**), (**b**) and (**d**); contour interval = 0.02 for (**c**); contour interval = 0.005 for (**e**); contour interval = 0.01 for (**f**)–(**h**). The *thicker solid line* denotes the outmost vorticity $\tilde{\omega}_z^*$ contour

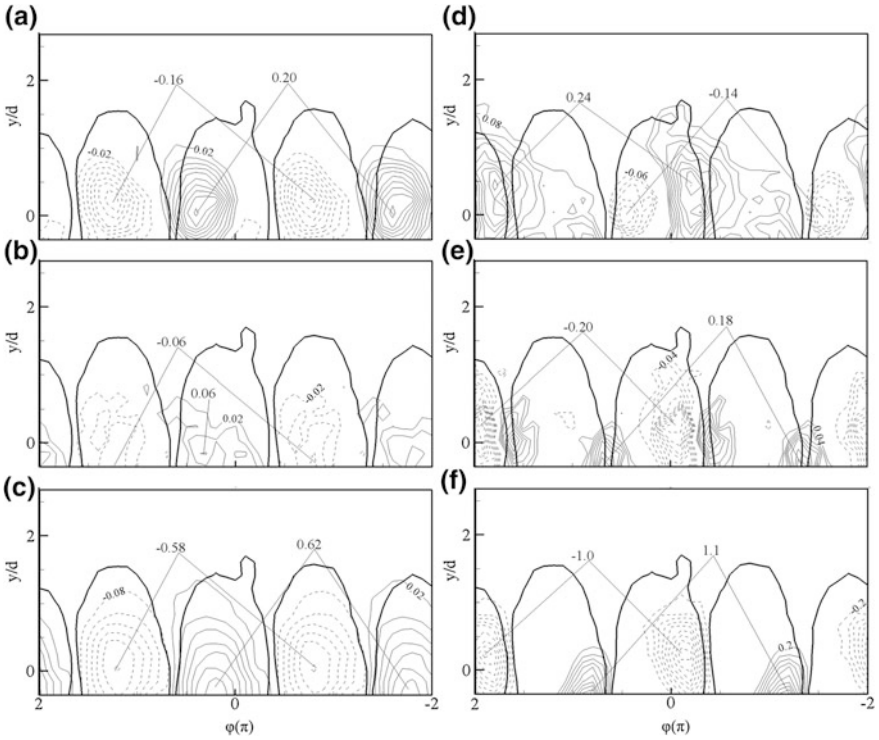


**Fig. 2** Phase averaged coherent $\left(\tilde{\omega}_x^*\tilde{\theta}^*, \tilde{\omega}_y^*\tilde{\theta}^*, \tilde{\omega}_z^*\tilde{\theta}^*\right)$ (**a–c**) and incoherent vorticity-heat correlation $\left(\langle\omega_{xr}^*\theta_r^*\rangle, \langle\omega_{yr}^*\theta_r^*\rangle, \langle\omega_{zr}^*\theta_r^*\rangle\right)$ (**d–f**). Contour interval = 0.02 for (**a**), (**b**), (**d**) and (**e**); contour interval = 0.1 for (**c**) and (**f**). The *thicker solid line* denotes the outmost vorticity $\tilde{\omega}_z^*$ contour

## 3.2 Phase-Averaged Reynolds Stress and Heat Fluxes

Figure 1 presents the coherent and incoherent Reynolds shear stress and heat fluxes. The $\tilde{u}^*\tilde{v}^*$ (Fig. 1a) positive and negative contours occur in pairs and are similar to that reported by Zhou et al. (2002b). The peak contour value of $\tilde{u}^*\tilde{v}^*$ is about an order smaller than that of $\tilde{v}^*\tilde{\theta}^*$. The $\tilde{v}^*\tilde{\theta}^*$ contours (Fig. 1c) alternate in sign but their size and magnitude are nearly the same, and the extrema of $\tilde{v}^*\tilde{\theta}^*$ occurs near the centerline while the extrema of $\tilde{u}^*\tilde{\theta}^*$ (Fig. 1b) moves away from the centerline and occurs between the neighboring vortices. There is a close similarity between $\tilde{v}^*\tilde{\theta}^*$ (Fig. 1c) and $\tilde{w}^*\tilde{\theta}^*$ (Fig. 1d), while the latter one has much smaller values and a change of sign. It also can be seen that the maximum incoherent heat fluxes $\langle v_r^*\theta_r^*\rangle$ (Fig. 1g) is quite comparable to that of the coherent

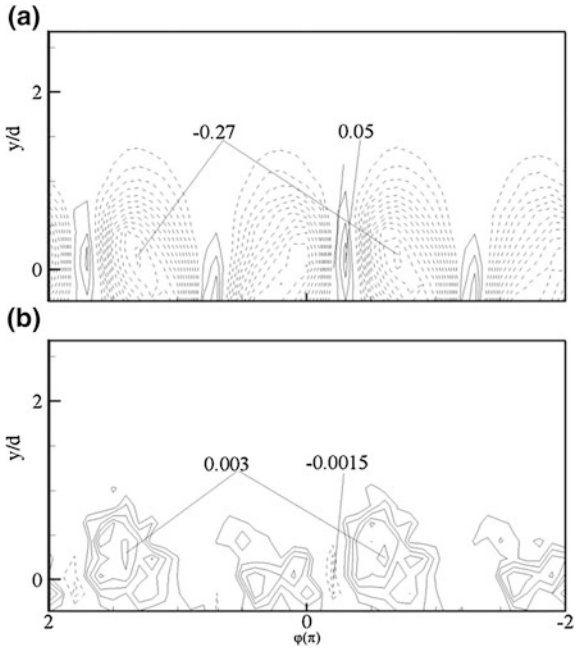


**Fig. 3** Phase-averaged coherent vorticity–velocity correlation $\widetilde{\omega}_z^*\widetilde{v}^*$ (**a**) and $\widetilde{\omega}_y^*\widetilde{w}^*$ (**b**). Interval for (**a**) = 0.02, for (**b**) = 0.0005

counterpart $\tilde{v}^*\tilde{\theta}^*$ (Fig. 1c), which means both coherent and incoherent motion contribute to the heat transport. However, the extrema of $\langle v_r^*\theta_r^*\rangle$ shifts outside the vortices and occurs in the alleyway between two vortices. It seems that the net heat transport within the vortex is due to the coherent motion, while the incoherent motion contributes to heat transport between two vortices.

### *3.3 Phase-Averaged Correlation Between Vorticity and Passive Heat*

The phase-averaged isocorrelation of vorticity and temperature fluctuations are shown in Fig. 2. It can be seen that $\tilde{\omega}_z^*\tilde{\theta}^*$ (Fig. 2c) is considerably greater in magnitude than that of $\tilde{\omega}_x^*\tilde{\theta}^*$ and $\tilde{\omega}_y^*\tilde{\theta}^*$ (Fig. 2a, b). There is a close similarity between spanwise vorticity (contours are not shown here) and $\tilde{\omega}_z^*\tilde{\theta}^*$, which would imply that the spanwise structures have a strong connection with passive heat and tend to retain heat. However, the longitudinal structures have very weak correlation with temperature fluctuations. Note that all of the incoherent correlations are significantly larger than those coherent counterparts. Further analysis on the correlation between vorticity and temperature dissipation rate will be examined.

### 3.4 Time-Averaging and Phase-Averaged Vorticity–Velocity Correlations

The time-averaging profile of vorticity–velocity correlations $\left(\overline{\omega_z' v'}, \overline{\omega_y' w'}\right)$ are not shown here. As *y/d* increases, $|\overline{\omega_z' v'}|$ decrease significantly, and the trough value occurs at $y/d = 0$, while $|\overline{\omega_y' w'}|$ behaves quite evenly. The phase-averaged contours are shown in Fig. 3. The $|\widetilde{\omega_y^* \widetilde{w}^*}|$ is about two orders of magnitude smaller than $|\widetilde{\omega}_z^* \widetilde{v}^*|$, which indicate that the contribution to the gradient of Reynolds shear stress are dominated by the correlation involving the spanwise vorticity component. Other velocity–vorticity correlations such as $\overline{\omega_z' u'}, \overline{\omega_x' w'}, \overline{\omega_y' u'}$ and $\overline{\omega_x' v'}$ will be further discussed in the future.

## 4 Conclusions

The three components of vorticity were measured simultaneously with the temperature fluctuations in a slightly heated cylinder wake and analyzed using the phase-averaging technique. It has been found that the coherent motion contributes significantly to the heat transport within the vortices while the incoherent motion mainly contributes heat transport between two vortices. The correlation of vorticity–velocity involving spanwise vorticity component mainly contributes to the gradient of Reynolds shear stress.

**Acknowledgments** The support from the Natural Science Foundation of China (11172085) is gratefully acknowledged.

## References

Matsumura M, Antonia RA (1993) Momentum and heat transport in the turbulent intermediate wake of a circular cylinder. J Fluid Mech 250:651–668

Yiu MW, Zhou Y, Zhou T, Cheng L (2004) Reynolds number effects on three-dimensional vorticity in a turbulent wake. AIAA 42(5):1009–1016

Zhou T, Antonia RA, Chua LP (2002a) Performance of a probe for measuring turbulent energy and temperature dissipation rates. Exp Fluids 33:334–345

Zhou Y, Zhang HJ, Yiu MW (2002b) The turbulent wake of two side-by-side circular cylinders. J Fluid Mech 458:303–332

Zhou T, Zhou Y, Yiu MW et al (2003) Three dimensional vorticity in a turbulent cylinder. Exp Fluids 35:459–471

# Turbulent Intensity Effect on Low Reynolds Number Airfoil Wake

**S. Wang, Y. Zhou, M. M. Alam and H. X. Yang**

**Abstract** The work investigates the effect of turbulent intensity ($T_u$) on the force and wake of a NACA0012 airfoil at chord Reynolds number $\mathrm{Re}_c = 5.3 \times 10^3$ and $2 \times 10^4$. Lift and drag coefficients ($C_L$ and $C_D$) on and flow fields around the airfoil were measured with $T_u$ varied from 0.6 to 6.0 %. Four $\mathrm{Re}_c$ regimes are identified based on the characteristics of the maximum lift coefficient ($C_{L,\,\max}$), i.e., ultra-low ($\mathrm{Re}_c < 10^4$), low ($10^4 \sim 3 \times 10^5$), moderate ($3 \times 10^5 \sim 5 \times 10^6$), and high ($> 5 \times 10^6$). It is noted that at $\mathrm{Re}_c = 5.3 \times 10^3$ (ultra-low $\mathrm{Re}_c$ regime) the stall is absent for $T_u = 0.6$ % but occurs for $T_u = 2.6$ and 6.0 %. As $\mathrm{Re}_c$ increases to low $\mathrm{Re}_c$ regimes, the $T_u$ influence decreases. So does the critical $\mathrm{Re}_c$, above which stall occurs. The effect of increasing $T_u$ on flow bears similarity to that of increasing $\mathrm{Re}_c$, albeit with a difference; the flow separation point shifts upstream with increasing $\mathrm{Re}_c$ but downstream with increasing $T_u$.

**Keywords** Low Reynolds number · Turbulence intensity · Lift and drag forces · Airfoil wake

## 1 Introduction

The flow around an airfoil at $\mathrm{Re}_c < 10^5$ is of interest for the design of micro air vehicles and wind turbines (Alam et al. 2010), attracting a surge attention of

S. Wang (✉) · Y. Zhou
Department of Mechanical Engineering, The Hong Kong Polytechnic University, Kowloon, Hong Kong
e-mail: wsv@outlook.com

Y. Zhou · M. M. Alam
Shenzhen Graduate School, Harbin Institute of Technology, Shenzhen, China

H. X. Yang
Department of Building Services Engineering, The Hong Kong Polytechnic University, Kowloon, Hong Kong

Y. Zhou et al. (eds.), *Fluid-Structure-Sound Interactions and Control*,
Lecture Notes in Mechanical Engineering, DOI: 10.1007/978-3-642-40371-2_29,

researchers recently (Akbari and Price 2003; Chen and Choa 1999; Cleaver et al. 2011; Grager et al. 2011; Schlüter 2009; Sunada et al. 2002). It has been previously reported that at $Re_c > 10^4$ the separated shear layer reattaches on the airfoil surface, which enhances the airfoil lift (Carmichael 1981; Huang and Lin 1995). In contrast, at $Re_c < 10^4$ the separated shear layer does not reattach to the airfoil surface, adversely affecting the lift (Alam et al. 2010). Investigations on the aerodynamics of airfoils at $Re_c < 10^4$ are very few (Alam et al. 2010; Sunada et al. 2002). There is also a lack of data in the literature on how the turbulent intensity ($T_u$) of oncoming flow affects the airfoil aerodynamics particularly at $Re_c < 10^4$. The objective of this work was (1) to investigate the effect of $T_u$ on the force and wake of a NACA0012 airfoil at $Re_c = 5.3 \times 10^3$ and $2 \times 10^4$ and (2) to classify the $Re_c$-dependent flow structure based on the maximum lift ($C_{L,\,max}$) and intrinsic features of the shear layer around the airfoil.

## 2 Experimental Details

Experiments were performed in a closed-loop water tunnel, with a test section of 0.3 m (width) × 0.6 m (height) × 2.4 m (length). The water speed in the test section ranges from 0.05 to 4 m/s. A NACA0012 airfoil, with a span length of $s = 0.27$ m and a chord length of $c = 0.1$ m, was used as the test model and mounted horizontally in the test section. A grid placed upstream of the airfoil model was used to generate turbulence in free stream. A variation in $T_u$ from 0.6 to 6.0 % was achieved by changing the distance between the grid and airfoil. While the lift and drag coefficients ($C_L$ and $C_D$) of the airfoil were measured using a load cell, the flow field was estimated using particle image velocimetry. Laser induced fluorescence (LIF) flow visualization was conducted to visualize flow.

## 3 Results and Discussion

### 3.1 *Classification of* $Re_c$ *Regimes*

Figure 1 shows the $C_{L,\,max}$ dependence on $Re_c$, based on a collection of both present and previous measurements, all obtained at $T_u \leq 1$ %. In the absence of stall, $C_{L,\,max}$ is defined as the turning point where the rate of increase in $C_L$ drops appreciably. Interestingly, the data shows four types of the $C_{L,\,max}$ dependence on $Re_c$, referred to as the ultra-low ($Re_c < 10^4$), low ($10^4 \sim 3 \times 10^5$), moderate ($3 \times 10^5 \sim 5 \times 10^6$), and high ($> 5 \times 10^6$) $Re_c$ regimes, each characterized by distinct flow patterns and stall types, which are mostly connected to the shear/boundary layer behaviors. While the shear layer is laminar in the ultra-low $Re_c$ regime, shear layer transition followed by a reattachment occurs in both low and moderate $Re_c$ regimes. The low $Re_c$ regime corresponds to a relatively longer

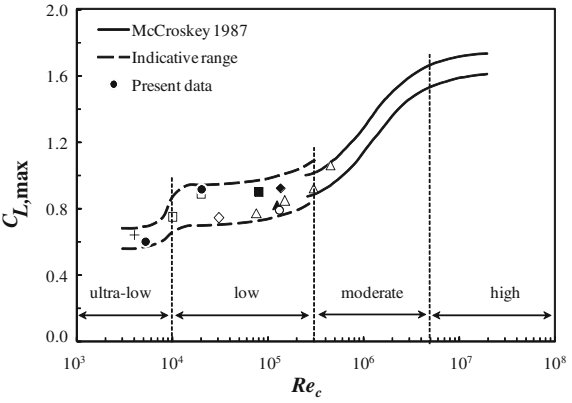


**Fig. 1** Dependence of $C_{L,\max}$ on $\mathrm{Re}_c$ of NACA0012 airfoil [+ Sunada et al. (2002); *black square* Chen and Choa (1999); × Akbari and Price (2003); *lozenge* Schlüter (2009); *square* Cleaver et al. (2011); *circle* Grager et al. (2011); *black lozenge* Lee and Gerontakos (2004); *black triangle* Wong and Kontis (2007); *triangle* Sant and Ayuso (2011)]

separation bubble than the moderate $\mathrm{Re}_c$ regime. The boundary layer transition to turbulence occurs in the high $\mathrm{Re}_c$ regime, where no reattachment occurs. This work is focused on the first two regimes.

## 3.2 $T_u$ Effects on Airfoil Load and Critical $\mathrm{Re}_c$

Figures 2 and 3 present the dependence of $C_D$, $C_L$, and $C_D/C_L$ on $\alpha$ for different $T_u$ levels, respectively. At $\mathrm{Re}_c = 5.3 \times 10^3$ (ultra-low $\mathrm{Re}_c$ regime), the airfoil stall appears absent for $T_u = 0.6$ % but occuring at $\alpha = 12°$ for $T_u = 2.6$ and 6.0 %, resulting in marked changes in $C_L$ and $C_D$ variations, and a considerably improved $C_L/C_D$. The maximum $C_L$ and $C_L/C_D$ at $T_u = 6.0$ % increase by 52 and 45 %, respectively, with respect to those at $T_u = 0.6$ %. At $\mathrm{Re}_c = 2 \times 10^4$ (low $\mathrm{Re}_c$ regime, Fig. 3) the stall occurs for all three $T_u$ levels. When $T_u$ grows from 0.6 to 6.0 %, the maximum $C_L$ rises by 12 %, much less than that at $\mathrm{Re}_c = 5.3 \times 10^3$. The $T_u$ effect on $C_L/C_D$ is, however, less appreciable at $\mathrm{Re}_c = 2.0 \times 10^4$; that is, in the low $\mathrm{Re}_c$ regime, the airfoil performance is less sensitive to a variation in $T_u$. The critical $\mathrm{Re}_c$ ($\mathrm{Re}_{c,\,cr}$), above which the stall occurs, divides the ultra-low and low $\mathrm{Re}_c$ regimes. Figure 4 presents the dependence of $\mathrm{Re}_{c,\,cr}$ on $T_u$ based on a collection of present and previous data (Carmichael 1981; Huang and Lin 1995). $\mathrm{Re}_{c,\,cr}$ drops with increasing $T_u$. This is reasonable because a higher $T_u$ is required to promote transition in the shear layer at a smaller $\mathrm{Re}_c$.

## 3.3 Flow Field

LIF flow visualization photographs (Fig. 5) reveal that the increased $T_u$ results in an earlier occurrence of transition in the shear layer, which triggers a shear layer reattachment and the formation of a laminar separation bubble, which accounts for

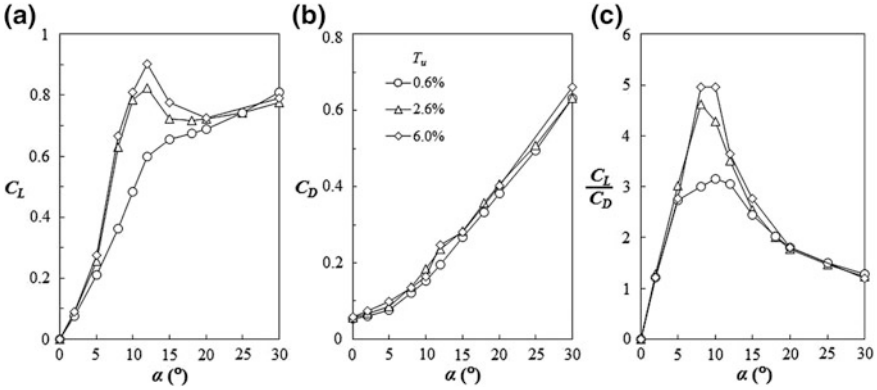


**Fig. 2** Dependence on α (the angle of attack) of $C_L$ (**a**), $C_D$ (**b**) and $C_L/C_D$ (**c**) at different $T_u$. $\mathrm{Re}_c = 5.3 \times 10^3$

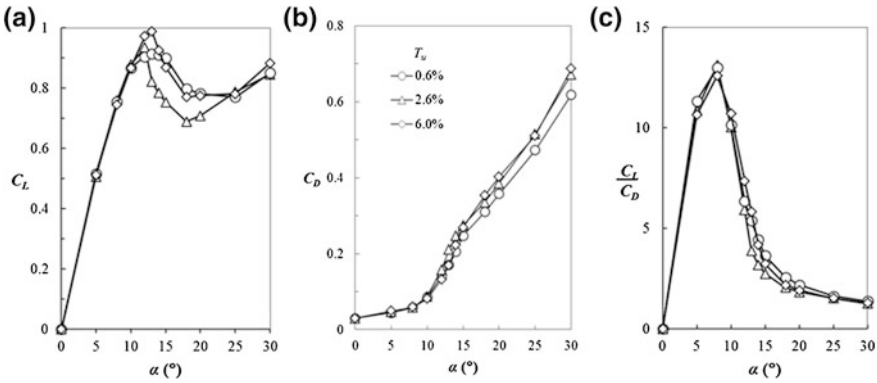


**Fig. 3** Dependence on α of $C_L$ (**a**), $C_D$ (**b**) and $C_L/C_D$ (**c**) at different $T_u$. $\mathrm{Re}_c = 2.0 \times 10^4$

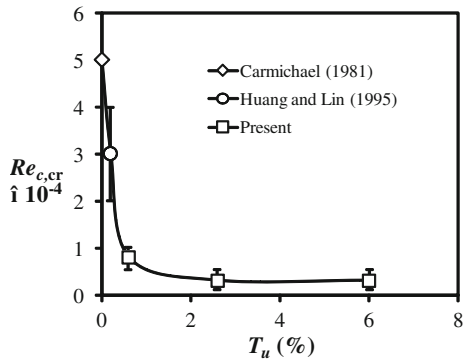


**Fig. 4** Dependence on $T_u$ of the critical Reynolds number $\mathrm{Re}_{c,\ cr}$

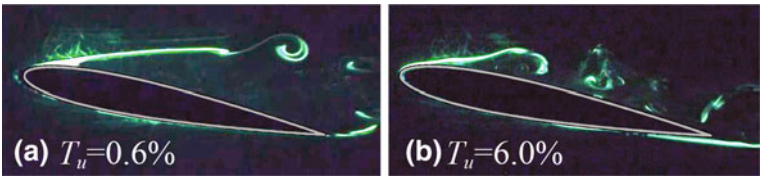


**Fig. 5** Typical photographs captured in LIF flow visualization at $\alpha = 10°$. $\mathrm{Re}_c = 5.3 \times 10^3$

the improved lift (Fig. 2). The separation bubble bursts when $\alpha$ exceeds the stall angle, corresponding to the maximum $C_L$ in Fig. 2. Figure 6 presents a comparison between the effects of increasing $\mathrm{Re}_c$ and $T_u$ on the separation point at $\alpha = 5°$, with the LIF visualization snapshots (left column) and the contours of the PIV measured time-averaged streamwise velocity $\overline{U}^*$ (right column), where asterisk denotes normalization by free stream velocity and/or $c$. As indicated in the snapshots, flow separation is postponed from 0.23 (Fig. 6c) to 0.45$c$, measured from the leading edge (Fig. 6a), as $T_u$ varies from 0.6 to 6.0 %; on the other hand, flow separation is advanced to 0.18$c$ (Fig. 6e) from $\mathrm{Re}_c = 5.3 \times 10^3$ to $2.0 \times 10^4$. The observation is confirmed by the $\overline{U}^*$ contours. For given $\mathrm{Re}_c$ and $T_u$, the flow separation point identified from the LIF image (instantaneous flow) may deviate slightly from that of the $\overline{U}^*$ contours (mean flow) because of the oscillating nature of the separation point with time.

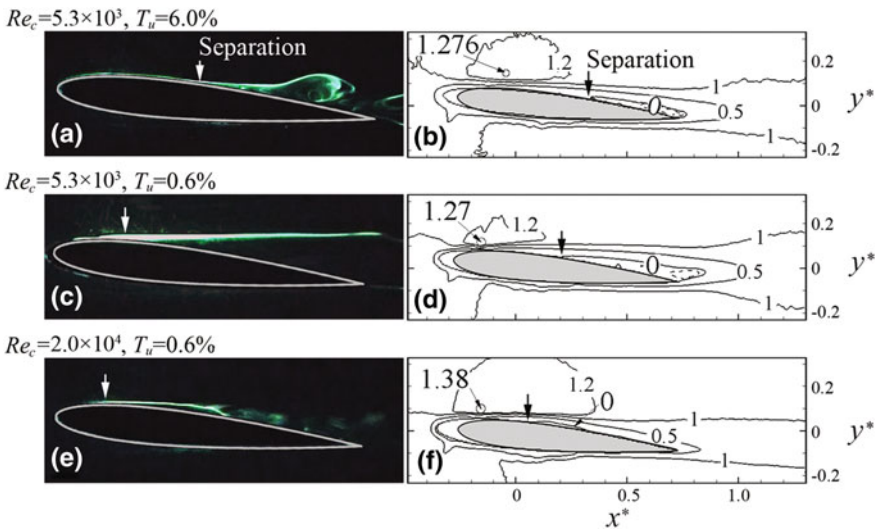


**Fig. 6** The effect of $\mathrm{Re}_c$ and $T_u$ on the separation point at $\alpha = 5°$. *Left column*, LIF visualization photographs; *right column*, time-mean streamwise velocity $\overline{U}^*$ contours

## 4 Conclusions

The work leads to following conclusions.

1. Four $Re_c$ regimes, i.e., ultra-low, low, moderate, and high $Re_c$, are proposed on the basis of $C_{L,\,\max}$ and boundary/shear layer characteristics.
2. A remarkable influence of $T_u$ is observed at $Re_c = 5.3 \times 10^3$ (ultra-low $Re_c$), increasing $C_L$ and $C_L/C_D$ by 52 and 45 %, respectively, when $T_u$ grows from 0.6 to 6.0 %. Stall does not occur at $T_u = 0.6$ % but does at $T_u = 2.6$ and 6.0 %.
3. The influence of $T_u$ wanes with increasing $Re_c$, and the critical $Re_c$ that divides the ultra-low and low $Re_c$ regimes decreases with increasing $T_u$.
4. The effect of increasing $T_u$ on flow bears similarity to that of increasing $Re_c$, albeit with a difference. While the increased $T_u$ delays the boundary layer separation due to the enhanced mixing ability, the increased $Re_c$ does the opposite, promoting flow separation.

**Acknowledgments** YZ wishes to acknowledge support given to him from Research Grants Council of HKSAR through grant B-Q33J.

## References

Akbari M, Price S (2003) Simulation of dynamic stall for a NACA 0012 airfoil using a vortex method. J Fluid Struct 17(6):855–874

Alam MM, Zhou Y, Yang HX, Guo H, Mi J (2010) The ultra-low Reynolds number airfoil wake. Exp Fluids 48(1):81–103

Carmichael B (1981) Low Reynolds number airfoil survey. NASA CR-165803

Chen JM, Choa C-C (1999) Freestream disturbance effects on an airfoil pitching at constant rate. J Aircraft 36(3):507–514

Cleaver DJ, Wang Z, Gursul I, Visbal MR (2011) Lift enhancement by means of small-amplitude airfoil oscillations at low Reynolds numbers. AIAA J 49(9):2018–2033

Grager T, Rothmayer A, Hu H (2011) Stall suppression of a low-Reynolds-number airfoil with a dynamic burst control plate. In: Proceedings of 49th AIAA aerospace sciences meeting including the New Horizons forum and aerospace exposition, 04 Jan, Orlando, Florida

Huang RF, Lin CL (1995) Vortex shedding and shear-layer instability of wing at low-Reynolds numbers. AIAA J 33(8):1398–1403

Lee T, Gerontakos P (2004) Investigation of flow over an oscillating airfoil. J Fluid Mech 512:313–341

Sant R, Ayuso L (2011) Aerodynamic study of airfoils geometric imperfections at low Reynolds number. In: Proceedings of 13th international conference on wind engineering, 10–15 Jul, Amsterdam, The Netherlands

Schlüter JU (2009) Lift enhancement at low Reynolds numbers using pop-up feathers. In: Proceedings of 39th AIAA fluid dynamics conference, 25 June, San Antonio, Texas

Sunada S, Kawachi K, Yasuda K, Yasuda T (2002) Comparison of wing characteristics at an ultralow Reynolds number. J Aircraft 39(2):331–338

Wong C, Kontis K (2007) Flow control by spanwise blowing on a NACA 0012. J Aircraft 44(1):338–341

# Part II
# Acoustics and Flow-Sound Interaction

# Temporal and Spectral Quantification of the 'Crackle' Component in Supersonic Jet Noise

**Woutijn J. Baars and Charles E. Tinney**

**Abstract** Measurements of the pressure waveforms along a grid in the far-field of an unheated Mach 3 jet were conducted in order to study crackle. A detection algorithm is introduced which isolates the shock-type structures in the temporal waveform that are responsible for crackle. Ensemble averages of the structures reveal symmetric shocks at shallow angles, while they appear to be asymmetric near the Mach wave angle. Spectral quantification is achieved through time–frequency analyses and shows that crackle causes the expected high-frequency energy gain. The increase in energy due to crackle is proposed as a more reliable metric for the perception of crackle, as opposed to the Skewness of the pressure or pressure derivative.

## 1 Introduction

There is practical interest in suppressing *crackle* as it is responsible for the excessive sound power that personnel, working in close proximity to aviation operations, are exposed to. This work aims to quantify crackle in a temporal and spectral sense, which is necessary for a systematic approach in noise reduction. The current experimental campaign, on an unheated shock-free Mach 3 jet, comprises turbulent mixing noise which consists of two components. The first is emitted by large-scale turbulence convection in the jet. These structures radiate Mach waves in a cone with half angle $\phi = \cos^{-1}(a_\infty/U_c)$, as measured from the

W. J. Baars (✉) · C. E. Tinney
Department of Aerospace Engineering and Engineering Mechanics, The University of Texas at Austin, 210 E. 24th Street, Austin, TX 78705, USA
e-mail: baars@utexas.edu

C. E. Tinney
e-mail: cetinney@utexas.edu

Y. Zhou et al. (eds.), *Fluid-Structure-Sound Interactions and Control*,
Lecture Notes in Mechanical Engineering, DOI: 10.1007/978-3-642-40371-2_30,

jet axis; $U_c$ is the convective speed of the most energetic instability waves. The second component is associated with fine-scale turbulence, which causes an omni-directional sound pattern.

In general, nonlinear acoustic phenomena are a prerequisite to understand the noise that radiates to the far-field from jets with a supersonic convective acoustic Mach number. The topic of nonlinear acoustics governs all forms of acoustic waveform distortion in progressive waves, beyond the change in amplitude from spherical spreading ($p \propto 1/r$). Two types of nonlinear effects—local and cumulative—can affect the waveform shape and create steep waveform gradients (Hamilton and Blackstock 2008); a review in the context of jet noise can be found in the dissertation by (Baars 2013). The simplest example of *cumulative* distortion—more pronounced with distance—is a sinusoid that gradually evolves into an *N*-wave when progressing through a lossless fluid. Conversely, *local* nonlinear distortions are instantaneous effects, such as a displacement of the source. When observing the pressure waveforms in laboratory-scale jet studies, shock-type structures (Fig. 1) are often ascribed to cumulative steepening. While this might be the case in full-scale jet noise (Gee et al. 2007), it was recently shown that it is nearly impossible to measure these cumulative effects in range-restricted environments using laboratory-scale nozzles (Baars 2013).

The shock-type waveform structures, which are responsible for *crackle*, are thus the result of *local* nonlinear phenomena. When (Ffowcs Williams et al. 1975) investigated crackle, emitted by a static full-scale engine, they formulated it as *spasmodic bursts of a rasping fricative sound*. They stated that the crackle signatures are formed in the near vicinity of, or within, the turbulent jet. This statement seems to be adapted by most researchers and the current work supports this hypothesis. One of the major challenges in studying crackle are the issues of perception (Gee et al. 2007). Various observers may perceive a waveform as crackle-free, while others do not. Furthermore, there is no unique measure of crackle, i.e. only a few metrics have been applied to jet data in an attempt to assess its presence. The Skewness of the pressure's PDF was used to establish a criterion (Ffowcs Williams et al. 1975), which has a shortcoming in the sense that the rise times of the compressive waveform parts are omitted. Henceforth, the perception of crackle may be better quantified with statistics of the pressure derivative, as was

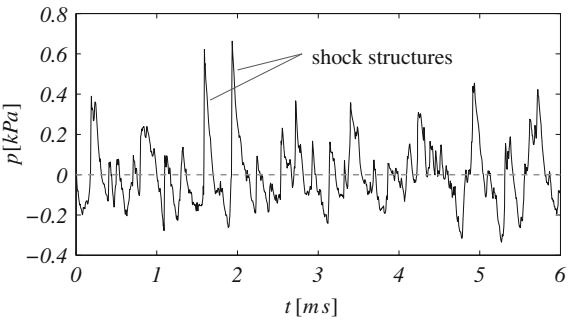


**Fig. 1** Temporal pressure waveform of far-field jet noise indicating shock-type intermittent events that are responsible for producing crackle

noticed by (McInerny 1996, Gee et al. 2007). This article presents a new unique measure associated with the crackle structures, based on time-preserving analyses techniques, in particular, wavelet transforms.

## 2 Experimental Campaign

The experiments were conducted in the fully anechoic jet facility of The University of Texas at Austin, as shown in Fig. 2 (Baars 2013). The jet under investigation comprises a Method of Characteristics contour with an exit gas dynamic Mach number of $M_e = 3.00$ and an exit diameter of 1 in (25.4 mm). The nozzle was operated at perfectly expanded conditions with an unheated flow ($T_0 = 288.2\,\mathrm{K}$). The convective Mach number was computed to be $M_c = U_c/a_\infty = 1.43$ and results in a Mach angle of $\phi = 45.6^\circ$ (Baars 2013). Acoustic waveforms were acquired at a rate of 102.4 kS/s using four 1/4 in pressure-field microphones (PCB 377B10) on a translatable beam. The array was used to measure (non-synchronized) pressure waveforms on an ($x$, $r$)-grid, spanning from 5 $D_j$ to 145 $D_j$ in the axial direction and from 25 $D_j$ to 95 $D_j$ in the radial direction with a uniform spacing of 10 $D_j$ (Fig. 2b).

## 3 Quantifying Crackle

To quantify crackle in a time-preserving fashion, a Shock Detection Algorithm (SDA) is applied to identify temporal instances of sharp pressure rises in the broadband jet noise pressure waveforms. A raw waveform, $p(t)$, is shown in Fig. 3a.

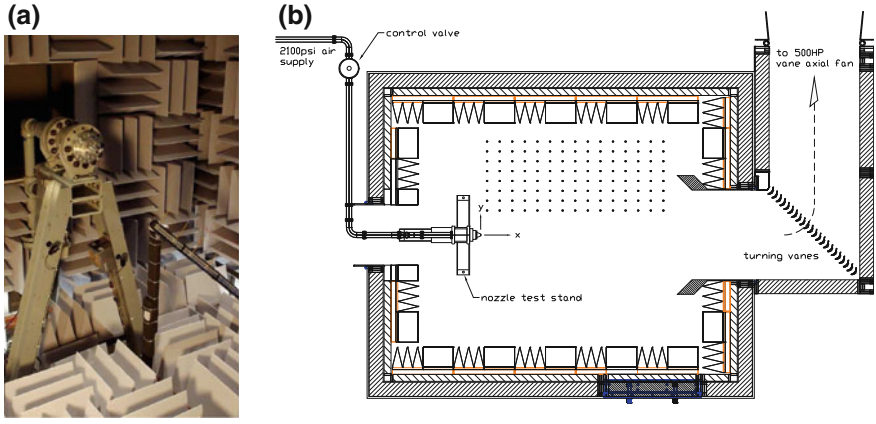


**Fig. 2** **a** The Mach 3 nozzle assembly and translatable microphone array. **b** Facility plan-view with an indication of the ($x$,$r$)-grid measurement positions (○)

The SDA finds all peaks of the pressure derivative $\dot{p}(t)$ exceeding a threshold of $T = 3 \times 10^{-6}\,\sigma/(6\mathrm{d}t)$ [kPa/ms]; $\sigma$ is the pressure standard deviation and d$t$ is the discrete time-step of $10^{-5}$ s. Subsequently, shocks in which the pressure jump does not exceed an amplitude of $A = 2.7\sigma$ [Pa] are omitted. The two thresholds are based on an effective acoustic shock thickness of $\Delta x_s = 10^{-6} a_\infty A/T = 0.0185$ m. The instances when structures were identified are marked at the top of Fig. 3a. To reveal the temporal waveform structure of crackle, an ensemble-average of all shocks is performed in a local time-frame (shock fronts aligned at $\tau = 0$) at each grid location. Fig. 4 presents the signatures at three locations. In general, shocks are point-symmetric around $\tau = 0$ at shallow angles, while they are less

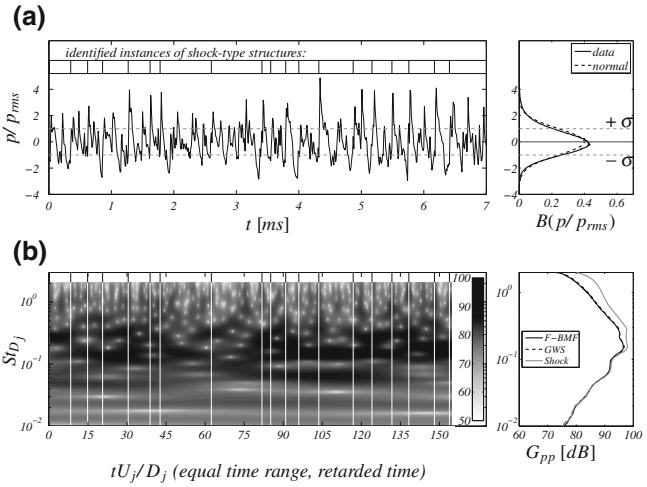


**Fig. 3** **a** Pressure waveform at location $B$ (see Fig. 6a) and the associated PDF. **b** WPS of the pressure signal and the GWS and shock spectrum

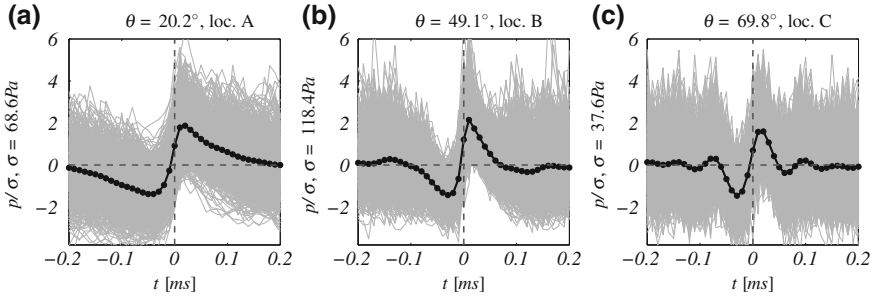


**Fig. 4** Ensemble-averages (*black* –) of the individual shock structures (*grey* –) at three locations in the measurement grid (see Fig. 6a for a mapping). Around 6, 28, and 13 k ensemble-averages were taken at locations **a** $\theta = 20.2°$, loc. $A$, **b** $\theta = 49.1°$, loc. $B$, **c** $\theta = 69.8°$, loc. $C$, respectively

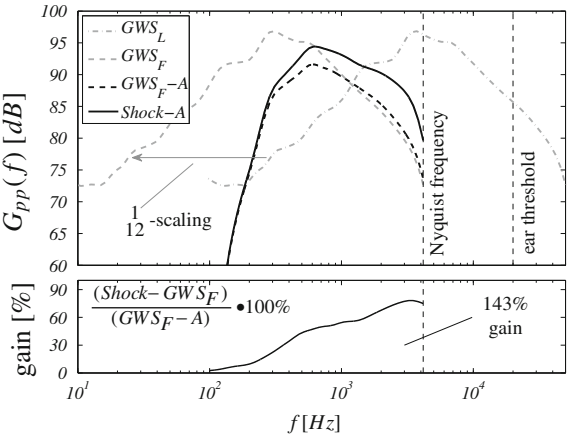


**Fig. 5** The laboratory-scale spectrum at grid location $B$ (subscript $L$) is scaled down to a full-scale scenario (subscript $F$). Adjacent, the $A$-weighting is applied to the spectrum, and the shock spectrum is presented (*solid black* –). The percentage gain (from *dashed to solid black*) is shown at the *bottom*

point-symmetric near the Mach wave angle. A contour of the average number of shocks per second is shown in Fig. 6a. The contours follow spherically spreading lines emanating from the end of the potential core (Baars 2013) and shows the absence of shock coalescence.

The continuous Morlet wavelet transform was applied to extract the energy content as function of time and frequency; the Wavelet Power Spectrum (WPS) is shown in Fig. 3b, for the signal shown in Fig. 3a. With these results, the SDA was verified, since at the instances of shocks (white –), the spectral content is broad-band, with an expected high-frequency energy gain associated with the sharp compressive parts in the waveforms. The principle of extracting a measure of the energy increase in the signal due to the presence of these crackle signatures is presented in Fig. 5.

The consequence of the laboratory-scale data is that high-frequency energy appears above the upper bound of the human ear (20 kHz). Therefore, the

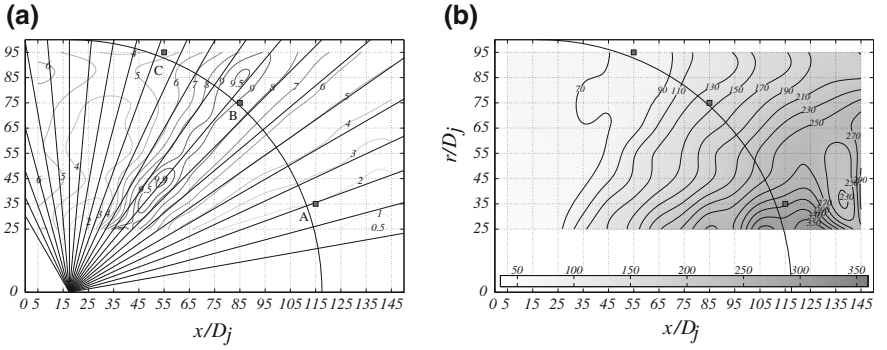


**Fig. 6** **a** Contours of the average number of shocks/s (normalized by 1,835/s at $(x, r)/D_j = (55, 45)$, and $\times$ 10). **b** The crackle gain in percentage

frequency is scaled down (FfowcsWilliams et al. 1975) by a factor of $\approx 12$ to replicate the perception of a full-scale scenario with the following conditions: $D_j = 24$ in, $M_j = 1.5$ and $T_j = 1,500$ K (constant Strouhal # scaling). *A*-weighting is then applied to account for the relative sound energy perceived by the human ear (Fig. 5).

The spectral content of the crackle structures is obtained by an ensemble-average of the local wavelet spectra at the instances provided by the SDA (white lines in Fig. 3b). The obtained spectrum is denoted as the *shock* spectrum (see Figs. 5 and 3b). The energy increase due to crackle is measured as the energy gain from the $GWS_F$ - A spectrum (scaled and *A*-weighted; computed from the complete signal) to the shock spectrum (143 % for location *B*). Fig. 6b shows the gain for the entire grid. From the crackle gain contour it is observed that the shock gain is independent of the distance travelled by the sound. More importantly, this measure seems to be an appropriate metric for the perception of crackle, as is concluded from blind jury trials performed at UT Austin. The crackle is perceived dominantly at shallow angles and becomes gradually less pronounced at larger angles.

**Acknowledgments** The authors gratefully acknowledge the support of the AFOSR (grant FA9550-11-1-0203) and the ONR (award N00014-11-1-0752).

## References

Baars WJ (2013) Aeroacoustics from high-speed jets with crackle. Ph.D. thesis. The University of Texas at Austin, Austin, TX

Ffowcs Williams JE, Simson J, Virchis VJ (1975) 'Crackle': an annoying component of jet noise. J Fluid Mech 71:251–271

Gee KL, Sparrow VW, Atchley A, Gabrielson TB (2007) On the perception of crackle in high amplitude jet noise. AIAA J 45(3):593–598

Hamilton MF, Blackstock DT (2008) Nonlinear acoustics. Acoustical Society of America, Melville, NY

McInerny SA (1996) Launch vehicle acoustics part 2: statistics of the time domain data. J Aircraft 33(3):518–523

# Sound Generated by a Wing with a Flap Interacting with a Passing Vortex

**A. Manela and L. Huang**

**Abstract** We study the acoustic signature of a rigid wing, equipped with a movable downstream flap and interacting with a line vortex, in a two-dimensional low-Mach number flow. The flap is attached to the airfoil via a torsion spring, and the coupled nonlinear fluid–structure interaction problem is analyzed using thin-airfoil methodology and the Brown and Michael equation. Passage of the incident vortex above the airfoil initiates flap oscillations at the system natural frequency, amplified over all other frequencies excited by the vortex. Far-field sound radiation is analyzed, yielding the leading order dipole-type signature of the system. The acoustic radiation is dominated by vortex sound, consisting of relatively strong leading and trailing edge interactions of the airfoil with the incident vortex, together with late-time wake sound resulting from induced flap oscillations. In comparison with counterpart rigid (non-flapped) configuration, we find that the flap may act as sound amplifier or absorber, depending on the value of flap-fluid natural frequency.

## 1 Background and Problem Formulation

Airframe noise, and in particular sound generated by high-lift devices, is known to be a major cause for acoustic radiation, particularly during airplanes approach for landing (Smith 1989). Significant efforts have therefore been made to analyze the sound generated by such devices, in various setups and flight conditions. Common

A. Manela (✉)
Faculty of Aerospace Engineering, Technion, Haifa 32000, Israel
e-mail: amanela@technion.ac.il

L. Huang
Laboratory of Aerodynamics and Acoustics, HKU Zhejiang Institute of Research and Innovation, Department of Mechanical Engineering, The University of Hong Kong, Hong Kong SAR, China
e-mail: lixi@hku.hk

Y. Zhou et al. (eds.), *Fluid-Structure-Sound Interactions and Control*,
Lecture Notes in Mechanical Engineering, DOI: 10.1007/978-3-642-40371-2_31,

to almost all of these works is a *static* configuration of a *detached* lift device, where the acoustic field is affected mainly by vortex shedding and flow separation phenomena occurring at the gap between the airfoil and the flap (Howe 1982; Guo 2001; Zheng et al. 2010). Motivated by recent investigations of continuous "mold-line link" flap configurations (Hutcheson et al. 2011), the objective of the this study is to consider an *attached-flap* configuration and examine the effect of flap *motion* on its acoustic radiation.

A schematic of the problem is given in Fig. 1. We consider a two-dimensional airfoil of chord $2a$ consisting of a stationary upstream part, aligned with the $x_1$ -axis, and attached to a flap at $x_1 = \bar{\eta}a$ (with $0 < \bar{\eta} < 1$). The flap is hinged to the airfoil through a torsion spring of constant $k_\theta$, and the system is subject to low-Mach high-Reynolds number flow of mean density $\rho_0$ and speed $U$ in the $x_1$-direction. An incident line vortex of strength $\Gamma$ is released into the flow at a given location, and moves past the airfoil-flap system. Fluid vorticity is assumed concentrated at the incident vortex location and along a trailing edge wake, with the latter discretized and modeled using the Brown and Michael equation (Howe 1996). The near-field flow is treated by means of potential thin-airfoil methodology, while the far-field sound is analysed using Powell-Howe acoustic analogy (Howe 2003).

To obtain a nondimensional problem, the length, velocity, time, and pressure are scaled by $a, U, a/U$ and $\rho_0 U^2$, respectively. The initial-value problem coupling between flap motion and near-field flow then consists of an angular equation of motion for the flap angle $q$ together with equations for the incident and trailing edge vortices dynamics. These are supplemented by a no-penetration condition on the airfoil, an unsteady Kutta condition ensuring finite fluid velocity at the trailing edge, and initial conditions specifying the system state at time $t = 0$. Omitting the presentation of full problem for brevity, we note the scaled form of the flap equation of motion for later reference,

$$\frac{\mathrm{d}^2\theta}{\mathrm{d}t^2} + \omega^2\theta = \beta \int_{\eta}^{1} \Delta p(x_1, t)(x_1 - \eta)\mathrm{d}x_1, \tag{1}$$

where $\Delta p(x_1, t)$ marks the pressure jump across the airfoil owing to fluid loading, and is calculated via Bernoulli equation. Equation (1) is governed by the parameters $\eta, \omega = \sqrt{k_\theta a^2}/\sqrt{I_f U^2}$ and $\beta = \rho_0 a^4/I_f$, with the latter two denoting the

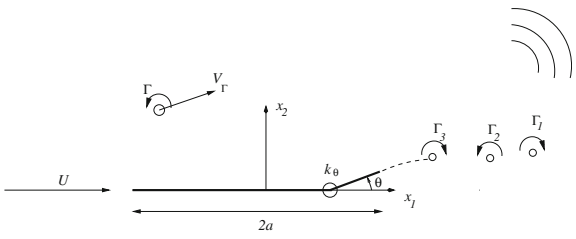


**Fig. 1** Schematic of the problem

*system natural frequency* and *fluid-loading number,* respectively, and $I_f$ marking the flap moment of inertia about its hinge. In addition, the problem is governed by $\gamma = \Gamma/2\pi aU$ and $\boldsymbol{x}_\gamma(0)$, specifying the scaled incident vortex circulation and initial location, respectively. To illustrate our findings, we focus on a case of an incident vortex with $\gamma = 0.2$, initially located at $\boldsymbol{x}_\gamma(0) = (-20, 0.2)$, sufficiently far upstream of the airfoil, where it essentially convects along the mean-flow direction. In addition, we fix $\bar{\eta} = 0.8$, which corresponds to a trailing edge flap capturing ten percent of the airfoil chord. The remaining free parameters are, therefore, the system natural frequency co and fluid-loading number $\bar{\beta}$ which effects are studied below. The solution for the dynamical problem is obtained numerically using a fourth-order Runge–Kutta algorithm.

To calculate the far-field acoustic radiation, we consider a case where the airfoil is acoustically compact. We, therefore, assume that $a/\lambda \ll 1$, where $\lambda = 2\pi c_0/\Omega$ is the dimensional acoustic wavelength, with $\Omega$ the dimensional counterpart of c. The condition for airfoil compactness is then given by $a/\lambda = M(\Omega a/2\pi U) \ll 1$, where $M = U/c_0$ is the mean stream Mach number. This restriction is in accordance with the low-Mach assumption set for the study of the near-field flow. Making use of Powell-Howe analogy for a compact body (Howe 2003), and adopting the scaling introduced, we obtain the following form for the *dipole-type* acoustic pressure

$$\frac{p(\mathbf{x},t)}{\rho_0 U^2} = \sqrt{\frac{M}{8|\mathbf{x}|}}\Pi_{\text{tot}}([t]) = \sqrt{\frac{M}{8|\bar{\mathbf{x}}|}}\left(\Pi_f([t]) + \Pi_\gamma([t]) + \Pi_w([t])\right), \tag{2}$$

where $\Pi_f$, $\Pi_\gamma$ and $\Pi_w$ denote separate contributions of flap motion, incident vortex, and wake to the total radiation $\Pi_{\text{tot}}$, respectively (explicit expressions are not given here for brevity), and $[t]$ marks the scaled retarded time. The acoustic radiation is governed, in addition to the above nondimensional parameters, by the observer directivity, $\alpha = \cos^{-1}(x_2/|\boldsymbol{x}|)$. Dipole sound is radiated along both lift $(\alpha\cos\alpha)$ and suction $(\alpha\sin\alpha)$ directions: while all three components appearing in (2) contribute to the lift dipole, suction dipole results only from vortices motion in the normal direction, reflecting the effect of nonlinear vortex-airfoil interactions.

## 2 Results and Discussion

Figure 2 summarizes some of our results for the dynamical and acoustic problems, by comparing between flap motion and sound radiation in the normal direction for non-flapped airfoil ($\beta = 0$), torsion-free flap ($\beta = 10$, $\omega = 0$), and flapped airfoil with $\beta = 10$, $\omega = 1$. Focusing on the latter case (solid line) and examining Fig. 2a, we observe that at early times the incident vortex induces only vanishingly small flap oscillations. Yet, shortly after the incident vortex passes above the airfoil leading edge significant flap oscillations are initiated, characterized by the

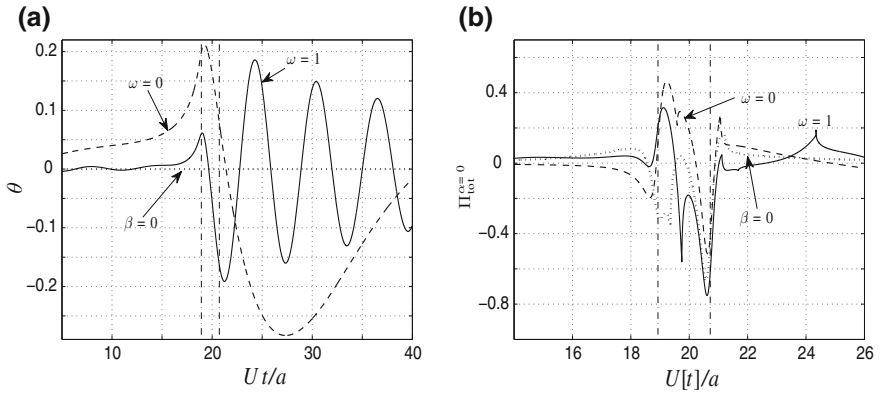


**Fig. 2** Flap angle (Fig. 2a) and total acoustic pressure in the $x_2$-direction (Fig. 2b) generated by passage of the incident vortex above the airfoil for non-flapped airfoil ($\beta = 0$, *dotted lines*), torsion- free flap ($\beta = 10$ and $\omega = 0$, *dashed lines*), and flapped airfoil with $\beta = 10$ and $\omega = 1$ (solid lines). Vertical dash-dotted lines confine the time interval during which the vortex passes above the airfoil

system natural frequency $\omega = 1$. Remarkably, this frequency is amplified by the fluid-flap system above all other frequencies contained in the spectrum of the forcing vortex. At late times, and as the vortex propagates away from the airfoil, flap oscillations decay. Traversing to the flap motion in the torsion-free $\omega = 0$ case (dashed line in Fig. 2a), we observe qualitatively different behavior: in the absence of a counter-acting spring, the incident vortex freely pulls the flap as it approaches the airfoil (in accordance with the counterclockwise velocity it induces) and pushes it away as it passes above it. This simple "passive-motion" mechanism reduces the singularity of incident vortex interaction with airfoil trailing edge, which, in turn, causes reduction in sound radiation at trailing edge time, as demonstrated below.

The total acoustic radiation along the $x_2$-direction presented in Fig. 2b can be viewed as a combination of relatively strong leading and trailing edge interactions of the airfoil with the incident vortex, together with late-time sound reflecting the motion of the flap. Interestingly, our results indicate that while flap motion is the indirect cause for late-time radiation, direct flap sound $(\Pi_f)$ is always negligible, and the acoustic radiation is dominated by incident and trailing edge wake sound at all times. Examining the flap-on-spring (solid), torsion-free (dashed), and non-flapped (dotted) signatures, we find that at trailing edge time (i.e., when the incident vortex passes above airfoil trailing edge, which is typically the time when strongest sound is radiated), the flap may have an amplifying (for $\omega = 1$) or absorbing (for $\omega = 0$) effect on radiation compared with the rigid case (cf. the levels of sound in the vicinity of the vertical right line in Fig. 2b). This result is in accordance with the "passive-motion" mechanism described in Fig. 2a for the $\omega = 0$ case.

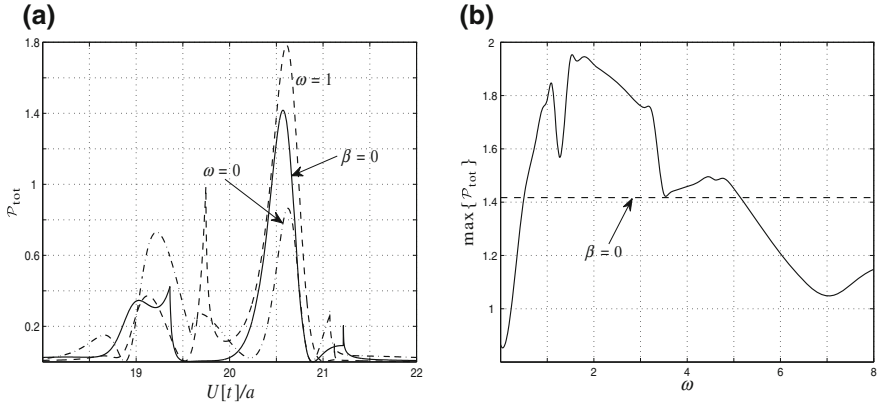


**Fig. 3** Effect of system natural frequency on sound energy amplitude $P_{\rm tot}$. (**a**) Comparison between $P_{\rm tot}$ for different flap configurations (line types as in Fig. 2). (**b**) Variation of maximum $P_{\rm tot}$ with $\omega$, achieved at trailing edge time

To clarify the effect of $\omega$ on system acoustic signature, Fig. 3a presents the far-field sound energy amplitude $p_{\rm tot}(|\bar{t}|)$, obtained by quadrature of the squared total acoustic pressure (2) over a circle of radius $|\bar{\mathrm{x}}| \to \infty$. The solid line shows the acoustic amplitude for a non-flapped airfoil ($\beta = 0$), and the dashed and dash-dotted lines present the counterpart results for $\beta = 10$ with $\omega = 0$ and $\omega = 1$, respectively. As noted in Fig. 2b, we observe that the largest sound energy amplitude is obtained in the proximity of trailing edge time (at $U[t]/a \approx 20.7$), and thus focus on the effect of $\omega$ at that time. This effect is illustrated in Fig. 3b, where the maximum value of $P_{\rm tot}$ is shown as function of $\omega$. For reference, the counterpart sound energy amplitude in the case of a rigid airfoil (i.e., the maximum value of the solid line in Fig. 3a) is given by the dashed line. In support of Fig. 2b, the results confirm that the flap may act as sound "amplifier" or "absorber", depending on the value of system natural frequency: at $0.5 < \omega < 5.2$, the flap amplifies the sound energy amplitude above the reference rigid-airfoil value, while at lower and larger frequencies the flap attenuates radiation. Note that at large values of $\omega$ (not presented here), $P_{\rm tot}$ converges to its non-flapped form, as flap oscillations vanish and the airfoil becomes essentially rigid. Further results, rationalizing the above findings in terms of the Fourier spectrum of the acoustic signal, are discussed elsewhere (Manela and Huang 2013).

**Acknowledgments** A. M. acknowledges support by the Marie Curie International Reintegration Grant PIRG-GA-2010-276837. L. H. acknowledges the support of a "973" Grant from China (2012CB720202).

## References

Guo YP (2001) A discrete vortex model for slat noise prediction. AIAA Paper 2001-2157
Howe MS (1982) On the generation of side-edge flap noise. J Sound Vib 80:555–572
Howe MS (1996) Emendation of the Brown and Michael equation, with application to sound generation by vortex motion near a half-plane. J Fluid Mech 329:89–101
Howe MS (2003) Theory of vortex sound. Cambridge University Press, Cambridge, p 216
Hutcheson FV, Brooks TF, Humphreys WM (2011) Noise radiation from a continuous mold- line link flap configuration. Int J Aeroacoustics 10:565–588
Manela A, Huang L (2013) Point vortex model for prediction of sound generated by a wing with flap interacting with a passing vortex. J Acoust Soc Am 133:1934–1944
Smith MJT (1989) Aircraft noise. Cambridge University Press, Cambridge, p 382
Zheng ZC, Tan BK, Xu Y (2010) Near-field fluctuations and far-field noise of a three-element airfoil system by a discrete vortex method. Appl Math Comput 216:1072–1086

# Modes of Pressure Fluctuations Around a Leading-Edge Slat

**Peng Chen, Xunnian Wang and Yuchang Wen**

**Abstract** Numerical simulations were conducted to investigate the pressure fluctuations (PF) around a leading-edge slat, which was assumed to have close relationship with the far-field slat noise. The PF predicted that not only the reattachment region of the free shear layer shedding from the slat cusp, but the region close to the leading edge of main element were the crucial regions that radiated noise into far field. Proper orthogonal decomposition (POD) was applied to the PF around the slat. By checking the temporal sequence of vorticity distribution around the slat, the crucial flow features corresponding to the first four POD modes were examined, in particular the first mode was induced by the vortical structures convecting through the slat gap.

## 1 Introduction

The noise generated from a leading-edge slat represents a complex aeroacoustic problem. Over the past several decades, extensive studies have been conducted with the aim of understanding of the underlying mechanisms of the slat noise generation. It is generally agreed that the slat noise is broadband in nature, with highest level appearing at a Strouhal (St) number of around 2 (based on the slat chord). In some cases, the noise can be superimposed by tonal components. Several models have been proposed to account for the broadband slat noise generation. For example, Molin and Roger (2000) attributed the broadband component to an interaction between turbulent structures in the slat cove region with the leading edge of the main element. Dobrzynski and Pott-Pollenske (2001) stated that the slat noise arose from the interaction between the vortices originating from

P. Chen (✉) · X. Wang · Y. Wen
China Aerodynamics Research and Development Center, Mianyang, China
e-mail: pht128@163.com

Y. Zhou et al. (eds.), *Fluid-Structure-Sound Interactions and Control*,
Lecture Notes in Mechanical Engineering, DOI: 10.1007/978-3-642-40371-2_32,

the unsteadiness in the slat cove and the slat trailing edge. Another view regarding the slat noise generation is that discrete vortices are rolled up from the free shear layer shed from the slat cusp through the Kelvin–Helmholtz instability. These rolled up vortices then experience severe stretching and distortion. Then, when the unsteady flow is shed from the slat trailing edge, noise is generated (Dobrzynski 2010; Molin and Roger 2000; Konig et al. 2009). In this current work, first to obtain the flow properties around the slat, a delayed detached eddy simulation (DDES) was performed. The value distributions of the pressure fluctuations (PF) in the vicinity of the slat were calculated. Meanwhile, the regions which were in key responsibility for the far-field slat noise were predicted through the PF distribution. Proper orthogonal decomposition (POD) was applied to the PF around the slat. By checking the temporal sequence of vorticity distribution around the slat, the crucial flow features corresponding to the POD modes were deduced.

## 2 Geometric Model and Setup for Numerical Simulation

For a generic wing in a landing configuration, it is known that the leading-edge slat and trailing-edge flap are the main components of noise. To isolate the slat component of high lift device noise, tests were conducted with a two-element model (Fig. 1). The model used in this study had a RA16SC1 section. The deflection angle of the slat ($\delta_s$) was set to 30°. The horizontal gap ($o_s$) and overlap ($g_s$) were respectively −2.4 and 2.7 % of the chord, in the stowed configuration. The main element chord ($c_m$) was 0.35 m and the slat chord was 0.088 m ($c_s$). The computational domain extended from −20 to 20 $c_m$ in both the $x$ and $y$ directions. An extension of 0.41 $c_s$ and 37 grid points was used in the spanwise direction. The entire three-dimensional domain consisted of $5 \times 10^6$ points. An incompressible S-A DDES technique, along with a second order temporal discretization was employed. Across all the solid surfaces no-slip boundary conditions were imposed. Periodic boundary conditions were employed across the spanwise boundaries of the computational domain. A dual time-stepping algorithm was used, with 20 subiterations within each time step of $7.14 \times 10^{-4}$ flow time unit (time non-dimensionalised by $c_m/u_\infty$). The freestream velocity was set to 25 m/s, and the angle of attack (AOA) was set to 8°.

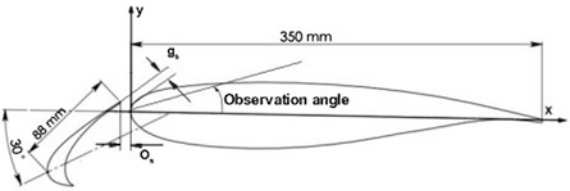


**Fig. 1** Model size

# 3 Results and Discussions

## 3.1 Pressure Fluctuations Around the Slat

Several studies had linked the slat noise sources with PF values around a slat. PF on or close to solid surface are known to play an important role in noise generation. Figure 2 shows the $p'_{\mathrm{rms}}$ (root mean square of PF) around the slat. $p'_{\mathrm{rms}}$ had high values not only in the reattachment region but also in the region close to the leading edge of the main element. The distributions pattern predicted that the dominant slat noise was generated from the two regions.

## 3.2 Modes of PF in Vicinity of Slat

To further investigate the behaviour of PF and the flow feature in the vicinity of the slat, POD technique was applied to the PF. The POD is a post-processing technique that takes a set of data and extracts basis functions. The technique was originally developed to identify the most energetic coherent structures contained in a turbulent flow. The POD calculation presented that the first four modes contributed to approximately 75 % of the total 'energy'. Therefore, understanding the flow features corresponding to those modes will help to understand the processes involved in the production of slat noise.

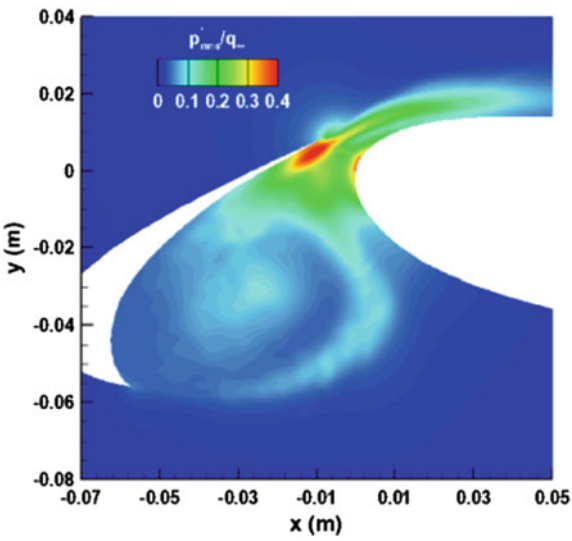


**Fig. 2** $p'_{\mathrm{rms}}$ distribution

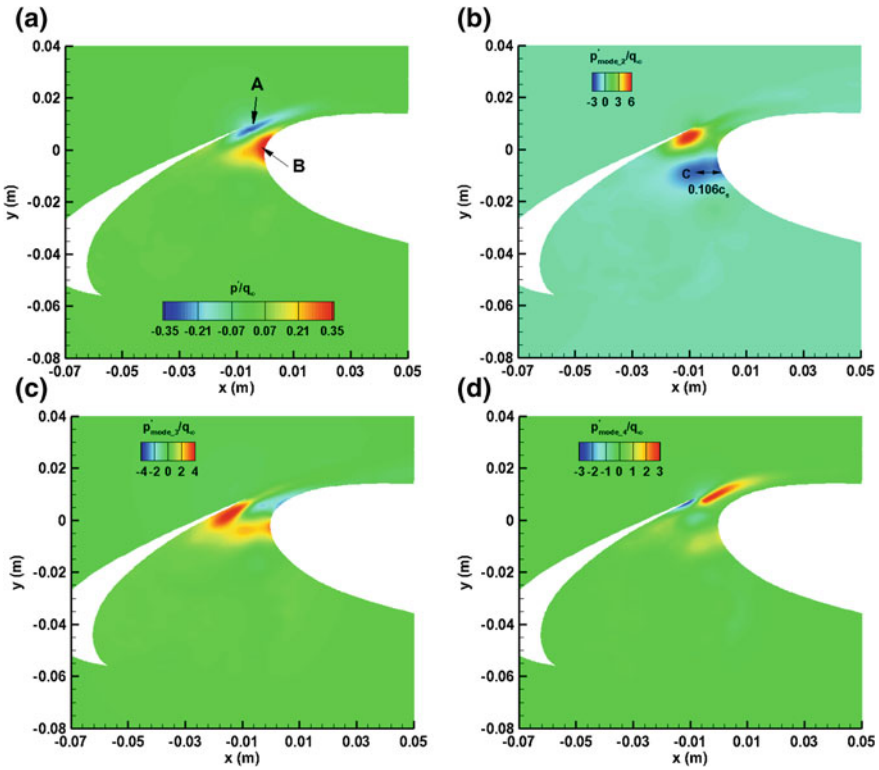


**Fig. 3** The first four modes of fluctuating pressure around slat. **a** Mode 1. **b** Mode 2. **c** Mode 3. **d** Mode 4

As shown in Fig. 3a, the first mode, appearing in the wake of the trailing edge of slat and the region close to the leading edge of the main element, had the highest values of PF. The time history of PF at positions *A* and *B* (shown in Fig. 4) revealed a crucial feature, the PF at the two positions had identical magnitude but opposite phase. To gain insight into the flow feature corresponding to the first mode, the typical vorticity distribution around the slat at time $\tau_1$ was examined (Fig. 5). From this figure, it can be observed that a large vortical structure was stretched by the mean flow through the slat gap. As the front part of the vortical structure approached the suction surface of main element, it altered the vorticity in the boundary layer above the main element surface. At the same time, a vortex was forced to shed from the trailing edge by the rear part of the vortical structure. It can be reasonably assumed that the rapid alternation of vorticity in the boundary layer arises the intense PF in the region close to the leading edge of main element, whilst the vortex shedding from the trailing edge leads to the PF in the wake of the slat trailing edge. By checking the temporal sequence of the vorticity distribution, it was shown that vortical structures were intermittently convected through the slat gap. The second mode (Fig. 3b) denotes that PF in region *C* and the reattachment

region are spatially correlated. The second mode was similar to the conventional interpretation associated with the slat noise generation, which claims that the intense PF in the reattachment region results from that the turbulent free shear layer impinging on the slat cove surface. In addition, relatively high PF in the region *C* was assumed to result from the local flow acceleration.

The third mode (shown in Fig. 3c) was related to the PF in the reattachment region and slat region. By checking the temporal sequence of the vorticity distribution, two kinds of vortex interaction could be seen. The first is shown in Fig. 6a. As a vortex approached the reattachment region, it induced a vortex to be shed from the trailing edge. This shed vortex flowed towards the slat cove, rather than towards the wake of the trailing edge. Then, the vortex interacts with a succeeding vortex convected by the free shear layer. This second vortex interaction pattern is illustrated in Fig. 6b. Once a vortex convected by the free shear layer impinged on the slat cove surface, part of it was trapped in the circulation region. Subsequently, the trapped vortex interacts with a succeeding vortex convected by the free shear layer. These two kinds of vortex interactions are assumed to be the flow features corresponding to the third mode, because they occur at the same spatial position where the PF was high.

The fourth mode (Fig. 3d) indicated that PF in the reattachment region was correlated with the PF in the wake of the trailing edge. Two kinds of possible flow features can account for this mode pattern. The first is that as the circulation around the slat was altered, by the vortex convecting with the free shear layer, a vortex would be shed from the trailing edge of the slat due to the Kutta-Joukowski condition. The second flow feature is that the unsteady flow was shed from the slat trailing edge after the vortices impinged on the slat cove surface.

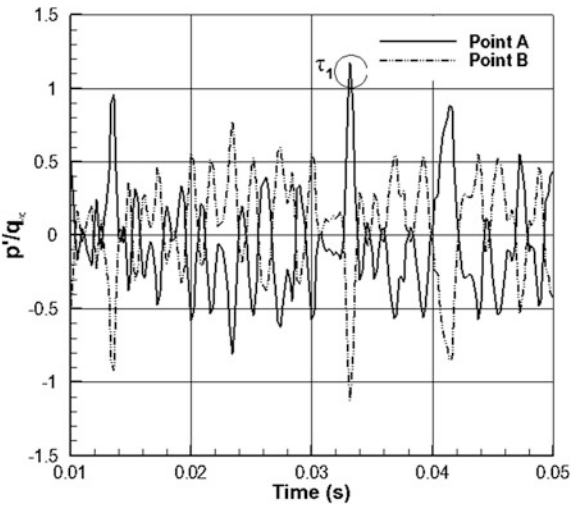


**Fig. 4** Time history of the first mode

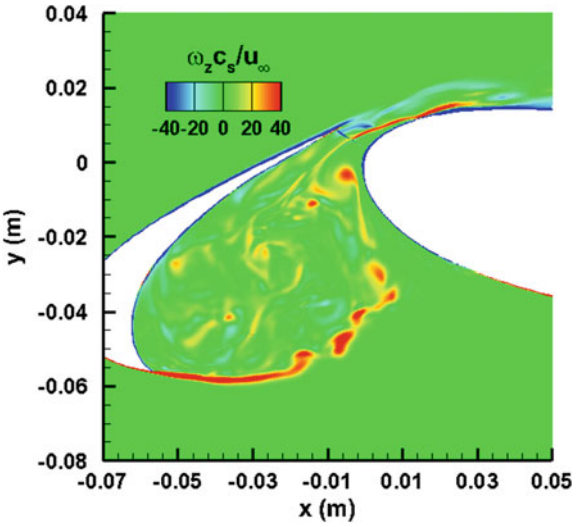


**Fig. 5** Vorticity around slat at $t = \tau_1$

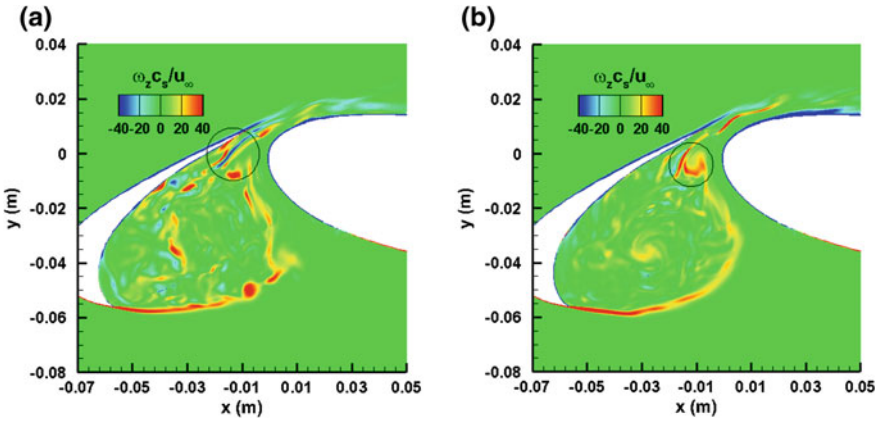


**Fig. 6** Vortex interaction in the slat gap region in the third mode

## 4 Summary

Numerical simulations were conducted to investigate the features, and possible mechanisms of generation, of slat noise. POD was applied on PF around the slat and the main flow features corresponding to the first four modes were discussed. The first mode was the outcome of vortical structures convecting through the slat

gap. The second mode related to the flow accelerating near the slat gap and the vortex impinging on the slat cove surface. The third mode corresponded to complex vortex interaction. Finally, the fourth mode related to the unsteady flow shed from the slat trailing edge, or vortex shedding due to the Kutta-Joukowski condition.

## References

Dobrzynski W (2010) Almost 40 years of airframe noise research: what did we achieve? J Aircr 47:353–367

Dobrzynski W, Pott-pollenske M (2001) Slat noise source studies for farfield noise prediction. In: Proceedings of 7th AIAA/CEAS aeroacoustics conference and exhibit, AIAA paper, Maastricht, Netherlands

Konig D, Koh SR, Schroder W, Meinke M (2009) Slat noise source identification. In: Proceedings of 30th AIAA aeroacoustics conference, AIAA paper, Miami, Florida

Molin N, Roger M (2000) The use of Amiet's methods in predicting the noise from 2D high-lift devices. In: Proceedinngs of 6th AIAA/CEAS aeroacoustics conference, AIAA paper, Lahaina

# On the Flow and Noise of a Two-Dimensional Step Element in a Turbulent Boundary Layer

**Danielle J. Moreau, Jesse L. Coombs and Con J. Doolan**

**Abstract** This paper presents results of a study on the flow and noise generated by two-dimensional step elements attached to a flat plate. The step elements used in this study are equivalent to a forward–backward facing step pair and have length to height ratio of $l/h = 8$, 4 and 2.7. Aerodynamic and acoustic measurements have been taken in an anechoic wind tunnel at the University of Adelaide. Numerical simulations of turbulent boundary layer flow over the step with $l/h = 2.7$ are also presented. The data given in this paper provide fundamental information on how a sub-boundary layer step element affects the noise and flow field.

**Keywords** Sub-boundary layer step noise · Step flow

## 1 Introduction

Aerodynamic sound is an important source of the noise produced by modern air, land and underwater vehicles. Surface discontinuities due to rivets, ribs, joints, environmental contamination or errors in machining can disturb the turbulent boundary layer that develops over a vehicle and generate increased levels of aerodynamic noise. Given the prevalence of surface discontinuity noise, it is important from a practical design perspective that this noise source is well understood and the baseline case of a step element attached to a flat plate is ideal for such a fundamental investigation. Previous research on step flows has largely focused on aerodynamic aspects of problem (Moss and Baker 1980) and the backward facing step is the most commonly studied configuration (Jacob et al. 2001). Leclerq et al. (2001) have conducted one of the few experimental studies on

D. J. Moreau (✉) · J. L. Coombs · C. J. Doolan
School of Mechanical Engineering, The University of Adelaide, Adelaide, SA 5005, Australia
e-mail: danielle.moreau@adelaide.edu.au

Y. Zhou et al. (eds.), *Fluid-Structure-Sound Interactions and Control*,
Lecture Notes in Mechanical Engineering, DOI: 10.1007/978-3-642-40371-2_33,

the sound generated by flow over a forward–backward facing step pair with length to height ratio of $l/h = 10$. This paper presents results of a study on the flow and noise generated by a two-dimensional forward–backward facing step pair with $l/h = 8$, 4 and 2.7 in low Mach number turbulent flow. Aeroacoustic measurements taken in an anechoic wind tunnel at the University of Adelaide are presented along with a numerical simulation of turbulent boundary layer flow over the step element with $l/h = 2.7$.

## 2 Experimental Method

Experiments were conducted in the University of Adelaide's anechoic wind tunnel with rectangular test section of 275 mm (width) × 75 mm (height) (Moreau et al. 2011). The test model consists of a rectangular step element attached to a flat plate as shown in Fig. 1. Three different step elements are used in this study with height of $h = 2.5$, 5 and 7.5 mm corresponding to 26, 52 and 77 % of the local unperturbed boundary layer thickness. The step elements are located (one at a time) on the flat plate at a distance of 30 mm downstream of the jet exit plane.

Acoustic measurements were recorded at two locations using two B&K 1/2 inch microphones (No. 4190). The first microphone was located at an observer angle of $\theta = 90°$ to the step at $x = 30$, $y = 137.5$, $z = 520$ mm while the second microphone was located at an angle of $\theta = 45°$ to the step at $x = 550$, $y = 137.5$, $z = 520$ mm. Hot-wire anemometry was used to measure the mean flow velocity and turbulence characteristics downstream of the step. The sensor used was a TSI 1210-T1.5 single wire probe connected to a TSI IFA300 constant temperature anemometer system and positioned using a Dantec automatic traverse. Experiments were conducted at a flow speed of $U_\infty = 35$ m/s. Acoustic and flow data were recorded using a National Instruments board at a sampling frequency of $5 \times 10^4$ Hz for a sample time of 8 and 4 s, respectively.

## 3 Experimental Results

One-third-octave band noise spectra at the two observer locations for the side plate with and without a step are shown in Fig. 2. This figure shows the sound radiated by the step is broadband in nature and increases with step height. The smallest step

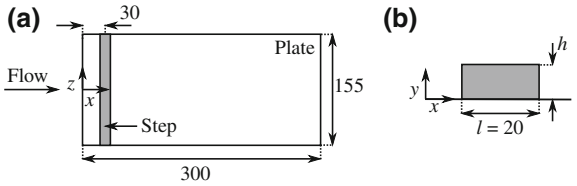


**Fig. 1** Step element attached to the plate. **a** Front and **b** side view. Dimensions in mm

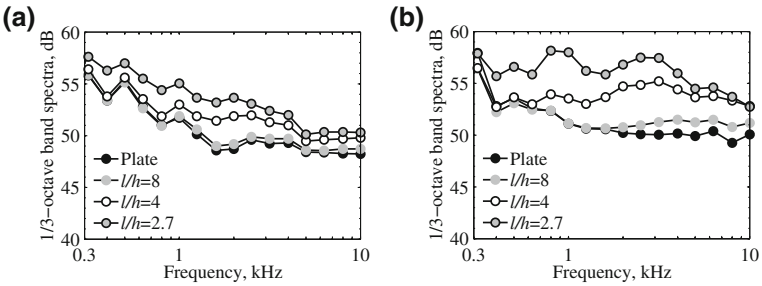


**Fig. 2** One-third-octave band spectra at an observer angle of **a** $\theta = 90°$ and **b** $\theta = 45°$

with $l/h = 8$ only slightly increases the noise levels above those of the plate (no step) at high frequencies (above 1 kHz). In comparison, the spectra for the step with $l/h = 2.7$ sit well above the plate spectra at all frequencies, especially at an observer angle of $\theta = 45°$. The step is expected to act as a dipole noise source which explains the higher levels of noise measured at an angle of $\theta = 45°$.

Figures 3 and 4 show the normalised mean velocity ($U/U_\infty$) and rms velocity ($u'/U_\infty$) profiles measured at two locations downstream of the step. The mean velocity profiles show a significant increase in the boundary layer thickness with step height and downstream distance. The rms velocity profiles show the turbulent energy levels in the boundary layer downstream of the step increase with step height. Additionally, the point of maximum energy occurs further from the plate surface as step height is increased. The turbulent intensity peaks are observed to reduce in amplitude and move further from the plate surface as the measurement location moves further downstream of the step.

Spectral maps of the fluctuating velocity measured 50 mm downstream of the step in Fig. 5 show a significant increase in low frequency energy content (below 500 Hz) as the step height is increased. In agreement with the rms velocity profiles, regions of intense low frequency energy move further from the plate surface with increasing step height.

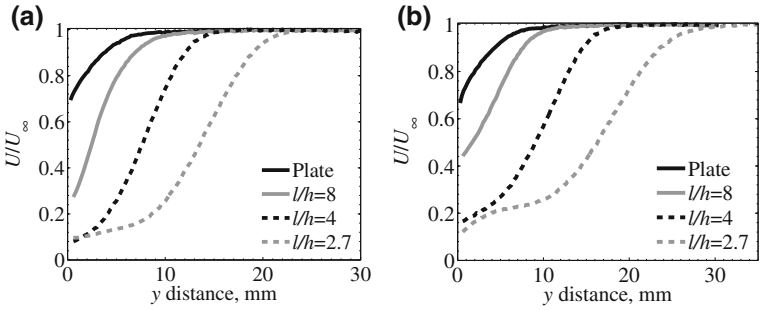


**Fig. 3** Normalised mean velocity profiles at **a** 20 and **b** 50 mm downstream of the step

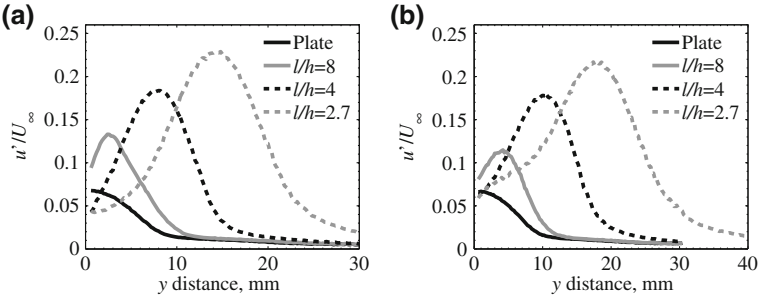


**Fig. 4** Normalised rms velocity profiles at **a** 20 and **b** 50 mm downstream of the step

## 4 Numerical Simulation

A large eddy simulation (LES) of the experimental test case of flow over the step element with $l/h = 2.7$ was performed. The simulation used the one equation eddy model on a structured hexahedral mesh of $1.775 \times 10^6$ cells with upstream, vertical, downstream and cross-stream boundaries of 10, 30, 12.5 and 0.05 $l$, respectively. The LES was run from a steady state Reynolds Averaged Navier–Stokes solution using the realisable k-$\varepsilon$ model for over 20 freestream passes (0.0115 s) of the step element, with statistical averages gathered over the final 10 freestream passes (0.00573 s).

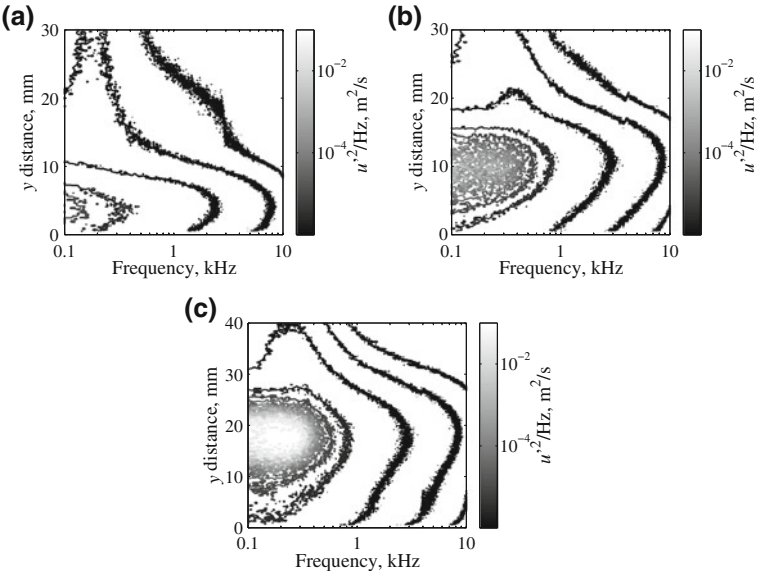


**Fig. 5** Velocity spectral maps 50 mm downstream of the step with $l/h$ of **a** 8, **b** 4 and **c** 2.7

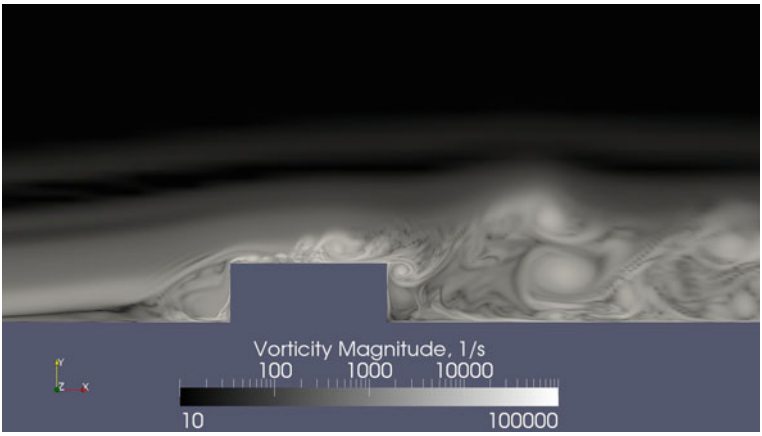


**Fig. 6** Instantaneous vorticity magnitude at time $t = 0.0068$ s for the step with $l/h = 2.7$

Figure 6 shows instantaneous vorticity magnitude of flow over the step at time $t = 0.0068$ s. A recirculation region can be seen upstream of the step leading edge which periodically ejects flow onto the top surface of the step in the leading edge region. Vortices form at the leading and trailing edge corners and large vortex structures are observed downstream of the step. This is in agreement with the velocity spectral map in Fig. 5c which shows a region of high energy low frequency fluctuations downstream of the step. The reattachment point was determined from the mean flow field to occur at 9.9 $h$ (74.1 mm) downstream of the step which is in broad agreement with the findings of others (Mohsen 1967).

## 5 Conclusion

A study on the flow and noise produced by a sub-boundary layer step element has been presented in this paper. Experimental results include far-field noise spectra as well as information on the mean and unsteady turbulent characteristics downstream of the step. A numerical simulation of flow over the step element has also been presented providing information on the important features of the flow field.

**Acknowledgments** This work has been supported by the Australian Research Council under linkage grant LP110100033.

## References

Jacob MC, Louisot A, Juve D, Guerrand S (2001) Experimental study of sound generated by backward-facing steps under wall jet. AIAA J 39:1254–1260

Leclerq DJ, Jacob MC, Louisot A, Talotte C (2001) Forward-backward facing step pair: aerodynamic flow, wall pressure and acoustic characterisation. In: Proceedings of 7th AIAA/CEAS aeroacoustics conference on AIAA Paper 2001–2249, Maastricht, Netherlands, 28–30 May

Mohsen AM (1967) Experimental investigation of the wall pressure fluctuations in subsonic separated flows. Boeing Commercial airplane division report, D6–17094

Moreau DJ, Brooks LA, Doolan CJ (2011) Broadband trailing edge noise from a sharp-edged strut. J Acoust Soc Am 129(5):2820–2829

Moss WD, Baker S (1980) Re-circulating flows associated with two-dimensional steps. Aeronaut Q: 151–172

# The Study of Prediction Method on Propeller Broadband Noise

**Yihong Chen, Denghai Tang, Zhuqing Liu and Hongxing Sun**

**Abstract** In this paper, a prediction method of hydrofoil broadband noise is developed based on large eddy simulation (LES) methods and Ffowcs Williams-Hawkings (FW-H) equations. The broadband noise of an airfoil is calculated and the comparison of computed and measured sound pressure spectra shows good agreement over approximately a decade of frequency. The broadband noise of five different hydrofoils are calculated and presented in this paper. The relationship between the broadband noise of hydrofoils and the hydrofoil thickness and camber distributions are discussed. An optimized hydrofoil is presented in this paper for which the broadband noise is about 4 dB lower than NACA-66mod foil.

## 1 Introduction

The propeller broadband noise spectrum is contributed by the sound radiation of the trailing edge flow of propeller blade and interaction between tip vortex and blade. Turbulence with various scales eddies in these flows is directly related to generation of the noise. So, how to obtain the detail structures of flow field around the propeller becomes one of the key points in propeller broadband noise prediction by numerical methods. Large eddy simulation (LES) method can get adequate flow details with relatively high accuracy, as well as satisfy the requirement of the sound source simulation calculation for noise prediction.

Wang and Moin (2000) used numerical methods to simulate trailing edge flow, and then the trailing edge noise was predicted by the acoustic disturbance

Y. Chen (✉) · D. Tang · Z. Liu · H. Sun
China Ship Scientific Research Center, Wuxi, China
e-mail: 5784362@qq.com

Y. Chen · D. Tang · Z. Liu · H. Sun
National Key Laboratory on Ship Vibration & Noise, Wuxi, China

Y. Zhou et al. (eds.), *Fluid-Structure-Sound Interactions and Control*,
Lecture Notes in Mechanical Engineering, DOI: 10.1007/978-3-642-40371-2_34,

equations. Moreauy used LES methods to calculate foil flow field, then solved the foil trailing edge noise by FW-H equations, and the comparison of computed and experimental results shows good agreement. In conclusion, the numerical prediction method of broadband noise using LES combined with acoustical methods have already been studied and validated in different fields.

In order to predict the hydrofoil broadband noises, the turbulent flow around a two-dimensional hydrofoil is calculated as a time series by LES, and then the broadband noise is predicted using the FW-H equations. The broadband noises of five different two-dimensional hydrofoils are calculated, and the relationships between the broadband noise of hydrofoil and the hydrofoil thickness and camber distributions are discussed.

## 2 LES Numerical Calculation Method

The basic assumptions of LES are that: (1) transport is largely governed by large—scale unsteady flow and these structures can be computationally resolved; (2) small—scale flow features can be under taken by using appropriate subgrid scale turbulence models. In LES, the motion is separated into small and large eddies, and the large eddies is achieved by means of a low—pass filter. The filter function $G(x, y)$ implied here is following:

$$\int_v G(x,y)\mathrm{d}y = 1 \tag{1}$$

Filtering the Navier—Stokes equation, one obtain equations as follows:

$$\frac{\partial \rho}{\partial t} + \frac{\partial}{\partial x_i}(\rho \overline{u}_i) = 0 \tag{2}$$

$$\frac{\partial}{\partial t}(\rho \overline{u}_i) + \frac{\partial}{\partial x_j}(\rho \overline{u}_i \overline{u}_j) = \frac{\partial}{\partial x_j}\left(\mu \frac{\partial \sigma_{ij}}{\partial x_j}\right) - \frac{\partial \overline{p}}{\partial x_j} - \frac{\partial \tau_{ij}}{\partial x_j} \tag{3}$$

$\tau_{ij} = -\left(\overline{u_i u_j} - \overline{u}_i \overline{u}_j\right)$ is subgrid scale stress tensor. The subgrid scale stresses resulting from the filtering operation are unknown, and require modeling.

## 3 Broadband Noise Numerical Calculation Method

Ffowes Williams and Hawkings (1969) utilized the generalized function theory to obtain the classic equation that has become associated with their names. If we take a time derivative of the generalized continuity equation, subtract the divergence of the generalized momentum equation, and then rearrange terms, the FW-H equation can be written as the following inhomogeneous wave equation:

$$\frac{1}{c^2}\frac{\partial p'}{\partial t} - \nabla^2 p' = \frac{\partial}{\partial t}[(\rho_0 v_n + \rho(u_n - v_n)]\delta(f) - \frac{\partial}{\partial x_i}\left[P_{ij}n_j + \rho u_i(u_n - v_n)\right]\delta(f) + \frac{\partial^2}{\partial x_i \partial x_j}[T_{ij}H(f)] \quad (4)$$

where $u$ is the velocity vector in fluids, $v$ is the velocity vector of subject surface, $c$ is the acoustic velocity in stable fluids, $T_{ij}$ is Lighthill stress tensor, $\delta(f)$ is Dirac delta function, $H(f)$ is Heaviside unit function, which is 0 when $f < 0$ and 1 when $f \geq 0$.

The FW-H approach has several advantages. First, the three source terms in the FW-H equation each have clear physical meaning, which is helpful in understanding the noise generation. The thickness noise (monopole source) is determined completely by the geometry and kinematics of the body. The loading noise (dipole source) is generated by the force that acts on the fluid as a result of the presence of the body. The quadrupole source term accounts for nonlinear effects. Second, the separation of the source term also is an advantage numerically because not all terms must be computed at all times if a particular source does not contribute to the sound field.

## 4 The Broadband Noise Computation and Validation of Foil

In order to validate the prediction method of foil broadband noise, the noise of a three-dimension foil is computed and compared with the measured result. The model foil is a 45° asymmetrically beveled trailing edge attached to a flat strut with an elliptical leading edge. The chord length $L$, thickness $H$, and span length $D$ of the foil are 910, 50.8, and 610 mm, respectively, the foil profile schematic diagram is shown in Fig. 1. The noise of foil was measured in anechoic wind tunnel of Notre Dame University, the wind speed is 30 m/s, and the attack angle is 0°.

The Large eddies simulation are performed in the calculated area as $4L$ (streamwise, $x$) × $2L$ (normal, $y$). A structured grid is adopted with total grid number of about 600,000. The time step for the calculations is $5 \times 10^{-5}$ s, so the relating noise analytical frequency can reach 10 kHz.

The compared results between the computed and measured sound pressure spectra are shown in Fig. 2. The comparison result shows good agreement both in the frequency spectrum characteristics and sound pressure spectra.

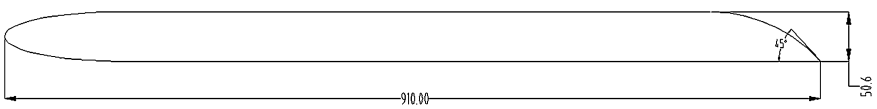


**Fig. 1** Schematic of foil profile geometry

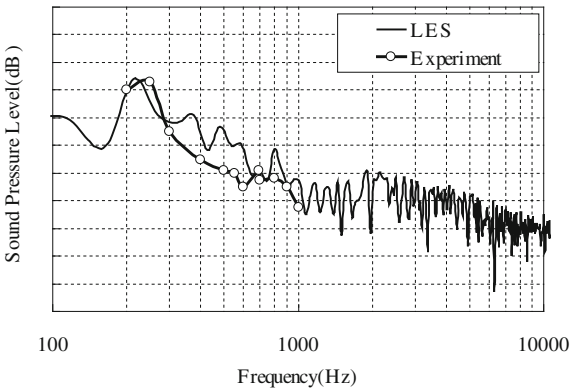


**Fig. 2** Comparison of computed and experimental sound pressure spectra

## 5 The Noise of Five Different Hydrofoils and Discuss

The broadband noise of five hydrofoils with different thickness and camber distribution are computed using the broadband noise prediction method based on LES and FW-H. The chord and maximum thickness of all of five hydrofoils are 45 and 4.5 mm, respectively.

### *5.1 The Broadband Noise of Hydrofoils with Different Thickness Distribution*

NACA-66mod is the basic scheme foil and named NO. 1, NO. 2 and NO. 3 are two new foils with different thickness distributions (Fig. 3), and camber distributions of the two new foils are same a NO. 1 (Fig. 4).

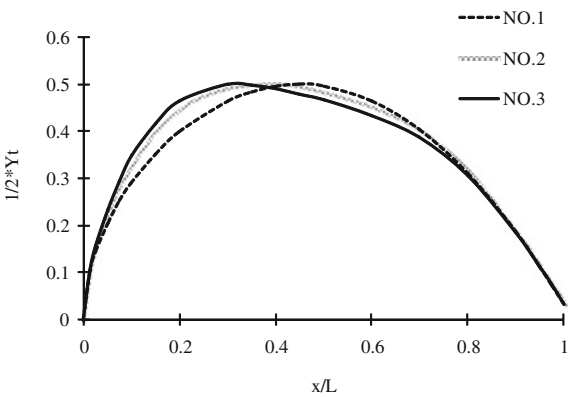


**Fig. 3** Thickness distributions of three hydrofoils

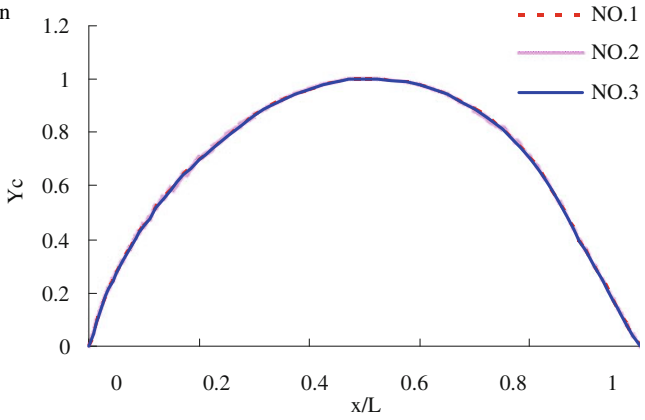


**Fig. 4** Camber distribution of three hydrofoils

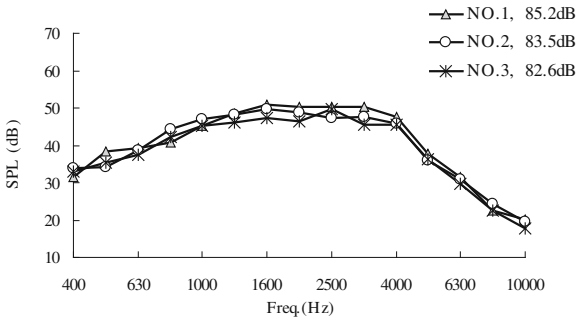


**Fig. 5** The broadband noise of three hydrofoils with different thickness distributions

The broadband noise of three hydrofoils are compared and shown in Fig. 5. The prediction results of three hydrofoils broadband noise show that the thickness distribution of hydrofoils induces the broadband noise. The noise of NO. 3 hydrofoil is the lowest of three hydrofoils, and that is 2.6 dB lower than noise of NO. 1 hydrofoil. Forwarding the maximum thickness position of hydrofoils is effective in reducing broadband noise of hydrofoils.

## *5.2 The Broadband Noise of Hydrofoils with Different Camber Distribution*

NO. 4 and NO. 5 are another two new hydrofoils that have different camber distributions from the NACA-66mod (Fig. 6), and the thickness distributions of NO. 4 and NO. 5 hydrofoils are the same as NO. 3 (Fig. 7).

The broadband noise of three hydrofoils are compared and shown in Fig. 8. The prediction results of three hydrofoils broadband noise show that the camber distribution of hydrofoils also induces the broadband noise. The noise of NO. 5 hydrofoil is the lowest of three hydrofoils and, that is, 2 dB lower than noise of

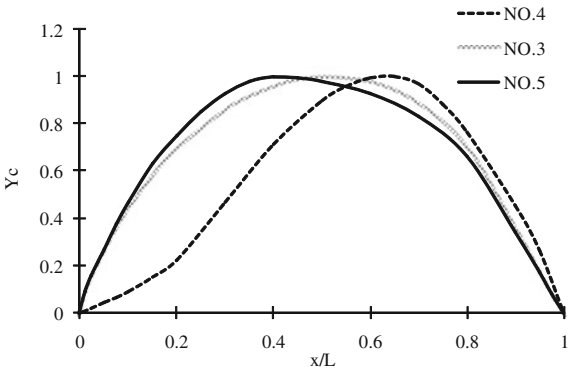


**Fig. 6** Camber distributions of three hydrofoils

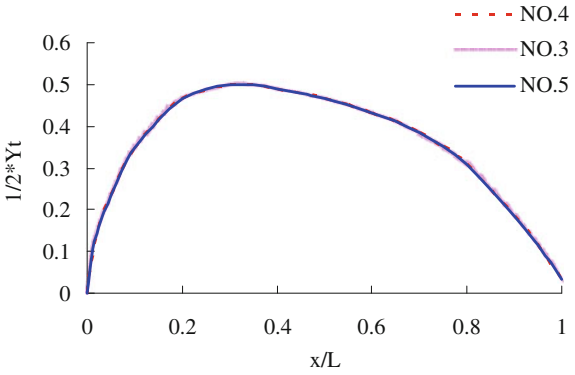


**Fig. 7** Thickness distributions of three hydrofoils

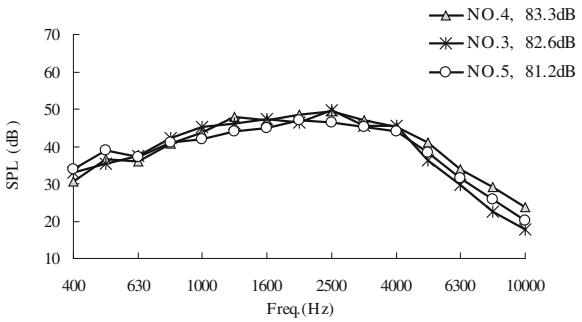


**Fig. 8** The broadband noise of three hydrofoils with different camber distributions

NO. 3 hydrofoil. Forwarding the maximum camber position of hydrofoils is also effective in reducing broadband noise of hydrofoils.

Based on the predicted results of all five hydrofoils, both maximum thickness and camber position forwarding are effective in reducing broadband noise of hydrofoil. As the optimized design model, NO. 5 hydrofoil is about 4.0 dB lower than NACA-66mod foil.

## 6 Conclusions

In this paper, a prediction method of foil broadband noise is developed based on LES methods and FW-H equations. An airfoil broadband noise is calculated using the prediction method, and the comparison of computed and measured sound pressure spectra shows good agreement. The noise of five hydrofoils with different thickness and camber distributions are computed by the prediction method that developed in this paper. The calculation results of five hydrofoils show that both moving the maximum thickness and camber forward are effective in reducing broadband noise. As the optimized design model, NO. 5 hydrofoil is about 4.0 dB lower than NACA-66mod foil.

## References

Ffowcs-Williams JE, Hawkings DL (1969) Sound generation by turbulence and surfaces in arbitrary motion. Proc. Roy. Soc. London A264:321–342

Wang M, Moin P (2000) Computation of trailing-edge flow and noise using large-eddy simulation. AIAA J 38(12):2201–2209

# A Class of High Order Compact Schemes with Good Spectral Resolution for Aeroacoustics

**Xuliang Liu and Shuhai Zhang**

**Abstract** In this paper, we design a class of linear compact schemes based on the cell-centered compact scheme of ((Lele, J Comput Phys 103:16–42, 1992). These schemes equate a weighted sum of the nodal derivatives of a smooth function to a weighted sum of the function on both the grid points and the cell-centers. Through systematic Fourier analysis and numerical tests, we observe that the schemes have good properties of high order, high resolution, and low dissipation. It is an ideal class of schemes for the simulation of multiscale problems such as aeroacoustics and turbulence.

**Keywords** Compact scheme · High order · High resolution · Computational aeroacoustics

## 1 Introduction

Direct numerical simulation (DNS) and large eddy simulation (LES) are two important methods to reveal the mechanism of multiscale problems such as turbulence and aeroacoustics. DNS for multiscale problems requires that the numerical grid should be fine enough to resolve the structure of smallest scales. However, due to the limitation of computational resources, most DNS studies have been carried out with marginal grid resolution. Besides the common problems in DNS of turbulence, there are computational issues that are unique to aeroacoustics (Tam 1995). First, the aerodynamic noise is broadband and the spectrum is fairly wide. Second, the amplitudes of the physical variables of the aerodynamic noise are far smaller than those of the mean flow. Third, the distance from the noise

X. Liu (✉) · S. Zhang
State Key Laboratory of Aerodynamics, China Aerodynamics Research and Development Center, Mianyang 621000 Sichuan, China
e-mail: xlliu@foxmail.com

Y. Zhou et al. (eds.), *Fluid-Structure-Sound Interactions and Control*,
Lecture Notes in Mechanical Engineering, DOI: 10.1007/978-3-642-40371-2_35,

source to the location of interest in aeroacoustic problems is quite long. To ensure that the computed solution is uniformly accurate over such a long propagation distance, the numerical scheme should have minimal numerical dispersion, dissipation, and anisotropy.

The most influential compact schemes for derivatives, interpolation, and filtering were proposed by Lele (1992). Through systematic Fourier analysis, it is shown that these compact schemes have spectral-like resolution for short waves.

In this paper, we propose a new idea to design the compact scheme based on the cell-centered compact scheme of Lele (1992). Instead of using only the values on cell centers, both the values of cell centers and grid nodes are used on the right hand side of compact schemes. Both the accuracy order and the wave resolution property are improved significantly. Numerical tests show that this is an ideal scheme for the DNS for multiscale problems.

## 2 Central Compact Schemes

In this section, we present the methodology to design central compact schemes (CCS). We start our work from the cell-centered compact scheme (CCCS) proposed by Lele (1992). Then we extend this scheme to a class of higher order schemes with good spectral resolution.

### *2.1 Lele's Compact Scheme*

Lele (1992) proposed two kinds of central compact schemes. One is a linear CCCS given by

$$\beta f'_{j-2} + \alpha f'_{j-1} + f'_j + \alpha f'_{j+1} + \beta f'_{j+2} = a\frac{f_{j+\frac{1}{2}} - f_{j-\frac{1}{2}}}{\Delta x} + b\frac{f_{j+\frac{3}{2}} - f_{j-\frac{3}{2}}}{3\Delta x} + c\frac{f_{j+\frac{5}{2}} - f_{j-\frac{5}{2}}}{5\Delta x} \tag{1}$$

The other is a cell-noded compact scheme (CNCS) given by

$$\beta f'_{j-2} + \alpha f'_{j-1} + f'_j + \alpha f'_{j+1} + \beta f'_{j+2} = a\frac{f_{j+1} - f_{j-1}}{2\Delta x} + b\frac{f_{j+2} - f_{j-2}}{4\Delta x} + c\frac{f_{j+3} - f_{j-3}}{6\Delta x} \tag{2}$$

The stencil involved in the CCCS and CNCS is shown in Fig. 1. The constraints on the coefficients $\alpha$, $\beta$, $a$, $b$, and $c$ corresponding to different orders of accuracy can be derived by matching the Taylor series coefficients and these have been listed in Lele (1992).

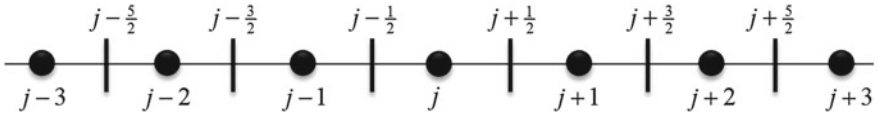


**Fig. 1** The stencil of cell-centerd and cell-noded compact schemes

## *2.2 A New Class of Central Compact Schemes*

In Lele's cell-centered compact schemes given by Eq. (1), the stencil contains both the grid point and half grid points. However, only the values at the cell-centers are used to calculate the derivatives at the cell-nodes. If the values at both the cell-nodes and the cell-centers are used, one could get a compact scheme with higher order accuracy and better resolution.

Based on this idea, we design a class of CCS given by the following formula. We use the scheme (3) to compute the values on cell-nodes, and the scheme (4) to compute the values on cell-centers.

$$\begin{aligned}\beta f'_{j-2} + \alpha f'_{j-1} + f'_j + \alpha f'_{j+1} + \beta f'_{j+2} = a\frac{f_{j+\frac{1}{2}} - f_{j-\frac{1}{2}}}{\Delta x} + b\frac{f_{j+1} - f_{j-1}}{2\Delta x} \\ + c\frac{f_{j+\frac{3}{2}} - f_{j-\frac{3}{2}}}{3\Delta x} + d\frac{f_{j+2} - f_{j-2}}{4\Delta x} \\ + e\frac{f_{j+\frac{5}{2}} - f_{j-\frac{5}{2}}}{5\Delta x}\end{aligned} \tag{3}$$

$$\begin{aligned}\beta f'_{j-\frac{5}{2}} + \alpha f'_{j-\frac{3}{2}} + f'_{j-\frac{1}{2}} + \alpha f'_{j+\frac{1}{2}} + \beta f'_{j+\frac{3}{2}} = a\frac{f_j - f_{j-1}}{\Delta x} + b\frac{f_{j+\frac{1}{2}} - f_{j-\frac{3}{2}}}{2\Delta x} \\ + c\frac{f_{j+1} - f_{j-2}}{3\Delta x} + d\frac{f_{j+\frac{3}{2}} - f_{j-\frac{5}{2}}}{4\Delta x} \\ + e\frac{f_{j+2} - f_{j-3}}{5\Delta x}\end{aligned} \tag{4}$$

We note that the cell-centered compact schemes (CCCS) given by Eq. (1) and cell-noded compact schemes (CNCS) given by Eq. (2) of Lele (1992) are both special cases of this class of CCS.

The physical values on cell-centers can be interpolated from the physical values of cell-nodes. In fact, a high order compact interpolation was proposed by Lele (1992), which has the following form:

$$\begin{aligned}\beta\hat{f}_{j-\frac{3}{2}} + \alpha\hat{f}_{j-\frac{1}{2}} + \hat{f}_{j+\frac{1}{2}} + \alpha\hat{f}_{j+\frac{3}{2}} + \beta\hat{f}_{j+\frac{5}{2}} = \frac{a}{2}\left(f_j + f_{j+1}\right) + \frac{b}{2}\left(f_{j-1} + f_{j+2}\right) \\ + \frac{c}{2}\left(f_{j-2} + f_{j+3}\right)\end{aligned} \tag{5}$$

Taking the Fourier transformation to Eq. (3) and using Euler's formula, the modified wavenumber of CCS can be obtained. It is:

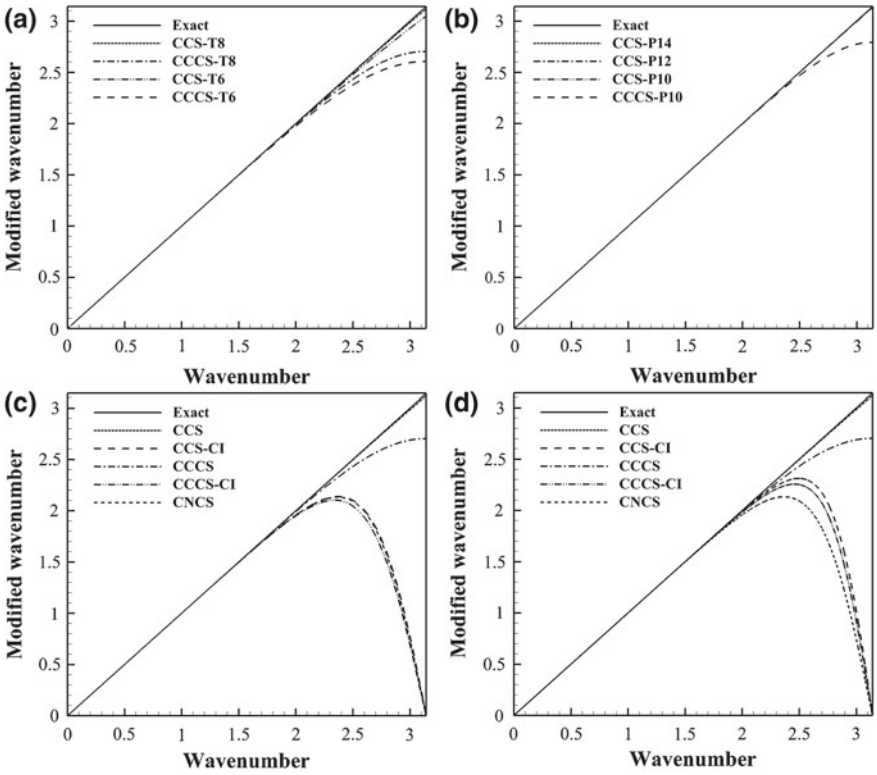


**Fig. 2** Modified wavenumber of CCS and comparison with CCCS and CNCS. **a** tridiagonal schemes; **b** pentadiagonal schemes; **c** eighth order tridiagonal CCS and CCCS combined with eighth order compact interpolation; **d** eighth order tridiagonal CCS and CCCS combined with tenth order compact interpolation

$$w' = 2\frac{a\sin\left(\frac{w}{2}\right) + \frac{b\sin(w)}{2} + \frac{c\sin\left(\frac{3w}{2}\right)}{3} + \frac{d\sin(2w)}{4} + \frac{e\sin\left(\frac{5w}{2}\right)}{5}}{2\beta\cos(2w) + 2\alpha\cos(w) + 1} \tag{6}$$

Figure 2 shows the modified wavenumber of CCS, it is clear that the resolutions of CCS are much better than those of CNCS and CCCS.

## 3 Numerical Experiments

In this section, we apply eighth order tridiagonal central compact scheme CCS-T8 as an example of CCS to simulate Euler and Navier–Stokes equations. The filter is chosen to be eighth order tridiagonal scheme, the time advancement is a third order TVD Runge–Kutta method.

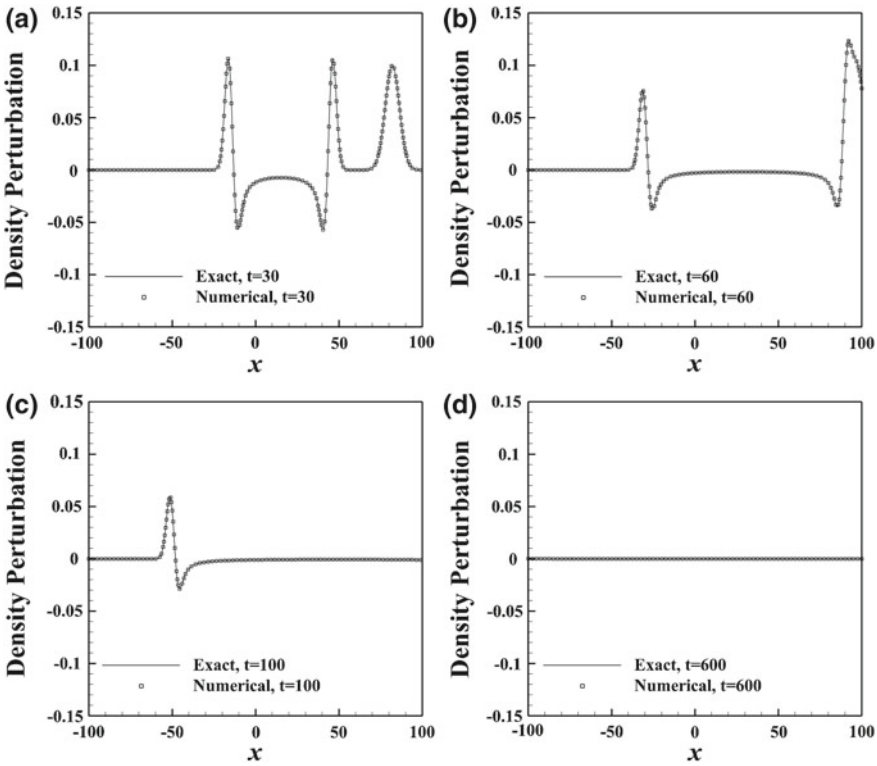


**Fig. 3** The distribution of density along $y = 0$ and the comparison with the exact solution at typical times of the benchmark of CAA

## *3.1 Benchmark of Computational Aeroacoustics*

We test a benchmark of Computational Aeroacoustics (Hardin et al. 1995). Sponge zones are used to absorb and minimize reflections from the computational boundaries. We take a $400 \times 400$ equally spaced mesh and perform the simulation until $t = 600$.

Figure 3 contains the distributions of density along $y = 0$ at typical times and their comparison with the exact solution. No noticeable difference is observed between the numerical results and the exact solution.

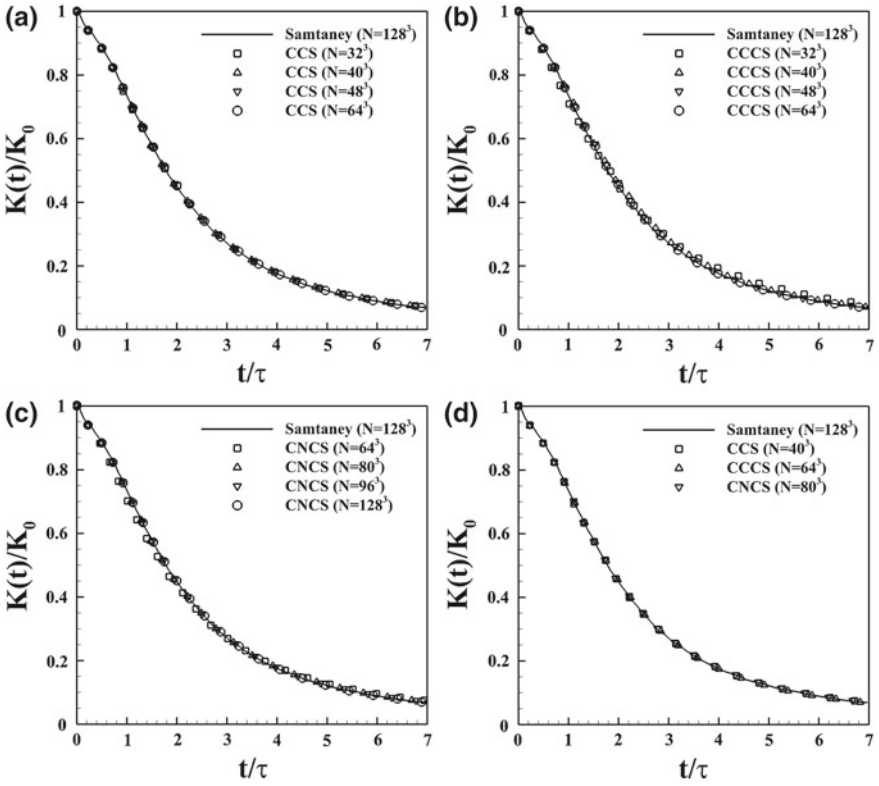


**Fig. 4** Grid convergence of the turbulent kinetic energy with different schemes

## *3.2 Three-Dimensional Decaying Isotropic Turbulence*

We start with a specified spectrum for the initial velocity field which is divergence free. The normalized temperature and density are simply initialized to unity at all spatial points. The dimensionless parameters are $Re = 519$ and $M = 0.308$, yielding the initial turbulent Mach number $M_t$ to be 0.3 and the initial Taylor microscale Reynolds number $\mathrm{Re}_\lambda$ to be 72.

The computational domain is $[0, 2\pi] \times [0, 2\pi] \times [0, 2\pi]$. Periodic boundary conditions are used in all boundaries. Figure 4 shows the grid converged results agree well with the numerical result of Samtaney et al. (2001). From this figure, we find that CCS needs $40^3$ grid density to reach grid converged solution, while the smallest grid density to obtain the grid converged results are $64^3$ and $80^3$ for CCCS and CNCS respectively. Again, we find that the resolution of CCS is much better than those of CNCS and CCCS. It is an ideal numerical scheme for DNS of turbulence.

## 4 Conclusions

In this paper, we design a new family of linear compact schemes, named central compact schemes, for the spatial derivatives in the Navier–Stokes equations based on the CCCS proposed by Lele (1992). Compared to other linear compact schemes, CCCS has nice spectral-like resolution, which may be a good method for the computation of multiscale problems. However, previous cell-centered compact schemes have the drawback that not all physical values on the stencil are used, which results in the numerical scheme not reaching its maximum accuracy order. The central compact scheme designed in this paper overcomes the drawbacks mentioned above. First, all physical values on the stencil are used. The schemes could reach the maximum accuracy order.

A systematic comparison with previous compact schemes, including cell-noded compact schemes and the cell-centered compact scheme, is made. The comparison shows the superiority of the central compact scheme over the previous compact schemes in accuracy and resolution. It appears to be an ideal numerical method for the computation of multiscale problems such as turbulence and aeroacoustics.

## References

Hardin JC, Ristorcelli JR, Tam CKW (1995) ICASE/LaRC workshop on benchmark problems in computational aeroacoustics (CAA). In: Proceedings of NASA conference publication 3300

Lele SK (1992) Compact finite difference schemes with spectral-like resolution. J Comput Phys 103:16–42

Samtaney R, Pullin DI, Kosovic B (2001) Direct numerical simulation of decaying compressible turbulence and shocklet statistics. Phys Fluids 13(5):1415–1430

Tam CKW (1995) Computational aeroacoustics: issues and methods. AIAA Journal 33(10): 1788–1796

# Stator Vane-Based Active Control of Turbofan Engine Noise

**I. Vinogradov and Y. Zhou**

**Abstract** Active control of rotor–stator interaction noise is studied numerically based on the surface oscillation of stator vanes. The problem is formulated in terms of 3D Euler equations linearized around uniform steady flow. Governing equations are solved with an explicit numerical technique based on a high-order approximation of spacial derivatives. It is found that the acoustic response with actuation on the suction side of the vanes differs considerably from that on the pressure side. The noise radiation also exhibits a strong dependence on the actuation frequency and position on the vane. Noise reduction of up to 80 % can be achieved.

**Keywords** Active noise control · Fan noise

## 1 Introduction

A significant portion of engine noise for modern transport aircraft comes from the fan stage, and is expected to be increased further with the introduction of ultra high bypass ratio engines. Traditional ways of noise reduction such as increasing rotor–stator distance and covering parts of the duct with acoustic liners are not effective for those engines, and alternative techniques are needed.

Active control is based on the idea that it is possible to generate a secondary acoustic field which can cancel upstream and/or downstream propagating sound waves. This work considers the case to mount oscillating actuators on the stator

I. Vinogradov (✉) · Y. Zhou
Institute for Turbulence-Noise-Vibration Interaction and Control, Shenzhen Graduate School, Harbin Institute of Technology, Shenzhen, China
e-mail: ivinogra@hitsz.edu.cn

Y. Zhou
Department of Mechanical Engineering, The Hong Kong Polytechnic University, Hung Hom, Hong Kong

Y. Zhou et al. (eds.), *Fluid-Structure-Sound Interactions and Control*,
Lecture Notes in Mechanical Engineering, DOI: 10.1007/978-3-642-40371-2_36,

vanes. Tonal noise is produced by the interaction between vanes and rotor wakes. Arranging actuators at the same location as the sources of noise to cancel may minimize the required input power (Curtis 1999).

One problem with active control in turbomachinery is to generate a secondary acoustic field of adequately high intensity. Therefore, it is important to have a clear understanding of how the position and size of the actuators and other parameters influence the acoustic response. Numerical simulation is highly suitable for this task but existing studies are mostly based on 2D techniques. This work aims to develop a 3D numerical simulation of sound produced in turbomachinery and to investigate the fundamentals of sound generation, propagation, and active control based on stator-mounted actuators.

## 2 Description of the Problem and Numerical Method

A stator is modeled as an isolated annular cascade of 24 vanes inside an infinite coaxial duct of inner radius $r_h$ and outer radius $r_t$, $r_h/r_t = 0.6$. A cylindrical coordinate system $(x, \theta, r)$ is used, as shown in Fig. 1. Flow inside the duct is assumed to be subsonic, inviscid, and non-heat conducting, while the flow variables $(\boldsymbol{u}, \rho, p)$ are represented as a sum of the steady flow variables $(\boldsymbol{U}, \rho_0, p_0)$ and small-amplitude unsteady distortions $(\tilde{\boldsymbol{u}}, \tilde{\rho}, \tilde{p})$, viz.:

$$(\boldsymbol{u}, \rho, p)(x, \theta, r, t) = (\boldsymbol{U}, \rho_0, p_0)(x, \theta, r) + (\tilde{\boldsymbol{u}}, \tilde{\rho}, \tilde{p})(x, \theta, r, t), \tag{1}$$

where $t$, $\rho$, $p$, $U$ and $\tilde{\boldsymbol{u}}$ denote time, density, pressure, steady and unsteady velocity vectors, respectively. $(U_x, U_\theta, U_r)$ and $(\tilde{u}_x, \tilde{u}_\theta, \tilde{u}_r)$ represent axial, circumferential, and radial velocity components of steady and unsteady parts, respectively. It is assumed that $|\tilde{\boldsymbol{u}}| \ll |\boldsymbol{U}|$, $|\tilde{\rho}| \ll |\rho_0|$ and $|\tilde{p}| \ll |p_0|$. Steady flow is assumed to be axial and uniform, while the evolution of the unsteady variables is described by Linearized Euler equations. Rotor wakes are modeled as a vortical gust imposed upstream (Atassi et al. 2004),

$$(\tilde{\rho}, \tilde{u}_x, \tilde{u}_\theta, \tilde{u}_r, \tilde{p}) = (0, -(m_g U_x)/(\omega r), 1, 0, 0)\exp(i(m_g\theta - \omega t)), \tag{2}$$

where $m_g$ is circumferential wave number and $\omega$ is frequency. Vanes have zero thickness and are placed along the steady flow streamlines, a single blade passage with $\theta$ varying from 0 to $2\pi/24$ is considered. Vane surface at $\theta = 0$ and $\theta = 2\pi/24$ will be called suction side and pressure side, respectively. Actuators are

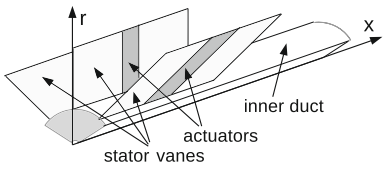


**Fig. 1** Stator cascade

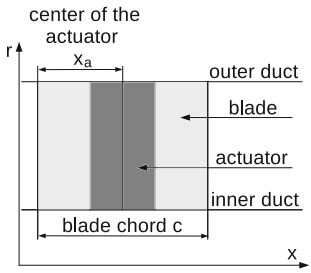


**Fig. 2** Stator-mounted actuator

modeled as stripes (Figs. 1, 2), are mounted on each vane at the axial position $x_a$ (Fig. 2) oscillating with the same $\omega$ as the gust. Non-dimensional variables, normalized with mean radius $r_m$, steady flow speed of sound $c_0$ and density $\rho_0$, are used. Non-impermeability condition is imposed at the rigid surfaces. The same boundary condition as (Farassat and Dunn 1999) is deployed for the surfaces of actuation. Non-reflecting boundary conditions (Atassi and Ali 2002) are imposed at the inlet and outlet of the domain, and the quasi-periodicity boundary condition (Atassi et al. 2004) is used at the free streamlines. The governing equations are solved in frequency domain with an explicit numerical technique based on a high-order approximation of spacial derivatives. The current approach is the extension of the algorithm used to analyze gust-cascade interaction noise (Vinogradov 2006).

## 3 Results and Discussion

The following uniform distribution of steady flow parameters is used:

$$(\rho_0, U_x, U_\theta, U_r, p_0) = (1, 0.5, 0, 0, 1/\gamma), \tag{3}$$

where $\gamma$ is the ratio of specific heats. The chord length is $c = 0.3491$, the actuator axial span is $0.2c$ and $m_g = 16$. Three cases with $\omega = 10$, 14 and 20 are examined corresponding to two, four, and seven downstream and upstream propagating modes, respectively. For each $\omega$ actuator position $x_a$ was varied from $x_a = 0.2c$ to $x_a = 0.8c$.

In the absence of incoming gust, the entire noise radiation results from actuation. Figure 3 presents the dependence on the actuator position $x_a$ of the downstream radiated modal power for suction- and pressure-side actuations. Each mode is denoted as ($m$ ,$n$) where $m$ is its circumferential wave number and $n$ is the number of zeroes of its pressure eigenfunction. It can be seen that the acoustic response differs greatly between suction- and pressure-side actuations. The dominant mode is (16 ,0) for the former and (8,0) for the latter, except for approaching $x_a = 0.2c$ (near the leading edge) where both modes contribute comparably. The $x_a$ has a significant influence on the acoustic response; even a small change may considerably alter the sound radiation. The ratio of downstream-to-upstream-radiated power is also

influenced by $x_a$ (Fig. 4). Note that the actuation amplitude is fixed. The problem is linear and the entire sound field is actuator-induced; the total power and the contribution from each mode are proportional to the square of the amplitude. As such, relative quantities such as the ratios of modal-to-total (Fig. 3) or downstream-to-upstream radiated power (Fig. 4) are independent of the amplitude.

In the presence of an incoming gust (2), downstream radiated sound power depends on the phase and amplitude of actuator oscillations. As such, steepest decent method (Press et al. 1992) was deployed to search for the optimum phase and amplitude in terms of the minimized downstream radiated sound power for given $\omega$ and $x_a$ When actuation is imposed simultaneously on both sides of the vane, the optimum phase and amplitude of each actuator were obtained similarly. Meanwhile, the upstream radiated sound power is subjected to two constraints, i.e., under its level without control (c1) and allowing an increase by 10 % of the gust-induced downstream radiated power (c2). Figure 5 shows that $x_a$ has a pronounced impact on the noise reduction, compared with the reference level, i.e., no control when the actuation amplitude is made zero. Due to the distinct distributions of power among propagating modes (Fig. 3), actuation on the pressure side is much more effective than on the suction side. Evidently, the control performance is greatly enhanced when actuation is imposed on both sides of the vane (Fig. 5). Active control using jets near the rotor suggested a difficulty in reducing noise when multiple propagating modes are present (Steger et al. 2010). There are seven propagating modes for the case considered but a good performance can still be achieved given a right $x_a$. Further investigation is underway to improve the control performance and to understand the physical mechanisms behind.

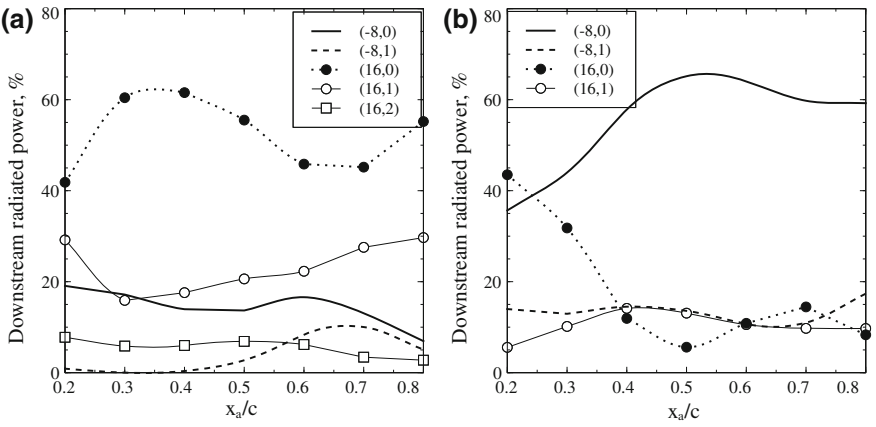


**Fig. 3** Dependence on $x_a$ of actuator-induced modal power as a percentage of the total power, actuation is imposed at $\omega = 20$ on **a** the suction side and **b** the pressure side

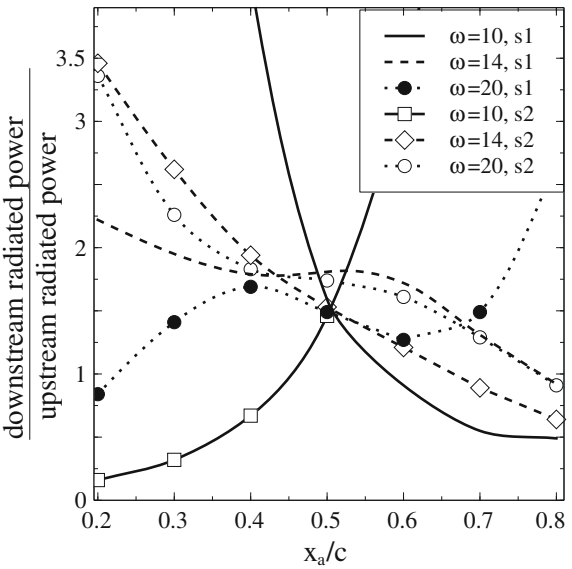


**Fig. 4** Dependence on $x_a$ of the ratio of downstream-to-upstream radiated actuator-induced powers, s1 and s2 denote suction- and pressure-side actuation, respectively

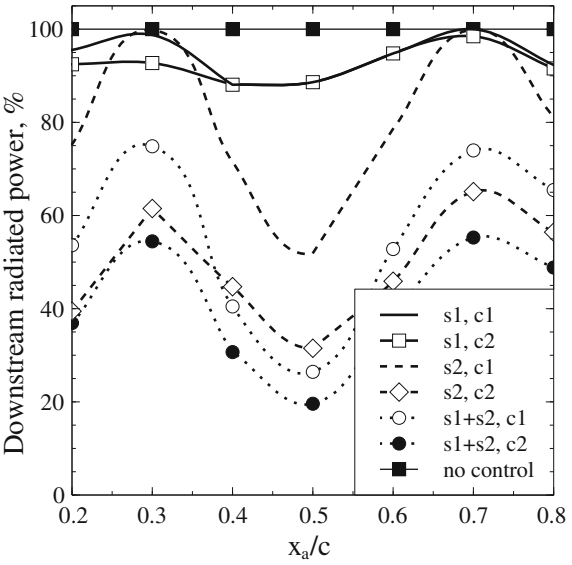


**Fig. 5** Downstream radiated power under control ($\omega = 20$), c1 and c2 are constraints imposed on upstream radiated power

## 4 Conclusions

Investigation has been conducted on active control of rotor–stator interaction noise based on unsteady actuation on stator vanes. The following conclusions can be drawn:

1. The proposed control has been demonstrated to be highly effective, reducing downstream radiated noise by up to 80 % given actuation on both sides of the vane and the optimum actuation position.
2. The control performance may depend on, *inter alia*, the actuation frequency, the side of the vane where actuation is imposed, and the axial position of actuation.
3. The present technique allows an effective control of noise even when multiple modes are present given the right position of the actuators.

**Acknowledgments** Yu Zhou wishes to acknowledge support given to him from the Natural Science Foundation of China through grants 11172085 and 50930007.

## References

Atassi O, Ali A (2002) Inflow/outflow conditions for time-harmonic internal flows. J Comput Acoust 10:155–182

Atassi H, Ali A, Atassi O et al (2004) Scattering of incident disturbances by an annular cascade in a swirling flow. J Fluid Mech 499:111–138

Curtis A (1999) Active control of fan noise by vane actuators. NASA/CR-1999-209156

Farassat F, Dunn M (1999) A simple derivation of the acoustic boundary condition in the presence of flow. J Sound Vib 224:384–386

Press W, Teukolsky S, Vetterling W et al (1992) Numerical recipes in Fortran 77: the art of scientific computing. Cambridge University Press, Cambridge, p 414

Steger M, Michel U, Ashcroft G et al (2010) Turbofan tone noise reduction by flow-induced unsteady blade forces. In: King R (ed) Active flow control II, NNFM 108:157-170. Springer, Berlin

Vinogradov I (2006) Interaction of acoustic and vortical waves with an annular cascade. PhD thesis, University of Notre Dame, Indiana, USA

# Controlling the Acoustic Resonance in a Corrugated Flow Pipe

**M. Amielh, F. Anselmet, Y. Jiang, U. Kristiansen, P. O. Mattéi, D. Mazzoni and C. Pinhède**

**Abstract** A new experimental study, aimed at investigating the coupling between the flow in a corrugated pipe, the acoustically generated flow oscillations, and the emitted resulting noise is carried out. Hot-wire anemometry, Particle Image Velocimetry, and microphone measurements are associated to characterize the flow. The flow response to the corrugation is shown to fit to the sixth to ninth acoustic modes of the pipe according to the flow rate. When low frequency acoustically generated oscillations interfere with this, one checks that they either significantly reduce the noise level or modify the peak frequencies. In addition, theoretical/numerical works are also performed, in order to provide an analytical framework describing the acoustical properties of such corrugated pipe flows.

**Keywords** Corrugated pipe · Acoustic control · Turbulent flow

## 1 Introduction

Our study is focused on a phenomenon often encountered in flow carrying pipes, since flow instabilities caused by geometric features may generate acoustic signals and thereafter interact with these signals in such a way that powerful pure tones are

M. Amielh · F. Anselmet (✉)
IRPHE, CNRS-AMU-ECM, UMR 7342, Marseille, France
e-mail: anselmet@irphe.univ-mrs.fr

F. Anselmet · D. Mazzoni
ECM, Marseille, France

Y. Jiang · U. Kristiansen
NTNU, Acoustics Research Centre, Trondheim, Norway

P. O. Mattéi · D. Mazzoni · C. Pinhède
LMA, CNRS, UPR 7051, Marseille, France

Y. Zhou et al. (eds.), *Fluid-Structure-Sound Interactions and Control*,
Lecture Notes in Mechanical Engineering, DOI: 10.1007/978-3-642-40371-2_37,

produced. Classic examples of flow generated tones are the Aeolian tones heard when a cylinder is put in an air flow, and the tone heard when blowing across the opening of a bottle. In industrial applications such tones may be powerful and, in addition to being annoying, damage machinery due to induced vibrations.

A modern example is found in the so-called "singing risers", or the gas pipes connecting gas production platforms to the transport network. These pipes can be very long, i.e., hundreds of meters, and are constructed in such a way that on the inside there is a periodic arrangement of cavities (corrugated pipes). The main reason for such a construction is to make the pipes flexible. Dry gas flowing across the cavities may generate high sound levels at some gas velocities. The high sound levels are both annoying and may cause vibrations with subsequent mechanical failures. No general mitigation technique has yet been found for this phenomenon, other than reducing the velocity and thereby the gas transport rate. Therefore, the industrial problems caused by singing risers are the inspiration for the present research.

Our general objective is to study the sound producing mechanisms involved when gas is flowing in pipes having one or a system of small cavities (Kristiansen et al. 2011). Velocity measurements will, in particular, enable us to determine the modifications which are induced on the flow organization (in terms of coherent structures, turbulence levels, regions of most intense shear, …). We aim at both understanding the origin of the noise generation, and then controlling it by acoustically generated oscillations that interfere with this and finally induce a significant reduction of the noise level or a shift in its peak frequency.

## 2 Experimental Setup

The whistling behavior of a corrugated pipe is investigated through a dedicated experiment (Fig. 1a). A pipe of length $L_{\text{pipe}} = 2$ m and rectangular cross-section $L_c \times L_s$, with $L_c = 100$ mm and $L_s = 25$ mm is inserted in the downstream part of the S6 IRPHE wind tunnel supplied by a low noise blower. The two opposite lateral walls occupying the long sides of the pipe section ($L_c$) are regularly corrugated with square-section cavities of length $L_{\text{cav}} = 10$ mm in the stream-wise direction and depth $D_{\text{cav}} = 10$ mm. The two opposite walls occupying short sides of the pipe section ($L_s$) are smooth walls. The pitch-length, i.e., the space-period of the corrugations in the stream-wise direction, is $L_p = 20$ mm. The pitch and cavity lengths are chosen such as $L_p = 2L_{\text{cav}}$. The upstream edges of these cavities are rounded precisely with a radius $\text{R}_{\text{cav}} = 3$ mm. The corrugated vein is machined in transparent plexiglass for optical diagnostics use (PIV, LDA…). A wooden acoustic box is placed downstream the corrugated vein. Two loudspeakers (subwoofers, SONIC-10MK2) are mounted face-to-face on this box in order to control the whistling of the corrugated pipe when working in phase. A long PVC (17 m) pipe of 200 mm diameter is placed downstream the box in order to play the role of a resonator. Two single hot-wires are used to characterize the flow velocity, the

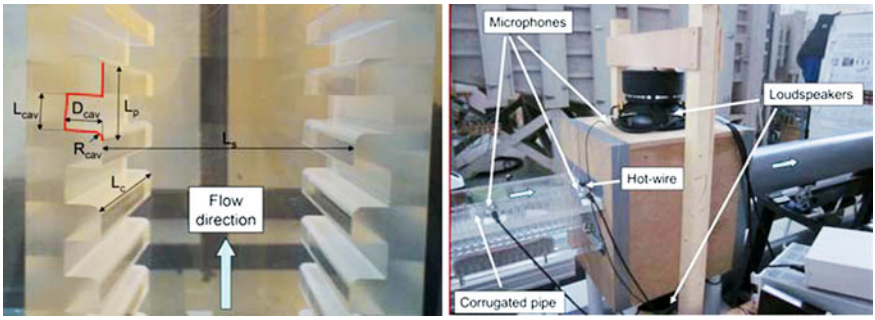


**Fig. 1** Experimental setup of the corrugated pipe. **a** Corrugation geometry and **b** Aero-acoustics measurement techniques associated to the flow investigation

first is located 5 mm upstream the vein entry and the other is put downstream, inside the vein, 19 mm just upstream its exit section. The vein is also equipped with three microphones that measure the acoustic response of the system (Fig. 1b).

## 3 Theoretical Approach

The sound emission by corrugated pipes in presence of a flow has been studied for quite a long time. A reference paper was proposed by Silverman and Cushman in 1989. More recently, Tonon et al. (2010) extended this study to multiple side branches system.

This whistling noise occurs from a frequency coincidence between the longitudinal eigenmodes of the pipe and the oscillation of the fluid in the separated boundary layer that develops over the cavities constituting the pipe corrugations. The longitudinal eigenfrequencies of a corrugated pipe are not equal to the eigenfrequencies of non-corrugated pipe of the same length. The presence of the corrugation induces a reduction of the speed of sound waves in the pipe. An approximation for the eigenfrequencies of a corrugated pipe was proposed by Elliott (2005). It consists in considering the frequencies of the same pipe without corrugations but with a modified speed of sound $c_{\text{eff}}$ given by:

$$c_{\text{eff}} = \frac{c_0}{\sqrt{1 + V_{\text{cav}} / \left(S_{\text{pipe}}\, L_p\right)}} \tag{1}$$

where $c_0 = 342$ m.s$^{-1}$ is the speed of sound in air, at normal ambient pressure/temperature conditions, $V_{\text{cav}}$ denotes the volume of the cavities contained between two sections of pipe separated by the pitch length $L_p$, $V_{\text{cav}} = 2\, L_{\text{cav}}\, D_{\text{cav}}\, L_c$ and $S_{\text{pipe}}\, L_p = 2\, S_{\text{pipe}}\, L_{\text{cav}}$ is the volume of the pipe between two sections with distance of $L_p$. The efficient speed of sound for the pipe used in our experiment is then

estimated as $c_{\text{eff}} = 289$ m.s$^{-1}$. The evaluated eigenfrequencies of our corrugated pipe are consequently given by:

$$f_c = n \frac{c_{\text{eff}}}{2 L_{\text{pipe,eff}}} \tag{2}$$

where $n = 1, 2, 3, \ldots$, and $L_{\text{pipe, eff}}$ is the effective pipe length that takes into account the end correction at each end.

## 4 Results

The velocities of the flow measured at the vein exit are varied in the range 0–25 m.s$^{-1}$. For the previously described arrangement, the whistling begins to be detected on the upstream hot-wire signal at 16 m.s$^{-1}$. The upstream hot-wire captures the pure tone of the oscillations while the turbulence that develops all along the corrugated pipe is superimposed to this sinusoidal oscillation on the downstream hot-wire signal (Fig. 2a). The response of the system in presence of a

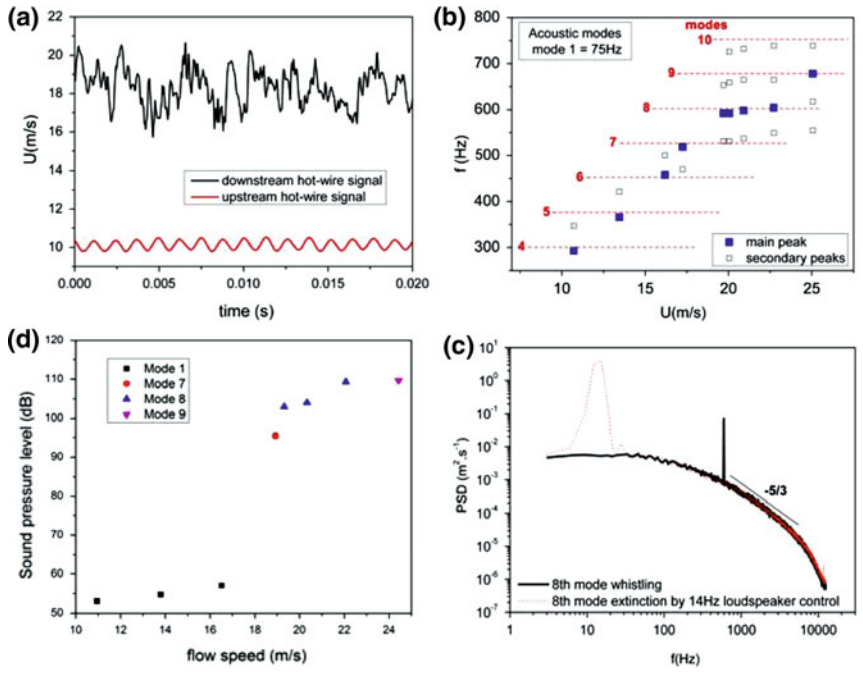


**Fig. 2** Response of the corrugated pipe to an internal flow. **a** Velocity time series from hot-wire, **b** Whistling frequencies with velocities, **c** Sound pressure levels (in dB) from microphone measurements, **d** Whistling control (extinction) by a low frequency sound

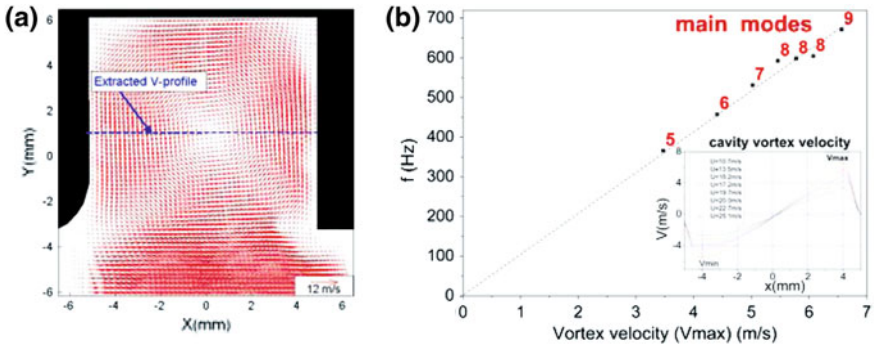


**Fig. 3** Mean vortex in the cavity. **a** Velocity vectors measured by PIV, **b** Relation between whistling frequency (main modes) and vortex velocity inside the cavity: $Vmax \approx L_{cav}.f$

flow is checked to be in agreement with the predicted eigenfrequencies. The whistling is confirmed by both air velocity and pressure measurements where spectral analyses highlight peaks at frequencies associated to sixth to ninth modes as shown in Fig. 2b. As indicated by Lattice Boltzmann simulations of the flow over a single cavity (Kristiansen et al. 2012), the noise emission occurring when a corrugated pipe is submitted to an internal flow of fluid is associated to the formation of vortices. These vortex structures are convected downstream by the flow to the downstream edge of the cavity and contribute to give a non-null time averaged acoustic power.

In the range of velocity 20–25 m/s measured by the downstream hot-wire, four modes were simultaneously detected with the spectral analysis of the upstream hot-wire signal. Above 17 m/s, only one strong mode is highlighted that is to be related to the sudden increase of sound pressure level as shown in Fig. 2c. This pure tone was checked to be completely extinguishable by a low frequency signal emitted at 14 Hz by the two loudspeakers as shown on the downstream velocity spectral analysis, and without any obvious modification of the turbulence at the pipe exit (Fig. 2d).

## 5 Conclusion: Perspectives

This new experimental setup will be interesting for the aero-acoustics study of flow in a corrugated pipe as shown by the first comparisons between theoretical analysis and experimental results. The flow structure will be thoroughly investigated by PIV, in particular in the cavities where vortices are highlighted (Fig. 3a and b). We plan to synchronize velocity snapshots with the pressure signal in order to analyze a possible vortex emission and its contribution to the corrugated pipe whistling. An associated numerical simulation is also developed for this purpose.

## References

Elliott JW (2005) Corrugated pipe flow. In: Wrigth MCM (ed.) Lecture notes on the mathematics of acoustics, Imperial College Press, London, pp 207–222

Kristiansen UR, Mattei P-O, Pinhede C, Amielh M (2011) Experimental study of the influence of low frequency flow modulation on the whistling behavior of a corrugated pipe. J Acoust Soc Am 130(4):1851–1855

Kristiansen U, Mazzoni D, Krogvig AB (2012) Aeroacoustic investigation of a flow pipe with a small cavity using the lattice Boltzmann method, 35th Scandinavian symposium on physical acoustics, Geilo, Norway

Silverman MP, Cushman GM (1989) Voice of the dragon: the rotating corrugated resonator. Eur J Phys 10(4):298–304

Tonon D, Landry BJT, Belfroid SPC, Willems JFH, Hofmans GCJ, Hirschberg A (2010) Whistling of a pipe system with multiple side branches: comparison with corrugated pipes. J Sound Vib 329(8):1007–1024

# A Three-Dimensional Semi-analytical Model for the Prediction of Underwater Noise Generated by Offshore Pile Driving

**A. Tsouvalas and A. V. Metrikine**

**Abstract** In this work, the problem of underwater noise generated during the offshore installation of steel monopiles is addressed. The monopiles are driven into place with the help of hydraulic hammers. During installation, the underwater noise levels generated can be very high and harmful for the marine life. A linear semi-analytical model is developed which is able to represent the dynamics of the coupled vibro-acoustic system. The pile is modelled using a high order thin shell theory whereas both water and soil are modelled as three-dimensional continua. The results indicate that the near-field response in the water column consists of pressure conical waves due to the the supersonic compressional waves in the pile generated by the impact hammer. The soil response is dominated by vertically polarised shear waves. Scholte waves are also generated at the water-seabed interface and can produce pressure fluctuations in the water column that are particularly significant close to the sea floor.

**Keywords** Pile driving · Underwater noise · Vibro-acoustics · Solid-fluid interface

## 1 Introduction

Underwater noise from offshore pile driving has gained considerable attention in recent years due to the large-scale offshore construction activities. The majority of the models used nowadays for the prediction of the sound levels is based on numerical techniques and are computationally very demanding for the frequency bandwidth of interest. A novel approach is adopted in this study, in which the coupled vibro-acoustic problem is solved at once both for the near- and the

A. Tsouvalas (✉) · A. V. Metrikine
Delft University of Technology, Stevinweg 1, 2628 CN Delft, The Netherlands
e-mail: a.tsouvalas@tudelft.nl

Y. Zhou et al. (eds.), *Fluid-Structure-Sound Interactions and Control*,
Lecture Notes in Mechanical Engineering, DOI: 10.1007/978-3-642-40371-2_38,

far-field. The model is similar to, but significantly more advanced than, the one presented by the authors in (Tsouvalas and Metrikine 2013). The advance is associated with a three-dimensional description of the soil adopted in the new model. The paper is composed as follows. At first, the mathematical background of the model and the solution procedure are briefly introduced. Subsequently, the response of the system is studied for different soil conditions. Emphasis is placed on the examination of the influence of soil elasticity on the pressures in the water column. To the authors' knowledge the latter effect has not been reported in the literature so far.

## 2 Model Description

The pile is described by an appropriate thin shell theory which includes the effects of shear deformation and rotational inertia (Belov et al. 1999). The water is treated as a three-dimensional compressible medium with a pressure release boundary describing the sea surface. The soil is described as a three-dimensional continuum able to support both dilatational and shear waves and is terminated at the pile tip level with a rigid boundary as shown in Fig. 1. The governing equations describing the shell vibrations in the time domain read:

$$\boldsymbol{L}\boldsymbol{u}_p + \boldsymbol{I}_m\boldsymbol{u}_p = -H(z-z_2)\boldsymbol{t}_s + (H(z-z_1) - H(z-z_2))\boldsymbol{p}_f + \boldsymbol{f}_e \qquad (1)$$

In Eq. 1, $\mathbf{u}_p(z,\boldsymbol{\theta},t)$ is the displacement vector of the mid-surface of the shell and $\boldsymbol{L}$, $\boldsymbol{I}_m$ are the stiffness and modified inertia operators of the shell structure, respectively, based on the chosen thin shell theory (Tsouvalas and Metrikine 2013). The term $\boldsymbol{t}_s(R,\boldsymbol{\theta},z,t)$ represents the boundary traction vector that takes into

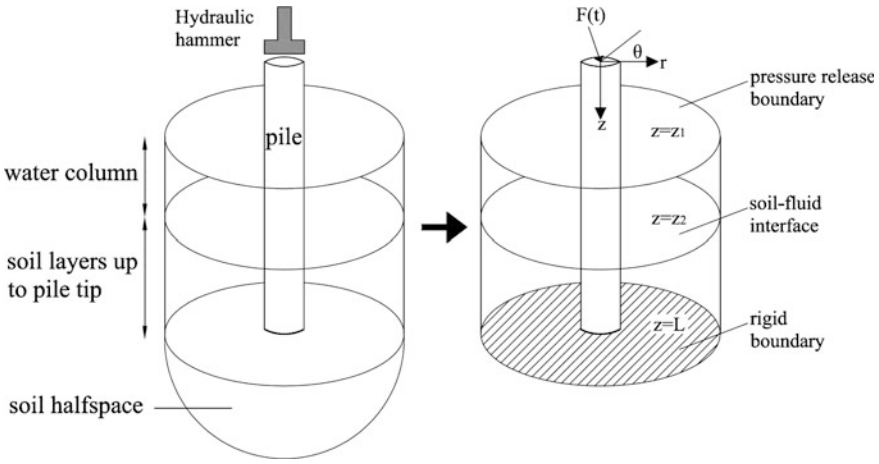


**Fig. 1** Geometry of the model

account the reaction of the soil at $z_2 < z < L$. The term $\boldsymbol{p}_f(R, \boldsymbol{\theta}, z, t)$ represents the fluid pressure exerted at the outer surface of the shell at $z_1 < z < z_2$ and $\boldsymbol{f}_e(z, \boldsymbol{\theta}, t)$ is the external force vector. The functions $H(z - z_i)$ are the Heaviside step functions, which account for the fact that the soil and the fluid are in contact with different segments of the shell. The motion of the inviscid fluid can be fully described by a velocity potential $\phi_f(r, \boldsymbol{\theta}, z, t)$:

$$\nabla^2 \phi_f(r, \boldsymbol{\theta}, z, t) - \frac{1}{c_f^2} \frac{\partial^2 \phi_f(r, \boldsymbol{\theta}, z, t)}{\partial t^2} = 0, \tag{2}$$

where $c_f$ is the sound speed in the water column. The motion of the soil medium is described by the following set of linear equations:

$$\mu_s \nabla^2 \boldsymbol{u}_s - (\lambda_s + \mu_s) \nabla \nabla \cdot \boldsymbol{u}_s - \rho_s \frac{\partial^2 \boldsymbol{u}_s}{\partial t^2} = 0, \tag{3}$$

with $\lambda_s$ and $\mu_s$ being the complex *Lame* constants of the soil and $\boldsymbol{u}_s(r, \boldsymbol{\theta}, z, t)$ representing the soil displacement vector. The body waves generated at the tip of the pile are not accounted for in the framework of this model since they are not expected to contribute significantly to the acoustic field (Masoumi and Degrande 2008). The solution of the system of coupled partial differential equations is based on the dynamic sub-structuring technique, in which the total system is divided into two subsystems; the shell structure and the soil-fluid exterior. The analytical approach is based on the following steps: (1) solution of the eigenvalue problem of the shell without the presence of the fluid and the soil; (2) solution of the eigenvalue problem of the acousto-elastic domain; (3) solution of the coupled system of equations resulting from the substitution of the obtained solutions for the shell and the soil–water domain into the interface conditions. The pile vibrations can be expressed as a superposition over the *in vacuo* shell modes:

$$u_{j,p}(z, \boldsymbol{\theta}, t) = \sum_{n=0}^{\infty} \sum_{m=1}^{\infty} A_{nm} \; U_{jnm,p}(z) \cos\left(\delta_{j\theta} \frac{\pi}{2} - n\boldsymbol{\theta}\right) e^{i\omega t}, \tag{4}$$

where $\delta_{j\theta}$ is the Kronecker delta. The subscript $p$ refers to the pile, $n = 0, 1, 2, \ldots, \infty$ is the circumferential order and $m = 0, 1, 2, \ldots, \infty$ is the axial order. The functions $U_{jnm,p}(z)$ with $j = z, \theta, r$ describe the axial distributions for the axial, circumferential, and radial displacement fields, respectively. $A_{nm}$ are the undetermined modal factors. For the exterior soil-fluid domain the solution is found by using the classical Lamb decomposition of Eq. 3, in terms of three scalar potential functions. The displacement field can be represented as:

$$u_{j,s;f}(r, z, \boldsymbol{\theta}, t) = \sum_{n=0}^{\infty} \sum_{k=1}^{\infty} C_{nk} U_{jnk,s;f}(z) S_{nk}(r, \boldsymbol{\theta}) e^{i\omega t} \tag{5}$$

The subscripts $s$ and $f$ refer to the soil and fluid respectively. The eigenfunctions $U_{jnk,s;f}(z)$, along the vertical coordinate (index $k$), are obtained by satisfying the set

of boundary and interface conditions at $z = z_i, L$ with $i = 1, 2$ in this case. The functions $S_{nk}(r, \theta)$ are Fourier–Bessel components. The field in the radial direction is described by Hankel functions of the second type and of different order $n$. The field in the tangential coordinate consists of trigonometric functions. By enforcing force equilibrium and displacement compatibility in the shell-soil/fluid interface, the original system of coupled partial differential equations is reduced to a system of coupled algebraic equations. To achieve this, the orthogonality condition of the shell structure *in vacuo* and the one of the exterior (to the pile) acousto-elastic domain is used in order to correlate the unknown sets of modal coefficients $A_{nm}$ and $C_{nk}$.

## 3 Results and Discussion

In this section results are presented for a system with the geometrical configuration and the material properties as shown in Table 1. The load is applied vertically at the head of the pile and corresponds to a hammer input energy of 90 kJ. The maximum force magnitude equals 12MN and the duration of the main pulse is equal to 0.005 s. The generated wave field for the two soil configurations is shown in Fig. 2. As can be seen, the near-field response in the water column consists of pressure conical waves due to the supersonic compressional waves in the pile generated by the impact hammer. The soil response is dominated by vertically polarised shear waves. In addition, Scholte waves are generated at the water-seabed interface which can produce pressure fluctuations in the water column that are particularly significant close to the sea floor. Regarding the influence of soil elasticity, it can be noticed that the pressures in the water column close to the

**Table 1** System parameters and material properties

| Parameter | Symbol | Value | Unit |
|---|---|---|---|
| Young modulus of steel | $E_p$ | 210,000 | MPa |
| Poisson ratio | $\nu_p$ | 0.28 | – |
| Density of steel | $\rho_p$ | 7,850 | $\text{kgm}^{-3}$ |
| Pile length | $L$ | 32.4 | m |
| Pile diameter | $D$ | 0.92 | m |
| Pile wall thickness | $t$ | 0.02 | m |
| Sea surface level | $z_1$ | 6.5 | m |
| Seabed level | $z_2$ | 13.4 | m |
| Soil elasticity modulus | $E_s$ | 100 | MPa |
| Soil density | $\rho_s$ | 1,600 | $\text{kgm}^{-3}$ |
| Poisson ratio of the soil | $\nu_s$ | 0.40 | – |
| [a]Soil elasticity modulus | $E_s$ | 500 | MPa |
| Water density | $\rho_s$ | 1,000 | $\text{kgm}^{-3}$ |
| Water sound speed | $c_f$ | 1,500 | $\text{ms}^{-1}$ |

[a] Value adopted for the case of a stiff soil only

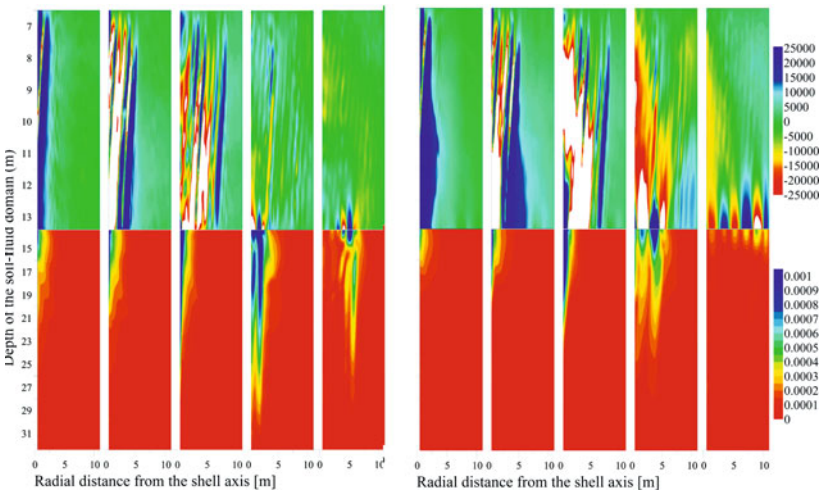


**Fig. 2** Pressures in the water in Pascals (*top*) and displacement norm in the soil in metres (*bottom*) for different time moments after the impact, in the case of a soft soil (*left*) and of a stiff soil (*right*). In both figures from left to right: $t = 0.004$ s; $t = 0.006$ s; $t = 0.008$ s; $t = 0.02$ s; $t = 0.045$ s

seabed-water interface are increased for the stiffer soil configuration. It is observed that for stiffer soil sediments, the penetration depth of the Scholte wave into the soil decreases and the energy is mainly localised in the fluid zone.

## 4 Conclusions

In this paper, a novel approach is presented for the study of the coupled vibro-acoustics of piles in layered media. The results indicate that the near-field response in the water column consists mainly of pressure conical waves. The soil response is dominated by shear waves with almost vertical polarisation. Scholte waves are generated at the sea bottom which can produce pressure fluctuations in the water column that are particularly significant close to the sea floor. It becomes apparent from the present analysis that a description of the soil by a *Winkler* type foundation or by an equivalent acoustic fluid is far from being realistic. In the first case, the non-local distribution of the soil reaction is neglected, whereas in the second case the ability of the soil to provide shear resistance in unaccounted for. It is shown here that it is the latter property that gives rise to considerable shear deformations in the soil which an acoustic model intrinsically disregards.

## References

Belov AV, Kaplunov JD, Nolde EV (1999) A refined asymptotic model of fluid-structure interaction in scattering by elastic shells. Flow Turbul Combust 61:255–267

Masoumi HR, Degrande G (2008) Numerical modeling of free field vibrations due to pile driving using a dynamic soil-structure interaction formulation. J Comput Appl Math 215(2):503–511

Tsouvalas A, Metrikine AV (2013) A semi-analytical model for the prediction of the underwater noise from offshore pile driving. J Sound Vib 332(13):3232–3257

# Vibroacoustic Coupling of Piping with Rubber Hose and Elastic Supports

**Zhiyong Yin, Wenwei Wu and Zhenping Weng**

**Abstract** The free stress and pressure waves in fluid filled piping are investigated numerically. The motivation of this work is to find measures and rules for the low frequency vibration and noise reduction for piping designers. The Timoshenko beam equation and extended water hammer equation are used to calculate the transfer matrix of two piping configurations. And the wave propagation constants are then obtained by get the eigenvalue of the transfer matrix. It's found that when the support stiffness reaches a critical value $k_c$ the piping will be a long bend wave filter. It's the same as obtained by increasing the support distance. The flexible hose shows good performance in controlling both stress and pressure waves, but the support shows insignificant capability in pressure wave reduction.

**Keywords** Wave propagation · Pipe support · Flexible hose · Vibration reduction

## 1 Introduction

Piping systems in vessels, power plants, and oil supply system always undergo vibration, flow excitation and pulsations from pump and valve. Flexible hoses and dampers are commonly used to reduce the vibration and noise caused by these sources. Generally, most of the middle and high frequency noise reduced by these components readily. However, for the low frequency noise control, it's necessary to tend to the layout of piping. Moreover, vibration from pump and the fluid borne sources are mainly long waves. It would be helpful to piping designers if there are instructions on how to make use of those measures. Unfortunately, few studies in the literature touch upon this area. Koo and Park (1998) had investigated the

Z. Yin (✉) · W. Wu · Z. Weng
China Ship Scientific Research Center, Wuxi, Jiangsu, China
e-mail: wq_708@163.com

Y. Zhou et al. (eds.), *Fluid-Structure-Sound Interactions and Control*,
Lecture Notes in Mechanical Engineering, DOI: 10.1007/978-3-642-40371-2_39,

possibility of reduce the fluid conveying piping vibration by using periodic supports. Their research validated the applicability of the periodic supports to vibration reduction, but didn't give advice on how to place the supports. The present paper focuses on the low frequency vibration and acoustic wave propagation features in liquid filled piping with flexible hoses and supports. A comprehensive parametric study has been made to get the relationship between the configuration of the piping and the attenuation of waves, and general design rules are put forward accordingly.

## 2 Parametric Study

### *2.1 Numerical Method*

Fluid filled cylindrical pipe behaves as a beam below its cut-on frequency. For most of the industry piping, vibration sources from rotating machine and fluid flow are well below its cut-on frequency. So the extended water hammer equations and a fluid filled Timoshenko beam equation (Wiggert and Tijsseling 2001) is adopted to study the axial and bend wave transmission in piping, respectively. According to these equations, the wave propagation constants for piping with flexible hose and supports, are calculated by a numerical method. Figure 1 presents the piping configurations. For each case, the over all transfer matrix [*T*] is calculated and then the wave propagation constants are get by

$$\boldsymbol{\lambda}(f,k,l) = \ln(\mathrm{eig}(\mathbf{T})) \tag{1}$$

where $f$ is frequency, $k$ is the stiffness of pipe support, $l$ is the axial length of waveguide, while eig($\mathbf{T}$) means get the eigenvalues of matrix $\mathbf{T}$ in diagonal form. For piping with flexible hoses and dampers, $\boldsymbol{\lambda}$ is a diagonal complex matrix. The absolute value of its real part is the wave attenuation index, while the imaginary part represents the phase change. By the formula above, the wave number frequency spectrum at a variety of parameters is plotted.

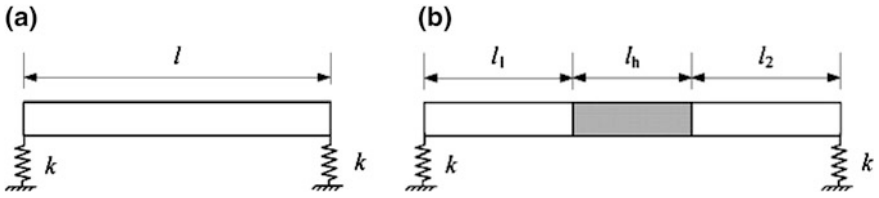


**Fig. 1** Piping configurations with (**a**) supports, and (**b**) supports and flexible hose. Pipe wall: $E = 2.0 \times 10^{11}$ N/m$^2$, $\rho = 7{,}850$ kg/m$^3$, $\mu = 0.3$. Fluid: $K = 1.9 \times 10^9$ N/m$^2$, $\rho = 1{,}000$ kg/m$^3$. Hose: $E = 1.5 \times 10^8$ N/m$^2$, $\rho = 1{,}700$ kg/m$^3$, $\mu = 0.35$, $l_h = 0.175$ m, inner radius $d = 0.08$ m, wall thickness $h = 0.01$ m

# 3 Results and Discussion

## 3.1 Configuration 1: Piping with Supports

Figure 2 shows the bend wave propagation characteristics for piping with supports. The effects of $l$ and $k$ are studied. $\lambda_1$ and $\lambda_2$ corresponds to shear wave and bend wave, respectively. It can be observed that there exists a frequency, below which the two waves are all evanescent (with the real part nonzero, imaginary part equals 0 or $\pm\ \pi$). It will move to high frequency and stop at a certain value $f_c$ with the supports stiffness $k$ increase. This feature is similar to the cut-on frequency of higher-order wave in fluid filled cylindrical pipe. $f_c$ is the natural frequency of the pipe. With the pipe length $l$ increases, $f_c$ moves to low frequency. From the point view of wave dynamics, when the simply supported pipe resonates, the bend wave will pass the support without resistance, but the shear wave will not. This can be verified from the fact that $f_c$ appears in $\lambda_2$, but doesn't come up in $\lambda_1$.

It should be noted that there also exists a $k_c$ that corresponds to $f_c$. Figure 3 plots the dimensionless stiffness $k_c^* = k_c l^3/EI$ to $l$ at three pipe sections. It's interesting that $k_c^*$ rapidly drops to a limit value with $l$ increases. This value, denoted by $k_{cl}^*$, approximately equals 78. When $l$ is small, the discrepancy between $k_c^*$ and $k_{cl}^*$ diminishes as the radius and thickness decreases. In fact, it is due to shear deformation in the pipe. The effect of shear deformation is significant in short pipe. It's necessary to take this into account in piping design. Theoretically, the results above demonstrates the wave propagation characteristic of periodic piping made up of cells in Fig. 1. As we didn't introduce any boundary conditions during the simulation, the results based on one cell are still instructive for a non-periodic piping.

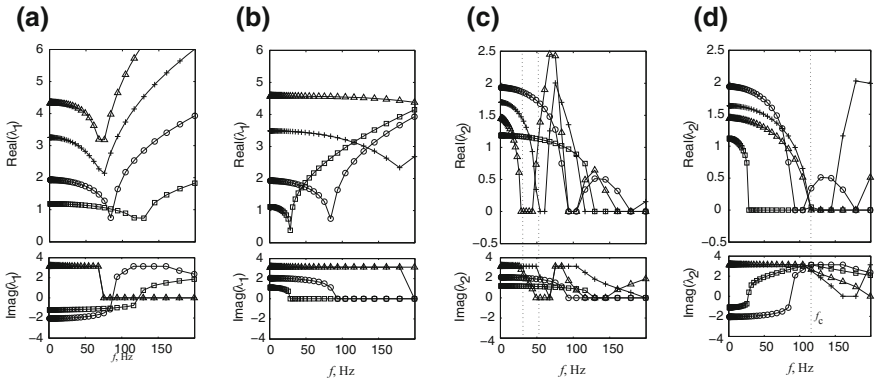


**Fig. 2** Wave propagation constants for piping configuration (**a**). **a, c** is the effects of $l$ ($k = 1.5 \times 10^6$ N/m): *squarebox*, $l = 0.5$ m, *circle*, $l = 1.0$ m, *plus*, $l = 1.5$ m, *triangle*, $l = 2.0$ m. **b, d** is the effects of $k$ ($l = 1.0$ m): *squarebox*, $k = 1.0 \times 10^5$ N/m, *circle*, $k = 1.0 \times 10^6$ N/m, *plus*, $k = 4.0 \times 10^6$ N/m, *triangle*, $k = 1.0 \times 10^7$ N/m

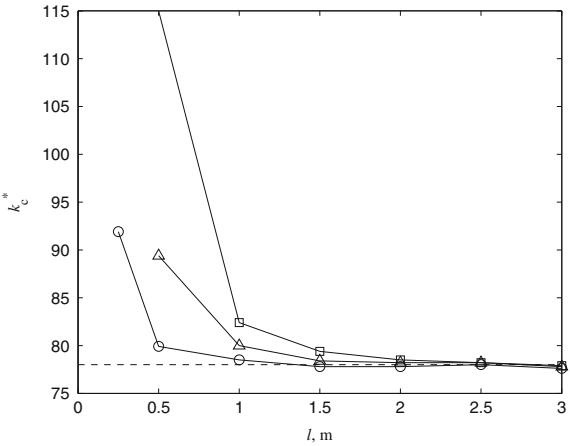


**Fig. 3** Dimensionless support stiffness $k_c$* for piping with different length $l$ and section size (inner diameter $d$, and wall thickness $h$): *squarebox*, $d = 0.1$ m, $h = 7$ mm, *triangle*, $d = 0.08$ m, $h = 4.5$ mm, *circle*, $d = 0.04$ m, $h = 4.5$ mm

## 3.2 Configuration 2: Piping with Flexible Hose and Supports

Figure 4 plots $k_c, f_c$ at different $l_1/l_2$ ratio and at different $l_2$ ($l_1 = 0$). In Fig. 4a, $k_c$ and $f_c$ monotonically decrease with $l_1/l_2$ increase. It means that for a fixed support distance, flexible hose supported at one of its end have the widest wave stop band, while hose placed at middle have the least stop band width. Figure 4b shows that when a hose supported at one side, and the connected pipe supported at another side, with the length of the pipe increases, $k_c$ and $f_c$ are all drop. One may get a wide wave stop band in low frequency by supporting the hose at its two ends, but the support stiffness would be too high to fulfill.

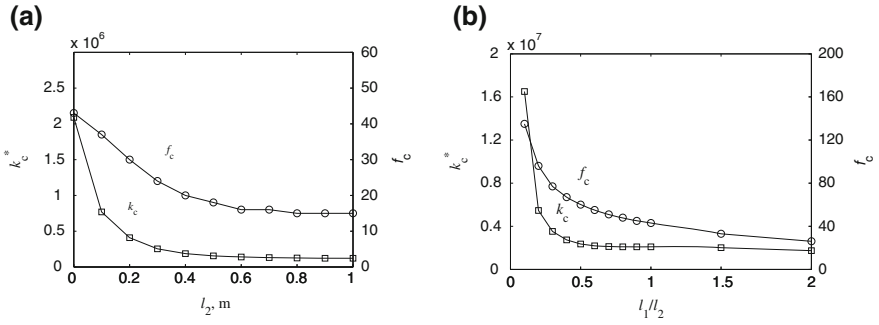


**Fig. 4** The $k_c$ and $f_c$ for the piping configuration (**b**). (**a**) is the effects of $l_1/l_2$, (**b**) is the effects of $l_2$ ($l_1 = 0$)

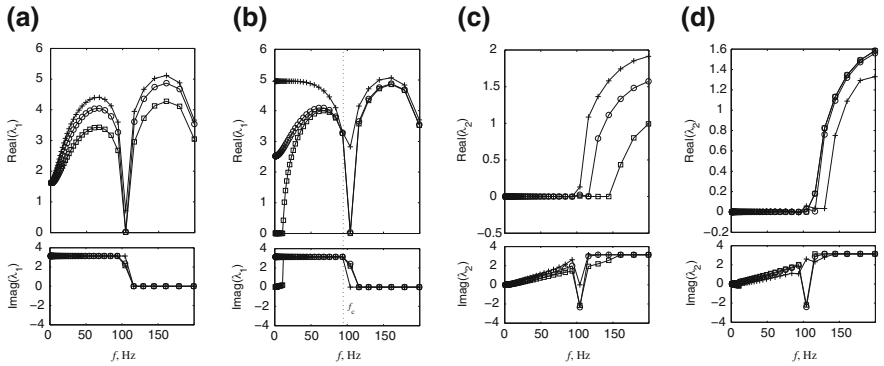


**Fig. 5** Wave propagation constants for piping configuration (**b**). **a**, **c** is the effects of $l$ ($k = 5.0 \times 10^6$ N/m): *squarebox*, $l = 0.5$ m, *circle,* $l = 1.0$ m, *plus*, $l = 1.5$ m. **b**, **c** is the effects of $k$ ($l = 1.0$ m): *squarebox*, $k = 1.0 \times 10^6$ N/m, *circle*, $k = 1.0 \times 10^7$ N/m, *plus*, $k = 1.0 \times 10^8$ N/m

The axial and pressure wave reduction capability of the flexible hose and support combination is also investigated. In this case, the hose jointed with only one pipe, and they are supported at axial direction. Figure 5 presents wave propagation constants at different $k$ and $l$, where $\lambda_1$ and $\lambda_2$ are propagation constants for the longitudinal wave and pressure wave, respectively. We can also find a low frequency wave stop band in $\lambda_1$, but no longer in $\lambda_2$. The corresponding $k_c$ to $f_c$ is much more higher than that of configuration (a), due to the high axial stiffness of pipe. The support stiffness makes much less impact on $\lambda_2$ compared with pipe length. As the hose is much more "softer" than the steel pipe, pressure wave still exhibits a higher frequency wave stop band. The lower bound move towards low frequency when increase the adjacent pipe length.

## 4 Conclusions

The bend and axial free wave propagation characteristics in fluid filled piping with hose and supports are studied numerically based on the Timoshenko beam equation and the extended waterhammer formula. The influence of support distance and stiffness are investigated parametrically. It's manifested that piping with supports characterize a potential low frequency bending and axial wave filter. It's important to choose a stiff enough support to guarantee the wave stop capability for long waves. But, as the weak coupling of the stress wave and pressure wave, its hard to control the pressure wave by choosing the support stiffness.

## References

Koo GH, Park YS (1998) Vibration reduction by using periodic supports in a piping system. J S V 210(1):53–68

Wiggert DC, Tijsseling AS (2001) Fluid transients and fluid-structure interaction in flexible liquid-filled piping. ASME Applied Mechanics Reviews

# Low-Frequency Noise Propagation from a Small Wind Turbine Tower

**Ehsan Mollasalehi, Qiao Sun and David H. Wood**

**Abstract** A major barrier to the acceptance of small wind turbines is that they are perceived to be noisy particularly when mounted on monopole towers rather than traditional guy-wired ones. Noise emission from a 2.4 kW downwind turbine due to its 10.2 m monopole tower was investigated. Tower vibration was measured using 24 accelerometers. A finite-element tower model combined with simple assumptions for the turbine and wind loads allowed the noise to be obtained from solution of the wave equation. The measured vibration levels were matched to the tower model amplitudes. Sound pressure level produced by the fluid–structure interaction reached 30 dB at about 11 m from the tower and decreased to 5 dB 1 km away. Propagation switched from cylindrical to hemispherical when the distance was about 200 times larger than the tower height.

**Keywords** Small wind turbine tower · Low frequency noise propagation · Fluid–structure interaction · Acoustic-structure interaction

## 1 Introduction

Vibration generation and consequent noise propagation have been one of the issues in the development of sustainable wind energy. Less noisy turbines have become available in recent decades due to improved design of airfoils and other components such as bearings and generators. Still, there are some missed areas which need more investigation. One of those is how the tower contributes to total noise generation. Monopole towers are thought to amplify the generated noise like a speaker, at low frequency and particularly in the infrasound range. Furthermore,

E. Mollasalehi · Q. Sun · D. H. Wood (✉)
Department of Mechanical and Manufacturing Engineering, University of Calgary, Calgary, Canada
e-mail: dhwood@ucalgary.ca

Y. Zhou et al. (eds.), *Fluid-Structure-Sound Interactions and Control*,
Lecture Notes in Mechanical Engineering, DOI: 10.1007/978-3-642-40371-2_40,

a tower will behave more like a line source than the nacelle and blades, and thus may cause significant noise even if its sound power level is low. Vibration from nacelle components and blades can be easily transferred to the tower (Marmo and Carruthers 2010) and amplified. The generated noise is propagated cylindrically because of tower's height. The authors showed in (Mollasalehi et al. 2012) that most of vibration energy is concentrated in lower frequency bands, i.e., below 20 Hz, using 24 accelerometers on the 10.2 m tower of a 2.4 kW wind turbine. The first three natural frequencies were excited more often than the higher modes while blade rotational speed varied up to 250 rpm. This work aims to estimate noise level produced by the tower using fluid/acoustic-structure interaction model, and conclude whether it is significant. The main reason to determine the noise level computationally is that the overall noise levels are low and are generated by multiple sources, which are difficult to separate without using microphone arrays and sophisticated signal processing (Bowdler and Leventhall 2011).

## 2 Model Development

The studied turbine was a 2.4 kW with 10.2 m monopole tower with downwind rotor of 3.7 m diameter. The base and top diameters of the tower were 27.56 and 15.67 cm, respectively. The tower thickness was 3.416 mm. In terms of vibration analysis, the tower and turbine can be considered as a beam with a mass at the top due to the nacelle and blades with specific center of mass. In other words, although blades have aerodynamic interactions with the tower, structural and modal parameters are affected only by the tip load with correct mass properties to represent the turbine and nacelle components contribution to the tower vibration. Other than the tower, three acoustic domains were added to model the fluid/acoustic domain. The first and main one represents the computational domain called "Air 1". Its size was chosen in reference to IEC 61400-11 (2002). For determining the sound power level of horizontal axis turbines, the microphone should be placed at $R = H + D/2$ where $H$ and $D$ are the height of the turbine axis, and the blade diameter, respectively. The outer domain is defined due to avoid any reflections with a perfectly matched layer on the boundaries named "Air 2". Last but not least, there is an air domain inside of the tower. This configuration is shown in Fig. 1a. Air 1 was set to be one-way coupled because it was assumed that the wave propagation in such a large domain in reality has no feedback on the tower. This means the vibration generated from the tower produces sound, while the generated sound does not affect the tower vibration. In contrast, because the space inside of the tower is too small to neglect sound pressure effect on the structure, two-way coupling was defined for inside air domain.

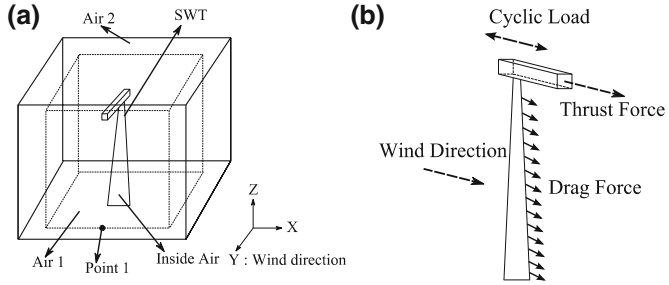


**Fig. 1** **a** Domains schematic. **b** Loads on the tower

## 3 Forces on the Tower

According to the IEC Simple Load Model (2006), the main turbine forces transmitted to the tower are the thrust and drag as noncyclic forces, and fatigue as cyclic which is the consequence of other loads. They are shown in Fig. 1b.

Thrust, $T$, and drag, $D$, are defined as:

$$T = \frac{1}{2} C_T \rho U^2 A \text{ and } D = \frac{1}{2} C_D \rho U^2 d \tag{1}$$

where $C_T$, $C_D$, $A$, and $d$ are thrust coefficient, drag coefficient, air density, blade swept area, and tower diameter, respectively. At wind speed of $U = 6$ m/s, which we estimate was the approximate speed during the accelerometer measurements, the following values can be considered: $C_T = 1.0$ (consistent with the value at the Betz Limit), $C_D = 1.0$ (cylinder in low Reynolds number), $=1.2$ kg/m$^3$, and $d = 21.6$ cm. Thrust and drag, therefore, are: $T = 239$, $D = 5$ N.

The cyclic load, $F_{\text{sh}}$, on the shaft is given by Eq. (24) of (IEC 2006):

$$F_{\text{sh}} = \frac{3}{2} \frac{\lambda Q}{R} \tag{2}$$

where $R$, and $Q$ are rotor radius, tip speed ratio, and shaft torque, respectively. Shaft torque is determined by dividing output power $P_r$ by shaft speed . Therefore, $F_{\text{sh}} = 75$ N.

## 4 Results and Discussions

Harmonic analysis was performed in 0–100 Hz range with a 1 Hz interval. Point 1, at $H + D/2 = 11.3$ m as shown in Fig. 1a in downwind direction, was chosen to plot the frequency spectrum in Fig. 2a. The most noticeable peak occurs at the frequency of 48 Hz which extends to 53 dB even though no structural resonance was indicated in modal analysis. After this frequency, sound pressure level (SPL)

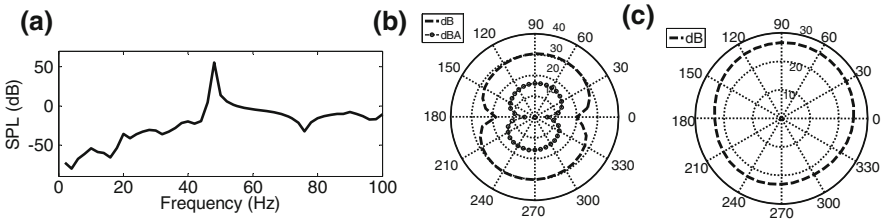


**Fig. 2** **a** SPL spectrum. **b** Overall SPL with loads. **c** Overall SPL without loads

values are roughly constant. In the infrasound region, SPL becomes negative even though the first and third structural natural frequencies cause small peaks. Values less than 0 dB can be ignored. Values indicate that only the frequency of 48 Hz can reach hearing threshold and the rest are too quiet. Figure 2b displays overall SPL by dB and dBA at the same distance but around the tower where 90° represents the wind direction. Noise level varies from 26 to 31 dB for most angles even though loads have been applied in the wind direction. However, deficits appear near side directions (0° and 180°). Removing the loads gives Fig. 2c where those deficits disappeared. The loads produced a difference of 6 dB in noise level suggesting that a more accurate determination of them should be made in future investigations. As a rough comparison with actual turbine noise output (Miglore et al. 2004), the background noise was taken to be 45 dBA at the wind speed of 6 m/s. It is environment-specific, but it can be estimated that the noise from the tower is masked out by the ambient noise as the maximum values reached 18 dBA. Although not shown here because of space limitations, calculations showed as the distance increases and ratio of height to distance becomes small, the tower changed from line to point source at a distance about 200 times the tower height.

## 5 Conclusions

A numerical noise prediction of the noise output from the 10.2 m tower of a 2.4 kW wind turbine at the wind speed of 6 m/s was made based on previous measurements of the tower vibration and the turbine loads estimated from the IEC Simple Load Model. The overall noise levels from the tower are small but are sensitive to the assumed loads as seen by comparison of Fig. 2b and c. This suggests that placing an accelerometer on the nacelle would yield important information on the forcing functions.

## References

Bowdler D, Leventhall G (2011) Wind turbine noise. Multi-Science Publishing Co. Ltd
IEC 61400-11 ed 3.0 (2002) Wind turbine generator systems. Part 11–acoustic noise measurement techniques
IEC 61400-2 ed 2.0 (2006–2003) Wind turbines. Part 2–design requirements for small turbines
Marmo BA, Carruthers BJ (2010) Modelling and analysis of acoustic emission and structural vibration in a wind turbine. Proceeding of the COMSOL conference, Paris
Miglore P, Van Dam J, Huskey A (2004) Acoustic tests of small wind turbines. Nat Renew Energy Lab
Mollasalehi E, Wood DH, Sun Q (2012) Small wind turbine tower structural vibration. Proceeding of the ASME IMECE, Houston, TX

# Combined Spherical Nearfield Acoustic Holography and Sound Quality Analyses

**Jiangming Jin, Huancai Lu, Weijie Hu, Minzhong Li and Fang Yuan**

**Abstract** The Spherical Nearfield Acoustic Holography—Sound Quality (SNAH-SQ) hybrid methodology is proposed in this paper. This methodology builds the mapping model from distribution of sound pressure to sound quality parameters on basis of reconstruction of the three-dimensional distribution of interior acoustic parameters reconstructed by SNAH. The three-dimensional distribution of sound quality parameters related to the human's subjective auditory experience can be obtained. The sound field which contained two monopole sound sources is used to conduct numerical simulation study. The distribution of sound quality parameters and the sound source localization results varied with the sound field reconstruction distance, sound frequency, and intersection angle between two sound sources. The advantages of the traditional sound source localization by nearfield acoustic holography and the sound quality sound field evaluation are adopted in the SNAH-SQ method which could provide an approach to revealing the three-dimensional inherent correlation between noise source locations and sound quality parameters distribution, and locate the noise sources with most annoyance.

**Keywords** Nearfield acoustic holography · Sound quality · Matrix mapping

J. Jin (✉) · H. Lu · W. Hu · M. Li · F. Yuan
Sound and Vibration Lab, College of the Mechanical Engineering, Zhejiang University of Technology, No. 18, Chao Wang Road, Hangzhou, People's Republic of China
e-mail: jjm@zjut.edu.cn
URL: http://www.acoustics.zjut.edu.cn

Y. Zhou et al. (eds.), *Fluid-Structure-Sound Interactions and Control,*
Lecture Notes in Mechanical Engineering, DOI: 10.1007/978-3-642-40371-2_41,

## 1 Introduction

The method of nearfield acoustic holography (NAH) (Lu and Li 2012) cannot reveal the global psychoacoustic attributes features of indoor sound field, which could be obtained by sound quality objective analysis. While traditional sound quality analysis (Blauert and Jekosch 2003) cannot show the 3D sound source distribution, we introduced a new way to find the 3D sound source distribution which is the Spherical Nearfield Acoustic Holography—Sound Quality (SNAH-SQ) hybrid method. The essential idea of this method is that from 3D distribution of interior acoustic parameters (Song 2008; Song et al. 2008) reconstructed by (SNAH) we can find the three-dimensional distribution of sound quality parameters can be obtained, which represent the human auditory percetion.

The sound field with two monopole sources and a certain angle is considered for numerical simulation in this work. The accuracy and validation of the method are verified by the numerical simulation. Errors of numerical simulation are calculated with varying reconstruction distance and frequency of sound field. The 3D distribution trend of sound quality parameters varied with the sound field reconstruction distance, sound frequency, and intersection angle between two sound sources in a sound field with two monopole sources are also studied in this paper.

Compared with the traditional sound source localization by nearfield acoustic holography and the sound quality sound field evaluation, the SNAH-SQ method is able to identify and locate sound source based on people's auditory feeling, and the results of SNHA-SQ are showed by 3D holography image.

## 2 Theory Model

### *2.1 Theory Model of Spherical Nearfield Acoustic Holography*

As shown by Jacobsen et al. (2011), the sound pressure inside and just outside of an acoustically transparent sphere of radius a can be expressed in terms of the pressure on the surface of the sphere as follows:

For the sound field shown in Fig. 1, the sound pressure can be written by:

$$p_i(r,\theta,\phi) = \sum_{n=0}^{N} \sum_{m=-n}^{n} \tilde{B}_{mn} j_n(kr) Y_n^m(\theta,\phi) \tag{1}$$

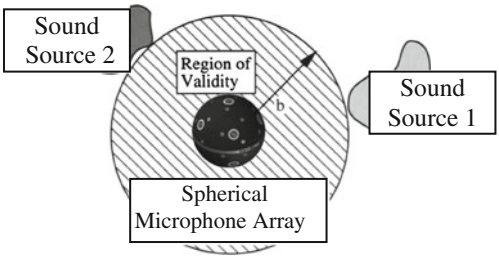


**Fig. 1** Sound field diagram

The coefficient Matrix $\tilde{B}_{mn}$ in Eq. 1 can be written as:

$$\tilde{B}_{mn} = \frac{\sum_{i=1}^{I} w_i p_t(a, \theta_i, \phi_i) Y_n^m(\theta_i, \phi_i)^*}{\left(j_n(ka) - \frac{j_n'(ka)}{h_n'(ka)} h_n(ka)\right)} \tag{2}$$

where the degree of harmonics truncated at $N$ because of the numerical integration.

## 2.2 Theory Model of Sound Quality Parameter Based on Moore Loudness Model

According to American standard: (ANSI3.4_2007), the special loudness model can be written as:

$$N_i' = \begin{cases} I_n[(GE_i + 2E_{\mathrm{THRQ}})^{\alpha} - (2E_{\mathrm{THRQ}})^{\alpha}] & E_{\mathrm{THRQ}} < E_i < 10^{10} \\ I_n\left(\frac{2E_i}{E_i + E_{\mathrm{THRQ}}}\right)[(GE_i + 2E_{\mathrm{THRQ}})^{\alpha} - (2E_{\mathrm{THRQ}})^{\alpha}] & E_i < E_{\mathrm{THRQ}} \\ I_n\left(\frac{E_i}{1.0707}\right)^{0.2} & E_i > 10^{10} \end{cases} \tag{3}$$

Then, the total loudness can be calculated:

$$N = 2\sum_{i=1}^{372} N_i' \tag{4}$$

and the sharpness is:

$$S = 0.11 \times \frac{\int_0^{24(\mathrm{bark})} N'(z) g(z) z \mathrm{d}z}{N} \tag{5}$$

## 2.3 Theory Model of SNAH-SQ Model

The special loudness for each point can be directly calculated by multiplying the sound pressure matrix by the sound quality mapping matrix, which is constructed

according the Moore loudness model. This process can be written as the following equation:

$$\begin{aligned}&[p_i(r,\theta,\phi,\omega_1)\ldots p_i(r,\theta,\phi,\omega_m)]_{1\times m}\begin{bmatrix} w_1 & \ldots & w_{372} \\ w_1 & \ldots & w_{372} \\ \vdots & \ldots & \vdots \\ w_1 & \ldots & w_{372} \end{bmatrix}_{m\times 372} \\ &= \left[N_1'(r,\theta_1,\phi_1)\ldots N_{372}'(r,\theta_1,\phi_1)\right]_{1\times 372}\end{aligned} \tag{6}$$

or: $P_i W = N'$

where $P_\mathrm{i}$ is the sound pressure vector in different frequency at one point, $W$ is the filter vector, and $N'$ is the specific loudness vector.

## 3 Numerical Simulation for Two monopole Source Sound Field

### 3.1 Monopole Sound Source

The sound pressure of a position which is also a radius vector measured form the origin generated by the monopole source is given by:

$$p = \frac{-i\rho_0 ck}{4\pi} \quad Q_s \frac{e^{ik|\vec{r}-\vec{r}_0|}}{|\vec{r}-\vec{r}_0|} \tag{7}$$

where $\rho_0$ is density of media, $c$ is wave speed, $k$ is wave number, and $Q_s$ is its source strength. Consider the condition $r < r_0$ in our study. Then expanding this equation into a series of spherical harmonics yields,

$$p = \rho_0 ck^2 Q_s \sum_{n=0}^{\infty} j_n(k,r) h_n(k,r_0) \sum_{m=-n}^{n} Y_n^m(\theta,\phi) Y_n^m(\theta_0,\phi_0)^* \tag{8}$$

### 3.2 3D Distribution of the Sound Quality Parameter

In case of this paper, the two monopole sources (center frequency of one sound source is 200 Hz, the other one is 800 Hz) were placed with an intersection angle with 30°, 60°, 90°, 120°, 150°, 180°, $d_1 = d_2 = 0.1$ m, The intensities of the two sound sources are $Q_{s1} = 2.5 \times 10^{-5}$和$Q_{s2} = 2.0 \times 10^{-5}$ ($Q_{s1} > Q_{s2}$). The 3D distribution of the sound quality parameters and the identification and localization of the sound sources by SNHA-SQ are shown in Fig. 2. As Fig. 2, the localization results of the main sound source in sound field based on the distribution of the

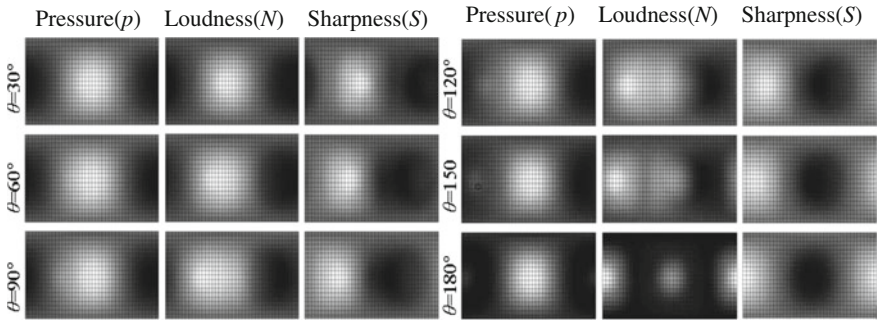


**Fig. 2** 3D distribution of the sound pressure, loudness, sharpness varying with inter angle $\theta$ between two sound source ($f_1 = 150$ Hz, $f_2 = 800$ Hz, $r = 0.1$ m) Pressure ($p$) Loudness ($N$) Sharpness ($S$)

sound pressure is different from the results based on the distribution of sound quality parameters. So, it is not reasonable to only suppress the sound source with the highest sound. The 3D distribution of the sound quality parameter is more effective to identify the most annoying sound source.

## 4 Conclusions

Hence, the following conclusions also can be obtained:

1. Only the sound pressure distribution cannot reflect people's auditory feeling of a specific sound field. High sound pressure does not mean high loudness or sharpness.
2. Through SNHA-SQ method, we can get an approach to revealing the inherent correlation between noise source locations and sound quality parameters, and target the noise sources in three-dimensional space which contribute most to the sound quality at the specified locations.
3. Combining different source localization methods which could reflect some unique attributes of sound sources respectively is a useful way for identifying multiple sound sources existing in space.

## References

ANSI3.4_2007 (2007) Procedure for the computation of loudness of stead sound. American National Standards Institute

Blauert J, Jekosch U (2003) Concepts behind sound quality: some basic considerations. Proceedings of 2003 inter noise: Seogwipo, Korea, pp 72–76

Jacobsen F, Moreno G, Fernandez Grande E (2011) Near field acoustic holography with microphones on a rigid sphere. J Acoust Soc Am 129:3461–3464

Lu H, Li M (2012) Reconstruction of sound field based on near-field acoustic holography with a rigid spherical microphone array. Proceedings of the Hong Kong: ACOUSTIC 2012 Hong Kong conference and exhibition, pp 3258–3258

Song W (2008) Beamforming applied to psychoacoustics -sound source localization based on psychoacoustic attributes and efficient auralization of 3D sound fields. Phd Thesis, Aalborg University

Song W, Ellermeier W, Hald J (2008) Using beamforming and binaural synthesis for the psychoacoustical evaluation of target sources in noise. J Acous Soc Am 123(2):910–924

# Making Use of Turbulence and its Interaction with Sound: A Non-Invasive Flow Monitor

**A. Nichols, K. Horoshenkov, S. Tait and S. Shepherd**

**Abstract** A novel acoustic sensor has been developed which is capable of remotely monitoring the free surface 'fingerprint' of shallow flows. The temporal and spatial properties of this fingerprint are shown to contain a wealth of information regarding the nature of the flow itself. The remote measurement can thereby be used to infer the bulk flow properties such as depth, velocity, and hydraulic roughness to within 8 % accuracy. The instrument is totally non-invasive and as such is low cost, low maintenance, and low power. Such a device will allow for widespread monitoring of flow conditions in drainage and river networks, informing flood models, and facilitating pro-active maintenance and real time control.

## 1 Introduction

Natural river systems and urban drainage infrastructure are becoming more frequently overloaded by heavy flows. Rising urbanization is bypassing the natural infiltration processes, while increasing population is demanding a greater capacity from our flow conduits. Additional loading is being generated by climate change, with the UK Meteorological Office predicting significantly greater peak flows over the next 80 years.

Flow properties and conduit conditions must be monitored more effectively in order to minimise failures through pro-active maintenance and real-time control, but the best technologies at present are too invasive, too costly for mass deployment, and require regular maintenance.

A. Nichols (✉) · K. Horoshenkov · S. Tait · S. Shepherd
University of Bradford, Richmond Road, Bradford BD71DP, UK
e-mail: a.nichols2@brad.ac.uk

Y. Zhou et al. (eds.), *Fluid-Structure-Sound Interactions and Control*,
Lecture Notes in Mechanical Engineering, DOI: 10.1007/978-3-642-40371-2_42,

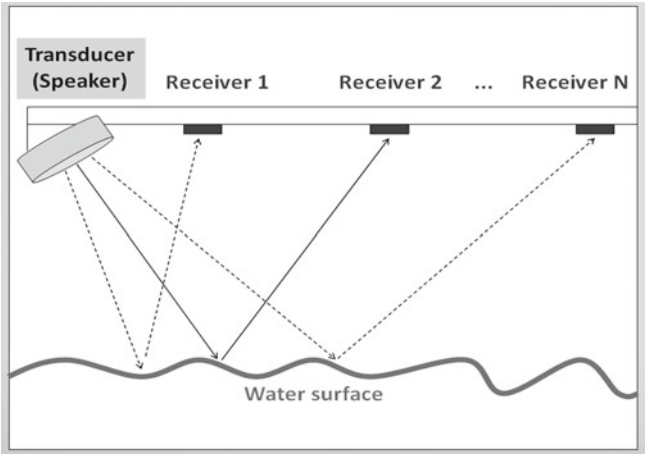


**Fig. 1** Source-receiver geometry

Flowing water exhibits a unique surface pattern driven by the flow induced turbulence (3). This pattern appears to be a function of the underlying flow properties (1). In this work, an airborne acoustic sensor is developed which is capable of remotely characterizing the free surface pattern of shallow flows Nichols and Horoshenkov (2012). Using this device it is possible to track to the pattern to obtain a velocity measurement, but also to analyse the spatial properties of the pattern in order to infer additional flow information such as hydraulic roughness, turbulence scale, and sediment properties.

A field version of the device was constructed and trialled in a foul sewer pipe in order to test the ability to measure velocity and flow depth, while a more precise laboratory version was developed in order to investigate the additional information contained within shallow flow surfaces.

## 2 Principles of the New Sensor

Consider a monochromatic ultrasonic wave reflected from an acoustically hard surface toward a microphone some distance away (Fig. 1). The received signal will have a difference in phase when compared to the transmitted signal, due to the time taken for the acoustic wave to travel from source to receiver. When the reflecting boundary is stationary this phase difference is constant. If the surface is displaced vertically, the phase difference is altered due to the change in path-length. A fluctuating surface will thereby generate a fluctuating phase difference.

Since the relative positions of source and receiver are known, the phase measurements may be converted into units of length representing the fluctuations of the flow surface at the point of specular reflection. In the laboratory tests, at the

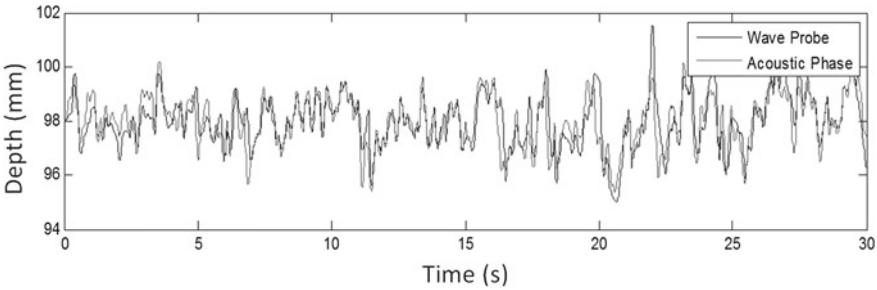


**Fig. 2** Accuracy of acoustic wave probe

point of specular acoustic reflection, a conductive wave probe is installed in order to assess the accuracy of the acoustic technique. Figure 2 shows an example of the acoustically measured surface wave fluctuations compared with standard conductance wave probe measurements. Comparison indicates that the acoustic technique can measure water surface fluctuations to within ± 5 % of those measured with the invasive conductive wave probes. The use of multiple acoustic receivers allows for fluctuation measurements to be synchronously recorded at several spatially distributed locations on the flow surface (see Fig. 1).

## 3 Surface Velocity and Mean Depth Measurement

A device was constructed with 7 receivers. Since each receiver has a unique point of specular reflection, and the location of these points is accurately known based on the location of the individual receivers, the phase pattern can be monitored as the surface passes each microphone, and a flow velocity can be calculated using cross-correlation. Figure 3(a) shows the surface pattern recorded at two locations in an arbitrary flow regime, with a clear temporal lag which reveals the surface

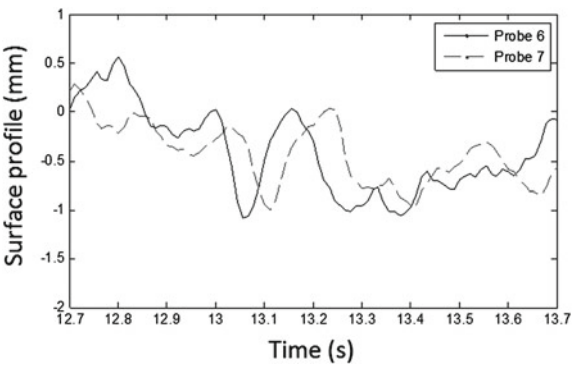


**Fig. 3** Spatially separated phase fluctuations

**Table 1** Flow measurement results

| Flow regime | Point gauge (mm) | Acoustic depth (mm) | Depth error (%) | Mean velocity (m/s) | Acoustic velocity (m/s) | Velocity error (%) |
|---|---|---|---|---|---|---|
| 1 | 15 | 15.8 | 5 | 0.58 | 0.59 | 2 |
| 2 | 16 | 15.7 | 2 | 0.59 | 0.54 | 8 |
| 3 | 9 | 8.7 | 3 | 0.29 | 0.27 | 7 |

flow velocity. Mean flow depth is measured using a standard time-of-flight technique. A pulse is emitted from the transducer, reflected from the flow surface, and received at each microphone. The time difference between emission and reception allows the location of the flow surface to be determined.

Measurements were taken in a 150 mm diameter foul sewer pipe using real flows. Reference measurements of depth and velocity were recorded using a point gauge and a saline tracer respectively. Data was recorded for three flow regimes, with the results given in Table 1. It can be seen that the maximum errors for depth and velocity were 5 % and 8 % respectively.

## 4 Deciphering Information Hidden in the Surface Pattern

It can be observed that the roughness pattern on shallow flow evolves gradually as it travels downstream. This evolution in surface pattern may be quantified from the surface fluctuation data obtained at multiple locations on the flow surface using the acoustic device. The dependence of the correlation upon the spatial separation follows an oscillatory relationship. This is known as the spatial correlation function (SCF). Examples of this are shown in Fig. 4 for three arbitrary regimes.

This spatial correlation function may be approximated by Eq. 1:

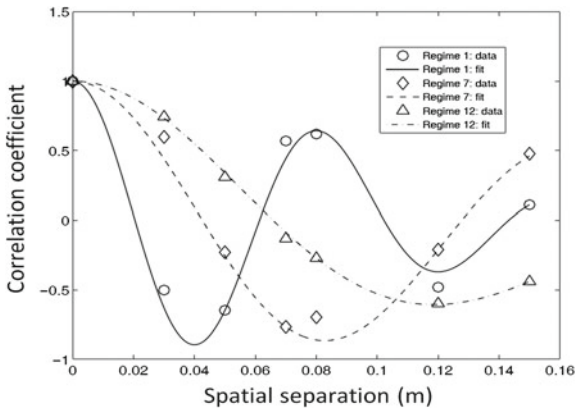


**Fig. 4** Spatial correlation functions

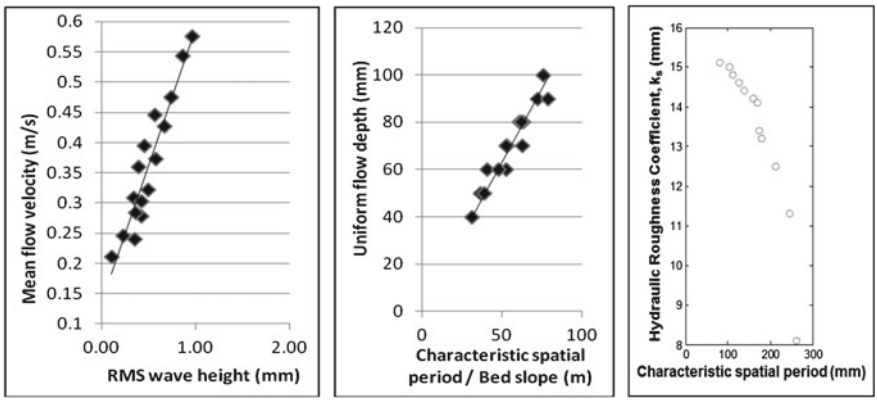


**Fig. 5** Relationships between surface roughness and flow properties

$$W(\rho) = e^{-\frac{\rho^2}{\sigma_w^2}} \cos\left(\frac{2\pi}{L_0}\rho\right) \tag{1}$$

where $\rho$ is the spatial separation, $\sigma_w$ the correlation radius and $L_0$ the characteristic spatial period. Also measurable is the root-mean-square (RMS) wave height. Data was collected from several regimes established in a laboratory flume using an array of wave probes, and an SCF was calculated for each regime. Analysis of the SCF revealed the following relationships (Fig. 5):

It can be seen that the physical nature of the surface roughness itself contains information about the flow. Not only may it provide independent measures of velocity and depth, but it may also infer hydraulic roughness. Additional research suggests it may be possible to learn about sediment structure and transport rates solely by remote measurement of the free surface pattern.

## 5 Conclusions

A sensor has been developed which makes use of the turbulent nature of depth limited flows. The device measures the free surface roughness acoustically, and uses this data to obtain depth and velocity measurements to within 8 %. It is also possible to measure hydraulic roughness, and future work will investigate the detection of physical bed roughness and sediment transport properties. The sensor is totally non-invasive and as such is low cost, low maintenance, and low power.

## References

Nichols A, Horoshenkov KV, Shepherd SJ, Attenborough K, Tait SJ (2010) Sonic Characterisation of Water Surface Waves. Proceedings ISHPF2010

Nichols A, Horoshenkov K (2012) Methods and apparatus for detection of fluid interface fluctuations. WO 2012/117261 A1

Tamburrino A, Gulliver J (2002) Free-surface turbulence and mass transfer in a channel flow. AIChE J 48 (12):2732–2743

# Part III
# Fluid-Structure Interaction

# The Swimming of Manta Rays

**Alexander J. Smits, Keith W. Moored and Peter A. Dewey**

**Abstract** Manta rays propel themselves by combining oscillating and undulating motions of flexible surfaces. We describe two experiments to study the effects of excitation and flexibility on the wake flowfield: experiments on undulating and flapping three-dimensional fins of elliptical planform, and experiments on pitching two-dimensional panels of rectangular planform with varying flexibility. To interpret the results on thrust and efficiency, we propose scalings for aspect ratio and flexibility, and develop a stability analysis called wake resonance theory. Here we focus on the insights provided by wake resonance theory.

**Keywords** Manta ray · Swimming · Flexibility · Wake resonance

## 1 Introduction

Aquatic animals propel themselves using a wide variety of mechanisms. Jellyfish, squid, and salps use pulsatile jets to produce locomotion. Whales, dolphins, and many fish use body and caudal fin oscillations, while penguins, sea turtles, and some fish employ paired pectoral fin locomotion to propel themselves forward. Sfakiotakis et al. (1999) has classified fish propulsion mechanisms based on the types of fins and the kinematic motions that are employed. For cruise locomotion, where fish are oscillating their fins in a periodic motion, there are two main categories for all fish species; body and/or caudal fin (BCF) locomotion and median and/or paired fin (MPF) locomotion. BCF swimmers propagate a traveling

A. J. Smits (✉) · K. W. Moored · P. A. Dewey
Mechanical and Aerospace Engineering, Princeton University,
Princeton, NJ 08544, USA
e-mail: asmits@princeton.edu

A. J. Smits
Mechanical and Aerospace Engineering, Monash University, Melbourne, Australia

Y. Zhou et al. (eds.), *Fluid-Structure-Sound Interactions and Control*,
Lecture Notes in Mechanical Engineering, DOI: 10.1007/978-3-642-40371-2_43,

wave down the length of their bodies. They are classified along an undulation continuum where the wavelength of motion ($\lambda$) as compared to the body length (L) ranges from values less than or near one, such as in eels using *anguilliform* motion, to values that are much greater than one, such as in tuna using *thunniform* motion. The more undulatory *anguilliform* motion typically engages nearly the entire body in active swimming, whereas the less undulatory *carangiform* or *thunniform* motions only engage part of the body or the caudal fin alone.

MPF fish include boxfish, seaperch, sunfish, and notably rays. Similar to BCF swimmers, rays, which include but are not limited to stingrays, cownose rays, eagle rays, and manta rays, have been classified based on the nondimensional wavelength of the traveling wave that is propagated down their pectoral fins (Rosenberger 2001). Benthic rays such as the Atlantic stingray typically utilize highly undulatory motions ($\lambda/L < 1$), whereas pelagic species such as an eagle and manta rays use less undulatory motions ($\lambda/L > 2$).

Regardless of the swimming mechanism employed, all of the oscillating motions used by aquatic species shed a series of vortices into the wake. These vortex wake structures impart momentum and impulse to the fluid environment and propel the animal forward. In the case of pulsatile jet production, individual vortex rings are ejected in the downstream direction, which can be seen to produce a jet structure through the center of the rings (Dabiri et al. 2005). For BCF and MPF swimmers, typically either a series of connected vortex rings or pairs of laterally ejected vortex rings are shed into the wake (Fish and Lauder 2006). When particle image velocimetry (PIV) is used to measure the velocity field in a plane at the midspan of the wake, a two-dimensional slice of the three-dimensional vortex rings is revealed (see Fig. 1). Here, the series of connected vortex rings is seen to be a three-dimensional analog to a reverse von Kármán street, also known as a 2S wake structure where two single vortices are shed per oscillation cycle. In addition, the pairs of laterally ejected vortex rings are seen to be the three-dimensional analog to what is known as a 2P wake structure where two pairs of vortices are shed per flapping cycle. In flapping airfoils that model animal locomotion other wake structures have also been observed (Lentink et al. 2008).

In nature, animals utilize unsteady fluid mechanics and flexible appendages to swim effectively. In contrast, typical design principles for underwater vehicles employ steady fluid mechanics principles and rigid propulsors. Exploring and understanding the swimming mechanisms of aquatic species may help to develop novel underwater vehicle designs that could outperform current technology.

Rays offer a unique biological focal point to explore MPF propulsion. Specifically in manta rays, propulsion is achieved by combining oscillating and undulating motions of flexible surfaces. Oscillations produce a spanwise flapping, and undulations produce a traveling wave that moves in the downstream direction (see Fig. 2). We are interested in studying the unsteady hydrodynamics of such motions to understand and model the wake structure. Ultimately, our goal is to understand the connection between the wake structure and the swimming performance exhibited by manta rays. Experiments suggest a rich set of phenomena exist, depending on the nondimensional frequency of flapping, the wavelength of the

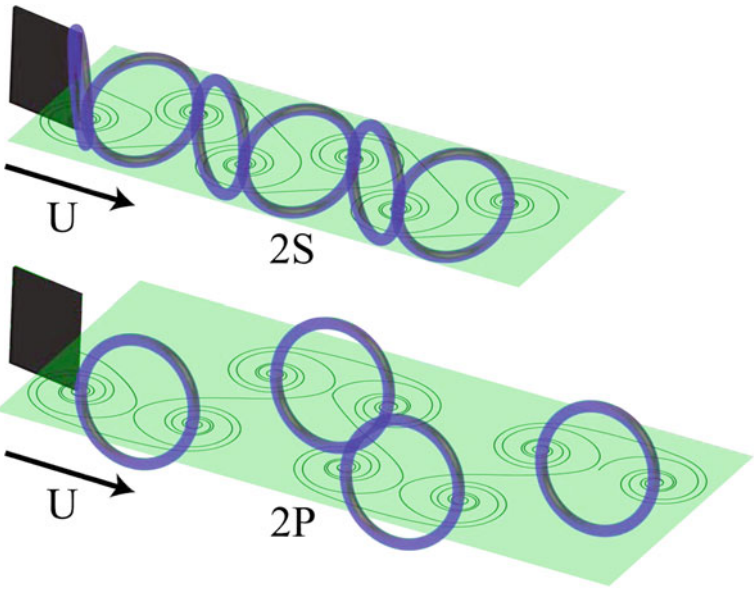


**Fig. 1** Typical three-dimensional vortex wake structures produced by swimming animals. The *top* is a reverse von Kármán street otherwise known as a 2S wake, where two single vortices are shed per cycle. The *bottom* is a 2P wake where two pairs of vortices are shed per cycle

undulation, the aspect ratio of the fin, and its bending rigidity. Under certain conditions, simple 2S wake structures are observed that bear a strong resemblance to the structure of co-flowing jets and wakes. In other cases, 2P bifurcating wakes are seen, and both cases appear to correspond to a peak in efficiency.

We describe two principal sets of experiments to study the effects of excitation and flexibility on the wake flowfield: one set to study undulating and flapping three-dimensional fins of elliptical planform, and one set to study pitching two-dimensional panels of rectangular planform with varying flexibility. To interpret the results on thrust and efficiency, we propose scalings for aspect ratio and flexibility, and develop a stability analysis called wake resonance theory. Here we focus on the insights provided by wake resonance theory.

**Fig. 2** Manta birostris, off the coast of Yap. *Photo credit* Keith Moored

## 2 Undulating and Flapping Three-Dimensional Elliptical Fin

The motivating result is shown in Fig. 3, which displays the efficiency $\eta_p$ of a mechanical analog of a manta ray pectoral fin, actuated using four rigid spars to produce an undulatory motion, as implemented by Clark and Smits (2006). Two observations are important: the maximum efficiency exceeds 40 %, and there are two peaks in efficiency, one at a Strouhal number $St = 0.2$ corresponding to a 2P wake, and one at a Strouhal number of 0.3 corresponding to a 2S wake. Here, $St = fA/U$, where $f$ is the frequency of actuation, $A$ is the peak-to-peak amplitude of the trailing edge motion at the half-span, and $U$ is the freestream velocity.

To provide insight into this behavior, we can examine the stability of the time-averaged wake profile. A linear spatial stability analysis reveals the frequency of maximum spatial growth, that is, the hydrodynamic resonant frequency of the time-averaged jet (see Moored et al. 2012 for details). It is found that: (1) optima in propulsive efficiency occur when the driving frequency of a flapping fin matches the resonant frequency of the jet profile; (2) there can be multiple wake resonant frequencies and modes corresponding to multiple peaks in efficiency; and (3) some wake structures transition from one pattern to another when the wake instability mode transitions.

The results are illustrated in Fig. 4, which shows stability curves formed from the most unstable eigenvalues at a given forcing frequency. There are two distinguished frequencies marked on each stability curve: the driving frequencies at which the velocity profiles and the stability curves were generated, and the most unstable frequency of the velocity profile. When the driving frequency coincides with the most unstable frequency of a velocity profile, we define this special frequency as a wake resonant frequency. It is postulated that when the fin is operated at a wake resonant frequency, the spatial growth rate of instability waves will be maximized,

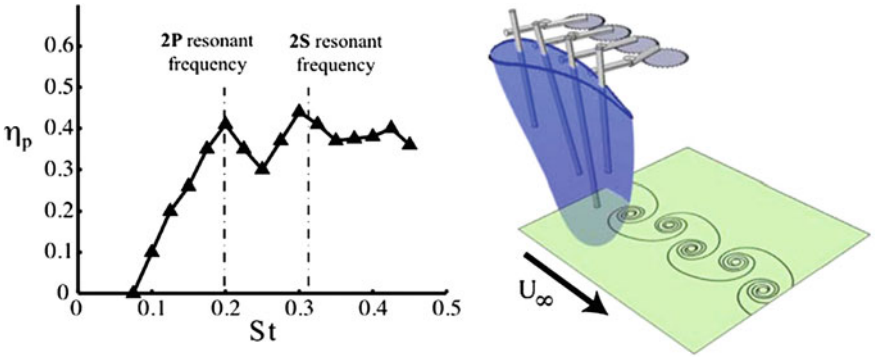


**Fig. 3** *Left* Efficiency of a batoid-like fin actuated in undulatory motion with a wavelength four times the chord length (adapted from Clark and Smits 2006). *Right* Fin schematic, showing 2S wake

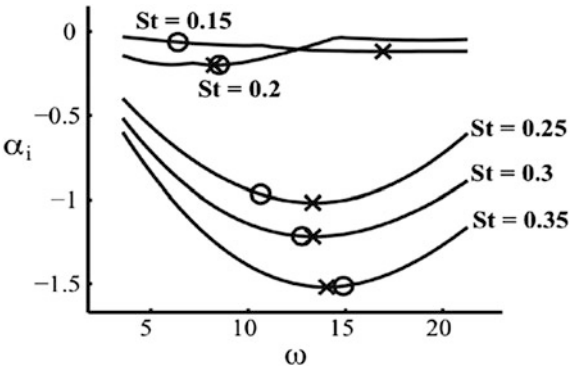


**Fig. 4** Stability curves for five velocity profiles taken from PIV data measured by Dewey et al. (2011). *Symbols x*, most unstable frequency of the stability curve; *o*, driving frequency used to generate the velocity profile (adapted from Moored et al. 2012)

amplifying the mean flow per unit input energy, and leading to a peak in efficiency (Triantafyllou et al. 1993). The cases where $St = 0.2$ and 0.35 in Fig. 3 correspond to the two cases shown in Fig. 4 where wake resonant frequencies are found, and indeed there is a close correspondence. The theoretical framework is termed wake resonance theory, which is a compilation of conclusions drawn by Moored et al. (2012, 2013). The analysis, although one-dimensional, captures the performance exhibited by a three-dimensional propulsor as seen in this case of an elliptical fin, showing the robustness and broad applicability of the technique.

## 3 Pitching Two-Dimensional Flexible Panels

Although rigid materials can be found throughout nature such as bone and nacre (Jackson et al. 1988), manta rays, and other aquatic species flap and undulate fins that are made from flexible materials (Lauder and Madden 2007). We propose that flexible materials have been evolutionarily selected to gain a hydrodynamic advantage over propulsors that use rigid materials. To explore this hypothesis, Dewey et al. (2013) isolated the role of flexibility in unsteady locomotion by experimentally measuring the performance of two-dimensional pitching panels (see Fig. 5) of varying flexibility.

The performance parameters included the coefficient of thrust, $C_T = T/(1/2\ \rho S U^2)$, the coefficient of power, $C_P = P/(1/2\ \rho S U^3)$, and the Froude efficiency, $\eta_p = C_T/C_P$. The time-averaged thrust, $T$, the time-averaged power input to the fluid, $P$, the fluid density, $\rho$, the planform area, $S$, and the freestream flow speed, $U$, are all used in the nondimensional force and power coefficients. Dewey et al. (2013) observed that thrust production could be more than doubled for a flexible panel as compared to a rigid panel at the same operating frequency. Also, the power consumed by a flexible panel can be reduced as compared to a rigid panel with the net effect being that flexible panels can be more than twice as efficient as their rigid counterparts. The Froude efficiency for seven panels is shown in Fig. 5a. The efficiency data from Dewey et al. (2013) shows that

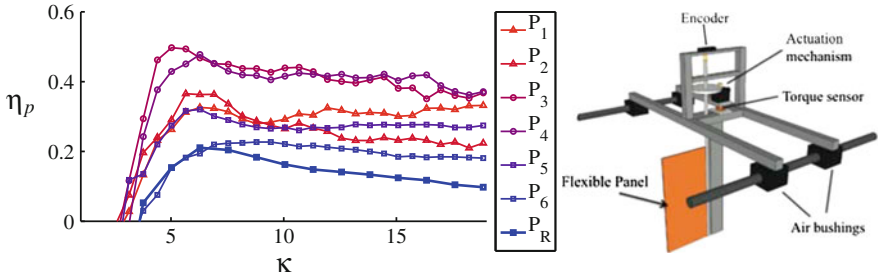


**Fig. 5** **a** Froude efficiency of seven panels of varying flexibility. The panels range from the most flexible, $P_1$, to the least flexible, $P_6$, with the rigid panel denoted as $P_R$. **b** Pitching panel apparatus (adapted from Dewey et al. 2013)

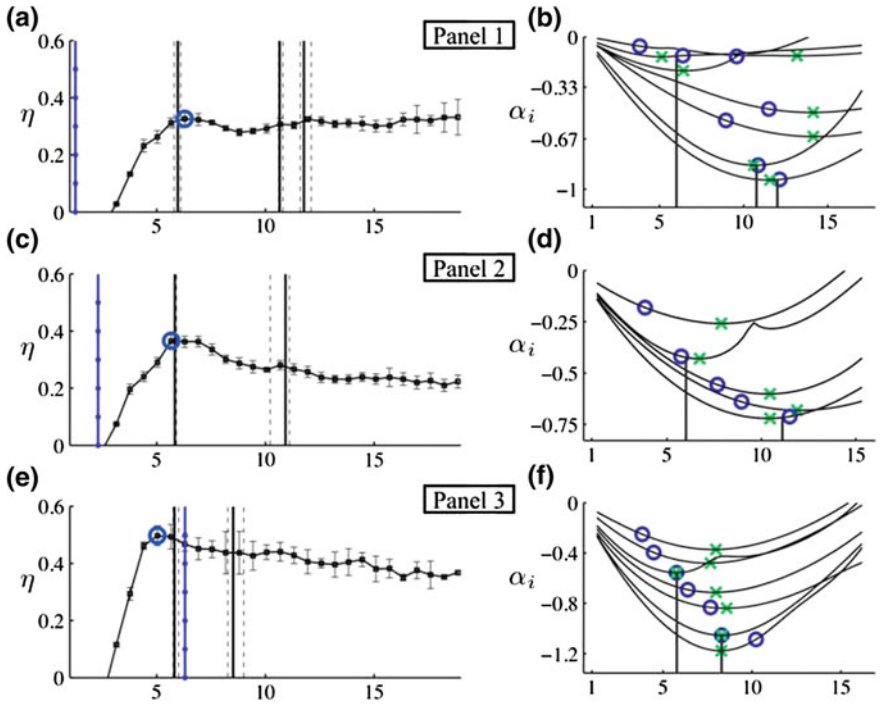


**Fig. 6** Panels one through three: (*left*) efficiency curves marked with the wake resonant frequencies (*solid black lines*) and the structural resonant frequencies (*dot-solid blue lines*). The *dashed black lines* denote wake resonant frequency uncertainty. (*right*) Stability curves generated from the linear stability analysis of velocity profiles extracted from the time-averaged PI V data (adapted from Moored et al. 2012)

there is an optimal flexibility (panels $P_3$ and $P_4$), where the efficiency is maximized across a range of reduced frequencies. The reduced frequency, $k = 2\pi fc/U$, where $f$ is the driving frequency and $c$ is the chord length.

Previously, it was shown that local peaks in efficiency occurred when the driving frequency of a fin was matched to its wake resonant frequency. The principles of wake resonance theory have been extended to flexible propulsors, specifically to understand the observed phenomena of an optimally efficient flexibility. Moored et al. (2012) postulated that driving a *flexible* fin at a wake resonant frequency would also lead to local peaks in efficiency and that operating at a structural resonant frequency was not sufficient to achieve a local peak in efficiency. In fact, the optimally efficient flexibility was proposed to occur when the structural resonant frequency of a flexible panel was nearly aligned with a wake resonant frequency.

To show that the optimal flexibility did indeed occur under these conditions, the same linear stability analysis was applied to the flowfields generated by flexible

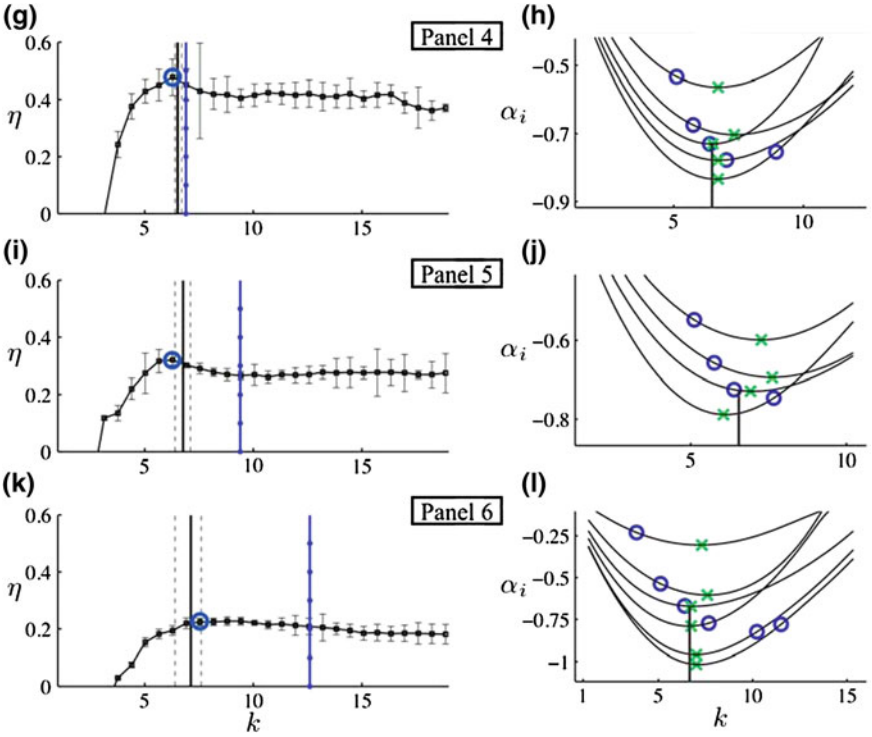


**Fig. 7** Panels four three six: (*left*) efficiency curves marked with the wake resonant frequencies (*solid black lines*) and the structural resonant frequencies (*dot-solid blue lines*). The *dashed black lines* denote wake resonant frequency uncertainty. (*right*) Stability curves generated from the linear stability analysis of velocity profiles extracted from the time-averaged PI V data (adapted from Moored et al. 2012)

fins of rectangular planform. The wake resonant frequencies and structural resonant frequencies of the flexible panels are marked on the efficiency data for each panel in Figs. 6 and 7. The associated stability curves generated from the linear stability analysis of the PIV data are also shown. Here, as hypothesized the efficiency displays a maximum in a global sense when the structural resonant frequencies of the panels are nearly aligned with their wake resonant frequencies, which is seen for panels $P_3$ and $P_4$. It can also be seen that operating at a structural resonant frequency does not lead to local peak in efficiency as suggested in Moored et al. (2012).

## 4 Conclusions and Future Directions

We have reviewed recent literature on wake resonance theory, which is a set of conclusions that clarify the mechanisms leading to efficient unsteady locomotion at high Reynolds numbers. Wake resonance theory states that local peaks in efficiency are achieved when the driving frequency of motion is matched to a wake resonant frequency for either flexible or rigid propulsors. The theory also states that there may be multiple wake resonant frequencies leading to multiple peaks in efficiency. The case of multiple wake resonant frequencies was first shown for an undulating elliptical fin. In this case, the first peak in efficiency was shown to relate to a 2P wake structure while the second efficiency peak was paired with a 2S wake structure. This observation established that both 2S and 2P wake structures can lead to efficient locomotion and that both wake structures had independent wake resonant frequencies. Many caudal fin swimmers such as tuna typically produce a 2S wake structure while other elongated fish such as eels typically produce a 2P wake structure (Tytell et al. 2010, Fish and Lauder 2006). Now, it may be concluded that both wakes may be efficient ways for animals to control the fluid flow around their bodies and appendages. The undulatory motion exhibited by manta rays has been shown to produce both wake structures depending on the nondimensional wavelength of the motion. Lastly, recent literature has shown that there is a flexibility that optimizes the efficiency of swimming. A tuning condition has been shown to characterize the optimal flexibility. When a structural resonant frequency is tuned to a wake resonant frequency then the global optimal efficiency of a flexible propulsor is achieved.

Thus far, wake resonance analysis has only been applied to fixed velocity biorobotic devices. The next step would be to explore whether wake resonance theory applies to free-swimming devices and computations, which is a step closer to autonomous underwater vehicles and animal swimming. It is possible that tuning to a wake resonant frequency may be a ubiquitous design principle used throughout nature, but this postulate has not been directly demonstrated. To clearly show that animals indeed tune into the resonances of their wakes, PIV data from animals must be analyzed. If it can be demonstrated that animals operate at their wake resonant frequencies then a strong conclusion may be made that animals are

tuned for high efficiency. Currently, it is proposed that at a wake resonant frequency the time-averaged jet produced behind an unsteady propulsor is amplified per unit input energy leading to the observed local peaks in efficiency. A detailed energy budget analysis of the mean flow production must be explored to confirm the amplification-efficiency mechanism. Lastly, the Orr-Sommerfeld equations may be studied to help determine scaling laws of Froude efficiency for unsteady swimmers and flyers.

We have made considerable progress in understanding the swimming of manta rays. We have determined underlying principles leading to their efficient locomotion, and we have also gained understanding into their fin kinematics (Fish et al. 2011), swimming performance (Clark and Smits 2006, Moored et al. 2011b), maneuverability (Parson et al. 2011), biomechanics (Russo et al. 2011), and wake structure (Dewey et al. 2011). Scaling laws (Dewey et al. 2013) and effective artificial fins (Moored et al. 2011a) have also been developed to aid in the engineering of ray-like mechanisms. This new understanding of manta rays may lead to a more complete understanding of the aerodynamics and hydrodynamics of flying and swimming animals, and to the development of a new class of biorobotic underwater vehicles that are tuned for high efficiency and may outperform their classic counterparts.

## References

Clark RP, Smits AJ (2006) Thrust production and wake structure of a batoid-inspired oscillating fin. J Fluid Mech 562:415–429

Dabiri JO, Colin SP, Costello JH, Gharib M (2005) Flow patterns generated by oblate medusan jellyfish: field measurements and laboratory analyses. J Exp Biol 208(7):1257–1265

Dewey PA, Carriou A, Smits AJ (2011) On the relationship between efficiency and wake structure of a batoid-inspired oscillating fin. J Fluid Mech 691:245–266

Dewey PA, Boschitsch B, Moored KW, Stone HA, Smits AJ (2013) Scaling laws for the thrust production of flexible pitching panels. J Fluid Mech (Under review)

Fish FE, Lauder GV (2006) Passive and active flow control by swimming fishes and mammals. Annu Rev Fluid Mech 38:193–224

Fish FE, Nichols RH, Dudas MA, Moored KW, Bart-Smith H (2011) Kinematics of swimming in the manta ray (Manta birostris): 3D analysis of open water maneuverability. Integr Comp Biol 51:E42

Jackson AP, Vincent JFV, Turner RM (1988) The mechanical design of nacre. Proc Royal Soc B 234(1277):415–440

Lauder GV, Madden PG (2007) Fish locomotion: kinematics and hydrodynamics of flexible foil-like fins. Exp Fluids 43(5):641–653

Lentink D, Muijres FT, Donker-Duyvis FJ, van Leeuwen JL (2008) Vortex-wake interactions of a flapping foil that models animal swimming and flight. J Exp Biol 211(2):267–273

Moored KW, Kemp TH, Houle NE, Bart-Smith H (2011a) Analytical predictions, optimization, and design of a tensegrity-based artificial pectoral fin. Int J Solids Struct 48(22):3142–3159

Moored KW, Dewey PA, Leftwich MC, Bart-Smith H, Smits AJ (2011b) Bioinspired propulsion mechanisms based on manta ray locomotion. Marine Technol Soc J 45(4):110–118

Moored KW, Dewey PA, Smits AJ, Haj-Hariri H (2012) Hydrodynamic wake resonance as an underlying principle of efficient unsteady propulsion. J Fluid Mech. doi:10.1017/jfm.2012.313

Moored KW, Dewey PA, Smits AJ, Haj-Hariri H (2013) Mechanisms for optimally efficient locomotion with flexible propulsors. Phys Fluids (Under review)

Parson J, Fish FE, Nicastro AJ (2011) Turning performance in batoid rays: limitations of a rigid body. J Exp Mar Biol Ecol 402:12–18. doi:10.1016/j.jembe.2011.03.010

Rosenberger LJ (2001) Pectoral fin locomotion in batoid fishes: undulation versus oscillation. J Exp Biol 204(2):379–394

Russo RS, Blemker SS, Fish F, Moored KW, Bart-Smith H (2011) Form-function relationship between ray skeletal architecture and ray locomotion. Integr Comp Biol 51:E119

Sfakiotakis M, Lane DM, Davies JBC (1999) Review of fish swimming modes for aquatic locomotion. IEEE J Oceanic Eng 24(2):237–252. doi:10.1109/48.757275

Triantafyllou GS, Triantafyllou MS, Grosenbaugh MA (1993) Optimal thrust development in oscillating foils with application to fish propulsion. J Fluids Struct 7:205–224

Tytell ED, Borazjani I, Sotiropoulos F, Baker TV, Anderson EJ, Lauder GV (2010) Disentangling the functional roles of morphology and motion in the swimming of fish. Integr Comp Biol 50(6):1140–1154

# Flow and Sound Generation in Human Lungs: Models of Wheezes and Crackles

**Yingying Hu, Shiyao Bian, Marcel Filoche, John C. Grotberg, Joshua White, Shuichi Takayama and James B. Grotberg**

**Abstract** We present a broad review of our laboratory's contributions to the understanding of flow generated sounds which emanate from the lung and are used by clinicians to ascertain the status of health of the respiratory system. Important sounds from diseased lungs include wheezing, which occurs primarily during expiration, and crackles which occur primarily during inspiration. We have analyzed flow-induced flutter of flexible tubes as the mechanism of wheezing sounds and connected its appearance to the onset of flow limitation in a lung. Wheezes and difficulty expiring air are common to asthma and emphysema. The flutter theory is for both linear and nonlinear wall properties, while using potential flow with a friction factor as well as a coupled Orr-Sommerfeld system using the Navier–Stokes equations coupled to the wall. Both the value of the critical flow velocity that instigates flutter, as well as the flutter frequency, compares well with experiments on isolated flexible tubes as well as an excised lung. We also studied the propagation and rupture of simulated mucus plugs using carbopol 940 gels to investigate the source of crackling sounds which occur in lungs with an abnormal amount of liquid in the airways, congestive heart failure, or small airway inflammation. The non-Newtonian properties of yield stress, storage modulus, and loss modulus were matched well with normal and abnormal mucus. A collapsed airway of the 12th generation was modeled using a quasi-two-dimensional polydimethylsiloxane channel. The plug yields at a plane about one-third of the half channel width away from the lateral channel walls and then ruptures, creating a

Y. Hu · S. Bian · M. Filoche · J. White · S. Takayama · J. B. Grotberg (✉)
Department of Biomedical Engineering, University of Michigan, Ann Arbor, MI 48109, US
e-mail: grotberg@umich.edu

Y. Hu
e-mail: yinghu@bu.edu

M. Filoche
Physique de la Matière Condensée, Ecole Polytechnique, CNRS, 91128 Palaiseau, France

J. C. Grotberg
University of Illinois at Chicago, Chicago, IL 60607, US

Y. Zhou et al. (eds.), *Fluid-Structure-Sound Interactions and Control*,
Lecture Notes in Mechanical Engineering, DOI: 10.1007/978-3-642-40371-2_44,

crackle sound, and reopening the model airway to gas flow. The relatively high shear stresses during rupture, and crackle sound production, may increase epithelial cell damage.

**Keywords** Mucus · Wheeze · Crackles · Flow limitation · Lungs · Non-Newtonian · Wall shear

## 1 Introduction

The airways of the lung are a branching network of tubes, starting with the trachea which is considered generation as n = 0. It branches into two main bronchi, one goes to the right lung and the other to the left lung, and they form generation n = 1. See Fig. 1. The system continues to branch by bifurcations primarily, so that there are essentially $2^n$ tubes at any generation, n. Typically in an adult $0 \leq n \leq 23$ and then the final branches are into the end sac alveoli. Once past the first few generation, the tube diameters are smaller and smaller as n increases, and the total cross-sectional area is larger and larger. The diameter of the trachea is typically 1.8 cm in an adult, so the initial cross section of the tree is $\sim 2.5$ cm$^2$. By comparison, the total surface area of the end sac alveoli is 90 m$^2$, roughly the surface area of a tennis court. As air flows into and out of the lung during respiration, a number of fluid dynamical interactions with the airway tree can occur that produce sounds in disease that can be heard by a physician through a stethoscope. We will discuss two such interactions: one with the wall flexibility leading to flutter instability and wheezing sounds, and one with the wall liquid layer or mucus where liquid plugs that block the airway are forced to rupture making a crackling sound.

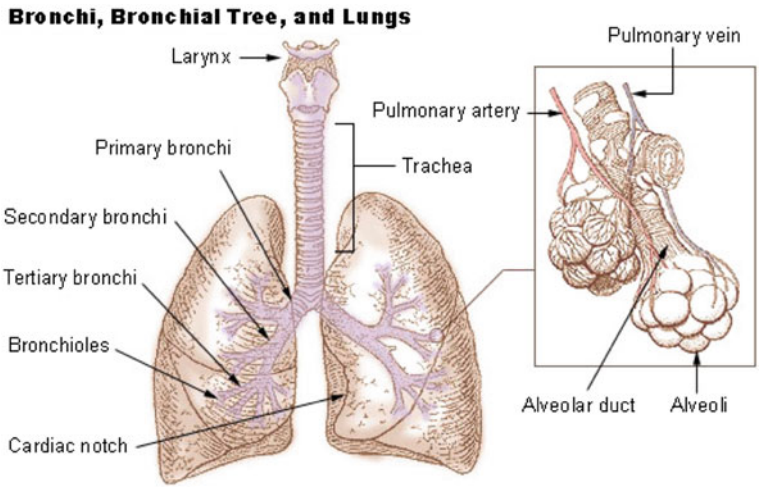


**Fig. 1** Human airway anatomy and geometry

*Flutter and Wheezing* The original intent of our presentation was to discuss mucus plug rupture and crackling sounds. This is a topic that relies on low Reynolds number flows which have significant surface tension and non-Newtonian fluid dynamics contributions to the resulting phenomena. However, the assembly of talks at the FSSIC2013 meeting concerning flow-induced vibrations over flexible surfaces related to aerospace applications encouraged us also to cover the history of our previous work on flutter related to wheezing breath sounds. This was meant to reach out further to our colleagues who may bring additional insights and investigations into this complex and important biofluid mechanics application. In gas flow through the pulmonary airways there are well-recognized phenomena associated with forced expiration: airway collapse, flow limitation, and often wheezing breath sounds (Gavriely et al. 1984, 1987, 1989). Wheezing is prevalent in obstructive pulmonary diseases such as asthma and emphysema. Flow limitation in this setting means that increased increments of driving pressure for flow through a flexible tube do not result in additional increments of flow through it. That may result from viscous effects where the increased pressure drop also increases the partial collapse of the tube. In forced expiration, for example, the upstream driving pressure, $P_u$ in Fig. 2a, is also proportional to the surrounding external pressure of the main flexible airways involved, $P_{ext}$. So, increased effort also increases the partial collapse of the airway. In that situation, the narrowing tube cross section increases the resistance to flow that the larger driving pressure encounters. The two competing effects can balance with the result of no additional flow but instead, a maximal flow, see the pressure-flow relationship of Fig. 2b. This is flow limitation, a common problem in asthma and emphysema patients struggle to force air out of their lungs. Another mechanism of flow limitation is that the fluid speed reaches the local fluid-elastic wave speed of the tube so that pressure information cannot propagate upstream. This is called the wave speed theory of flow limitation (Shapiro 1977; Grotberg and Davis 1980). The experimental evidence so far is that wheezing only occurs in the presence of flow limitation, as Fig. 2b indicates at the maximum flow rate. It also appears that flow limitation can occur without wheezing, which may be a distinguishing feature between the two mechanisms.

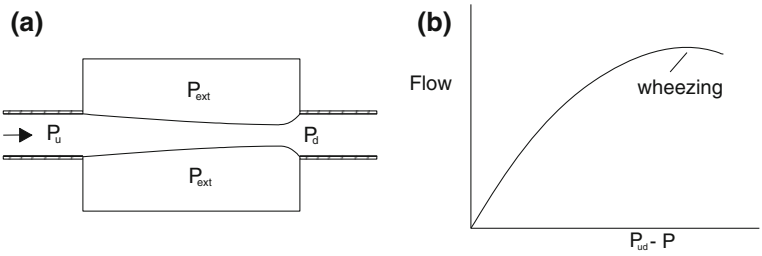


**Fig. 2** **a** Typical flow in flexible tube experiment with rigid upstream and downstream sections. In the lung, $P_u$ and $P_{ext}$ are proportional to one another. **b** Maximum flow, i.e., flow limitation, accompanied by flutter/wheezing for a collapsible tube

Our measurements have included hardware experiments of a collapsible tube segment similar to Fig. 2a (Gavriely et al. 1989), an excised dog lung arranged into a constant flow and constant volume status (Gavriely and Grotberg 1988), and recordings of flow and wheezes in humans (Gavriely et al. 1984; Gavriely et al. 1987). A wide range of oscillation frequencies occur in these settings but are bounded mostly by 100–1,000 Hz with very sharp peak in the power spectrum.

The idea that flow limitation and flutter are related by a general theory was first presented by our group (Grotberg and Davis 1980) for a model of an infinitely long, undamped, flexible channel conveying a frictionless fluid. Increasing the imposed fluid velocity first encounters the wave speed of long waves on the wall, the wave speed theory of flow limitation. Then it loses stability in a flutter mode at a slightly higher speed. That flutter theory was later extended to include a fluid friction term linear with velocity and wall friction (Grotberg and Reiss 1984). Interestingly, a channel flow system with a frictionless fluid and a damped wall loses stability by static divergence at zero frequency, but any amount of fluid friction changes the instability to flutter. The theory was advanced into the nonlinear range using a Poincare-Lindstedt method which showed it to be a supercritical bifurcation instability which stiffens to higher frequencies (Grotberg and Reiss 1984; Grotberg and Gavriely 1989). We then moved to the more complicated approach of solving a small perturbation of the Navier–Stokes equations coupled to a flexible channel wall and solved the resulting Orr-Sommerfeld system analytically for long waves and numerically for finite wavelengths (Larose and Grotberg 1997). The predictions of the linear friction loss system and the Orr-Sommerfeld systems were compared to the benchtop experiments (Gavriely et al. 1989) and found to give reasonable correlations to the measured flutter frequencies and critical fluid velocities that initiate flutter, i.e., the flutter velocity. While this is older work from our lab, presenting it at this meeting will hopefully raise interest from those currently involved in flow-structure interactions with more powerful methods to investigate the key issues of the relationship between flow limitation and flow-induced oscillations, and what other mechanisms may contribute such as vortex shedding or a combination of mechanisms.

*Airway Liquid Plug Rupture and Crackles.* Human lung airways are coated with a viscous mucus layer above a watery serous layer. In healthy airways, the mucus layer traps particles in the lung and is continuously moved toward the mouth by ciliary beating in the serous layer. Such a mucociliary clearance system forms one of the major mechanisms for mucus clearance, besides gravitational drainage and cough (King 2006; Ragavan et al. 2010). Non-Newtonian rheological properties of human respiratory mucus, viscoelasticity, yield stress, and shear-thinning, play significant roles in mucus clearance (King 2006; Ragavan et al. 2010; Rubin et al. 1990). In lung diseases of cystic fibrosis (CF), asthma, severe bronchitis or chronicle obstructive pulmonary diseases (COPD), mucus is hypersecreted, and highly viscoelastic. Mucus hypersecretion causes reduced gas exchange, inflammation, dysfunction of mucus as a selective barrier, and impairment of the mucus clearance mechanism (Lai et al. 2009). Plugs are more likely to form to block partial or total airways (Kant et al. 2007; Kuyper et al. 2003).

To reopen the plug-blocked airway requires the plug to move and rupture, usually from the imposed driving air pressure during breathing. In the plug rupture process, extra forces are imposed on airway walls. The forces have their maximum magnitudes at the front meniscus of the plug (Fujioka and Grotberg 2004), and reach their peaks shortly after rupture. The high forces (and their gradients) may cause lethal damage to the underlying epithelial cells (Bilek et al. 2003; Huh et al. 2007). Yield stress of the plug is more dangerous to the epithelial cells by increasing the force gradients (though reducing shear stress to a degree) (Zamankhan et al. 2011). High surface tension at the plug-air interface can also increase peaks of forces and their gradients, increasing the risk of cell damage (Fujioka and Grotberg 2004). Therefore exogenous surfactant delivering to reduce surface tension has been effective treatment to surfactant deficiency related lung diseases such as respiratory distress syndrome happening to premature infants (Carnielli et al. 2009; Willson and Notter 2011). Besides epithelial cell damage, the rupture may suggest a link to crackles (Hassan et al. 2011).

To further understand rupture of mucus plugs with rheological properties in the human respiratory system, we established a 2D experimental model to study mucus plug rupture in a collapsed lung airway of the 12th generation. Aqueous carbopol 940 (C940) was used as a mucus simulant due to its stable, controllable rheological properties (Gomez et al. 2010). The fluid mechanics features of the plug in the rupture process were to be studied, for instance, critical-driven pressure drop, strain rate of plug deformation, and shear stress in the plug.

## 2 Experimental Methods

### *2.1 Mucus Simulant*

C940 powder (from Lubrizol Co. as an appreciated courtesy) was dissolved in deionized water to make aqueous C940 solutions at concentrations $c = 0.15$, 0.2, 0.25, and 0.3 % (weight/weight). The C940 solutions are acidic and were neutralized by 18 % sodium hydroxide to acquire clear gels with non-Newtonian properties of viscoelasticity, yield stress, and shear-thinning.

The viscoelasticity of the C940 gels was measured by an AR1000 rheometer (TA Instruments Com.). A 60 mm-2° cone-plate with a truncation gap of 58 μm was used in the oscillatory measurement mode. The storage modulus, $G'$, and the loss modulus, $G''$, components of the complex shear modulus $G^* = G' + iG''$, were derived as well as their relationship to the complex viscosity, $\eta^* = \eta' - i\eta'' = -iG^*/\omega$. To measure the static yield stress of the gels, we ran a rate-controlled RVDV-III Ultra rheometer with the vane spindle-74 (Brookfield Engineering Laboratories, Inc.) at 0.7 revolutions per minute in normal room conditions.

Yield stress inherent in C940 gels makes it difficult to accurately measure surface tension using conventional methods (Balmforth et al. 2010). Here, surface tension between the gel and air was set as $\sigma = 0.04$ N/m, a constant for parameter estimation.

## 2.2 Microchannel Fabrication

To simulate a collapsed airway at the 12th generation, we made a microfluidic channel 1.5 mm wide, 120 μm high, and 5 cm long, as shown in Fig. 3. Due to the large aspect ratio (= 12.5) of the $y$- to $z$-direction, quantities may be integrated with respect to $z$ to reduce the 3D effects. Such a selected geometry provides optical clarity to view plug evolvement. The channel was fabricated through standard soft lithography. Both the pattern and non-pattern layers were made of polydimethylsiloxane (Slygard 184, Dow Corning Corp.) for the same surface properties.

## 2.3 Plug Manufacture

We manually made plugs inside the channel with a syringe. The plugs had no precursor and trailing films to reduce film thickness uncertainty in experiments. A C940 gel was infused into the channel to partially fill the channel, and then air was infused to break the gel filling into two thin films attached to the lateral walls. A plug was formed with a micro spatula slowly pressing down the channel until the film layers partially touched each other. Finally the plug was detached from films (using the spatula repeatedly pressing-releasing from the channel above the films). The initial plug length varied from $2.27a$ to $0.59a$.

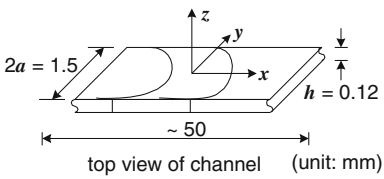


**Fig. 3** The channel dimensions: $a$ = half channel width, and $h$ = channel height. The $x$-axis is located at the channel centerline; $z = 0$ is at the middle of the channel height. Lateral walls: $y = \pm a$, parallel to the $zx$-plane; and top/bottom walls: $z = \pm h/2$, parallel to the $xy$-plane

## 2.4 Experiment Operation

Figure 4 shows the experimental setting. The 2D channel was used to simulate a collapsed lung airway of the 12th generation. The channel with the plug was placed on a slide and then mounted on the platform of an inverted microscope (Eclipse Ti-U, Nikon). A 12-bit CCD camera (CoolSnap EZ, Photometrics) was connected to a 2 × objective lens to capture images of plug motion. All experiments were done at room temperatures between 22.5 and 25.5 °C.

A syringe pump compressed air to build up a pressure drop upon the plug, $\Delta p = p_1\text{-}p_2$ ($p_2$ equal to the atmosphere pressure), as shown in Fig. 4. To find a critical pressure drop, a minimum pressure drop for the plug to rupture, a series of pressure drops were imposed upon the plug ordered in steps, $i$, from low to high to observe if the plug ruptures. When the plug does not rupture at the lower value, $\Delta p^{i-1}$, but ruptures at the next pressure drop, $\Delta p^{i}$, average the two successive pressure drops—re-denoted as $\Delta p_c^{i-1}$ and $\Delta p_c^{i}$—to approximate the actual critical pressure drop, $\Delta p_c = (\Delta p_c^{i-1} + \Delta p_c^{i})/2$.

The initial infused air was set as 0.1 ml for 0.1 and 0.15 % plugs (about a pressure drop of $4.27 \times 10^3$ dyn/cm$^2$) or 0.2 ml for 0.2 and 0.3 % plugs (about a pressure drop of $8.25 \times 10^3$ dyn/cm$^2$). The increment of infused air volume was 0.025 ml, equivalent to a pressure drop about $1.0 \times 10^3$ dyn/cm$^2$. Before each plug rupture experiment was done, the piston of the air syringe was set at a zero position, and any remained pressure in the channel system was fully released. The syringe pump was run in volume mode at an infused flow rate of 0.5 ml/min. The pressure drop $\Delta p^{i}$ was recorded using a differential pressure transducer (PX139-001D4 V, Omega Engineering Inc.) triggered by a program coded in LabView (National Instruments Co.). The imaging program, MetaMorph (Universal Imaging Co.), was turned on just before the pressure was recorded.

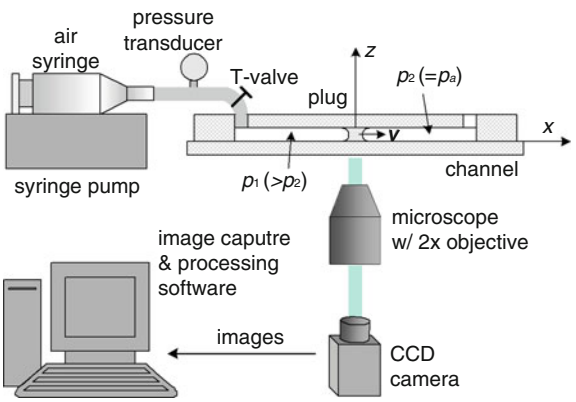


**Fig. 4** Experiment setting to simulate mucus plug dynamics in a collapsed lung airway of the 12th generation

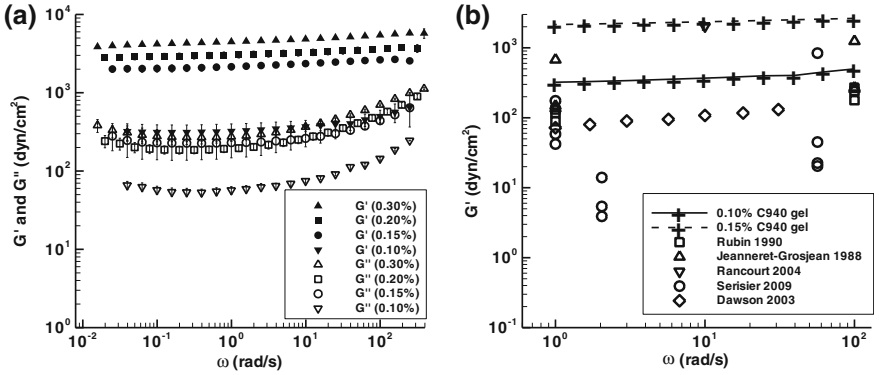


**Fig. 5** **a** The storage and loss moduli, $G'$ and $G''$ (mean ± SD, repeating each measurement three times), vary with angular frequency $\omega$. **b** $G'$ of the 0.1 % (—) and 0.15 % (- - -) gels and human respiratory mucus from literature at $1 \leq \omega \leq 100$ rad/s. White square (Rubin et al. 1990), White up-pointing triangle, White down-pointing triangle (Rancourt et al. 2004) (here the value is $G^*$ instead of $G'$), White circle (Serisier et al. 2009), Diamond (Dawson et al. 2003)

## 2.5 Imaging

The imaging and $\mu$-PIV technique followed the method given in the study of Bian et al. (Bian et al. 2010). Images were captured by the CCD camera at a speed of 27.96 frames per second. The image resolution provided by MetaMorph is 348 × 260 pixels, equivalent to a spatial resolution of 12.6 μm per pixel. Particles with size of 1-μm (Titanium dioxide) were uniformly seeded into the gels.

## 2.6 Scales and Parameters

The plug rupture problem involves nine-dimensional parameters, $\rho$, $U, a, L_0, h, \sigma$, $|\eta^*|$, $G'$, $\tau_y$, in which $\rho$ is gel density. The characteristic velocity parameter, $U$, is derived from the simplified $x$-momentum balance, $\mathrm{d}p/\mathrm{d}x \sim \partial(|\eta^*|\partial u/\partial y)/\partial y$. Defining the characteristic pressure gradient as the initial pressure drop across the plug, $\mathrm{d}p/\mathrm{d}x \sim \Delta p_c/L_0$, we find $\Delta p_c/L_0 \sim |\eta^*|U/a^2$, so $U = \Delta p_c a^2/(|\eta^*|L_0)$. Six dimensionless parameters are further generated, the reciprocal Bingham number $Bn^{-1}$=$\Delta p_c a/(\tau_y L_0)$, the capillary number $Ca = \Delta p_c a^2/(\sigma L_0)$, the Reynolds number $Re = \rho \Delta p_c a^3/\left(|\eta^*|^2 L_0\right)$, the ratio of elastic to surface forces, $G'/(\sigma/a)$, the geometric ratios $L_0/a$ and $h/a$. Neither $Bn^{-1}$ nor $Ca$ depends directly on viscosity, but rather indirectly through the imposed pressure drop.

# 3 Results

## 3.1 Rheology of C940 Gels

### 3.1.1 Viscoelasticity

Figure 5a shows the storage and loss moduli, $G'$ and $G''$, as functions of $\omega$ from 0.04 to 250 rad/s. Generally they both increase with gel concentration. Due to $G' > G''$, the gel is more elastic, also a feature of human respiratory mucus. The storage modulus $G'$ increases with $\omega$ except that $G'$ of the 0.1 % gel has a local minimum at $\omega = 0.16$ rad/s. The $G$"-curves have local minima in $0.1 < \omega < 1$ rad/s. Figure 5b plots the storage modulus $G'$ of the measured values of the 0.1 % and 0.15 % gels and literature data of human respiratory mucus at $1 \leq \omega \leq 100$ rad/s. The storage modulus $G'$ of human respiratory mucus varies in a large range, including mucus from normals, CF, COPD, and treatment with atropine which dehydrates secretions (Rubin et al. 1990; Dawson et al. 2003; Rancourt et al. 2004; Serisier et al. 2009). These abnormal mucus properties will be found in the upper airway as well in a similar thin channel geometry. Generally, human respiratory mucus is on the order of those for the 0.1 % gel, and has lower $G'$ than the 0.15 % gel. Diseased airway mucus usually has higher $G'$ than normals. In some lung diseases, $G'$ can be as high as that of the 0.15 % gel.

The values of the complex viscosity $\eta^*$ and the dynamic viscosity $\eta' = G$"$/\omega$ in Fig. 6a increase with gel concentration and decrease with the angular frequency $\omega$, showing shear-thinning behavior. Using the power-law relationship to fit the curves, $\eta' \propto \omega^{n-1}$, we find the flow behavior index, $n$, varies within 0.09 and 0.16. For human respiratory mucus, $n$ is in the range 0–0.5 (average of 0.15) (Yeates and Wong 1997). Therefore the C940 gels can simulate the shear-thinning feature of the physiologic mucus. Figure 6b further shows the dynamic viscosity $\eta'$ of the 0.1 and 0.15 % gels and human respiratory mucus from the same literature sources as Fig. 5b. The 0.1 % gel may approximate the dynamic viscosity of most human respiratory mucus of both pathologic and healthy people. At $\omega = 1$ rad/s, human respiratory mucus has the dynamic viscosity of about 22–207 Poise (Rubin et al. 1990; Dawson et al. 2003; Serisier et al. 2009; Jeanneret-Grosjean et al. 1988), which is comparable to $\eta' = 57$ Poise of the 0.1 % gel. The dynamic viscosity of mucus is higher in some lung diseases, in which the 0.15 % gel can be used as a simulant in terms of dynamics viscosity.

### 3.1.2 Yield Stress

The yield stress in the static tests increases from $55 \pm 21$, $324 \pm 59$, $504 \pm 57$ to $744 \pm 163$ dyn/cm$^2$ for the four gel concentrations from 0.1 to 0.3 %. The yield stress of 504 dyn/cm$^2$ at $c = 0.2$ % is comparable to the normal human lung

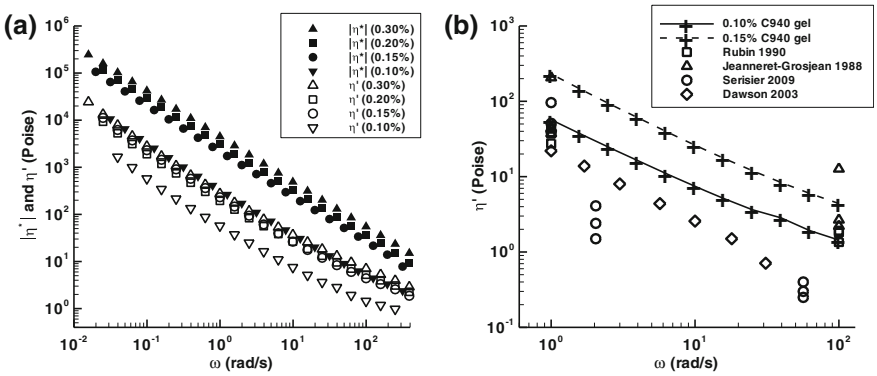


**Fig. 6** **a** The magnitude of complex viscosity $\eta^*$ and the dynamic viscosity $\eta'$ vary with angular frequency $\omega$. The viscosities were calculated from the mean values of $G'$ and $G$" in Fig. 5a. **b** The dynamic viscosity $\eta'$ of the 0.1 % (—) and 0.15 % (- - -) gels and human respiratory mucus from literature at $1 \leq \omega \leq 100$ rad/s. White square (Rubin et al. 1990), White up-pointing triangle (Jeanneret-Grosjean et al. 1988), White circle (Serisier et al. 2009), Diamond (Dawson et al. 2003)

mucus around 400–600 dyn/cm$^2$ (Davis 1973). Due to property variation among batches, the yield stress of the batch used in the plug rupture experiments is 55, 257, 440, and 580 dyn/cm$^2$, respectively.

## 3.2 Critical Pressure Drop

The critical pressure drop, $\Delta p_c$, used in the experiments to yield rupture varies in the range $7.7 \times 10^3 \leq \Delta p_c \leq 1.88 \times 10^4$ dyn/cm$^2$ for all plugs at the gel concentrations from 0.1 to 0.3 %. This pressure drop is physiologic, compared with a typical pressure difference between the alveoli and mouth of $2 \times 10^3$ dyn/cm$^2$ during quiet breathing and up to $4 \times 10^4$ dyn/cm$^2$ or higher during forced expiration. In Fig. 7a, increasing $L_0/a$ or gel concentration usually requires an increased $\Delta p_c$. In the dimensionless form in Fig. 7b, the essentially linear $Bn^{-1}$-$L_0/a$ relationship suggests the proper choice of the velocity scale, $U = \Delta p_c a^2/(|\eta^*|L_0)$. The 0.1 %-line is steeper than the other three nearly co-linear lines.

## 3.3 Rupture Experiments

### 3.3.1 Motion and Rupture Process

Here the plug motion with a final rupture is presented for two plugs in the conditions of $c = 0.1$ %, $L_0/a = 1.15$, $\Delta p_c = 8.0 \times 10^3$ dyn/cm$^2$, and $c = 0.3$ %, $L_0/a = 1.33$, $\Delta p_c = 1.6 \times 10^4$ dyn/cm$^2$, which are named plug-0.1 % and

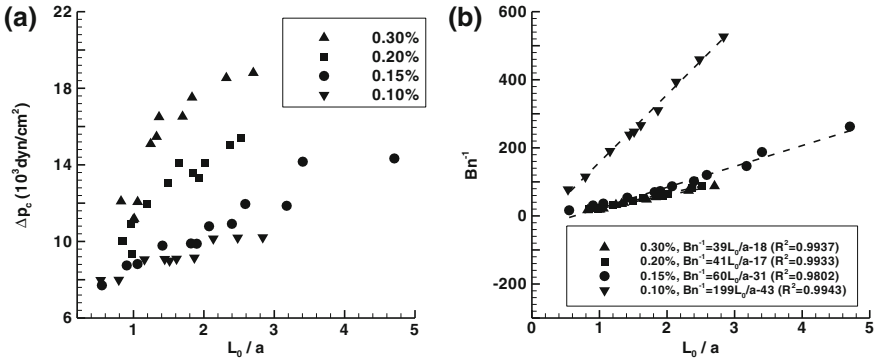


**Fig. 7** **a** The critical pressure drop, $\Delta p_c$, and **b** the reciprocal of the Bingham number, $Bn^{-1}$, increases with $L_0/a$ at $c = 0.1$, 0.15, 0.2, and 0.3 %. The dashed lines are linear fit to data. $R^2$ is the squared determination coefficient

plug-0.3 %, respectively. Figure 8a shows the moving and rupturing process of plug-0.1 %. Once $\Delta p_c$ is imposed, the time to final rupture is about 9 s. The plug deforms and moves as a whole with the plug meniscus tips protruding forward as shown from Fig. 8(a1) to 8(a2). In this case droplets (three) are also formed in Fig. 8(a8). Plug-0.3 % in Fig. 8b shares similar motion and rupture features as plug-0.1 % in Fig. 8a, but has slower motion. The speed at Fig. 8(b3) is 0.12 mm/s, much slower than 0.88 mm/s for plug-0.1 % at Fig. 8(a3). One droplet appears in Fig. 8(b8). The sketch in Fig. 8c shows the approximate plug positions in the channel. Plug-0.3 % covers over a shorter overall distance, less than half that of plug-0.1 %.

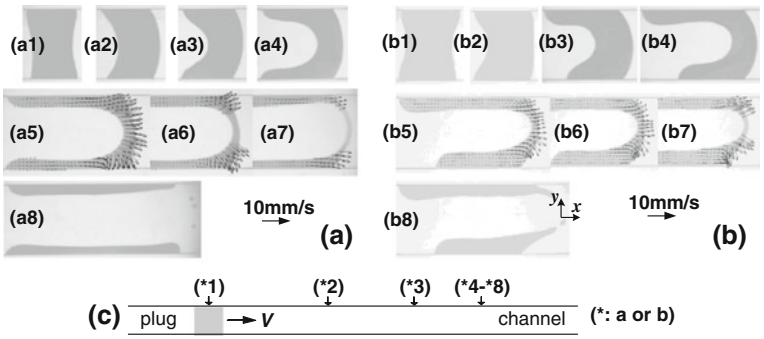


**Fig. 8** The deformation and rupture process of **a** plug-0.1 % and **b** plug-0.3 %. (*a1*) and (*b1*) are plug length $L = L_0$ at the moment when $\Delta p_c$ is imposed, (*a2–a3*) and (*b2–b3*) are translation phases, (*a4–a7*) and (*b4–b7*) are the rupture phase. The velocity vector fields from $\mu$-PIV are shown for (*a5–a7*) and (*b5–b7*). **c** The sketch shows the approximate plug position in the channel

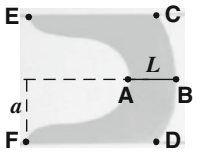


**Fig. 9** Six points are selected on the plug: *A*—back plug tip, *B*—front plug tip, *C*—front wall attachment point ($y = a$), *D*—front wall attachment point ($y = -a$), *E*—back wall attachment point ($y = a$), and *F*—back wall attachment point ($y = -a$). *L*: plug length

### 3.3.2 Average Strain Rates and Shear Stress

Figure 9 shows six selected points on the plug. The distance between the two plug tips located at the channel centerline, A and B, is defined as the time-dependent plug length, *L*. Near rupture, the velocities at A, B, C, and D, dramatically increase to a final value about 10–16 mm/s. The velocity averaged in the time period $t|_{L/a=0.5} \leq t \leq 0$ ($t|_{L/a=0.5} = -0.29$ s for plug-0.1 %, and -0.72 s plug-0.3 %) at A and B is 5.7 mm/s for plug-0.1 %, four times that of plug-0.3 %, 1.4 mm/s.

An averaged shear strain rate and normal strain rate are introduced to describe the average plug deformation in the rupture process, $\bar{\dot{\gamma}}_{xy} = (V_A - V_{EF})/a$ and $\bar{\dot{\gamma}}_{xx} = (V_B - V_A)/L$, in which $V_{EF} = (V_E + V_F)/2$. The magnitudes of both rates increase dramatically at rupture from nearly zero, as shown in Fig. 10. Plug-0.1 % has higher values of $\bar{\dot{\gamma}}_{xy}$ than plug-0.3 % until they both reach about 21 $s^{-1}$ at the rupture moment $t = 0$, whereas the two plugs have little difference in $\bar{\dot{\gamma}}_{xx}$ until $\bar{\dot{\gamma}}_{xx}$=28 $s^{-1}$ for both at $t = 0$. Over the interval $t|_{L/a=0.5} \leq t \leq 0$, the time averaged strain rates of plug-0.1 %, $<\bar{\dot{\gamma}}_{xy}>_{0.1\%} = 8.24$ $s^{-1}$ and $<\bar{\dot{\gamma}}_{xx}>_{0.1\%} = 6.37$ $s^{-1}$, are both higher than those of plug-0.3 %, $<\bar{\dot{\gamma}}_{xy}>_{0.3\%} = 2.07$ $s^{-1}$ and $<\bar{\dot{\gamma}}_{xx}>_{0.3\%} = 2.33$ $s^{-1}$.

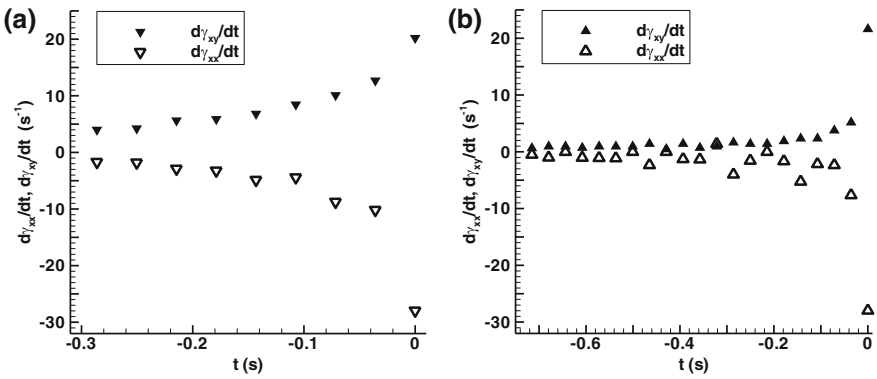


**Fig. 10** The averaged shear and strain rates near rupture for **a** plug-0.1 % and **b** plug-0.3 %

### 3.3.3 Film Thickness

After rupture, two trailing films attach to the lateral channel walls (at $y = \pm a$), as shown in Fig. 8(a8) and (b8). Defining the average length of the two films as the final film length, $L_f$, we calculated the film thickness $H$ according to mass conservation as $H/a = L_0/L_f$. The thickness $H/a$ is nearly a constant of $0.34 \pm 0.06$ for all the plugs, independent of $Ca$ and $Bn^{-1}$.

## 4 Discussion

### *4.1 Rheology of C940 Gels*

C940 gels have both viscoelastic and viscoplastic properties. They have higher storage modulus than the loss modulus, as shown in Fig. 5a and literature (Oppong and de Bruyn 2011). The gels show a shear-thinning feature that the (complex and dynamic) viscosity decreases with angular frequency (or shear rate). The moduli and viscosity increase with gel concentration. The gels at concentrations 0.1–0.15 % may be used to simulate human mucus with comparable viscoelasticity moduli and viscosity (Rubin et al. 1990; Lai et al. 2009; Dawson et al. 2003; Serisier et al. 2009; Jeanneret-Grosjean et al. 1988), particularly in infection or dehydration where mucus clearance is a significant issue. The yield stress of the gels also increases with concentration. According to our protocol, the 0.2 % gel has properties similar to normal mucus with a yield stress of 504 dyn/cm$^2$, whereas 0.3 % gel can be used to simulate pathological mucus with a high yield stress.

### *4.2 Critical Pressure Drop*

The imposed pressure drop caused two types of motion. The initial movement is translational with some deformation. As a strategy for clearing mucus with airflow, translation is a meaningful event to move the mucus downstream. However, it does not allow continuity between the two air columns, upstream and downstream. In the respiratory application that would imply the lack of gas exchange of oxygen and carbon dioxide between the atmosphere and the lung portions distal to the location of the blocking plug. The other motion is rupture, where the plug length at the centerline going to zero establishes the airflow without further blockage.

The linear relationship between $Bn^{-1}$ and $L_0/a$ (Fig. 7b) indicates, as $L_0/a \rightarrow 0$, $Bn^{-1} \rightarrow 0$, or equivalently $\Delta p_c \rightarrow 0$. However, a finite, nonzero limit may exist for $\Delta p_c$ as $L_0/a \rightarrow 0$ due to surface tension, since the surface tension force on the plug front and rear surfaces is not directly related to the plug length, but rather the

channel width and height, to which the plug surface curvature is related. The gradient, $Bn^{-1}/(L_0/a)$, is the dimensionless critical value of the pressure gradient to cause rupture. The $Bn^{-1}$-$L_0/a$ line has a much larger slope for $c = 0.1$ % than the nearly co-linear lines for the higher concentrations, which implies the importance of surface tension for the mixture. The ratio of elasticity to surface tension for $c = 0.1$ %, $G'/(\sigma/a) = 0.6$ (at $\omega = 1$ rad/s), indicates surface tension is roughly as important as elasticity, whereas surface tension is far less important for $c > 0.1$ %, in which $G'/(\sigma/a)$ increases from 4 at $c = 0.15$ % to 8.4 at $c = 0.3$ % (at $\omega = 1$ rad/s). Likewise, the comparison of surface tension to yield stress, $\sigma/(a_y)$, has values 9.7, 2.1, 1.2, and 0.9 for the concentrations from 0.1 to 0.3 %, respectively. Clearly the 0.1 % plugs is more controlled by surface tension effects than the other mixtures, which sets it aspart from them in the critical driving pressure required for rupture. The fact that surface tension of the gels generally decreases with concentration increasing (Baek et al. 2011) would further distinguish the 0.1 % plugs from the plugs at the other three higher concentrations.

### *4.3 Plug Motion and Rupture*

The deformation of the rear interface for the plug permits the normal pressure at its interface to have a component in the $y$-direction that increases the friction of the wall and eventually can pin the trailing three-phase line of the plug to the wall [Fig. 8(a4) and (b4)]. Around this moment, the plug ceases to simply translate, but instead goes through a rupture deformation while depositing mass to the lateral walls to form films. The rear meniscus moves faster and catches up with the front meniscus, causing rupture with two deposited trailing film layers attached to the lateral walls [Fig. 8(a8) and 8(b8)].

The formation of the two deposited films with $H/a \sim 0.34 \pm 0.06$, implies that the plug yields at a line of $y \sim 0.66a$ from the channel center line. Little dependence of $H/a$ while changing $Bn$ and $Ca$ might imply a 3D effect from the $z$-height of the channel near the lateral boundaries at $y = \pm a$. Fluid in that corner will feel that influence of additional wall shear more than the fluid near the centerline. However, we have found a similar yield plane position, $y \sim 0.7a$ in a 2D study of a Bingham plug with a precursor and trailing film (Zamankhan et al. 2011). In most cases, the rupture process is accompanied by the generation of satellite droplets depositing in the channel. The droplets, together with the films on the lateral walls, are possible for further formation of plugs due to periodic airway closure-reopening (Tai et al. 2011).

### 4.4 Average Shear Rate and Shear Stress

The maximum average shear rate appears at rupture. The average shear stress is approximated using $<\tau_{xy}> = \eta(<\bar{\dot{\gamma}}>)<\bar{\dot{\gamma}}_{xy}>$, in which $<\bar{\dot{\gamma}}> = \sqrt{<\bar{\dot{\gamma}}_{xx}>^2/2 + <\bar{\dot{\gamma}}_{xy}>^2}$ (normal strain rate is neglected), and viscosity is approximated by $\eta(<\bar{\dot{\gamma}}>) = |\eta^*|(\omega)_{\omega=<\bar{\dot{\gamma}}>}$ (Cox and Merz 1958). Using the viscosity data in Fig. 6a, we acquire average shear stress of 362 dyn/cm$^2$ for plug-0.1 %, about one-tenth of 3.69 × 10$^3$ dyn/cm$^2$ for plug-0.3 %.

The relevant numerical studies indicate that wall shear stress (WSS), and the axial gradients of shear stress and pressure along the wall are sources of injury and/or death for epithelial cells (Bilek et al. 2003; Huh et al. 2007; Zamankhan et al. 2011). An in vivo–in vitro experiment showed that cells may have been damaged at the WSS about 100 dyn/cm$^2$, estimated from a numerical study of steady Newtonian plug motion (Fujioka and Grotberg 2004; Huh et al. 2007), which is much lower than the averaged shear stress obtained here. A numerical study of non-Newtonian plugs also predicted the existence of yield stress may result in higher WSS, and increase the possibility of epithelial cell damage (Zamankhan et al. 2011). Furthermore, high WSS may lead to more mucus secretion from epithelial cells, and more likely block airways (Even-Tzur et al. 2008).

## 5 Conclusion

We studied the propagation of non-Newtonian plugs in an otherwise dry channel as a model of mucus plug clearance in the lung. Clearance of mucus plugs from airways is an important self-defense of human physiology that can be compromised by particularly difficult mucus properties of yield stress, viscosity, and elasticity found in some lung diseases. In this study the mucus simulant, carbopol 940, showed its properties overlap with those measured in human mucus during health and disease.

In these experiments, both the translational phase of the plug propagation and the rupture phase were studied using average shear strain rates. The explosive rupture of a liquid plug can severely damage airway epithelial cells causing injury or death (Huh et al. 2007). Plug rupture is linked to the creation of lung sounds of crackles, a very important clinical finding heard with a stethoscope. Understanding the dynamics of that sound formation will help to link mucus properties to recorded acoustic signatures, potentially allowing a non-invasive diagnostic tool to follow disease and results of treatments.

**Acknowledgments** This work is supported by NIH grants: HL84370 and HL85156. The authors are particularly grateful to Dr. Parsa Zamankhan, Dr. Cheng-Feng Tai, and Yi-Cheng Chen in the Grotberg lab for helpful discussions. We are grateful to the lab of Dr. Michael J. Solomon of the University of Michigan for use and instruction of their rheometer.

## References

Baek G, Kim S, Han J, Kim C (2011) Atomization characteristics of impinging jets of gel material containing nanoparticles. J Nonnewton Fluid Mech 166(21–22):1272–1285

Balmforth NJ, Dubash N, Slim AC (2010) Extensional dynamics of viscoplastic filaments: II. Drips and bridges. J Nonnewton Fluid Mech 165(19–20):1147–1160

Bian S, Tai CF, Halpern D, Zheng Y, Grotberg JB (2010) Experimental study of flow fields in an airway closure model. J Fluid Mech 647:391–402

Bilek AM, Dee KC, Gaver DP (2003) Mechanisms of surface-tension-induced epithelial cell damage in a model of pulmonary airway reopening. J Appl Physiol 94(2):770–783

Carnielli VP, Zimmermann LJI, Hamvas A, Cogo PE (2009) Pulmonary surfactant kinetics of the newborn infant: novel insights from studies with stable isotopes. J Perinatol 29:S29–S37

Cox WP, Merz EH (1958) Correlation of dynamic and steady flow viscosities. J Poly Sci 28(118):619–622

Davis SS (1973) Rheological examination of sputum and saliva and the effect of drugs. In: Gabelnick HL, Litt M (ed) Rheology of Biological Systems. Springfield: Charles C. Thomas pp 157–194

Dawson M, Wirtz D, Hanes J (2003) Enhanced viscoelasticity of human cystic fibrotic sputum correlates with increasing microheterogeneity in particle transport. J Biol Chem 278(50):50393–50401

Even-Tzur N, Kloog Y, Wolf M, Elad D (2008) Mucus secretion and cytoskeletal modifications in cultured nasal epithelial cells exposed to wall shear stresses. Biophys J 95(6):2998–3008

Fujioka H, Grotberg JB (2004) Steady propagation of a liquid plug in a two-dimensional channel. J Biomech Eng 126(5):567–577

Gavriely N, Palti Y, Alroy G, Grotberg JB (1984) Measurement and theory of wheezing breath sounds. J Appl Physiol 57(2):481–492

Gavriely N, Kelly KB, Grotberg JB, Loring SH (1987) Forced expiratory wheezes are a manifestation of airway flow limitation. J Appl Physiol 62(6):2398–2403

Gavriely N, Grotberg JB (1988) Flow limitation and wheezes in a constant flow and volume lung preparation. J Appl Physiol 64(1):17–20

Gavriely N, Kelly KB, Grotberg JB, Loring SH (1989a) Critical pressures required for generation of forced expiratory wheezes. J Appl Physiol 66(3):1136–1142

Gavriely N, Shee TR, Cugell DW, Grotberg JB (1989b) Flutter in flow-limited collapsible tubes: a mechanism for generation of wheezes. J Appl Physiol 66(5):2251–2261

Gomez C, Derakhshandeh B, Hatzikiriakos SG, Bennington CPJ (2010) Carbopol as a model fluid for studying mixing of pulp fibre suspensions. Chem Eng Sci 65(3):1288–1295

Grotberg JB, Davis SH (1980) Fluid-dynamic flapping of a collapsible channel: sound generation and flow limitation. J Biomech 13(3):219–230

Grotberg JB, Reiss EL (1984) Subsonic flapping flutter. J Sound Vib 92(3):349–361

Grotberg JB, Gavriely N (1989) Flutter in collapsible tubes: a theoretical model of wheezes. J Appl Physiol 66:2262–2273

Hassan EA, Uzgoren E, Fujioka H, Grotberg JB, Shyy W (2011) Adaptive Lagrangian-Eulerian computation of propagation and rupture of a liquid plug in a tube. Int J Numer Meth Fluids 67(11):1373–1392

Huh D, Fujioka H, Tung YC, Futai N, Paine R, Grotberg JB, et al. (2007) Acoustically detectable cellular-level lung injury induced by fluid mechanical stresses in microfluidic airway systems. In: Proceedings of the National Academy of Sciences of the United States of America. 104:18886–18891. PMCID: PMC2141877

Jeanneret-Grosjean A, King M, Michoud MC, Liote H, Amyot R (1988) Sampling technique and rheology of human tracheo-bronchial mucus. Am Rev Respiratory Disease 137(3):707–710

Kant S, Verma S, Sanjay (2007) Complete left lung collapse secondary to mucus plug in COPD patient. Pulmon 9(1):35–36

King M (2006) Physiology of mucus clearance. Paediatr Respir Rev 7:S212–S214

Kuyper L, Pare P, Hogg J, Lambert R, Ionescu D, Woods R et al (2003) Characterization of airway plugging in fatal asthma. Am J Med 115(1):6–11

Lai SK, Wang Y–Y, Wirtz D, Hanes J (2009) Micro-and macrorheology of mucus. Adv Drug Deliv Rev 61(2):86–100

Larose PG, Grotberg JB (1997) Flutter and long wave instabilities in compliant channels conveying developing flows. J Fluid Mech 331:37–58

Oppong FK, de Bruyn JR (2011) Mircorheology and jamming in a yield-stress fluid. Rheol Acta 50(4):317–326

Ragavan AJ, Evrensel CA, Krumpe P (2010) Interactions of airflow oscillation, tracheal inclination, and mucus elasticity significantly improve simulated cough clearance. Chest 137(2):355–361

Rancourt RC, Tai SS, King M, Heltshe SL, Penvari C, Accurso FJ et al (2004) Thioredoxin liquefies and decreases the viscoelasticity of cystic fibrosis sputum. Am J Physiol-Lung Cellular Molecular Physiol 286(5):L931–L938

Rubin BK, Finegan B, Ramirez O, King M (1990) General-anesthesia does not alter the viscoelastic or transport properties of human resiratory mucus. Chest 98(1):101–104

Serisier DJ, Carroll MP, Shute JK, Young SA (2009) Macrorheology of cystic fibrosis, chronic obstructive pulmonary disease and normal sputum. Respiratory Research 10

Shapiro AH (1977) Steady flow in collapsible tubes. J Biomech Eng 99:126–147

Tai CF, Bian S, Halpern D, Zheng Y, Filoche M, Grotberg JB (2011) Numerical study of flow fields in an airway closure model. J Fluid Mech 677:483–502

Willson DF, Notter RH (2011) The future of exogenous surfactant therapy. Respiratory Care 56(9):1369–1386

Yeates DB BG, Wong LB (1997) Physicochemical properties of mucus and its propulsion. In: Crystal RG WJ, Weibel ER et al. (ed) The Lung: Scientific Foundations. Philadelphia: Lippincott-Raven pp 487–503

Zamankhan P, Helenbrook BT, Takayama S, Grotberg JB (2011) Steady motion of Bingham liquid plugs in two-dimensional channels. J Fluid Mech. doi:10.1017/jfm.2011.438

# Stability of a Spring-Mounted Cantilevered Flexible Plate in a Uniform Flow

**R. M. Howell and A. D. Lucey**

**Abstract** A new system in fluid-structure interaction (FSI) is studied wherein a cantilevered thin flexible plate is aligned with a uniform flow with the upstream end of the plate attached to a spring-mass system. This allows the entire system to oscillate in a direction perpendicular to that of the flow as a result of the dynamic interaction of the mounting with the flow-induced oscillations, or flutter, of the flexible plate. While a fundamental problem in FSI, the study of this variation on classical plate flutter is also motivated by its potential as an energy-harvesting system in which the reciprocating motion of the support system would be tapped for energy production. In this paper, we formulate and deploy a hybrid of theoretical and computational models for the fluid-structure system and map out its linear stability characteristics. The computational model detailed is a novel fully implicit solution that is robust to spatial and temporal discretization. Compared to a fixed cantilever, the introduction of the dynamic support system is shown to yield lower flutter-onset flow speeds and a reduction of the order of the mode that yields the critical flow speed; these effects would be desirable for energy-harvesting applications.

## 1 Introduction

In the recent study of simply supported or cantilevered plates in uniform axial flow first studied by Kornecki et al. (1976), a popular idea has been that of using the flutter instabilities observed in the system to generate useful electrical energy harvested by various means; see for examples Allen and Smits (2001) and Tang et al. (2009). This has led us to investigate the linear stability of a new fundamental

R. M. Howell (✉) · A. D. Lucey
Fluid Dynamics Research Group, Department of Mechanical Engineering, Curtin University of Technology, GPO Box U1987 Perth WA 6845, Australia
e-mail: richard.howell@curtin.edu.au

Y. Zhou et al. (eds.), *Fluid-Structure-Sound Interactions and Control*,
Lecture Notes in Mechanical Engineering, DOI: 10.1007/978-3-642-40371-2_45,

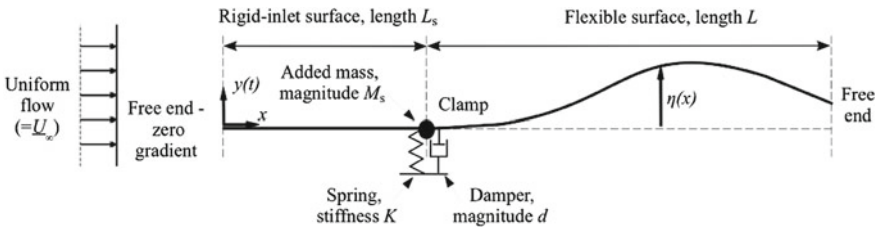


**Fig. 1** The fluid-structure interaction under consideration

system, where the cantilever is not fixed but can move freely in the vertical axis being attached at its leading edge to a rigid base by mounting it upon a linear spring; this new system is depicted in Fig. 1 that also shows the inclusion of a rigid-inlet surface upstream and fixed to the cantilever. A future application of this system would be an energy-harvesting device; this would be achieved through the addition of a linear damper as part of the spring-mass system as shown in Fig. 1. In this paper we combine the exploratory findings of our preliminary studies—see Howell and Lucey (2012a, b)—and present definitive key results. In the absence of damping we map out the dynamics of the parameter space that we find depends upon the mass ratio and the critical velocity and additionally the natural frequency of the support of the spring-mass system and the length and mass of the rigid-inlet.

## 2 Method

The methods detailed in Howell et al. (2009, 2011) that mixed numerical simulation with eigenvalue analysis and incorporated the effects of added point mass are further extended to in-corporate the new system mechanics; these methods have been thoroughly validated in Howell et al. (2009) against other theoretical and experimental studies. An ideal two-dimensional flow is assumed wherein the rotationality of the boundary-layers is modelled by vortex elements on the solid–fluid interface and the imposition of the Kutta condition at the trailing edge of the plate. The Euler–Bernoulli beam model is used for the structural dynamics. Simply supported free beams where the support can move vertically are analysed in studies of insect flight, for example see Manela (2012), and constrain that the leading edge must follow (1) the heaving motion and (2) the pitching motion of the actuating force. In our study these constraints are applied through enforcing that the cantilever displacement is equal to that of the first mass point along the flexible beam. The fluid-structure system is solved both as an initial value problem using a time-stepping fully implicit solution and as a boundary value problem using a state-space method.

## 3 Results

We first introduce the system parameters and the values used to plot the results. To non-dimensionalise properties we use a reference time and length scale $t_r = (\rho h)^{5/2}/(\rho_f^2 B^{1/2})$ and $L_r = \rho h/\rho_f$ respectively where $\rho_f$ is the fluid density and $\rho$, $h$ and $B$ are respectively the flexible plate density, thickness and flexural rigidity. The mass ratio $\bar{L}$ is equal to $L/L_r$ where $L$ is the plate length. The rigid-inlet length $L_s$ in non-dimensional form is $\bar{L}_s = L_s/L$. The dimensionless natural frequency of the spring mount $\bar{\omega}_s$ is equal to $t_r\sqrt{K/(M+M_s)}$ where $K$, $M$ and $M_s$ are respectively the spring stiffness, the flexible plate mass and the splitter-plate mass lumped at the spring mount. The free stream velocity $U_\infty$ in non-dimensional form is $\bar{U} = U_\infty t_r/L_r$. In all the results of this paper damping is absent in both the flexible plate and the spring mounting. The real and imaginary parts of eigenvalues in non-dimensional form are $\bar{\omega}_R = \omega_R t_r$ and $\bar{\omega}_I = \omega_I t_r$ respectively, the non-dimensional fluid work done $\bar{W}$ is the sum of the product of the fluid pressure and wall velocity up to the current time $t$ divided by the initial strain energy in the plate, non-dimensional time is $\bar{t} = t/t_r$, non-dimensional horizontal distance along the flexible plate is $\bar{x} = x/L$ and non-dimensional beam vertical displacement is $\bar{\eta} = \eta/\eta_0$ where $\eta_0$ is the maximum displacement of the flexible plate at $t = 0$.

We first review the results for a rigidly held 'short' plate with a mass ratio of 1 presented in Howell et al. (2009) with a rigid-inlet length of $\bar{L}_s = 1$. Figure 2a shows the variation of system eigenvalues with applied flow speed. In this and subsequent eigenvalue plots the broken lines denote the oscillatory (imaginary) part of the eigenvalue while the solid lines show the associated growth/decay (real) part of the eigenvalue. The modes are numbered in the plots following their order of increasing frequency at zero flow speed. Instability sets in at the lowest flow speed (the critical flow speed, $\bar{U}_c$) for which the real part of the eigenvalue becomes positive. In Fig. 2a it is seen that modal-coalescence flutter of the third system mode—highlighted by a thicker line type—is the critical instability at a non-dimensional flow speed of 13.48. Figure 2c shows the numerical simulation of the critical mode at this flow speed. The simulation was started by releasing the plate from an applied deformation—the thick black line—in the shape of the second *in-vacuo* mode. The critical mode, seen to contain strong contributions from the second and third *in-vacuo* modes, then evolves from the initial excitation. In Howell et al. (2009), the phase angle was monitored between the pressure loading and plate velocity in numerical simulations showing that both the leading-edge singularity and the trailing-edge Kutta condition contribute to non-orthogonality of the pressure and plate velocity. The product of these terms yields the localised rate of work done (per unit area of plate). For unstable motions the sum, over the plate area, of these local transfers is nonzero when integrated over one period of oscillation. The plate-energy record for the simulation of Fig. 2c is shown in Fig. 2e. In Fig. 2e, the thick line represents the total energy transferred from the flow to the plate exactly at the critical flow speed where neutral stability

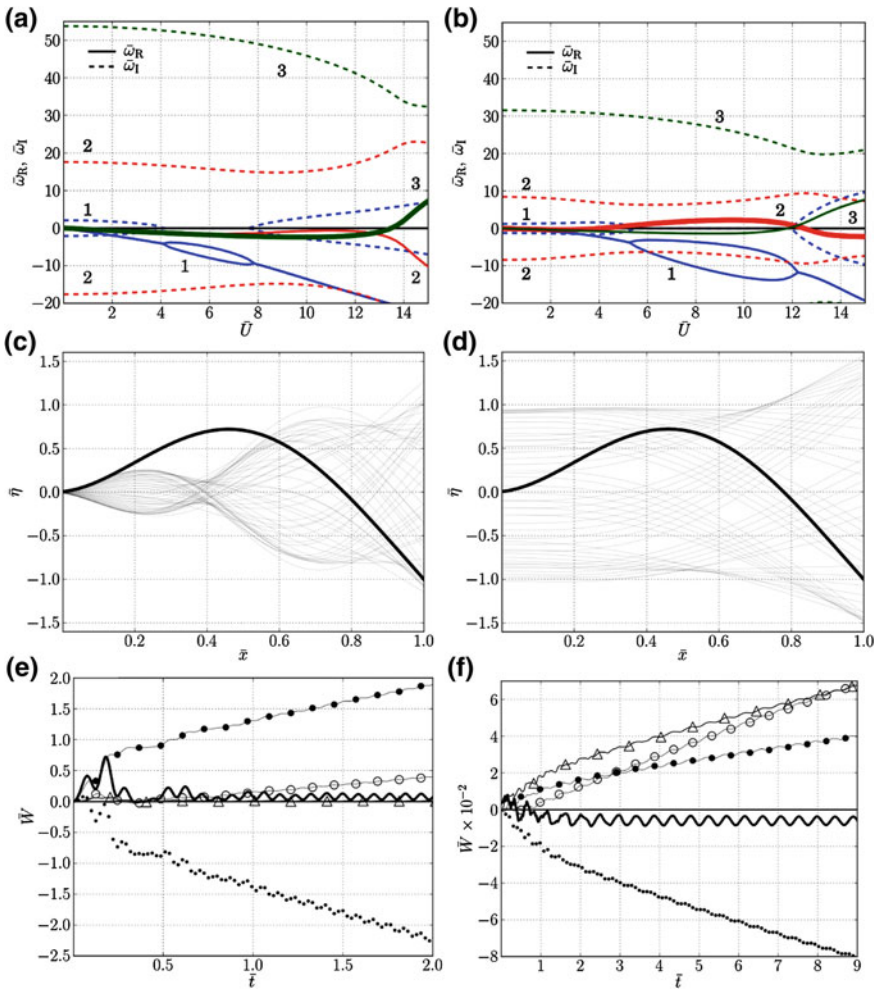


**Fig. 2** **a** and **b** Variation of numbered eigenvalues with flow speed (oscillatory and growth/decay parts represented by *broken* and *full lines* respectively) with the real part that becomes unstable highlighted through a *thicker line* type. **c** and **d** Time-sequence of instantaneous plate position at critical speed (the *thick line* being the initial deflection with early oscillations removed). **e** and **f** Time series of cumulative energy transferred from flow to plate in *triangle*—first, *open circle*—second, *filled circle*—third and *dotted lines*—fourth quarters of the plate while *thick line* is the total of these. **a**, **c** and **e** adapted from Howell et al. (2009) for a fixed cantilever; **b**, **d** and **f** are for a spring-mounted cantilever with $\bar{\omega}_s^{-1} = 0.1$

occurs, while the other four lines show the contributions to this total from each of the four quarters of the plate. After transients due to mode adjustment have died away, the time-averaged value of the total energy is constant. However, it is also seen that the energy exchanges between plate and flow are spatially dependent.

Figure 2b, d and f show the effect on these results of the now oscillating mounting support of the cantilever. The introduced spring stiffness gives $\bar{\omega}_s^{-1} = 0.1$ for the spring-mass system at the leading edge of the flexible beam. Figure 2d shows that the critical mode shape loses its higher order mode content and the reason for this is clearly seen in Fig. 2b as the previously stable Mode 2 has been destabilised by the introduced spring and causes the system to experience flutter at a far lower critical velocity—$\bar{U}_c$ has dropped to 4.0—through single-mode flutter (Mode 2 in Fig. 2b—thick red line). Figure 2f shows that the destabilising work done by and on the fluid has also changed: it is now the first and second quarters of the plate where the greatest energy transfer is occurring in the system instead of the third quarter observed in the fixed-cantilever system.

Figure 2b, d and f illustrate the system behaviour for just one value, $\bar{\omega}_s^{-1} = 0.1$, of the mass-spring support. This type of investigation has then been conducted over a range of $\bar{\omega}_s^{-1}$ and the variation of instability onset flow speed, instability type and oscillation frequency at onset is summarised in Fig. 3a, b. Three types of instability mechanism are identified: the crosses denote the neutral-stability boundary for Mode 2 single-mode flutter, the circles denote the boundary for modal-coalescence of system Modes 2 and 3 and the triangles the boundary for Mode 4 single-mode flutter. Instability occurs within (to the right) of each of the neutral-stability loops while $\bar{U}_c$ for system instability onset is the envelope of minimum flow speed generated by the three loops as $\bar{\omega}_s^{-1}$ is increased from zero.

The vertical dashed lines in Fig. 3a, b show the critical velocity and oscillation frequency values for the rigidly mounted cantilever case. Thus, Fig. 3a shows that the spring-mounted cantilever is always more unstable than when it is rigidly held and that the latter case is approached as the stiffness of the support system is increased ($\bar{\omega}_s^{-1}$ is decreased). Figure 3b shows the large frequency jumps between

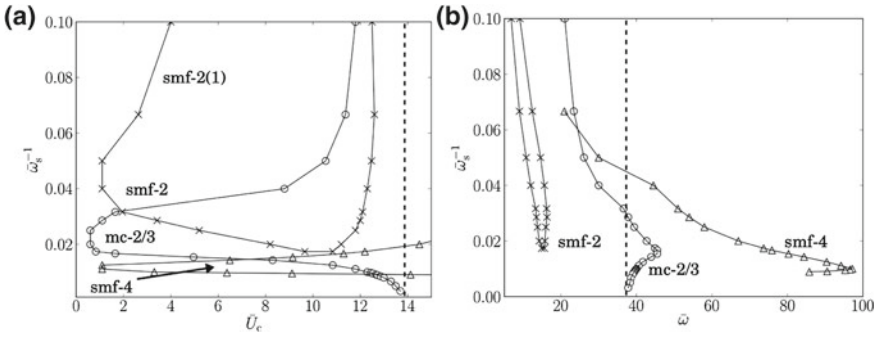


**Fig. 3** Plots of $\bar{\omega}_s^{-1}$ against **a** $\bar{U}_c$ flow speed and **b** $\bar{\omega}$ mode frequency of neutral stability. The labels smf and mc denote regions of single-mode and modal-coalescence flutter respectively; *cross sign*—single-mode flutter of Mode 2 (smf-2) and of a mix of Mode 2 and Mode 1 (smf-2(1)), *open circle*—coupled-mode (Modes 2 and 3) flutter with Mode 3 unstable, triangle—single-mode flutter of Mode 4; the *vertical dashed lines* denote $\bar{U}_c$ and $\bar{\omega}$ at $\bar{U}_c$ for the fixed cantilever case

the predicted types of instabilities and that as the rigidly held cantilever state is approached, the oscillation frequency of the critical mode in the spring-mounted system actually exceeds that of the fixed case.

## 4 Conclusions

We have developed a model for predicting the two-dimensional linear behaviour of a spring-mounted cantilevered flexible plate in a uniform flow and we have used the model to map the stability characteristics of the system when a rigid upstream splitter plate is present for which the rigidly held system would succumb to modal-coalescence flutter at a sufficiently high flow speed.

It has been shown that the introduction of a spring mounting is generally destabilising in that it leads to lower values of the critical flow speed of the onset of both single-mode and modal-coalescence types of flutter. The results also show that the minimum values of critical flow speed for each of the three types of instability encountered as the support stiffness is reduced from the rigidly held state are lower than the values that they asymptotically approach with decreasing stiffness for which rigid-body motion of the flexible plate prevails. This indicates a resonance-type of behaviour between the frequencies of the unstable modes of the fluid-loaded deforming plate and the natural frequency of the mounting system.

The present stability results augur well for the introduction of means to extract power from the reciprocating motion of the support. This is readily modelled by introducing a dashpot damper alongside the spring and the present methods can then be used to determine optimal system parameters for energy harvesting.

## References

Allen JJ, Smits AJ (2001) Energy harvesting eel. J Fluids Struct 15(3–4):629–640

Howell RM, Lucey AD (2012a) The fluid-structure interaction of a spring-mounted cantilevered-free flexible plate in a uniform flow. In: Proceedings of 10th International Conference on flow induced vibration, Dublin, Ireland, 3–6 July 2012 pp 219–226

Howell RM, Lucey AD (2012b) Energy production characteristics of a spring-mounted cantilevered-free flexible plate in a uniform flow. In: Proceedings of FEDSM 2012, Puerto Rico, July 8–12 2012. http://www.asme.org. Paper no FEDSM2012-72071

Howell RM, Lucey AD, Carpenter PW, Pitman MW (2009) Interaction between a cantilevered-free flexible plate and ideal flow. J Fluids Struct 25:544–566

Howell RM, Lucey AD, Pitman MW (2011) The effect of inertial inhomogeneity on the flutter of a cantilevered flexible plate. J Fluids Struct 27:383–393

Kornecki A, Dowell EH, OBrien J (1976) On the aeroelastic instability of two-dimensional panels in uniform incompressible flow. J Sound Vib 47:163–178

Manela A (2012) Vibration and sound of an elastic wing actuated at its leading edge. J Sound Vib 331(3):638–650

Tang L, Païdoussis MP, Jiang J (2009) Cantilevered flexible plates in axial flow: energy transfer and the concept of flutter mill. J Sound Vib 326:529–542

# The Effect of Localised Stiffening on the Stability of a Flexible Panel in Uniform Flow

**Ben H. Tan, Anthony D. Lucey and Richard M. Howell**

**Abstract** The three-dimensional stability of a fluid-loaded flexible panel is studied to determine the effectiveness of adding localised stiffening to control or postpone instability. A hybrid of computational and theoretical modelling is used to cast an eigenvalue problem for the fluid-structure system. It is shown that the addition of each of transverse and streamwise stiffening strips postpones divergence onset but for the former there is a threshold strip stiffness above which no further postponement is possible. Streamwise stiffening is additionally shown to be effective for increasing post-divergence flutter-onset flow speeds while in aeroelastic applications a transverse stiffening strip can be used to replace flutter instability with divergence. The present results suggest a relatively economical and practicable way to ameliorate panel instability in both hydro- and aero-elastic applications.

## 1 Introduction

This paper considers the classical aero/hydro-elastic system comprising a flexible panel exposed to a one-sided incompressible uniform flow; linear studies include Dugundji et al. (1963), Weaver and Unny (1971), Ellen (1973), Lucey and Carpenter (1993), Guo and Païdoussis (2000). The system is representative of the high Reynolds number situations found in many engineering applications that range from the hydrodynamic loading of panels making up the hull of a ship through to the axial wind loading of glass panels of curtain walls that have become a feature of contemporary high-rise buildings for both aesthetic and thermal-control reasons. In such applications, the concern is that at some critical speed the

B. H. Tan · A. D. Lucey (✉) · R. M. Howell
Department of Mechanical Engineering, Curtin University of Technology, GPO Box U1987, Perth, WA 6845, Australia
e-mail: a.d.lucey@curtin.edu.au

Y. Zhou et al. (eds.), *Fluid-Structure-Sound Interactions and Control*,
Lecture Notes in Mechanical Engineering, DOI: 10.1007/978-3-642-40371-2_46,

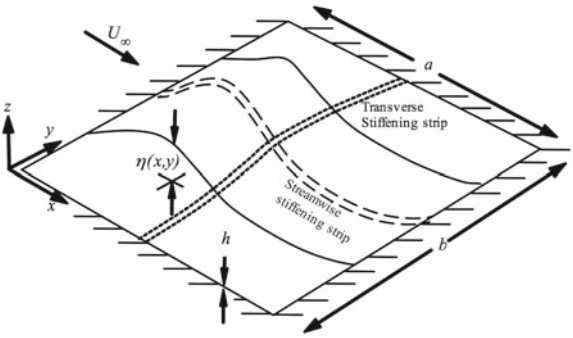


**Fig. 1** Schematic of the problem studied: a fluid-loaded elastic plate has a localised stiffening strip, in either transverse or streamwise direction, bonded to the underside of the panel

panel loses stability, usually through divergence that can lead to a buckled nonlinearly saturated state, e.g. Ellen (1977), Lucey et al. (1997), or a highly destructive flutter instability at higher flow speeds. Strategies to postpone critical flow speeds to values beyond the speed for which a panel is designed are usually based upon material selection or uniform thickening of the panel that results in increased cost and dead weight. By contrast, the goal of this paper is to control instability through the judicious use of highly localised structural inhomogeneity (stiffening) based upon a full understanding of instability modes. Our previous work Tan et al. (2010), Tan et al. (2011) demonstrated the utility of this stabilisation strategy for a two-dimensional system wherein an isolated spring support provides the added structural inhomogeneity. A preliminary exploration of the effect of a transverse stiffening strip on the equivalent full three-dimensional system of Fig. 1 was presented in Tan et al. (2012) revealing similar dynamics and stabilisation benefits found in the two-dimensional system. In this paper, we extend the hybrid of theoretical and computational methods of Pitman and Lucey (2009) to conduct an eigenanalysis of the three-dimensional system when a streamwise stiffening strip is incorporated. Our immediate goal is to determine the effectiveness of this type of additional structural component on stability relative to transverse stiffening. The broader goal is to optimise the use of multiple stiffeners to postpone instability of the panel for a given material (weight) cost of added structural material.

## 2 Overview of Methods

The fluid-structure system is modelled by fully coupling a finite-difference representation of the structural mechanics with a boundary-element solution for the ideal-flow fluid mechanics. Solution of the structural dynamics modelled by classical thin-plate mechanics yields displacement, velocity and acceleration conditions that provide the boundary conditions for the flow solution while the resulting flow-perturbation pressure drives the motion of the panel. The full system

is cast as a single differential equation for the displacement-field of the solid–fluid interface and its time derivatives. This equation is transformed into state-space form and, assuming single-frequency response, the resulting eigenvalue problem for complex frequency is solved. In the procedure, we compute all $2N$ eigenvalues of a system discretised into $N$ collocation points. Details of the modelling are provided in Tan et al. (2012), Pitman and Lucey (2009) for the results of this paper the modelling has been extended to incorporate a streamwise stiffening strip. The homogeneous fluid-structure system is controlled by three parameters, namely the fluid-to-solid mass and stiffness ratios, respectively defined by $L' = \rho a/(\rho_m h)$ and $\Lambda^{\mathrm{F}} = \rho U_\infty^2 a^3/B$, and the aspect ratio of the plate, $A = b/a$, in which a, $b$ and $h$ are respectively the length (in the flow direction), width and thickness of the plate that has density and flexural rigidity $\rho_m$ and $B$; the fluid has density $\rho$ and speed $U_\infty$. In the structurally inhomogeneous system, the stiffness of the added strip is described relative to the flexural rigidity of the plate; i.e. $EI/B$. For each of the transverse and streamwise cases studied in this paper, the stiffening strip is respectively located at the mid-chord and mid-width of the panel although our methods can be used for its addition at any position. For the results of this paper, we use a plate that is hinged along its edges and throughout has aspect ratio $A = 1$ discretised into 1,600 square panels.

## 3 Results and Discussion

Figure 2a, b shows the variation of system eigenvalues with applied flow speed for two very different values of mass-ratio, $L' = 38.5$ and 0.049, that respectively typify water flow over the aluminium panel of a high-speed ship and airflow over the glass panel of a curtain wall of a high-rise building. The upper and lower panels show the real ($\Omega_R$) and imaginary ($\Omega_I$) parts of the system eigenvalues (frequencies), non-dimensionalised with respect to the frequency of the fundamental mode of the corresponding two-dimensional system, that respectively indicate the growth(+ve)/decay(-ve) and oscillatory motion of the mode. In each of Fig. 2a, b, we plot the eigenvalues for the homogeneous case and when each of a transverse and streamwise stiffening strip with $EI/B = 1$ has been added to the panel. For both the homogeneous cases, Mode-1 divergence is first seen to occur when $\Lambda^F = 202$ because exactly at onset the panel is static through the balance of flow and structural stiffnesses; this critical value, along with the post-divergence features of the eigenplot, is in excellent agreement with the results of Lucey and Carpenter (1993) obtained using a Galerkin analysis and serves to validate the present modelling. Both transverse and streamwise stiffening strips are seen to increase the value of divergence onset flow speed ($\Lambda^F$ for a given panel geometry and material properties) in both water- and air-flow applications. However, it is seen that the streamwise stiffening strip also confers a marked postponement to modal-coalescence flutter. This is because streamwise stiffening beneficially

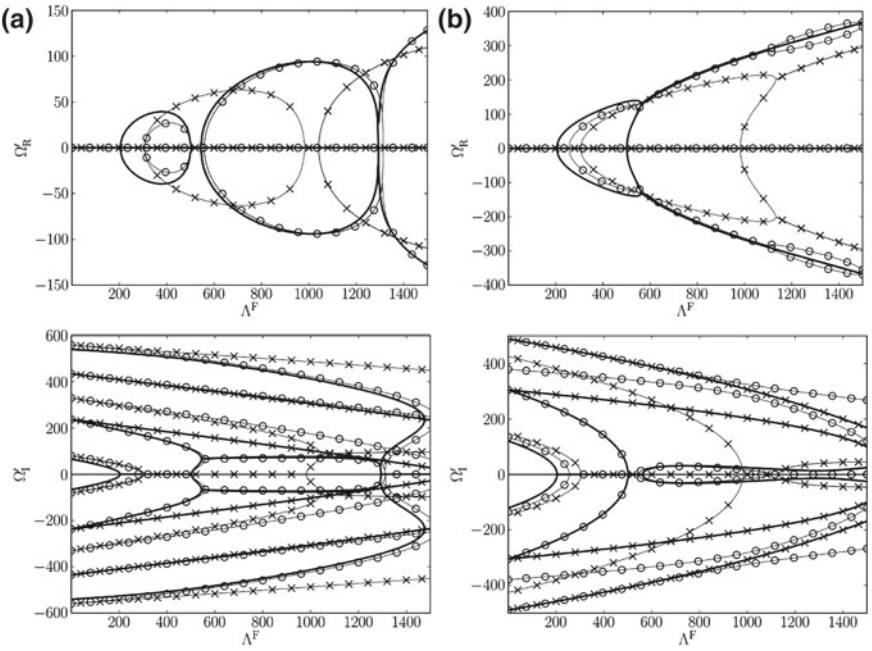


**Fig. 2** Variation of system eigenvalues with non-dimensional flow speed for—(*thick*) a homogenous panel, and a panel with each of— o —transverse and— × —streamwise stiffening strips included, for **a** high and **b** low mass-ratios, respectively representing water and air-flow applications

affects both of the coalescing (streamwise) Modes 1 and 2 whereas a mid-chord transverse stiffening strip has little effect on Mode 2 because it is located at that mode's nodal line. Note that these figures also feature eigenstates of the second transverse mode but these have much higher divergence- and flutter-onset flow speeds than those with the fundamental transverse mode discussed above. Clearly, Fig. 2a, b indicates that the addition of a localised stiffening strip is a very effective way to postpone divergence onset and, for a streamwise orientation, the modal coalescence flutter that replaces divergence instability at higher flow speeds. Figure 3 serves to quantify these benefits for the addition of transverse and streamwise stiffening strips for the two cases of applications to high (water) mass-ratio—Figs. 3a, c—and low (air) mass-ratio—Fig. 3b, d. Accordingly, the variations of the critical flow speeds (as $\Lambda^F$) for each of divergence onset, divergence-recovery or two-mode divergence and modal-coalescence flutter onset are plotted against *EI*/*B*, the stiffness of the added strip.

For the typical high mass-ratio case, the results of Fig. 3a, c show that while both types of stiffening strip can be used to increase the divergence onset flow speed, there exists a maximum value of stiffness for which this strategy can be used when a transverse strip is used. This is because further increases to its

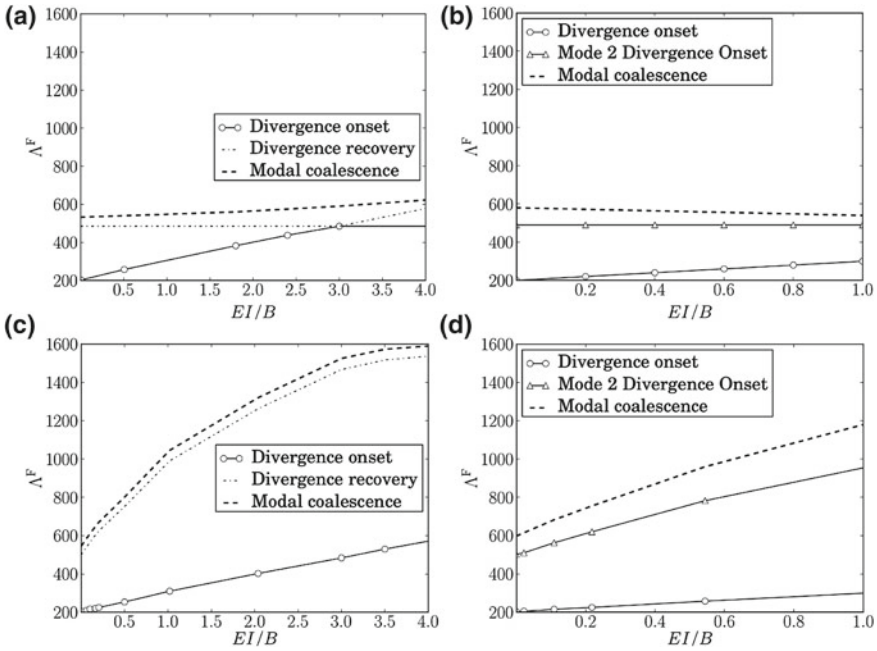


**Fig. 3** Variation of critical speeds with stiffness of **a** and **b** transverse and **c** and **d** streamwise stiffening strips: **a** and **c** for a high mass-ratio system typical of water flow applications and **b** and **d** for a low mass-ratio system typical of air-flow applications

stiffness see Mode 2 become the critical mode for divergence as the stiffener is effectively located at the (transverse) nodal line of Mode 2. The typical low mass-ratio case summarised by Fig. 3b, d features a different sequence of (increasing) critical speeds wherein initial Mode-1 divergence onset is then followed by Mode 2 divergence onset and finally by flutter due to the coalescence of the two divergence modes. Both transverse and streamwise stiffening strips are seen to be effective for the postponement of Mode-1 divergence while a streamwise strip is also effective in the postponement of modal-coalescence flutter. Higher values of transverse stiffening (results not shown here) also evidence a limit beyond which Mode 2 becomes the critical mode and no further postponement is obtained. However, beyond this threshold value of *EI*/*B* modal-coalescence flutter no longer exists and this may be advantageous for glass panels that have little ductility and are therefore readily damaged by a vibrational instability over even a short duration of loading.

## 4 Conclusions

A hybrid of computational and theoretical methods has been developed and deployed to compare and contrast the effectiveness of transverse and streamwise stiffening strip for the control of hydro- and aero-elastic instabilities of an otherwise homogeneous elastic panel. It is shown that both forms of stiffening can be used to postpone divergence onset flow speeds. However, there is a threshold stiffness above which no further gains are obtained when a transverse strip is used. For high mass-ratio systems typical in hydro-elasticity, the use of a streamwise stiffening strip also gives substantial increases to the onset flow speed of post-divergence flutter while for low mass-ratios typical in aero-elasticity a transverse orientation is able to suppress flutter. These findings set the basis for the study and optimisation of more complex arrangements of stiffening strips as a strategy for the control of flow-induced panel instability.

## References

Dugundji J, Dowell E, Perkin B (1963) Subsonic flutter of panels on a continuous elastic foundation. AIAA J 1:1146–1154

Ellen CH (1973) The stability of simply supported rectangular surfaces in uniform subsonic flow. ASME J Appl Mech 95:68–72

Ellen CH (1977) The non-linear stability of panels in incompressible flow. J Sound Vib 54:117–121

Guo CQ, Paidoussis MP (2000) Stability of rectangular plates with free side-edges in two-dimensional inviscid channel flow. ASME J Appl Mech 67:171–176

Lucey AD, Carpenter PW (1993) The hydroelastic stability of three dimensional disturbances of a finite compliant wall. J Sound Vib 165:527–552

Lucey AD, Cafolla GJ, Carpenter PW, Yang M (1997) The nonlinear hydroelastic behaviour of flexible walls. J Fluids Struct 11:717–744

Pitman MW, Lucey AD (2009) On the direct determination of the eigenmodes of finite flow-structure systems. Proc Roy Soc A 465:257–281

Tan BH, Lucey AD, Pitman MW (2010) Hydroelastic stability of flexible panel: eigen-analysis and time-domain response. ASME Paper FEDSM-ICNMM2010-30057

Tan BH, Lucey AD, Pitman MW (2011) Controlling hydroelastic instability of hull panels through structural inhomogeneity. In: Proceedings of the Royal Institute of Naval Architects (RINA) international conference on high speed marine vessels, 2nd–3rd March 2011, Fremantle, Australia, 51–60

Tan BH, Lucey AD, Pitman MW (2012) Stability of a structurally inhomogeneous flexible plate in uniform axial flow. In: Meskell C, Bennett G (eds) Proceedings of the 10th international conference on flow induced vibration (and flow-induced noise), pp 203–210

Weaver DS, Unny TS (1971) The hydroelastic stability of a flat plate. ASME J Appl Mech 37:823–827

# Eigen-Analysis of an Inviscid Channel Flow with a Finite Flexible Plate in One Wall

**M. A. Burke, A. D. Lucey, R. M. Howell and N. S. J. Elliott**

**Abstract** A state-space method is used to investigate the surface instabilities of a flexible plate comprising one wall of an inviscid channel flow computationally modelled with a finite-difference method coupled with a boundary-element method. Simple elastic and spring-backed plates are considered and in both cases it is found that reducing the height of the channel causes divergence and modal-coalescence to occur at lower flow velocities. An analytical prediction for an infinitely long plate is also developed and the divergence-onset predictions are compared with those obtained by the state-space method for a spring-backed plate.

**Keywords** Fluid–structure interaction · Boundary-element · Finite-difference · Divergence · Flutter

## 1 Introduction

The aim of the present study is to determine the stability of a flexible plate—or compliant wall—that comprises a section of one wall of a two-dimensional channel in which there is a uniform (inviscid), incompressible flow; the system is depicted in Fig. 1. This problem may be considered an extension of the large body of work on the behaviour of flexible plates and compliant walls in open flows; e.g., see Carpenter and Garrad (1986) and Pitman and Lucey (2009). These show that a flexible plate first loses its stability to divergence, and at higher applied flow speeds to a flutter-type instability caused by modal-coalescence. The closely related problem of (inviscid) fluid-conveying two-dimensional flexible pipes for which symmetric (sinuous) deformation of both walls occur has been studied using

M. A. Burke (✉) · A. D. Lucey · R. M. Howell · N. S. J. Elliott
Fluid Dynamics Research Group, Department of Mechanical Engineering, Curtin University, GPO Box U1987Perth, WA 6845, Australia
e-mail: m.burke@postgrad.curtin.edu.au

Y. Zhou et al. (eds.), *Fluid-Structure-Sound Interactions and Control*,
Lecture Notes in Mechanical Engineering, DOI: 10.1007/978-3-642-40371-2_47,

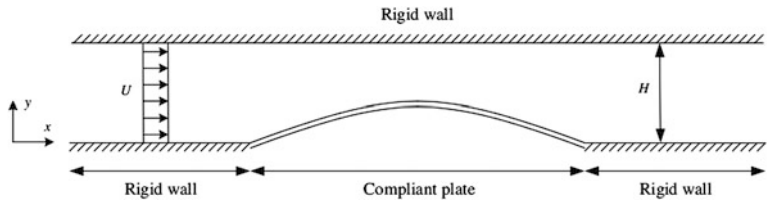


**Fig. 1** Schematic of the fluid–structure interaction system

a quasi-one-dimensional plug-type flow. Pipe buckling (divergence) and flutter are predicted at sufficiently high flow speeds, e.g. Doaré and De Langre (2002) and observed experimentally by Dodds and Runyan (1965) and Weaver and Païdoussis (1977). The latter also modelled potential flow in a flexible channel undergoing varicose deformations using a Galerkin method for a finite extent of the channel and a three-dimensional travelling-wave approach for an infinitely long channel. This system is similar to that studied herein. The present results are, therefore, compared against those of Weaver and Païdoussis (1977) especially with regard to the differing predictions between analyses for finite and infinite flexible walls. Viscous fluid-flow models for the system of Fig. 1 have been developed for linear deformations of a flexible insert, see Heil and Jensen (1996), Davies and Carpenter (1997) and Huang (2001), demonstrating a range of instabilities that include divergence, travelling-wave flutter, and Tollmien-Schlichting waves. These more complex flow models are restricted to low (laminar-flow) Reynolds numbers. In contrast, the potential flow results herein correspond to very high (infinite) Reynolds-number flows relevant to engineered, and some biological, systems. The main goal in this paper is to characterise the effect of channel height on the stability of the flexible channel wall.

## 2 Methods

The motion of the flexible insert, or plate, of length $L$ is described by the one-dimensional beam equation and solved using a finite-difference method, where it is discretised into $N$ mass points. Hinged-hinged boundary conditions are applied at the plate ends. Potential flow is assumed, giving a perturbation which satisfies Laplace's equation, and the pressure is obtained from the unsteady Bernoulli equation. The flow solution is obtained using an unsteady boundary-element method, constructed using source/sink singularities, following the linear theory developed by Lucey and Carpenter (1992) in which the singularities on the flexible surface remain on the undisturbed plane, analogous to the approach of thin-aerofoil theory. Boundary-elements are also used on the rigid upper and lower walls of the channel to enforce the no-flux condition on these boundaries. A fully-coupled system is developed by matching the pressure at the fluid–solid boundary

and a single matrix equation is derived. Using the state-space approach of Pitman and Lucey (2009), the system eigenvalues, *s,* and eigenvectors, *W,* are extracted. Complex *s* gives the oscillation frequency and growth/decay rate, and is used to determine instability onset, while *W* can be used to construct the plate deflections.

An extension, to account for channel walls, of the analysis of Carpenter and Garrad (1986) is also developed by considering the harmonic form of a travelling-wave disturbance. This theory is only appropriate for spring-backed flexible plates for which deformation wavelengths are much shorter than the length of the flexible insert. A characteristic equation for the continuous spectrum of eigenvalues is derived from which the critical flow speed for divergence is found.

## 3 Results

For a simple elastic plate, Fig. 2a shows the variation of system eigenvalues with the stiffness ratio, $\Lambda^{\mathrm{F}} = \rho_{\mathrm{f}} U^2 L^3/B$, for three different non-dimensional channel heights, $H/L$, at a mass ratio, $\mu = \rho_{\mathrm{f}} L/(\rho_{\mathrm{w}} h)$ of 92.3. In the foregoing $\rho_{\mathrm{f}}$ and $\rho_{\mathrm{w}}$ are, respectively, the fluid and plate-material densities, $U$ is the flow speed, $L$ is the flexible plate length, and $B$ and $h$ are, respectively, its flexural rigidity and thickness; $H$ is the channel height. For constant plate dimensions and material properties, $\Lambda^{\mathrm{F}}$ is a non-dimensional form of the flow speed. For $H/L = 2$, divergence-onset, divergence-recovery and modal-coalescence flutter are, respectively, seen to occur at $\Lambda^{\mathrm{F}} = 40$, 275 and 316, which closely match the open-flow results of Pitman and Lucey (2009) and Tan et al. (2010). For an aluminium plate 0.6 m long and 2.5 mm thick, these correspond to dimensional flow speeds 3.77, 9.88 and 10.59 m/s. Figure 2b summarises the effect of $H/L$ on these landmark values. Reducing $H/L$ causes instability onset to occur at lower flow speeds with a maximum reduction of 29% to divergence-onset that agrees with the finite-wall analysis of Weaver and Paidoussis (1977). Figure 2b also indicates that beyond $H/L = 1.5$, the upper rigid-wall exerts negligible influence on instability onset; the critical values of $\Lambda^{\mathrm{F}}$ asymptote to those of an open-flow analysis. In the neutral-stability range of flow speeds, the imaginary parts of the eigenvalues in Fig. 2a also indicate that modal-oscillation frequencies are reduced by narrowing the channel.

We now consider divergence-onset for a flexible plate surmounting a distributed spring foundation with coefficient $K$. This introduces a further control parameter for the system and therefore a set of divergence-onset flow speed curves of the type seen in Fig. 2b. However, by redefining the stiffness ratio as $\Lambda^{\mathrm{I}} = 3\pi\rho_{\mathrm{f}} U^2/(3BK^3)^{(1/4)}$ and scaling channel height with the wavelength of the critical mode, $\lambda_{\mathrm{C}}$, a single non-dimensional result for the variation of divergence-onset flow speed with channel height is obtained; this is presented in Fig. 3a. The present results have been validated by recovering, for large $H/\lambda_{\mathrm{C}}$, the open-flow results of Tan et al. (2010) and Carpenter and Garrad (1986), respectively, for the analyses of finite and infinitely long flexible walls.

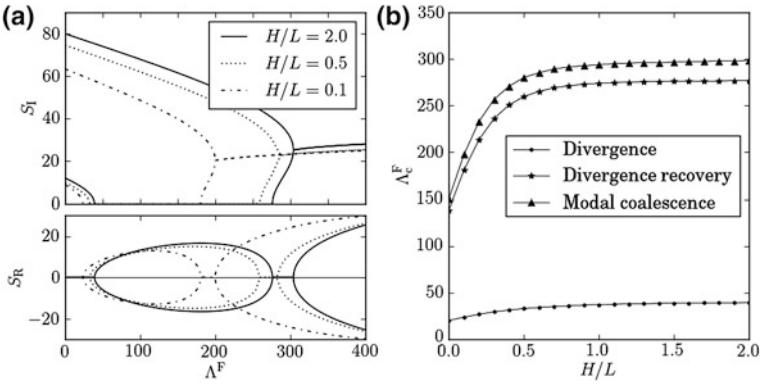


**Fig. 2** **a** Imaginary (*top*) and real (*bottom*) parts of eigenvalues of the first two modes for three different channel heights, and **b** dependence of divergence-onset, divergence-recovery and flutter-onset flow speed on channel height

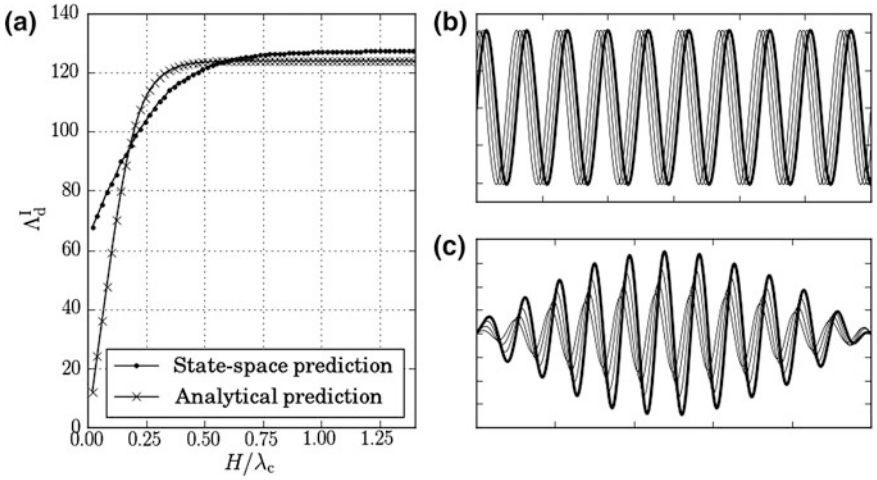


**Fig. 3** **a** The dependence of divergence-onset flow speed on the channel height for a spring-backed flexible plate; and predicted wall motion at $\Lambda^I = 104$ and $H/\lambda_c = 0.2$ as a time sequence of instantaneous wall profiles for **b** travelling-wave analysis (infinitely long wall) and **c** state-space analysis (finite-length wall). *Thick line* highlights the final deflection

Also plotted in Fig. 3a is our analytical prediction of divergence-onset based upon the assumption of an infinitely long flexible plate. In both these and the results of the finite-wall state-space analysis, reducing the channel height causes a reduction in the divergence-onset flow speed. While there is good agreement between the two methods for the larger values of channel height in Fig. 3a, this is not true as the channel is narrowed. The finite-flexible-wall analysis predicts that divergence-onset flow speed is reduced by a maximum of 29 % (agreeing with

Weaver and Païdoussis (1977), whereas it reduces to zero in the travelling-wave analysis of an infinitely long flexible wall. A similar dependence on the modelling assumptions used was also found by Weaver and Païdoussis (1977) whose experiments suggested that the finite-wall prediction was the more realistic of the two. In Fig. 3b, c we contrast our calculations of wall motion (for a damped wall with $\mu = 70.4$) just above divergence-onset for the two models, showing that the differing predictions of divergence-onset may be explained by the amplitude modulation always present in the analysis of a flexible wall of finite extent.

## 4 Conclusions

The stability of flexible plates comprising an insert in an otherwise rigid-walled channel conveying an ideal flow has been studied. The key findings are that: (1) Modal vibration frequencies of unsupported plates are decreased by reducing the channel height, (2) Reducing the channel height is destabilising in that it leads to a lower divergence-onset flow speed for both unsupported and spring-backed flexible plates and (3) The effect of channel height on stability scales with plate length for simple plates and with the wavelength of the critical divergence mode for spring-backed plates.

## References

Carpenter PW, Garrad AD (1986) The hydrodynamic stability of flow over Kramer-type compliant surfaces. Part 2. Flow-induced surface instabilities. J Fluid Mech 170:199–232

Davies C, Carpenter PW (1997) Instabilities in a plane channel flow between compliant walls. J Fluid Mech 352:205–234

Doaré O, De Langre E (2002) Local and global instability of fluid-conveying pipes on elastic foundations. J Fluids Struct 16:1–14

Dodds HL, Runyan HL (1965) Effect of high-velocity fluid flow on the bending vibrations and static divergence of a simply supported pipe. NASA Technical Note NASA TN D-2870

Heil M, Jensen OE (1996) A numerical simulation of unsteady flow in a two-dimensional collapsible channel. J Fluid Mech 72:15–49

Huang L (2001) Viscous flutter of a finite elastic membrane in Poiseuille flow. J Fluids Struct 15:1061–1088

Lucey AD, Carpenter PW (1992) A numerical simulation of the interaction of a compliant wall and inviscid flow. J Fluid Mech 234:121–146

Pitman MW, Lucey AD (2009) On the direct determination of the eigenmodes of finite flow-structure systems. Proc Roy Soc 465:257–281

Tan BH, Lucey AD, Pitman, MW (2010) Hydroelastic stability of flexible panel: eigen-analysis and time-domain response. ASME FEDSIM-ICNMM2010-30057

Weaver DS, Païdoussis MP (1977) On collapse and flutter phenomena in thin tubes conveying fluid. J Sound Vib 50:117–132

# Instability of Axial Flow Over a Plate Hinged at Its Leading Edge

**Chao Zhang, Naitong Liu and Lixi Huang**

**Abstract** This paper describes a study of the flow instability over a plate hinged at its leading edge by the pseudospectral numerical method for fluid loading and the Galerkin method for the eigen-value problem. The mechanism of modal coupling for the plate flutter is illustrated. It is found that flutter arises from the coupling between the first and second in-vacuo modes, with flow-to-structure energy transfer. The fluid loading on the second in-vacuo mode is found to be the dominant source of instability. Compared with a cantilever plate with the same material property, the plate with a simply supported leading edge has similar threshold of flutter velocity, which suggests that the bending stiffness of the plate is crucial for the stability instead of the structural boundary condition at the leading edge. This conclusion is also validated by the analytical study for a simplified model in which the flexible plate is replaced by two rigid plates connected by a hinge.

**Keywords** Flutter · Simply supported plate · Modal analysis

## 1 Introduction

The stability of cantilever plate in axial flow is of great importance in engineering. Many methods for this theoretical model have been applied. The first study was given by Kornecki et al. (1979) with Theodorsen's thin airfoil theory and Kutta condition. Watanabe et al. (2002) adopted the Navier–Stokes equation, and also gave a good collection of the comparison between various experiments and theories on the flutter of a cantilever plate. His summary showed that the theoretical

C. Zhang (✉) · N. Liu · L. Huang
Laboratory of Aerodynamics and Acoustics, Zhejiang Institute of Research and Innovation, Department of Mechanical Engineering, The University of Hong Kong, Hong Kong, China
e-mail: zchku@hku.hk

Y. Zhou et al. (eds.), *Fluid-Structure-Sound Interactions and Control*,
Lecture Notes in Mechanical Engineering, DOI: 10.1007/978-3-642-40371-2_48,

results by various methods were consistent, but typical measured flutter speed was about twice as much as the theoretical predictions. The precise reason for such significant discrepancy remains to be identified and it is beyond the scope of the current study.

In this paper, we investigate the effect of the structural boundary condition at the leading edge of the flexible plate on the flutter occurrence. We extend our numerical method originally written for a cantilever plate to simulate the flutter of plate with a simply supported leading edge, and conduct the modal analysis for the new configuration. The analysis first focuses on the flutter mechanism. The flutter properties for simply supported and cantilever configurations are compared in order to illustrate the dominant control parameter for the instability. A simplified model with two rigid plates is proposed to further clarify the effects of the structural boundary condition and the bending stiffness of the plate.

## 2 Numerical Method

The fundamental model is shown in Fig. 1. A rectangular flexible plate, which becomes a beam in the two-dimensional flow model, is immersed in the axial flow of a wind tunnel. The leading edge of the plate is simply supported, while the trailing edge is free with a thin wake extending from it.

With the time harmonic assumption, the beam vibration is governed by the following equation, written in dimensionless form,

$$\begin{gathered} -\omega^2 m_p \eta + \frac{\partial^2}{\partial x^2}\left((1+i\delta_d)B\frac{\partial^2 \eta}{\partial x^2}\right) = \Delta p = p_{\text{lower}} - p_{\text{upper}}, \\ m_p = \frac{\rho_p^* s^*}{\rho_a^* L_p^*},\ B = \frac{E^* s^{*3}}{12\rho_a^* U^{*2} L_p^{*3}},\ \omega = \frac{\omega^* L_p^*}{U^*},\ \Delta p = \frac{\Delta p^*}{\rho_a^* U^{*2}}, \end{gathered} \tag{1}$$

where $\eta = \eta^*/L_p^*$ is the normalized upward displacement, $m_p$ is the mass ratio, $B$ is the normalized plate stiffness, $\omega$ is the normalized angular frequency, $\Delta p$ is the

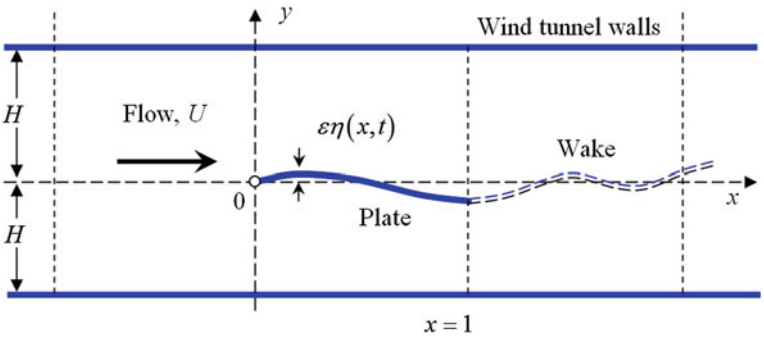


**Fig. 1** Schematic of the numerical model

normalized pressure difference over the two sides of the plate and $\delta_d$ is the damping ratio. In this paper, all variables with superscript '*' is the dimensional version of the same variable without the superscript. Here, $s^*$ is the plate thickness, $L_p^*$ is the length of the plate, $\rho_p^*$ is the density of the plate, $\rho_a^*$ is the density of the air, $E^*$ is the Young's modulus, $\omega^*$ is the angular frequency of the vibration, and $U^*$ is the mean-flow speed.

An accurate pseudospectral method is adopted for the aerodynamic calculation of $\Delta p$ with Kutta condition implemented at the trailing edge. The standard Galerkin procedure is used for the eigen-value problem derived from Eq. (1). The displacement $\eta$ and the fluid pressure loading $\Delta p$ are expanded in terms of the in-vacuo modes of a simply supported beam,

$$\eta(x) = \sum_n C_n \eta_n(x), \Delta p(x) = \sum_n C_n \sum_m \eta_m(x) P_{mn}, \tag{2}$$

where $\eta_m$ is the modal displacement and $P_{mn}$ is the modal loading matrix in which the $n$th column contains the modal responses caused by the vibration of the $n$th in-vacuo mode. Substitution of Eq. (2) into Eq. (1) yields a system of linear equations for mode coefficients $C_n$:

$$\begin{gathered} [\mathrm{M}][\mathrm{C}] = [0], \\ [\mathrm{M}] = \mathrm{diag}\left[\left((\omega/\omega_m)^2 - (1 + i\delta_d)\right)\right] + \mathrm{diag}\left(m_p^{-1}\omega_m^{-2}\right)[P_{mn}] \end{gathered} \tag{3}$$

The control parameters here are $\omega$ and $\omega_m$, where $\omega_m = k_m^2\sqrt{B/m_p}$ are the normalized angular frequencies. For a plate with a hinged leading edge and a free trailing edge, the first five characteristic wavenumbers are given by

$$k_m = 0,\ 3.927,\ 7.069,\ 10.210,\ 13.352. \tag{4}$$

Note that the first eigen-value $k_1$ is zero. We normalize the mean-flow speed by the second in-vacuo mode as follows,

$$U = \frac{U^*}{\omega_2^* L_p^*} = \frac{1}{\omega_2} = \frac{\sqrt{12}}{k_2^2} \frac{L_p^* U_c^*}{s^* \sqrt{E^*/\rho_p^*}}. \tag{5}$$

Therefore, the control parameters $(\omega, \omega_m)$ can be converted to $(\omega, U)$. The normalized mean-flow speed at which the flutter occurs will be defined as the dimensionless critical flutter speed $U_c$. Eigen frequency and critical flutter speed are found when the system of linear equations [Eq. (3)] has nontrivial solutions.

# 3 Results and Discussion

## 3.1 Modal Analysis

In this part, the flutter simulation results for a simply supported plate with $m_p = 1.46$, $\delta_d = 0$ in a wind-tunnel whose half height $H$ is 0.75 are presented for modal analysis. The numerical solution using the first 5 in-vacuo modes for this eigen-value problem established by Eq. (3) gives $U_c = 0.303, \omega = 2.602$. The magnitudes of these 5 modes are:

$$|C_n| = 0.7282,\ 0.6851,\ 0.0203,\ 0.0013,\ 0.0003. \tag{6}$$

The first and second modal coefficients are dominant.

Figure 2 shows the details of the coupled flutter mode. The left figure shows 22 instantaneous vibration positions (thin lines). The solid and dashed thicker lines represent the real and imaginary parts of the eigen solution $\eta(x)$, respectively. We can see that there is single bottle neck around 70 % of the plate length, which is similar with the solution for a cantilever plate. The right sub-figure in Fig. 2 shows the complex-valued fluid loading on the lower and upper surfaces of the plate.

For the coupled eigen vibration, the rate of energy transfer from the flow to the plate, $W$, is expressed by

$$W = \frac{1}{2}\mathrm{Re}\left(-i\omega \sum_m \sum_n C_m^c P_{mn} C_n\right) \equiv \sum_{m,n} W_{mn}, \tag{7}$$

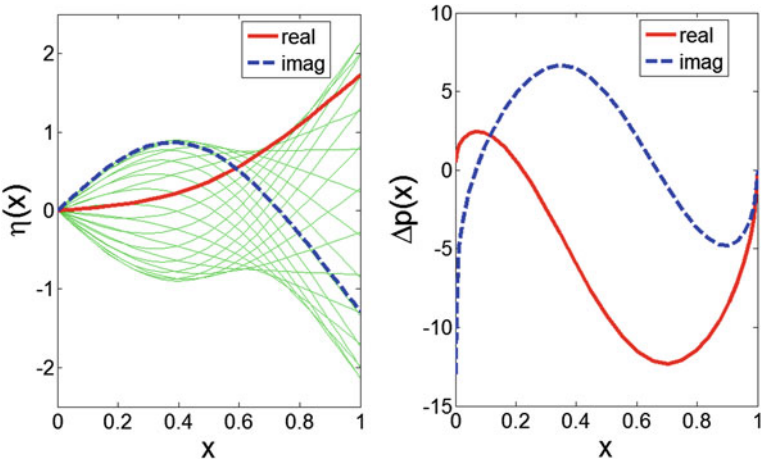


**Fig. 2** Flutter a hinge-fee plate with $m_p = 1.46$, $\delta_d = 0$, $H = 0.75$

where superscript '$c$' in $C_m^c$ signifies complex conjugate. The element $W_{mn}$ represents the power contribution by the fluid loading arising from the $n$th mode coupled to the $m$th mode vibration velocity. Collecting those elements and rewriting them into a matrix form $[W_{mn}]$, we obtain:

$$\left.\frac{[W_{mn}]}{|W_{11}|}\right|_{\delta_d=0} = \begin{bmatrix} -1 & 1.034 & -0.030 & \cdots \\ 0.191 & -0.189 & -0.002 & \cdots \\ -0.003 & 0.003 & -0.000 & \cdots \\ \cdots & \cdots & \cdots & \cdots \end{bmatrix}. \tag{8}$$

A positive value in the matrix means energy transfer from the flow to the plate, which is unstable. The dominant unstable coupling is $W_{12}$, which is between the fluid loading of the second in-vacuo mode and the vibration velocity of the first in-vacuo mode. The self-coupling by the first and second in-vacuo modes are both stable. To further simplify the conclusion, it may be said that the first in-vacuo mode is stable but the second is not.

## 3.2 Comparison Between Simply Supported and Cantilever Configurations

The dimensional critical flutter speed and flutter frequency are compared between the current hinge-free configuration and the cantilever plate for $m_p \in [1, 4], \delta_d = 0$, $H = 0.75$ in Fig. 3. In this range of mass ratio, there are little in-vacuo modes above the in-vacuo modal index of 2, and the configuration of the coupled mode is similar to Fig. 2a. The solid line in Fig. 3 is the ratio of dimensional critical flutter speed for hinge-free and cantilever plates, while the dashed line is the ratio of dimensional angular frequencies. The result illustrates that the two configurations have similar flutter speeds, while the vibration frequency for the hinge-free plate is lower than that for the cantilever plate. This suggests that the boundary condition at the leading edge is not the main factor for the flutter instability. Because the in-vacuo modes for the hinge-free plate and the cantilever plate are quite similar, except for the vicinity of

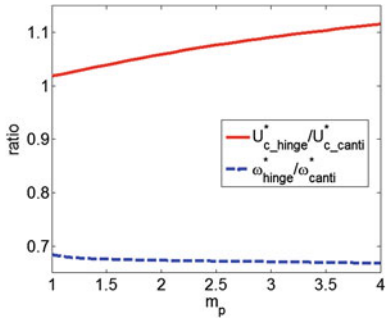


**Fig. 3** Comparison of the critical flutter speed and the flutter frequency between simply supported and cantilever configurations at the leading edge

the leading edge, the aerodynamic loading on the plate has little difference. In Eq. (5), the dimensionless flutter speed is normalized by the stiffness of the plate, so the dimensional flutter speed depends directly on the stiffness. Since the value of the dimensional flutter speed is roughly a constant for different boundary conditions, it is argued that the dominant parameter controlling the flutter instability is the bending stiffness of the plate.

In order to clarify the effects of structural boundary condition and the bending stiffness on flutter, we study a simplified 2D model. This model consists of two rigid flat plates linked by a torsional spring in the mid-chord, and the hinge at the leading edge of the upstream plate is also replaced by a torsional spring. It is assumed that the mid-chord torsional spring has the similar effect as the bending stiffness of a uniform, flexible plate, while the spring at the leading edge simulates the boundary condition effect of a cantilever plate. Theodorsen's thin airfoil theory is adopted to calculate the aerodynamics. Details are left out due to page limitations. The conclusion is that the torsional stiffness of the spring at the leading point is not as crucial as that of the spring at the conjoint point. It is therefore concluded that the flutter instability is mainly controlled by the bending stiffness rather than the structural boundary condition at the leading edge.

## 4 Conclusions

We use a pseudospectral method with the Galerkin procedure to simulate the flutter for a plate with a hinged leading edge. It is found that the flutter is caused by the coupling between the first and second in-vacuo modes, the fluid loading on the latter being the dominant source of instability with energy transfer from the flow to the vibration. The flutter instability is mainly determined by the bending stiffness of the plate, not the structural boundary condition at the leading edge in these particular cases.

## References

Kornecki A et al (1979) On the aeroelastic instability of two-dimensional panels in uniform incompressible flow. J Sound Vib 47:163–178

Watanabe Y et al (2002) A theoretical study of paper flutter. J Fluids Struct 16:543–560

# An Immersed Boundary Method for Simulating an Oscillating Airfoil

**Guotun Hu, Lin Du and Xiaofeng Sun**

**Abstract** The numerical simulation associated with fluid–structure interaction problems is very complicated for the grid regeneration in the traditional method. In the present work, a fast explicit numerical method is established to solve the unsteady flow with oscillation of a rotor blade on the basis of the immersed boundary method. The governing equations are discretized on simple Cartesian meshes by using the immersed boundary method and the blade can move arbitrarily in the computational domain. It is found that the oscillation of rotor blades is influenced greatly by the reduced velocity and cascade solidity.

**Keywords** Immersed boundary method · Fluid–structure interaction

## 1 Introduction

Flutter is a severe problem in the design of turbomachinery. It is known that the compressor/turbine blade rows flutter issues have become more and more serious because the phenomenon has caused countless engine breakdowns in various practical applications. The flutter of compressor/turbine blade is one of the critical factors that need to be considered during the engine design period. It is intended to find a way to improve the physical understanding of blade instability in turbomachinery, which involves the fluid/blade interaction of cascade. Effective flutter prediction tools and the understanding of the physics of mutual interaction between the flow and oscillating airfoil is essential for improving overall efficiency, durability, and reliability.

G. Hu (✉) · L. Du · X. Sun
School of Energy and Power Engineering, Beihang University, Beijing, China
e-mail: huguotun@126.com

Y. Zhou et al. (eds.), *Fluid-Structure-Sound Interactions and Control*,
Lecture Notes in Mechanical Engineering, DOI: 10.1007/978-3-642-40371-2_49,

Based on the immersed boundary method proposed by Peskin et al. (1977), a fast simulation for solving unsteady, incompressible, viscous flow associated with the oscillating airfoil is established on a quasi-three-dimensional coordinate system (Hu and Sun 2011). Using this method, the coupling processes are simulated on simple Cartesian meshes, which avoid re-gridding for moving boundary. The interfacial force is calculated using Virtual Boundary Formulation. Zhong and Sun (2009) combined the immersed boundary method with the operator splitting technique to investigate the two-dimensional fluid–structure interaction problems. The main advantage of this method is that it enables the calculation of this force field, even if the interface is moving or deforming. Using this method, the vortex-induced vibration of cascade in turbomachinery has been simulated (Hu and Sun 2011).

## 2 Numerical Scheme

As described in the past work (Hu and Sun 2011), the incompressible Navier–Stokes equations on a quasi-three-dimensional coordinate system can be given as below:

$$\left(\frac{\partial u_m r}{\partial m}+\frac{\partial u_\theta}{\partial \theta}\right)=0 \tag{1a}$$

$$\rho\frac{\partial u_m r}{\partial t}+\rho\frac{\partial u_m^2 r}{\partial m}+\rho\frac{\partial u_\theta u_m}{\partial \theta}=-\frac{\partial pr}{\partial m}+F_m r+\left(\frac{\partial r\sigma_{11}}{\partial m}+\frac{\partial \sigma_{12}}{\partial \theta}\right) \tag{1b}$$

$$\rho\frac{\partial u_\theta r}{\partial t}+\rho\frac{\partial u_\theta u_m r}{\partial m}+\rho\frac{\partial u_\theta^2}{\partial \theta}=-\frac{\partial p}{\partial \theta}+F_\theta r+\left(\frac{\partial r\sigma_{12}}{\partial m}+\frac{\partial \sigma_{22}}{\partial \theta}\right) \tag{1c}$$

We demonstrated the robustness of our program with two canonical examples (Hu and Sun 2011). It is important to note the application of immersed boundary method in these problems does reveal obvious advantages, particularly in its simple mesh generation. Ignoring the mesh regeneration in each time step means that the computational time can be reduced.

## 3 Model of Oscillating Cascade on a Stream Surface

It is known that the compressor/turbine blade rows flutter issues have been more and more serious because the phenomenon has caused countless engine breakdowns in various practical applications. It is intended to find a way to improve the physical understanding of coupled instability in compressor/turbine blade rows, which involve the interaction between the fluid and blade and also involve the

interaction between every adjacent blade. In addition, the flow in the rotating machinery is quite complex. Thus, the rotor blade row is simplified to be a single rotor blade, and we first simulate the oscillating blade whose speed is zero. Next, a single rotor blade is simulated in which $v \neq 0$. All these steps just lay a foundation for the simulating of whole row of rotor blades.

As shown in Fig. 1, the blade has 2° of freedom. Similar to Piperno (Piperno 1997) the equations for the blade are given as follows:

$$m\ddot{h} + S_\theta \ddot{\theta} + c_h \dot{h} + k_h h = F_h \tag{2}$$

$$S_\theta \ddot{h} + I_\theta \ddot{\theta} + c_\theta \dot{\theta} + k_\theta \theta = F_\theta \tag{3}$$

We define the reduced velocity $U^* = U_\infty / f_n D = 2\pi U_\infty / \omega_h D$. We also define $\lambda = \omega_h / \omega_\theta$, then $\omega_\theta = \omega_h / \lambda$.

## 3.1 Numerical Analysis and Discussion of an Oscillating Blade with $v = 0$

In the following simulation, the initial stagger angle of blade is set to 15°. The inlet flow is set to $u = 1$ and $\mathrm{Re} = 500$, moving velocity: $v = 0$. Time step $\Delta t = 4 \times 10^{-4}$ is used for this calculation. Several parameters are defined as: $F_y$, frequency of transverse oscillation; $F_{cl}$, frequency of lift coefficient; $A$, the amplitude of transverse oscillations.

Figure 2 shows variation of the frequency and the amplitude of transverse oscillations with reduced velocity $U^*$ at different mass ratio. When $m = 0.5$, the frequency is almost the same in the lower range of $U^*$. This frequency is just the vortex-shedding frequency, but when $U^*$ increases close to 2.6, the frequency jump phenomenon is observed, and then the frequency is reduced when $U^*$ increases. Also, the amplitude of transverse oscillation is almost zero when $U^*$ is less than 2.6. But When $U^*$ is greater than 2.6, the amplitude of transverse oscillation increases rapidly. From the result, it is found that the trend of the curve is very close except the frequency jumping point and the amplitude jumping point are different at different mass. It is also shown that in the jumping section, the frequency is locked into the natural frequency just like the oscillating cylinder.

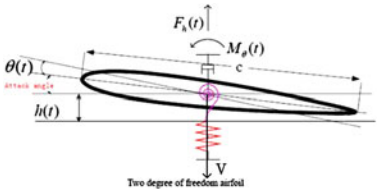


**Fig. 1** Oscillating blade with two degrees of freedom

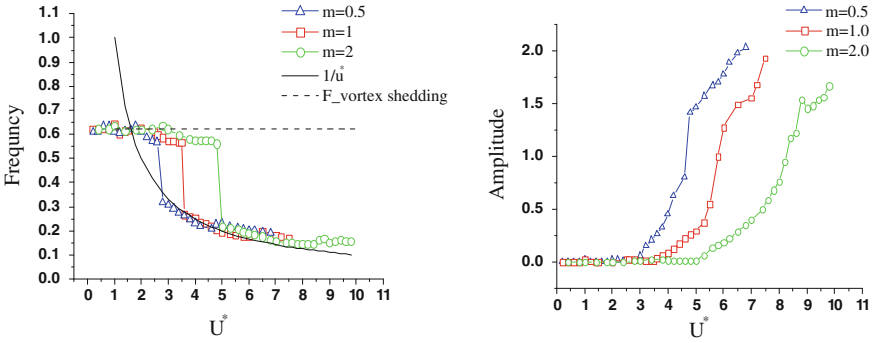


**Fig. 2** Variation of the frequency and the amplitude of transverse oscillation with $U^*$

Figure 3 shows the variation of the frequency of transverse oscillation and the frequency of lift coefficient with $U^*$ when mass is 0.5. In the present example, it shows that the frequency of transverse oscillation and the frequency of lift coefficient are almost the same at different $U^*$. Figure 4 shows the time evolution of the transverse displacement and the amplitude-frequency spectrum of blade oscillations when $U^* = 5.0$. From these results, it is found that the frequency of transverse oscillation is related to the frequency of the lift coefficient. The small lift coefficient is corresponding to the low amplitude of the transverse oscillation and the large lift coefficient corresponds to the high amplitude of the transverse oscillation. It is shown that the amplitude of the second harmonic is the largest.

From these examples, it is found that the frequency of transverse oscillation and the frequency of lift coefficient are very close in ranges of $U^*$. And the frequency 'jump' phenomena are observed. The phenomenon is almost the same in different mass except the 'jumping' point. The amplitude of transverse oscillation increases slowly in the lower range of $U^*$ and increases rapidly when $U^*$ reaches a certain value.

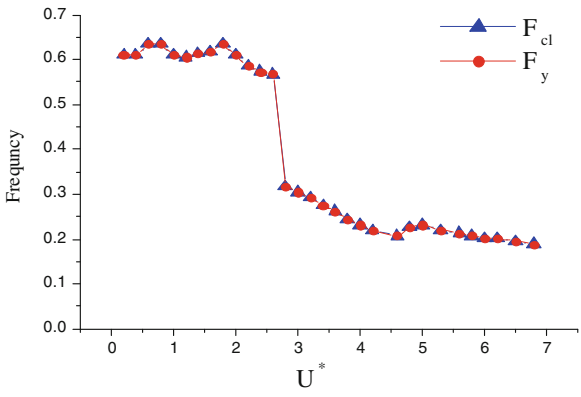


**Fig. 3** Variation of the frequency of transverse oscillation and the frequency of lift coefficient with $U^*$, $m = 0.5$

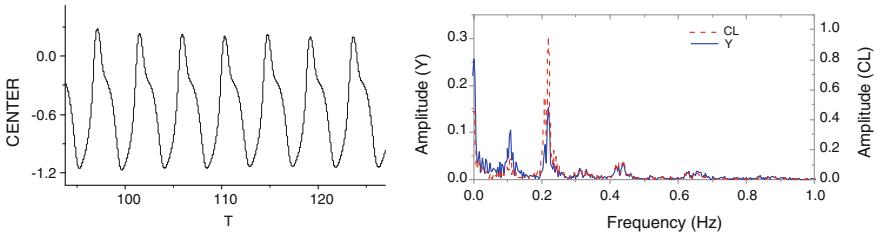


**Fig. 4** The time evolution of the transverse displacement and amplitude-frequency spectrum of blade oscillations, $U^* = 5.0$

## 3.2 *Numerical Analysis and Discussion of Oscillating Blade with* $v \neq 0$

The oscillating blade simulated above is $v = 0$, which is not moving. But it is known that the compressor/turbine is rotating machinery and compressor/turbine blade rows flutter issues have become more and more serious. So the rotating oscillating blade will be simulated in order to improve the physical understanding of coupled instability in compressor/turbine rotating blade rows.

Figure 5 shows the computational domain and grid where Fig. 5a is the same as Fig. 5b except the blade number. The cascade solidity for Fig. 5a is 1/3 and for Fig. 5b is 2/3. The initial stagger angle of blade is set to 53.43°. For inlet flow: $u = 0.5$ and $\mathrm{Re} = 500$, moving velocity: $v = -1$, $m = 0.1$, $\lambda = 1.16$. A time step of $\Delta t = 4 \times 10^{-4}$ is used for this calculation. The parameters $F_y$, $F_{cl}$, $A$ have the same meaning as previously mentioned.

Figure 6 shows variation of the frequency and the frequency of lift coefficient with reduced velocity $U^*$ for a different case. It is found that the trend of the curve is almost the same to the one whose moving speed is zero. It also has the frequency 'jump' phenomenon. Figure 7 shows variation of the frequency of transverse oscillations and variation of the amplitude of transverse oscillations with reduced velocity $U^*$ for a case with different cascade solidity. It is found that the 'jumping' point is apparently different, and the trend of the curve is almost the same as the single rotor blade case.

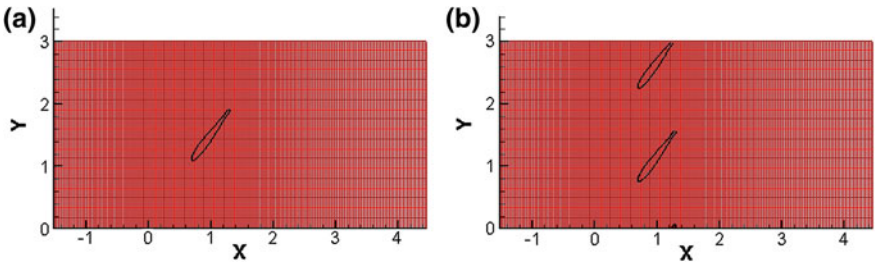


**Fig. 5** The computational domain and grid: **a** single blade; **b**: two blades

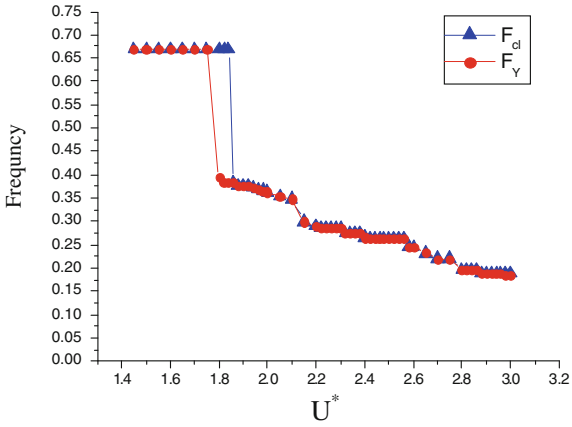


**Fig. 6** Variation of the frequency of transverse oscillation and the frequency of lift coefficient with $U^*$, single blade

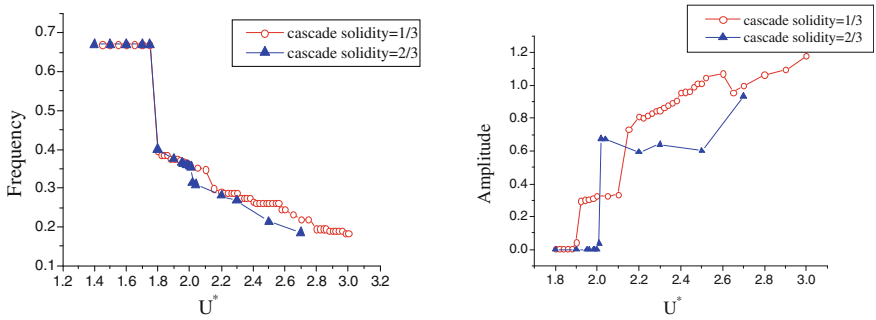


**Fig. 7** Variation of the frequency and the amplitude of transverse oscillation with $U^*$ at different case

## 4 Conclusions

Based on the immersed boundary method, a fast scheme for solving unsteady, incompressible, viscous flow associated with an oscillating cascade is established on a quasi-three-dimensional coordinate system. It is found that the cascade solidity is also a very sensitive factor except the reduced velocity. The results are presented with emphasis on physical understanding of fluid-cascade interaction. It is worth noting that the coupling process is not necessary to be generated by any body-fitting grid, which makes it much faster in computational process for such a complicated fluid–structure interaction problem.

## References

Hu GT, Sun XF (2011) A numerical modeling of the vortex-induced vibration of cascade in turbomachinery using immersed boundary method. J Therm Sci 20:229–237

Peskin CS (1977) Numerical analysis of blood flow in the heart. J Comput Phys 25(3):220–252

Piperno S (1997) Explicit/implicit fluid/structure staggered procedures with a structural predictor and fluid subcycling for 2D inviscid aeroelastic simulations. Int J Numer Meth Fluids 25:1207–1226

Zhong GH, Sun XF (2009) A simulation strategy for an oscillating cascade in the turbomachinery using immersed boundary method. AIAA J Propul Power 25(2):312–321

# Passive Morphing of Solar Powered Flying Wing Aircraft

**Pezhman Mardanpour and Dewey H. Hodges**

**Abstract** High Altitude, Long Endurance (HALE) aircraft can achieve sustained uninterrupted flight time if they use solar power. Wing morphing of solar powered HALE aircraft can significantly increase solar energy absorbency. An example of the kind of morphing considered in this paper requires the wings to fold so as to orient a solar panel to be hit more directly by the sun's rays at specific times of the day. In this paper solar powered HALE flying wing aircraft are modeled with three beams with lockable hinge connections. Such aircraft are shown to be capable of morphing passively, following the sun by means of aerodynamic forces and engine thrusts. The analysis underlying Nonlinear Aeroelastic Trim And Stability of HALE Aircraft (NATASHA), a computer program that benefits from geometrically exact, fully intrinsic beam equations, and a finite-state-induced flow model was extended to include the ability to simulate morphing of the aircraft into a "Z" configuration. Because of the "long endurance" feature of HALE aircraft, such morphing needs to be done without relying on actuators and as near zero energy cost as possible. The emphasis of this study is to substantially demonstrate the processes required to passively morph a flying into a Z- shaped configuration and back again.

## 1 Introduction

A morphing flying wing can maximize the energy absorption of solar panels on the wing surfaces by changing its configuration such that the panels have highest exposure to the sun. In this study a solar powered High Altitude, Long Endurance

P. Mardanpour (✉) · D. H. Hodges
Daniel Guggenheim School of Aerospace Engineering, Georgia Institute of Technology, Georgia 30332-0150, Atlanta
e-mail: Pezhman.Mardanpour@GaTech.edu

D. H. Hodges
e-mail: dhodges@GaTech.edu

Y. Zhou et al. (eds.), *Fluid-Structure-Sound Interactions and Control*,
Lecture Notes in Mechanical Engineering, DOI: 10.1007/978-3-642-40371-2_50,

(HALE) flying wing aircraft is considered to morph into a "Z" configuration to allow for sustained uninterrupted flight. Energy absorption of this aircraft is maximized if the sun exposure of the solar panels distributed on the wings is maximized; see Fig. 1. For this purpose a three-wing HALE flying wing follows the sun and morphs passively (without actuators at the hinges and only making use of aerodynamic force and thrust) into a *Z*-shaped configuration, while the bending moments about hinge lines at the beam connections are zero. To capture these phenomena, NATASHA has been augmented with new equations to analyze aeroelastic trim, stability, and time marching of such aircraft. Local bending moments are zeroed out at the beam connection points while the hinges are locked and kept at zero while the aircraft morphs. The morphing motion is brought to a stop before the hinges are again locked. The emphasis of this study is to demonstrate the systematic processes required for passive morphing of a flying wing with Z-shaped configuration.

## 2 Theory Behind NATASHA and Morphing

NATASHA is based on a geometrically exact composite beam formulation of Hodges (2006) and finite-state induced flow aerodynamic model of Peters et al. (1995). The governing equations for structural model are geometrically exact, fully intrinsic, and capable of analyzing the dynamical behavior of a general, nonuniform, twisted, curved, anisotropic beam undergoing large deformation. The partial differential equations' dependence on $x_1$ is approximated by spatial central differencing detailed in Patil and Hodges (2006). The resulting nonlinear ordinary differential equations are linearized about a steady-motion state governed by nonlinear algebraic equations which NATASHA solves a discretized version of those equations in obtaining the steady-state trim solution using the Newton–Raphson procedure. This system of nonlinear aeroelastic equations, when linearized about the resulting trim state, leads to a standard eigenvalue problem, which NATASHA uses to assess stability.

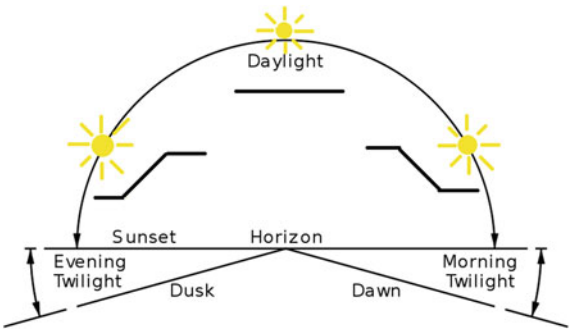


**Fig. 1** Schematic view of the flying wing morphing and the sun position

## 2.1 Trimming

The trim condition of the aircraft can be found by finding the steady-state solution of the aeroelastic equations with all time-dependent terms of the equations removed. NATASHA trims the aircraft for equality of lift to weight and thrust to drag by finding the controls of the aircraft (angle of flaps and thrusts) for a prescribed speed and climb angle. The symmetric trim equations at the aircraft reference node as described in Patil and Hodges (2006) are

$$\begin{aligned} \hat{g}_2\hat{V}_2 + \hat{g}_3\hat{V}_3 - \tan\phi\left(\hat{g}_3\hat{V}_2 + \hat{g}_2\hat{V}_3\right) &= 0 \\ \hat{V}_2^2 + \hat{V}_3^2 - \hat{V}_\infty^2 &= 0 \end{aligned} \tag{1}$$

In order to passively morph the flying wing (i.e., avoiding actuators) using aerodynamic forces and thrust, a new set of equations in addition to the former trim equations is required to trim the aircraft. It is noted that these forces should fold the wings in a quasi-static morphing process so as to avoid inducing vibrations. It is also required that the moment about the folding hinge stays zero at each prescribed fold angle. For this purpose, a unit hinge vector ($\boldsymbol{h}$) is introduced in the direction in which the hinges are designed to fold. The scalar product of the hinge vector and wing bending moment ($\boldsymbol{M}$) at the hinge location needs to be maintained zero, so that there is no resistance while folding occurs; thus,

$$\boldsymbol{M}_n \cdot \boldsymbol{h}_n = 0 \qquad n = 1, 2, \ldots \tag{2}$$

Finally, for each hinge, a new equation is added to the system of aeroelastic equations. Hence, a new set of flaps needs to be introduced to the unknown variables so that the number of equations and unknowns remains equal. A detailed explanation on the aeroelastic equations and variables for non-morphing configuration is available in the work done by Patil and Hodges (2006).

## 2.2 Time Marching

NATASHA is capable of time marching the aeroelastic system of equations using the scheduled control of the aircraft that comes from the trim solution. When time marching the morphing process, four aircraft controls (a value for all engines and three flap settings) with prescribed location are scheduled to morph the aircraft over a suitable time period and time steps. The fold angles are the unknown variables in the state vector of the time marching, whereas in the trim solution they were prescribed. During the morph process, the morph speed (the time rate of the change of the fold angle) at each hinge is governed by

$$\left(\hat{\boldsymbol{\Omega}}_{l,n} - \hat{\boldsymbol{\Omega}}_{r,n}\right) \cdot \boldsymbol{h}_n = \dot{\theta}_n \qquad n = 1, 2, \ldots \tag{3}$$

where for the $n$th hinge, $\hat{\mathbf{\Omega}}_{l,n}$ and $\hat{\mathbf{\Omega}}_{r,n}$ are the nodal left and right values for the angular velocity in the deformed basis and $\dot{\theta}$ is the time rate of change of the $n$th fold angle.

## 3 Aeroelastic Simulation of Passive Morphing

***Flying Wing Model*** In this study a very high aspect ratio flying wing is modeled with three beams connected to each other with two hinges about which folding takes place. There are four identical engines with prescribed mass, inertia, and angular momentum placed at the outer portion of the beams with zero offset from elastic axis; see Fig. 2. Three sets of flaps are distributed on the wings: one set (set 1) is on the side wings; the middle beam was divided into equal portions for the two other sets of flaps (sets 2 and 3); see Figs. 2, 3.

***Aeroelastic Simulation of Morphing Process*** For this maneuver, the controls of the aircraft obtained from the trim conditions were curve fitted to experience seven time marching phases over a time interval of 106 s. Stability analysis shows that this configuration of the flying wing has directional instability with lead-lag motion with very small amplitude and as the aircraft's shape is changing the amplitude of the eigenvalue changed with no apparent regularity. These phases are (a) 10 s time-march while the flying wing is unfolded and hinges are locked and loaded, (b) 10 s to gradually remove the bending moment in the direction in which the fold occurs, (c) 10 s to unlock the hinge while $d\theta_n/dt = 0$, (d) 45 s to morph from fold angle of $0^\circ - 45^\circ$ and come to Z-shaped configuration, (e) 10 s to lock while $d\theta_n/dt = 0$, (f) 10 s to gradually load the hinges and (g) a 10 s time march while the hinges are locked and loaded. A choice for $\Delta t = 10^{-6}$ s turns out to be suitable. For time marching on a global scale, for the purpose of saving time in calculations, the variables of the state vectors were evaluated at each converged time-march solution for every second of this maneuver and then curve-fitted separately for each phase with polynomials up to the order of 20.

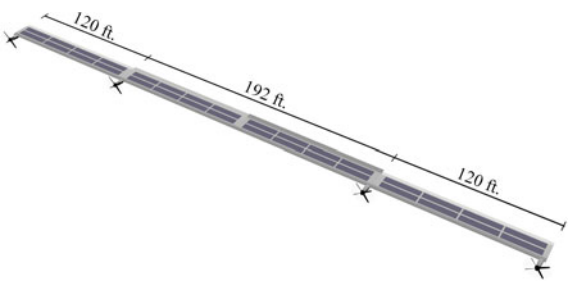


**Fig. 2** Geometry of the flying wing

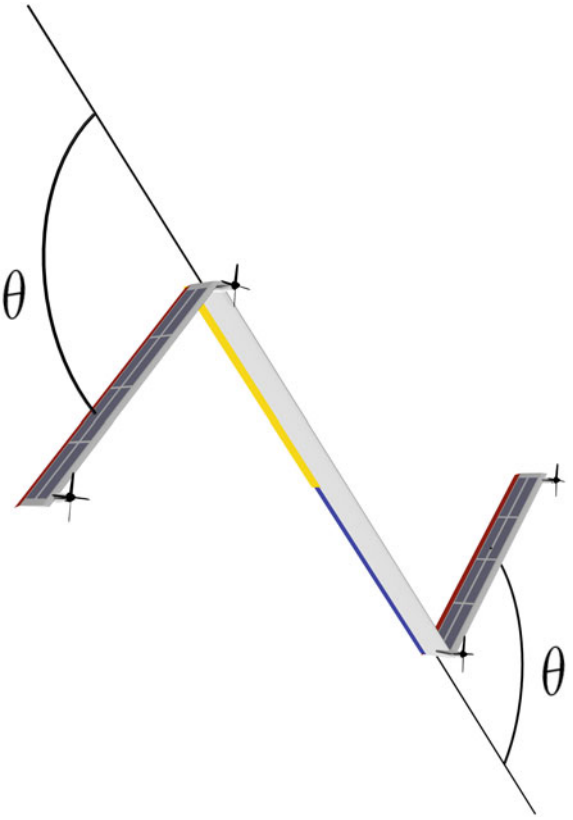


**Fig. 3** Schematic front view of the morphed configuration of the flying wing

## 4 Concluding Remarks

The analysis underlying NATASHA was extended to include the ability to simulate morphing of the aircraft using a new set of trim and kinematical differential equations. An example of the kind of morphing considered in this study requires the wings to fold so as to orient a solar panel to be hit more directly by the sun's rays at specific times of the day. Because of the "long endurance" feature of HALE aircraft, such morphing needs to be done with as near zero energy cost as possible, i.e., without relying on actuators at the hinges and use of aerodynamic forces and engine thrust. The three-wing solar powered HALE aircraft morphs passively into a Z-shaped configuration while local bending moments are zeroed out at the beam connection points while the hinges are locked and are held at zero while the aircraft morphs. The morphing motion is brought to a stop before the hinges are again locked. A systematic process for trim and time marching for passively morphing flying wing is presented. The present study does not account for stiffness and damping in the hinges. These aspects are recommended for future study.

## References

Hodges DH (2006) Nonlinear composite beam theory. AIAA, Reston

Patil MJ, Hodges DH (2006) Flight dynamics of highly flexible flying wings. J Aircr 43(6):1790–1799

Peters DA, Karunamoorthy S, Cao WM (1995) Finite state induced flow models; part I: two-dimensional thin airfoil. J Aircr 32(2):313–322

# Active Control of Self-Excited Roll Oscillations of LAR Wings

**Z. Wang, T. Hu and I. Gursul**

**Abstract** Large amplitude roll oscillations are inherent to fixed-wing MAVs. This paper reviews our recent works on the suppression of the self-induced roll oscillations of LAR rectangular wings using active flow control techniques. Both acoustic excitation and synthetic jet blowing have been used to attenuate the self-excited roll oscillations. Three rectangular wings, of flat plate, NACA0012 and SD7003-085-88 profiles were tested. It was found that roll oscillations can be completely suppressed and the onset of the roll oscillations can be delayed by active flow control approaches. PIV measurements indicated that the excitations could restore a symmetric vortex flow over free-to-roll wings thus stabilize the roll oscillations.

## 1 Introduction

MAVs have been receiving increasing interest because of their broad applications. MAVs with fixed LAR wings have operating speeds around 10 m/s with dimensions between 10 and 15 cm (Torres and Mueller 2004). Roll instabilities and oscillations are inherent to the fixed-wing MAVs due to their low aspect ratio wings and low mass moment of inertia (Mueller 2001). The vortex induced limit-cycle rotary oscillation is often referred to as 'wing rock' (Katz 1999). Early studies of wing rock focused on slender delta wings (Arena and Nelson 1994). Recent studies showed that self-induced roll oscillations also exist for nonslender

Z. Wang (✉)
Shenzhen Graduate School, Harbin Institute of Technology, Shenzhen, 518055, People's Republic of China
e-mail: Z.Wang@bath.ac.uk

Z. Wang · T. Hu · I. Gursul
Department of Mechanical Engineering, University of Bath, Bath BA2 7AY, UK

Y. Zhou et al. (eds.), *Fluid-Structure-Sound Interactions and Control*,
Lecture Notes in Mechanical Engineering, DOI: 10.1007/978-3-642-40371-2_51,

delta wings, but with a nonzero mean roll angle (Gursul et al. 2005). More recently, investigations on relatively higher aspect ratio rectangular wings suggested that, even at pre-stall incidences, self-excited roll oscillations occur (Gresham et al. 2010).

Previous studies of suppressing the slender wing rock have been conducted by applying both passive (Mabey 1997) and active (Sreenatha and Ong 2002) flow control techniques. It has been found that the active techniques, which can often be regarded as steady or periodic addition of momentum that affects the boundary layers and shear layers (Greenblatt and Wygnanski 2000), tend to be more effective (Katz 1999). The present research focuses on control of the self-induced roll oscillations of rectangular wings with aspect ratio 2 using active flow control techniques, say acoustic excitation and synthetic jet blowing.

## 2 Acoustic Excitation

Acoustic excitation has been previously employed to delay the boundary layer separation as well as to enhance the shear layer reattachment over an airfoil (Yarusevych et al. 2007). As separated flows are dominant over the leading-edge and tips of a LAR wing, active flow control with acoustic excitation offers the potential to increase MAV robustness to atmospheric disturbances.

The experiments were conducted in a closed-loop wind tunnel located at the University of Bath. The experimental arrangements are shown in Fig. 1. Three rectangular wings, of flat plate, NACA0012 and SD7003-085-88 profiles, with an aspect ratio of AR = 2 were tested. The physical properties of the wings can be found in Hu et al. (2011). The wings were attached to the high-alpha rig, which allows the angle of attack to be varied as the wind tunnel is running, through the free-to-roll device. The acoustic excitation was provided by an Eminence Omega PRO-18A speaker mounted on the side wall of the test section and aligned with the wing facing the suction surface (Fig. 1). Quantitative flow measurements were undertaken using two different PIV systems, a TSI 2D-PIV system (the maximum repetition rate of 7.25 Hz) for time-averaged and phase-averaged velocity measurements and a TSI high frame rate PIV system (the maximum repetition rate of 3,000 Hz) for spectral features of the shear layer separated from leading edge.

For the flat plate wing, when there was no acoustic excitation, prior to $\alpha = 11°$, nonzero mean roll angles were observed (Fig. 2) due to the asymmetric leading-edge bubbles and therefore asymmetric tip vortices were possible at low incidences (Gresham et al. 2010). Further increase the wing incidence to $\alpha = 12°$, small amplitude roll oscillations occurred and the mean roll angle remains close to 0°. The roll amplitude increased gradually with increasing angle of attack until $\alpha = 15°$. A sharp increase in the amplitude of the wing roll oscillations can be observed at about $\alpha = 15°$. For $\alpha \geq 17°$, the amplitude of the wing roll oscillations increased gradually and eventually saturated. When an acoustic excitation was applied at the optimum frequency of St = 1.5, the onset of the self-excited roll

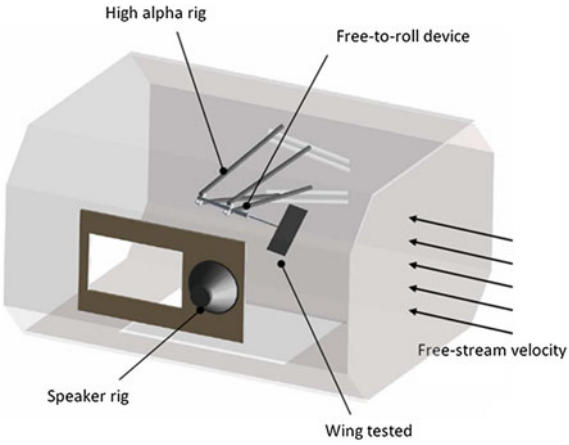


**Fig. 1** Experimental arrangements of attenuation of self-excited roll oscillations of LAR wings by means of acoustic forcing

oscillations was delayed by approximately 4° to about $\alpha = 16°$. A sharp increase in the amplitude of the wing roll oscillations was observed at about $\alpha = 18.5°$. At about $\alpha = 20°$, the amplitude of the wing roll oscillations approached the same values as that of the experiments without acoustic excitation. The acoustic excitation had little effect on the mean roll angle (Fig. 2). The maximum effectiveness of roll angle suppression was achieved at $\alpha = 17°$, $\Delta\Phi_{\text{rms, max}} \approx 30°$ (Fig. 2). Similar results have also been obtained for the NACA0012 wing and SD7003-085-88 wing.

Acoustic forcing is a global flow control approach, thus both tip vortex and shear layer separated from leading-edge are excited. HF PIV measurements suggested that, at the optimum acoustic excitation frequency of St = 1.5, the velocity power spectra of the shear layer instabilities over the stationary flat plate wing exhibit a sharp dominant peak at the same frequency as the acoustic excitation,

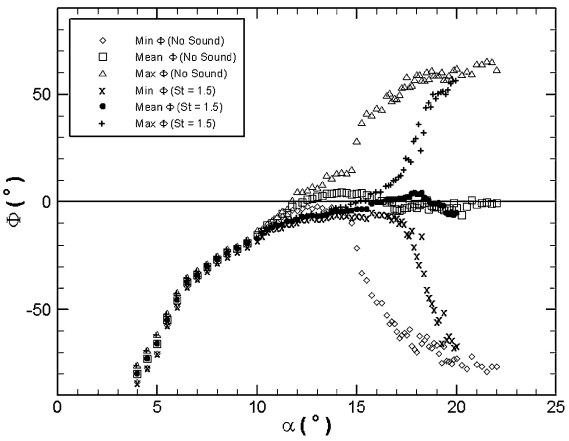


**Fig. 2** Variation of roll angle with angle of attack for the flat plate wing with AR = 2 without and with acoustic excitation at St = 1.5

suggesting strong resonance between the acoustic forcing and shear layer instabilities. The strong resonance energizes the shear layers and results in local reattachment or smaller separated region closer to the wing surface (Fig. 3), which restores the vorticity field back to a symmetric pattern and attenuates the roll oscillations.

## 3 Synthetic Jet

Synthetic jet has been applied as an effective active flow control technique in the past decades (Smith and Glezer 1998) in delaying stall (Seifert et al. 1996), lift enhancement (Amitay et al. 2001), thrust enhancement (Whitehead and Gursul 2006), tip-vortex control (Margaris and Gursul 2006), and leading-edge separated flow control (Amitay and Glezer 2002). The present study employed synthetic jet to attenuate the self-induced roll oscillations of a LAR rectangular wing. The experiments were conducted in the same wind tunnel as aforementioned acoustic excitation project. A rectangular flat plate wing of aspect ratio AR = 2 with synthetic jet installed along the leading-edge was tested. The synthetic jet was generated by diaphragm (membrane with a thickness of 0.2 mm) motions actuated by APCI 40-2010 piezoelectric actuators. Quantitative flow measurements in various streamwise planes were undertaken using the aforementioned TSI HF PIV system.

Generally, the variations of mean, minimum, and maximum roll angle with increasing angle of attack for the flat plate wing without and with synthetic jet excitation exhibit similar trends to those of acoustic excitations (Fig. 2). By applying leading-edge synthetic jet blowing at the optimum frequency of St = 1, the onset of self-excited roll oscillation was delayed by approximately 3°. Figure 4a presents the RMS values of free-to-roll flat plate wing roll angle as a

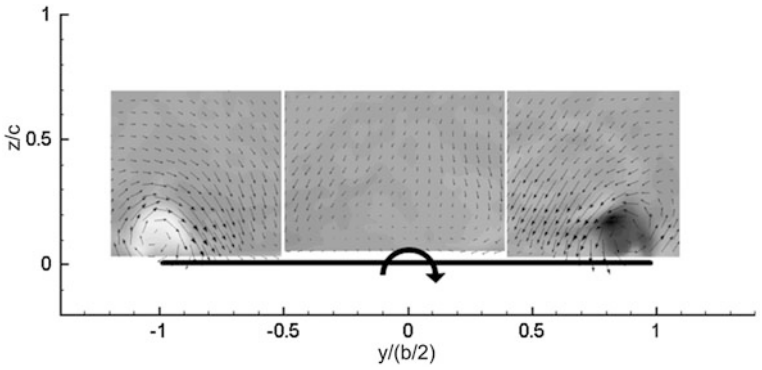


**Fig. 3** Vorticity pattern in the cross-flow plane near the trailing edge of the rolling flat plate wing. $\alpha = 17°$, $\Phi = 0°$, and the acoustic excitation was applied at St = 1.5

function of angle of attack without and with synthetic jet excitations of various frequencies. The reduction of RMS values of the wing roll angle is presented in Fig. 4b. It can be observed that, for all the excitation frequencies tested, St = 1 was the most effective case, which result in a maximum reduction of $\Delta\Phi_{rms,max} = 27°$ at $\alpha = 17.5°$. Again, HF PIV measurements indicated strong resonance between shear layer instabilities and the synthetic jet at St = 1. The resonance resulted earlier reattachment of the separated shear layer which may restore the flow over the rolling wing back to a symmetric pattern and thus attenuate the oscillations.

## 4 Concluding Remarks

Experimental investigations of attenuation of self-excited roll oscillations of LAR wings using acoustic excitation and synthetic jet have been performed. It was found that the roll oscillations first appeared at pre-stall incidences and increased with angle of attack. When the external excitation was applied at the optimum excitation frequencies, these roll oscillations can be effectively suppressed.

Velocity measurements taken over the flat plate wing in a cross-flow plane near the trailing edge and in various streamwise planes indicated that the excitation could return asymmetric flows over the free-to-roll wing back to a symmetric pattern, which attenuates the self-excited roll oscillations. Time-resolved HF PIV measurements taken in various streamwise planes revealed strong resonance between external forcing and instabilities of the shear layer separated from the leading edge when the excitation was applied at the optimum frequency. The excitation energizes the separated shear layer and generates a flow field similar to that of a smaller incidence, and attenuates the self-excited wing roll oscillations.

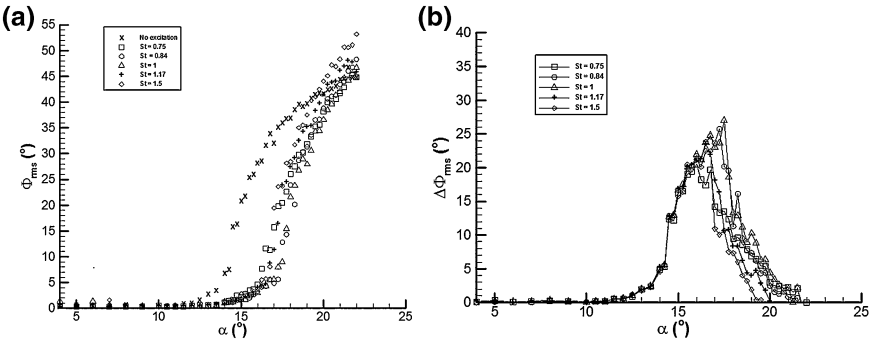


**Fig. 4** **a** RMS values of free-to-roll flat plate wing roll angle as a function of angle of attack without and with synthetic jet excitation; **b** Reduction of RMS values of the roll angle

## References

Amitay M, Glezer A (2002) Role of actuation frequency in controlled flow reattachment over a stalled airfoil. AIAA J 40(2):209–216

Amitay M, Smith DR, Kibens V, Parekh DE, Glezer A (2001) Aerodynamic flow control over an unconventional airfoil using synthetic jet actuators. AIAA J 39(3):361–370

Arena ASJ, Nelson RC (1994) Experimental investigation on limit cycle wing rock of slender wings. J Aircr 31(5):1148–1155

Greenblatt D, Wygnanski IJ (2000) The control of flow separation by periodic excitation. Prog Aerosp Sci 36:487–545

Gresham NT, Wang Z, Gursul I (2010) Low Reynolds number aerodynamics of free-to-roll low aspect ratio wings. Exp Fluids 49:11–25

Gursul I, Gordnier R, Visbal M (2005) Unsteady aerodynamics of nonslender delta wings. Prog Aerosp Sci 41:515–557

Hu T, Wang Z, Gursul I (2011) Control of self-excited roll oscillations of low-aspect-ratio-wings using acoustic excitation. AIAA-2011-36, AIAA conference, Orlando, 4–7 Jan 2011

Katz J (1999) Wing/vortex interactions and wing rock. Prog Aerosp Sci 35:727–750

Mabey DG (1997) Similitude relations for buffet and wing rock on delta wings. Prog Aerosp Sci 33:481–511

Margaris P, Gursul I (2006) Wing tip vortex control using synthetic jets. Aeronaut J 110(1112):673–681

Mueller T (2001) Fixed and flapping wing aerodynamics for micro air vehicle applications, published by the AIAA

Seifert A, Darabi A, Wyganski I (1996) Delay of airfoil stall by periodic excitation. J Aircr 33(4):691–698

Smith BL, Glezer A (1998) The formation and evolution of synthetic jets. Phys Fluids 10(9):2281–2297

Sreenatha AG, Ong TK (2002) Wing rock suppression using recessed angle spanwise blowing. J Aircr 39(5):900–903

Torres GE, Mueller TJ (2004) Low-aspect-ratio wing aerodynamics at low Reynolds numbers. AIAA J 42(5):865–873

Whitehead J, Gursul I (2006) Interaction of synthetic jet propulsion with airfoil aerodynamics at low Reynolds numbers. AIAA J 44(8):1753–1766

Yarusevych S, Sullivan PE, Kawall JG (2007) Effect of acoustic excitation amplitude on airfoil boundary layer and wake development. AIAA J 45(4):760–771

# A New Stall Delay Model for HAWT Based on Inviscid Theory

**Q. Wang, Y. Xu and J. Z. Xu**

**Abstract** Aeroelastic analysis of wind turbine blade is one of the most important studies, which is a typical phenomenon of the fluid–structure interaction. In order to increase the accuracy of the aeroelastic analysis, in this paper, we developed a new three-dimensional (3D) stall delay model for horizontal axis wind turbine (HAWT), which is inviscid stall delay model (ISDM). The model is derived from the Navier–Stokes equations, in which we treat the stall delay effects differently by the delay of the separation point on the airfoil, and aim to capture the further negative pressure reduction in the separation area due to the span wise flow driven by the centrifugal force on the rotating blade. Based on the analytical solution, the ISDM is created and the correction factor $S$ is analyzed. In order to validate ISDM, the model is applied to the NREL Phase VI wind turbine blade. Both the corrected lift and drag coefficients and the power/torque results are compared with the experimental data. From the comparison it can be concluded that ISDM gives reasonable predictions of the 3D lift and drag coefficients as well as the corresponding power and thrust force obtained from blade element and moment (BEM) computation.

## 1 Introduction

The BEM theory is widely applied to the aeroelastic analysis of the wind turbine, which is a typical fluid–structure interaction phenomenon during the operation of wind turbine. However, as one important hypothesis of BEM, the span wise flow is

Y. Xu (✉) · J. Z. Xu
Key Laboratory of Wind Energy Utilization, Chinese Academy of Sciences, Beijing, China
e-mail: xuyu@iet.cn

Q. Wang
Graduate School of Chinese Academy of Sciences, Beijing, China

Y. Zhou et al. (eds.), *Fluid-Structure-Sound Interactions and Control*,
Lecture Notes in Mechanical Engineering, DOI: 10.1007/978-3-642-40371-2_52,

ignored and the local flow field is treated as two-dimensional (2D). For a rotating wind turbine blade, the stall delay effect is usually associated with the span wise flow, which may play an important role in determining the loads and output power, especially for the stall regular wind turbine (Hand et al. 2001). In order to take stall delay effect into consideration, it is necessary to add a 3D stall delay model in BEM computation.

During the past decades, different 3D stall delay models have been developed. Snel et al. analyzed the 3D boundary layer on wind turbine blade by dimensional analysis and set up a stall delay model which has quadratic relationship with the local ratio between the chord length and the span wise position (Snel et al. 1994). Based on his work, Chaviaropoulos and Hansen used a quasi-3D Navier-Stocks (N–S) solver to analyze the rotational effects of wind turbine blade and added the influence of the local twist angle to their stall delay model (Chaviaropoulos and Hansen 2000). Snel' work was also developed by Du and Selig by assuming the velocity profile in the boundary layer to be Pohlhausen type (Du and Selig 1998). Du's model is more comprehensive which contains the blade tip speed ratio and other parameters. Corrigan and Shillings thought that the stall delay effects can be modeled by the delay of the stall angle of attack (AOA) of the airfoil and an additional portion of lift coefficient should be added to the 2D lift coefficient through the slope of the inviscid lift-incidence curve (Corrigan and Schillings 1994).

Different from the stall delay study mentioned above, Lindenburg had made a deep analysis of the stall delay phenomenon based on the 'Centrifugal Pump' concept (Lindenburg 2003). Lindenburg proposed to add the ratio between the rotational speed at blade tip and the local relative speed to the model of Snel. Based on his analysis, Corten also developed 'Centrifugal Pump' model and made a dimensional analysis of the N–S equations instead of boundary layer equations (Corten 2001). Compared with the dimensional analysis of Snel, Corten pointed out that it may be impossible to analyze the separation flow by the boundary layer equations, because the flow separation point is a singular point, and in the separation area the hypothesis of the boundary layer theory is failed. Based on the experimental study, Corten proposed 12 hypotheses to simplify the N–S equations and established the inviscid stall model (ISM) which contains the general relationship among the inviscid flow in the separation area, the centrifugal force, and the Coriolis force, etc. In a word, the stall delay effect is not completely understood so far and the study of the 3D stall delay effects on wind turbine blade is still an open problem.

In this paper the analytical solution of the ISM is derived step by step, and based on the result the inviscid stall delay model (ISDM) is created. The ISDM is applied to the NREL Phase VI wind turbine blade and the results are compared with that of other models and the experimental data.

## 2 The Analytical Solution of ISM

### 2.1 The ISM

The ISM is aim to capture the mechanism of the stall delay effect influenced by the inviscid flow in the separation area. Under the cylinder coordinate, the equations of the ISM are listed below.

$$\frac{\partial V_\theta}{r\partial\theta}+\frac{\partial V_z}{\partial z}+\frac{\partial V_r}{\partial r}+\frac{V_r}{r}=0;\ \frac{\partial p}{\rho r\partial\theta}=2V_r\Omega;\ V_r\frac{\partial V_r}{\partial r}=r\Omega^2-\frac{\partial p}{\rho\partial r};\ V_r\frac{\partial V_z}{\partial r}=0 \tag{1}$$

### 2.2 The Analytical Solution

Assume the dimensionless span wise velocity has the following expression,

$$V_r^*=h(r^*)g(\theta);\ h=q(r^*)r^* \tag{2}$$

the analytical solution of ISM can be derived,

$$V_r^*=\lambda\left(-1\pm\sqrt{1+\frac{1}{\lambda}\frac{C_3}{r^{*2}}}\right)r^*\left(\theta+\frac{C_2}{C_1}\right) \tag{3}$$

$$p^*=A(\lambda,\ r^*)\left[\frac{1}{2}(\theta-\theta_t)^2+D_1(\theta-\theta_t)+D_2\right] \tag{4}$$

$$A(\lambda,\ r^*)=4\lambda^2r^{*2}\left(\sqrt{1+\frac{D_3}{\lambda r^{*2}}}-1\right) \tag{5}$$

where $C$ and $D$ are constants, $\lambda$ is the tip speed ratio, $r^*$ and $\theta$ are the span wise and chord wise cylinder coordinates, respectively.

Based on Eqs. (3)–(5), the ISDM is created and the lift and drag coefficients can be corrected as following:

$$C_{l3d}=C_{l2d}+H_1S\cos(\alpha) \tag{6}$$

$$C_{d3d}=C_{d2d}+H_2S\sin(\alpha) \tag{7}$$

$$S=\frac{r}{c}\left[\frac{1}{1+\lambda^2r^{*2}}A(\lambda,\ r^*)\left(\frac{1}{6}t^3+\frac{D_1}{2}t^2+D_2t\right)+D_4t\right] \tag{8}$$

$$t=\frac{fc}{r};\ r^*=\frac{r}{R};\ \lambda=\frac{\Omega R}{U_\infty} \tag{9}$$

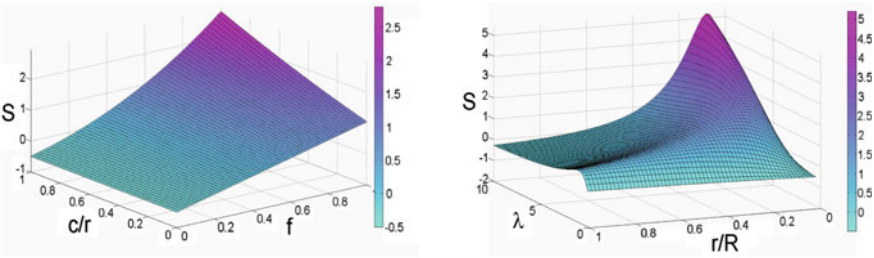


**Fig. 1** The relationship between $S$ and its variables

$$f = 1 - \left(2\sqrt{\frac{C_n}{(\alpha - \alpha_0)\frac{\partial C_{n,0}}{\partial \alpha}}} - 1\right)^2 \tag{10}$$

where $D_1$, $D_2$, $D_3$, $D_4$ and $H_1$, $H_2$ are empirical parameters and $S$ is named as the ISDM correction factor. In this paper these parameters are taken as $D_1 = 2$, $D_2 = 1$, $D_3 = 1.0$, $D_4 = -0.5$, $H_1 = 0.5$ and $H_2 = 0.5$. The relationship between $S$ and its dependent parameters under a typical condition of NREL Phase VI wind turbine is shown in Fig. 1.

## 3 Results and Discussion

### *3.1 NREL Phase VI Wind Turbine Case*

In order to validate the ISDM, the model is applied to NREL phase VI wind turbine blade. The results of the lift and drag coefficients modified by ISDM are compared with that of the other models and the experimental data (Bak et al. 2006), as plotted in Fig. 2.

From the comparison in Fig. 2, it can be seen that the 3D experimental data are different with the 2D data especially when the AOA is larger than the stall angle. The 3D rotational effects improve both of the lift and drag coefficients for most of the span positions. At 30 % span position, the ISDM is the only one that can predict the decrease trend of the lift coefficient and the high drag coefficient in the post stall area. However, it is also noticed that when the AOA is between 8 and 16°, both the lift and the drag coefficients predicted by the ISDM are over estimated. At 63.3 % span position, the lift and the drag coefficients of ISDM are similar to the results of Du and Chaviaropoulos models, respectively. At 95 % span position, all of the models failed to predict the low lift coefficient.

Based on these modified lift and drag coefficients, the power and the thrust force are computed by BEM code and the results are shown in Fig. 3. Compared with the unmodified 2D results, ISDM gives reasonable predictions of the power as well as the thrust force when the wind speed is larger than 13 m/s.

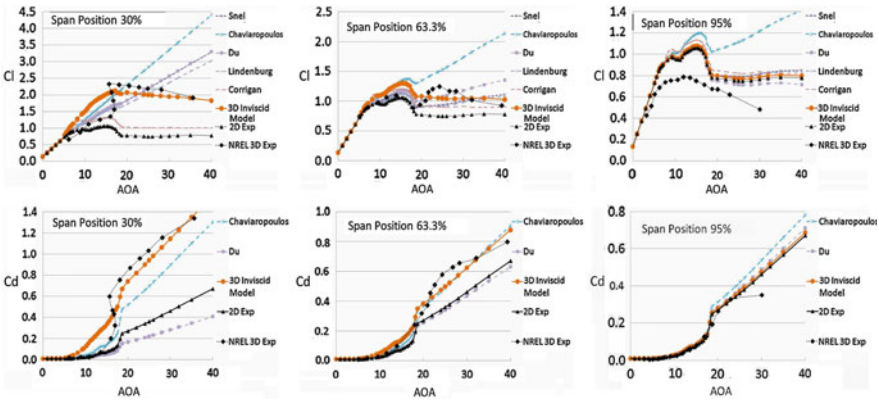


**Fig. 2** The modified lift and drag coefficients comparison for NREL phase VI rotor

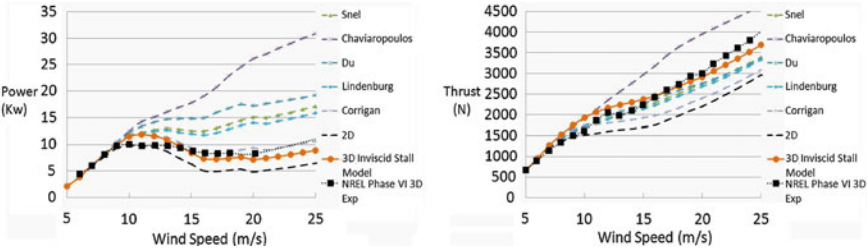


**Fig. 3** The power and the thrust comparison for NREL phase VI rotor

## 4 Conclusions

The analytical solution of ISM is derived in this paper. Based on this solution, the ISDM is created, which contains the mechanism of the stall delay induced by the span wise flow.

The ISDM is applied to the modification of the airfoil aerodynamic coefficients of the NREL Phase VI wind turbine blade. The corresponding power and the thrust force are computed by BEM code and compared with the experimental data. From the comparison it can be seen that, although the result of ISDM has mismatches at some conditions, it gives overall good prediction of the lift and drag coefficients considering the 3D rotational effects.

In the future, more test cases are needed to validate the accuracy of ISDM and the empirical parameters of the model are needed to be systematically studied.

**Acknowledgments** This work was supported by the National Nature Sciences Foundation of China (Grant No. 50876105), the Sino-Denmark Collaboration Project (Grant No. 2010DFA62830), and the National High Technology Research and Development Program of China (863 Program) (Grant No. 2012AA051303).

## References

Bak C, Johansen J, Andersen PB (2006) Three-dimensional corrections of airfoil characteristics based on pressure distributions. EWEC 06, Athens

Chaviaropoulos P, Hansen MOL (2000) Investigating three-dimensional and rotational effects on wind turbine blades by means of a quasi-3D Navier-Stokes solver. J Fluids Eng 122:330–336

Corrigan J, Schillings J (1994) Empirical model for stall delay due to rotation. American Helicopter Society Aeromechanics Specialists Conference San Francisco, CA

Corten GP (2001) Inviscid stall model. Proceedings of the European wind energy conference, Netherlands energy research foundation, pp 466–469

Du Z, Selig M (1998) A 3-D stall-delay model for horizontal axis wind turbine performance prediction. AIAA-98-0021, 36th AIAA aerospace sciences meeting and exhibit, ASME wind energy symposium Reno, NV, USA

Hand MM, Simms DA, Fingersh LJ, Jager DW, Cotrell JR (2001) Unsteady aerodynamics experiment phase V: test configuration and available data campaigns. Technical report, National renewable energy laboratories, 1617 Cole Boulevard, Golden, Colorado, United States of America, NREL/TP-500-29491

Lindenburg C (2003) Investigation into rotor blade aerodynamics. Netherlands society for energy and the environment, paper ECN-C-03-025

Snel H, Houwink R, Bosschers J (1994) Sectional prediction of lift coefficients on rotating wind turbine blades in stall. Neth Energy Res Found

# Flow Control for Vortex Shedding of a Circular Cylinder Based on a Steady Suction Method

**Wen-Li Chen, Hui Hu and Hui Li**

**Abstract** In this study, a suction flow control method was employed to suppress the vortex shedding of a circular cylinder based on a multi-point suction type. A digital particle image velocimetry (PIV) system was used to conduct detailed flow field measurements under different suction flow control conditions with simultaneously measuring the pressure distribution on the test models. Five steady suction flow rates of 20, 40, 60, 80, and 95 L/min were employed in the testing. The suction control effects were investigated under an angle of 90.0° of the suction holes; the effects of the suction flow control along the axial direction of the test model were investigated. The mean and fluctuating pressure coefficients, the lift and drag coefficients, the mean velocity fields of the circular cylinder, and the mean velocity profiles in the wake under the suction flow control were then analyzed. The results indicated that the steady suctions exhibited excellent control effects and could dramatically reduce the fluctuations of lift coefficients and the averages of the drag coefficients and distinctly suppress the alternating vortex shedding (changing into symmetric mode). The control effects of the suction along the axial direction of the model are not uniform and the control effects are improved from the section without suction to the suction section.

## 1 Introduction

As key components of cable-stayed bridges, inclined cables often vibrate under wind, rain, and traffic loads, such as the vortex-induced vibration (VIV) (Zuo et al. 2008) and rain-wind induced vibration (RWIV) (Hikami and Shiraishi 1988).

W.-L. Chen (✉) · H. Li
School of Civil Engineering, Harbin Institute of Technology, Harbin, China
e-mail: cwl_80@hit.edu.cn

W.-L. Chen · H. Hu
Department of Aerospace Engineering, Iowa State University, Ames, USA

Y. Zhou et al. (eds.), *Fluid-Structure-Sound Interactions and Control*,
Lecture Notes in Mechanical Engineering, DOI: 10.1007/978-3-642-40371-2_53,

Frequent wind-induced vibrations which are often induced by the alternating vortex shedding of the stayed cables may induce fatigue damages to the cables, so it is necessary to suppress the vortex shedding of the cables to mitigate the vibration.

Suction flow controls were also widely used to suppress the flow separation of circular cylinders (Fransson et al. 2004; Patil and Ng 2010) by tests or CFD numerical simulations. Patil and Ng (2010), Fransson et al. (2004) found that the continuous porosity could lead to a drag reduction, suppress the spanwise vortices formation, reduce the velocity fluctuation level, eliminate the oscillation of the lift, and delay the separation resulting in a narrower wake width.

In present paper, a steady suction flow control method is adopted to suppress the vortex shedding of a circular cylinder based on a multi-point suction type. Further details and comprehensive study on this method to control the vortex shedding of a circular cylinder will be submitted as a journal paper in the near future.

## 2 Experimental Setup

The experimental study was conducted in a closed-circuit low-speed wind tunnel located in the Aerospace Engineering Department of Iowa State University. The tunnel has a test section with a 1.0 × 1.0 ft (30.48 × 30.48 cm) cross section.

### *2.1 PIV System*

Figure 1 shows the schematic of the experimental setup used in the present study for the two-dimensional PIV measurements. Illumination was provided by a double-pulsed Nd:YAG laser with a repetition rate of 8 Hz. A high-resolution 12-bit (1,376 × 1,040 pixels) CCD camera was used to perform two-dimensional PIV image recording. The CCD camera and double-pulsed Nd: YAG lasers were connected to a workstation (host computer) via a Digital Delay Generator, which controlled the timing of laser illumination and image acquisition.

### *2.2 Model Setup with Suction Flow Control System and Pressure Measurement System*

The test model used in the present study was a circular cylinder. The circular cylinder had a diameter $d = 0.0508$ m and a width equal to the test section width of the wind tunnel. Its roots were mounted on two sides of the wind tunnel wall.

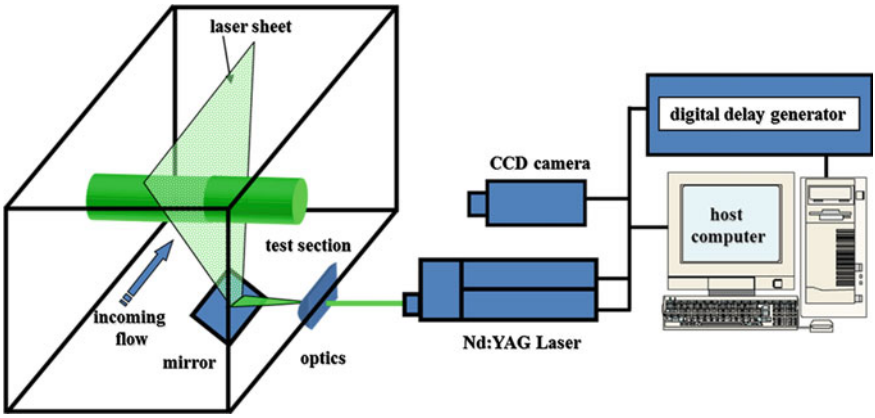


**Fig. 1** Schematic of the experimental setup for PIV measurement

During the experiments, the wind tunnel speed was adjusted to 8.0 m/s, which corresponds to a Reynolds number $\mathrm{Re} = 2.8 \times 10^4$.

Figure 2 shows the assemblage of the test model used in present study. The test model was employed in present test as shown in Fig. 2a. For the test model, four different suction sections were employed with the spaces of $L/8@L/4@L/8$, where $L$ is the length of the test model. The suction holes have the same diameter of 3 mm. Two suction holes were symmetrically distributed about $x$ axis at each suction section, i.e., the angle of suction holes: 90.0 (270.0)°. Omega FMA-2613A was used in the testing to control the suction flow rates of main suction tube which was separated into 8 branches: 8 suction tubes which were connected with 8 suction holes. The flow rate was corrected to a set of standard conditions which are 25 °C and one standard atmosphere pressure of 101.325 kPa. Five suction flow rates of main suction tubes: 20, 40, 60, 80, and 95 L/min were adopted.

To measure the pressure distribution on the cylinder model, a digital pressure measurement system based on the model DSA3217 pressure scanner (Scanivalve

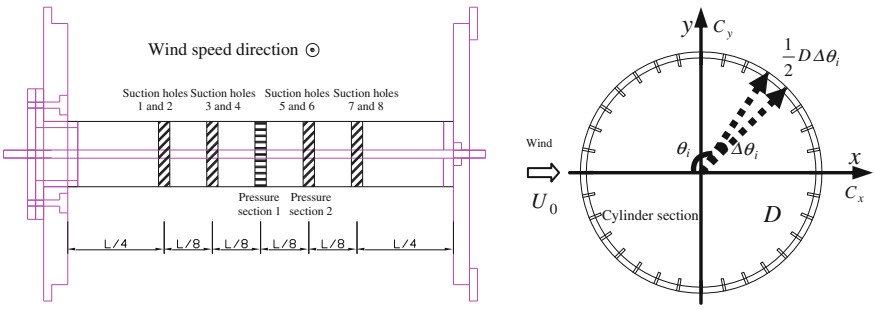


**Fig. 2** Setup of the test model. **a** Test models. **b** Pressure section 1

Corporation) was used in the wind tunnel tests. As shown in Fig. 2b, a total of 62 pressure taps were arranged on the model in two sections, 32 for pressure section 1 and only 30 for pressure section 2 because two pressure taps are replaced by two suction holes at each suction angle. Pressure section 1 was located on the middle of the test model and pressure section 2 was shared with one suction section as shown in Fig. 2a. The sampling rate was 300 Hz and the sampling time was 100 s for the pressure measurement of each tap.

## 3 Experimental Results and Discussions

Figure 3 shows the distributions of the mean pressure coefficients of the test model at two suction pressure sections, respectively. The suction flow control induces great change to the distributions of the mean pressure coefficients, especially in the flow separation region. As the flow rate increasing, the mean pressure coefficient absolutes in the flow separation region decrease resulting in drag reduction. The control effect will be not improved and tend to be steady when the suction flow rate exceeds 40 L/min. For pressure section 1, the position with the minimum mean pressure coefficient has no change under suction flow control with different flow rates. But, for pressure section 2, the point with the minimum mean pressure coefficient move to next point when the flow rate is larger than 40 L/min. It can be deduced that the separate point may move backward or the flow separation is delayed at this suction section. Figure 4 shows the distributions of the fluctuating pressure coefficients at two suction pressure sections, respectively. Similar with the analysis of the mean pressure coefficients, the small flow rate of 20 L/min can obtain better control effect, but the control effect tends to be steady when the suction flow rate exceeds 40 L/min. The fluctuating pressure coefficients of most taps decrease to 1/3 of the values without the suction flow control.

The lift and drag coefficients can be calculated by integral of pressure on the cylinder surface. Figure 5 shows the time histories of the lift and drag coefficients of the cylinder model. The fluctuations of the lift coefficient histories are dramatically suppressed. If the cylinder model can freely vibrate, the oscillation amplitude will also be suppressed under a suction flow control. Not only the amplitudes of the drag coefficients greatly are suppressed, but also the means of the drag coefficients are obviously decreased. It is shown that the suction flow control has the function of the flow drag reduction.

The control effects of the root mean squares (RMSs) of lift coefficients and the means of the drag coefficients are obtained as shown in Fig. 6. The control effect of the lift coefficients of pressure section 2 is just slightly better than that of pressure section 1; and the lift coefficients at two sections can reach about 80 % the amplitude reduction. But, for the drag coefficient reduction, the best control effect is about 30 % on pressure section 2, but only 25 % on pressure section 1. It is indicated that the control effect of the drag coefficients along the axial direction is different; the reason may be that the flow should behave a three-dimensional

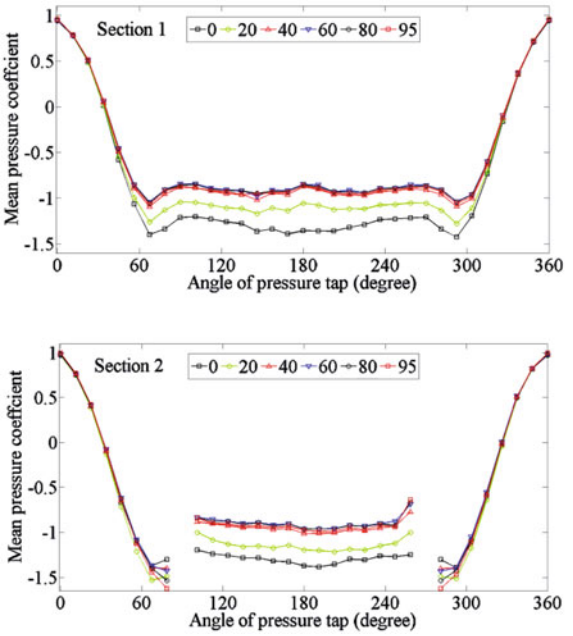


**Fig. 3** Mean pressure coefficient distribution of the test model

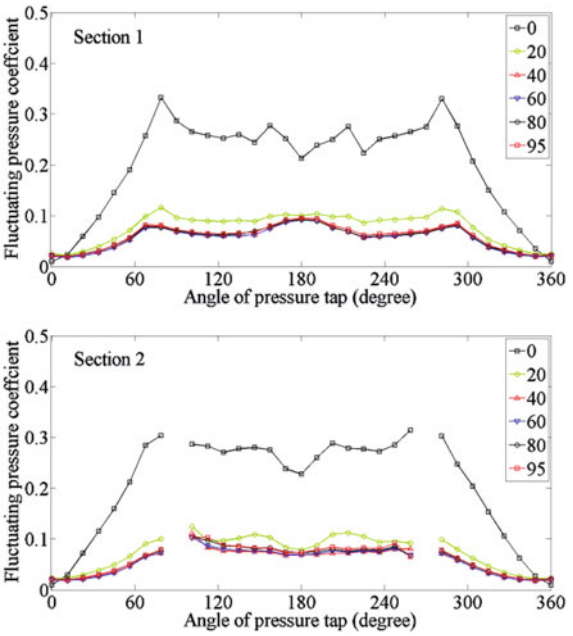


**Fig. 4** Fluctuating pressure coefficient distribution of the test model

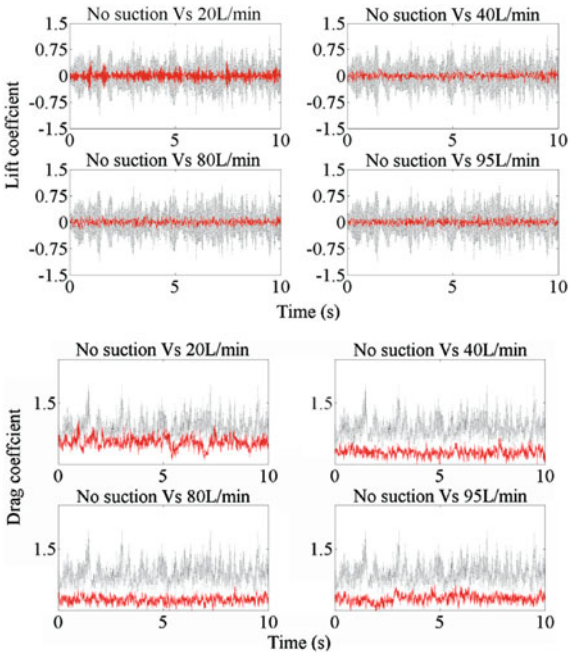


**Fig. 5** Time histories of lift and drag coefficients of section 1

feature along the axial direction. The PIV measurements were simultaneously performed when the wind pressures on the cylinder were measured for models 1 and 2. Two measured PIV planes are located on pressure section 1 and 2. Figure 7 shows the instantaneous vorticity on section 2 of the model. Under the suction flow control, the alternating vortex shedding was changed into a symmetric mode.

To investigate the effects of the suction flow control for the wake along the axial direction, only two measured PIV planes are not enough, so another two planes are added between section 1 and section 2, named section 11 and section 12 along the direction of section 1 to section 2. The PIV measurements are performed on these four planes at the flow rates of 0, 20, 40, and 95 L/min for the test model.

Figure 8 shows the mean velocity fields on four sections for the test model. The results indicate that the values of the T. K. E. are greatly reduced and the turbulence intensities of the wake are decreased under the suction flow control whatever on which section. But only for the section 2, the velocities in the wake have the same direction with the main flow and the velocities close to the centreline in the near wake of other three sections have the opposite direction with the main flow. Furthermore, the separation point of section 2 has been moved backward compared with those of other three sections. It can explain that the point with the minimum mean pressure coefficient move to next point as shown in Fig. 3a. So

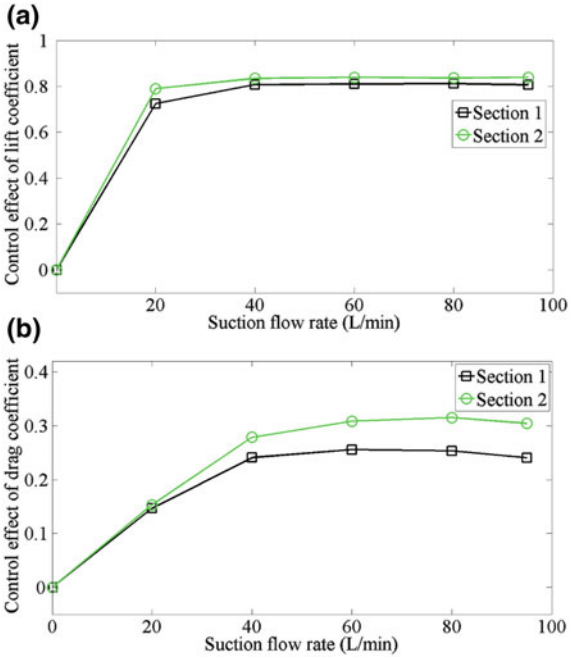


**Fig. 6** Comparison of control effects of aerodynamic coefficients. **a** Lift coefficients. **b** Drag coefficients

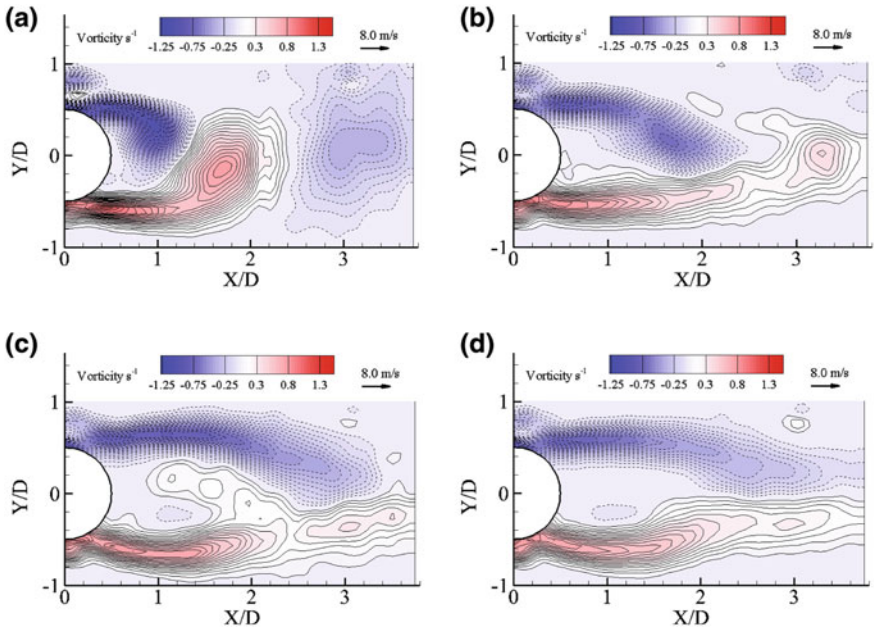


**Fig. 7** Instantaneous vorticity field of the test model for section 2. **a** 0 L/min. **b** 20 L/min. **c** 40 L/min. **d** 95 L/min

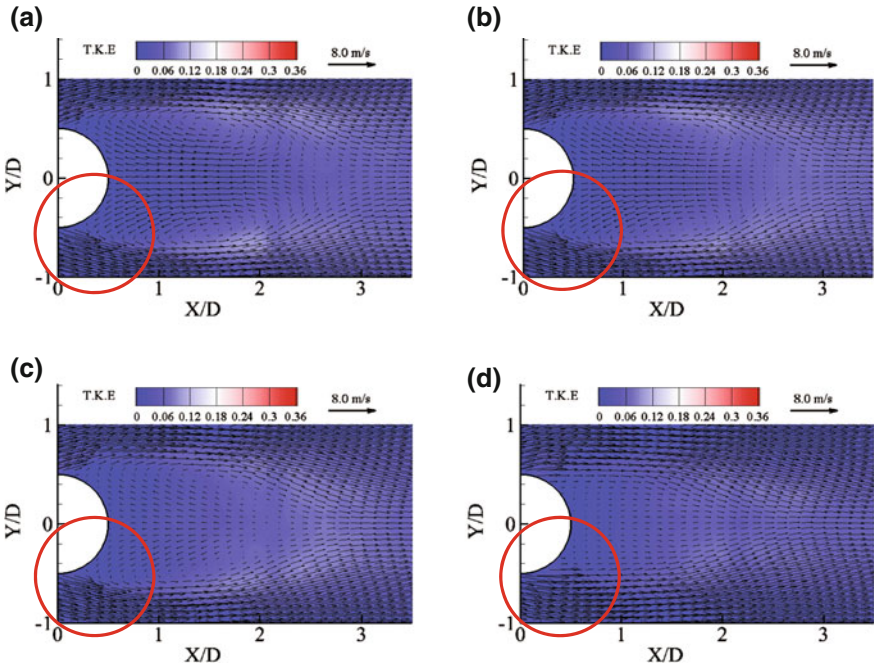


**Fig. 8** Mean velocity field of the test model under the flow rate of 95 L/min. **a** Section 1. **b** Section 11. **c** Section 12. **d** Section 2

combining the results of the distribution of the mean pressure coefficient, it can be deduced that the separate point may also move backward along the flow direction, i.e., the flow separation is delayed on the section 2.

## 4 Conclusions

In this study, the suction flow control for vortex shedding of a circular cylinder was investigated combining PIV and pressure measurements through wind tunnel tests. We obtained that: (1) When the suction holes (90.0°) are close to the flow separation point, one can achieve good control effects: Drag and lift fluctuation reduction, changing the alternating vortex shedding into a symmetric mode, and delaying the flow separation on the suction section; (2) The control effects of the drag and lift fluctuation reduction are improved from the section without suction to the suction section. Flow separation delay is only achieved on the suction section.

## References

Fransson JHM, Konieczny P, Alfredsson PH (2004) Flow around a porous cylinder subject to continuous suction or blowing. J Fluids Struct 19:1031–1048

Hikami Y, Shiraishi N (1988) Rain-wind induced vibrations of cables in cable stayed bridges. J Wind Eng Ind Aerodyn 29:409–418

Patil SKR, Ng TT (2010) Control of separation using spanwise periodic porosity. AIAA J 48(1):174–187

Zuo D, Jones NP, Main JA (2008) Field observation of vortex- and rain-wind-induced stay-cable vibrations in a three-dimensional environment. J Wind Eng Ind Aerodyn 96:1124–1133

# Numerical Investigation on the Flow-Induced Oscillation of Two Elastic Circular Cylinders in Tandem

**H. Chen, H. J. Zhang, C. J. Zhang and Z. D. Su**

**Abstract** The vortex-induced vibration of two elastic cylinders in tandem has been numerically simulated based on the Galerkin finite element method and dynamic mesh technique. Influences of the reduced velocity to the amplitude of vibration displacement of the cylinders was investigated, with cylinder spacing of $L/D = 5$ and a Reynolds number of 1,000. In the simulation, several classic vortex-induced vibration modes have been obtained, such as beat vibration and resonance. It was found that vortices shed periodically from both the upstream and downstream cylinders. The downstream cylinder undergoes larger amplitude of oscillations in both transverse and streamwise directions than those of the upstream cylinder. Variations in the maximum amplitudes of the oscillation displacement were found to agree with the "three-branch" model.

## 1 Introduction

Flow-structure interaction in an arrangement of two cylinders in tandem is an important project for the research works of fluid mechanics, which has not been well understood. Previous works reveal some characteristics of this kind of flow phenomenon. Assi et al. (2006) experimentally investigated the oscillations of the downstream cylinder in a two-tandem circular cylinder arrangement. They observed that the oscillating amplitude of the cylinder increased with the reduced velocity. For the same reduced velocity, this amplitude is 50 % larger than that of a single cylinder. Price et al. (2007) experimentally investigated the vortex pattern and the vortex shedding frequency as the upstream cylinder vibrates in the transverse direction. Kim et al. (2009a, b) investigated experimentally flow-induced

H. Chen · H. J. Zhang (✉) · C. J. Zhang · Z. D. Su
College of Metrology and Measurement Engineering, China Jiliang University, Hangzhou, China
e-mail: zhanghongjun@cjlu.edu.cn

Y. Zhou et al. (eds.), *Fluid-Structure-Sound Interactions and Control*,
Lecture Notes in Mechanical Engineering, DOI: 10.1007/978-3-642-40371-2_54,

oscillations of two cylinders in tandem arrangement. Five wake vortex flow patterns have been observed in their experiments. Flow-induced oscillation of two cylinders in tandem has been investigated numerically by Prasanth and Mittal (2009) for a low Reynolds number of 100. In their work, mass ratio m* = 10, damping ratio $\zeta_s = 0$, cylinder spacing $L/D = 5.5$. They found that the variation in the amplitude of the transverse oscillation is in accordance with a three-branch model which is suitable for that of a single cylinder. Numerical studies have been conducted for one-degree-of-freedom and two-degree-of-freedom vortex-induced vibrations of the downstream elastic circular cylinder in tandem arrangement by Chen et al. (2004, 2005). Their results showed that the peak value of the displacement of the cylinder for two degree of freedom is larger than that for one degree of freedom, and the lift of the downstream cylinder is larger than the upstream cylinder, while it is contrary for the drag. Although many research works have been made on the flow-structure interactions, numerical studies on the flow-induced vibration of two cylinders in tandem for a higher Reynolds number are still lacking. In this work, flow-structure interactions of two cylinders in tandem were investigated numerically at a Reynolds number of 1,000.

## 2 Mathematic Model and Calculation Method

### *2.1 Governing Equation*

For the unsteady incompressible flow of the fluid-induced vibration issue in this study, the continuity and momentum equations are:

$$\frac{\partial U_i}{\partial X_i} = 0 \tag{1}$$

$$\frac{\partial U_i}{\partial \tau} + U_j \frac{\partial U_i}{\partial X_j} = -\frac{\partial P}{\partial X_i} + \frac{1}{Re}\frac{\partial^2 U_i}{\partial X_j \partial X_j} \tag{2}$$

The dimensionless parameters in the equations are $X_i = x_i/D$, $U_i = u_i/U$, $P = (p - p_0)/\rho U^2$ and $\tau = Ut/D$, where the characteristic length $D$ is the diameter of the cylinder, $U$ is the uniform flow velocity, $p_0$ is the inlet pressure, the Reynolds number $Re = UD/\upsilon$, and $\nu$ is the kinematic viscosity.

Introducing the spring damping vibration model, the vibration equation of the cylinder for two degree of freedom is:

$$\frac{\mathrm{d}^2 Y_i}{\mathrm{d}\tau^2} + \frac{4\pi\zeta_s}{U_r}\frac{\mathrm{d}Y_i}{\mathrm{d}\tau} + \left(\frac{2\pi}{U_r}\right)^2 Y_i = \frac{F_i}{2m^*} \tag{3}$$

In which, $Y_i$ is the displacement of the cylinder in $x$ and $y$ directions, $\zeta_s$ is the dimensionless damping coefficient of the structure, $F_i = (C_D,\ C_L)$ is the cylinder's

stress coefficient, mass ratio $m^* = 4m/\rho\pi D^2$, $m$ is the mass of unit length of the cylinder, $\rho$ is the fluid density, the reduced velocity $U_r = U/f_n D$, $f_n$ is the natural frequency of the cylinder.

## 2.2 Computation Model and Grid

The computations were carried out with Galerkin finite element method, at a Reynolds number 1,000, and spacing ratio $L/D = 5$. The two cylinders can vibrate with two degrees of freedom. The mass ratio is $m* = 20.0$, and the non-dimensional damping ratio is $\zeta_s = 0.0$. A dynamic grid technology was introduced to calculate the vibration of the two elastic cylinders. The $k$-$\varepsilon$ model was chosen for the turbulence flow.

Two cylinders of equal diameter are placed in a 60 × 20 D rectangular domain, in which the length from the inlet to the upstream cylinder is 10 D. After defining $u$ and $v$ are the mean values of the streamwise and vertical velocity, the boundary conditions were set as: the inlet dimensionless $u = 1$ and $v = 0$, the outlet dimensionless pressure $P = 0$. The Neumann condition is employed in the inlet velocity, i.e., $\partial u/\partial x = 0$ , $\partial v/\partial x = 0$. The non-slip boundary condition is employed in the upper and lower walls, $u = 0$, $v = 0$. The six-node triangle mesh was introduced in the computational domain and the mesh near the cylinder was refined. The number of grids is more than 60,000.

# 3 Results and Discussions

Figure 1 shows the time histories of the lateral displacement of the cylinder vibration. It is found that as the reduced velocity is increased, the vibration mode undergoes successively small vibration, beat, resonance, and small beat vibration. The upstream and downstream cylinders appear to be of similar varying rule in terms of the vibration mode, but the amplitude of the downstream cylinder is larger than that of the upstream. As the relative values of the natural frequency of the cylinder and the vortex shedding frequency varying, i.e., the value of $U_r$ was set at different values, the clap-frequency is varied consequentially. There are five and two beats at $U_r = 5$ and $U_r = 5.5$, as shown in Fig. 1b and c.

Figure 2 presents the variations of maximum oscillating displacement amplitudes of the cylinder as the reduced velocity is changed. When the natural frequency of the cylinder $f_n$ was set at 0.175 and $U_r = 5.75$, the natural frequency is the same with vortex shedding frequency in magnitude, resonance phenomenon occurs both on the upstream and downstream cylinders, the displacement amplitudes reach maximum values. With the reduced velocity continuously increasing, the streamwise amplitudes of the upstream and downstream cylinders are both

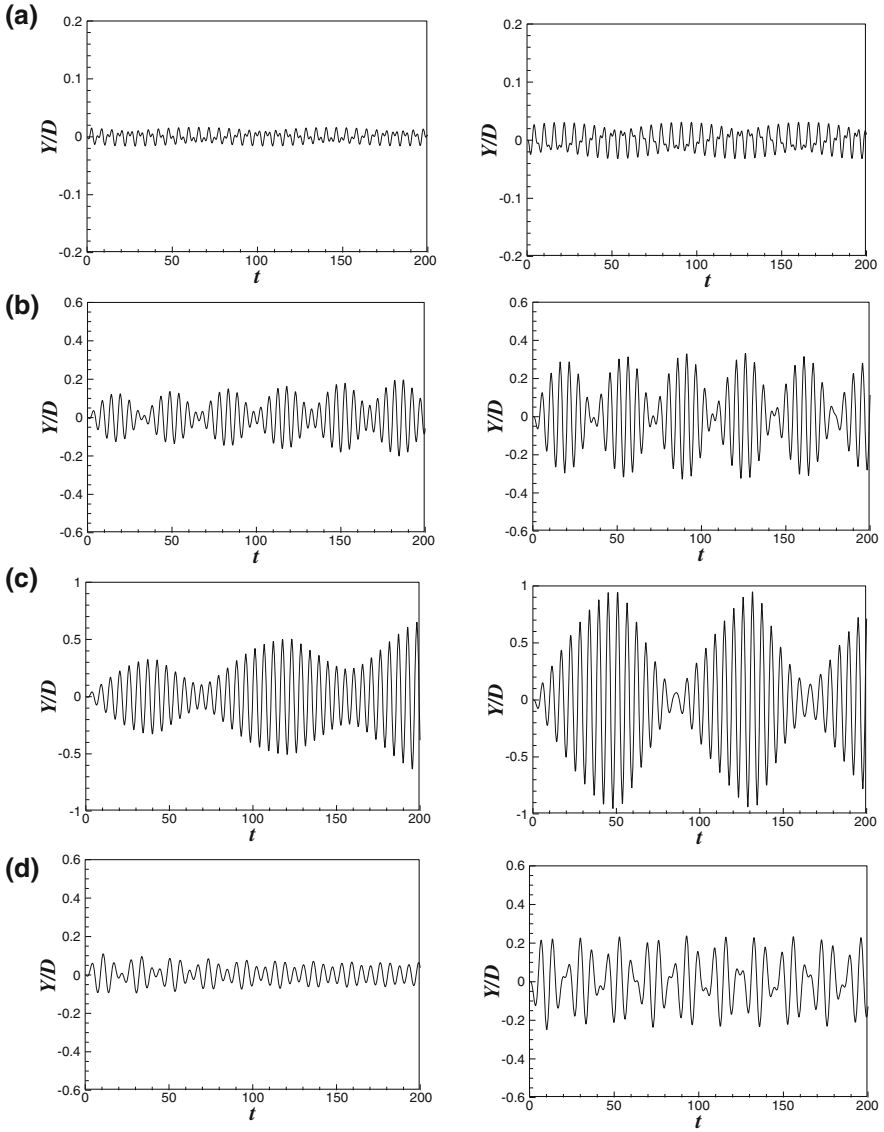


**Fig. 1** Transverse vibration displacement curve of the upstream cylinder (*left*) and the downstream cylinder (*right*). (**a**) $U_r = 4.0$ (**b**) $U_r = 5.0$ (**c**) $U_r = 5.5$ (**d**) $U_r = 8.0$

increasing, and the amplitude of the upstream cylinder is larger than that of the downstream cylinder (Fig. 2a). With regard to the maximum lateral displacement amplitude (Fig. 2b), the variation tendency of the upstream and downstream cylinders is the same. As being affected by the trailing vortex of the upstream, the amplitude of the downstream cylinder is larger than the upstream cylinder. The

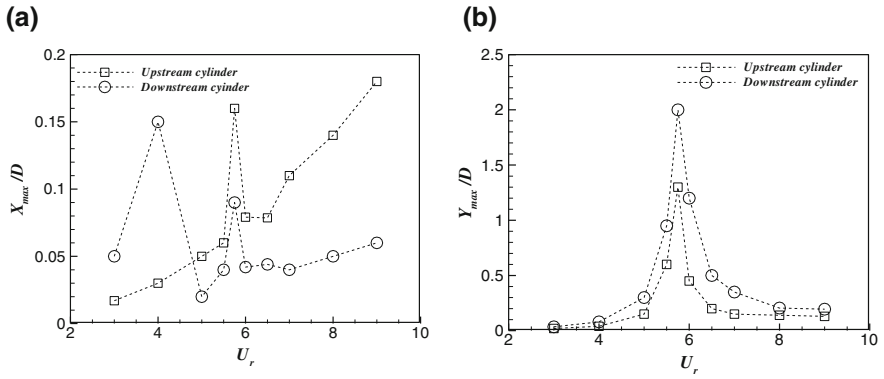


**Fig. 2** The maximal vibration displacement amplitudes of the cylinder

lateral variations of the two cylinders present a "three branch" mode. At the initial part, the amplitudes are very small. While for the middle part, the amplitudes reach maximum values, and those for the larger reduced velocity are smaller. These results are similar to the observations of Prasanth and Mittal's (2009) and Khalak and Williamson (1999), in spite of some differences in data magnitude due to the difference in the Reynolds number, spacing ratio, and mass ratio.

## 4 Conclusions

A numerical simulation has been carried out on the vortex-inducted vibrations of cylinders in tandem at the spacing ratio of $L/D = 5$, with two degrees of freedom. The behaviors of flow-induced responses of the cylinders were examined as the reduced velocity is varied. The main conclusions are summarized as follows:

1. The maximum lateral vibration amplitude of the downstream cylinder is larger than that of the upstream. The lateral vibration amplitude trend shows "three-branch" mode, which is similar to that of a single cylinder.
2. With the reduced velocity varied, several vortex-induced vibration modes were captured, i.e., small amplitude vibration, beat, and resonance. When the resonance occurs, the vortex shedding frequency is increased.

**Acknowledgments** This work was financially supported by the National Natural Science Foundation of China (10972210) and Zhejiang Province Key Sci-tech Innovation Team Project (2009R50024).

## References

Assi GRS, Meneghini JR, Aranha JAP, Bearman PW, Casaprima E (2006) Experimental investigation of flow-induced vibration interference between two circular cylinders. J Fluid Struct 22:819–927

Chen WQ, Ren AL, Li GW (2004) The numerical study of two-degree-of-freedom vortex-induced vibration of the downstream cylinder in tandem arrangement. Acta Mech Sinica 36(6):732–738 (in Chinese)

Chen WQ, Ren AL, Li GW (2005) Numerical simulation of flow-induced vibration on two circular cylinders in a cross-flow. Acta Aerodyn Sin 23(4):442–448 (in Chinese)

Khalak A, Williamson CHK (1999) Motion, forces and mode transitions in vortex-induced at low mass damping. J Fluid Struct 13:813–851

Kim S, Alam MM, Sakamoto H, Zhou Y (2009a) Flow-induced vibrations of two circular cylinders in tandem arrangement. Part 1: characteristics of vibration. J Wind Eng Ind Aerod 97:304–311

Kim S, Alam MM, Sakamoto H, Zhou Y (2009b) Flow-induced vibrations of two circular cylinders in tandem arrangement. Part 2: suppression of vibrations. J Wind Eng Ind Aerod 97:312–319

Prasanth TK, Mittal S (2009) Flow-induced oscillation of two circular cylinders in tandem arrangement at low Re. J Fluid Struct 25:1029–1048

Price SJ, Païdoussis MP, Krishnamoorthy S (2007) Cross-flow past a pair of nearly in-line cylinders with the upstream cylinder subjected to a transverse harmonic oscillation. J Fluid Struct 23:39–57

# Flow-Induced Vibrations of a Circular Cylinder Interacting with Another of Different Diameter

**Md. Mahbub Alam and Y. Zhou**

**Abstract** The work investigates flow-induced response of a circular cylinder interacting with another smaller diameter cylinder placed upstream. The upstream cylinder diameter $d$ was varied from 0.24 to 1.00 times the diameter $D$ of the downstream cylinder, which was cantilever-supported. Experimental observation was made at a spacing ratio, $L/d$, of 1–2, where $L$ is the center of the upstream cylinder to the forward stagnation point of the downstream. A violent vibration of the cylinder occurred at $d/D = 0.24$–$0.8$ for $L/d = 1$ or $d/D = 0.24$–$0.6$ for $L/d = 2$, but not at $d/D = 1$. The violent vibration occurs at a reduced velocity $U_r = 13$–$22.5$, depending on $d/D$ and $L/d$, and increases rapidly, along with the fluctuating lift, for a higher $U_r$. At a small $d/D$, the upstream cylinder wake narrows, hence the high-speed slice of the shear layer could flow alternately along the two different sides of this cylinder, thus exciting the downstream cylinder.

**Keywords** Two circular cylinders · Tandem · Flow-induced vibrations · Different diameter · Forces · Wake · Strouhal numbers

## 1 Introduction

Flow-induced vibrations of two interacting cylinders subjected to a cross flow have been the subject of intensive research because of relevance to the engineering structural design and acoustic emission problems. A detailed survey of the

Md. M. Alam (✉) · Y. Zhou
Institute of Turbulence-Noise-Vibration and Control, Shenzhen Graduate School, Harbin Institute of Technology, Shenzhen, China
e-mail: alamm28@yahoo.com

Y. Zhou
Department of Mechanical Engineering, The Hong Kong Polytechnic University, Hong Kong, China

Y. Zhou et al. (eds.), *Fluid-Structure-Sound Interactions and Control*, Lecture Notes in Mechanical Engineering, DOI: 10.1007/978-3-642-40371-2_55,

literature relating to flow-induced response of two cylinders suggests that previous investigations mostly were performed for two cylinders of an identical diameter (e.g., Bokaian and Geoola 1984). The literature mainly clarified $L/d$ range where vortex-resonance or galloping persists (see Fig. 1 for definition of symbols). Rahmanian et al. (2012) performed a numerical simulation on vortex-induced vibrations of two cylinders of $d/D = 0.1$ where the cylinders were mechanically coupled, behaving as one combined cylinder. The interaction between the coupled cylinders led to a very irregular vibration of the bundle both in-line and cross-flow directions. There does not seem to have a systematic study on flow-induced response of the downstream cylinder when the upstream cylinder size (diameter) is changed. Hence a number of questions are still unanswered. First, what is the effect of the upstream cylinder diameter on the flow-induced response of the downstream cylinder? Second, how much force on the base structure is induced when a structure experiences vortex-excitation (VE) or galloping? Finally, what is the physics behind the generation of galloping for tandem cylinders, though galloping in general is not generated on an isolated circular cylinder (axis-symmetric body)?

The objectives of the present study are to experimentally investigate flow-induced response of a cantilever circular cylinder in the presence of an upstream cylinder of different diameters. The flow-induced responses $A_x$ and $A_y$ in the $x$- and $y$-direction (where $A$ stands for amplitude of vibration at the free end of the cylinder) and fluctuating (rms) drag ($C_{\mathrm{Drms}}$) and lift ($C_{\mathrm{Lrms}}$) forces on the cylinder base are systematically measured for reduced velocity $U_r = 0.8$–$32$. Furthermore, wake and vortex-shedding frequency $f_v$ behind the downstream cylinder and in the gap between the cylinders are examined.

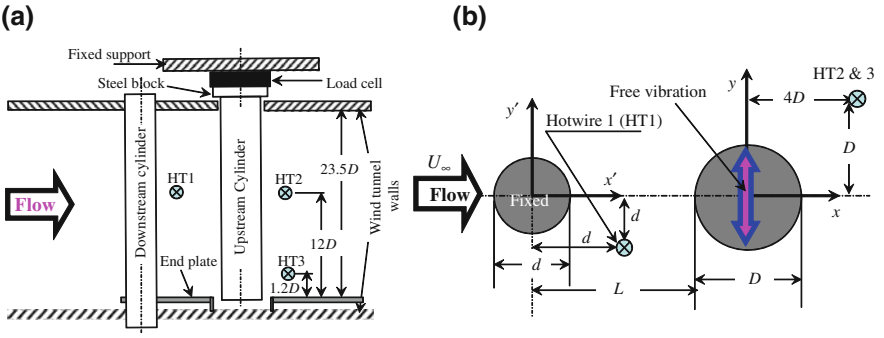


**Fig. 1** **a** Experimental setup, **b** definitions of symbols

## 2 Experimental Details

Experiments were conducted in a low-speed, close-circuit wind tunnel with a test section of 600 × 600 mm. The upstream cylinder of diameter $d$ was solid and fixed-mounted at both ends (Fig. 1). The downstream cylinder of outer diameter $D = 25$ mm was hollow, 700 mm in length, and cantilever-mounted on an external rigid support detached from the wind-tunnel wall. $d$ was 25, 20, 15, 10, and 6 mm, respectively. Free-stream velocity $U_\infty$ was varied from 0.5 to 20 m/s, corresponding to variation of $U_r$ from 0.8 to 32 and Reynolds numbers ($Re$) from 825 to $3.3 \times 10^4$ based on $D$ and $U_\infty$. Two hotwires were used to measure the frequencies of vortex shedding from the cylinders. A three-component strain-gauge load cell (KYOWA Model LSM-B-500NSA1) was installed at the base of the downstream cylinder to measure the force. Free-end vibration displacement of the cylinder was measured by using a standard laser vibrometer. To visualize the flow, smoke was introduced into the flow from the midspan of the upstream cylinder through six 0.75 mm-diameter pinholes, three at an azimuthal angle $\theta = +30°$ with a 2 mm spanwise spacing between the holes and the other three at $\theta = -30°$ with the same spanwise spacing, where $\theta$ is measured from the front stagnation point. A Dantec PIV CCD camera was used to capture the flow images.

## 3 Results and Discussion

### *3.1 Flow-Induced Response*

The cylinder system had a mass-damping ($m^*\zeta$) value of 4.33 with the first mode natural frequency $f_{n1} = 24.9$, where $m^*$ and $\zeta$ are the mass and damping ratios, respectively. Figure 2 illustrates vibration amplitude $A_y/D$ and $A_x/D$ at $L/d = 1$ for $d/D = 0$ (single cylinder), 0.24, 0.4, 0.6, 0.8, and 1.0. The horizontal axis $U_r$ is based on $f_{n1}$. Violent vibration is unveiled at $d/D = 0.24$, 0.4, 0.6, and 0.8 for $U_r > 13$, 13, 19.5, and 22.5, respectively, in addition to a visible VE at $U_r = 4.75$ for $d/D = 0.24$ and 0.4. For other $d/D$, a very tiny hump generated at the same $U_r$ (see the insert of Fig. 2) is the sign of VE, $A_y/D$ at the hump is less than 0.003 corresponding to 0.075 mm vibration amplitude; hence, it can be said that VE is practically suppressed. Note that VE speed $U_{r0}$ calculated from the Strouhal number of the cylinder fixed at both ends was 5, 5.3, 5.12, 5.1, 4.74, and 4.58 for $d/D = 0$, 0.24, 0.4, 0.6, 0.8, and 1.0, respectively. Vibration due to VE started at $U_r = 4.4$ and reached to a maximum at $U_r = 4.75$. On the other hand, the galloping occurred for $U_r > 11.3$. For the galloping generated cases $d/D = 0.24$–0.8, the starting $U_r$ of vibration generation is lower for lower $d/D$, implying that a decreasing $d/D$ anyhow causes a higher instability of flow and/or an increase of negative damping on the cylinder. At $L/d = 2$, vibration was generated for $d/D = 0.24$–0.6 (not shown).

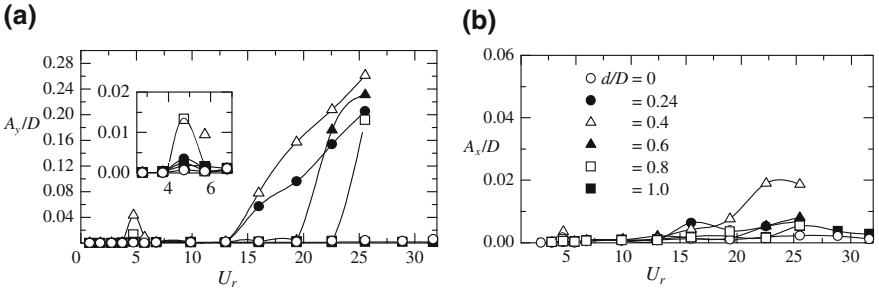


**Fig. 2** Normalized vibration amplitude $A_y/D$ **a** and $A_x/D$ **b** in $y$- and $x$-direction at $L/d = 1$

## 3.2 Forces on the Cylinder

Figure 3 shows variations of $C_{\mathrm{Drms}}$ and $C_{\mathrm{Lrms}}$ with $U_r$ at $L/d = 1$. $C_{\mathrm{Drms}}$ and $C_{\mathrm{Lrms}}$ are highly sensitive to $U_r$ for $d/D = 0.24$–$0.8$, but less for $d/D = 0$ and 1.0. For $d/D = 0$, they are more or less constant at about 0.11 and 0.23, respectively for $U_r < 25$. These values are however the same as those measured for both ends fixed. They however increase slightly for $U_r > 25$. This is due to a synchronization of the vortex-shedding frequency $f_v$ with the second-mode natural frequency $f_{n2}$ of the cylinder. Note that the value of $U_r$ corresponding to $f_v$ synchronization at $f_{n2}$ is 32, estimated from Strouhal number. The most important feature in the figure is that $C_{\mathrm{Lrms}}$ for $d/D = 0.24$, 0.4, 0.6, and 0.8 launches to intensify itself at $U_r = 13$, 13, 19.5, and 22.5, respectively, where vibration starts to occur. At $U_r = 25.5$, where $A_y/D$ is about 0.23, 0.26, 0.205 and 0.192 for $d/D = 0.24$, 0.4, 0.6, and 0.8, respectively, $C_{\mathrm{Lrms}}$ intensified by 48, 78, 57, and 45 times, respectively, compared with that for $d/D = 0$ or for a fixed cylinder. $C_{\mathrm{Drms}}$ is quite low even in the high-amplitude vibration regime, confirming vibration generated dominantly in the cross-flow direction. Similar observation is made at $L/d = 2$ (not shown).

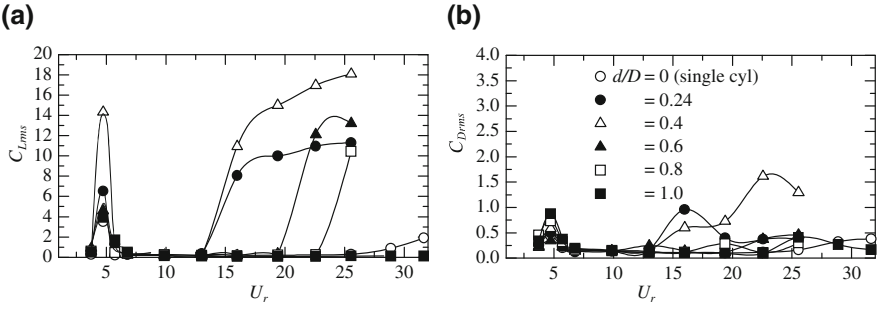


**Fig. 3** Fluctuating (rms) lift $C_{\mathrm{Lrms}}$ **a** and drag $C_{\mathrm{Drms}}$ **b** forces at $L/d = 1$

### 3.3 Fluid–Structure Interaction and Vibration Generation

For fixed cylinders (Fig. 4a), the two shear layers emanating from the upstream cylinder reattach steadily on the downstream cylinder. Indeed, the vibration mainly results from the switching instability of the shear layers emanating from the upstream cylinder. The switching instability is generated from whether the high-velocity slice of a shear layer passes on the same side or opposite side of the downstream cylinder (Fig. 4b). The high-velocity slice generates highly negative pressure on the surface over which it goes. When the cylinder is moving upward from its centerline (Fig. 4c, d), the high-velocity slice of the upper shear layer goes on the upper side and causes an upward lift force to pull the cylinder upward. On the other hand, when the cylinder is moving down (Fig. 4e, f), toward the centerline, the high-velocity slice of the same shear layer sweeps the lower side; hence a downward lift force is generated to pull the cylinder toward the centerline. Similarly, the next half cycle is associated with the lower shear layer. Previous sections proved that a smaller $d/D$ is more prone to generate vibration. Why? A smaller $d/D$ is accompanied by a narrow wake between the cylinders, hence the shear layers are more prone to switch and results in the vibration.

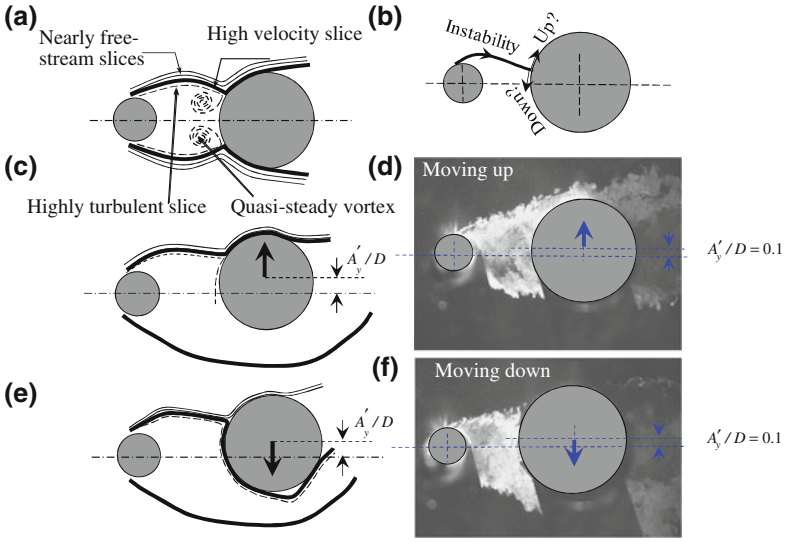


**Fig. 4** Flow structures generating vibration. **a** No vibration: steady-reattachment flow. **b** Instability generation. For a given displacement, visualized flow ($d/D = 0.4$, $L/d = 2$, $U_r = 19.9$) and sketch when cylinder moving (**c**, **d**) upward, (**e**, **f**) downward

## 4 Conclusions

1. The downstream cylinder experiences violent vibration when the upstream cylinder diameter is $d/D = 0.24$–$0.8$ for $L/d = 1$ and $d/D = 0.24$–$0.6$ for $L/d = 2$.
2. The vibration causes an intensification of $C_{\mathrm{Lrms}}$. Compared with that for $d/D = 0$ or for a fixed cylinder, $C_{\mathrm{Lrms}}$ for $d/D = 0.24$, 0.4, 0.6, and 0.8 intensified by 48, 78, 57, and 45 times, respectively at $U_r = 25.5$ where $A_y/D$ is about 0.23, 0.26, 0.205, and 0.192, respectively.
3. Decreasing $d/D$ is prone to generate vibration. At a small $d/D$, the upstream cylinder wake narrows, and the shear layer reattachment position on the downstream cylinder approaches the front stagnation point, and hence the high-speed slice of the shear layer could flow alternately along the two different sides of this cylinder, thus exciting the downstream cylinder.

**Acknowledgements** YZ wishes to acknowledge support given to him from Natural Science Foundation of China through grants 11172085 and 50930007. Alam wishes to acknowledge Shenzhen Govt support through grant JCYJ20120613145300404.

## References

Bokaian A, Geoola F (1984) Wake-induced galloping of two interfering circular cylinders. J Fluid Mech 146:383–415

Rahmanian M, Zhao M, Cheng L, Zhou T (2012) Two-degree-of-freedom vortex-induced vibration of two mechanically coupled cylinders of different diameters in steady current. J Fluids Struct 35:133–159

# Numerical Study on Vortex-Induced Vibration of Three Cylinders in Equilateral-Triangular Arrangements

**Feng Xu, Yi-qing Xiao, Hai-tao Liu and Jin-ping Ou**

**Abstract** In the present paper, a numerical study is performed on the vortex-induced vibrations of three elastically mounted cylinders in a regular triangle arrangement at low Reynolds number. The motion of every single cylinder, which is free to oscillate in two degrees-of-freedom in an uniform flow and has the same mass and natural frequency in both inflow and cross flow directions, is modeled by a mass-spring-damper system. The vibrating displacement, mean and fluctuating aerodynamic forces, Strouhal number (St) and vortex shedding pattern in the wake of each cylinder are analyzed with seven spacing ratios $L/D$ changing from 2.0 to 6.0. The results indicate that the simultaneous resonance may occur and the frequency of inflow vibration keeps consistent with that of cross flow vibration for the downstream cylinders. The cross flow oscillation amplitude of three cylinders significantly increased compared with the flow-induced vibration of a single elastically mounted cylinder and the cross oscillation of downstream cylinder is non-negligible for vortex-induced vibration of multi-cylinder system with low mass and damping.

**Keywords** Vortex-induced vibration · Three cylinders · Two degrees-of-freedom · Vortex shedding pattern

F. Xu (✉) · Y. Xiao · H. Liu
School of Civil and Environmental Engineering, Harbin Institute of Technology Shenzhen Graduate School, Shenzhen, China
e-mail: xufenghit@hit.edu.cn

J. P. Ou
School of Civil Engineering, Harbin Institute of Technology, Harbin, China

Y. Zhou et al. (eds.), *Fluid-Structure-Sound Interactions and Control*,
Lecture Notes in Mechanical Engineering, DOI: 10.1007/978-3-642-40371-2_56,

# 1 Introduction

Vortex-induced vibrations (VIV) of cylinder group are a very common phenomenon in engineering, such as high-rise building groups, suspended cables of long-span bridges, marine cables and subsea pipelines in offshore platform, and so on. The resulting vibration has significant influence of the fatigue life of structures and could cause disastrous failure of industrial facilities with heavy financial losses. Therefore, engineers and researchers have spent much effort to investigate the VIV of cylindrical structures (Govardhan and Williamson 2001; Sarpkaya 2004; Williamson and Govardhan 2004). Nevertheless, the study on VIV of the cross flow past more than one or two cylinders is still relatively scarce, especially numerical simulation (Meneghini et al. 2001; Lam et al. 2008). Computational fluid dynamics (CFD) has become a powerful tool for solving complex fluid flow problems in the last decade and has been used to calculate the flow around single and multiple cylinders cover a wide range of Reynolds number (Re).

In this study, a numerical simulation is presented for the VIV of three cylinders in equilateral-triangular arrangement at Re = 200. The 2D Navier-Stokes equations are solved by a finite volume method (FVM) with an industrial CFD code in which a coupling procedure has been implemented in order to obtain the cylinder response. The spacing ratio *L/D* is set from 2.0 to 6.0. The main objective of this study is to examine the effect of *L/D* on the flow pattern, aerodynamic forces, and inflow and cross flow vibrating response of the three cylinders.

# 2 Numerical Method

## *2.1 Computational Models and Boundary Conditions Setting*

The elastically mounted cylinder can be simplified as mass-spring-damper system having two degrees-of-freedom. The numbering and arrangement form of three equal diameter cylinders are shown in Fig. 1. The *L/D* is defined as spacing ratio, here, $L$ is the center-to-center distance, $D$ is the cylinder diameter and equal to 0.01 m. The unstructured grids are employed to discretize the flow field as shown in Fig. 2. The computational region is $45D \times 30D$ with $15D$ upstream, $30D$ downstream, and $15D$ on either side, respectively. The flow direction is from left to right. The left side is set as velocity-inlet, and the right side is set pressure-outlet. The relative pressure is set as 0, and the upper and lower free slip boundaries are set by symmetry. The three cylinder surfaces are set as wall.

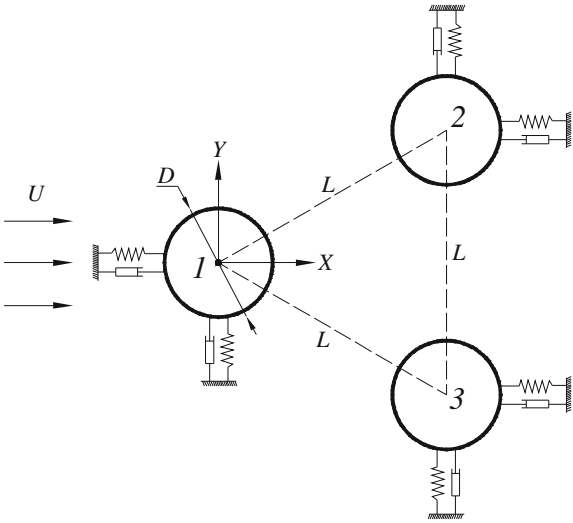


**Fig. 1** Calculation model and arrangement form of three elastically mounted cylinders

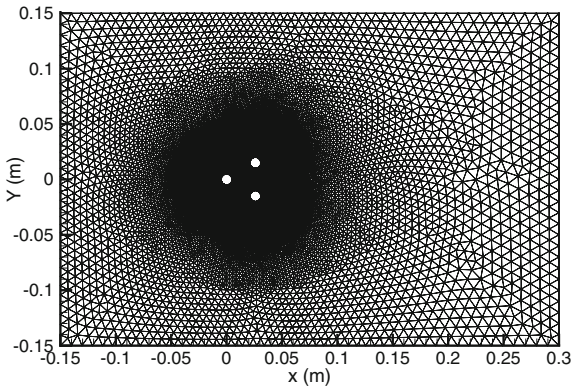


**Fig. 2** Computational region and mesh generation for space ratio $L/D = 3.0$

## *2.2 Solution Process of Fluid-Structure Interactions*

The fluid-structure interaction system was solved using a loosely coupled method. The 2D Navier-Stokes equations are solved by a CFD code (Fluent) based on a finite volume method (FVM) with a Pressure-Based algorithm in which a coupling procedure (Newmark-$\beta$) has been implemented in order to obtain the cylinder response. The grid domain is updated by a dynamic mesh model of the Fluent code.

## 3 Results and Discussion

Current studies confirm that the ratio between the natural frequency $f_n$ of elastic cylinder and the vortex shedding frequency $f_s^*$ of flow around rigid cylinder (hereinafter referred to as "frequency ratio $f_n/f_s^*$"), the dimensionless mass ratio $M^*=m/\rho D^2 l$ and reduced damping $Sg=8\pi^2 S_t^{*2} M^* \zeta$ are important parameters which have significant influence on the structural vibration. The parameters $Sg = 0.01$, $M^* = 1.0$ and $f_n/f_s^* = 1.30$ are chosen for each of the three cylinders, and a single cylinder with the same parameter subjected to VIV confined in the resonance band such as described by Zhou et al. (1999).

### 3.1 Aerodynamic Forces and Responses

Figure 3 shows the aerodynamic force coefficients and correlated frequency characteristics vary as the *L/D* for three cylinders, which include the mean and fluctuating lift coefficients $\bar{C}_l$ and $C_l'$, the mean and fluctuating drag coefficients $\bar{C}_d$ and $C_d'$, the Strouhal number $S_t$ and dominant frequency $f_{cd}$ of the drag coefficient, respectively.

In Fig. 3a, the mean of upstream cylinder 1 $\bar{C}_{l1}$ approximates 0 for entire *L/D* range, the $\bar{C}_{l2}$ and $\bar{C}_{l3}$ are equal in magnitude and opposite in direction, which means values increase at first then decrease with the increase of *L/D*. In Fig. 3b,

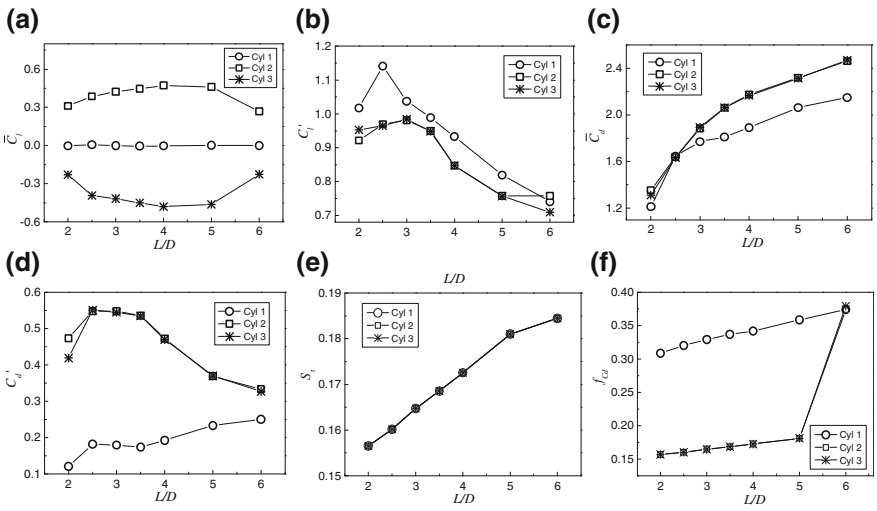


**Fig. 3** Characteristic parameters of aerodynamic force versus *L/D* for three cylinders: **a** $\bar{C}_l$, **b** $C_l'$, **c** $\bar{C}_d$, **d** $C_d'$, **e** $S_t$, **f** $f_{cd}$

the $C_l'$ of each cylinder initially increases and then decreases. When $L/D$=2.5, the maximum value of $C_{l1}'$ is 1.15, and the maximum values of $C_{l2}'$ and $C_{l3}'$ are close to 1.0 at $L/D$=3.0. It is seen that the $C_{l2}'$ is almost consistent with $C_{l3}'$, which are slightly less than the $C_{l1}'$, in the entire $L/D$. In Fig. 3c, the $\bar{C}_{d2}$ and $\bar{C}_{d3}$ increase as the $L/D$ increases and keep coincident with each other, which are larger than $\bar{C}_{d1}$ besides $L/D$=2.5. In Fig. 3d, the $C_{d2}'$ and $C_{d3}'$ show a convex trend and are significantly larger than $C_{d1}'$ in the $L/D$. It is noted that the impact force to the downstream cylinders due to the vortices shedding from upstream cylinders brings in a larger RMS of the drag coefficients compared to the case of flow around a single cylinder. In Fig. 3e, the $S_t$ for the three cylinders, ranging from 0.157 to 0.184, increases as the $L/D$ increases. In Fig. 3f, the $f_{cd1}$ is about twice that of $S_{t1}$, as expected result of flow around a single cylinder. Besides $L/D$=6.0, the $f_{cd2}$ and $f_{cd3}$ are equal to $S_{t2}$ and $S_{t3}$, it will result in the simultaneous resonance in cross flow and inflow directions for the downstream cylinders.

The ratios of vibrating displacement to diameter $D$, and corresponding frequency characteristics are shown in Fig. 4. In Fig. 4a, it is seen that all the $\bar{Y}/D$ behaves similar change law compared with Fig. 3a, and the $\bar{Y}_2/D$ and $\bar{Y}_3/D$ reach their maximum values 0.12 at $L/D = 4.0$. In Fig. 4b, when the $L/D \leq 2.5$, the $Y_1'/D$ increases and reaches their maxima 0.495 at $L/D = 2.5$, then slowly decreases and finally approaches to 0.463 at $L/D = 6.0$. The $Y_2'/D$ and $Y_3'/D$ show a convex trend with $L/D$=2.0–4.0, and reach their corresponding maximum value 0.45 at $L/D = 3.0$. As the $L/D$ further increases, the $Y_2'/D$ and $Y_3'/D$ gradually increase and obtain their maxima at $L/D = 6.0$, which approach very close to that of $Y_1'/D$. In Fig. 4c, the $\bar{X}/D$ of three cylinders gradually increases with increasing

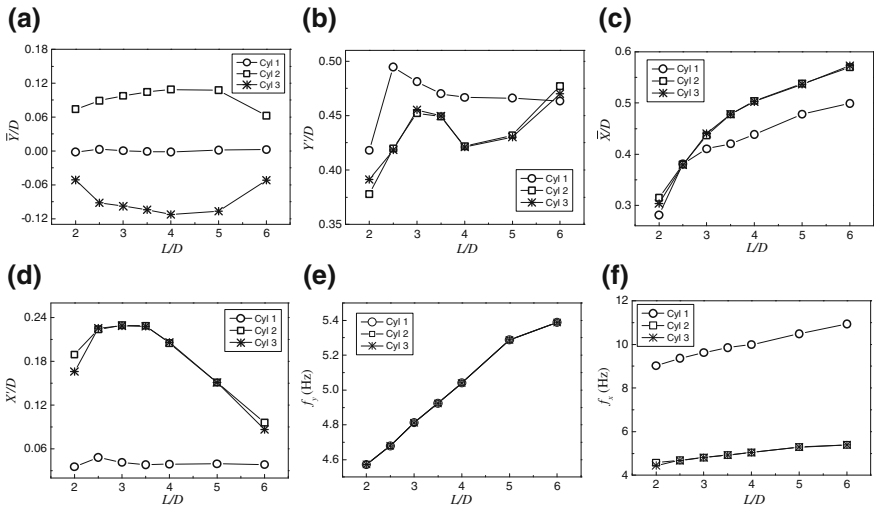


**Fig. 4** Characteristic parameters of aerodynamic response versus $L/D$ for three cylinders: **a** $\bar{Y}/D$, **b** $Y'/D$, **c** $\bar{X}/D$, **d** $X'/D$, **e** $f_y$, **f** $f_x$

*L/D*, which have a little change for $L/D \leq 2.5$. In Fig. 4d, it is noted that the fluctuating amplitude of inflow displacement of cylinder 1 is very small. The $X_2'/D$ and $X_3'/D$ increase first then decrease, which are much greater than that of $X_1'/D$ for the all *L/D*. In Fig. 4e, the $f_y$, which ranging from 4.572 to 5.388 Hz, of the three cylinders increases and is completely equal to each other as the *L/D* increases. In Fig. 4f, the values of $f_{x1}$ are about twice that of $f_{y1}$. For the downstream cylinders 2 and 3, the $f_{x2}$ and $f_{x3}$ are close to $f_{y2}$ and $f_{y3}$. It is indicated that both cross flow and inflow resonances have been occurred.

The centroid motion trajectories of the three cylinders are shown in Fig. 5. These plots obviously show that the vibrations of each cylinder are self-limiting. The cylinder 1 appears to have a "figure of 8" shape for all *L/D*, which indicates that the frequency of inflow oscillation is two times of that of cross flow direction. The motion trajectories of cylinder 2 and 3 present a distinct oblique ellipse. It indicated that the frequency of inflow oscillation is equal to that of the cross flow oscillation and there is a certain phase difference between the two downstream cylinders.

## *3.2 Flow Pattern*

In Fig. 6, the flow patterns are clearly illustrated by the instantaneous vorticity plots around the three cylinders, while the cross flow vibrating displacement of cylinder 1 reaches to the positive maximum value. Figure 6a–d show the free shear layers from the upstream cylinder 1 reattach onto the two downstream cylinder surfaces.

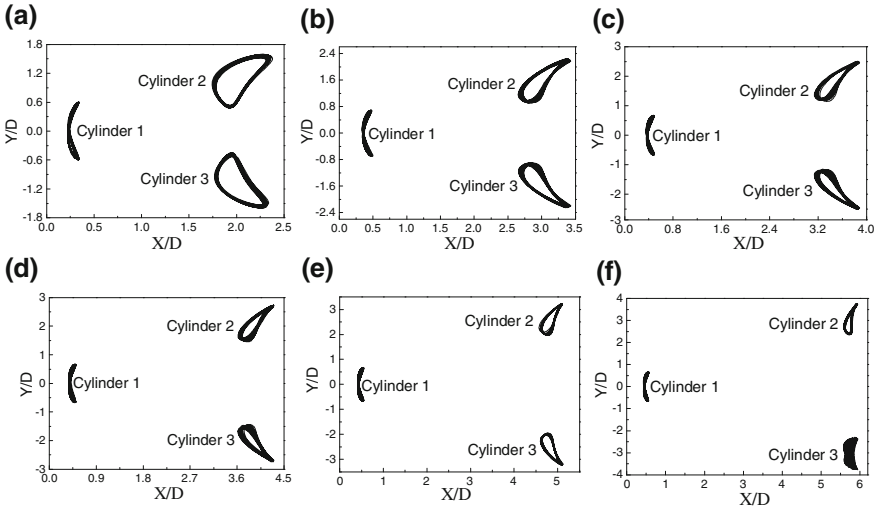


**Fig. 5** Centroid trajectories of three cylinders: **a** $L/D = 2.0$, **b** $L/D = 3.0$, **c** $L/D = 3.5$, **d** $L/D = 4.0$, **e** $L/D = 5.0$, **f** $L/D = 6.0$

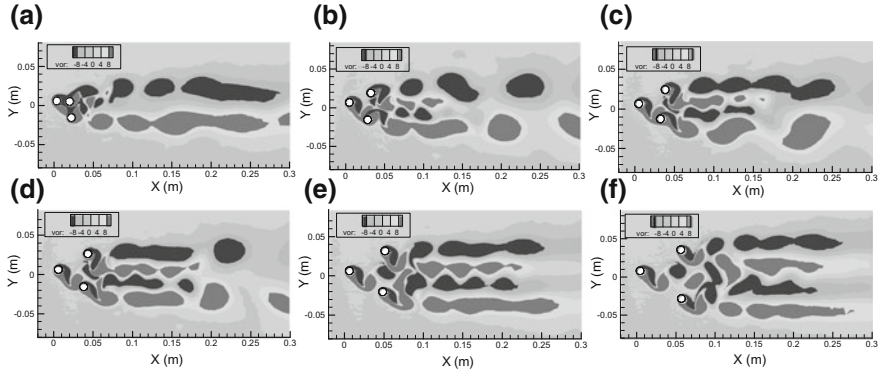


**Fig. 6** Instantaneous vorticity contours of three cylinders: **a** $L/D = 2.0$, **b** $L/D = 3.0$, **c** $L/D = 3.5$, **d** $L/D = 4.0$, **e** $L/D = 5.0$, **f** $L/D = 6.0$

At small $L/D = 2.0$, it is seen that the vortex shedding of flow around the three cylinders is very similar to that of flow over a single cylinder. As the $L/D$ further increases, the two inner side free shear layers from the downstream cylinder 2 and 3 are gradually developed and wiggled. In Fig. 6e and f, the downstream cylinder 2 and 3 have, respectively, fully developed vortex street, this signifies the weakening of flow interference between the two side by side cylinders.

## 4 Conclusions

In this study, the vortex-induced vibration of three elastically mounted cylinders in equilateral-triangular arrangements was investigated by numerical simulation. The following conclusions were obtained from this study:

1. The fluctuating lift coefficient of upstream cylinder is larger than that of the two downstream cylinders, but the mean and RMS values of the downstream cylinders are larger than that of the upstream cylinder for the entire $L/D$ range.
2. The motion trajectories of downstream cylinders represent the oblique oval orbits. It indicated that the frequency of inflow oscillation is equal to that of the cross flow oscillation, and there is a certain phase difference for the two downstream cylinders.
3. The resonances occur in the inflow and cross flow directions for the downstream cylinders. Hence, the inflow oscillating of the downstream cylinders increases significantly compared with the upstream cylinder.

**Acknowledgments** This research was funded by the National Natural Sciences Foundation of China (NSFC) (51008103 and 51008093).

## References

Govardhan R, Williamson CHK (2001) Mean and fluctuating velocity fields in the wake of a freely-vibrating cylinder. J Fluids Struct 15:489–501

Lam K, Gong WQ, So RMC (2008) Numerical simulation of cross-flow around four cylinders in an in-line square configuration. J Fluids Struct 24:34–57

Meneghini JR, Saltara F, Soqueira CLR (2001) Numerical simulation of flow interference between two circular cylinders in tandem and side-by-side arrangements. J Fluid Struct 15:327–350

Sarpkaya T (2004) A critical review of the intrinsic nature of vortex-induced vibrations. J Fluids Struct 19:389–447

Williamson CHK, Govardhan R (2004) Vortex-induced vibrations. Annu Rev Fluid Mech 36:413–455

Zhou CY, So RMC, Lam K (1999) Vortex-induced vibrations of an elastic circular cylinder. J Fluid Struct 13:165–189

# The Numerical Simulation of Fluid-Structure Interaction on a Simple Cluster in an Axial Flow

**Z. G. Liu, Y. Liu and J. Lu**

**Abstract** A cylinder/cluster subjected to axial flow is the most fundamental and revealing problem in the general subject of fluid-structure interaction (FSI). In this paper, the FSI of a system in which a simple cluster consisting of four cylinders is subjected to an axial flow is studied numerically with an explicit partitioned scheme. The cylinders are modeled by Euler–Bernoulli beams and the flow is solved based on Navier–Stokes equations with LES turbulence model. The effect of the dimensionless flow velocity on the dynamics of the cylinders is investigated in detail. For small dimensionless flow velocity, the initial strong vibration of the cylinder is damped and the buckling instability may occur if the dimensionless velocity is large enough.

**Keywords** FSI · LES · Vibration · Buckling

## 1 Introduction

When the water flows through fuel assemblies in pressurized water reactor (PWR) core, the rods, which constitute the assembly, are induced to vibrate by the fluid. This vibration is called axial flow-induced vibration and is important for the PWR safety. The amplitude of this vibration is very small, however, it would fret and wear the rods so that the radioactive material may be released (Païdoussis 2004). On the other hand, the instability may be induced (Païdoussis 2004).

Z. G. Liu · Y. Liu (✉)
Department of Mechanical Engineering, The Hong Kong Polytechnic University, Hong Kong, China
e-mail: yang.liu@polyu.edu.hk

J. Lu
Department of Mechanical and Biomedical Engineering, City University of Hong Kong, Tat Chee Avenue, Kowloon, Hong Kong, China

Y. Zhou et al. (eds.), *Fluid-Structure-Sound Interactions and Control*,
Lecture Notes in Mechanical Engineering, DOI: 10.1007/978-3-642-40371-2_57,

The axial flow-induced vibration is essentially a fluid-structure interaction (FSI) problem and has been studied theoretically by many researchers by simplifying the FSI. The rod can be considered as a cylinder. One important parameter influencing the dynamics of the system is the dimensionless flow velocity (Païdoussis 2004), which is defined in Eq. (1). For small dimensionless flow velocity, instabilities do not occur, however, they could occur if dimensionless flow velocity is large enough (Païdoussis 2004). This is also observed by experiments (Païdoussis 1979, 2004).

In this study, we try to simulate FSI numerically for a simple cluster consisting of four cylinders in an axial flow to avoid the difficulties and defects of the theoretical analyses and experiments (Liu et al. 2012).

## 2 Simulation Methods and Model

The flow governing equations are arbitrary Lagrangian-Eulerian (ALE) Navier-Stokes (N-S) equations (Donea et al. 2004) and the cylinders are modeled by Euler-Bernoulli beams (Thomson 1965). The cylinders can vibrate in any transverse directions. The FSI is solved by an explicit partitioned scheme, the interested readers could refer to Liu et al. (2012) for the details. The fluid flow solver is commercial CFD software Fluent, which solves ALE N-S equations with FVM (ANSYS 2009), and the structure solver is in-house developed FEM codes solving Euler–Bernoulli beam dynamic equation.

The model is shown in Fig. 1. The cylinders all have a diameter $D$ and length $20D$. The flow is confined by a cylindrical wall which is the same long as the cylinders with diameter of $6.8284D$, and is hollowed with the thickness $0.06D$. For each cylinder we define radial and tangential directions R and T (Gagnon and Païdoussis 1994a, b). The cylinders are respectively clamped at their two ends and the flow is assumed turbulent and solved numerically with LES model, in which the subgrid-scale (SGS) model is Smagorinsky–Lilly model (ANSYS 2009).

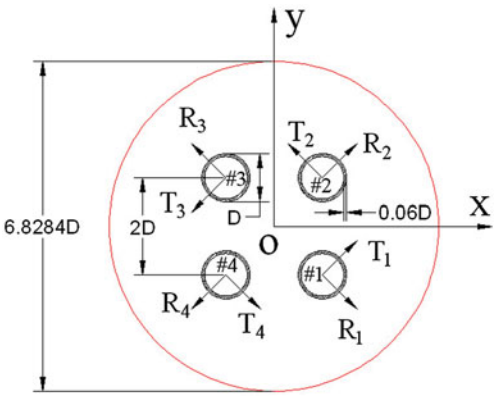


**Fig. 1** Schematic view of the model

## 3 Results and Discussion

We define the dimensionless flow velocity $\bar{U}$, mass ratio $\beta$, Reynolds number Re and the dimensionless time $\tau$ (Païdoussis 2004) as

$$\bar{U} = \upsilon_0 L\sqrt{\frac{\rho A_t}{EI}}, \beta = \frac{\rho A_t}{\rho A_t + \rho_b A_e}, \text{Re} = \frac{\rho \upsilon_0 D_h}{\mu}, \tau = \frac{t}{L^2}\sqrt{\frac{EI}{\rho_b A_e + \rho A_t}}, \quad (1)$$

where $\upsilon_0$ is the average flow inlet velocity; $\rho$ and $\rho_b$ are the density of the fluid and cylinders, respectively; $\mu$ is the viscosity of the fluid; $D_h$ is the hydraulic diameter; $A_t$, $A_e$ and $L$ are the total cross sectional area, effective sectional area and length of the cylinders. We investigate two cases, in which $\text{Re} = 1.05 \times 10^5$, $\beta = 0.4699$ but $\bar{U} = 4.4499$, 6.0173 respectively.

The vibrations of the mid-spans of cylinders #1 and #2 for $\bar{U} = 4.4499$ and 6.0173 are shown in Figs. 2 and 3, where the dimensionless displacements $d_r$ and $d_t$ in $R$ and $T$ directions are defined by normalizing the displacements in these two directions with the diameter $D$ of the cylinders. When $\bar{U} = 4.4499$, the cylinder #1 is initially located as the first beam shape with the maximum displacement $0.2D$ in its $R$ direction and equilibrium shape in $T$ direction, and all other cylinders have no displacement. As shown in Fig. 2, the initial strong vibration of cylinder #1 in its $R$ direction is damped rapidly into weak oscillation with the amplitude about $0.01D$. At the beginning, a strong vibration of cylinder #2 in its $R$ direction is induced but damped rapidly into weak oscillation with the amplitude about $0.01D$, which is similar to the case of cylinder #1. In $T$ direction, for both cylinders #1 and #2, only weak oscillations are induced by the flow and the amplitudes are comparable to those of final vibrations in $R$ direction. The weak oscillation could be categorized as sub-critical vibration as a result of turbulence (Païdoussis 2004). The vibrations of cylinders #3 and #4 are similar to that of cylinder #2.

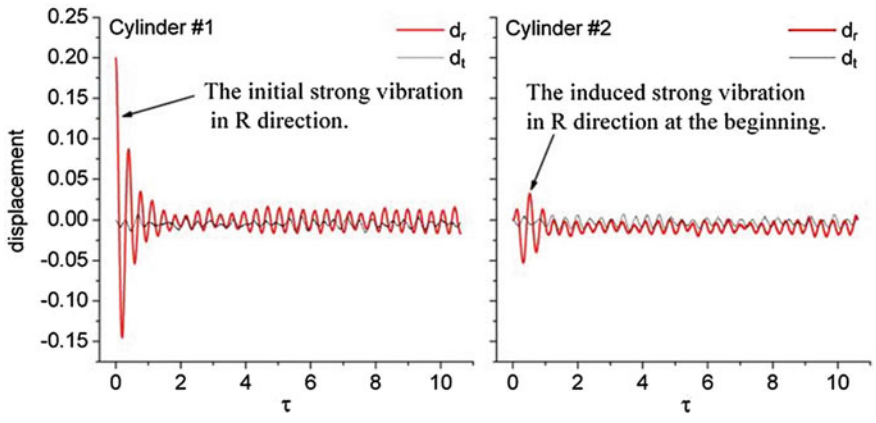


**Fig. 2** The displacements of cylinders #1 and #2 at their mid-spans for $\bar{U} = 4.4499$

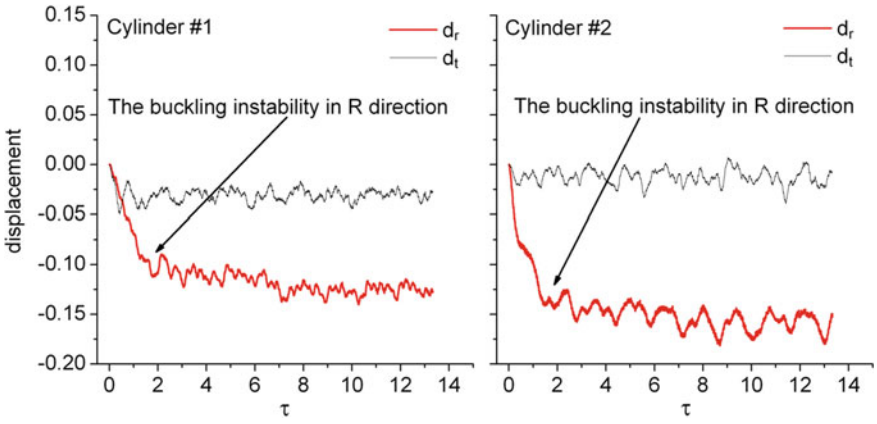


**Fig. 3** The displacements of cylinders #1 and #2 at their mid-spans for $\bar{U} = 6.0173$

If the dimensionless flow velocity is increased to 6.0173, the buckling instability is found, as shown in Fig. 3. To investigate the instability, all cylinders have no displacements in all directions at the beginning. It is very clear that the vibrations of both cylinders #1 and #2 are enhanced dramatically within a short time, e.g., the displacement of the mid-span of cylinder #1 in its $R$ direction is increased to about $0.14D$. The two cylinders seem buckled but with weak oscillations around the buckled shapes, respectively. In $T$ direction, there are only weak oscillations induced for the two cylinders, respectively. The amplitudes of the weak oscillations of the two cylinders in $R$ direction are comparable to those in $T$ direction and those of the final weak oscillations for $\bar{U} = 4.4499$. The cases for cylinders #3 and #4 are very similar to those for cylinders #1 and #2.

Thus, we could conclude that only weak vibration could be induced by the flow if the dimensionless flow velocity is small, however, the buckling instability may occur if the dimensionless flow velocity is large enough. This was also predicted by linear theoretical analysis and observed by experiment (Païdoussis 1979, 2004).

**Acknowledgments** Support given by the HKPolyU/AREVA collaboration fund under grant No. RPQ4 is gratefully acknowledged.

## References

ANSYS Inc (2009) ANSYS FLUENT 12.0 Documentation

Donea J, Huerta A, Ponthot JP, Rodríguez-Ferran A (2004) Arbitrary lagrangian-eulerian methods. In: Stein E et al (eds) Encyclopedia Comput Mech. Wiley, Barcelona

Gagnon JO, Païdoussis MP (1994a) Fluid coupling characteristics and vibration of cylinder clusters in axial flow, part 1: theory. J Fluid Struct 8:257–291

Gagnon JO, Païdoussis MP (1994b) Fluid coupling characteristics and vibration of cylinder clusters in axial flow, part 2: experiment. J Fluid Struct 8:293–324

Liu ZG, Liu Y, Lu J (2012) Fluid-structure interaction of single flexible cylinder in axial flow. Comput Fluids 56:143–151

Païdoussis MP (1979) The dynamics of clusters of flexible cylinders in axial flow: theory and experiments. J Sound Vib 65:391–417

Païdoussis MP (2004) Fluid-structure interactions: slender structures and axial flow, vol 2. Academic Press, Netherlands

Thomson WT (1965) Vibration theory and applications. Prentice-Hall, Englewood Cliffs

# Feedback Control of Flow-Induced Vibrations on Head Gimbals Assembly Inside Hard Disk Drives

**X. Y. Huang, H. Min and Q. D. Zhang**

**Abstract** High speed flows in working hard disk drives (HDDs) can induce off-track vibrations on a head gimbals assembly (HGA), which limit positioning accuracy of the slider magnetic head on the tip of the HGA for high magnetic storage density in disks. This paper presents experimental studies and numerical simulations on the flow-induced vibrations (FIV) of the HGA inside an HDD and active control of such vibrations. First, the HGA off-track vibration and the airflow pressure fluctuations around the HGA are measured to characterise the FIV of the HGA. Second, we propose an active control strategy for such FIV of the HGA, in which feedback acoustic pressures are employed to suppress pressure fluctuations in turbulence around the HGA. Numerical simulations have been carried out on this issue by introducing virtual sensors into the close regions around the HGA. Finally, by using the FIV on the HGA as feedback error signals through the laser Doppler vibrometer, the feedback control of FIV on the HGA has also been demonstrated.

**Keywords** Active control · Flow-induced vibration · Acoustic pressure · Hard disk drive · Head gimbals assembly

X. Y. Huang (✉) · H. Min
School of Mechanical and Aerospace Engineering, Nanyang Technological University, Nanyang, Avenue, Singapore
e-mail: mxhuang@ntu.edu.sg

Q. D. Zhang
Data Storage Institute, DSI Building, Singapore, Singapore

Y. Zhou et al. (eds.), *Fluid-Structure-Sound Interactions and Control*,
Lecture Notes in Mechanical Engineering, DOI: 10.1007/978-3-642-40371-2_58,

## 1 Introduction

Vibration of a head gimbals assembly (HGA) induced by high speed circumferential airflows in working hard disk drives (HDDs) limits the positioning accuracy of slider magnetic head on the HGA tip, and is therefore receiving much attention associated with the development of high magnetic storage density in disks, such as 10 Tb/in$^2$. Aerodynamic pressure fluctuation around the HGA plays an important role in the flow-induced vibration (FIV) on the HGA (Min et al. 2012a, b, c). Passive methods such as modification on the HDD inner structures have proved to be difficult for the fine control on this issue (Zhang et al. 2010). The previous work on active control of disk flutter inside working HDDs by Huang et al. (2004, 2005) suggested a possible active control strategy on the FIV of the HGA through suppressing unsteady airflows around the HGA by acoustic pressure disturbance. In this paper, the turbulence fluctuations and the FIV on the HGA are measured to show the correlations between them. Then, a possible active control architecture is proposed based on numerical simulations. Finally, an experiment is conducted to demonstrate the proposed active control strategy on the FIV of the HGA.

## 2 Measurement of FIV on HGA in HDDs

The setup for simultaneous measurements of pressure fluctuations and HGA-OTV inside a working 3.5 inch Seagate HDD is illustrated in Fig. 1. The HDD can operate at different rotation speeds driven by an HC6250B-PT motor driver. During the measurements, the HGA was fixed at middle track following position and a PCB 103B12 pressure transducer was used to measure the pressure fluctuation through a hole of diameter 3 mm drilled on the HDD cover right above the HGA. The HGA off-track (horizontal) vibrations were measured through a laser Doppler vibrometer (LDV) typed Polytec PSV300.

In the measurements, the HDD was working under three different rotation speeds and the corresponding results are presented in Fig. 2. It is shown that the pressure fluctuations inside the HDD are highly associated with the HGA off-track vibration in terms of principal peaks in the spectra, and the spectrum magnitudes of both the pressure fluctuation and the HGA off-track vibration increase with the HDD rotation speed. This reveals the correspondence of the turbulence fluctuations around the HGA to the FIV on the HGA, and suggests that an active control may be applied on the HGA vibrations by suppressing the turbulence fluctuations around the HGA.

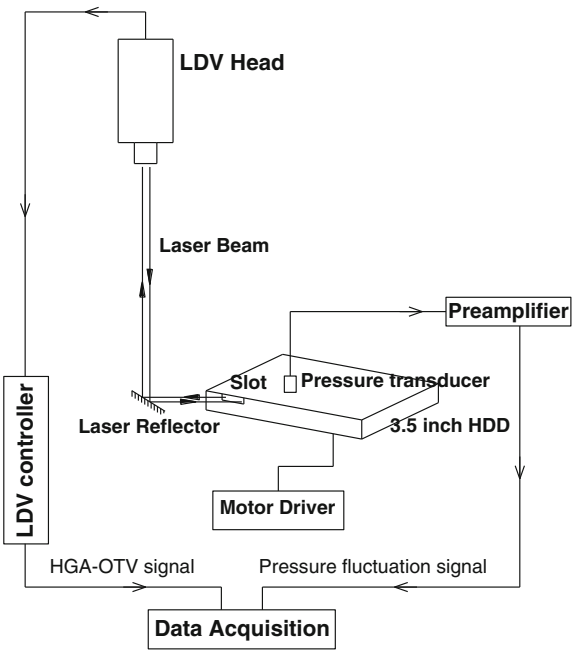


**Fig. 1** Setup of measurements on pressure fluctuations around an HGA and the HGA off-track vibration (HGA-OTV) in a 3.5 inch Seagate HDD

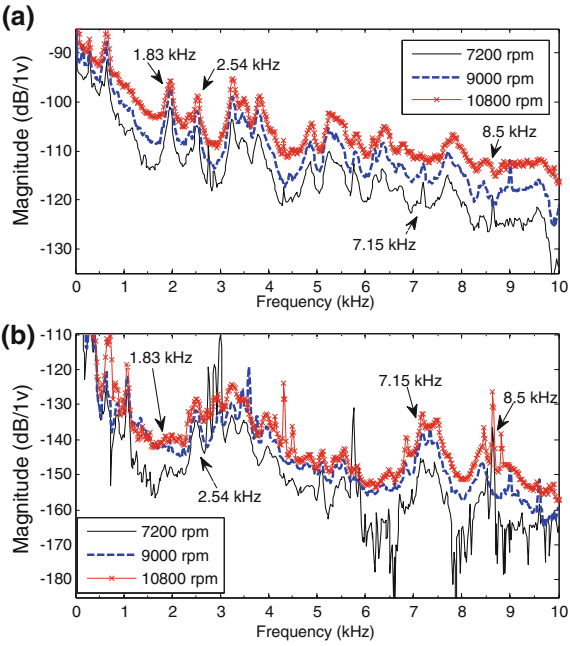


**Fig. 2** (Color online) Spectra of **a** pressure fluctuation around the HGA and **b** the HGA off-track vibration displacement at HDD different rotation speeds

## 3 Numerical Simulations on Active Control

Based on observations in measurements above, we proposed an active control strategy for the FIV on the HGA. In the active control strategy, a physical pressure sensor is assumed on the HDD cover to detect the pressure fluctuations for feedback error signals and a pressure actuator is on the inner surface of the HDD cover to actuate feedback acoustic pressures to suppress pressure fluctuations in airflow turbulence around the HGA. Two-dimensional numerical simulations were conducted to investigate the corresponding control effect. Turbulent model based on the large eddy simulation is applied through the commercial code of FLUENT. In prior to numerical and experimental investigations, it was found that the spatial coherence is low between the pressure fluctuations near the HDD cover and the FIV on the HGA (Min et al. 2012a, b, c). Those investigations also show that it is hard to achieve successful active control on the FIV of the HGA through a conventional feedback control system with feedback error signals directly from the physical pressure sensor on the HDD cover. In this work, a virtual sensing method (Elliott 2001) is employed to enable the system feedback signal changeable from the physical pressure sensor to specific "virtual pressure sensors" closely around the HGA. A feedback control architecture with pressure virtual sensing at a point right in the wake zone of the HGA, $CP_1$, was implemented as shown in Fig. 3. A pressure actuator chip with 10 mm width was assumed on the HDD cover inner surface in the upstream of the HGA, and a physical pressure sensor was assumed to pick up the pressure disturbance on the cover inner surface right above the wake zone of the HGA through a hole on the HDD cover. Given that a relationship function can be explicit through numerical evaluation between the spectra of pressure fluctuations at the physical and the virtual sensing position, the direct cancelation point for pressure fluctuations in the feedback control system can be moved from the physical sensing position onto the virtual sensing one (Elliott 2001).

The simulation results of pressure disturbance contour at frequency of 1480 Hz before and under control are presented in Figs. 4a and b. It is shown that successful suppression of pressure fluctuations is achieved in the wake zone and other close regions of the HGA with virtual sensing.

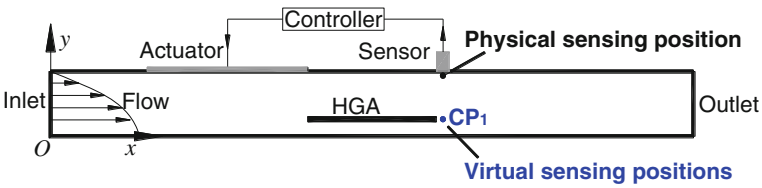


**Fig. 3** (Color online) Schematic architecture of the feedback active control loop with virtual sensing at $CP_1$ in the wake zone of the HGA

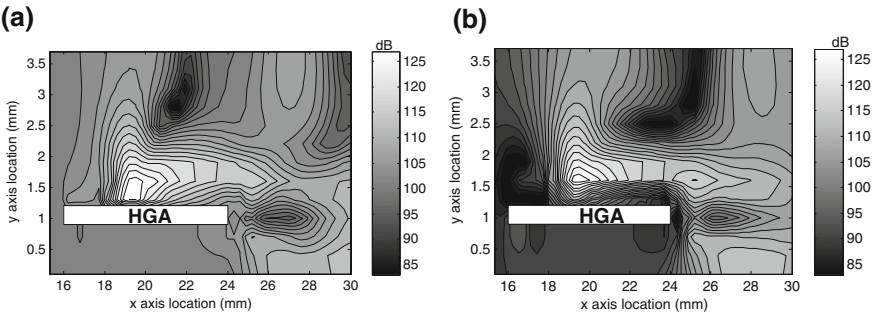


**Fig. 4** Contour of pressure disturbance around the HGA at the frequency of 1,480 Hz, **a** before control, **b** under feedback control with $CP_1$ (shown in Fig. 3) as the pressure fluctuation cancelation point

The drag coefficient of the HGA block was used to evaluate the HGA off-track vibration in simulations. The spectrum results of the drag coefficient of the HGA block before and under feedback control with virtual sensing at $CP_1$ are presented in Fig. 5. It is shown that most of the peaks in spectrum of the HGA off-track vibration become well suppressed with this feedback control system, especially for the maximum peaks around frequencies of 1,480 and 2,940 Hz. These results indicate that the feedback control system with the virtual sensing of pressure disturbance at the wake zone of the HGA can provide good suppression on the flow fluctuations around the HGA and then enable the successful control on the HGA off-track vibration.

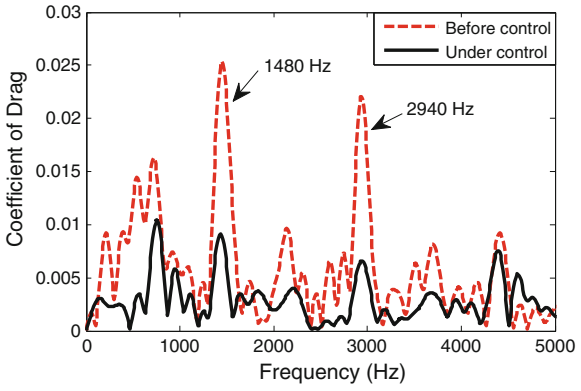


**Fig. 5** (Color online) Spectrum results of the drag coefficient of the HGA block before and under the feedback control with pressure virtual sensing

## 4 Experimental Demonstration

An experimental demonstration has been conducted to further validate the proposed active control solution of the FIV on the HGA. Figure 6 is a schematic diagram on the experimental setup. The feedback control close-loop consisted of a LDV, a narrowband frequency filter, a signal conditioner, an in-house made phase shifter, and a piezoelectric (PZT) disk mounted on the inner surface of the HDD cover. The HGA off-plate (vertical) vibrations detected by the LDV were used as feedback error signals, and the signals were then phase shifted and amplified to drive the PZT disk to generate feedback acoustic pressure around the HGA. The phase shift and gain of the feedback loop were adjusted such that the HGA off-plate vibrations were reduced.

By setting the center frequency of the narrow band filter, experiments have been conducted by focusing the active control separately on several principal peaks in the HGA off-plate vibration spectrum. In this paper, only the results from control focused on the principal peak around 1,256 Hz in the HGA vibration spectrum are presented in Fig. 7 for succinctness. It is shown that positive suppression up to

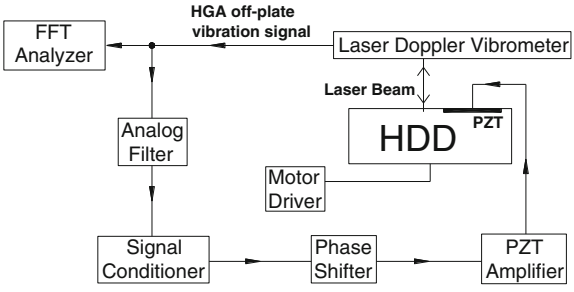


**Fig. 6** Schematic diagram of the experimental setup

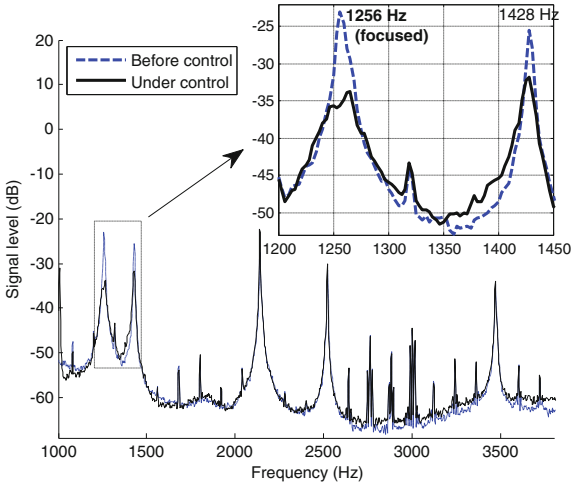


**Fig. 7** (Color online) Spectra of the HGA off-plate vibration before and under active control focused on the principal peak around 1,256 Hz

13 dB has been achieved at the principal peak around 1,256 Hz. The results demonstrate the physical validity of the active control strategy on the FIV of the HGA by acoustic pressures.

## 5 Conclusion

Experimental and numerical studies were conducted on active control of the FIV on the HGA in working HDDs through suppressing turbulence fluctuations around the HGA. The correspondence was found between the pressure fluctuations around the HGA and the FIV on the HGA. Numerical results show that the FIV on the HGA can be successfully controlled when the airflow pressure fluctuations in close regions around the HGA can be actively suppressed, which has been further demonstrated in experiments by using an analog feedback loop.

**Acknowledgments** This project (No. 092-156-0128) is funded by A*STAR of Singapore.

## References

Elliott SJ (2001) Signal processing for active control. Academic Press, London

Huang XY, Wang X, Yap FF (2004) Feedback control of rotating disk flutter in an enclosure. J Fluids Struct 19:917–932

Huang XY, Hoque ME, Wang X (2005) An experimental study on feedback control of rotating disk flutter. J Fluids Struct 20:71–80

Min H, Huang X, Zhang Q (2012a) Aerodynamic pressure fluctuations associated with flow-induced vibration of the head gimbals assembly inside a hard disk drive. IEEE Trans Magn 48:101–106

Min H, Huang X, Zhang Q (2012b) Active control of flow-induced vibrations on slider in hard disk drives by suppressing pressure fluctuations with virtual sensing. IEEE Trans Magn (to be published)

Min H, Huang X, Zhang Q (2012c) Active control of flow-induced vibrations on slider in hard disk drives: experimental demonstration. IEEE Trans Magn, under review

Zhang QD, Tan CS, Sundaravadivelu K et al (2010) Mitigation of flow induced vibration of head gimbals assembly. Microsyst Technol 16:213–219

# Towards the Numerical Modelling of Floating Offshore Renewables

**A. Viré, J. Xiang, M. D. Piggott, C. J. Cotter, J-P. Latham and C. C. Pain**

**Abstract** Two finite element models are coupled, with the aim of computing the mutual interactions between fluids and floating solids. The fluid and solid domains are discretised differently in space and time, and at every time step, the solid mesh is mapped onto the fluid mesh. The effect of the solid on the fluid dynamics, and vice versa, is modelled through a volumetric penalty force added to the momentum balances of the fluids and solids. A novel algorithm ensures that the action-reaction principle is satisfied at the discrete level. The coupled models are used to simulate uniform flow past a wind turbine, which is represented as a fixed actuator disc. Preliminary results on a floating pile also demonstrate the applicability of the models to fully coupled simulation of a floating spar. This work is a first-step towards the fully coupled modelling of floating wind turbines.

**Keywords** Fluid-structure interactions · Immersed-body approach · Finite element method · Actuator disc · Floating pile · Floating wind turbines

## 1 Introduction

The numerical modelling of fluid–structure interactions is important in the context of offshore renewables. This work targets floating wind turbines, where the turbine is supported by a floating pile moored to the seabed. Such devices are attractive in

A. Viré (✉) · J. Xiang · M. D. Piggott · J-P. Latham · C. C. Pain
Department of Earth Science and Engineering, Imperial College London, SW7 2AZ London, UK
e-mail: avire@imperial.ac.uk

M. D. Piggott
Grantham Institute for Climate Change, Imperial College London, SW7 2AZ London, UK

C. J. Cotter
Department of Aeronautics, Imperial College London, SW7 2AZ London, UK

Y. Zhou et al. (eds.), *Fluid-Structure-Sound Interactions and Control*,
Lecture Notes in Mechanical Engineering, DOI: 10.1007/978-3-642-40371-2_59,

deep seas (typically deeper than 50 m), where bottom-mounted foundations are too expensive. The numerical modelling of floating wind turbines is very challenging because of the dynamic interaction between the moving air–water and fluid–solid interfaces, and the presence of both rigid (i.e. the wind turbine) and deformable (i.e. the moorings) solids. Computer models are, however, attractive in studying such coupled fluid–solid problems, because they can analyse different configurations while limiting expensive laboratory or onsite testing. In this work, two finite element models are coupled in order to represent the mutual interactions between fluids and floating solids. The use of separate models, based on different spatial and temporal discretisations, allows for the mesh resolution to be tailored to the specific needs of the fluids and solids, respectively.

## 2 Numerical Models

Consider a solid $V_s$ immersed in a fluid domain $V_f$. In this work, the interactions between fluids and solids are modelled by filling the regions covered by solids with the surrounding fluid and relaxing the flow to the behaviour of the solids in those regions. The Navier–Stokes equations describing the fluid dynamics are thus modified in two ways. First, they are expressed in terms of monolithic fields, which are defined over the extended domain $V = V_f \cup V_s$. In particular, the monolithic velocity field is given by $u = \alpha_f u_f + \alpha_s u_s$, where $\alpha_f = V_f/V$ and $\alpha_s = V_s/V$ are the volume fractions of the fluid and solid, respectively. Second, the monolithic velocity is relaxed to the solid velocity in $V_s$. This is achieved by adding a volumetric penalty force to the right-hand side of the momentum balance. Considering incompressible fluids, the fluid-dynamics equations are given by:

$$\nabla \cdot u = 0, \tag{1}$$

and

$$\rho_f \frac{\partial u}{\partial t} + \rho_f (u \cdot \nabla) u - \nabla p + \nabla \cdot \left( 2\mu \overline{\overline{S}}^* \right) + F_f + B, \tag{2}$$

where $p$ is the pressure field, $\mu$ is the dynamic viscosity of the fluid, $\overline{\overline{S}}^*$ is the deviatoric part of the strain-rate tensor $S_{ij} = \partial_j u_i + \partial_i u_j$, $B$ represents external body forces (e.g. buoyancy), and $F_f$ is the penalty force. The latter is non-zero close to the fluid–solid interface only, and is expressed as

$$F_f = \beta \alpha_f \alpha_s \left( u_s - u_f \right) = \beta (\widehat{u}_s - \alpha_s u). \tag{3}$$

where $\widehat{u}_s = \alpha_s u_s, \beta = \rho_f / \Delta t$ is a factor which dictates how fast the fluid and solid velocities relax to one another at the interface, and $\Delta t$ is the time step. The magnitude of the relaxation factor is driven solely by inertial effects. The extension to viscous effects is the subject of further work.

Equations 1–2 are solved using the open-source model 'Fluidity-ICOM' (Pain et al. 2001). This fluid/ocean dynamics model uses unstructured finite elements and has the capability of adapting the mesh dynamically in time. The fluid mesh is therefore modified, either to track accurately the fluid–solid interfaces when a solid moves, or to refine the resolution around specific flow features which develop in the wake of a fixed solid.

The finite-element model 'Y3D' (Xiang et al. 2009) solves the solid-dynamics equations on a separate solid mesh, which covers the regions *Vs*. The solid-dynamics equations are expressed as

$$\mathcal{L}d_s + F_{\text{int}} = F_{\text{ext}} + F_c + F_s, \tag{4}$$

where $d_s$ denotes the solid displacement, $\mathcal{L}$ is an operator dependent on the velocity gradient, $F_{\text{int}}$ stands for the internal forces, $F_c$ is the contact force when multiple solids impact on each other, and $F_{\text{ext}}$ is the external force including the surface traction force and all the body forces other than the action–reaction force exerted by the fluid. A novel algorithm was implemented in order to ensure that the action–reaction principle is satisfied at a discrete level, when coupling 'Fluidity-ICOM' and 'Y3D'(Viré et al. 2012). The models are applied to two different cases, which are relevant for the modelling of floating wind turbines: (1) a fixed wind turbine modelled as a thin actuator-disc, and (2) a pile floating at the interface between air and water.

## 3 Results

### *3.1 Uniform Flow Past a Fixed Actuator Disc*

Wind turbines can be parameterised by thin discs, which exert a constant thrust force on the flow. The force is derived from actuator disc theory (Conway 1995), which assumes that the flow is homogeneous, incompressible, steady, frictionless and that no external force acts on the fluid upstream or downstream of the rotor. This formalism is used to model a fixed wind turbine subjected to a uniform flow. As described in the previous section, two meshes are used: the fluid mesh covers the whole computational domain, while the solid mesh only discretises the disc. Because the disc is fixed, the solid model does not solve the solid-dynamics equations. A solid-concentration field is defined on the fluid mesh, in order to identify the region occupied by the disc. This field is obtained by projecting a unitary field from the solid to fluid mesh. A thrust force acting on the fluid is spread uniformly across the disc, and is given by:

$$T = \frac{1}{2}\rho C_T A_d u_0^2, \tag{5}$$

where $\rho$ is the fluid density, $C_T$ is the thrust coefficient of the wind turbine, $A_d$ is the frontal area of the disc, and $u_0$ is the far-upstream velocity. The size of the computational domain is $25D \times 10D \times 10D$, where $D$ is the disc diameter. The disc centre is placed at a distance $5D$ from the domain inlet and sides. The disc normal is aligned with the flow. The Reynolds number is set to $Re_D = u_0 D/\nu = 10^3$, where $\nu$ is the kinematic viscosity of the fluid. Three values of the thrust coefficients are considered ($C_T = 0.2$; 0.45; 0.7). The fluid mesh adapts every $T = 1$ s, in order to refine the regions of high curvatures in the velocity and pressure fields. The total number of mesh nodes at steady state is of the order of $10^6$. The time step is such that the Courant number is fixed at 0.3. The streamwise evolution of the streamwise velocity at the disc centreline is shown in Fig. 1 where the numerical results are indicated by dashed lines and the continuous lines represent the semi-analytical solution (Conway 1995). The velocity deficit induced by the disc is well predicted by the present algorithm. The discrepancy between numerical and theoretical results in the far-wake is explained by the role of the fluid viscosity in the numerical simulation. No wake recovery is observed in the theoretical results, which are derived in the inviscid approximation. The effect of the resolution on the numerical results is under further investigation.

## 4 Dynamics of a Floating Pile

The dynamic response of a pile is analysed when placed at the interface between air ($\rho_1 = 1.2\,\mathrm{kg \cdot m^{-3}}, \mu_1 = 18.27\mu\mathrm{Pa \cdot s}$) and water ($\rho_2 = 1000\,\mathrm{kg \cdot m^{-3}}, \mu_2 = 1.002\,m\mathrm{Pa \cdot s}$). The pile density is uniform and equals half the water density. It is centred in a box of edge length $20D$, where $D$ is the pile diameter and $4D$ is its length. Initially, the fluids are at rest and the pile lies vertically across the fluid interface (Fig. 2 left). As time evolves, the pile moves in heave before falling into water. The pile eventually reaches an equilibrium position, that is horizontal and half submerged in water, in accordance with Archimedes' principle.

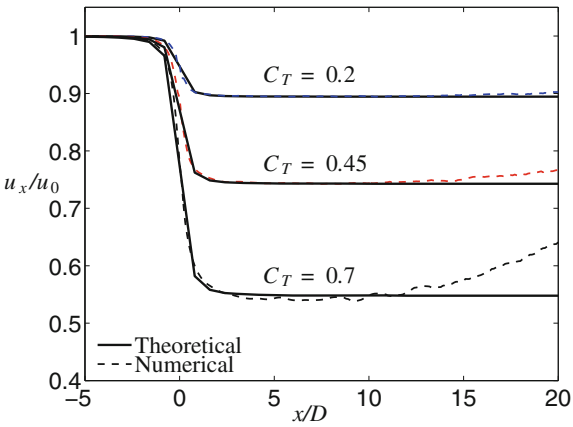


**Fig. 1** Streamwise evolution of the streamwise velocity (non-dimensionalised by the far-upstream velocity) for an actuator disc of diameter $D$, centred at $x = 0$, and three values of thrust coefficient $C_T$. The lines represent the semi-analytical solution (Conway 1995), while the dashed lines show the numerical results


**Fig. 2** Snapshots of the dynamics of a floating pile, at three different instants in time, when placed at the interface between air and water

## 5 Conclusions

This work presents a novel algorithm to couple two finite element models and demonstrates their ability to simulate: (1) the flow past a fixed wind turbine represented as an actuator disc, and (2) the dynamics of a cylindrical pile floating at the interface between air and water. Results in both cases are shown to be in good agreement with theoretical predictions, and the effect of different parameters will be the subject of further work. This study is a first step towards the fully coupled numerical simulation of floating solids, applicable to the next generation of offshore renewables.

**Acknowledgments** This work is supported by the European Union Seventh Framework Programme (FP7/2007-2013) under a Marie-Curie Intra-European Fellowship (grant agreement PIEF-GA-2010-272437). The authors also wish to acknowledge support from EPSRC, NERC, the Grantham Institute for Climate Change and the High Performance Computing Service at Imperial College London. The content of this paper reflects only the authors′ views and not those of the European Commission.

## References

Conway J (1995) Analytical solutions for the actuator disk with variable radial distribution of load. J Fluid Mech 297:327–355

Pain C, Umpleby A, de Oliveira C, Goddard A (2001) Tetrahedral mesh optimisation and adaptivity for steady-state and transient finite element calculations. Comput Methods Appl Mech Engrg 190:3771–3796

Viré A, Xiang J, Milthaler F, Farrell P, Piggott M, Latham JP, Pavlidis D, Pain C (2012) Modelling of fluid-solid interactions using an adaptive-mesh fluid model coupled with a combined finite-discrete element model. Ocean Dyn 62:1487–1501

Xiang J, Munjiza A, Latham JP (2009) Modelling of fluid-solid interactions using an adaptive-mesh fluid model coupled with a combined finite-discrete element model. Int J Numer Meth Engng 79:946–978